THE UNIVERSITY OF CHICAGO

TRANSLATING DOUBLY-THREADED [3]ROTAXANES INTO ADVANCED MATERIALS

A DISSERTATION SUBMITTED TO

THE FACULTY OF THE PRITZKER SCHOOL OF MOLECULAR ENGINEERING

IN CANDIDACY FOR THE DEGREE OF

DOCTOR OF PHILOSOPHY

BY

LAURA FRANCES HART

CHICAGO, ILLINOIS

JUNE 2023

“Chemists are dreamers. We think up new molecules and bring them to life.”

– Carolyn Bertozzi, 2022 Nobel Laureate in Chemistry

TABLE OF CONTENTS

LIST OF FIGURES

LIST OF TABLES

LIST OF EQUATIONS

ACKNOWLEDGEMENTS

Professor Stuart Rowan's passion for polymer chemistry has been a constant source of inspiration and motivation for me. Stuart, I cannot thank you enough for giving me the opportunity to work in your lab, which has allowed me to achieve my dream of becoming a synthetic chemist. Thank you for pushing me to be a better scientist and for never giving up on me.

I left New England and moved to Cleveland for two reasons: (1) I could not get the prospect of synthesizing rotaxanes and slide-ring gels out of my head, and (2) the graduate students I met during recruitment at the CWRU Macro Department. I would not be writing this without the unwavering support and friendship of my fellow polymer nerds: Dr. Jesse Gadley, Dr. Sidney Carson, Brandy Troxell, Mark Holland, Dr. Chase Thompson, and Dr. Melanie Hutnick.

My sincerest gratitude goes to the members of Rowan Group, past and present. I am indebted to my first mentor and hero in the lab, Dr. Qiong Wu, who taught me how to synthesize macrocycles, run fancy columns, and grow beautiful crystals. A special thank you to Dr. Katie Herbert and Dr. Elvis Cudjoe for being the best office mates and role models I could have ever asked for in my first year of graduate school. I would never have survived this wild rotaxane ride without Dr. Jerry Hertzog (rotaxanebro), a brilliant chemist and the kindest lab mate, mentor, and friend. Thank you to the rest of Team Interlocked for being a constant source of moral support and chemistry knowledge: Dr. Marissa Tranquilli, Dr. Benjamin Rawe, Dr. Phil Rauscher, Guancen (Mike) Liu, and Dr. Jongwon Oh. I have had the privilege of mentoring undergraduate Wilson Turner and watching him grow into a skilled (and clean!) synthetic chemist. Thanks to Dr. Forrest Etheridge and Dr. Debbie Schneiderman for teaching me valuable lab hacks and making long days in the lab fun. Shout-out to the Dynamic Crew for letting me crash subgroup to absorb all of your materials knowledge. Thank you, Dr. Neil Dolinski, for fostering such a great group culture over

these past few years. Charlie, thank you for always being there to help me fix or jerry-rig things in the lab, celebrate the small wins, and provide incredible emotional and mental support. I was fortunate to work with Dr. Joseph Dennis (GI Joe), who has become one of my favorite mentors. Thank you for answering my silly questions in the lab, helping me write my first paper, and giving me the confidence I needed to score my first job in industry. The Rowan Group has become my second family, and I want to thank each and every single one of you for making me feel like I belong. Cheers to the Friday beers crew; thank you for making me laugh and providing a safe space for me to vent about life and celebrate my good days.

This work would not have been possible without the incredible staff and facilities across the University of Chicago and PME. Shout-out to Paul Julson, Marco Calderon, Maurice Perry, and Matt Williams for keeping the lab up and running. I would like to recognize Rovana Popoff, Amanda Dennis, David Taylor, Hayley Huffman, and Novia Pagone for being so welcoming and supportive during my time in the PME. I am grateful to Dr. Jin Qin from the Mass Spec Facility, Dr. Sarah Brown from the Chicago Materials Research Center, and Dr. Josh Kurutz from the NMR Facility for maintaining friendly, clean, and safe work environments. A very special thank you to Dr. Philip Griffin from the Soft Matter Characterization Facility for his vast instrumentation knowledge and incredible patience. I also need to thank Tracy Walker for handling random chemical orders, booking conference rooms, and providing constant support for the entire Rowan Group.

I would not be here without my ladies downtown, who were there for me on my happiest and darkest days, and who I know will continue cheering me on as I enter the next phase of my life. I will never be able to thank Christine enough for keeping me motivated, teaching me how to access the logical side of my brain, and giving me the strength I needed to finish this dissertation.

And thank you, David Archuleta, for being the shining star that always guides me back to the light when the darkness closes in and carries me away.

My heart is overflowing with love and appreciation for my family. Thank you, Mom and Dad, for always believing in me and letting me chase my wildest dreams. I don't know where I would be without your continued support and unconditional love, and I owe you the world. Thank you to my compassionate big brother Nick, my gorgeous sister-in-law Meggin, and my two adorable little nephews, Nolan and Keegan, for being there to make me smile and remind me what is most important in life. I owe much of my sanity to my dog Nutmeg, an incredible source of unconditional love and warm cuddles who now lives in a special place in my heart. While writing this dissertation, Thoreau (Roni!), the current furry friend in my life, enjoyed boop-ing my elbow with his nose every 5 minutes. Thank you for being there!

My world changed when the stars aligned in Cleveland and brought Dr. William Lenart into my life, the most passionate, kind, and intelligent person I have ever known. Not only did I gain an excellent tutor for Polymer Physical Chemistry, but I found my very best friend in life. Bill, I love you with all my heart and cannot wait to share my vows with you at our wedding.

Dearest Auntie and Grandpa – I did it!

ABSTRACT

Crosslinking in polymer networks leads to intrinsic structural inhomogeneities that result in brittle materials. Replacing fixed covalent crosslinks with mobile ones results in mechanically interlocked polymers (MIPs) such as slide-ring networks (SRNs), where polymer chains threaded through rings form interlocked crosslinks that act as frequency-dependent pulleys to relax internal stresses, leading to tougher, more robust materials. SRNs are typically made by crosslinking rings on different polyrotaxanes, interlocked architectures comprised of a polymer chain threaded with rings and capped with stoppers to prevent dethreading, to form figure-of-eight crosslinks and an uncontrolled amount of singly-threaded (uncrosslinked) rings. MIP networks containing doubly-threaded rings are less explored because of the difficulty of synthesizing rings big enough to thread two polymer chains and the challenges in preventing slippage of the larger rings. This work explores different click chemistries to develop a new way to access doubly-threaded SRNs from a simple mixture of tetra-functional pseudo[3]rotaxane (P3R) crosslinker, difunctional monomer, and large stoppers to keep rings in the network. Ditopic rings comprised of two 2,6-bis(N-alkyl-benzimidazolyl)pyridine (BIP) ligands were threaded with two BIP threads using metal-templating to access the doubly-threaded P3R complex. SRNs were synthesized by incorporating the P3R crosslinker into a catalyst-free nitrile-oxide/alkyne click polymerization of PEG-based networks with varying amounts of interlocked crosslinks, where covalent crosslinks act as stoppers to prevent slippage of the rings. Studies on their mechanical properties show that metal ions fix the rings in the network, leading to similar behavior as the covalent PEG gels. Removal of the metal ion frees the rings resulting in a high-frequency transition attributed to the additional relaxation of polymer chains through the doubly-threaded rings at longer timescales. After remetallation, this transition disappears, and SRNs show similar trends as the original metallated network, proving

ring sliding can be turned off in the network by adding metal ions. The synthetic design of these doubly-threaded MIPs allows for systematic control over the number and type of rings, and other components and polymers, that can be added to the click polymerization. The versatility of the macrocycle synthesis used in this work provides a basis for controlling the rings' size, conformation, and valency to tune MIP material properties. To this end, monotopic rings were synthesized to assemble pseudo[2]rotaxanes that polymerize under catalyst-free conditions. The resulting pseudopolyrotaxanes can be incorporated into the network synthesis to form doubly-threaded SRNs embedded with singly-threaded rings. This straightforward, catalyst-free click approach is a promising platform for understanding the complex structure-property relationships in doubly-threaded MIPs.

1 Introduction: Material Properties and Applications of Mechanically Interlocked Polymers

[1] This chapter was adapted from: Hart, L. F.; Hertzog, J. E.; Rauscher, P. M.; Rawe, B. W.; Tranquilli, M. M.; Rowan, S. J. Material Properties and Applications of Mechanically Interlocked Polymers. *Nature Reviews Materials.* **2021**, *6* (6), 508–530.

1.1 Introduction

A key feature that controls the properties of a polymeric material is its architecture. Beyond the conventional linear polymer, architectures such as branched, cyclic, bottlebrush, star, and block co-polymers have expanded the property profile of polymeric materials and offered opportunities for polymer research and applications. Recently, the polymer field has seen the emergence of a new class of polymer architecture: mechanically interlocked polymers (MIPs), which are polymers that include a mechanical bond. MIPs present an attractive frontier in polymer science, as the presence of the mechanical bond allows for unprecedented degrees of motion within the polymer architecture. Conceptually, there are many ways the mechanical bond can be incorporated into polymer architectures (Figure 1.1), and these unique and varied structures can enable property profiles that have never been seen before.

The most common MIP is based on the rotaxane architecture: a ring (macrocycle) threaded onto a dumbbell-like component (Figure 1.1a) where the ring can slide back and forth along the dumbbell component but is prevented from dethreading by the presence of bulky stoppers. A polymeric analogy to this would be the main-chain polyrotaxane (Figure 1.1b), in which the ring(s) are trapped on the polymer backbone and can undergo a similar sliding motion over a much longer distance. Thus, by expanding or limiting the range of the rings' sliding motion (for example, by controlling the length of the polymer backbone or the number of rings on it), the properties of the

polyrotaxane can be tuned. Another important class of MIPs is slide-ring materials (SRMs), which are polymer networks where the crosslink itself is a rotaxane moiety. The term slide-ring gels, SRGs, is also commonly used to describe these materials, particularly if the network is swollen with a solvent. The most common of these systems contain figure-of-eight crosslinks (Figure 1.1c), and the resulting MIP networks have mobile junctions that can slide freely along the polymer

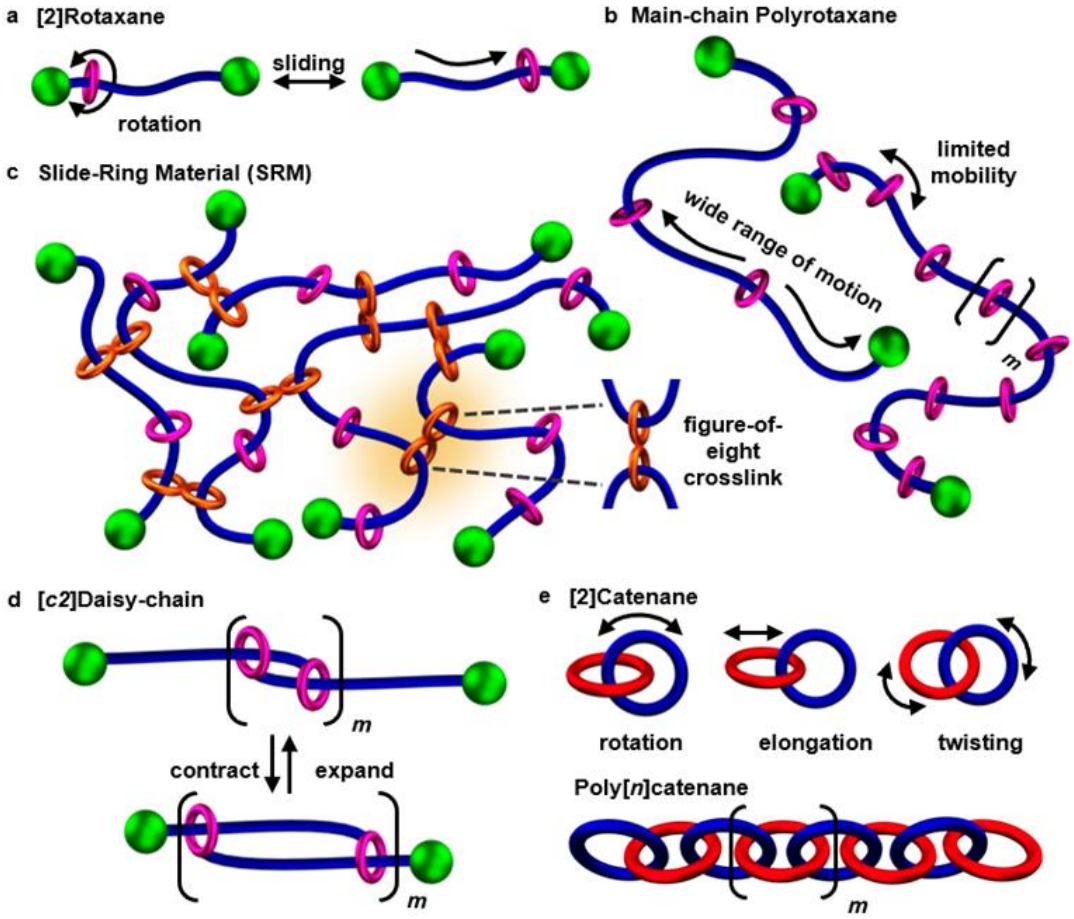

Figure 1.1. Mechanically interlocked molecules and polymers. a) Schematic of a [2]rotaxane, demonstrating the translational motion of a free ring along the dumbbell component. b) In a main-chain polyrotaxane, the m rings can exhibit translational motions similar to their small molecule counterparts but potentially over longer distances, depending on, for example, the number of rings. c) Interchain crosslinking of a main-chain polyrotaxane through the rings yields a slide-ring material with mobile figure-of-eight crosslinks (orange). d) The expansion and contraction motions of a polymeric [*c2*]daisy chain. e) A [2]catenane is capable of rotation, elongation, and twisting motions that can be expanded to n times in a poly[*n*]catenane, a polymer consisting only of n interlocked rings.

backbone. The final class of polyrotaxanes is the "daisy-chain" architectures, which feature interlocked monomeric units composed of two of the key polyrotaxane elements (the ring and thread) covalently bound together; the simplest form of this structure is the dimeric cyclic [*c2*]daisy chain (Figure 1.1d).

The other main class of MIPs is mechanically interlocked rings, or catenanes (such as a [2]catenane, Figure 1.1e). This chain-link structure can be incorporated into a polymer in many ways: as monomeric subunits (poly[2]catenane), pendant moieties, or even composing the entirety of the polymer (polymeric [2]catenane, Olympic gel, poly[*n*]catenane (Figure 1.1e)). Mechanically bonded rings do not allow for the long-range translational motion present in the polyrotaxanes; however, the components of a catenane possess several unusual degrees of freedom, such as elongation, twisting, and rotating motions (Figure 1.1e).

Although MIP synthesis remains a challenge, developments have been made over the years that have allowed access to a range of MIPs[2–7] and other classes of interlocked polymers, such as pseudopolyrotaxanes or knot-based materials,[6,8] that will not be discussed herein.

1.2 Rotaxanes

A mechanical bond occurs when two (or more) molecular components are constrained in space without being covalently bonded together and cannot disassemble unless there is enough energy to break covalent bonds (Figure 1.1). The mechanical linkage within these interlocked molecules gives rise to unusually high mobility and degrees of freedom while maintaining a permanent spatial association between the components.[9–12] Perhaps the most versatile of these molecules is the rotaxane: a ring (macrocycle) threaded onto a dumbbell-like component, where the ring can slide back and forth along the linear molecule but is prevented from dethreading by

the presence of bulky stoppers (Figure 1.1a). These pulley-like architectures can be incorporated into polymeric systems as part of a polymer backbone or side-chain (polyrotaxanes) or as movable crosslinks in polymer networks (slide-ring gels).

1.2.1 Early Synthesis of Rotaxanes

In 1967, the first reported rotaxane was synthesized through a multi-step reaction process. A solution of stopper and thread was passed over a resin coated in carbon-based macrocycles 70 times, ultimately forming the desired product in a 6% yield.[13] Although statistical methods were able to show that interlocked molecules are experimentally feasible, such methodologies led to poor yields and inhibited the progression of rotaxane chemistry. Since the 1960s, chemists have moved on from statistical methods to take advantage of self-assembly and molecular recognition techniques. Supramolecular interactions have been investigated to facilitate the assembly and threading of various organic fragments into interlocked architectures, such as hydrogen bonding, donor-acceptor, π-π stacking, and metal-ligand coordination, to name a few.[14–17]

In 1983, Jean-Pierre Sauvage published the first successful synthesis of a [2]catenane (composed of two interlocking rings) using transition metal templating, revolutionizing access to mechanically interlocked molecules.[16] To use as a metal template, Sauvage incorporated a ligand molecule into the architecture of his macrocycle, allowing another ligand to assemble into a stabilized tetrahedron geometry with the ring around a copper(I) species. Intra-ligand cyclization of this pseudo[2]rotaxane, rotaxane lacking stoppers, results in a ring-closed [2]catenane species, which can undergo free ring rotation post-demetallation.[16,18,19] End-capping the thread with bulky stopper groups converts the pseudo[2]rotaxane into the corresponding interlocked rotaxane species.[20] In 2017, a new methodology was developed in which the rotaxane was synthesized through the aminolysis of a phenolic pseudo-crown ether and a bulky stopper unit. This highly

selective synthesis yielded the corresponding rotaxane quantitatively ca. 100%.[17] In this way, metal-ligand templating synthesis changed how chemists viewed interlocked molecules and inspired them to develop new synthetic routes. Rotaxanes can now be accessed in 100% yield, a remarkable improvement from the original 6%.[21,17,15]

1.2.2 Accessing Multiply-Threaded Rotaxanes

Increasing the number of interlocked components in the rotaxane molecule is also possible, wherein several rings encircle the same thread, or two (or more) dumbbell molecules share the same ring cavity. Recent advances in synthesizing higher-order rotaxanes have inspired chemists to synthesize a library of unique rotaxane architectures (Figure 1.2a).[22] Additional rings can be added to a rotaxane in myriad ways, by introducing additional recognition sites and/or lengthening the thread component or building a molecular pump.[23,24] In this way, precise [n]rotaxane oligomers have been prepared, and threading rings onto a polymeric backbone gives rise to main-chain polyrotaxanes, which will be discussed in more detail later.

Multiply-threaded [n]rotaxanes are synthetically more challenging. The formation of the desired mechanical bond competes with the destabilization of the multicomponent system due to steric overcrowding.[25] The size of each rotaxane component is also crucial for isolating interlocked products. The macrocycle must be big enough to fit the desired number of threads through its cavity, and the stoppers sufficiently bulky to prevent ring slippage. Passive template approaches for assembling multiply-threaded rotaxanes that have been developed include “clipping” an acyclic ligand around the template site of dumbbell components and the covalent capture of a pseudo[3]rotaxane through a “stoppering” reaction. Furthermore, multivalent interactions between DNA strands have been shown to form doubly-threaded [3]rotaxanes by hybridizing a DNA ring with two DNA dumbbells.[26,27]

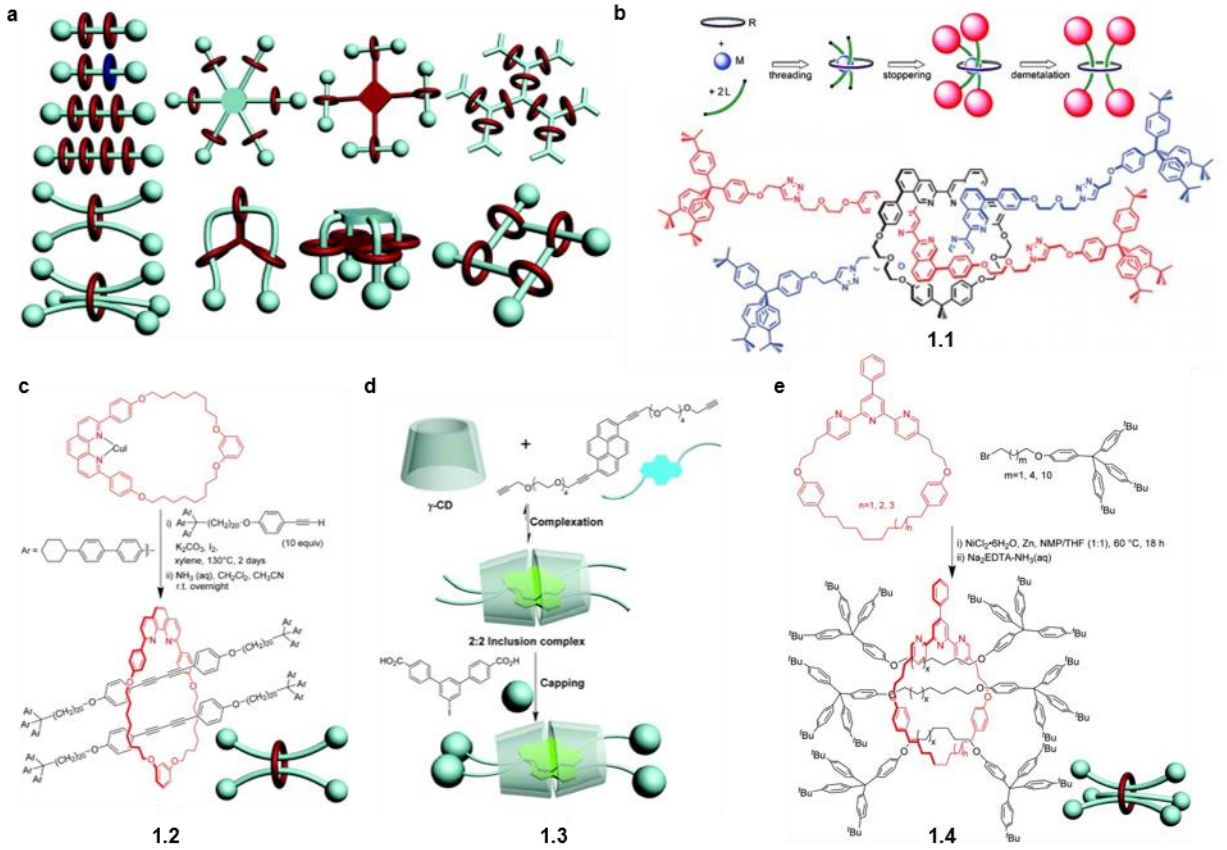

Figure 1.2. Multiply-threaded rotaxanes. a) Various higher-order rotaxane architectures containing more than one ring and/or axle. b) Iron(II)-templated synthesis of [3]rotaxanes by passing two threads through the same (41-atom) ring to form an octahedral metal center that can be stoppered using Cu-catalyzed azide-alkyne Huisgen cycloaddition (CuAAC) and demetallated to afford the [3]rotaxane **1.1** ($t_{1/2}$ ~200 hours at 298K). c) Active template Glaser coupling of [3]rotaxane **1.2** formed via second oxidative coupling of diyne half-dumbbells mediated by the pseudo[2]rotaxane-Cu complex. d) Doubly alkynyl pyrene-threaded [4]rotaxane **1.3** showing yellow-green emission. e) Leigh's active metal-template forms triply-threaded [4]rotaxanes **1.4** using a 37- or 38-atom ring. Adapted from Ref. 22 with permission from Royal Society of Chemistry, Ref. 28 with permission from American Chemical Society.

Doubly-threaded [3]rotaxanes have been previously synthesized by metal-template-driven methods by Sauvage, utilizing a single octahedral coordination complex between two threads and a monovalent ring (Figure 1.2b).[28] A bidentate ligand in the macrocycle and each thread component gather around a transition metal ion to form a pseudo[3]rotaxane. This complex is stoppered via Cu-catalyzed azide-alkyne Huisgen cycloaddition (CuAAC) and demetallated in the presence of a base to afford the doubly-threaded interlocked product **1.1**. Saito et al. used an active

template Glaser coupling method to make [3]rotaxanes **1.2** from the oxidative dimerization of an alkyne-terminated half-dumbbell mediated by the ring-Cu complex (Figure 1.2c).[29] A combination of active and passive metal template methods was also used to prepare [3]rotaxanes from the reaction of [2]rotaxanes (synthesized via copper-mediated oxidative coupling of alkyne) with metal and another ligand, which was stoppered and demetallated to afford a [3]rotaxane containing two different dumbbells.[30,31]

The large hydrophobic cavity of γ-CD was used to access doubly-threaded [4]rotaxanes by stoppering 2:2 inclusion complexes formed from a Sonogashira reaction between γ-CD and pyrene in water (Figure 1.2d).[32] The [4]rotaxane **1.3** showed strong circulatory polarized luminescence (CPL) with yellow-green emission attributable to the spatially restricted pyrene; changing the inner fluorescence core from pyrene to perylene resulted in a [4]rotaxane that showed orange emission.[33] Leigh et al. developed an active metal-templating strategy accessing triply-threaded [4]rotaxanes using Ni-catalyzed homocoupling of alkyl bromines, wherein the transition metal center gathers two reactive half dumbbells inside of the macrocycle and also mediates covalent bond formation (Figure 1.2e).[34] After the dumbbell molecule forms, the metal returns to its original state, and this catalytic cycle repeats to interlock a second or third dumbbell. A 35-atom ring allows two axles to fit through the cavity to form the [3]rotaxane. Increasing ring size to 37- and 38 atoms provided enough room to thread three axles, resulting in the triply-threaded [4]rotaxane **1.4**.

From a design standpoint, the most exciting feature of the rotaxane is the ease at which its molecular components can be designed to control ring sliding. Playing with the number of threaded rings and dumbbell molecules are ways to tune the molecular dynamics of rotaxanes; thus, using them as topological crosslinks in a polymer network should affect material properties. Polyrotaxanes and slide-ring materials containing singly-threaded macrocycles on polymer chains

have been studied extensively; however, networks containing two polymer chains through a single ring are rare because they are synthetically challenging.

1.3 Polyrotaxane Materials

Rotaxane moieties can be incorporated into macromolecules in a variety of ways (Figure 1.3a). The resulting architectures include main-chain polyrotaxanes (in which the polymer backbone is part of the rotaxane moiety, either as the thread or ring component (Figure 1.3a, left)), side-chain polyrotaxanes (Figure 1.3a, center), and polyrotaxanes in which the mechanical bond is incorporated into the polymer backbone, such as the poly[2]rotaxanes (top right) and poly[3]rotaxanes (Figure 1.3a, bottom right). Although these architectures have been synthesized,[6,35] the main-chain polyrotaxanes have provided the most insight into how an interlocked architecture impacts material properties.

1.3.1 Main-Chain Polyrotaxanes

As in traditional polymers, the chemistry and structure of the backbone play a role in the behavior of polyrotaxanes. However, their properties are also impacted by the ring(s) and stopper(s) and the interactions between these interlocked components. These relationships have been most extensively characterized in main-chain polyrotaxanes (Figure 1.3a, left).

The first report of a main-chain polyrotaxane was by Harrison and Harrison in 1967,[36] however, the field did not gain traction until 1992 when Wenz reported the threading of poly(iminooligomethylene)s through α-cyclodextrin (α-CD) rings[37] and Harada reported the threading of poly(ethylene glycol) (PEG) through α-CDs.[38] The PEG and α-CD pseudopolyrotaxane assembly is highly efficient and driven by a combination of hydrophobic

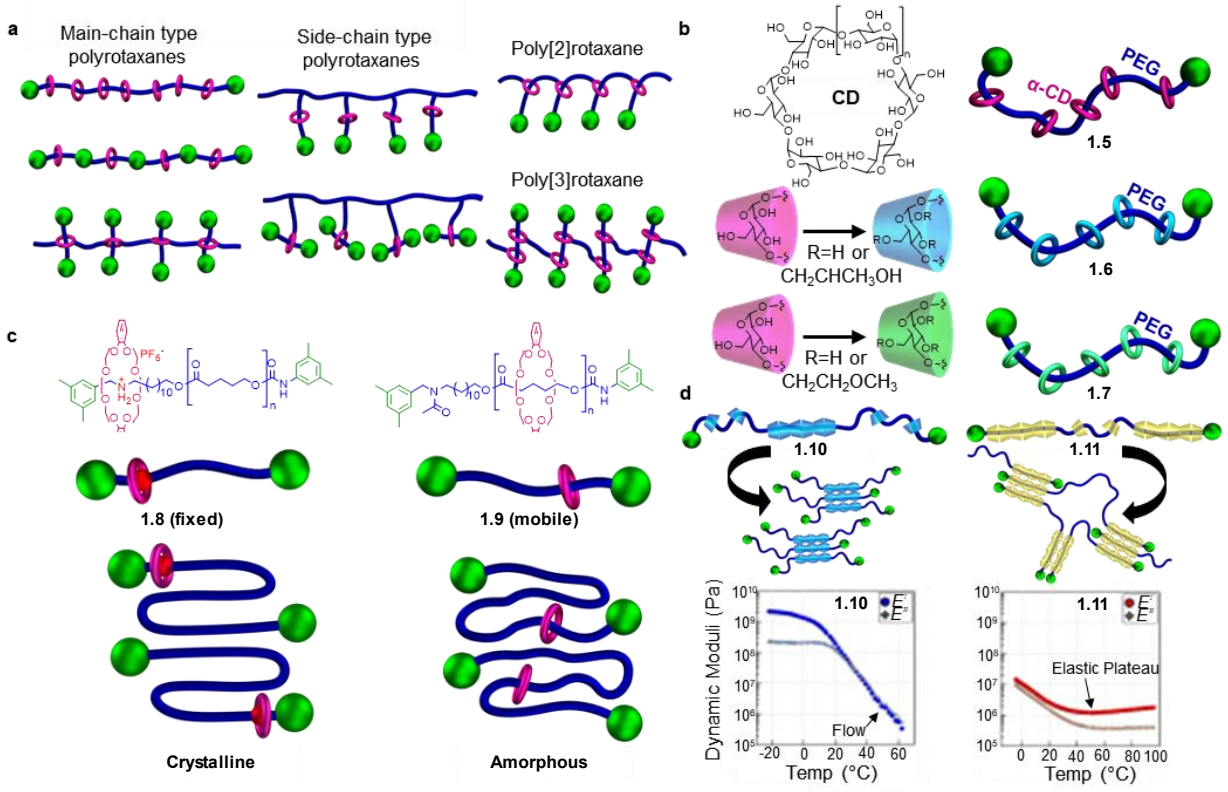

Figure 1.3. Polyrotaxanes. a) A selection of polyrotaxane architectures that includes main-chain polyrotaxanes (left), side-chain polyrotaxanes (center), poly[2]rotaxanes (or daisy chains) (top right), and poly[3]rotaxanes (bottom right). b) Polyrotaxanes are often synthesized using cyclodextrin (top left), which is commercially available in three ring sizes, α, β, and γ, where *n* = 1, 2, or 3 anhydroglucopyranoside units. A main-chain polyrotaxane composed of poly(ethylene glycol) (PEG) threaded through α-cyclodextrin (α-CD) (**1.5**) (top right). Partial hydroxypropylation of α-CD is used to access the PEG-based polyrotaxane, **1.6** (middle row). Partial methoxyethylation of α-CD is used to access the PEG-based polyrotaxane, **1.7** (bottom row). c) Chemical structure of the ammonium-containing polyvalerolactone-based polyrotaxane **1.8** with dibenzo[24]crown-8 and the related amine-protected polyrotaxane **1.9** with schematics highlighting their crystallization behavior. d) Cartoons showing the CD distribution in **1.10**, its proposed self-assembly and the temperature-sweep dynamic mechanical analysis (DMA) data of a **1.10** film (left), and cartoons showing the CD distribution in **1.11**, its proposed self-assembly and the temperature-sweep dynamic mechanical analysis (DMA) data of a **1.11** film (right).

interactions (between the polymer chain and the hydrophobic pocket of the CD) and hydrogen bonding between adjacent CDs.[39] The polyrotaxane **1.5** is formed when a stoppering reaction "traps" the α-CD rings on the polymer backbone (Figure 1.3b, top).[40] In addition to ease of synthesis, CDs are commonly used in polyrotaxanes because they are commercially available in three sizes that vary in the number of α-D-glucopyranoside units (Figure 1.3b, α-CD (n=1), β-CD

(n=2) and γ-CD (n=3)). As such, CD-based polyrotaxanes are the most studied, producing valuable insights into polyrotaxane structure-property relationships.

In **1.5**, the α-CD rings play a significant role in the properties of the material: hydrogen bonding between the rings favors their aggregation on the polymer backbone resulting in semi-crystalline materials, limiting ring mobility along the polymer backbone.[41] However, these hydrogen bonds can be disrupted, either by introducing a hydrogen-bond competing solvent or through partial hydroxypropylation or methoxyethylation of the CD rings, resulting in more soluble amorphous polyrotaxanes (**1.6** and **1.7**) (Figure 1.3b) with enhanced ring translational mobility (Figure 1.1b).[41,42] Studies have focused on how this mobility and the resulting material properties are affected by parameters such as ring-backbone interactions, ring–ring interactions, polymer concentration, and ring coverage (calculated either as the number of rings per repeat unit or the percent coverage of the backbone by the rings).[43–47]

The mobility and placement of the rings are controlled, in part, by the inherent interactions between the ring and polymer backbone. For instance, the energy barrier resulting from attractive interactions between the CD and PEG backbone in **1.5** leads to slower diffusion of the α-CD along the PEG backbone compared to unthreaded (free) CD.[45] Furthermore, the presence of the rings impacts the polymer backbone by, for example, decreasing the flexibility of the polymer with increasing ring coverage leading to stiffer polyrotaxanes.[39,48] The effect of the ring–backbone interactions has been studied in polyrotaxanes with rings other than CD, for instance, crown ethers. Early examples of polyrotaxanes based on crown ethers include those reported by Gibson, in which the stopper groups are incorporated into the polymer backbone.[49–56] These polyrotaxanes were synthesized by copolymerizing an alkyl diol monomer and a bulky diol monomer with either diacid chloride monomers (forming polyesters) or diisocyanate monomers (forming polyurethanes) in the

presence of a high concentration of [30]crown-10 rings. The sliding mobilities of the crown ethers in the resulting polyrotaxanes vary based on the differing backbone chemistries. In the polyester-based polyrotaxane, the crown ether rings move freely between the stoppers and appear as a range of broad signals in the ^{1}H nuclear magnetic resonance (NMR) spectrum. In contrast, the polyurethane-based polyrotaxanes exhibit hydrogen-bonding between the ring and the polymer backbone NH groups (in $CDCl_3$), which restricts ring mobility, as demonstrated by the methylene groups of the crown ethers appearing as a single peak in the NMR spectrum. In a hydrogen-bond competing solvent (for example, d_6-dimethyl sulfoxide (DMSO)), the hydrogen bonding is "switched off," increasing ring mobility and resulting in the methylenes showing up as a broad range of peaks in the ^{1}H NMR spectrum, similar to systems with no hydrogen bonding present.

This difference in ring mobility is also seen in the solid state properties of similar crown ether-based polyester and polyurethane polyrotaxanes.[49,53,55,56] The polyester polyrotaxanes exhibit two melting-to-crystallization transitions (as determined by differential scanning calorimetry (DSC)), suggesting that the rings are mobile enough to phase separate and allow the rings and polymer chains to crystallize separately. In contrast, hydrogen-bonding in the polyurethanes results in a single-phase material that only exhibits one glass transition temperature (T_g).

The effect of ring mobility on the solid-state properties of a polyrotaxane can even be observed with just a single mobile ring present. For example, Takata and coworkers[57] synthesized macromolecular [2]rotaxanes using poly(δ-valerolactone) (PVL) with a single secondary ammonium binding site on the thread component (M_n *ca.* 2,300 $gmol^{-1}$) and [24]crown-8 as the ring (**1.8**, Figure 1.3c, top). The secondary ammonium site interacts favorably with the crown ether ring limiting its motion and allowing crystallization of the PVL segment in **1.8**. However, if the

secondary amine is acetylated (**1.9**), the hydrogen bonding between the ring and thread is "switched off," increasing ring mobility and disrupting crystallization resulting in an amorphous material (Figure 1.3c, bottom).[57]

In addition to ring mobility, how the rings are distributed along the polymer backbone can affect the solid-state properties. For example, Ito and coworkers[58] studied a poly(ethylene oxide)-*b*-poly(propylene oxide)-*b*-poly(ethylene oxide) (PEO−PPO−PEO) triblock main-chain polyrotaxane with either fully-functionalized hydroxypropyl-α-CDs (100% HP-α-CDs, **1.10**) or trimethylsilyl-functionalized hydroxypropyl-α-CDs (100% TMS-α-CDs, **1.11**) as the ring components. In **1.10**, the α-CDs preferentially reside on the inner PPO block because of the more favorable hydrophobic interactions with PPO than PEO (Figure 1.3d, left).[59] In contrast, the TMS-α-CDs in **1.11** reside on the PEO end-blocks to shield the polar PEO segments from the hydrophobic TMS-α-CD outer wall (Figure 1.3d, right).[57] In both polymers, the CDs form crystalline domains; however, the different positioning of the CDs along the polymer backbone results in drastically different mechanical properties. In **1.10**, the concentration of the CDs on the central PPO block results in discrete crystalline assemblies, resulting in fluid-like behavior above T_g, as shown by dynamic mechanical analysis (DMA) (Figure 1.3d, left). In **1.11**, the CDs are concentrated on the outer PEO blocks so that the crystalline CD domains are bridged by polymer chains, resulting in an elastic plateau even above T_g (Figure 1.3d, right).

CD-crystallization in polyrotaxanes has also been used by Ke and coworkers to obtain 3D-printed cubic wood-pile lattices.[60–62] In these materials, obtained from the chemical photo-crosslinking of main-chain pseudopolyrotaxanes, the α-CDs hydrogen-bond into tubular arrays which form hexagonal crystalline domains that function as physical crosslinking sites.[60,61] Varying pH (Figure 1.4a, top) or solvent type (Figure 1.4a, bottom) can disrupt (or reform) these physical

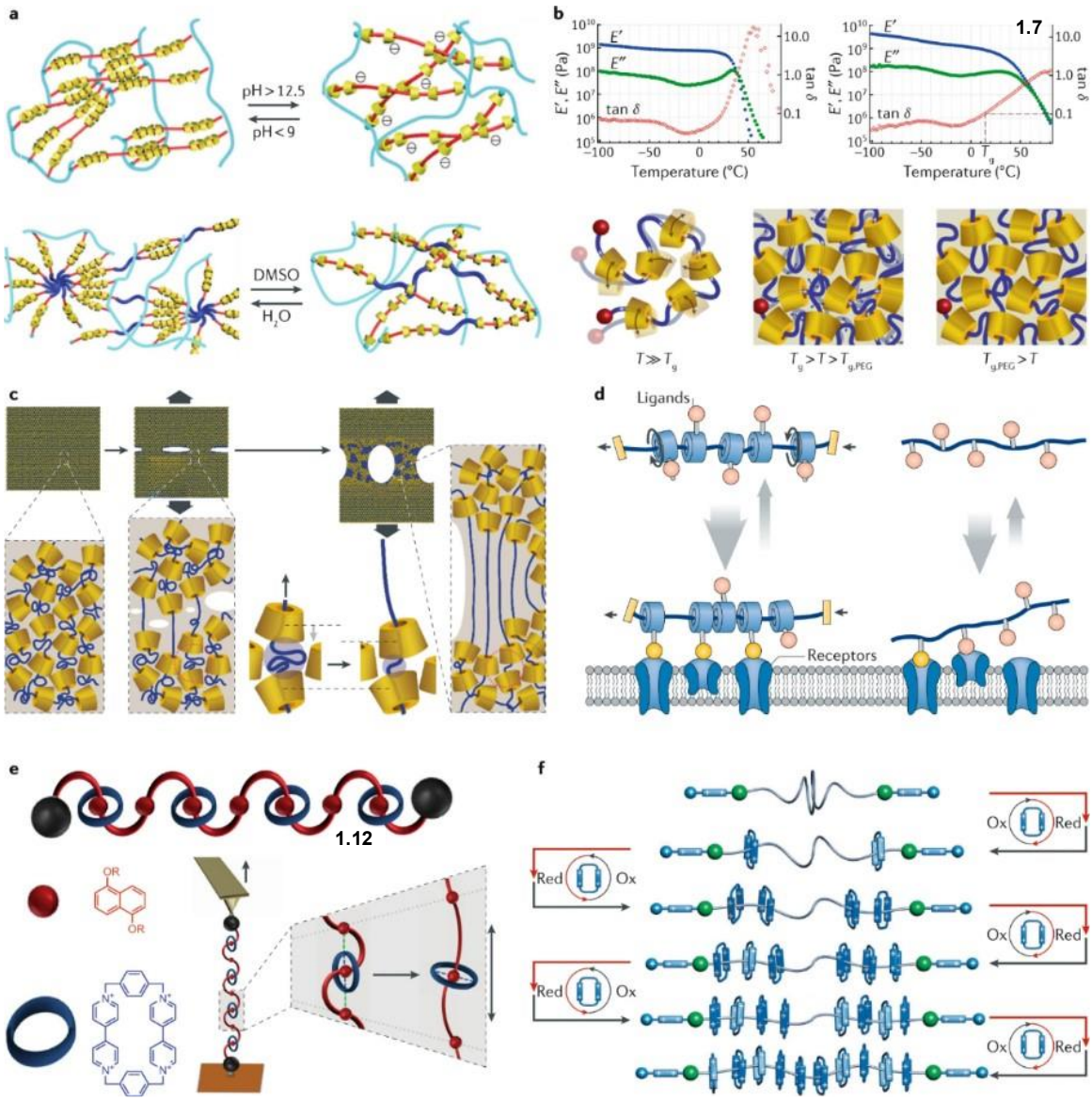

Figure 1.4. Main-chain polyrotaxane properties and behavior. a) Cartoon showing the effect of pH (top) or solvent change (bottom) on the aggregation of threaded cyclodextrins (CDs) in a photocrosslinked polyrotaxane. b) Temperature dependence of tensile storage modulus (E'), loss modulus (E''), and loss tangent (tan δ) of α-CD (46% methoxylated) glass (top left) and **1.7** polyrotaxane glass (poly(ethylene oxide) backbone, 25% ring coverage, 46% methoxylated α-CD rings)) (top right). Cartoon showing the vitrification of CD rings in **1.7**, highlighting the poly(ethylene glycol) (PEG) chain mobility above $T_{g,PEG}$ (bottom). c) Scheme showing how the structure of a polyrotaxane glass (**1.6** and **1.7**) changes during stress below the glass transition temperature T_g: homogenous CD distribution before stress (left), fragmentation of CD framework (center), stress-induced translational motion of the threaded PEG chains (bottom right) and microscopic phase separation of backbone PEG chains and CD framework (right). d) Cartoon highlighting the difference in multivalent binding of the more mobile ligands on polyrotaxane rings (left) versus them directly conjugated to a polymer backbone (right). Yellow ligands indicate successful ligand–receptor binding. e) Cartoon image of folded structure of **1.12** with blue

(Figure 1.4 Continued.) cyclobis(paraquat-p-phenylene) (CBPQT) rings and red 1,5-dioxynaphthalene backbone polymer (top). Cartoon showing breaking of π-stacking between the CBPQT rings and naphthalene backbone in the foldamer during a single-molecule atomic force microscopy experiment (bottom). f) Cartoon showing the stepwise addition of CBPQT rings (up to 10) onto a PEG backbone using chain-end redox-active molecular pumps.

crosslinks leading to a decrease (or increase) in moduli allowing access to shape memory properties. Such shape-memory behavior combined with the lattice structure allows the material to actuate in a controlled manner, exemplified by lifting a coin upon the reformation of the crystalline CD-domains. Related work using methylated CDs' lower critical solution temperature (LCST) behavior showed similar actuation behavior upon temperature cycling.[62]

All the films discussed so far were investigated above T_g (which allows movement of both polymer chains and rings). Still, polyrotaxanes may also have interesting properties in the glassy regime below T_g. Unfortunately, the rings in CD-based polyrotaxanes crystallize rather than vitrify; however, crystallization can be inhibited by partial functionalization of the CD rings allowing access to polyrotaxane glasses. For example, glassy polyrotaxane **1.7** consists of a PEO backbone (M_n 20,000 $gmol^{-1}$) threaded through partially 2-methoxyethylated α-CD (46% hydroxy groups reacted and a CD to repeat unit ratio of 1:8 (25% coverage)). As the CDs comprise *ca.* 80 wt.% of the material, there is a T_g at *ca.* 8 °C, comparable to the neat 2-methoxyethylated α-CDs (Figure 1.4b, top left). However, **1.7** also exhibits a secondary relaxation (subrelaxation) at *ca.* −30°C (Figure 1.4b, top right), close to the T_g of PEO (ca. −35 °C). Raising the temperature above this secondary relaxation reduces the modulus to about a third of its value at −100°C.[42] This subrelaxation is linked to the interlocked architecture and is consistent with the PEG backbone sliding through the glassy CD framework (Figure 1.4b, bottom). As a result, these polyrotaxane glasses can be extremely ductile because the polymer chains slide through the rings at points of high stress allowing material deformation and resulting in enhanced toughness (Figure 1.4c).[63]

Further research showed similar effects in **1.6** and demonstrated that the properties of both **1.6** and **1.7** could be tuned by changing either the amount of chemically-modified hydroxy groups on the CD or the ring coverage. For instance, less "fragile" glass-formers with reduced T_g and less cooperative dynamics were obtained by increasing the chemical modification of the CDs, which mitigates ring–ring interactions,[64] while increased CD coverage results in an additional relaxation slightly above T_g, attributed to correlated motions of neighboring CDs on the polyrotaxane backbone.[65]

The encapsulation of a polymer by rings results in reduced interpolymer chain interactions. This effect has been used to synthesize polyrotaxanes that can act a molecular wires.[66] Conjugated polymers have long been candidates for developing molecular-scale wires; unfortunately, strong interchain interactions make it difficult to isolate single polymers, and the conformational entropy of the polymer disfavors extended, straight chain configurations, limiting conjugation within the backbone.[67] Sheathing of a conjugated polymer with rings drastically improves its overall rigidity and "insulates" the threaded polymer chain. A number of conducting polymers have been investigated in such polyrotaxanes,[68] including poly(phenylenevinylene),[69] polyfluorene,[70] poly(paraphenylene),[71] poly(diphenylenevinylene),[72] and, polythiophene.[73] The most common ring component in these polyrotaxanes is CD, but other rings such as cyclophanes[74] and cucurbiturils[75] have been reported. Most studies on conjugated polyrotaxanes are focused on their optical properties. For example, CD-based conjugated polyrotaxanes exhibit sharper UV-Vis spectra, blue-shifted emission spectra, and higher quantum yields relative to their unthreaded conjugated polymer counterparts.[67,68] In these systems, the rings separate the polymer chains, preventing aggregation (and quenching) and leading to longer life-time excited states. In addition, threaded rings cause increases in the persistence length of the backbone, stretching the polymer

out and resulting in more extended, near-planar conformations, important for enhancing the conjugation along the backbone.[67,76,77] For example, poly(4,4'-diphenylenevinylene) polyrotaxanes with varying β-CD ring coverage (between 0% and 82%) showed an increase in the electroluminescence quantum efficiency and solid-state photoluminescence with increasing coverage.[78] Ring size is also an important feature in these polyrotaxanes; systems with larger rings (for example, γ-CD vs. α-CD) exhibit greater fluorescence quenching by methylviologen in aqueous solution.[79] It was suggested that these larger rings have greater mobility along the polyrotaxane backbone, allowing larger aggregate formation. Preliminary investigations into the electrical behavior of these polyrotaxanes have shown that their conductivity can be orders of magnitude higher than the unthreaded conjugated backbone,[80] although investigations in this area are primarily focused on pseudopolyrotaxanes.[81,82] None-the-less, such pseudopolyrotaxane studies have shown that the hole mobility along a threaded poly(phenylene ethynylene) backbone can be similar to amorphous silicon, highlighting the potential of these MIPs as well-insulated organic semiconductors.[83,84]

Main-chain CD-polyrotaxanes have also been investigated as functional biomaterials,[85–90] aided by the US FDA approving the components of **1.5** (α-CD and PEG) for drug use.[91] For example, controlled release of drugs covalently attached to the CD rings can occur with selective removal of the stopper groups.[85–88] CDs functionalized with cationic groups can form complexes with anionic nucleic acids, either DNA or RNA, for gene delivery. Owing to the mobility of the positively-charged CD rings, these polyrotaxane/nucleic acid complexes are much stronger than comparable systems comprising linear cationic polymers and nucleic acids.[92,93] Upon entering the cell, the stopper groups can be selectively removed, resulting in decomplexation and subsequent delivery of the nucleic acid payload.[85–88]

Ring mobility in polyrotaxanes has also been used to enhance the biological targeting of synthetic systems. In nature, multi-valency is commonly used to enhance the molecular recognition of weak ligand-receptor interactions,[94] however, this typically requires the binding sites to be precisely arranged in space. When ligands are attached to the polyrotaxane rings, the ring mobility (both translational and rotational) allows them to arrange themselves to optimize the multivalent interactions.[89,90] Such polyrotaxanes exhibit faster and more efficient multivalent binding to receptor proteins than ligands tethered to standard covalent polymers (Figure 1.4d).[95,96]

Building on the previously mentioned ability of MIMs to act as switches and machines[97,98] main-chain polyrotaxane architectures have also attracted attention as polymer-based switches and machines.[99,100] For instance, Stoddart and coworkers developed polyrotaxane "foldamers" capable of concerted motion at the macromolecular scale.[100–103] These polyrotaxanes (**1.12**) use π-stacking interactions between a cyclobis(paraquat-*p*-phenylene) ($CBPQT^{4+}$) rings and a 1,5-dioxynaphthalene backbone polymer (Figure 1.4e) to fold in a specific manner, which results in a conformation that is ca. 15% shorter and 92% wider than the free backbone.[100] Single-molecule force spectroscopy was used to observe the transition between folded and unfolded states under applied force and showed **1.12** could exert forces of up to 50 pN (under a load of 150 pN) during folding (Figure 1.4e).[104] Furthermore, π-stacking rupture events during extension can be observed with dynamic force spectroscopy confirming the folded structure.[105] These measurements also implied a rapid reformation of the folded structure because the interlocked structure prevents the disassembly of the components.

Strides towards accessing polyrotaxanes machines have been made by Stoddart and coworkers through synthesizing a high-energy polyrotaxane through successive controlled pumping of $CBPQT^{4+}$ rings onto a polymeric chain (Figure 1.4f).[106–108] Each chain-end contains a

viologen unit sandwiched between a pyridinium group (that acts as a Coulombic barrier) and an isopropyl group (acting as a steric speed bump).[106–108] Rings can be added to the polyrotaxane by reducing the viologen units and $CBPQT^{4+}$ ring allowing threading of the ring onto the viologen, driven by the formation of a trisradical tricationic association complex. Reoxidation then forces the ring over the isopropyl speed bump because of Coulombic repulsions, resulting in a stable polyrotaxane. This ring-addition ratchet mechanism can be repeated to drive the controlled pumping of between 2 and 10 rings onto the polymer backbone, resulting in highly-charged, high-energy systems with the potential to perform work.

1.4 Slide-Ring Materials (SRMs)

Crosslinking a polymeric material gives rise to an enhanced property profile that includes higher modulus and elasticity, solvent resistance, lower rates of creep, and improved temperature stability relative to its uncrosslinked counterpart.[109] Although crosslinking is commonly achieved through chemical or physical interactions, mechanical bonds can also be realized. For instance, crosslinking polyrotaxanes by covalently linking their rings results in the formation of slide-ring materials (SRMs) (also referred to as slide-ring networks, SRNs).[110] As the polymer chains are not fixed by permanent covalent bonds, the interlocked crosslinking site can slide along the polymer backbone akin to a pulley (Figure 1.5a); a process that can dramatically affect material properties. In chemical gels, fixed (covalent) crosslinks are not distributed evenly throughout the material, and upon deformation, the shorter strands can rupture, leading to mechanical failure (Figure 1.5b, left). However, mobile interlocked crosslinks allow polymer chains to slide through the network like a pulley system, allowing dissipation of stresses in a cooperative manner (Figure 1.5b, right).

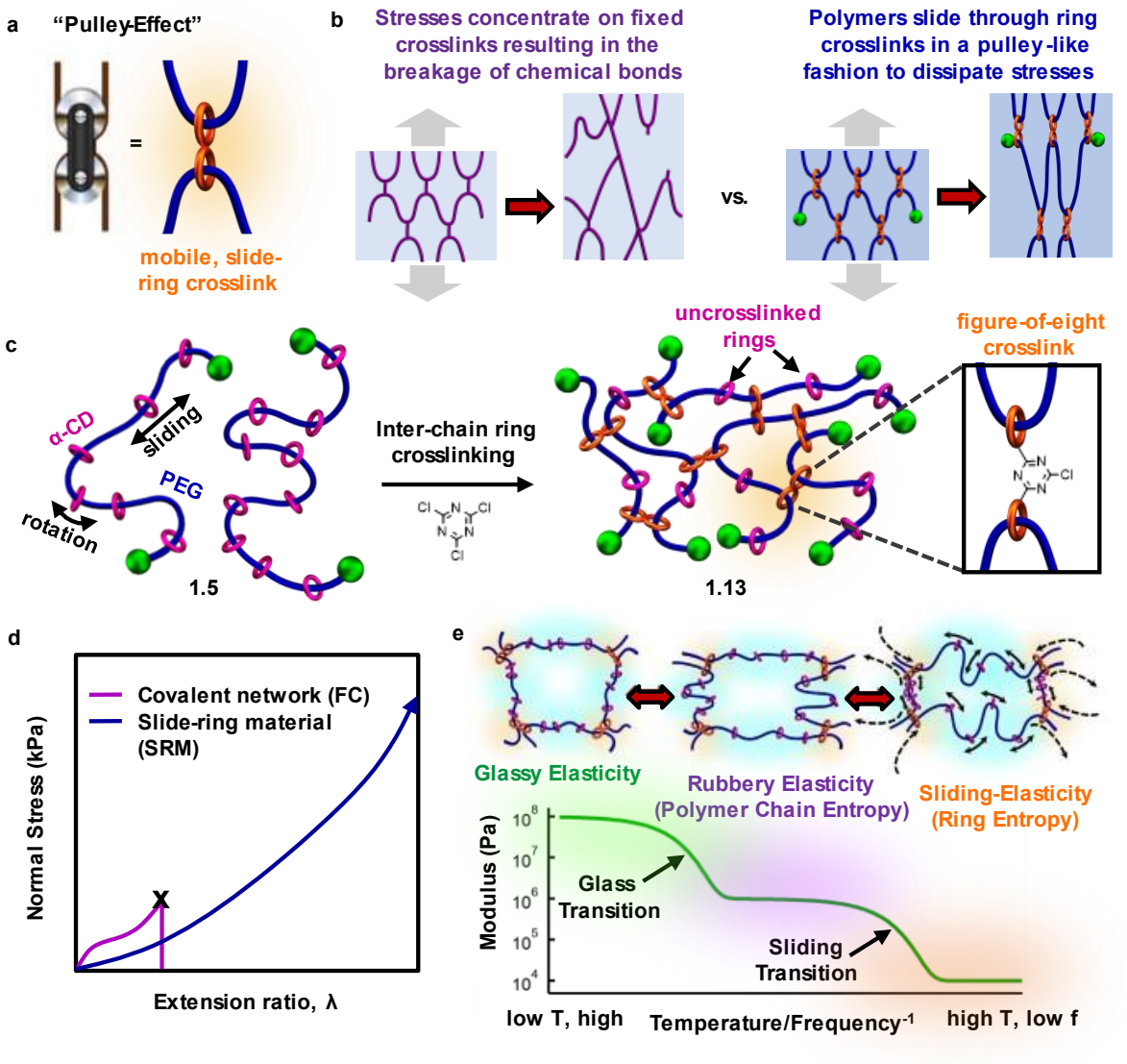

Figure 1.5. "Pulley effect" in figure-of-eight slide-ring materials. a) Visualization of the pulley effect that has been used to describe the mobile, slide-ring crosslinks (orange) of slide-ring materials (SRMs). b) The effects of strain on a fixed crosslinked network (left), where short network strands tend to rupture under strain, and a SRM (right), where the pulley effect allows for the dissipation of stress as polymer chains slide through the crosslinked rings in a cooperative manner, akin to a pulley system. c) Synthesis of a SRM (**1.13**) via interchain ring crosslinking of hydroxy groups on the α cyclodextrins (α-CDs) (pink) in **1.5** with cyanuric chloride, resulting in figure-of-eight crosslinks (orange) and residual, uncrosslinked α-CDs (pink). d) Schematic comparing the idealized tensile properties of figure-of-eight SRMs and conventional polymer networks with fixed crosslinks. e) Oscillatory compression rheology of **1.13** shows three plateaus: a glassy plateau (green), a rubber elasticity plateau (pink), and a high-temperature, low-frequency plateau (orange), referred to as sliding elasticity, wherein chain sliding and ring sliding occur simultaneously, a process that is not possible in covalent fixed-crosslinked networks.

Such interlocked networks have been broadly classified as slide-ring materials (SRMs) (or slide-ring networks, SRNs), and the mobility of their crosslinks imbues them with new property profiles.

1.4.1 Molecular Processes in SRMs

The first and most studied class of SRMs incorporates interlocked crosslinks by covalently bonding rings from different polyrotaxanes, yielding "figure-of-eight" topological crosslinks. The quintessential example of a slide-ring material, **1.13**, can be prepared by crosslinking the α-CD rings on **1.5** (Figure 1.5c).[110] Importantly, this synthetic protocol results in both figure-of-eight crosslinks and residual uncrosslinked rings in the polymer network; the latter also plays a role in the properties of these SRMs. Such polymer networks exhibit an impressive property profile; for example, **1.13** can absorb 24,000 times its mass in water and extend to 24 times in length without hysteresis.[110–113] The interlocked crosslinking architecture also influences the mechanical properties,[67] exemplified by the stress-strain behavior (Figure 1.5d). Although fixed-crosslink networks reveal the typical "S"-shaped curves, SRMs have a "J"-shaped profile with lower elastic (Young's) modulus and much greater strain-at-break. Other properties, such as fracture behavior[114] and strain recovery,[67] are also affected, as discussed later.

In the past two decades, there have been substantial investigations into the molecular processes and structure-property relationships of these topological materials.[115–119] The elasticity of conventional polymer networks arises from the conformational entropy of polymer segments between fixed crosslinks. Although this conformational entropy also plays a role in SRMs, two additional molecular mechanisms are at work: first, crosslink mobility, and second, configurational entropy of the uncrosslinked rings (if present). These mechanisms are unique to SRMs and, in combination with traditional network elasticity, lead to their exceptional properties. Although this section focuses on figure-of-eight SRMs that contain solvent (namely, slide-ring gels, SRGs) the

concepts apply to SRMs with different crosslink architectures (to be discussed later) with or without solvent.

Let us first consider the impact of crosslink mobility on the behavior of polymer networks. If crosslinks in polymer networks are fixed, they are constrained to a specific point on the polymer chains. However, in SRMs, these constraints are lifted because the crosslinks are free to slide along the backbone; from a thermodynamic perspective, the removal of any constraint always allows the system to relax to a state of lower free energy. In SRMs, this leads to a lower elastic (Young's) modulus. The concept of mobile crosslinks originated in the study of rubber elasticity and trapped entanglements, which are formed by the concatenation of network loops during the crosslinking process.[120–127] The point of contact between the two loops acts as a sort of crosslink whose position is not fixed, similar to the figure-of-eight crosslinks in SRMs. Thus, a number of slip-link models were developed to explain the nonlinear elasticity of rubbers.[120–127] Some authors even used a doubly-threaded [3]rotaxane model to illustrate these concepts.[124,125] The sliding junction model introduced by Ito[128,129] is conceptually similar to some of these theories: the free energy is minimized with respect to the distribution of monomers among several chains, leading to a lower Young's modulus than networks with fixed crosslinks. Furthermore, the lack of hysteresis in most SRMs is a consequence of the reversibility of the sliding motion of the rings.

Mechanical testing highlights the dramatic effect that a slide-ring crosslink can have on the properties of a polymer network. Small-amplitude oscillatory compression rheology[130] on SRGs of **1.13** in DMSO revealed a time-dependent stress relaxation modulus with two distinct plateaus at low frequencies: the first was attributed to the typical rubbery modulus, but the second (lower) plateau is not observed in networks with fixed crosslinks (Figure 1.5e). These features have also been observed in step strain experiments on similar SRMs.[131] The rubbery plateau implies a

molecular weight between crosslinks, M_C, and the relaxation time, τ, associated with the transition between the two regimes scales as $\tau \sim M_C^3$.[130] This dependence is the same as that predicted by reptation theory, which describes the sliding motion of a polymer chain,[132] and, as a result, the researchers associated this "sliding transition" with the sliding of the polymer chains through the ring crosslinks, accounting for the lower equilibrium modulus of figure-of-eight SRMs relative to fixed-crosslinked networks. However, the analogy with reptation theory may not be appropriate because there is no continuous confining tube in SRMs, and the timescale for the diffusion of tension along entangled chains actually scales as M_C^2.[132] Thus, further study is required to clarify the dynamic processes responsible for the sliding transition. Nevertheless, it seems likely that ring sliding is responsible for the phenomenon in some fashion.

Molecular simulations have also investigated the impact of mobile crosslinks on material properties.[129,133–135] These efforts demonstrate that the reduced modulus of SRMs is intimately related to the distance available for crosslink sliding, with greater freedom leading to softer materials.[129,133] Other in silico experiments have shown that SRMs exhibit excellent surface adsorption because the stretchable networks can readily deform to maximize surface contact.[135] Further simulations showed that SRMs can rapidly absorb nanoparticles with diameters much larger than the network mesh size because the mobile crosslinks allow for efficient expansion of the network.[135]

Given that mobility of crosslinks is a key factor in the properties of SRMs, the effective range of sliding strongly influences the behavior, as suggested by the simulation studies discussed above. This range can be widened by increasing the molecular weight of the axis polymer, which results in improved fracture energy. However, increasing the crosslink density appears to mitigate some of these effects. For instance, SANS and SAXS experiments have shown that SRGs remain

isotropic upon uniaxial deformation up to considerable strains and are homogeneous even at large extensions, in contrast to networks with fixed crosslinks.[113,136–138] However, the structural inhomogeneities typical of these fixed networks emerge when the ring-sliding range is suppressed, either by increasing the crosslink density [131,136] or using a solvent that favors ring aggregation.[113]

The picture of SRMs discussed so far is incomplete; it does not explain why the second (low frequency) plateau modulus has a finite, non-zero value. It also fails to address the unusually weak dependence of modulus, E, on crosslink density, ν, which seems to scale as $E \sim \nu^{0.2}$ rather than $E \sim \nu^{1}$ as expected for fixed-crosslinked networks,[139] and is sometimes even non-monotonic.[140] Furthermore, in the simple picture illustrated above, SRGs at swelling equilibrium should display the same modulus as fixed-crosslinked gels. This observation was first made by de Gennes,[141] who argued that the additional degrees of freedom afforded by mobile crosslinks would be entirely used to swell the gel further rather than lower the modulus upon deformation. As a result, SRGs at equilibrium should be as stiff as fixed-crosslinked gels of comparable swelling and density of elastic strands. The discrepancy between this theoretical model and experimental results might be explained by the presence of uncrosslinked rings in experimental SRGs (pink rings, **1.13**).

The free rings along the polymer backbone possess translational entropy that can affect crosslink mobility. In particular, rings on a polyrotaxane backbone can be modeled as hard particles confined to 1D space. In this system, analogous to the Tonks gas in statistical mechanics,[142] the configurational entropy of the rings gives rise to a pressure, which resists the motion of the crosslinks as this reduces the contour length available to the molecules. The connection to polyrotaxanes was made by Sevick and Williams,[143] who found that the presence of rings along the backbone (and the associated pressure) resists the sliding motion of the polymer chain through a fixed ring below a critical force, analogous to yield stress behavior.[144–148] In the

context of SRMs, the translational entropy of the uncrosslinked rings resists the sliding motion of the ring crosslinks, causing additional contributions to the elasticity, called ":sliding-elasticity."[130,149]

Ito and coworkers have attempted to explain various properties of SRMs in qualitative terms by applying the concepts of sliding elasticity. For instance, they propose that the finite storage modulus of SRMs at long times cannot be understood purely in terms of crosslink mobility and that the resistance to crosslink sliding caused by the uncrosslinked rings may furnish an explanation for this effect.[130,149] Young's modulus can also depend non-monotonically on crosslink density, increasing for small amounts of crosslinks and then decreasing at larger loadings; a model combining sliding crosslinks with the entropic effects of uncrosslinked rings can reproduce such an effect.[140] Ito and coworkers have also observed significant strain hardening upon compression of **1.13** (in DMSO), with the modulus transitioning from one constant value at low strains to another, higher-value at intermediate strains.[139] The initial (smaller) and intermediate (larger) moduli agree quantitatively with the two plateaus observed in rheological measurements (Figure 1.5e). If these regimes do indeed reflect polymer and sliding elasticity, then one may conclude that the entropy of the rings dominates at small deformations and the entropy of the chains becomes more important at larger strains.

Despite the progress described above, the details of how ring entropy affects SRM mechanical properties are still unclear. Mobile rings on polyrotaxanes lead to yield stress behavior, both in theory[145] and simulation,[150] but SRMs show no such effects. Moreover, if the low-frequency plateau in the viscoelastic data (Figure 1.5e) is associated with crosslink sliding, then the average force on each network strand must be greater than the yield force. However, the expected yield force appears quite large compared to the stresses observed in linear viscoelasticity

measurements.[130,145] In general, it is unclear how the microscopic properties of polyrotaxanes with mobile rings connect to the macroscopic properties of SRMs. Molecular simulations of model systems, such as those by Müller *et al.*,[150] may prove useful in resolving these questions.

1.4.2 Structure-Property Relationships in SRMs

As discussed above, the mobility of the figure-of-eight rings in SRM **1.13** influences its material properties. However, various factors impact this mobility, including the distance available for ring-sliding, crosslink density, ring size, and ring-thread interactions. As such, understanding the complex relationship between these factors is essential for creating a structure-property profile of these intriguing materials.

The ring coverage of a polyrotaxane is defined as the percent of the polymer backbone covered by the rings. Reducing the coverage increases the sliding distance between rings, therefore increasing crosslink mobility. This relationship was demonstrated by studying the mechanical properties of two related SRGs (**1.14**) with different ring coverages (2%: **1.14-02**, Figure 1.6a top, and 25%: **1.14-25**, Figure 1.6a bottom) but similar degrees of crosslinking.[116] The 25 wt.% **1.14-02** hydrogel exhibited excellent extensibility (up to 1,600%) and was capable of reaching over 1.1 MPa stress-at-break while, for comparison, fixed-crosslinked gels with similar elasticity usually exhibited < 10 KPa stress-at-break. Fatigue performance of **1.14-02** was determined via successive cyclic tensile tests, which showed that stretching the material to seven times its original length (extension ratio, $\lambda = 7$) for 100 cycles resulted in stress-strain curves that nearly overlap (Figure 1.6b left). Additionally, loading-unloading cyclic tensile tests on **1.14-02** showed almost no

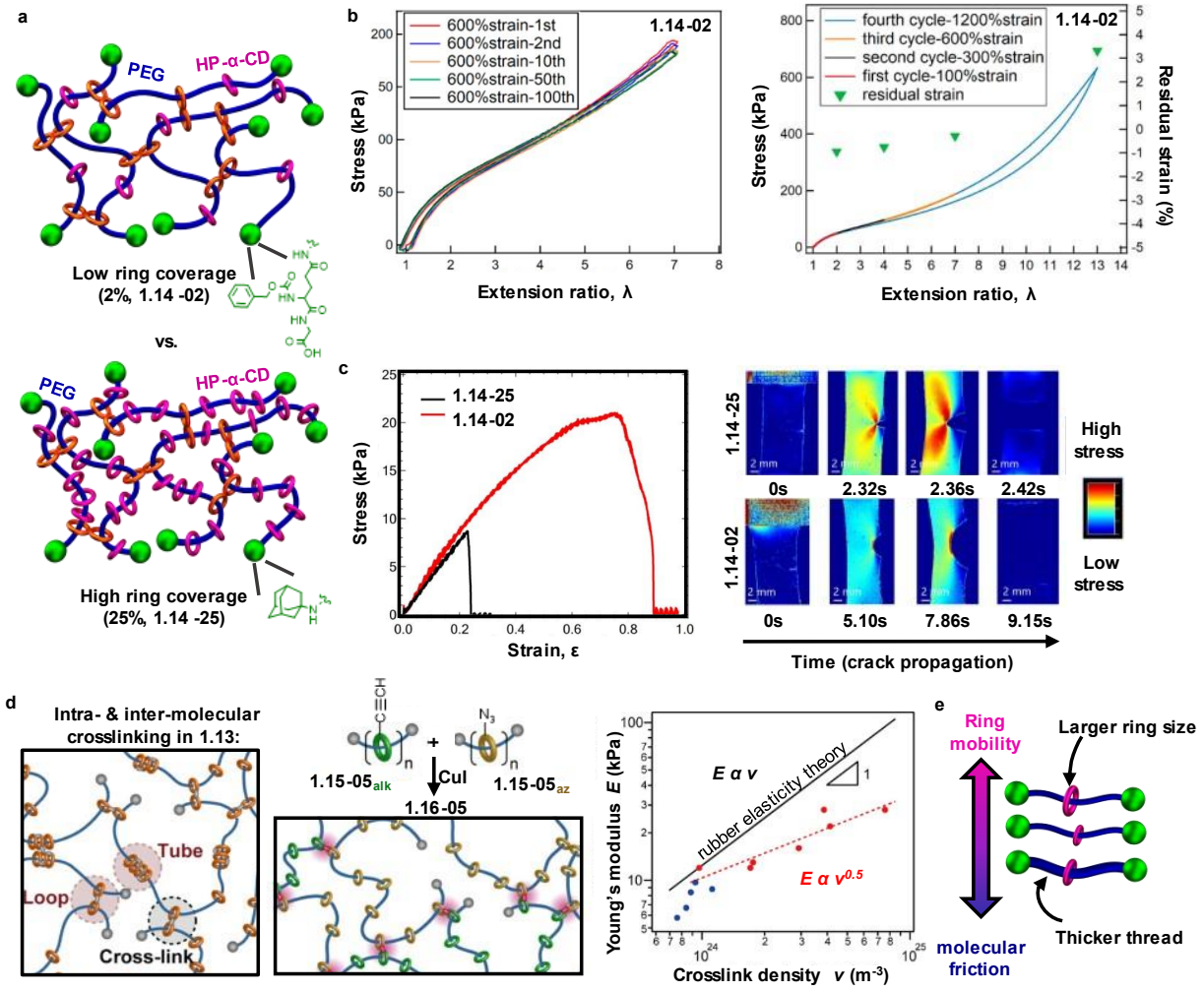

Figure 1.6. Structure-property relationships in SRMs. a) Schematic of the figure-of-eight **1.14-02** and **1.14-25** hydrogels that consist of PEG backbones and partially functionalized HP-α-CD, with similar crosslink density but different ring coverage: 2% (top) and 25% (bottom). b) Successive cyclic tensile tests (extension ratio, l, = 7 for 100 cycles) on **1.14-02** (25 wt% hydrogel) showed minimal hysteresis (left) and loading-unloading cyclic tensile tests on the same material at different strains with the residual strain after each cycle revealing little-to-no hysteresis at lower extensions, and small residual strain during the fourth cycle (1200% strain, λ = 12, right). c) Fracture tensile properties of notched 16 wt% hydrogel samples of **1.14-02** and **1.14-25**; the critical strain of crack propagation of **1.14-02** is three times that of **1.14-25** (left) and polarized-light images of notched samples of the same material mapping localized stresses throughout the material (warmer colors represent greater stress); a highly blunted notched region is observed in **1.14-02** in addition to a smaller area of high stress (red) relative to **1.14-25** (right). d) Intermolecular crosslinking of chemically identical polyrotaxanes (for example, **1.5**) yields slide-ring materials that contain "loops" and "tubes" as a result of unintended intramolecular crosslinking, as shown in **1.13** (left). Complimentary functionalities (azide (orange) and alkyne (green)) on the PR α-CDs of **1.15-05$_{az}$** and **1.15-05$_{alk}$** prevent intramolecular reactions during crosslinking forming **1.16-05** (center). Correlation between modulus, *E*, and crosslink density, *v*, for **1.16-25** ($E \alpha v^{0.5}$, red data points) showing an apparent deviation from rubber elasticity theory ($E \alpha v$), blue data points

correspond to **1.16-05** (right). e) PR ring mobility can be influenced by ring size (i.e., α-CD vs. γ-CD) and/or thread thickness (e.g., via different alkyl substituents on the thread) as a consequence of a change in molecular friction along the PR backbone. Adapted from Ref. 116 with permission from American Chemical Society.

hysteresis during the first 3 cycles at low extension, and only 3% residual strain during the 4th cycle ($\lambda = 12$, Figure 1.6b right).

The SRGs of different ring coverage were compared with the 16 wt.% hydrogels. Tensile studies showed that the lower coverage **1.14-02** exhibited vastly superior strain and stress-at-break relative to the higher coverage **1.14-25** (1,250% strain, 125kPa stress vs. 110% strain, 50kPa stress, respectively). A similar effect has been observed in SRGs (with DMSO solvent) prepared from related polyrotaxanes[151] as well as slide-ring hydrogels[131] and non-figure-of-eight SRGs.[152] These observations are consistent with the larger number of uncrosslinked rings limiting mobility and resulting in inferior mechanical properties.

Reducing ring coverage on polyrotaxane chains within SRMs also improves their fracture toughness. Notched samples of **1.14-02** (16 wt.%) had a critical strain of crack propagation three times that of **1.14-25** (Figure 1.6c, left), although both samples showed better fracture toughness than an equivalent fixed-crosslinked gel.[119,153] Plane polarized-light images (Figure 1.6c, right) of these stretched materials showed remarkable differences in the stress relaxation mechanism; **1.14-02** appears to undergo homogenous distribution of stresses throughout the material, whereas a butterfly-shaped pattern is observed in **1.14-25**, consistent with the heterogeneous distribution of stress. Furthermore, crack propagation occurred 40 times slower in the lower coverage SRMs.[154] From a molecular perspective, these observations are consistent with lower ring coverage allowing greater freedom of movement of the slide-ring crosslinks and, therefore, more efficient stress relaxation.

The number (or density) of sliding crosslinks will also impact the range of ring motion along polymer chains. Increasing the covalent crosslink density in fixed-crosslinked networks leads to a higher modulus, reduced strain-at-break, lower toughness, and lower swelling. The same qualitative trends are typically observed in SRMs when the sliding-crosslink density increases. However, the situation is more complicated because there are two forms of entropic elasticity: namely, from polymer chains and ring-sliding. As a result, SRMs do not exhibit a linear relationship between crosslink density and elastic modulus, as is expected for fixed-crosslinked networks. How the SRM mechanical properties are affected by changing the crosslink density can depend on the ring coverage of their polyrotaxane precursors. For example, SRMs with higher ring coverage (~25%) can show non-monotonic changes in elastic modulus as the crosslinking density varies, first increasing at small densities (up to about 1.0-1.5%) and then decreasing at higher values.[140,151] However, this behavior is not observed in all circumstances, suggesting a more complex relationship.[116] Such non-monotonic behavior is generally not seen in low-coverage figure-of-eight SRMs or other SRM architectures.[155,156] Other factors, such as microphase separation, can also complicate the relationship between modulus and crosslink density.[157] One feature observed in most SRMs is that Young's modulus scales slowly with crosslink density, having an exponent well below unity, in contrast to the linear scaling of networks with fixed crosslinks. This weak dependence suggests that chain entropy does not contribute as strongly to the elasticity of SRMs as ring entropy.

Understanding network elasticity can be difficult, even in fixed-crosslinked networks, because defects, such as loops and dangling ends, must be accounted for. SRMs present additional challenges because intramolecular reactions between CD rings on the same polyrotaxane chain can form "tubes"[158,159] (as in **1.13**, Figure 1.6d, left), which increase polymer segment stiffness

and, therefore, modulus. These confounding factors make it difficult to build a comprehensive understanding of the relationship between crosslink density and mechanical response. Ito and coworkers[115] addressed some of these issues by crosslinking alkyne- and azide-functionalized polyrotaxanes (**1.15$_{alk}$** and **1.15$_{az}$**) to form slide-ring material **1.16** (Figure 1.6d, center), thereby eliminating tube formation. This approach also reduces loop-formation because single-chain loops are not possible.[115] Furthermore, the resulting triazole crosslinks can be detected by UV spectroscopy, providing an accurate estimate of crosslink density.

The modulus of these specially-designed SRGs (in DMSO) exhibited a very weak dependence on crosslink density, $E \alpha \nu^{0.5}$ (Figure 6d right, red data points, *c.f.* $E \alpha \nu^{1}$ for fixed-crosslinked networks). As discussed above, the relationship between modulus and crosslink density is also affected by ring coverage; for instance, **1.16-05** made from 5% coverage polyrotaxanes (**1.15-05$_{az}$** and **1.15-05$_{alk}$**) exhibit a lower modulus than **1.16-25**, although the dependence on crosslink density appears to be stronger (Figure 1.6d right, blue data points). However, the range of synthetically accessible crosslink densities for **1.16-05** is narrow, so the precise relationship between *E* and *v* for lower-coverage SRMs is not fully established at this time.

Molecular dynamics simulations have shown that increasing ring size in polyrotaxanes can lead to faster ring diffusion (or reduced friction) along the backbone (Figure 1.6e).[46] As a result, the size of the ring component is expected to have a significant impact on the dynamical properties of SRMs. While SRGs have been synthesized and studied with various ring sizes (for example, α-CD compared with γ-CD),[118] solvent effects complicate the results and make them difficult to interpret. Taking a different approach, Takata and coworkers[160] investigated this concept using non-figure-of-eight rotaxane-crosslinked networks. Rather than change the diameter of the rings, they altered the width of the thread by using a polyrotaxane backbone with different alkyl

substituents. Although the thicker-thread SRMs have the same strain-at-break as those with thinner threads, their fracture stress (and energy) are actually larger. This suggests that greater force is required to pull the rings along thicker backbones, consistent with the idea that the "friction" associated with ring-sliding increases for thicker threads, smaller rings, or a combination of both.

1.4.3 SRM Architectures Beyond the Figure-of-Eight

As discussed at the end of the previous section, researchers have investigated SRM architectures beyond the original figure-of-eight gels. In this prior example, multiple polymerizable groups are installed on the polyrotaxane rings or stoppers, which allows the polyrotaxanes to act as crosslinkers for copolymerization or direct reaction with other polymers.[152,161–164] This approach has been used to synthesize SRMs with both covalent and sliding crosslinks,[162,165,166] so that material properties can be tuned smoothly between the fully-topological and fully-covalent limits.

An alternative SRM architecture can be prepared by grafting polymer chains onto the rings of a polyrotaxane and crosslinking through the chain-ends.[156] It is possible to introduce new chemistries and tailor material properties by varying the polymers used as grafting chains. For example, polyrotaxane **1.6**[110] grafted with polycaprolactone (PCL) (**1.17**, Figure 1.7a) is commercially available and can be used as a crosslinker to form SRM **1.18** upon the reaction of the grafted polymer chain ends with other monomers. Because of its excellent stress recovery, a highly-crosslinked, low-T_g SRM **1.18** has been commercialized as a UV-curable, scratch-resistant coating for automobiles and electronic devices.[167] When a scratching force is applied to these SRMs, the rings can slide away and then recover when the force is released, resulting in physical self-healing of the scratch (Figure 1.7b).

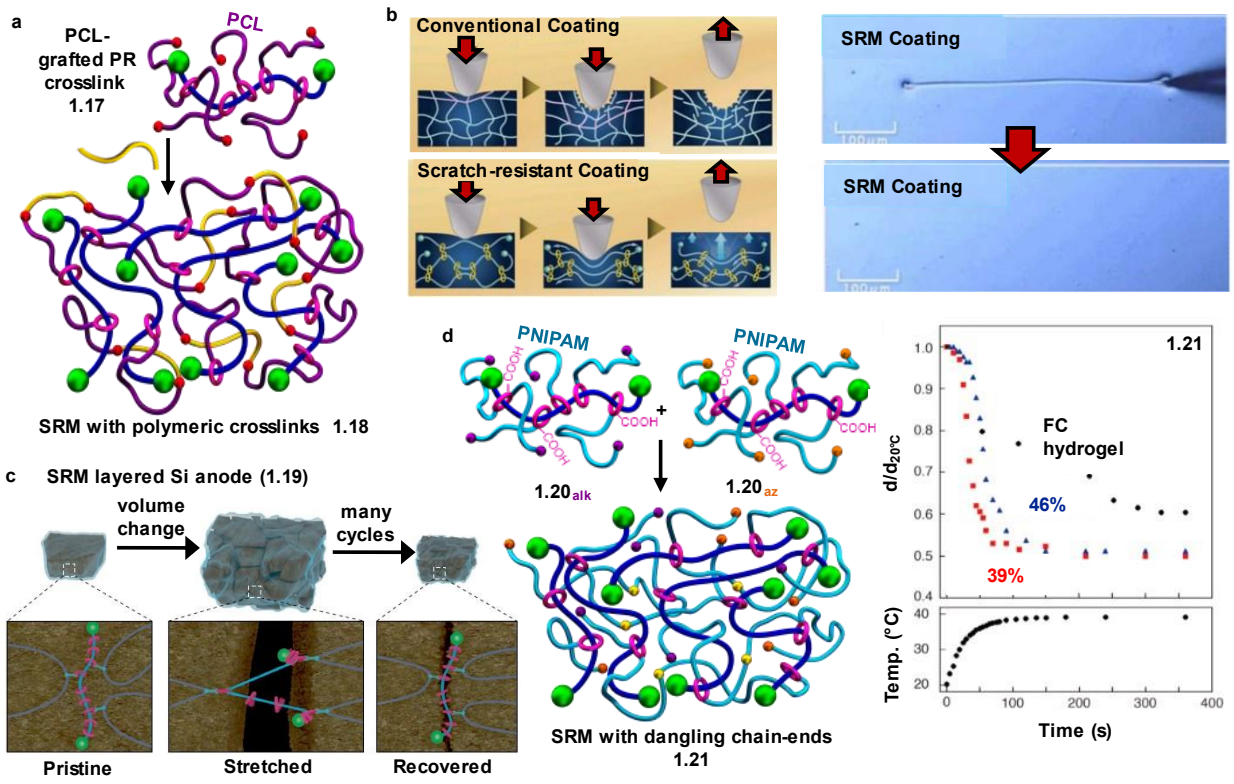

Figure 1.7. Engineering SRMs for targeted applications. a) Grafting of polycaprolactone (PCL) from the CDs of **1.6** yields the PCL-grafted polyrotaxane (**1.17**) with hydroxyl chain ends (red) that can be crosslinked with a diisocyanate (dibutyltin dilaurate (cat.)) to access **1.18**. b) Cartoon showing deformation of a conventional coating and a slide-ring coating; the latter exhibits physical healing. c) Graphical representation of the proposed stress dissipation mechanism in a silicon anode layered with **1.19** (which comprises **1.6** and poly(acrylic acid) (PAA)) during the charge/discharge cycles of a Li-ion battery. d) PNIPAM-grafted, carboxylated-CD PRs with alkyne (purple, **1.20alk**) and azide (orange, **1.20az**) chain-ends that crosslink (yellow) to form **1.21** with varying amounts of dangling PNIPAM chain-ends (left). Temperature-induced deswelling kinetics of **1.21** with 39% (red) and 46% (blue) dangling PNIPAM chains vs. a conventional PNIPAM hydrogel (crosslinked with *N*,*N*′-methylene-bis-acrylamide, black) upon raising the temperature from 20°C to 40°C, i.e., above the LCST (swelling ratio: $d/d_{20°C}$, where d = gel diameter at a certain temperature, and $d_{20°C}$ is the diameter at 20°C in water). Adapted from Ref. 167 with permission from John Wiley and Sons, and Ref. 188 with permission from American Chemical Society.

Using either of these strategies, sliding crosslinks have been incorporated in polylactones,[156,168] polylactides,[157] acrylates,[163,169] polyurethanes,[170] to name a few. Adding sliding crosslinks generally leads to lower (or similar) elastic modulus, higher extensibility, improved toughness, and greater swelling relative to comparable materials with fixed crosslinks.

Furthermore, the effects of changing ring coverage, crosslink density, and ring size discussed in the previous sections typically remain valid in these materials. However, some of these systems do not possess uncrosslinked rings like the figure-of-eight systems, so the "sliding-elasticity" described above is not always relevant.

1.4.4 Engineering SRMs toward Applications

Polyrotaxanes based on CD and PEG are commercially available,[167] leading to increased studies aimed at engineering SRMs toward applications. The discussion below highlights areas in which SRMs have attracted attention. However, the potential of SRMs goes beyond these areas, reaching fields as diverse as vibration- and sound-proof insulation materials,[167] ion transport,[171] and icephobicity[172].

As discussed above SRMs have allowed access to coatings that self-heal a scratch and this resiliency has made SRMs useful in other applications. For example, in Li-ion batteries with polymer-bound Si particle anodes, the particles experience large volume changes during charge-discharge cycles, leading to particle degradation and limited battery lifetime.[173,174] Stress from the volume changes can be mitigated with the use of an SRM as the anode binder (Figure 1.7c). For example, SRM **1.19** is prepared by the reaction of **1.6** (5 wt%) with a conventional polymer binder, polyacrylic acid (PAA), substantially improving the mechanical properties. As a result, the use of **1.19** as a binder for the anode yielded a 91% capacity retention after 150 cycles. In contrast, the anode with a more standard PAA binder attained only 48% of its original capacity after 50 cycles. The interlocked crosslinks were proposed to slide and equalize stress to cushion the silicon microparticles during charge-discharge cycles.

Dynamic covalent chemistry[175] has been introduced into SRMs to provide an additional mechanism for healing. For instance, boronic acid and diol moieties have been attached to CD

rings to access interlocked dynamic polyrotaxane crosslinkers.[176] This combination of sliding crosslinks and dynamic bonds makes SRMs capable of self-healing with greater efficiency than non-sliding dynamic covalent networks, making them excellent candidates for scratch-resistant coatings. Similarly, combining sliding crosslinks with carboxyl-Fe^{3+} coordination yields tough and highly recoverable metallosupramolecular hydrogels.[177]

Stimuli-responsive hydrogels have garnered interest in several fields, including drug delivery, biosensing, and artificial muscles.[178–180] Sliding-crosslinks hold great promise for improving the properties of existing stimuli-responsive hydrogels, particularly those that undergo large or rapid volume changes that cause stress concentrations in fixed-crosslinked networks. For example, α-CDs functionalized with photoresponsive azobenzene moieties provide access to SRMs with large photoinduced swelling-deswelling.[181] The sliding crosslinks distribute stresses evenly throughout the network, leading to more robust materials with longer lifetimes.

Polymers with an LCST are commonly used in stimuli-responsive hydrogel research, with poly(*N*-isopropylacrylamide) (PNIPAM) being the most widely studied.[182] However, these fixed-crosslink hydrogels often become brittle or lose transparency upon repeated swelling and deswelling. As such, it is not surprising that polyrotaxanes have been incorporated into PNIPAM networks[183–185] and other polyacylamides[186,187] to improve toughness, swelling capacity, optical properties, and material lifetime. In general, the better-performing materials used polyrotaxane **1.6** crosslinkers with carboxylated rings where the ionic groups enhance water solubility and uptake.

Building on such studies, it has been shown that the shrinking rate of PNIPAM-based SRMs can be tuned by varying the amount of "dangling chains" attached to the CD rings. In particular, Takeota and coworkers[188] prepared polyrotaxanes in which alkyne or azide end-capped PNIPAM chain-grafts were present on rings of carboxylated polyrotaxane **1.6** (**1.20$_{alk}$** and **1.20$_{az}$**,

Figure 1.7d, left)). Subsequent crosslinking of **1.20$_{alk}$** and **1.20$_{az}$** via click reaction yields SRM **1.21**, where the ratio of crosslinked to dangling chains was controlled by varying the reaction time. Increasing the number of dangling chains from 39% to 46% increased the equilibrium swelling ratio and accelerated the shrinking rate (Figure 1.7d, right). It was suggested that the ring mobility allows the thermoresponsive dangling ends to distribute themselves evenly throughout the network, improving the material response.

1.4.5 SRM Resins

Highly crosslinked, high-T_g resins are the oldest synthetic commercial polymers produced and are still commonly used today as structural, impact-resistant, or adhesive materials. Unfortunately, these materials are often brittle, trading toughness for high modulus. However, incorporating slide-ring crosslinks into the materials can improve both modulus and toughness. For example, Seo and coworkers[189] incorporated polyrotaxane **1.5** into a commonly-used epoxy resin. Here the α-CD hydroxy groups act as nucleophiles during the curing reaction, resulting in a material that has both covalent and sliding crosslinks. Given that each α-CD possesses 18 hydroxy groups, the resulting SRMs have a higher crosslinking density than the original material, which leads to greater stiffness and tensile strength. However, despite the stiffness of the surrounding matrix, the PEG chains of the polyrotaxane are still able to slide through the CDs, allowing the material to relieve internal stresses.[190] Such polymer chain mobility has also been observed in polyrotaxane glasses[42], leading to greater strains-at-break and toughness.

The mechanical properties of SRM resins can be tuned by controlling the amount of topological crosslinking by modifying the α-CDs in **1.5**. For instance, tertiary amines installed on the polyrotaxanes accelerate resin formation while limiting the number of hydroxyl groups available for crosslinking. As a result, the crosslink density increases when an average of one

tertiary amine per CD is used but decreases when a CD with an average of four tertiary amines per CD is used.[189] All SRM resins showed improved toughness compared to the fixed-crosslinked epoxy, and this toughness increased concomitantly with crosslink density and stiffness, in contrast to conventional resins and unlike the lightly-crosslinked, low-T_g SRMs discussed above.[191] Similar enhancements in toughness can be achieved by incorporating polyrotaxane **1.5** as a crosslinker into other high T_g resins,[192–194] in addition to improvements in adhesive strength.[195] In each case, the higher extensibility of the materials is attributed to the additional mobility of the slide-ring crosslinks in the network.

1.4.6 SRMs Containing [3]Rotaxane Crosslinks

Notably, an ever-expanding library of distinct SRM architectures is developing that continues to investigate how topological crosslinking enhances material properties. For example, oligomacrocycles and dumbbells can assemble SRMs to create recyclable or degradable materials.[161,196–200] Fluorescent, vinyl-based polymers have been made by crosslinking stimuli-degradable [3]rotaxane moieties **1.22** where upon heat, slippage of the dumbbell molecule causes decrosslinking of the network.[201,202] Fluorescence intensity monitors the dissociation process, where the blue fluorescence of the rotaxane crosslinked polymer **1.23** changes to green when the axel leaves the crosslinking moiety (Figure 1.8a).

Takata and coworkers recently extended investigations into crosslink mobility in slide-ring gels by exploiting different rotaxane architectures as crosslinks in PEG- and vinyl-based networks.[198,199] Supramolecular crosslinkers **1.24**, comprised of γ-CD doubly-threaded with terminal-bulky PEG- or poly(THF)-based macromonomers, were used as crosslinkers to make SRMs **1.25** (Figure 1.8b). Increasing the length of the axis polymer was shown to provide higher degrees of flexibility and, therefore, an improvement in the elongation of such networks because

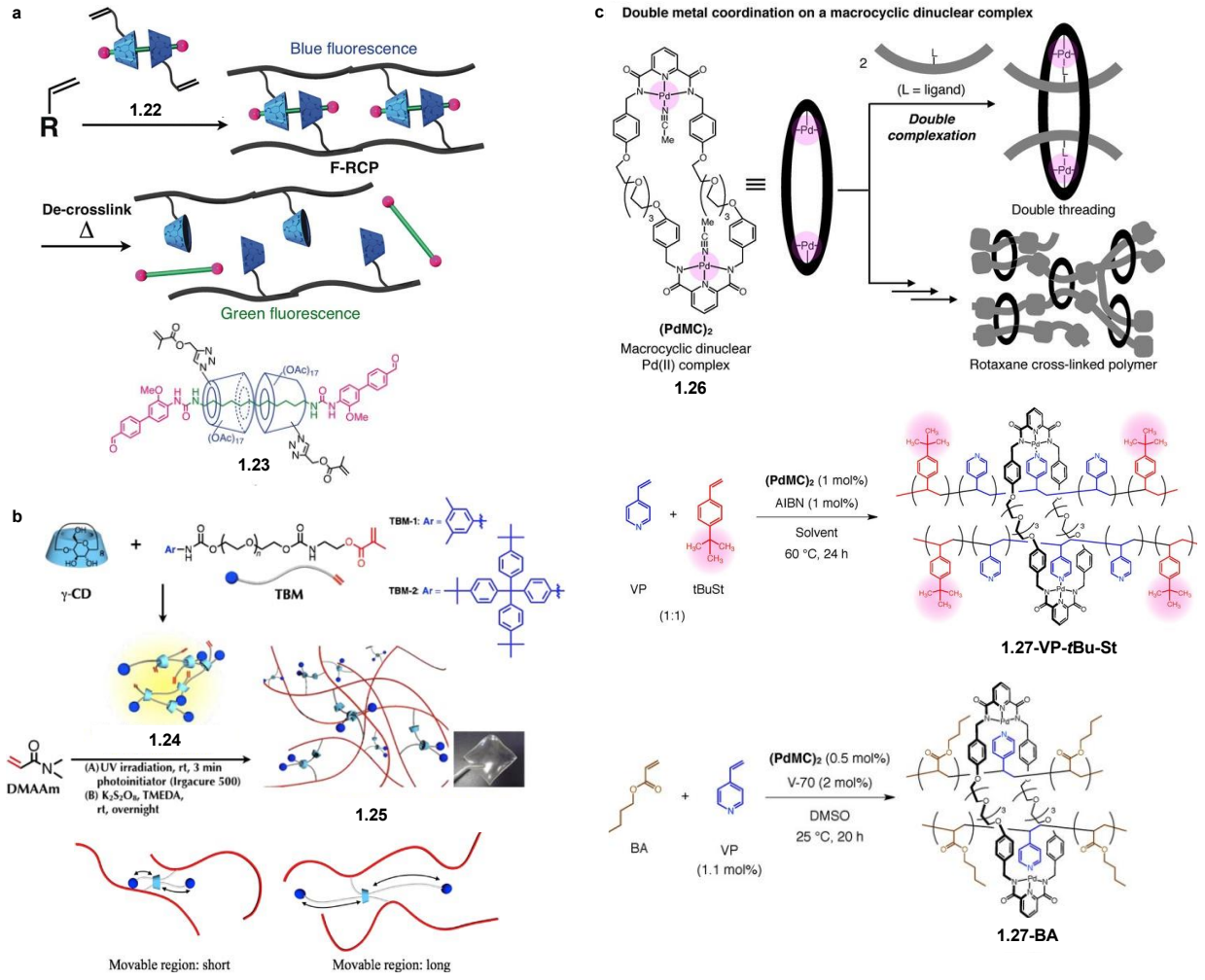

Figure 1.8. SRMs containing [3]rotaxane crosslinks. a) Size-complementary [3]rotaxane crosslinker **1.22** used to synthesize stimuli-degradable rotaxane networks (**1.23**) via radical polymerization; decrosslinking the network by heating changes fluorescence from blue to green as the axle is removed from the crosslink. b) Synthesis of rotaxane networks via radical polymerization of *N*,*N*-dimethyl acrylamide (DMAAm) with vinylic supramolecular crosslinkers **1.24** from γ-CD threaded with two terminal-bulky macromonomers (TBMs). Longer poly(THF) chains in TBM provide higher degrees of flexibility and mechanical properties in SRM **1.25** than shorter p(THF) chains. c) Double metal coordination on a macrocyclic dinuclear Pd(II) complex (**1.26**, top) used as a [3]rotaxane crosslink in the co-polymerization of vinyl pyridine (VP) with 4-tert-butylstyrene (middle) or *n*-butyl acrylate (BA, bottom) to make **1.27-VP-*t*Bu-St** and **1.27-BA** comprised of doubly-threaded rotaxane crosslinks. Adapted from Ref. 201 and Ref. 205 with permission from John Wiley and Sons, and Ref. 203 from Elsevier.

the rings have a longer distance to slide. This study shows that the movable region of a polymer chain at the crosslink points strongly influences mechanical properties.

The key to forming the doubly-threaded architecture mentioned above comes from designing a stable inclusion complex that can also undergo polymerization. Expanding on this concept, Takata also showed that a macrocyclic dinuclear palladium complex **1.26** could be used as a crosslinker in the polymerization of vinyl pyridine to form doubly-threaded SRMs (Figure 1.8c, top).[205] A copolymer was required to stabilize the PVP network; styrene was not bulky enough to prevent dethreading of the doubly-threaded ring, but tert-butyl styrene and butyl acrylate both provided insoluble materials (**1.27-VP-*t*Bu-St** and **1.27-BA**, Figure 1.8c, bottom). Mechanical properties were not reported for these doubly-threaded SR materials because of the difficulty in preparing the appropriate films required for tensile testing.

1.5 Conclusions

While MIPs may have initially been targeted as an intriguing synthetic challenge or for their aesthetic appeal, studies have shown that these polymers offer unique property profiles, potentially providing advantages in many applications. Their utility is, perhaps, most clearly demonstrated through polyrotaxane-based materials such as SRMs; the facile, scalable, and inexpensive synthesis of **1.5**, for example, has propelled the research beyond chemistry and into materials engineering. Over the past two decades, researchers have established relationships between structure and mechanical properties for such materials (at least at a qualitative level), while continued advances in material preparation and molecular simulations promise to improve our understanding further. As a result, these materials have already been applied toward (and in some cases even commercialized in) several technologies, such as Li-ion batteries and anti-scratch coatings.

New synthetic strategies are required to expand the library of interlocked architectures and synthesize these new MIPs in quantities large enough for detailed material characterization, both of which are significant challenges. While CD-based MIPs have provided access to a wealth of exciting and valuable materials, a greater diversity of MIP ring components would dramatically expand the materials design space. As discussed, the crosslink density, the number and size of the rings, and interactions between the ring and polymer all influence the figure-of-eight crosslink mobility. The potential of these gels is limited; current systems rely on the interaction between polyethylene glycol and α-cyclodextrin rings to form polyrotaxanes, so other polymers and macrocycles with different sizes and conformations cannot be incorporated into the crosslinked network (**1.13**, Figure 1.9a). Furthermore, intermolecular crosslinking between polyrotaxane chains results in an uncontrollable, inhomogeneous density distribution of uncrosslinked rings between figure-of-eight crosslinks.

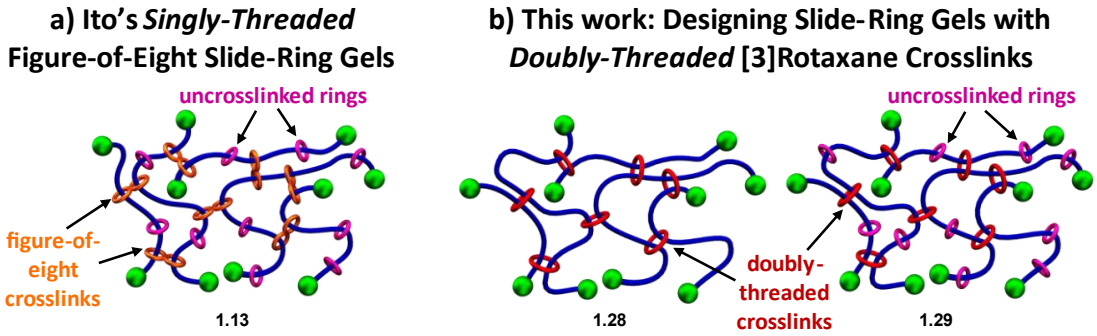

Figure 1.9. Crosslinking through doubly-threaded rings. a) Traditional slide-ring gel topology (**1.13**, synthesized by Ito) comprised of singly-threaded figure-of-eight crosslinking sites (orange) with an uneven distribution of uncrosslinked rings (pink). b) This dissertation aims to develop a new type of ring crosslink based on the doubly-threaded [3]rotaxane topology (red) and design a system to control the number and valency of threaded rings in **1.28** and **1.29**.

Ito's SRGs comprise only singly-threaded rings that prevent polymer chains from interacting as they slide through figure-of-eight crosslinks. This dissertation discusses the chemistry and components required for developing a new crosslink topology based on the doubly-

threaded [3]rotaxane topology to form fully interlocked doubly-threaded slide-ring gels **1.28** and **1.29** (Figure 1.9b). Chapter 2 explores the mobility of doubly-threaded rings along PEG chains through the design and synthesis of slide-ring polycatenane networks (SR-PCNs), a new type of MIP architecture, through mechanical analysis. Chapter 3 focuses on characterizing the poroelastic and viscoelastic relaxations of SR-PCNs in different solvents. Singly-threaded rings and polyrotaxane polymerizations are developed in Chapter 4 using nitrile-oxide/alkyne cycloaddition (NOAC) as a model system for adding uncrosslinked rings into doubly-threaded SR-PCNs and MIPs such as **1.29**. Chapters 5 and 6 explore the assembly and stoppering of pseudo[3]rotaxanes from new ditopic rings under different maleimide click conditions that will be used to functionalize new MIP and dynamic networks. The synthesis and characterization discussed in this dissertation lead to Chapter 7, which demonstrates how NOAC polymerization can be used to develop polycatenane networks and fully interlocked doubly-threaded slide-ring materials **1.28** and **1.29** with control over the number (and valency) of threaded rings in the network.

1.6 References

(1) Hart, L. F.; Hertzog, J. E.; Rauscher, P. M.; Rawe, B. W.; Tranquilli, M. M.; Rowan, S. J. Material Properties and Applications of Mechanically Interlocked Polymers. *Nat. Rev. Mater.* **2021**, *6* (6), 508–530. https://doi.org/10.1038/s41578-021-00278-z.

(2) Beves, J. E.; Blight, B. A.; Campbell, C. J.; Leigh, D. A.; McBurney, R. T. Strategies and Tactics for the Metal-Directed Synthesis of Rotaxanes, Knots, Catenanes, and Higher Order Links. *Angew. Chemie - Int. Ed.* **2011**, *50* (40), 9260–9327. https://doi.org/10.1002/anie.201007963.

(3) Hubin, T. J.; Busch, D. H. Template Routes to Interlocked Molecular Structures and Orderly Molecular Entanglements. *Coord. Chem. Rev.* **2000**, *200–202*, 5–52. https://doi.org/10.1016/S0010-8545(99)00242-8.

(4) Niu, Z.; Gibson, H. W. Polycatenanes. *Chem. Rev.* **2009**, *109* (11), 6024–6046. https://doi.org/10.1021/cr900002h.

(5) Fang, L.; Olson, M. A.; Benítez, D.; Tkatchouk, E.; Goddard III, W. A.; Stoddart, J. F. Mechanically Bonded Macromolecules. *Chem. Soc. Rev.* **2010**, *39* (1), 17–29. https://doi.org/10.1039/B917901A.

(6) Arunachalam, M.; Gibson, H. W. Recent Developments in Polypseudorotaxanes and Polyrotaxanes. *Prog. Polym. Sci.* **2014**, *39* (6), 1043–1073. https://doi.org/10.1016/j.progpolymsci.2013.11.005.

(7) Takata, T.; Kihara, N.; Furusho, Y. Polyrotaxanes and Polycatenanes: Recent Advances in Syntheses and Applications of Polymers Comprising of Interlocked Structures. *Adv. Polym. Sci.* **2004**, *171*, 1–75. https://doi.org/10.1007/b95529.

(8) Garcia-Rio, L.; Otero-Espinar, F. J.; Luzardo-Alvarez, A.; Blanco-Mendez, J. Cyclodextrin Based Rotaxanes, Polyrotaxanes and Polypseudorotaxanes and Their Biomedical Applications. *Curr. Top. Med. Chem.* **2014**, *14* (4), 478–493. https://doi.org/10.2174/1568026613666131219123910.

(9) Schill, G.; Zollenkopf, H. Rotaxan-Verbindungen, 1. *Justus Liebigs Ann. Chem.* **1969**, *721* (1), 53–74. https://doi.org/10.1002/jlac.19697210109.

(10) Wasserman, E. The Preparation of Interlocking Rings: A Catenane. *J. Am. Chem. Soc.* **1960**, *82* (16), 4433–4434. https://doi.org/10.1021/ja01501a082.

(11) Dietrich-Buchecker, C. O.; Sauvage, J.-P. A Synthetic Molecular Trefoil Knot. *Angew. Chemie Int. Ed. English* **1989**, *28* (2), 189–192. https://doi.org/10.1002/anie.198901891.

(12) Chichak, K. S.; Cantrill, S. J.; Pease, A. R.; Chiu, S.-H.; Cave, G. W. V.; Atwood, J. L.; Stoddart, J. F. Molecular Borromean Rings. *Science (80-.).* **2004**, *304* (5675), 1308–1312. https://doi.org/10.1126/science.1096914.

(13) Harrison, I. T.; Harrison, S. The Synthesis of a Stable Complex of a Macrocycle and a Threaded Chain. *J. Am. Chem. Soc.* **1967**, *89* (22), 5723–5724. https://doi.org/10.1021/ja00998a052.

(14) Takata, T.; Kihara, N.; Furusho, Y. Polyrotaxanes and Polycatenanes: Recent Advances in Syntheses and Applications of Polymers Comprising of Interlocked Structures. *Adv. Polym. Sci.* **2004**, *171*, 1–75. https://doi.org/10.1007/b95529.

(15) Griffiths, K. E.; Stoddart, J. F. Template-Directed Synthesis of Donor/Acceptor [2]Catenanes and [2]Rotaxanes. *Pure Appl. Chem.* **2008**, *80* (3). https://doi.org/10.1351/pac200880030485.

(16) Dietrich-Buchecker, C. O.; Sauvage, J. P.; Kern, J. M. Templated Synthesis of Interlocked Macrocyclic Ligands: The Catenands. *Journal of the American Chemical Society*. 1984, pp 3043–3045. https://doi.org/10.1021/ja00322a055.

(17) Hirose, K.; Nishihara, K.; Harada, N.; Nakamura, Y.; Masuda, D.; Araki, M.; Tobe, Y. Highly Selective and High-Yielding Rotaxane Synthesis via Aminolysis of Prerotaxanes Consisting of a Ring Component and a Stopper Unit. *Org. Lett.* **2007**, *9* (16), 2969–2972. https://doi.org/10.1021/ol070999w.

(18) Dietrich-Buchecker, C. O.; Sauvage, J. P.; Kintzinger, J. P. Une Nouvelle Famille de Molecules : Les Metallo-Catenanes. *Tetrahedron Lett.* **1983**, *24* (46), 5095–5098. https://doi.org/10.1016/S0040-4039(00)94050-4.

(19) Dietrich-Buchecker, C. O.; Sauvage, J. P. Synthese de Composes Polyethers Macrocycliques Derives de La Phenanthroline-1,10 Diphenyl-2,9. *Tetrahedron Lett.* **1983**, *24* (46), 5091–5094. https://doi.org/10.1016/S0040-4039(00)94049-8.

(20) Wu, C.; Lecavalier, P. R.; Shen, Y. X.; Gibson, H. W. Synthesis of a Rotaxane via the Template Method. *Chem. Mater.* **1991**, *3* (4), 569–572. https://doi.org/10.1021/cm00016a002.

(21) Hänni, K. D.; Leigh, D. A. The Application of CuAAC 'Click' Chemistry to Catenane and Rotaxane Synthesis. *Chem. Soc. Rev.* **2010**, *39* (4), 1240–1251. https://doi.org/10.1039/B901974J.

(22) Zhou, H. Y.; Zong, Q. S.; Han, Y.; Chen, C. F. Recent Advances in Higher Order Rotaxane Architectures. *Chem. Commun.* **2020**, *56* (69), 9916–9936. https://doi.org/10.1039/d0cc03057k.

(23) Qiu, Y.; Song, B.; Pezzato, C.; Shen, D.; Liu, W.; Zhang, L.; Feng, Y.; Guo, Q. H.; Cai, K.; Li, W.; Chen, H.; Nguyen, M. T.; Shi, Y.; Cheng, C.; Dean Astumian, R.; Li, X.; Fraser Stoddart, J. A Precise Polyrotaxane Synthesizer. *Science (80-.).* **2020**, *368* (6496), 1247–1253. https://doi.org/10.1126/science.abb3962.

(24) Amano, S.; Fielden, S. D. P.; Leigh, D. A. A Catalysis-Driven Artificial Molecular Pump. *Nature* **2021**, *594* (7864), 529–534. https://doi.org/10.1038/s41586-021-03575-3.

(25) McGonigal, P. R. Multiply Threaded Rotaxanes. *Supramol. Chem.* **2018**, *30* (9), 782–794. https://doi.org/10.1080/10610278.2018.1433832.

(26) Heckel, A.; Famulok, M.; Purohit, C. S.; Ackermann, D.; Schmidt, T. L.; Hannam, J. S. A Double-Stranded DNA Rotaxane. *Nat. Nanotechnol.* **2010**, *5* (6), 436–442. https://doi.org/10.1038/nnano.2010.65.

(27) Amici, G.; Caraglio, M.; Orlandini, E.; Micheletti, C. Topologically Linked Chains in Confinement. *ACS Macro Lett.* **2019**, *8* (4), 442–446. https://doi.org/10.1021/acsmacrolett.9b00114.

(28) Prikhod'ko, A. I.; Sauvage, J. P. Passing Two Strings through the Same Ring Using an Octahedral Metal Center as Template: A New Synthesis of [3]Rotaxanes. *J. Am. Chem. Soc.* **2009**, *131* (19), 6794–6807. https://doi.org/10.1021/ja809267z.

(29) Yamashita, Y.; Mutoh, Y.; Yamasaki, R.; Kasama, T.; Saito, S. Synthesis of [3]Rotaxanes That Utilize the Catalytic Activity of a Macrocyclic Phenanthroline-Cu Complex: Remarkable Effect of the Length of the Axle Precursor. *Chem. - A Eur. J.* **2015**. https://doi.org/10.1002/chem.201405090.

(30) Saito, S.; Nakazono, K.; Takahashi, E. Template Synthesis of [2]Rotaxanes with Large Ring Components and Tris(Biphenyl)Methyl Group as the Blocking Group. The Relationship between the Ring Size and the Stability of the Rotaxanes. *J. Org. Chem.* **2006**, *71* (19), 7477–7480. https://doi.org/10.1021/jo060829h.

(31) Hayashi, R.; Mutoh, Y.; Kasama, T.; Saito, S. Synthesis of [3]Rotaxanes by the Combination of Copper-Mediated Coupling Reaction and Metal-Template Approach. *J. Org. Chem.* **2015**, *80* (15), 7536–7546. https://doi.org/10.1021/acs.joc.5b01120.

(32) Inouye, M.; Hayashi, K.; Yonenaga, Y.; Itou, T.; Fujimoto, K.; Uchida, T.; Iwamura, M.; Nozaki, K. A Doubly Alkynylpyrene-Threaded [4]Rotaxane That Exhibits Strong Circularly Polarized Luminescence from the Spatially Restricted Excimer. *Angew. Chemie Int. Ed.* **2014**, *53* (52), 14392–14396. https://doi.org/10.1002/anie.201408193.

(33) Hayashi, K.; Miyaoka, Y.; Ohishi, Y.; Uchida, T. aki; Iwamura, M.; Nozaki, K.; Inouye, M. Observation of Circularly Polarized Luminescence of the Excimer from Two Perylene Cores in the Form of [4]Rotaxane. *Chem. - A Eur. J.* **2018**, *24* (55), 14613–14616. https://doi.org/10.1002/chem.201803215.

(34) Danon, J. J.; Leigh, D. A.; McGonigal, P. R.; Ward, J. W.; Wu, J. Triply Threaded [4]Rotaxanes. *J. Am. Chem. Soc.* **2016**, *138* (38), 12643–12647. https://doi.org/10.1021/jacs.6b07733.

(35) Huang, F. H.; Gibson, H. W. Polypseudorotaxanes and Polyrotaxanes. *Prog. Polym. Sci.* **2005**, *30* (10), 982–1018. https://doi.org/10.1016/j.progpolymsci.2005.07.003.

(36) Harrison, I. T.; Harrison, S. Synthesis of a Stable Complex of a Macrocycle and a Threaded Chain. *J. Am. Chem. Soc.* **1967**, *89* (22), 5723–5724. https://doi.org/10.1021/ja00998a052.

(37) Wenz, G.; Keller, B. Threading Cyclodextrin Rings on Polymer Chains. *Angew. Chem. Int.* **1992**, *31* (2), 197–199.

(38) Harada, A.; Li, J.; Kamachi, M. The Molecular Necklace: A Rotaxane Containing Many Threaded α-Cyclodextrins. *Nature* **1992**, *356* (March), 325–327.

(39) Fleury, G.; Brochon, C.; Schlatter, G.; Bonnet, G.; Lapp, A.; Hadziioannou, G. Synthesis and Characterization of High Molecular Weight Polyrotaxanes: Towards the Control over a Wide Range of Threaded α-Cyclodextrins. *Soft Matter* **2005**, *1* (5), 378–385. https://doi.org/10.1039/b510331b.

(40) Miyake, K.; Yasuda, S.; Harada, A.; Sumaoka, J.; Komiyama, M.; Shigekawa, H. Formation Process of Cyclodextrin Necklace−Analysis of Hydrogen Bonding on a Molecular Level. *J. Am. Chem. Soc.* **2003**, *125* (17), 5080–5085. https://doi.org/10.1021/ja026224u.

(41) Inomata, A.; Sakai, Y.; Zhao, C.; Ruslim, C.; Shinohara, Y.; Yokoyama, H.; Amemiya, Y.; Ito, K. Crystallinity and Cooperative Motions of Cyclic Molecules in Partially Threaded Solid-State Polyrotaxanes. *Macromolecules* **2010**, *43* (10), 4660–4666. https://doi.org/10.1021/ma100259t.

(42) Kato, K.; Mizusawa, T.; Yokoyama, H.; Ito, K. Polyrotaxane Glass: Peculiar Mechanics Attributable to the Isolated Dynamics of Different Components. *J. Phys. Chem. Lett.* **2015**, *6* (20), 4043–4048. https://doi.org/10.1021/acs.jpclett.5b01782.

(43) Mayumi, K.; Ito, K. Structure and Dynamics of Polyrotaxane and Slide-Ring Materials. *Polymer (Guildf).* **2010**, *51* (4), 959–967. https://doi.org/10.1016/j.polymer.2009.12.019.

(44) Zhao, C.; Domon, Y.; Okumura, Y.; Okabe, S.; Shibayama, M.; Ito, K. Sliding Mode of Cyclodextrin in Polyrotaxane and Slide-Ring Gel. *J. Phys. Condens. Matter* **2005**, *17* (31), S2841–S2846. https://doi.org/10.1088/0953-8984/17/31/009.

(45) Yasuda, Y.; Hidaka, Y.; Mayumi, K.; Yamada, T.; Fujimoto, K.; Okazaki, S.; Yokoyama, H.; Ito, K. Molecular Dynamics of Polyrotaxane in Solution Investigated by Quasi-Elastic Neutron Scattering and Molecular Dynamics Simulation: Sliding Motion of Rings on Polymer. *J. Am. Chem. Soc.* **2019**, *141*, 9655–9663.

(46) Yasuda, Y.; Toda, M.; Mayumi, K.; Yokoyama, H.; Morita, H.; Ito, K. Sliding Dynamics of Ring on Polymer in Rotaxane: A Coarse-Grained Molecular Dynamics Simulation Study. *Macromolecules* **2019**, *52* (10), 3787–3793. https://doi.org/10.1021/acs.macromol.9b00118.

(47) Mayumi, K.; Osaka, N.; Endo, H.; Yokoyama, H.; Sakai, Y.; Shibayama, M.; Ito, K. Concentration-Induced Conformational Change in Linear Polymer Threaded into Cyclic Molecules. *Macromolecules* **2008**, *41* (17), 6480–6485. https://doi.org/10.1021/ma801021g.

(48) Yamada, S.; Sanada, Y.; Tamura, A.; Yui, N.; Sakurai, K. Chain Architecture and Flexibility of α-Cyclodextrin/PEG Polyrotaxanes in Dilute Solutions. *Polym. J.* **2015**, *47*

(6), 464–467. https://doi.org/10.1038/pj.2015.18.

(49) Gibson, H. W.; Liu, S.; Gong, C.; Ji, Q.; Joseph, E. Studies of the Formation of Poly(Ester Rotaxane)s from Diacid Chlorides, Diols, and Crown Ethers and Their Properties. *Macromolecules* **1997**, *30* (13), 3711–3727. https://doi.org/10.1021/ma961362n.

(50) Gong, C.; Gibson, H. W. Controlling Microstructure in Polymeric Molecular Shuttles: Solvent-Induced Localization of Macrocycles in Poly(Urethane/Crown Ether) Rotaxanes. *Angew. Chemie (International Ed. English)* **1997**, *36* (21), 2331–2333. https://doi.org/10.1002/anie.199723311.

(51) Shen, Y. X.; Xie, D.; Gibson, H. W. Polyrotaxanes Based on Polyurethane Backbones and Crown Ether Cyclics. 1. Synthesis. *J. Am. Chem. Soc.* **1994**, *116* (2), 537–548. https://doi.org/10.1021/ja00081a014.

(52) Gong, C.; Glass, T. E.; Gibson, H. W. Poly(Urethane/Crown Ether Rotaxane)s with Solvent Switchable Microstructures. *Macromolecules* **1998**, *31* (2), 308–313. https://doi.org/10.1021/ma970812o.

(53) Gong, C.; Ji, Q.; Subramaniam, C.; Gibson, H. W. Main Chain Polyrotaxanes by Threading Crown Ethers onto A Preformed Polyurethane: Preparation and Properties. *Macromolecules* **1998**, *31* (6), 1814–1818. https://doi.org/10.1021/ma9713116.

(54) Gong, C.; Gibson, H. W. Synthesis and Characterization of a Polyester/Crown Ether Rotaxane Derived from a Difunctional Blocking Group. *Macromolecules* **1996**, *29* (22), 7029–7033. https://doi.org/10.1021/ma960769p.

(55) Gong, C. G.; Gibson, H. W. Polyrotaxanes and Related Structures: Synthesis and Properties. *Curr. Opin. Solid State Mater. Sci.* **1997**, *2* (6), 647–652. https://doi.org/10.1016/S1359-0286(97)80004-6.

(56) Gong, C.; Gibson, H. W. Dethreading during the Preparation of Polyrotaxanes. *Macromol. Chem. Phys.* **1997**, *198* (7), 2321–2332. https://doi.org/10.1002/macp.1997.021980723.

(57) Chen, Z.; Aoki, D.; Uchida, S.; Marubayashi, H.; Nojima, S.; Takata, T. Effect of Component Mobility on the Properties of Macromolecular [2]Rotaxanes. *Angew. Chemie - Int. Ed.* **2016**, *55* (8), 2778–2781. https://doi.org/10.1002/anie.201510953.

(58) Uenuma, S.; Maeda, R.; Kato, K.; Mayumi, K.; Yokoyama, H.; Ito, K. Drastic Change of Mechanical Properties of Polyrotaxane Bulk: ABA-BAB Sequence Change Depending on Ring Position. *ACS Macro Lett.* **2019**, *8* (2), 140–144. https://doi.org/10.1021/acsmacrolett.8b00896.

(59) Uenuma, S.; Maeda, R.; Takahashi, S.; Kato, K.; Yokoyama, H.; Ito, K. Self-Assembled Structure of Polyrotaxane Consisting of β-Cyclodextrin and Poly(Ethylene Oxide)-Block-Poly(Propylene Oxide)-Block-Poly(Ethylene Oxide) Triblock Copolymer in Bulk System. *Chem. Lett.* **2016**, *45* (8), 991–993. https://doi.org/10.1246/cl.160490.

(60) Lin, Q.; Li, L.; Tang, M.; Hou, X.; Ke, C. Rapid Macroscale Shape Morphing of 3D-Printed Polyrotaxane Monoliths Amplified from PH-Controlled Nanoscale Ring Motions. *J. Mater. Chem. C* **2018**, *6* (44), 11956–11960. https://doi.org/10.1039/c8tc02834f.

(61) Lin, Q.; Hou, X.; Ke, C. Ring Shuttling Controls Macroscopic Motion in a Three-Dimensional Printed Polyrotaxane Monolith. *Angew. Chemie - Int. Ed.* **2017**, *56* (16), 4452–4457. https://doi.org/10.1002/anie.201612440.

(62) Lin, Q.; Tang, M.; Ke, C. Thermo-Responsive 3D-Printed Polyrotaxane Monolith. *Polym. Chem.* **2020**, *11* (2), 304–308. https://doi.org/10.1039/c9py01510h.

(63) Kato, K.; Nemoto, K.; Mayumi, K.; Yokoyama, H.; Ito, K. Ductile Glass of Polyrotaxane Toughened by Stretch-Induced Intramolecular Phase Separation. *ACS Appl. Mater. Interfaces* **2017**, *9* (38), 32436–32440. https://doi.org/10.1021/acsami.7b10845.

(64) Kato, K.; Mizusawa, T.; Yokoyama, H.; Ito, K. Effect of Topological Constraint and Confined Motions on the Viscoelasticity of Polyrotaxane Glass with Different Interactions between Rings. *J. Phys. Chem. C* **2017**, *121* (3), 1861–1869. https://doi.org/10.1021/acs.jpcc.6b11362.

(65) Kato, K.; Ohara, A.; Yokoyama, H.; Ito, K. Prolonged Glass Transition Due to Topological Constraints in Polyrotaxanes. *J. Am. Chem. Soc.* **2019**, *141* (32), 12502–12506. https://doi.org/10.1021/jacs.9b06063.

(66) Cardin, D. J. Encapsulated Conducting Polymers. *Adv. Mater.* **2002**, *14* (8), 553–563. https://doi.org/10.1002/1521-4095(20020418)14:8<553::AID-ADMA553>3.0.CO;2-F.

(67) Mayumi, K.; Ito, K.; Kato, K. *Polyrotaxane and Slide-Ring Materials*; Monographs in Supramolecular Chemistry; Royal Society of Chemistry: Cambridge, 2015.

(68) Frampton, M. J.; Anderson, H. L. Insulated Molecular Wires. *Angew. Chemie - Int. Ed.* **2007**, *46* (7), 1028–1064. https://doi.org/10.1002/anie.200601780.

(69) Terao, J.; Tang, A.; Michels, J. J.; Krivokapic, A.; Anderson, H. L. Synthesis of Poly(Para-Phenylenevinylene) Rotaxanes by Aqueous Suzuki Coupling. *Chem. Commun.* **2004**, 56–57.

(70) Cacialli, F.; Wilson, J. S.; Michels, J. J.; Daniel, C.; Silva, C.; Friend, R. H.; Severin, N.; Samori, P.; Rabe, J. P.; O'connell, M. J.; Taylor, P. N.; Anderson, H. L. Cyclodextrin-Threaded Conjugated Polyrotaxanes as Insulated Molecular Wires with Reduced Interstrand Interactions. *Nat. Mater.* **2002**, *1* (3), 160–164. https://doi.org/10.1038/nmat750.

(71) Taylor, P. N.; O'Connell, M. J.; McNeill, L. A.; Hall, M. J.; Aplin, R. T.; Anderson, H. L. Insulated Molecular Wires: Synthesis of Conjugated Polyrotaxanes by Suzuki Coupling in Water. *Angew. Chemie - Int. Ed.* **2000**, *39* (19), 3456–3460. https://doi.org/10.1002/1521-3773(20001002)39:19<3456::AID-ANIE3456>3.0.CO;2-0.

(72) Michels, J. J.; O'Connell, M. J.; Taylor, P. N.; Wilson, J. S.; Cacialli, F.; Anderson, H. L.

Synthesis of Conjugated Polyrotaxanes. *Chem. - A Eur. J.* **2003**, *9* (24), 6167–6176. https://doi.org/10.1002/chem.200305245.

(73) Van Den Boogaard, M.; Bonnet, G.; Van't Hof, P.; Wang, Y.; Brochon, C.; Van Hutten, P.; Lapp, A.; Hadziioannou, G. Synthesis of Insulated Single-Chain Semiconducting Polymers Based on Polythiophene, Polyfluorene, and β-Cyclodextrin. *Chem. Mater.* **2004**, *16* (23), 4383–4385. https://doi.org/10.1021/cm049665g.

(74) Ikeda, T.; Higuchi, M.; Kurth, D. G. From Thiophene [2]Rotaxane to Polythiophene Polyrotaxane. *J. Am. Chem. Soc.* **2009**, *131* (26), 9158–9159. https://doi.org/10.1021/ja902992c.

(75) Farcas, A.; Aubert, P. H.; Mohanty, J.; Lazar, A. I.; Cantin, S.; Nau, W. M. Molecular Wire Formation from Poly[2,7-(9,9-Dioctylfluorene)-Alt-(5,5′-Bithiophene/Cucurbit[7]Uril)] Polyrotaxane Copolymer. *Eur. Polym. J.* **2015**, *62*, 124–129. https://doi.org/10.1016/j.eurpolymj.2014.11.021.

(76) Belosludov, R. V.; Mizuseki, H.; Ichinoseki, K.; Kawazoe, Y. Theoretical Study on Inclusion Complex of Polyaniline Covered by Cyclodextrins for Molecular Device. *Jpn. J. Appl. Phys* **2002**, *41* (4 B), 2739–2741. https://doi.org/10.1143/JJAP.41.2739.

(77) Belosludov, R. V.; Sato, H.; Farajian, A. A.; Mizuseki, H.; Ichinoseki, K.; Kawazoe, Y. Molecular Enamel Wires for Electronic Devices: Theoretical Study. *Jpn. J. Appl. Phys.* **2003**, *42* (4 B), 2492–2494. https://doi.org/10.1143/jjap.42.2492.

(78) Brovelli, S.; Latini, G.; Frampton, M. J.; McDonnell, S. O.; Oddy, F. E.; Fenwick, O.; Anderson, H. L.; Cacialli, F. Tuning Intrachain versus Interchain Photophysics via Control of the Threading Ratio of Conjugated Polyrotaxanes. *Nano Lett.* **2008**, *8* (12), 4546–4551. https://doi.org/10.1021/nl802775a.

(79) Oddy, F. E.; Brovelli, S.; Stone, M. T.; Klotz, E. J. F.; Cacialli, F.; Anderson, H. L. Influence of Cyclodextrin Size on Fluorescence Quenching in Conjugated Polyrotaxanes by Methyl Viologen in Aqueous Solution. *J. Mater. Chem.* **2009**, *19* (18), 2846–2852. https://doi.org/10.1039/b821950h.

(80) Farcas, A.; Assaf, K. I.; Resmerita, A. M.; Sacarescu, L.; Asandulesa, M.; Aubert, P. H.; Nau, W. M. Cucurbit[7]Uril-Threaded Poly(3,4-Ethylenedioxythiophene): A Novel Processable Conjugated Polyrotaxane. *European J. Org. Chem.* **2019**, *2019* (21), 3442–3450. https://doi.org/10.1002/ejoc.201801724.

(81) Terao, J.; Tsuji, Y. New Synthetic Methods of π-Conjugated Inclusion Complexes with High Conductivity. *J. Incl. Phenom. Macrocycl. Chem.* **2014**, *80* (3–4), 165–175. https://doi.org/10.1007/s10847-014-0381-y.

(82) Grigoras, M.; Stafie, L. Electrically Insulated Molecular Wires. *Supramol. Chem.* **2010**, *22* (4), 237–248. https://doi.org/10.1080/10610270903410496.

(83) Terao, J.; Tanaka, Y.; Tsuda, S.; Kambe, N.; Taniguchi, M.; Kawai, T.; Saeki, A.; Seki, S.

Insulated Molecular Wire with Highly Conductive π-Conjugated Polymer Core. *J. Am. Chem. Soc.* **2009**, *131* (50), 18046–18047. https://doi.org/10.1021/ja908783f.

(84) Terao, J.; Wadahama, A.; Matono, A.; Tada, T.; Watanabe, S.; Seki, S.; Fujihara, T.; Tsuji, Y. Design Principle for Increasing Charge Mobility of π-Conjugated Polymers Using Regularly Localized Molecular Orbitals. *Nat. Commun.* **2013**, *4*, 1691. https://doi.org/10.1038/ncomms2707.

(85) Wankar, J.; Kotla, N. G.; Gera, S.; Rasala, S.; Pandit, A.; Rochev, Y. A. Recent Advances in Host–Guest Self-Assembled Cyclodextrin Carriers: Implications for Responsive Drug Delivery and Biomedical Engineering. *Adv. Funct. Mater.* **2020**, 1909049.

(86) Tamura, A.; Yui, N. Threaded Macromolecules as a Versatile Framework for Biomaterials. *Chem. Commun.* **2014**, *50* (88), 13433–13446. https://doi.org/10.1039/C4CC03709J.

(87) Li, J. J.; Zhao, F.; Li, J. Polyrotaxanes for Applications in Life Science and Biotechnology. *Appl. Microbiol. Biotechnol.* **2011**, *90* (2), 427–443. https://doi.org/10.1007/s00253-010-3037-x.

(88) Loethen, S.; Kim, J.-M.; Thompson, D. H. Biomedical Applications of Cyclodextrin Based Polyrotaxanes. *Polym. Rev.* **2007**, *47* (3), 383–418. https://doi.org/10.1080/15583720701455145.

(89) Arisaka, Y.; Yui, N. Polyrotaxane-Based Biointerfaces with Dynamic Biomaterial Functions. *J. Mater. Chem. B* **2019**, *7* (13), 2123–2129. https://doi.org/10.1039/C9TB00256A.

(90) Yui, N.; Ooya, T. Molecular Mobility of Interlocked Structures Exploiting New Functions of Advanced Biomaterials. *Chem. Eur. J.* **2006**, *12* (26), 6730–6737. https://doi.org/10.1002/chem.200600370.

(91) Patel, P.; Pol, A.; Jain, R.; Dandekar, P. Cyclodextrin Polyrotaxanes: Drug and Nucleic Acid Delivery. In *Encyclopedia of Biomedical Polymers and Polymeric Biomaterials*; Mishra, M., Ed.; CRC press: Boca Raton, 2015.

(92) Ooya, T.; Yamashita, A.; Kurisawa, M.; Sugaya, Y.; Maruyama, A.; Yui, N. Effects of Polyrotaxane Structure on Polyion Complexation with DNA. *Sci. Technol. Adv. Mater.* **2004**, *5* (3), 363–369. https://doi.org/10.1016/j.stam.2003.12.014.

(93) Ooya, T.; Choi, H. S.; Yamashita, A.; Yui, N.; Sugaya, Y.; Kano, A.; Maruyama, A.; Akita, H.; Ito, R.; Kogure, K.; Harashima, H. Biocleavable Polyrotaxane-Plasmid DNA Polyplex for Enhanced Gene Delivery. *J. Am. Chem. Soc.* **2006**, *128* (12), 3852–3853. https://doi.org/10.1021/ja055868+.

(94) Mammen, M.; Choi, S.-K.; Whitesides, G. M. Polyvalent Interactions in Biological Systems: Implications for Design and Use of Multivalent Ligands and Inhibitors. *Angew. Chem. Int.* **1998**, *37* (20), 2754–2794. https://doi.org/10.1002/chin.199909293.

(95) Seo, J.-H.; Kakinoki, S.; Inoue, Y.; Yamaoka, T.; Ishihara, K.; Yui, N. Inducing Rapid Cellular Response on RGD-Binding Threaded Macromolecular Surfaces. *J. Am. Chem. Soc.* **2013**, *135* (15), 5513–5516. https://doi.org/10.1021/ja400817q.

(96) Ooya, T.; Eguchi, M.; Yui, N. Supramolecular Design for Multivalent Interaction: Maltose Mobility along Polyrotaxane Enhanced Binding with Concanavalin A. *J. Am. Chem. Soc.* **2003**, *125* (43), 13016–13017. https://doi.org/10.1021/ja034583z.

(97) Sluysmans, D.; Stoddart, J. F. The Burgeoning of Mechanically Interlocked Molecules in Chemistry. *Trends Chem.* **2019**, *1* (2), 185–197. https://doi.org/10.1016/j.trechm.2019.02.013.

(98) Berná, J.; Leigh, D. A.; Lubomska, M.; Mendoza, S. M.; Pérez, E. M.; Rudolf, P.; Teobaldi, G.; Zerbetto, F. Macroscopic Transport by Synthetic Molecular Machines. *Nat. Mater.* **2005**, *4* (9), 704–710. https://doi.org/10.1038/nmat1455.

(99) Sun, X.; Amabilino, D. B.; Ashton, P. R.; Parsons, I. W.; Fraser Stoddart, J.; Tolley, M. S. Towards the Self-Assembly of Polyrotaxanes. *Macromol. Symp.* **1994**, *77* (1), 191–207. https://doi.org/10.1002/masy.19940770123.

(100) Zhang, W.; Dichtel, W. R.; Stieg, A. Z.; Benitez, D.; Gimzewski, J. K.; Heath, J. R.; Stoddart, J. F. Folding of a Donor-Acceptor Polyrotaxane by Using Noncovalent Bonding Interactions. *Proc. Natl. Acad. Sci.* **2008**, *105* (18), 6514–6519. https://doi.org/10.1073/pnas.0711072105.

(101) Zhu, Z.; Bruns, C. J.; Li, H.; Lei, J.; Ke, C.; Liu, Z.; Shafaie, S.; Colquhoun, H. M.; Stoddart, J. F. Synthesis and Solution-State Dynamics of Donor–Acceptor Oligorotaxane Foldamers. *Chem. Sci.* **2013**, *4* (4), 1470–1483. https://doi.org/10.1039/c3sc00015j.

(102) Basu, S.; Coskun, A.; Friedman, D. C.; Olson, M. A.; Benítez, D.; Tkatchouk, E.; Barin, G.; Yang, J.; Fahrenbach, A. C.; Goddard, W. A.; Stoddart, J. F. Donor-Acceptor Oligorotaxanes Made to Order. *Chem. - A Eur. J.* **2011**, *17* (7), 2107–2119. https://doi.org/10.1002/chem.201001822.

(103) Zhu, Z.; Li, H.; Liu, Z.; Lei, J.; Zhang, H.; Botros, Y. Y.; Stern, C. L.; Sarjeant, A. A.; Stoddart, J. F.; Colquhoun, H. M. Oligomeric Pseudorotaxanes Adopting Infinite-Chain Lattice Superstructures. *Angew. Chemie Int. Ed.* **2012**, *51* (29), 7231–7235. https://doi.org/10.1002/anie.201202513.

(104) Sluysmans, D.; Hubert, S.; Bruns, C. J.; Zhu, Z.; Stoddart, J. F.; Duwez, A. S. Synthetic Oligorotaxanes Exert High Forces When Folding under Mechanical Load. *Nat. Nanotechnol.* **2018**, *13* (3), 209–213. https://doi.org/10.1038/s41565-017-0033-7.

(105) Sluysmans, D.; Devaux, F.; Bruns, C. J.; Stoddart, J. F.; Duwez, A.-S. Dynamic Force Spectroscopy of Synthetic Oligorotaxane Foldamers. *Proc. Natl. Acad. Sci.* **2018**, *115* (38), 9362–9366. https://doi.org/10.1073/pnas.1712790115.

(106) Pezzato, C.; Nguyen, M. T.; Cheng, C.; Kim, D. J.; Otley, M. T.; Stoddart, J. F. An Efficient

Artificial Molecular Pump. *Tetrahedron* **2017**, *73* (33), 4849–4857. https://doi.org/10.1016/j.tet.2017.05.087.

(107) Qiu, Y.; Zhang, L.; Pezzato, C.; Feng, Y.; Li, W.; Nguyen, M. T.; Cheng, C.; Shen, D.; Guo, Q. H.; Shi, Y.; Cai, K.; Alsubaie, F. M.; Astumian, R. D.; Stoddart, J. F. A Molecular Dual Pump. *J. Am. Chem. Soc.* **2019**, *141* (44), 17472–17476. https://doi.org/10.1021/jacs.9b08927.

(108) Qiu, Y.; Song, B.; Pezzato, C.; Shen, D.; Liu, W.; Zhang, L.; Feng, Y.; Guo, Q.-H.; Cai, K.; Li, W.; Chen, H.; Nguyen, M. T.; Shi, Y.; Cheng, C.; Dean Astumian, R.; Li, X.; Fraser Stoddart, J. A Precise Polyrotaxane Synthesizer. *Science (80-.).* **2020**, *368* (June), 1247–1253.

(109) Whittaker, A. K. The Structure of Polymer Networks. In *Modern Magnetic Resonance*; Webb, G. A., Ed.; Springer, Cham: Dordrecht, 2006; pp 583–589.

(110) Okumura, Y.; Ito, K. The Polyrotaxane Gel: A Topological Gel by Figure-of-Eight Cross-Links. *Adv. Mater.* **2001**, *13* (7), 485–487. https://doi.org/doi:10.1002/1521-4095(200104)13:7<485::AID-ADMA485>3.0.CO;2-T.

(111) Ito, K. Slide-Ring Materials Using Topological Supramolecular Architecture. *Curr. Opin. Solid State Mater. Sci.* **2010**, *14* (2), 28–34. https://doi.org/10.1016/j.cossms.2009.08.005.

(112) Neal, E. A.; Goldup, S. M. Chemical Consequences of Mechanical Bonding in Catenanes and Rotaxanes: Isomerism, Modification, Catalysis and Molecular Machines for Synthesis. *Chem. Commun.* **2014**, *50* (40), 5128–5142. https://doi.org/10.1039/C3CC47842D.

(113) Karino, T.; Okumura, Y.; Ito, K.; Shibayama, M. SANS Studies on Spatial Inhomogeneities of Slide-Ring Gels. *Macromolecules* **2004**, *37* (16), 6177–6182. https://doi.org/10.1021/ma049598b.

(114) Liu, C.; Kadono, H.; Yokoyama, H.; Mayumi, K.; Ito, K. Crack Propagation Resistance of Slide-Ring Gels. *Polymer (Guildf).* **2019**, *181*, 121782. https://doi.org/10.1016/j.polymer.2019.121782.

(115) Kato, K.; Ikeda, Y.; Ito, K. Direct Determination of Cross-Link Density and Its Correlation with the Elastic Modulus of a Gel with Slidable Cross-Links. *ACS Macro Lett.* **2019**, *8* (6), 700–704. https://doi.org/10.1021/acsmacrolett.9b00238.

(116) Jiang, L.; Liu, C.; Mayumi, K.; Kato, K.; Yokoyama, H.; Ito, K. Highly Stretchable and Instantly Recoverable Slide-Ring Gels Consisting of Enzymatically Synthesized Polyrotaxane with Low Host Coverage. *Chem. Mater.* **2018**, *30* (15), 5013–5019. https://doi.org/10.1021/acs.chemmater.8b01208.

(117) Wang, Z.; Li, W.; Yang, X.; Cao, J.; Tu, Y.; Wu, R.; Wang, W. Highly Stretchable and Compressible Shape Memory Hydrogels Based on Polyurethane Network and Supramolecular Interaction. *Mater. Today Commun.* **2018**, *17*, 246–251. https://doi.org/10.1016/J.MTCOMM.2018.09.006.

(118) Kato, K.; Karube, K.; Nakamura, N.; Ito, K. The Effect of Ring Size on the Mechanical Relaxation Dynamics of Polyrotaxane Gels. *Polym. Chem.* **2015**, *6* (12), 2241–2248. https://doi.org/10.1039/C4PY01644K.

(119) Liu, C.; Mayumi, K.; Hayashi, K.; Jiang, L.; Yokoyama, H.; Ito, K. Direct Observation of Large Deformation and Fracture Behavior at the Crack Tip of Slide-Ring Gel. *J. Electrochem. Soc.* **2019**, *166* (9), B3143–B3147. https://doi.org/10.1149/2.0241909jes.

(120) Higgs, P. G.; Ball, R. C. Trapped Entanglements in Rubbers. A Unification of Models. *Europhys. Lett.* **1989**, *8* (4), 357–361. https://doi.org/10.1209/0295-5075/8/4/010.

(121) Kość, M. "Belt-Loop" Model of Chain Entanglement. *Colloid Polym. Sci.* **1988**, *266* (2), 105–113. https://doi.org/10.1007/BF01452807.

(122) Adolf, D. Origins of Entanglement Effects in Rubber Elasticity. *Macromolecules* **1988**, *21* (1), 228–230. https://doi.org/10.1021/ma00179a043.

(123) Kholodenko, A. L.; Vilgis, T. A. Some Geometrical and Topological Problems in Polymer Physics. *Phys. Rep.* **1998**, *298* (5–6), 251–370. https://doi.org/10.1016/S0370-1573(97)00081-1.

(124) Edwards, S. F.; Vilgis, T. The Effect of Entanglements in Rubber Elasticity. *Polymer (Guildf).* **1986**, *27* (4), 483–492. https://doi.org/10.1016/0032-3861(86)90231-4.

(125) Graessley, W. W.; Pearson, D. S. Stress–Strain Behavior in Polymer Networks Containing Nonlocalized Junctions. *J. Chem. Phys.* **1977**, *66* (8), 3363–3370. https://doi.org/10.1063/1.434421.

(126) Ziabicki, A. Contribution of Entrapped Entanglements to Equilibrium Elasticity of Rubber Networks. *Colloid Polym. Sci.* **1976**, *254* (1), 1–5. https://doi.org/10.1007/BF01526734.

(127) Marrucci, G. A Mechanical Model for Rubbers Containing Entanglements. *Rheol. Acta* **1979**, *18* (2), 193–198. https://doi.org/10.1007/BF01542766.

(128) Ito, K. Novel Cross-Linking Concept of Polymer Network: Synthesis, Structure, and Properties of Slide-Ring Gels with Freely Movable Junctions. *Polym. J.* **2007**, *39* (6), 489–499. https://doi.org/10.1295/polymj.pj2006239.

(129) Yasuda, Y.; Masumoto, T.; Mayumi, K.; Toda, M.; Yokoyama, H.; Morita, H.; Ito, K. Molecular Dynamics Simulation and Theoretical Model of Elasticity in Slide-Ring Gels. *ACS Macro Lett.* **2020**, *9*, 1280–1285.

(130) Kato, K.; Yasuda, T.; Ito, K. Viscoelastic Properties of Slide-Ring Gels Reflecting Sliding Dynamics of Partial Chains and Entropy of Ring Components. *Macromolecules* **2013**, *46* (1), 310–316. https://doi.org/10.1021/ma3021135.

(131) Fleury, G.; Schlatter, G.; Brochon, C.; Hadziioannou, G. From High Molecular Weight Precursor Polyrotaxanes to Supramolecular Sliding Networks. The "Sliding Gels." *Polymer*

(Guildf). **2005**, *46* (19), 8494–8501. https://doi.org/10.1016/j.polymer.2005.02.125.

(132) Rubinstein, M.; Colby, R. H. *Polymer Physics*; Oxford University Press: Oxford, 2003.

(133) Koga, T.; Tanaka, F. Elastic Properties of Polymer Networks with Sliding Junctions. *Eur. Phys. J. E* **2005**, *17* (2), 225–229. https://doi.org/10.1140/epje/i2004-10142-9.

(134) Zhang, Z.; Hou, G.; Shen, J.; Liu, J.; Gao, Y.; Zhao, X.; Zhang, L.; Zhang, Z.; Hou, G.; Shen, J.; Liu, J.; Gao, Y.; Zhao, X.; Zhang, L. Designing the Slide-Ring Polymer Network with Both Good Mechanical and Damping Properties via Molecular Dynamics Simulation. *Polymers (Basel).* **2018**, *10* (9), 964. https://doi.org/10.3390/polym10090964.

(135) Gavrilov, A. A.; Potemkin, I. I. Adaptive Structure of Gels and Microgels with Sliding Cross-Links: Enhanced Softness, Stretchability and Permeability. *Soft Matter* **2018**, *14* (24), 5098–5105. https://doi.org/10.1039/C8SM00192H.

(136) Karino, T.; Okumura, Y.; Zhao, C.; Kataoka, T.; Ito, K.; Shibayama, M. SANS Studies on Deformation Mechanism of Slide-Ring Gel. *Macromolecules* **2005**, *38* (14), 6161–6167. https://doi.org/10.1021/ma050624v.

(137) Karino, T.; Shibayama, M.; Okumura, Y.; Ito, K. SANS Study on Pulley Effect of Slide-Ring Gel. *Phys. B Condens. Matter* **2006**, *385–386*, 807–809. https://doi.org/10.1016/j.physb.2006.06.095.

(138) Shinohara, Y.; Kayashima, K.; Okumura, Y.; Zhao, C.; Ito, K.; Amemiya, Y. Small-Angle X-Ray Scattering Study of the Pulley Effect of Slide-Ring Gels. *Macromolecules* **2006**, *39* (21), 7386–7391. https://doi.org/10.1021/ma061037s.

(139) Kato, K.; Yasuda, T.; Ito, K. Peculiar Elasticity and Strain Hardening Attributable to Counteracting Entropy of Chain and Ring in Slide-Ring Gels. *Polymer (Guildf).* **2014**, *55* (10), 2614–2619. https://doi.org/10.1016/j.polymer.2014.03.022.

(140) Mayumi, K.; Tezuka, M.; Bando, A.; Ito, K. Mechanics of Slide-Ring Gels: Novel Entropic Elasticity of a Topological Network Formed by Ring and String. *Soft Matter* **2012**, *8* (31), 8179–8183. https://doi.org/10.1039/c2sm25508a.

(141) de Gennes, P.-G. Sliding Gels. *Phys. A Stat. Mech. its Appl.* **1999**, *271* (3–4), 231–237. https://doi.org/10.1016/S0378-4371(99)00227-7.

(142) Tonks, L. The Complete Equation of State of One, Two and Three-Dimensional Gases of Hard Elastic Spheres. *Phys. Rev.* **1936**, *50* (10), 955–963. https://doi.org/10.1103/PhysRev.50.955.

(143) Sevick, E. M.; Williams, D. R. M. Piston-Rotaxanes as Molecular Shock Absorbers. *Langmuir* **2010**, *26* (8), 5864–5868. https://doi.org/10.1021/la903801x.

(144) Gao, Y.; Williams, D. R. M.; Sevick, E. M. Dynamics of Molecular Shock-Absorbers: Energy Dissipation and the Fluctuation Theorem. *Soft Matter* **2011**, *7* (12), 5739.

https://doi.org/10.1039/c1sm05161j.

(145) Pinson, M. B.; Sevick, E. M.; Williams, D. R. M. Mobile Rings on a Polyrotaxane Lead to a Yield Force. *Macromolecules* **2013**, *46* (10), 4191–4197. https://doi.org/10.1021/ma4000094.

(146) Boesten, R. J. J.; Sevick, E. M.; Williams, D. R. M. Piston Rotaxane Monolayers: Shear Swelling and Nanovalve Behavior. *Macromolecules* **2010**, *43* (17), 7244–7249. https://doi.org/10.1021/ma902824t.

(147) Sevick, E.; Williams, D.; Sevick, E. M.; Williams, D. R. M. A Piston-Rotaxane with Two Potential Stripes: Force Transitions and Yield Stresses. *Molecules* **2013**, *18* (11), 13398–13409. https://doi.org/10.3390/molecules181113398.

(148) Metzler, R.; Kantor, Y.; Kardar, M. Force-Extension Relations for Polymers with Sliding Links. *Phys. Rev. E - Stat. Physics, Plasmas, Fluids, Relat. Interdiscip. Top.* **2002**, *66* (2), 022102. https://doi.org/10.1103/PhysRevE.66.022102.

(149) Ito, K. Novel Entropic Elasticity of Polymeric Materials: Why Is Slide-Ring Gel so Soft? *Polym. J.* **2012**, *44* (1), 38–41. https://doi.org/10.1038/pj.2011.85.

(150) Müller, T.; Sommer, J.-U.; Lang, M. Tendomers – Force Sensitive Bis-Rotaxanes with Jump-like Deformation Behavior. *Soft Matter* **2019**, *15* (18), 3671–3679. https://doi.org/10.1039/C9SM00292H.

(151) Kato, K.; Okabe, Y.; Okazumi, Y.; Ito, K. A Significant Impact of Host-Guest Stoichiometry on the Extensibility of Polyrotaxane Gels. *Chem. Commun.* **2015**, *51* (90), 16180–16183. https://doi.org/10.1039/c5cc07122d.

(152) Murakami, T.; Schmidt, B. V. K. J.; Brown, H. R.; Hawker, C. J. Structural Versatility in Slide-Ring Gels: Influence of Co-Threaded Cyclodextrin Spacers. *J. Polym. Sci. PART A-POLYMER Chem.* **2017**, *55* (7), 1156–1165. https://doi.org/10.1002/pola.28490.

(153) Liu, C.; Kadono, H.; Yokoyama, H.; Mayumi, K.; Ito, K. Crack Propagation Resistance of Slide-Ring Gels. *Polymer (Guildf).* **2019**, *181*, 121782. https://doi.org/10.1016/j.polymer.2019.121782.

(154) Liu, C.; Mayumi, K.; Hayashi, K.; Jiang, L.; Yokoyama, H.; Ito, K. Direct Observation of Large Deformation and Fracture Behavior at the Crack Tip of Slide-Ring Gel. *J. Electrochem. Soc.* **2019**, *166* (9), B3143–B3147. https://doi.org/10.1149/2.0241909jes.

(155) Araki, J.; Kataoka, T.; Ito, K. Preparation of a ``sliding Graft Copolymer'', an Organic Solvent-Soluble Polyrotaxane Containing Mobile Side Chains, and Its Application for a Crosslinked Elastomeric Supramolecular Film. *Soft Matter* **2008**, *4* (2), 245–249. https://doi.org/10.1039/b715231k.

(156) Kato, K.; Hori, A.; Ito, K. An Efficient Synthesis of Low-Covered Polyrotaxanes Grafted with Poly(ε-Caprolactone) and the Mechanical Properties of Its Cross-Linked Elastomers.

Polymer (Guildf). **2018**, *147*, 67–73. https://doi.org/10.1016/J.POLYMER.2018.05.072.

(157) Li, X.; Kang, H.; Shen, J.; Zhang, L.; Nishi, T.; Ito, K.; Zhao, C.; Coates, P. Highly Toughened Polylactide with Novel Sliding Graft Copolymer by in Situ Reactive Compatibilization, Crosslinking and Chain Extension. *Polymer (Guildf).* **2014**, *55* (16), 4313–4323. https://doi.org/10.1016/J.POLYMER.2014.06.045.

(158) Fleury, G.; Schlatter, G.; Brochon, C.; Hadziioannou, G. Unveiling the Sliding Motion in Topological Networks: Influence of the Swelling Solvent on the Relaxation Dynamics. *Adv. Mater.* **2006**, *18* (21), 2847–2851. https://doi.org/10.1002/adma.200600107.

(159) Fleury, G.; Schlatter, G.; Brochon, C.; Travelet, C.; Lapp, A.; Lindner, P.; Hadziioannou, G. Topological Polymer Networks with Sliding Cross-Link Points: The "Sliding Gels". Relationship between Their Molecular Structure and the Viscoelastic as Well as the Swelling Properties. *Macromolecules* **2007**, *40* (3), 535–543. https://doi.org/10.1021/ma0605043.

(160) Sawada, J.; Aoki, D.; Otsuka, H.; Takata, T. A Guiding Principle for Strengthening Crosslinked Polymers: Synthesis and Application of Mobility-Controlling Rotaxane Crosslinkers. *Angew. Chemie - Int. Ed.* **2019**, *58* (9), 2765–2768. https://doi.org/10.1002/anie.201813439.

(161) Koyama, Y. Synthesis of Topologically Crosslinked Polymers with Rotaxane-Crosslinking Points. *Polym. J.* **2014**, *46* (6), 315–322. https://doi.org/10.1038/pj.2014.9.

(162) Sawada, J.; Aoki, D.; Uchida, S.; Otsuka, H.; Takata, T. Synthesis of Vinylic Macromolecular Rotaxane Cross-Linkers Endowing Network Polymers with Toughness. *ACS Macro Lett.* **2015**, *4* (5), 598–601. https://doi.org/10.1021/acsmacrolett.5b00242.

(163) Iijima, K.; Aoki, D.; Otsuka, H.; Takata, T. Synthesis of Rotaxane Cross-Linked Polymers with Supramolecular Cross-Linkers Based on γ-CD and PTHF Macromonomers: The Effect of the Macromonomer Structure on the Polymer Properties. *Polymer (Guildf).* **2017**, *128*, 392–396. https://doi.org/10.1016/j.polymer.2017.01.024.

(164) Arai, T.; Jang, K.; Koyama, Y.; Asai, S.; Takata, T. Versatile Supramolecular Cross-Linker: A Rotaxane Cross-Linker That Directly Endows Vinyl Polymers with Movable Cross-Links. *Chem. – A Eur. J.* **2013**, *19* (19), 5917–5923. https://doi.org/10.1002/chem.201204402.

(165) Tan, S.; Blencowe, A.; Ladewig, K.; Qiao, G. G. A Novel One-Pot Approach towards Dynamically Cross-Linked Hydrogels. *Soft Matter* **2013**, *9* (21), 5239–5250. https://doi.org/10.1039/c3sm50638j.

(166) Sawada, J.; Aoki, D.; Sun, Y.; Nakajima, K.; Takata, T. Effect of Coexisting Covalent Cross-Links on the Properties of Rotaxane-Cross-Linked Polymers. *ACS Appl. Polym. Mater.* **2020**, *2* (3), 1061–1064. https://doi.org/10.1021/acsapm.9b00994.

(167) Noda, Y.; Hayashi, Y.; Ito, K. From Topological Gels to Slide-ring Materials. *J. Appl.*

Polym. Sci. **2014**, *131* (15), app.40509. https://doi.org/10.1002/app.40509.

(168) Minato, K.; Mayumi, K.; Maeda, R.; Kato, K.; Yokoyama, H.; Ito, K. Mechanical Properties of Supramolecular Elastomers Prepared from Polymer-Grafted Polyrotaxane. *Polymer (Guildf).* **2017**, *128*, 386–391. https://doi.org/10.1016/J.POLYMER.2017.02.090.

(169) Koyanagi, K.; Takashima, Y.; Yamaguchi, H.; Harada, A. Movable Cross-Linked Polymeric Materials from Bulk Polymerization of Reactive Polyrotaxane Cross-Linker with Acrylate Monomers. *Macromolecules* **2017**, *50* (15), 5695–5700. https://doi.org/10.1021/acs.macromol.7b00797.

(170) Shi, C.-Y.; Zhang, Q.; Yu, C.-Y.; Rao, S.-J.; Yang, S.; Tian, H.; Qu, D.-H. An Ultrastrong and Highly Stretchable Polyurethane Elastomer Enabled by a Zipper-Like Ring-Sliding Effect. *Adv. Mater.* **2020**, *32*, 2000345. https://doi.org/10.1002/adma.202000345.

(171) Sugihara, N.; Nishimura, K.; Nishino, H.; Kanehashi, S.; Mayumi, K.; Tominaga, Y.; Shimomura, T.; Ito, K. Ion-Conductive and Elastic Slide-Ring Gel Li Electrolytes Swollen with Ionic Liquid. *Electrochim. Acta* **2017**, *229*, 166–172. https://doi.org/10.1016/J.ELECTACTA.2017.01.118.

(172) Zhuo, Y.; Li, T.; Wang, F.; Håkonsen, V.; Xiao, S.; He, J.; Zhang, Z. An Ultra-Durable Icephobic Coating by a Molecular Pulley. *Soft Matter* **2019**, *15* (17), 3607–3611. https://doi.org/10.1039/c9sm00162j.

(173) Choi, S.; Kwon, T.; Coskun, A.; Choi, J. W. Highly Elastic Binders Integrating Polyrotaxanes for Silicon Microparticle Anodes in Lithium Ion Batteries. *Science (80-.).* **2017**, *357* (6348), 279–283. https://doi.org/10.1126/science.aal4373.

(174) Yoo, D.-J.; Elabd, A.; Choi, S.; Cho, Y.; Kim, J.; Lee, S. J.; Choi, S. H.; Kwon, T.; Char, K.; Kim, K. J.; Coskun, A.; Choi, J. W. Highly Elastic Polyrotaxane Binders for Mechanically Stable Lithium Hosts in Lithium-Metal Batteries. *Adv. Mater.* **2019**, *31* (29), 1901645. https://doi.org/10.1002/adma.201901645.

(175) Rowan, S. J.; Cantrill, S. J.; Cousins, G. R. L.; Sanders, J. K. M.; Stoddart, J. F. Dynamic Covalent Chemistry. *Angew. Chemie Int. Ed.* **2002**, *41* (6), 898–952. https://doi.org/10.1002/1521-3773(20020315)41:6<898::AID-ANIE898>3.0.CO;2-E.

(176) Nakahata, M.; Mori, S.; Takashima, Y.; Yamaguchi, H.; Harada, A. Self-Healing Materials Formed by Cross-Linked Polyrotaxanes with Reversible Bonds. *Chem* **2016**, *1*, 766–775. https://doi.org/10.1016/j.chempr.2016.09.013.

(177) Zheng, S. Y.; Liu, C.; Jiang, L.; Lin, J.; Qian, J.; Mayumi, K.; Wu, Z. L.; Ito, K.; Zheng, Q. Slide-Ring Cross-Links Mediated Tough Metallosupramolecular Hydrogels with Superior Self-Recoverability. *Macromolecules* **2019**, *52*, 6748–6755. https://doi.org/10.1021/acs.macromol.9b01281.

(178) Sood, N.; Bhardwaj, A.; Mehta, S.; Mehta, A. Stimuli-Responsive Hydrogels in Drug Delivery and Tissue Engineering. *Drug Deliv.* **2016**, *23* (3), 748–770.

https://doi.org/10.3109/10717544.2014.940091.

(179) Imran, A. Bin; Seki, T.; Takeoka, Y. Recent Advances in Hydrogels in Terms of Fast Stimuli Responsiveness and Superior Mechanical Performance. *Polym. J.* **2010**, *42* (11), 839–851. https://doi.org/10.1038/pj.2010.87.

(180) Koetting, M. C.; Peters, J. T.; Steichen, S. D.; Peppas, N. A. Stimulus-Responsive Hydrogels: Theory, Modern Advances, and Applications. *Mater. Sci. Eng. R Reports* **2015**, *93*, 1–49. https://doi.org/https://doi.org/10.1016/j.mser.2015.04.001.

(181) Sakai, T.; Murayama, H.; Nagano, S.; Takeoka, Y.; Kidowaki, M.; Ito, K.; Seki, T. Photoresponsive Slide-Ring Gel. *Adv. Mater.* **2007**, *19* (15), 2023–2025. https://doi.org/10.1002/adma.200700457.

(182) Haq, M. A.; Su, Y.; Wang, D. Mechanical Properties of PNIPAM Based Hydrogels: A Review. *Mater. Sci. Eng. C* **2017**, *70*, 842–855. https://doi.org/https://doi.org/10.1016/j.msec.2016.09.081.

(183) Imran, A. Bin; Seki, T.; Ito, K.; Takeoka, Y. Poly(N-Isopropylacrylamide) Gel Prepared Using a Hydrophilic Polyrotaxane-Based Movable Cross-Linker. *Macromolecules* **2010**, *43* (4), 1975–1980. https://doi.org/10.1021/ma902349j.

(184) Bin Imran, A.; Esaki, K.; Gotoh, H.; Seki, T.; Ito, K.; Sakai, Y.; Takeoka, Y. Extremely Stretchable Thermosensitive Hydrogels by Introducing Slide-Ring Polyrotaxane Cross-Linkers and Ionic Groups into the Polymer Network. *Nat. Commun.* **2014**, *5* (1), 5124. https://doi.org/10.1038/ncomms6124.

(185) Ohmori, K.; Abu Bin, I.; Seki, T.; Liu, C.; Mayumi, K.; Ito, K.; Takeoka, Y. Molecular Weight Dependency of Polyrotaxane-Cross-Linked Polymer Gel Extensibility. *Chem. Commun.* **2016**, *52* (95), 13757–13759. https://doi.org/10.1039/C6CC07641F.

(186) Kobayashi, Y.; Zheng, Y.; Takashima, Y.; Yamaguchi, H.; Harada, A. Physical and Adhesion Properties of Supramolecular Hydrogels Cross-Linked by Movable Cross-Linking Molecule and Host-Guest Interactions. *Chem. Lett.* **2018**, *47* (11), 1387–1390. https://doi.org/10.1246/cl.180646.

(187) Ikura, R.; Ikemoto, Y.; Osaki, M.; Yamaguchi, H.; Harada, A.; Takashima, Y. Preparation of Hydrophilic Polymeric Materials with Movable Cross-Linkers and Their Mechanical Property. *Polymer (Guildf).* **2020**, *196*, 122465. https://doi.org/https://doi.org/10.1016/j.polymer.2020.122465.

(188) Yasumoto, A.; Gotoh, H.; Gotoh, Y.; Imran, A. Bin; Hara, M.; Seki, T.; Sakai, Y.; Ito, K.; Takeoka, Y. Highly Responsive Hydrogel Prepared Using Poly(N-Isopropylacrylamide)-Grafted Polyrotaxane as a Building Block Designed by Reversible Deactivation Radical Polymerization and Click Chemistry. *Macromolecules* **2017**, *50* (1), 364–374. https://doi.org/10.1021/acs.macromol.6b01955.

(189) Seo, J.; Yui, N.; Seo, J.-H. Development of a Supramolecular Accelerator Simultaneously

to Increase the Cross-Linking Density and Ductility of an Epoxy Resin. *Chem. Eng. J.* **2019**, *356*, 303–311. https://doi.org/https://doi.org/10.1016/j.cej.2018.09.020.

(190) Wang, X.-S.; Kim, H.-K.; Fujita, Y.; Sudo, A.; Nishida, H.; Endo, T. Relaxation and Reinforcing Effects of Polyrotaxane in an Epoxy Resin Matrix. *Macromolecules* **2006**, *39* (3), 1046–1052. https://doi.org/10.1021/ma051888k.

(191) Levita, G.; De Petris, S.; Marchetti, A.; Lazzeri, A. Crosslink Density and Fracture Toughness of Epoxy Resins. *J. Mater. Sci.* **1991**, *26* (9), 2348–2352. https://doi.org/10.1007/BF01130180.

(192) Ohtsuka, K.; Zhao, C. Properties of Bismaleimide Resin Modified with Polyrotaxane as a Stress Relaxation Material. *Polym. Int.* **2018**, *67* (8), 1112–1117. https://doi.org/10.1002/pi.5619.

(193) Li, X.; Kang, H.; Shen, J.; Zhang, L.; Nishi, T.; Ito, K. Miscibility, Intramolecular Specific Interactions and Mechanical Properties of a DGEBA Based Epoxy Resin Toughened with a Sliding Graft Copolymer. *Chinese J. Polym. Sci.* **2015**, *33* (3), 433–443. https://doi.org/10.1007/s10118-015-1596-0.

(194) Seo, J.; Moon, S. W.; Kang, H.; Choi, B.-H.; Seo, J.-H. Foldable and Extremely Scratch-Resistant Hard Coating Materials from Molecular Necklace-like Cross-Linkers. *ACS Appl. Mater. Interfaces* **2019**, *11* (30), 27306–27317. https://doi.org/10.1021/acsami.9b05738.

(195) Pruksawan, S.; Samitsu, S.; Yokoyama, H.; Naito, M. Homogeneously Dispersed Polyrotaxane in Epoxy Adhesive and Its Improvement in the Fracture Toughness. *Macromolecules* **2019**, *52* (6), 2464–2475. https://doi.org/10.1021/acs.macromol.8b02450.

(196) Oku, T.; Furusho, Y.; Takata, T. A Concept for Recyclable Cross-Linked Polymers: Topologically Networked Polyrotaxane Capable of Undergoing Reversible Assembly and Disassembly. *Angew. Chemie - Int. Ed.* **2004**, *43* (8), 966–969. https://doi.org/10.1002/anie.200353046.

(197) Bilig, T.; Oku, T.; Furusho, Y.; Koyama, Y.; Asai, S.; Takata, T. Polyrotaxane Networks Formed via Rotaxanation Utilizing Dynamic Covalent Chemistry of Disulfide. *Macromolecules* **2008**, *41* (22), 8496–8503. https://doi.org/10.1021/ma801687y.

(198) Kohsaka, Y.; Nakazono, K.; Koyama, Y.; Asai, S.; Takata, T. Size-Complementary Rotaxane Cross-Linking for the Stabilization and Degradation of a Supramolecular Network. *Angew. Chemie - Int. Ed.* **2011**, *50* (21), 4872–4875. https://doi.org/10.1002/anie.201008020.

(199) Zhang, Y. M.; Liu, Y. H.; Liu, Y. Cyclodextrin-Based Multistimuli-Responsive Supramolecular Assemblies and Their Biological Functions. *Adv. Mater.* **2019**, *32*, 1806158. https://doi.org/10.1002/adma.201806158.

(200) Iijima, K.; Kohsaka, Y.; Koyama, Y.; Nakazono, K.; Uchida, S.; Asai, S.; Takata, T. Stimuli-Degradable Cross-Linked Polymers Synthesized by Radical Polymerization Using

a Size-Complementary [3]Rotaxane Cross-Linker. *Polym. J.* **2014**, *46* (1), 67–72. https://doi.org/10.1038/pj.2013.63.

(201) Akae, Y.; Sogawa, H.; Takata, T. Cyclodextrin-Based [3]Rotaxane-Crosslinked Fluorescent Polymer: Synthesis and De-Crosslinking Using Size Complementarity. *Angew. Chemie Int. Ed.* **2018**, *57* (45), 14832–14836. https://doi.org/10.1002/anie.201809171.

(202) Lu, Y.; Aoki, D.; Sawada, J.; Kosuge, T.; Sogawa, H.; Otsuka, H.; Takata, T. Visualization of the Slide-Ring Effect: A Study on Movable Cross-Linking Points Using Mechanochromism. *Chem. Commun.* **2020**, *56* (23), 3361–3364. https://doi.org/10.1039/c9cc09452k.

(203) Jang, K.; Iijima, K.; Koyama, Y.; Uchida, S.; Asai, S.; Takata, T. Synthesis and Properties of Rotaxane-Cross-Linked Polymers Using a Double-Stranded γ-CD-Based Inclusion Complex as a Supramolecular Cross-Linker. *Polymer (Guildf).* **2017**, *128*, 379–385. https://doi.org/10.1016/j.polymer.2017.01.062.

(204) Iijima, K.; Aoki, D.; Otsuka, H.; Takata, T. Synthesis of Rotaxane Cross-Linked Polymers with Supramolecular Cross-Linkers Based on γ-CD and PTHF Macromonomers: The Effect of the Macromonomer Structure on the Polymer Properties. *Polymer (Guildf).* **2017**, *128*, 392–396. https://doi.org/10.1016/j.polymer.2017.01.024.

(205) Yamamoto, K.; Nameki, R.; Sogawa, H.; Takata, T. Macrocyclic Dinuclear Palladium Complex as a Novel Doubly Threaded [3]Rotaxane Scaffold and Its Application as a Rotaxane Cross-Linker. *Angew. Chemie Int. Ed.* **2020**, *59* (41), 18023–18028. https://doi.org/10.1002/anie.202007866.

2 Doubly-Threaded Slide-Ring Polycatenane Networks

[*] This chapter was adapted from: Hart, L. F.; Lenart, W. R.; Hertzog, J. E.; Oh, J.; Turner, W. R.; Dennis, J. M.; Rowan, S. J. Doubly-Threaded Slide-Ring Polycatenane Networks. [*Accepted.*]

2.1 Introduction

The mobility and subsequent relaxations of polymer chains between crosslinks in networks often dictate many of the material's properties, such as modulus, elasticity, creep rate, stress relaxation, and impact mitigation.[1–3] However, kinetic limitations during network formation introduce topological defects, such as loops and dangling ends, reducing the number of elastically effective chains and producing a weaker and softer material. In addition, inhomogeneous distributions of covalent crosslinks lead to stress localization and brittle behavior (Figure 2.1a).[2–4] Over the years, many different approaches have been taken to improve the mechanical behavior and energy dissipation of polymer networks and gels.[3,5,6] A structural approach to this is a double-network gel (a class of interpenetrating networks),[7]

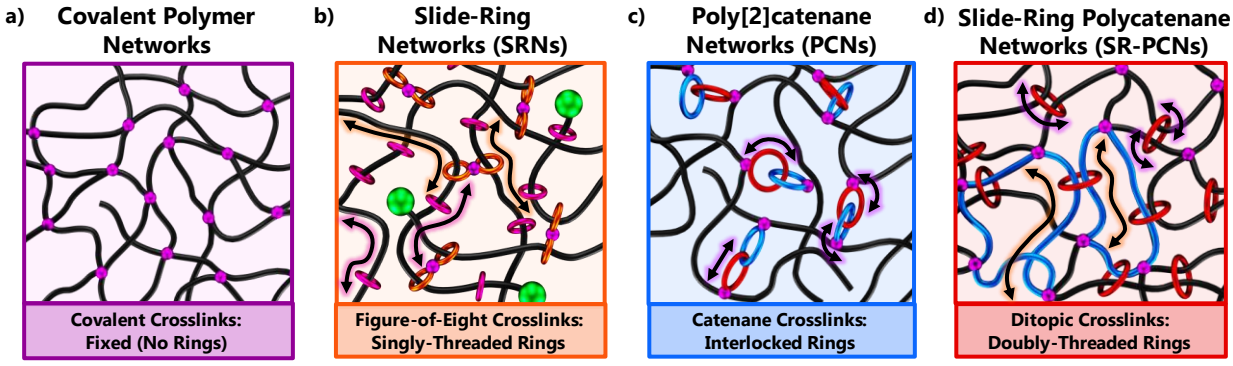

Figure 2.1. Schematics of covalent and selected mechanically interlocked polymer (MIP) networks. a) Fixed crosslinking in covalent polymer network leads to an inhomogeneous distribution of covalent crosslinks (purple), where the shortest chains break under deformation. b) A slide-ring network (SRN) comprised of figure-of-eight crosslinks (orange rings) and singly-threaded rings (pink) that can slide along polymer chains (arrows) but cannot dethread in the presence of stoppers (green). c) A polycatenane network (PCN) with [2]catenane crosslinks that impart mobility elements, such as elongation, rotation, and twisting (arrows) to the networks. d) Slide-ring polycatenane networks (SR-PCNs) consisting of doubly-threaded rings (red) embedded into covalent gels. The catenated crosslink, comprised of the red ring and the (highlighted) blue chains in the network, can rotate, twist and slide along chains (arrows) between covalent crosslinks.

which exhibits impressive enhancements in mechanical properties. It has been shown that the toughening mechanism in such gels relies on the different properties of the two or more networks that are partially interlocked on a molecular scale but not covalently bonded.

Interpenetrating networks are one class of mechanically interlocked polymers (MIPs),[6] which consist of non-covalently bonded components held together by mechanical bonds. Another class of MIPs is the slide-ring network (SRN), a subset of polyrotaxane[8] materials where polymer threaded rings are the crosslinking units within the polymer network. One method of accessing SRNs is by covalently crosslinking the rings on polyrotaxanes to form mobile figure-of-eight crosslinks (Figure 2.1b).[9–15] The sliding motion of the rings along the polymer chain allows these mobile crosslinks to adjust during applied loads, which can result in a range of interesting mechanical properties that include improved ductility and fracture behavior,[16–18] frequency-dependent relaxations,[11–15] isotropic chain deformation during elongation,[19] and suppressed stretch-induced swelling.[20] The most studied class of such materials are cyclodextrin (CD)-based SRNs, and these materials have been explored in applications such as vibration- and sound- dampening insulation,[21] superabsorbent materials,[22] elastic binders for Li-ion battery anodes,[23] coatings for anti- fouling applications,[24,25] and a wide selection of self-healing[26–29] and stimuli-responsive systems.[30–33]

Polycatenane networks (PCNs),[34–37] polymers that contain interlocked rings, are a less developed class of MIP networks that utilize mechanical bonding between two or more interlocked rings (macrocycles) within the polymer architecture.[6] The presence of elastically active concatenated rings in elastomers without covalent crosslinks[38] provides the basis for an elastic response, suggesting that incorporating cyclic components can influence material properties through the motion of interlocked rings in the network. Figure 2.1c is a schematic of a poly[2]catenane network in which the crosslinking unit is a [2]catenane (two interlocked rings) moiety.[36,37] The presence of these [2]catenane crosslinks imbues the

networks with increased mobility derived from the elongation, rotation, and twisting (arrows, Figure 2.1c) of the interlocked rings. As with the SRNs, the mobility elements introduced by the nature of the interlocked architecture impact the properties of the network. For example, controlling the mobility of the interlocked crosslinks in the poly[2]catenane networks through metallation/demetallation[37] or intercomponent hydrogen bonding[36] leads to mechanically adaptive networks that can reversibly switch between rigid and flexible states.

Of course, SRNs and PCNs have very different types of mobility elements. The most apparent difference between the two is the translational motion of the ring along the polymer backbone in the SRNs (the magnitude of which depends on the total length of the polymer chain and the number of rings threaded onto the polymer).[6,39] Combining elements of these two types of networks within a single crosslink moiety produces a new class of MIP, called here a slide-ring polycatenane network (SR-PCN, Figure 2.1d), where catenane crosslinks can slide along the network backbone as well as rotate, and twist. Furthermore, changing the crosslink topology should influence the coupled network relaxations between ring mobility and chain diffusion,[40] and potentially impact other properties such as solvent transport through the network during deformation.

MIP networks that only contain doubly-threaded rings are less explored as synthetic access to such materials is not well developed.[41] Early studies of SRNs with doubly-threaded rotaxane moieties as the crosslinker leveraged γ-CD as the ring, but the cavity size of CDs and the solvent interactions that drive complex formation limit the variety of polymers available as the threading component.[42–44] Previous attempts with template-directed assembly of doubly-threaded rings have shown low quality gels form when the rings remain bound to the chain and ring dethreading limits practical utility. Rather than inserting a stopper after polymerization to prevent dethreading, this work shows doubly-threaded rings are maintained in a network by incorporating a tetrafunctional pseudo[3]rotaxane (P3R) crosslinker into the

synthesis of a crosslinked PEG-based network. This is achieved by copolymerizing the tetrafunctional P3R with a tetrafunctional PEG-based crosslinker and appropriate ditopic monomer to yield a gel with large catenated crosslinks, where one ring component is the doubly-threaded ring, and the other ring components are formed by the polymer network (blue chains in Figure 2.1d). The incorporation of rings introduces a new frequency dependent relaxation into the PEG gel, while also drastically increasing the rate of poroelastic draining.

2.2 Results and Discussion

2.2.1 Synthesis of Slide-Ring Polycatenane Networks (SR-PCNs)

In targeting the SR-PCNs, a doubly-threaded pseudo[3]rotaxane (P3R) moiety that is stable under the network reaction conditions is required. Metal ion templating is a common route to interlocked molecules, and many different ligand and metal ion combinations have been used to form interlocked compounds under different reaction conditions.[45–47] Recently, the terdentate 2,6-bis(*N*-alkyl-benzimidazolyl)pyridine (Bip)[48,49] ligand and its derivatives have been used to build doubly-threaded mechanically interlocked compounds, such as poly[*n*]catenanes[50–52] and [3]rotaxanes.[53] Building on this prior work, the Bip-containing ditopic macrocycle **2.1** and bis-alkyne thread component **2.2** were synthesized from their corresponding bis-phenolic Bip derivatives[48,50] via Williamson ether synthesis (see Experimental). The ditopic macrocycle incorporates two Bip ligands joined by rigid naphthalene linkers that prevent both ligands in the ring from binding to the same Zn^{2+} ion.[53] As such, the most thermodynamically favorable way for these ligands to form 2:1 Bip:metal complexes is by forming the doubly-threaded P3R complex (**2.1:2.2$_2$:Zn(II)$_2$**, Figure 2.2a). A solution of $Zn(NTf_2)_2$ is titrated into a 2:1 mixture of the ditopic macrocycle **2.1** and bis-alkyne thread **2.2** and monitored via ^{1}H-NMR to achieve the stoichiometry required for the P3R formation (see Experimental). The template-directed assembly of

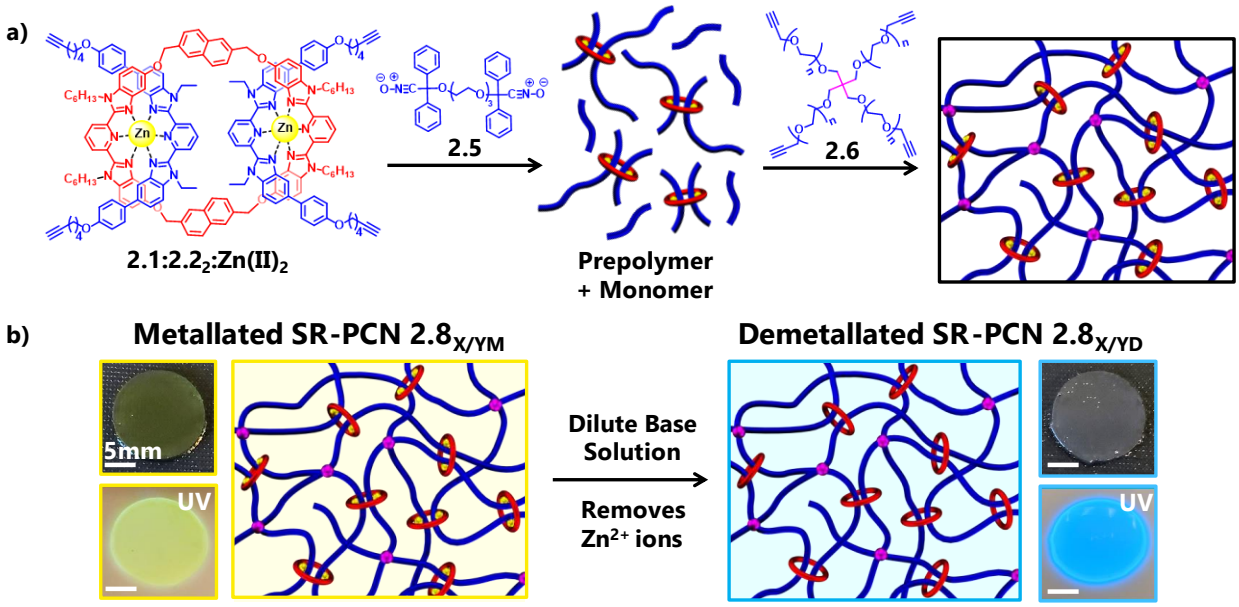

Figure 2.2. a) The two-step reaction of tetra-alkyne pseudo[3]rotaxane crosslinker **2.1:2.2$_2$:Zn(II)$_2$** (Y = 0 – 30 mol%) with nitrile-oxide monomer **2.5** and a 4-arm PEG-Alkyne **2.6** (X = 100 – Y mol%) to yield the metallated gels (**2.8$_{X/YM}$**) with varying amounts of fixed and metallated ring crosslinks. b) Treating **2.8$_{X/YM}$** with a dilute solution of base (tetrabutylammonium hydroxide, TBAOH) removes Zn^{2+} ions from the network, causing an observable change in color under visible and 365 nm UV light (**6$_{80/20M}$** and **6$_{80/20D}$** pictured, 5mm scale bar).

the desired P3R complex was confirmed by the downfield shift of the aromatic Bip protons on **2.1** and **2.2** in the NMR spectrum after adding two equivalents of Zn^{2+} (see Experimental).

With the P3R complex as a suitable doubly-threaded crosslinking moiety, the next step was to find reaction conditions that minimized its dethreading during network formation while maximizing the incorporation of macrocycle **2.1** into the network. The catalyst-free nitrile-oxide/alkyne click[54–58] reaction was chosen as the network-forming reaction because it should allow access to the SR-PCN gels by simply mixing the components in solution. This click reaction has been shown by Takata to be useful in the synthesis of low molecular weight rotaxanes,[59,60] main-chain poly[2]rotaxanes, and poly[3]rotaxanes.[61] Reaction of the tetra-alkyne end-capped 4-arm poly(ethylene glycol) (4-arm PEG-Alkyne) (**2.6**, M_n = 5 kg mol^{-1}) and the difunctional nitrile-oxide monomer[62] **2.5** yields the covalent gel **2.7$_{96}$** with a high gel fraction (GF, determined

gravimetrically, Equation 2.1, see Experimental)[63] of >96% (number subscript refers to the GF of the covalent gel) confirming the overall suitability of the nitrile-oxide/alkyne click reaction. A series of SR-PCNs that vary in the amount of catenane crosslinks was accessed by reacting the difunctional nitrile-oxide monomer **2.5** with different ratios of the P3R crosslinker (**2.1:2.2$_2$:Zn(II)$_2$**) and **2.6** (keeping the [nitrile-oxide]:[alkyne] ratio 1:1) (Figure 2.2a).

A two-step, one-pot reaction was utilized to access the SR-PCNs (**Figure 2.2a,** and Experimental). The P3R crosslinker (**2.1:2.2$_2$:Zn(II)$_2$**) was initially reacted with a large excess of a difunctional nitrile-oxide monomer **2.5** for four hours (the total amount of **2.5** is kept constant regardless of P3R crosslinker content) before sufficient 4-arm PEG-Alkyne crosslinker (**2.6**) was added to balance the stoichiometric ratio between alkyne and nitrile-oxide. The resulting SR-PCNs (**2.8$_{X/Y}$**) were prepared with varying amounts of P3R crosslinker, where X and Y are the molar percentage of **2.6** and **2.1:2.2$_2$:Zn(II)$_2$** crosslinkers used in the network synthesis, respectively. The gels were washed by heating in chloroform (~5 mL/mg of dry sample) for 4 hours to remove any low molecular weight components. After washing, the metallated SR-PCNs (**2.8$_{X/YM}$**) (Figure 2.2b) have a light yellow color, and exhibit a yellow fluorescence under 365 nm UV light originating from the Bip/Zn^{2+} complexes[51] and qualitatively confirms the successful incorporation of P3R crosslinker into the network. Base treatment of the metallated SR-PCNs, utilizing a dilute solution of tetrabutylammonium hydroxide (TBAOH), is accompanied by a shift in the UV-Vis spectra (see Experimental) and as a change in the color of the material under visible and UV light (Figure 2.2b). The demetallated gels (**2.8$_{X/YD}$**) were washed repeatedly to ensure the complete extraction of metal salts and any soluble fractions (including rings) not connected to the network structure.

Controlling the monomer composition in this reaction provided a series of SR-PCNs (**2.8**$_{90/10}$, **2.8**$_{80/20}$, **2.8**$_{70/30}$) with an increasing number of doubly-threaded rings (Y = 0 – 30 mol%; Figure 2.3a). Quantitative NMR (qNMR) studies were (see Experimental) used to determine the amount of macrocycle (MC) retained in the network by measuring the number (moles) of MC in the demetallated soluble fractions. Perhaps not surprisingly, the total amount of free macrocycle **2.1** obtained in the soluble fraction, X_{MC} (mol) calculated from Equation 2.3 (see Experimental), increases with the amount of P3R crosslinker used in the synthesis (Figure 2.3b, red circles).

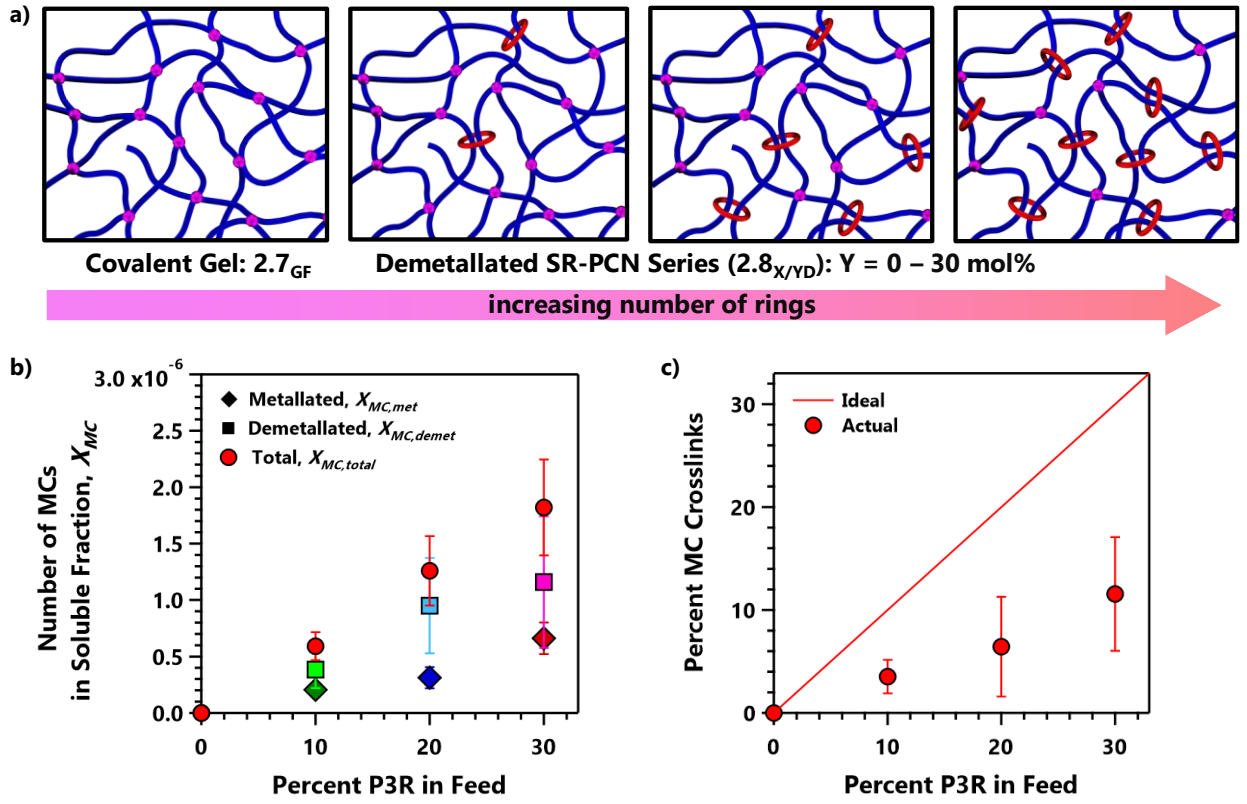

Figure 2.3. a) Schematic of a covalent gel (**2.7**$_{GF}$) and demetallated SR-PCNs (**2.8**$_{X/YD}$) with an increasing number of doubly-threaded rings (Y = 0 – 30 mol%). b) The average number (moles) of macrocycle (MC) in the metallated ($X_{MC,met}$, diamonds; **2.8**$_{90/10M}$ green, **2.8**$_{80/20M}$ blue, **2.8**$_{70/30M}$ dark red) and demetallated ($X_{MC,demet}$, squares; **2.8**$_{90/10D}$ light green, **2.8**$_{80/20D}$ light blue, **2.8**$_{70/30D}$ pink) soluble fractions determined from qNMR experiments and Equation 2.3. The total number of MC in the soluble fraction ($X_{MC,total}$) is plotted in red (circles). c) The percent of MC crosslinks in the network, calculated from Equation 2.7, plotted against the percent of total crosslinker in the feed that is P3R (100 x [**2.1:2.2**$_2$**:Zn(II)**$_2$]/([**2.1:2.2**$_2$**:Zn(II)**$_2$] + [**2.6**])) content. The ideal percent of MC crosslinks (solid red line), assuming 100% incorporation based on the crosslinker feed ratio, is plotted for comparison.

However, importantly for this study, the percent of MC (**2.1**) crosslinks that remain in the SR-PCN (calculated from Equation 2.7, see Experimental) increases with the increasing fraction of P3R crosslinker used in the polymerization (Figure 2.3c).

The successful incorporation of the rings is further confirmed by thermal gravimetric analysis (TGA) studies of the dry demetallated SR-PCNs, which show an increase in residual mass as the amount of macrocycle **2.1** is increased in the synthesis (see Experimental), consistent with increased incorporation of more aromatic rings in these networks. Furthermore, Differential Scanning Calorimetry (DSC) thermograms of both the metallated and demetallated (dry) SR-PCNs reveal a reduction in the PEG crystallinity as the relative amount of 4-arm PEG-alkyne crosslinker is reduced with the addition of more P3R crosslinker (Table 2.3, see Experimental).

It is important to note that the introduction of the P3R crosslinker into the synthesis results in a drop in the overall SR-PCN gel fraction (GF, wt%, Equation 2.1) based on the weight of the (dry) demetallated SR-PCN after washing and the original weight of the (dry) metallated SR-PCN after gelation (see Experimental). Therefore, in addition to the covalent gel $\mathbf{2.7_{96}}$ (with a GF of 96%) two covalent networks ($\mathbf{2.7_{GF}}$) were prepared at different reaction times which resulted in gel fractions of 86% ($\mathbf{2.7_{86}}$, 24 hrs), and 74% ($\mathbf{2.7_{74}}$, 12 hrs) to provide GFs similar to $\mathbf{2.8_{X/YM}}$ and $\mathbf{2.8_{X/YD}}$ for better comparison (see Experimental). Swelling studies show that the average weight-based swelling ratios for $\mathbf{2.8_{X/YM}}$ and $\mathbf{2.8_{X/YD}}$ (Equation 2.10, see Experimental)[64] in *N*-methyl-2-pyrrolidone (NMP) are relatively similar to the covalent control $\mathbf{2.7_{74}}$. Therefore, all gels were swollen to approximately the same extent over 24 hrs before mechanical testing.

2.2.2 Relationship between Macrocycle Content and SR-PCN Mechanical Properties

With a series of SR-PCNs in hand, the next goal was to explore the influence of the ring crosslinks on the gels' mechanical properties. The metallated gels were included in this

investigation to determine if replacing a covalent crosslink with a ring crosslink influences the material properties while in the bound state, and to help separate and aid the comparison of the demetallated SR-PCNs to covalent controls. To this end, compressive stress relaxation experiments were carried out on the NMP swollen SR-PCNs (**2.8$_{90/10M}$, 2.8$_{80/20M}$, 2.8$_{70/30M}$**) and the two covalent networks with comparable GF (**2.7$_{86}$, 2.7$_{74}$**). The long relaxation time of the swollen covalent gels, measured under compression, generally corresponds to the poroelastic relaxation of the solvent draining from the network.[65–67] The rate of this draining is related to the viscosity of the fluid and the average mesh size of the network, defined as the linear distance between two adjacent crosslinks.[68,69] Generally, in a system with fixed crosslinks, there is a distribution of mesh sizes that dictates fluid draining, and the corresponding distribution of relaxation times can be described with a stretched exponential function (Equation 2.11):[70]

$$E(t)/E_0 = exp\left(-\left(\frac{t}{\tau}\right)^{\beta}\right) \tag{2.11}$$

where *E(t)* is the modulus at time *t*, E_0 is the initial modulus at time zero, $E(t=0)/E_0 = 1$ after normalization, τ is the relaxation time, and β ($0 \leq \beta \leq 1$) is the stretching parameter that captures a distribution in relaxation time (Table 2.4, see Experimental). In both the covalent controls **2.7$_{GF}$** and metallated SR-PCNs **2.8$_{X/YM}$**, the stretched exponential fits well (dashed lines, Figure 2.4a), indicating that a single relaxation distribution governs the poroelastic relaxation process in these gels. By normalizing the relaxation time (taken when $E(t) = 1/e$) of the catenated gels to covalent controls of equivalent GF (see Experimental), it is possible to estimate the contribution of the MC content to this relaxation time. Incorporating the metallated ring crosslinks substantially decreases the relaxation time relative to the equivalent covalent gel of similar GF, increasing solvent draining.

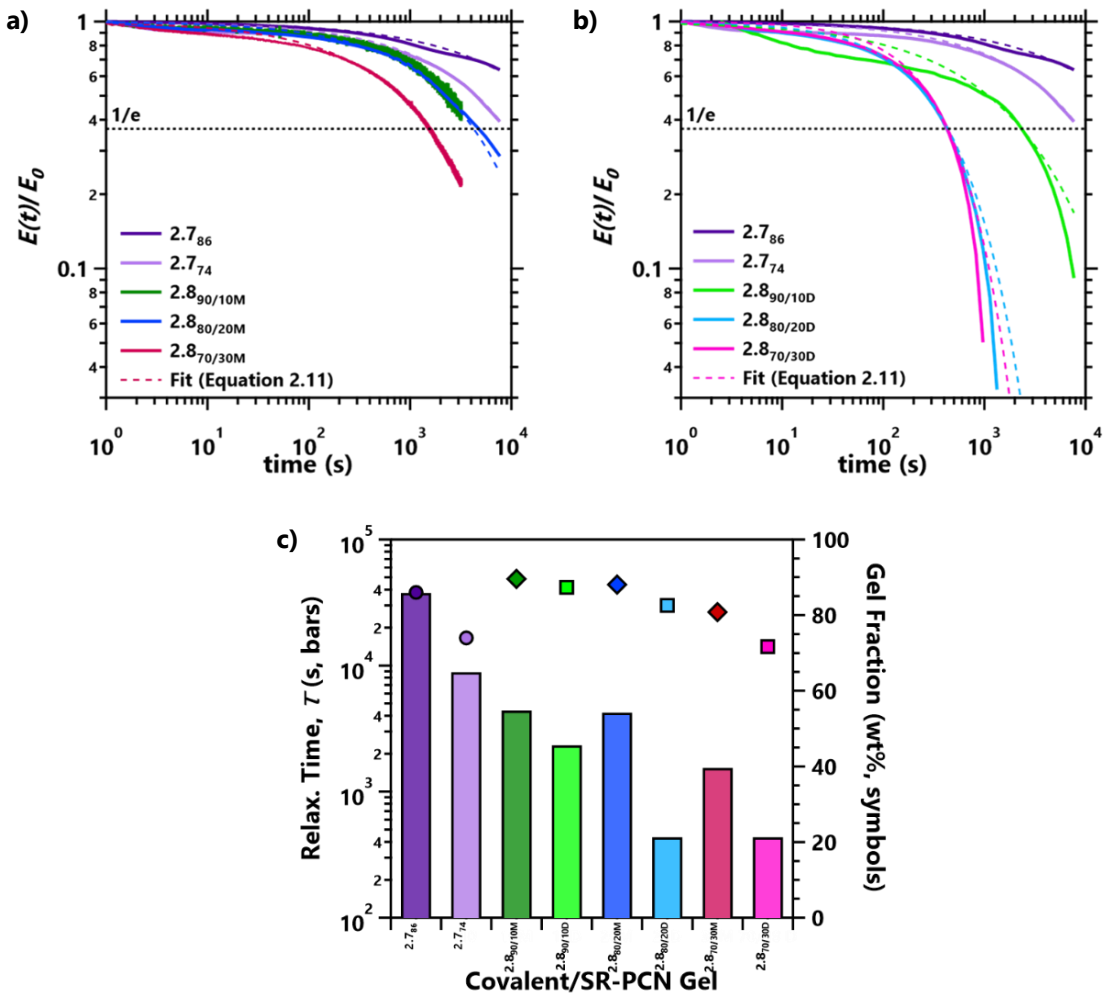

Figure 2.4. a) Overlay of the normalized stress relaxation moduli, $E(t)/E_0$, for the metallated SR-PCNs (**2.8**$_{90/10M}$ green, **2.8**$_{80/20M}$ blue, **2.8**$_{70/30M}$ red) swollen in NMP (including the covalent controls: **2.7**$_{86}$ dark purple, **2.7**$_{74}$ light purple). b) $E(t)/E_0$ overlay for the demetallated SR-PCNs (**2.8**$_{90/10D}$ light green, **2.8**$_{80/20D}$ light blue, **2.8**$_{70/30D}$ pink), highlighting the failure of the stretched exponential (Equation 2.11, dashed lines) to capture the changes in relaxation behavior. The dashed line at $E(t)=1/e$ determined the relaxation time, τ (s). c) Comparison of τ (on a log scale) for all gels (bars) shows a significant decrease in estimated τ for **2.8**$_{X/YD}$ irrespective of the decrease in GF (symbols, calculated from Equation 2.1).

After demetallating these three SR-PCNs with base, to yield **2.8**$_{90/10D}$, **2.8**$_{80/20D}$ and **2.8**$_{70/30D}$, there is a substantial decrease in the long relaxation time of the gels, with a decrease of about an order of magnitude for the gels with the highest MC content (Figure 2.4b and 2.4c). The relaxation times of the SR-PCNs, when normalized by the relaxation time of a covalent gel with equivalent GF (see Experimental), are much smaller than one, indicating there are other

contributions to the decrease in relaxation time beyond GF. A possible explanation for this effect is that the average mesh size is increasing as the rings can slide to accommodate the stress on the network, facilitating faster flow of the solvent. Another indication of the ring crosslink mobility in the network is the failure of a single stretched exponential to fully capture the poroelastic relaxation time. While a single stretched exponential function can capture a single relaxation event with a distribution of times, the dynamic nature of the mesh size distributions and the mobility of the rings themselves likely impact the poroelastic relaxation times, suggesting convolution of relaxation phenomena in the network. Previous quasi-elastic[71] and inelastic[72] neutron scattering studies on CD-SRNs suggest that when the rings are well dispersed, the timescale for ring sliding is slow and on the order of the poroelastic relaxation seen in this system. An additive model (see Experimental) might be expected to fit if the measurement of these relaxations do not interact, usually when the relaxation timescale is significantly different. Using this model, leaving the relaxation times unbound and the stretching parameters bound between 0 and 1, gives a better fit to the experimental data, however, it still fails to accurately capture the behavior of the curve (Equation 2.12, see Experimental). If the relaxation events interact (e.g. through energy transfer) then a product model could better capture the relaxation times.[73] The simplest way to model this interaction would be the product of the two exponential decays from the same initial stress (Equation 2.13, see Experimental). This fit was performed with the same parameter bounds as the additive model (see Experimental) but also failed to capture the stress relaxation of the of PC-SRNs. The interaction of ring sliding with poroelastic draining is clearly more complex than these three simple models can account for.

To further probe the properties of these SR-PCNs, small-amplitude oscillatory compression (SAOC) studies were performed to explore the frequency-dependent mechanical

response as well as the faster relaxation process. Figure 2.5 summarizes the frequency dependence of the storage modulus E' and tan δ of metallated and demetallated SR-PCNs swollen in NMP (see Experimental for loss modulus E"). The storage moduli of the covalent control and metallated samples display minimal frequency dependence above 1 rad/s. While below this frequency, typical poroelastic behavior is observed wherein the modulus decreases with frequency because of solvent draining from the network[74] (Figure 2.5a).

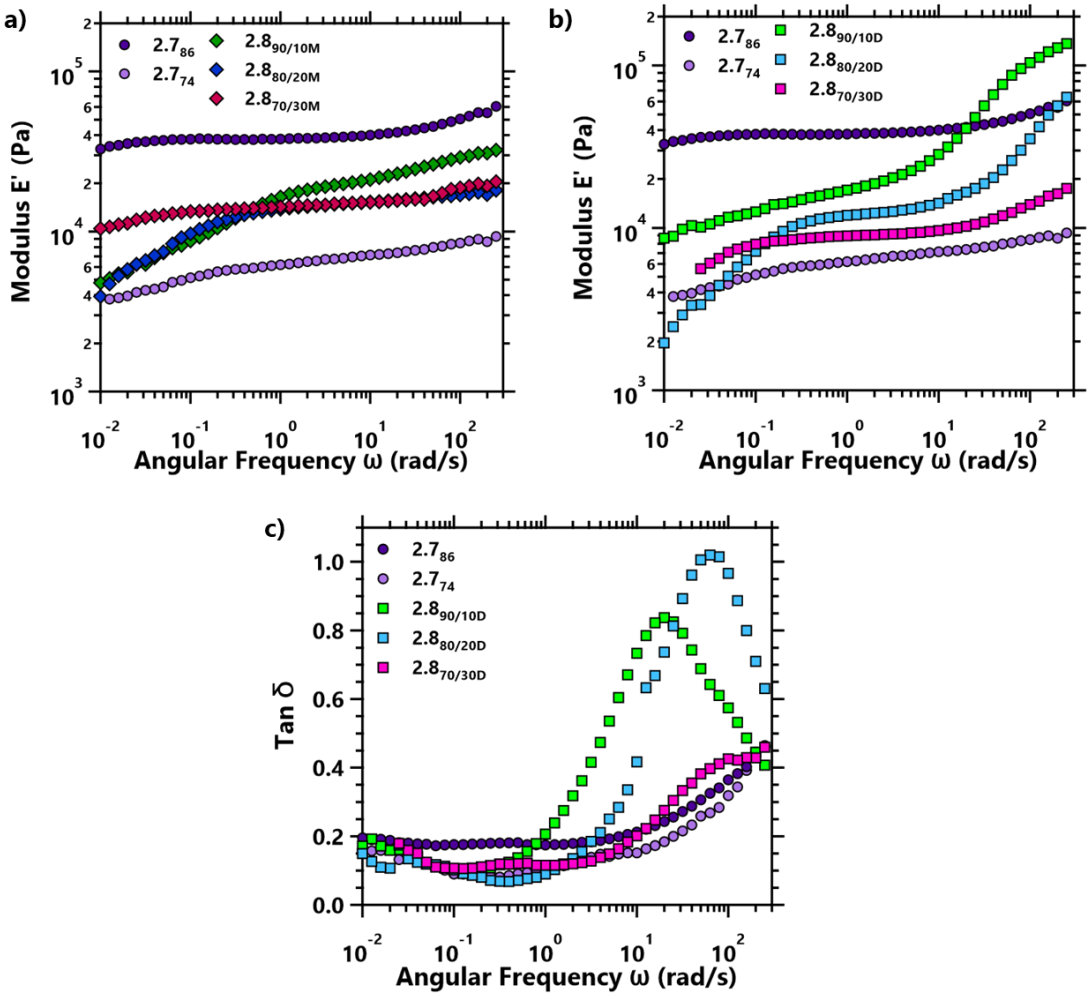

Figure 2.5. Small-amplitude oscillatory compression (SAOC) frequency sweeps for a) covalent (**2.7$_{86}$**, dark purple; **2.7$_{74}$**, light purple), and metallated (diamonds) SR-PCNs (**2.8$_{90/10M}$**, green; **2.8$_{80/20M}$,** blue; **2.8$_{70/30M}$,** red), and b) demetallated (squares) SR-PCNs (**2.8$_{90/10D}$,** light green; **2.8$_{80/20D}$,** light blue; **2.8$_{70/30D}$,** pink) swollen in NMP. c) Tan δ vs. angular frequency for covalent and demetallated NMP gels. Samples were preloaded with 0.025 N to ensure uniform contact between the sample and plates. Frequency sweeps were performed from 1000 rad/s to 0.01 rad/s with a strain amplitude of 1%.

Demetallation resulted an additional higher-frequency relaxation observed as an increase in storage modulus with frequency (Figure 2.5b) and peak in the tan δ (Figures 2.5c and Experimental). Using the frequency at the peak intensity of the tan δ, a characteristic relaxation time of 50 and 16 ms was estimated for the **2.8**$_{\mathbf{90/10D}}$ and **2.8**$_{\mathbf{80/20D}}$, respectively. While the peak of the tan δ for the **2.8**$_{\mathbf{70/30D}}$ is beyond the limits of the instrument, the onset of a relaxation is observed at the higher frequencies and suggests this sample would continue the trend of a decreasing characteristic relaxation time. Rationalized as a change in network mobility, this faster relaxation occurs as mobile ring crosslinks replace the covalent crosslinks. Interestingly, as this ring relaxation is traversed from low to high frequencies, the sliding appears to become restrained and behaves similarly to an entrapped entanglement resulting in a higher concentration of elastically effective chains in the network and a higher modulus than the covalent control of similar GF.[75] Similar to the stress relaxation studies, as the ring content increases a number of complex catenated structures can form and contribute to the relaxation behavior in convoluted ways. Harnessing the variety of relaxations available in SR-PCNs could prove valuable in a range of advanced applications, such as impact mitigation.

2.3 Conclusions

Catalyst-free NOAC polymerization of a tetra-alkyne pseudo[3]rotaxane and a tetra-alkyne covalent crosslinker with a difunctional nitrile-oxide monomer can be used to synthesize slide-ring polycatenane networks (SR-PCNs) with varying amounts of interlocked and covalent crosslinks. Incorporating metallated ring crosslinks into a PEG gel hastens the slow poroelastic relaxation behavior seen in the stress relaxation studies. At higher strain rates, the metallated gel behaves similarly to the covalent controls, indicating that the metallated rings act as fixed

crosslinks at fast timescales. Demetallation frees the catenated rings to move in the system providing new avenues of mechanical relaxation showing similar behavior to a glass transition in the storage modulus and tan δ, while the time for poroelastic draining rapidly decreases. Copolymerization of doubly-threaded pseudo[3]rotaxanes and covalent crosslinkers offers a simple way to include complex catenane moieties into a network structure and provides a platform for deeper investigations of the structure-property relationships in these SR-PCNs.

2.4 Experimental

2.4.1 Materials and Methods

All chemicals were purchased from Sigma-Aldrich and used without further purification unless otherwise mentioned. Benzophenone imine was purchased from Oakwood Chemical. Zinc di[bis(trifluoromethylsulfonyl)imide] was purchased from Strem Chemicals and stored in a nitrogen desiccator. Sodium hydride, dry powder, and thymol standard for quantitative NMR *Trace*CERT® were purchased from Sigma-Aldrich and stored in a nitrogen desiccator. 4-arm PEG-Alkyne (**2.6**, M_n = 5.3 $kgmol^{-1}$) was purchased from Creative PEGWorks. Difunctional nitrile-oxide monomer **2.5**,[62] 2,6-bisbenzimidazolylpyridine ligands,[48,53] and 2,6-bis(bromomethyl)naphthalene[76] were prepared following literature procedures. Solvents for chromatography were purchased from Fisher Scientific. Deuterated solvents and nitromethane were purchased from ACROS Organics. Tetrahydrofuran (THF) was dried over sodium and benzophenone. Dichloromethane was distilled over calcium hydride. Dimethylformamide (DMF) was dried with activated 4Å molecular sieves. All synthesized components were stored in a freezer at -8°C before use.

Room Temperature Nuclear Magnetic Resonance Spectroscopy (NMR) was performed using a Bruker Ascend AVANCE III 500 MHz spectrometer, a Bruker AVANCE II+ 500 MHz spectrometer, or a Bruker DRX 400 MHz spectrometer at the University of Chicago Chemistry Department's NMR Facility. ^{1}H NMR spectra were referenced to the residual protonated solvent signal, and ^{13}C NMR spectra were referenced to the deuterated solvent carbon resonance signal.

Matrix-Assisted Laser Desorption/Ionization Mass Spectrometry (MALDI-TOF MS) was performed on a Bruker Ultraflextreme MALDI-TOF-TOF spectrometer at the University of Chicago Mass Spectrometry Facility in linear (or reflectance) mode using dithranol or trans-2-[3-

(4-tert-butylphenyl)-2-methyl-2-propenylidene]malononitrile (DCTB) as matrix and silver trifluoroacetate as ionizer (or no ionizer).

UV-Vis Spectrometry was measured using a Shimadzu UV-3600 Plus UV-Vis-NIR spectrophotometer and a 1 cm width quartz cuvette. Gels were cut into squares (~1mm/1mm) and placed onto quartz glass slide.

Thermogravimetric Analysis (TGA) was performed using a TA Instruments Discovery Thermogravimetric Analyzer in the Soft Matter Characterization Facility at the University of Chicago. Samples were tested under a nitrogen atmosphere using platinum pans. Tests were conducted using a ramp of 10°C/min from 30°C to 700°C.

Differential Scanning Calorimetry (DSC) was performed using a TA Instruments Discovery 2500 Differential Scanning Calorimeter in the Soft Matter Characterization Facility at the University of Chicago. Dried gel samples were prepared in aluminum Tzero pans from TA Instruments and were sealed. Typical test conditions involved a heat-cool-heat procedure (200°C/-90°C/200°C) run at 10°C/min with a 5 min isotherm between each ramp.

Compressive Stress Relaxation was performed using a TA Instruments RSA GS2 with the 25 mm compression plate geometry operating in compression. Gel samples (swollen in NMP) were cut using a die punch of 16 mm, and an instantaneous strain of 7% was applied.

Small Amplitude Oscillatory Compression (SAOC) Rheology was performed using a TA Instruments RSA GS2 with the 25 mm compression plate geometry. Gel samples (swollen in NMP) were cut using a die punch of 16 mm and preloaded with 0.025 N to ensure uniform contact between the sample and plates. Frequency sweeps were performed from 1000 rad/s to 0.01 rad/s with a strain amplitude of 1%.

2.4.2 Synthetic Procedures

2.4.2.1 Synthesis of ditopic macrocycle **2.1**.

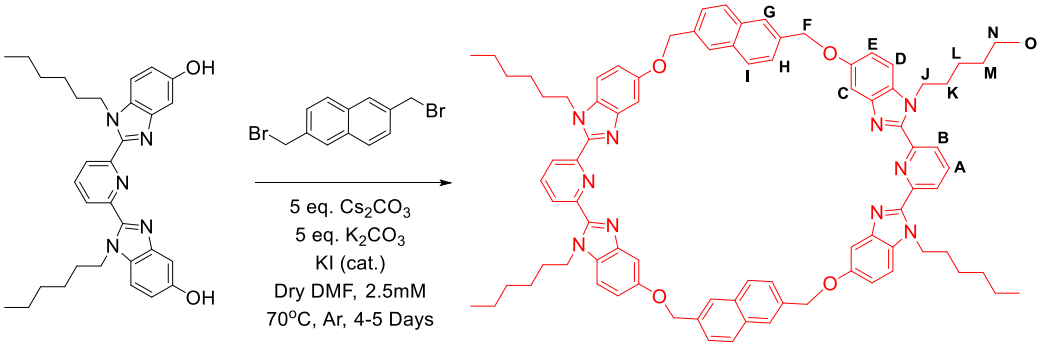

***N*-hexyl Bip** **2.1**

A 3-neck 1 L round bottom flask was charged with Cs_2CO_3 (3.18 g, 9.77 mmol), K_2CO_3 (1.35 g, 9.77 mmol), and KI (catalytic amount) under an Ar atmosphere. Dry DMF (450 mL) was injected, and the mixture was heated to 70°C and stirred while a DMF (330 mL) solution of *N*-hexyl Bip[53] (1.0 g, 1.95 mmol) and 2,6-bis(bromomethyl)naphthalene (0.61, 1.95 mmol)[76] was added dropwise (at an approximate rate of one drop every 20 s) over 4 d. After complete addition of components, the final concentration of the reaction was 2.5 mM. The reaction was allowed to stir at 70°C for one more day, after which the reaction mixture was cooled to room temperature and the solvent was removed under vacuum. The residue was dissolved in $CHCl_3$, and the insoluble material (salts) was removed by filtration. The filtrate was collected, and the solvent removed under vacuum. The resulting material was purified using column chromatography (TEA treated silica gel, chloroform/methanol gradient as eluent) followed by recrystallization (chloroform/methanol mixture) to yield white crystals of **2.1** in 33% yield by mass. ^{1}H NMR (500 MHz, $CDCl_3$) δ 8.08 (d, *J* = 7.9 Hz, 4H, B), 7.83 – 7.75 (m, 6H, A+C), 7.71 (d, *J* = 8.5 Hz, 4H, H), 7.50 (dd, *J* = 8.5, 1.6 Hz, 4H, I), 7.20 – 7.13 (m, 8H, G+D), 6.97 (dd, *J* = 8.9, 2.3 Hz, 4H, E), 5.44 (s, 8H, F), 4.45 (t, *J* = 7.5 Hz, 8H, J), 1.54 (p, *J* = 7.2 Hz, 8H, K), 0.97 – 0.85 (m, 24H, L+M+N), 0.53 – 0.47 (m, 12H, O). ^{13}C NMR (101 MHz, $CDCl_3$) δ 154.50, 150.16, 149.83, 143.29, 137.70, 135.43, 132.90,

131.19, 128.48, 125.67, 125.23, 125.00, 114.89, 110.72, 104.82, 70.46, 44.84, 31.14, 30.02, 26.30, 22.38, 13.74. MALDI-TOF MS: 1329.1 ([M]+H^+).

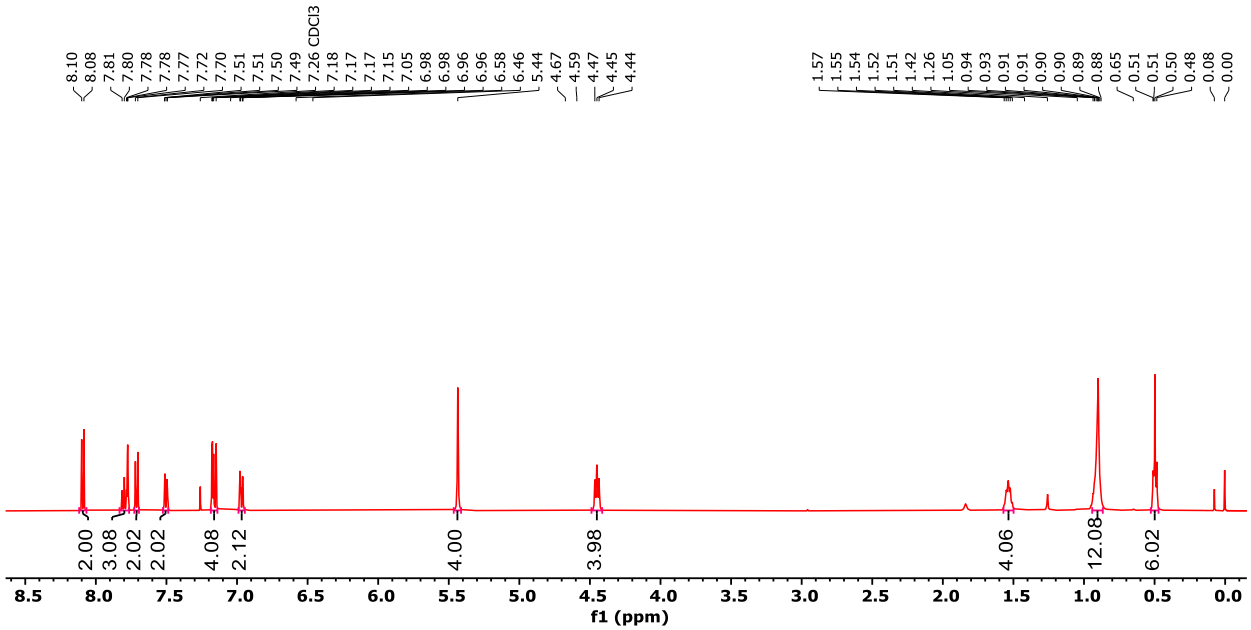

Figure 2.6. ^{1}H-NMR (400 MHz, 25°C, $CDCl_3$) of ditopic ring **2.1**.

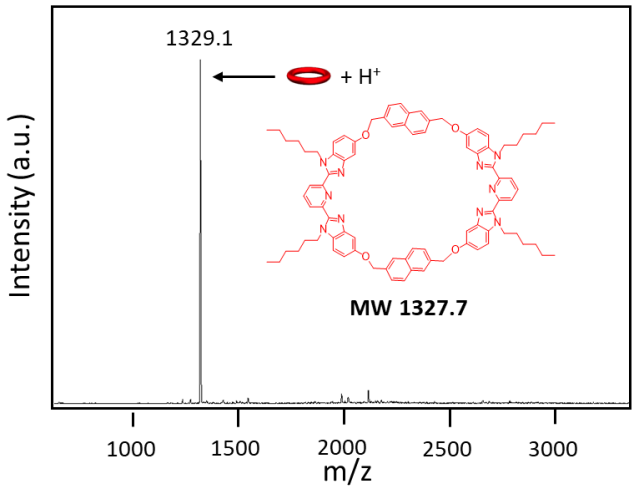

Figure 2.7. MALDI-TOF MS (Dithranol, no salt) of ditopic ring **2.1**.

2.4.2.2 Synthesis of bis-alkyne thread **2.2**.

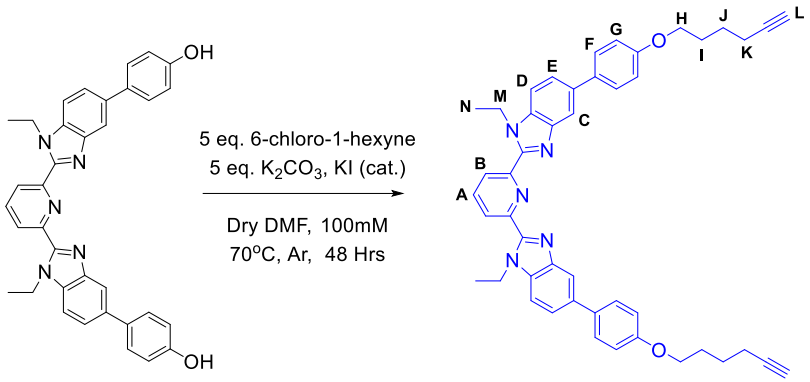

***N*-ethyl Bip** **2.2**

N-Ethyl Bip[53] (2.0 g, 3.91 mmol), K_2CO_3 (2.7 g, 19.5 mmol), and KI (catalytic amount) were added to a 100 mL round bottom flask under an Ar atmosphere. Dry DMF (39 mL) and 6-chloro-1-hexyne (2.37 mL, 19.5mmol.) were injected into the flask, and the reaction stirred at 70°C for 48 hours. After this time the reaction mixture was cooled to room temperature and then precipitated dropwise into cold deionized water (~300 mL). The white solid was collected by vacuum filtration and subsequently recrystallized in a mixture of chloroform and methanol to yield the desired thread **2.2** in 95% yield by mass. ^{1}H NMR (400 MHz, $CDCl_3$) δ 8.36 (d, *J* = 7.9 Hz, 2H, B), 8.12 – 7.99 (m, 3H, A+C), 7.65 – 7.48 (m, 8H, E+F+D), 7.05 – 6.97 (m, 4H, G), 4.83 (q, *J* = 7.2 Hz, 4H, M), 4.06 (t, *J* = 6.2 Hz, 4H, H), 2.31 (td, *J* = 7.0, 2.6 Hz, 4H, I), 2.02 – 1.90 (m, 6H, K+L), 1.82 – 1.71 (m, 4H, J), 1.40 (t, *J* = 7.2 Hz, 6H, N). ^{13}C NMR (101 MHz, $CDCl_3$) δ 158.46, 150.46, 150.07, 143.60, 138.24, 136.36, 135.24, 134.31, 128.48, 125.80, 123.28, 118.17, 114.97, 110.45, 84.22, 68.79, 67.50, 40.05, 28.43, 25.18, 18.28, 15.60. MALDI-TOF MS: 712.30 ([M]+H^+).

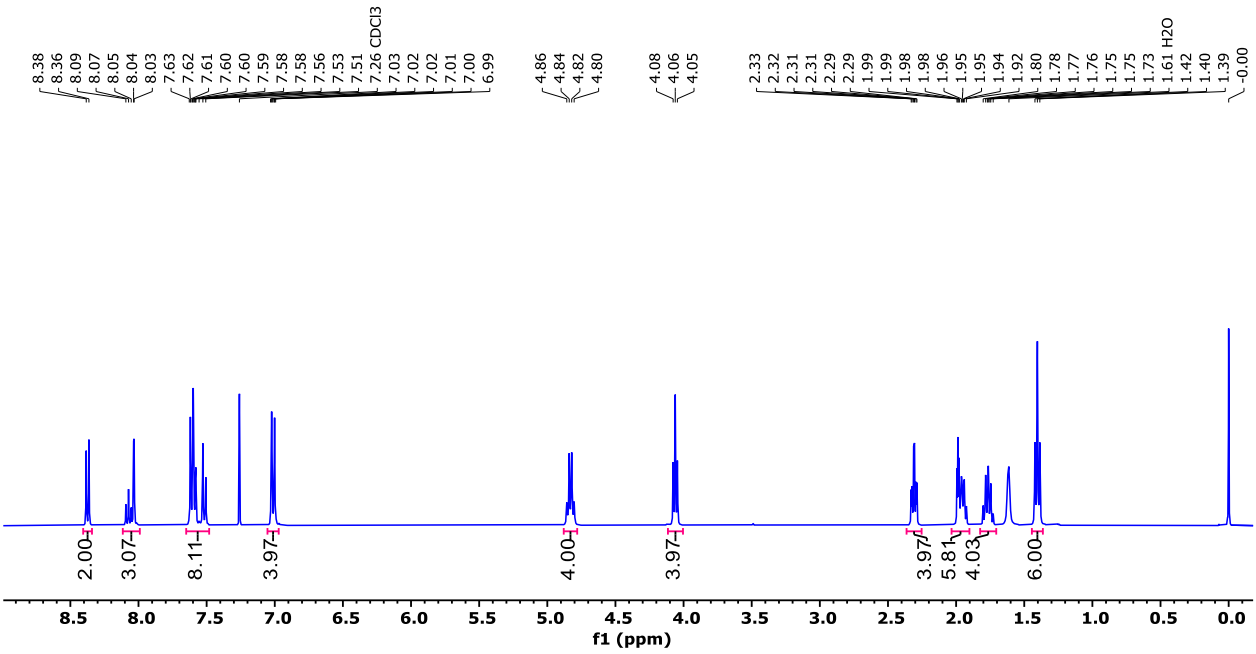

Figure 2.8. ^{1}H-NMR (400 MHz, 25°C, $CDCl_3$) of bis-alkyne Bip **2.2**.

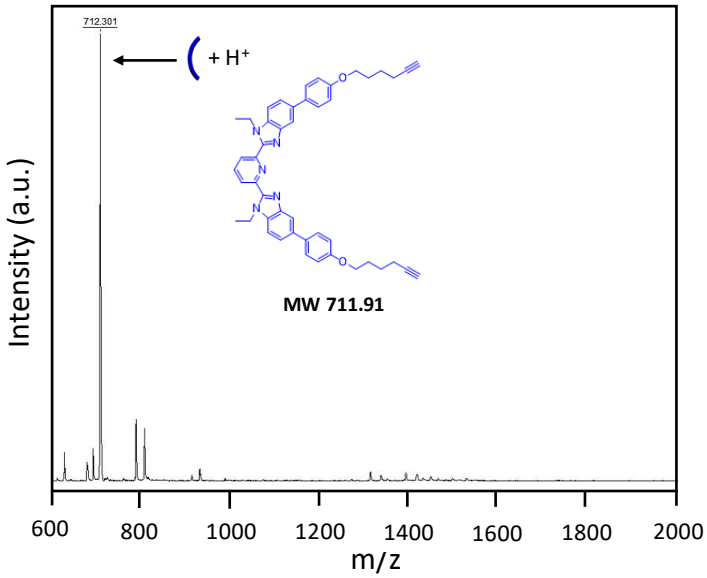

Figure 2.9. MALDI-TOF MS (Dithranol, no salt) of bis-alkyne Bip **2.2**.

2.4.2.3 Zn(II) assembly of Pseudo[3]rotaxane (P3R) crosslinker **2.1:2.2$_2$:Zn(II)$_2$**

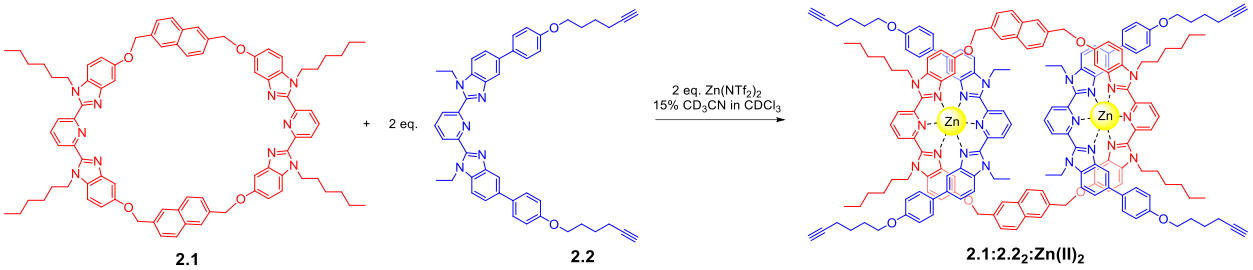

2.1 **2.2** **2.1:2.2$_2$:Zn(II)$_2$**

Macrocycle **2.1** (0.0500 g, 0.0377 mmol) was dissolved in 1.0 mL $CDCl_3$. Thread **2.2** (0.0536 g, 0.0753 mmol) was dissolved in 500 µL $CDCl_3$ and titrated into the solution of **2.1** until an exact 2:1 (**2.2**:**2.1**) ratio was formed (done by monitoring both the N-CH_2 peaks on the alkyl groups of the Bip ligands). $Zn(NTf_2)_2$ (0.0471 g, 0.0753 mmol) was dissolved in 500 µL of 4:1 $CDCl_3$:CD_3CN and was added until no free (unbound) Bip peaks appeared at ~2 equivalents of $Zn(NTf_2)_2$. The complete disappearance of the doublets at 8.09 and 8.37 ppm (and the corresponding growth of the peaks at 8.78 and 8.58 ppm) indicates that all Bip ligands are bound with Zn^{2+} ions in a 2:1 Bip:metal ratio. The resulting pseudo[3]rotaxane solution was dried under vacuum to obtain a yellow powder that was stored in the freezer at -8°C before use.

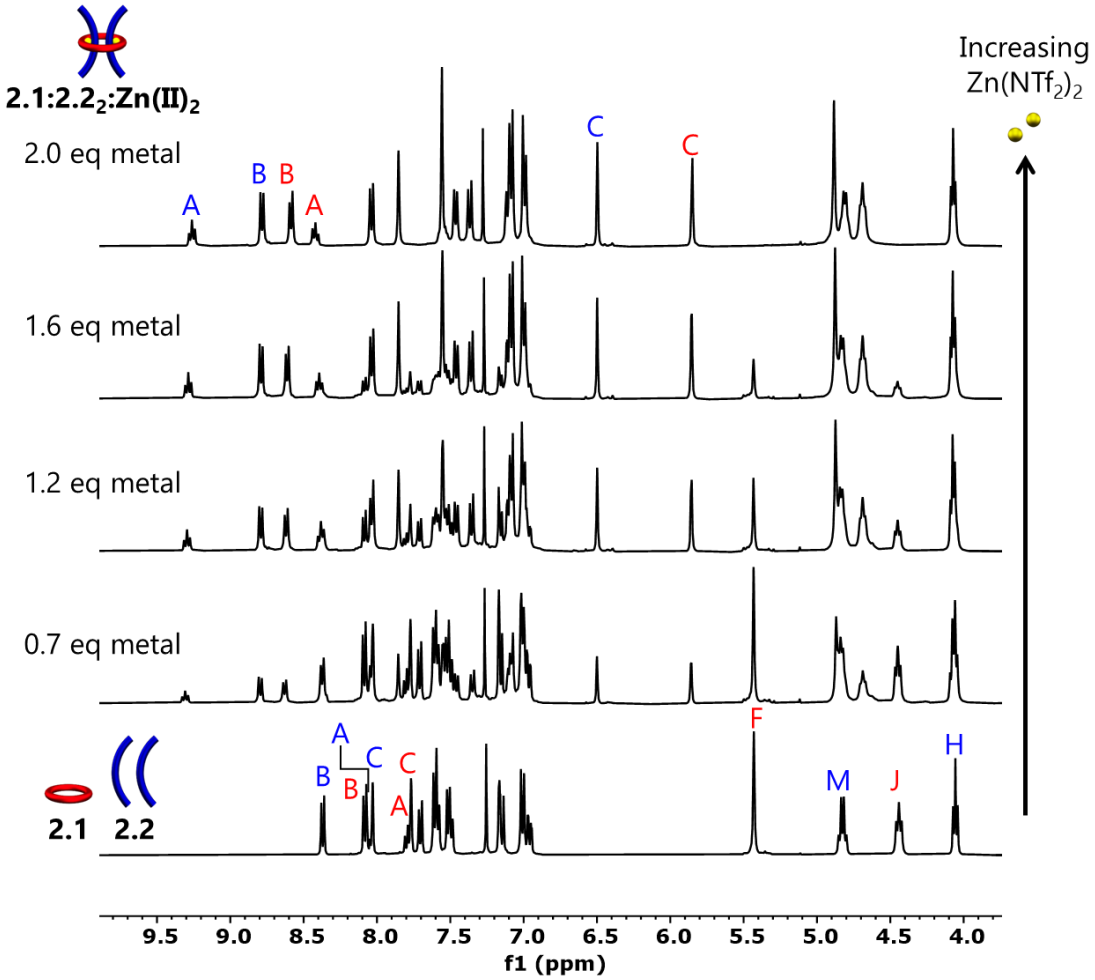

Figure 2.10. Partial ^{1}H-NMR overlay (500 MHz, 25°C, Solvent: 0, 5.25, 9, 12, 15% d_3-MeCN in $CDCl_3$ increasing upwards) of metal addition to form **2.1:2.2$_2$:Zn(II)$_2$**.

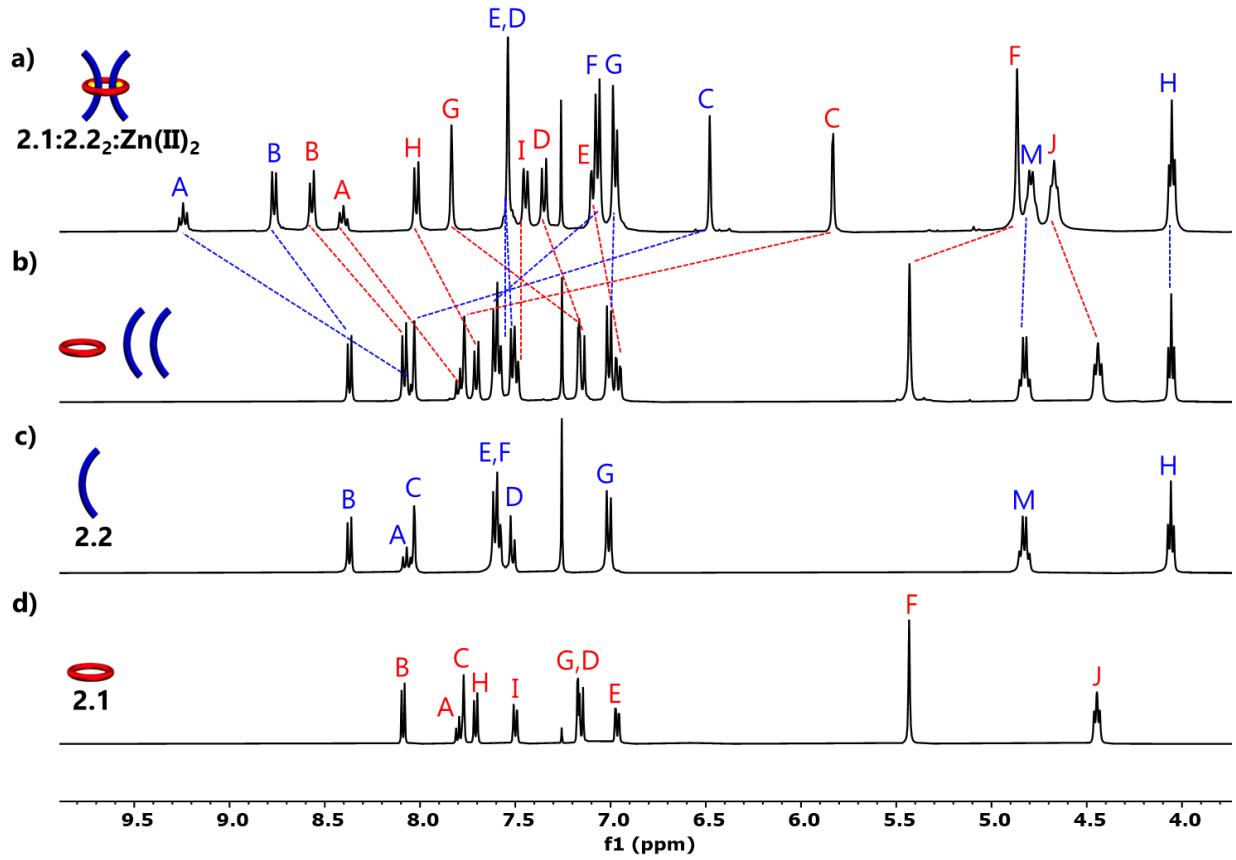

Figure 2.11. Partial ^{1}H-NMR overlay (500 MHz, 25°C) of a) **2.1:2.2$_2$:Zn(II)$_2$** (15% d_3-MeCN in $CDCl_3$), b) 2:1 mixture of **2.2**:**2.1** ($CDCl_3$), c) **2.2** ($CDCl_3$) and d) **2.1** ($CDCl_3$).

2.4.2.4 Synthesis of difunctional nitrile-oxide monomer **2.5**

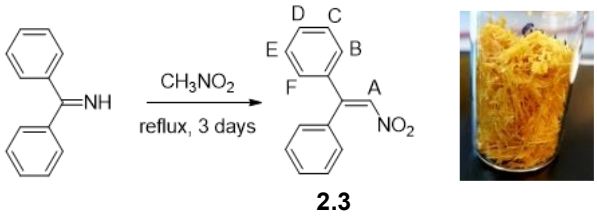

1,1-Diphenylnitroethene (**2.3**) was first prepared according to a literature procedure.[56,77] Benzophenone imine (29.12 g, 34.64 mL, 160.68 mmol) and nitromethane (39.04 g, 34.64 mL, 639.51 mmol) were added to an oven-dried round bottom flask equipped with two condensers under argon. The reaction was slowly heated to 100°C and the colorless solution refluxed for 3 days (behind blast shields). The resulting yellow/orange solution was cooled to room temperature and excess nitro methane was removed under vacuum. The yellow/orange oil was recrystallized

(x2) in hexanes and ethyl acetate, revealing large golden-yellow crystals of **2.3** in 96% yield (35 g) by mass. ^{1}H NMR (500 MHz, $CDCl_3$) δ 7.48 – 7.41 (m, 5H, A+E+C), 7.39 (m, 2H, D), 7.30 – 7.27 (m, 2H, F), 7.25 – 7.22 (m, 2H, B).

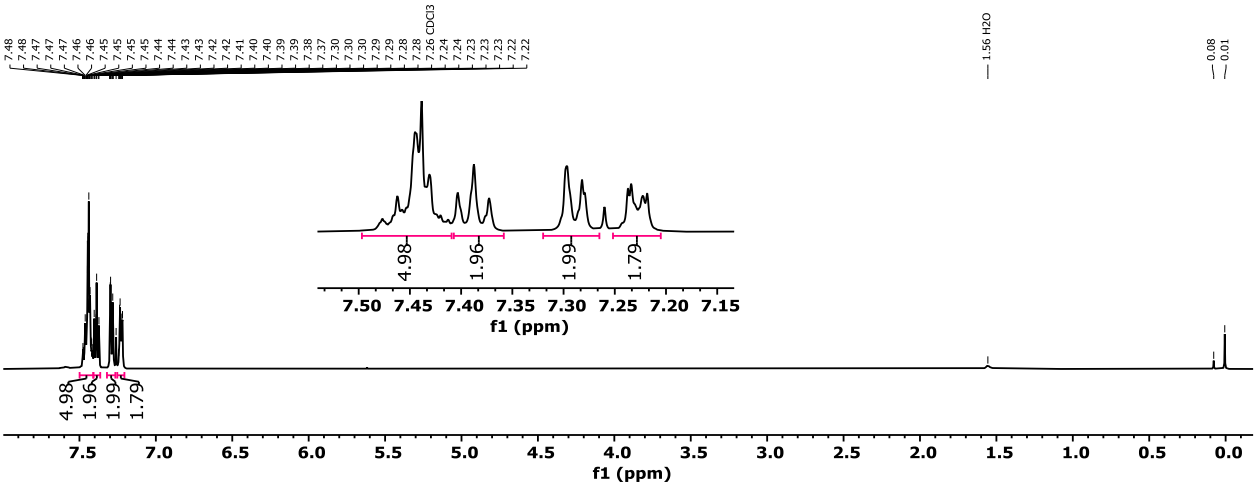

Figure 2.12. ^{1}H-NMR (500 MHz, 25°C, $CDCl_3$) of 1,1- diphenylnitroethene **2.3**.

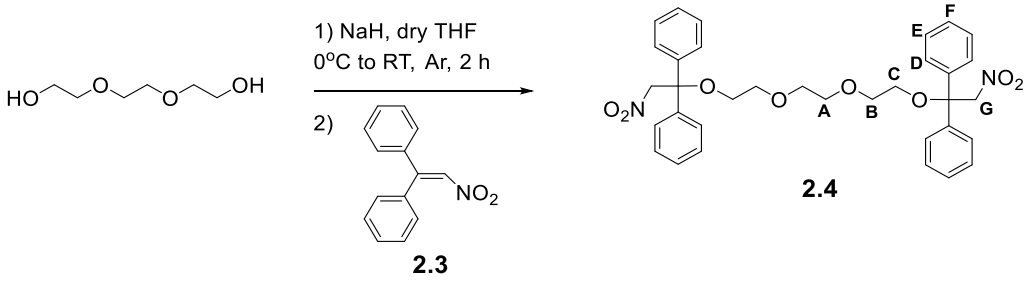

The difunctional nitro compound **2.4** was synthesized as previously reported by Takata and coworkers.[62] All glassware was dried in the oven at 130°C overnight and then flame-dried under vacuum before use. Triethylene glycol was dried with magnesium sulfate and filtered before use. Sodium hydride powder (2.59 g, 107.9 mmol) was weighed out and added immediately to a schlenk flask under argon. Anhydrous THF (10 mL) was injected, and the flask was placed in a 0°C ice bath to stir. A solution of triethylene glycol (3.0 g, 20.0 mmol) in anhydrous THF (15 mL) was added dropwise. After one hour, the ice bath was removed, and the reaction mixture was stirred for one more hour at room temperature. A solution of 1,1-diphenylnitroethene[56] **2.3** (13.5 g, 59.9 mmol) in 10 mL anhydrous THF was then added dropwise at room temperature. After 18

hours, the reaction was cooled to 0°C with an ice bath and then quenched with acetic acid. The mixture was diluted with DCM and washed three times with 1.0 M HCl and brine. The organic layer was collected, dried over magnesium sulfate, and the solvent was removed under vacuum. The resulting material was purified using column chromatography (silica gel, hexanes to ethyl acetate gradient) to yield **2.4** as a pale-yellow oil in 94% yield by mass. ^{1}H NMR (500 MHz, $CDCl_3$) δ 7.32 – 7.22 (m, 20H, D+E+F), 5.30 (s, 4H, G), 3.70 (t, *J* = 5.4 Hz, 4H, C), 3.64 (s, 4H, A), 3.50 (t, *J* = 5.4 Hz, 4H, B). ^{13}C NMR (101 MHz, $CDCl_3$) δ 141.31, 128.54, 128.18, 126.89, 81.81, 80.16, 70.83, 70.21, 62.97. MALDI-TOF MS: 622.8 ([M]+Na^+), 638.9 ([M]+K^+), 708.0 ([M]+Ag^+).

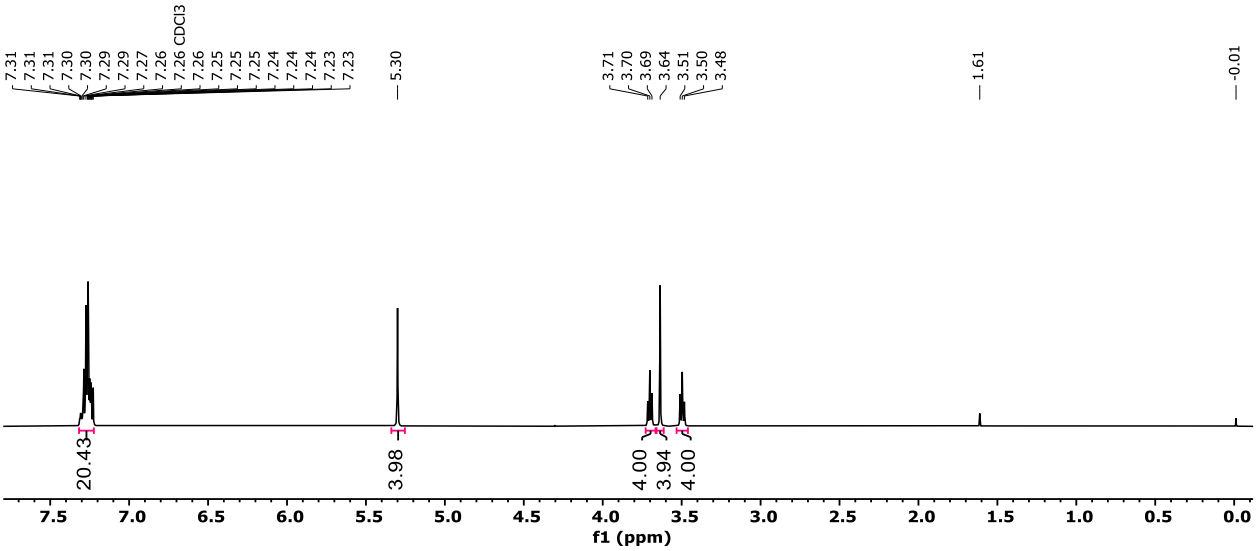

Figure 2.13. ^{1}H-NMR (500 MHz, 25°C, $CDCl_3$) of nitro monomer **2.4**.

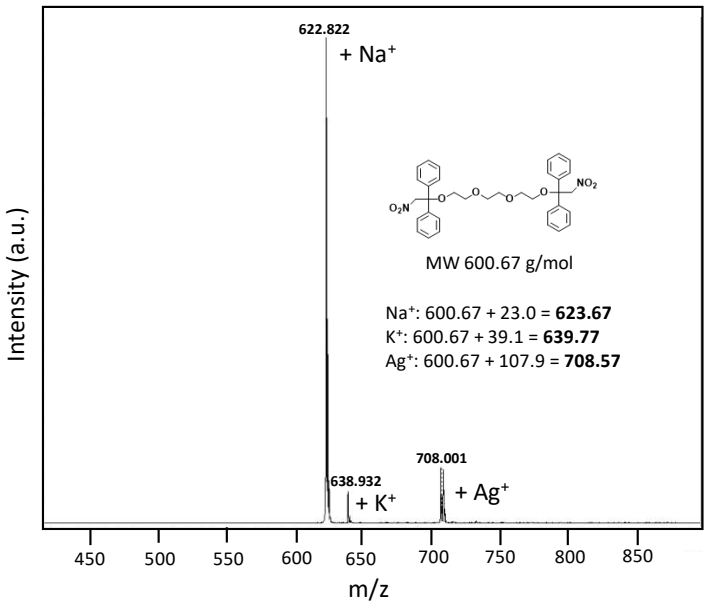

Figure 2.14. MALDI-TOF MS (DCTB: *trans*-2-[3-(4-*tert*-Butylphenyl)-2-methyl-2-propenylidene]malononitrile, sodium trifluoroacetate) of nitro monomer **2.4**.

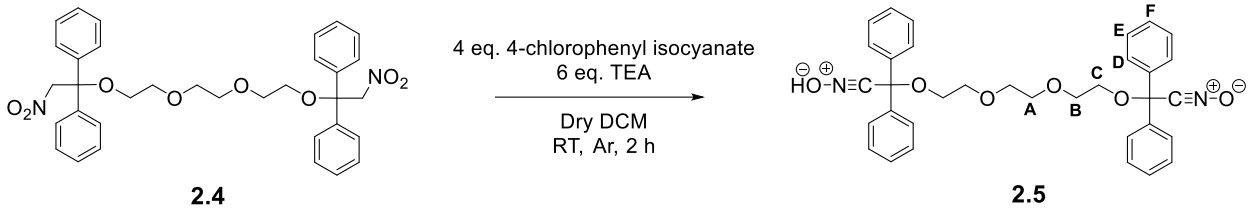

The nitrile-oxide monomer **2.5** was synthesized as previously reported by Takata and coworkers.[62] The difunctional nitro compound **2.4** (2.0 g, 3.33 mmol) and 4-chlorophenyl isocyanate (2.05 g, 13.3 mmol) were added to a round bottom flask under an argon atmosphere. Dry DCM (11.1 mL) and triethylamine (2.78 mL, 2.02 g, 20.0 mmol) were injected, and a white precipitate formed within the first minute. After stirring at room temperature for 2 hours, the reaction solution was filtered to remove the 1,3-bis(4-chlorophenyl)urea byproduct, and the filtrate was dried under vacuum. The remaining residue was dissolved in chloroform and filtered (x2). The filtrate was collected, and the solvent was removed under vacuum, leaving behind a yellow solid that was purified using column chromatography (silica gel, hexanes to ethyl acetate gradient) to yield nitrile-oxide **2.5** as a colorless oil in 45% yield by mass. ^{1}H NMR (500 MHz, $CDCl_3$) δ 7.46 – 7.39

(m, 8H, D), 7.36 – 7.29 (m, 12H, E+F), 3.75 (t, *J* = 4.2 Hz, 4H, C), 3.68 (s, 4H, A), 3.63 (t, *J* = 4.2 Hz, 4H, B). MALDI-TOF MS: 698.09 ([M]+Cs^+), 812.33 ([M]+DCTB).

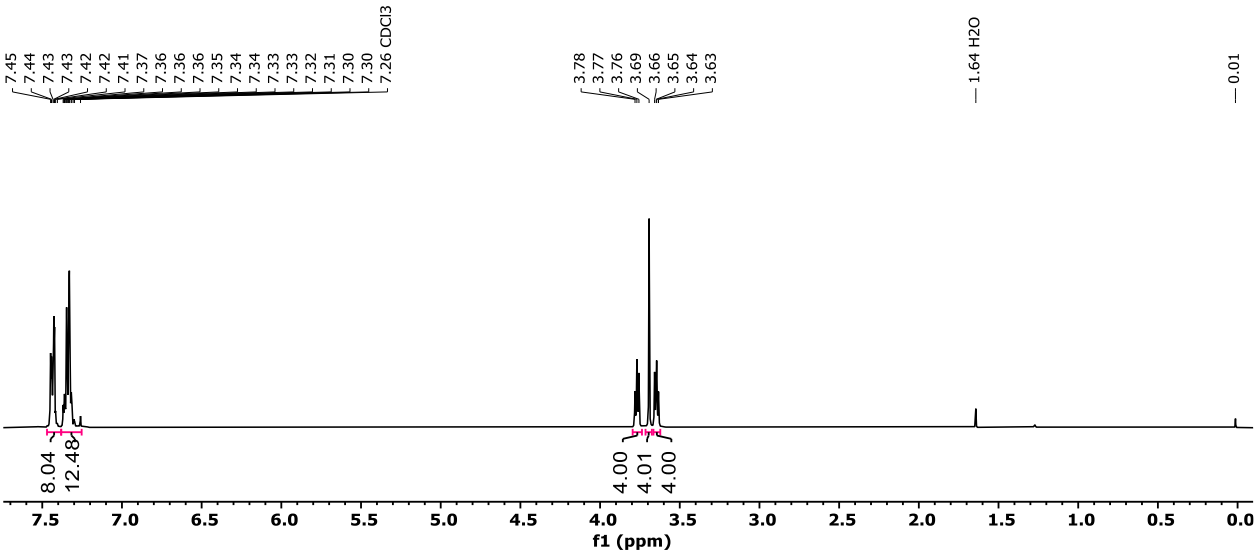

Figure 2.15. ^{1}H-NMR (500 MHz, 25°C, $CDCl_3$) of nitrile-oxide monomer **2.5**.

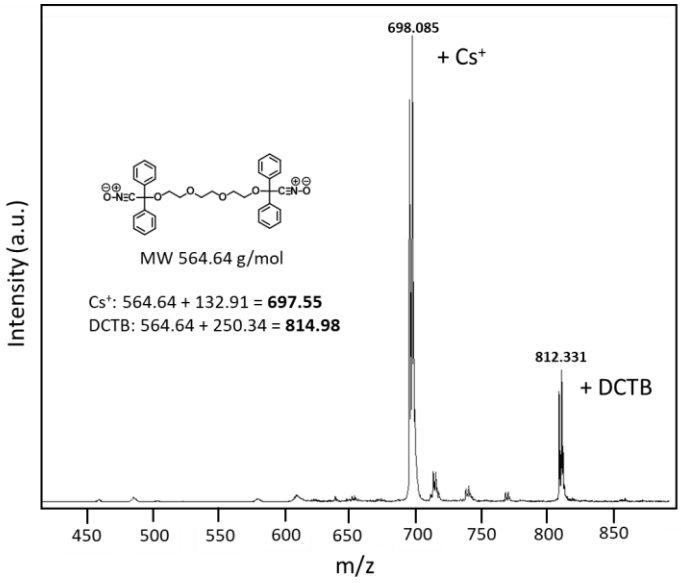

Figure 2.16. MALDI-TOF MS (DCTB: *trans*-2-[3-(4-*tert*-Butylphenyl)-2-methyl-2-propenylidene]malononitrile) of nitrile-oxide monomer **2.5**.

2.4.2.5 Doubly-Threaded Slide-Ring Polycatenane Network (SR-PCN) Synthesis

2.4.2.5.1 Nitrile-Oxide/Alkyne Cycloaddition (NOAC) Polymerization

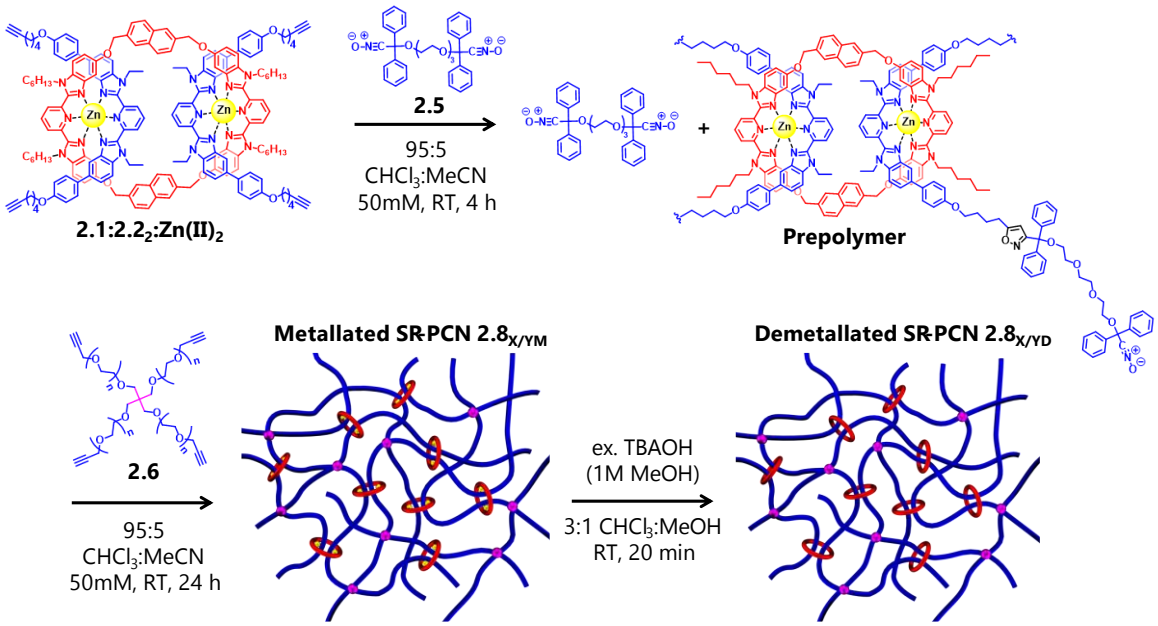

Figure 2.17. Polymerization of doubly-threaded SR-PCN series **2.8$_{X/YM}$** with varying amounts of **2.1:2.2$_2$:Zn(II)$_2$** (n_{P3R} mol, Y mol%) and 4 (n_{PEG} mol, X mol%), and demetallation with a dilute solution of tetrabutylammonium hydroxide (TBAOH) to **2.8$_{X/YD}$**.

P3R crosslinker **2.1:2.2$_2$:Zn(II)$_2$** (n_{P3R} mol, see Table 2.1) and nitrile-oxide monomer[62] **2.5** (0.010 g, 0.0177 mmol) were dissolved in 95:5 $CHCl_3$:MeCN (~250 µL) and added to a glass shell vial with a stir bar and capped. The solution was left to stir at room temperature for 4 hours. The small amount of acetonitrile helps solubilize the metal complex and allows the final crosslinking reaction to occur at a higher concentration (50mM vs. 25mM required for pure chloroform). During the first step, the difunctional nitrile-oxide **2.5** reacts with some of the terminal alkynes on **2.1:2.2$_2$:Zn(II)$_2$** to form isoxazole prepolymers/oligomers in the presence of the excess monomer. The 4-arm PEG-alkyne **2.6** (M_n = 5.3 kgmol^{-1}, n_{PEG} mol, see Table 2.1) was dissolved in 95:5 $CHCl_3$:MeCN (~100 µL) then added to the vial. A viscous solution formed within minutes; the stir bar was removed, and then the vial was capped and left to gel at room temperature for ~48 hours.

A disposable smartSpatula® was used to transfer the metallated gels (**2.8$_{X/YM}$**) to Teflon dishes to dry overnight, and then the crude masses of the metallated gels were recorded. The gel samples were swollen in *N*-methyl-2-pyrrolidone (NMP) and cut using a die punch of 16 mm to make samples for mechanical testing.

Covalent gels with different GF (**2.7$_{GF}$**) were made by reacting **2.5** and **2.6** at different reaction times which resulted in gel fractions of 96% (**2.7$_{96}$,** 48 hrs), 86% (**2.7$_{86}$,** 24 hrs), and 74% (**2.7$_{74}$**, 12 hrs).

Table 2.1. Composition of covalent **2.7$_{GF}$** and doubly-threaded SR-PCN series **2.8$_{X/YM}$**

Covalent/ SR-PCN	Nitrile-oxide monomer **2.5**	P3R **2.1:2.2$_2$:Zn(II)$_2$**	4-arm PEG **2.6**
2.7$_{96}$	0.010 g, 1.8E-05 mol	0	0.047 g, 8.86E-06 mol
2.8$_{90/10M}$	0.010 g, 1.8E-05 mol	0.0035 g, 8.86E-07 mol	0.042 g, 7.97E-06 mol
2.8$_{80/20M}$	0.010 g, 1.8E-05 mol	0.0071 g, 1.77E-06 mol	0.038 g, 7.08E-06 mol
2.8$_{70/30M}$	0.010 g, 1.8E-05 mol	0.011 g, 2.66E-06 mol	0.033 g, 6.20E-06 mol

To remove low molecular weight components from the crude samples and calculate the gel fraction (GF), the metallated samples were submerged in a large beaker full of ~200 mL of chloroform at 48°C on a hot plate. A watch glass was placed on top of the beaker, and the gels were left heating for 4 hours to extract low molecular weight components into the soluble fraction. The extracted metallated soluble fractions were dried under high vacuum for qNMR analysis. The swollen metallated gels were dried slowly overnight at room temperature, and the gels were considered dry after measuring a consistent mass over three days. The mass of each dry, washed (metallated) sample was used to calculate the GF from Equation 2.1 (Figure 2.22, diamonds):[63]

$$\text{GF (wt \%)} = \frac{m_{dry,washed}}{m_{dry,crude}} \text{ x } 100 \quad (2.1)$$

Where $m_{dry,crude}$ is the weight of the crude (metallated) dried network after gelation. The washed metallated SR-PCNs (**2.8$_{X/YM}$**, Figure 2.2b) exhibited a yellow fluorescence under 365 nm UV light on account of the Bip/Zn^{2+} complexes[53] and qualitatively confirms the successful incorporation of P3R moieties into the network.

2.4.2.5.2 Demetallation

To demetallate, the washed, metallated SR-PCNs (**2.8$_{X/YM}$**) were submerged in 35 mL of chloroform and 5 mL of methanol in a Teflon dish. 10 µL of tetrabutylammonium hydroxide solution (1M in MeOH) was added dropwise to demetallate the rings, resulting in a rapid color change from yellow to light blue under 365 nm UV light, the fluorescence color of the free ligand, consistent with the decomplexation/demetallation of the gels. After 20 minutes, the demetallated SR-PCNs (**2.8$_{X/YD}$**) were transferred to a second Teflon dish containing 40 mL of 50/50 chloroform/methanol for 2-3 hours, changing the solvent every 30 minutes (for a total of 6 different washes). Then the gels were submerged in a large beaker full of ~200 mL of chloroform at 48°C on a hot plate. A watch glass was placed on top of the beaker, and the gels were left heating for 4 hours to ensure the complete extraction of any residual soluble fractions of the network. The soluble fractions (from the 50/50 chloroform/methanol washes and the 100% chloroform washes) were combined and dried under vacuum, then dissolved in 10 mL of DCM. The samples were washed with 20 mL of deionized water (x3) and dried under vacuum for qNMR analysis. The demetallated gels dried slowly overnight at room temperature, and then the mass of each dry, washed (demetallated) sample was used to calculate the GF from Equation 2.1. TGA confirmed that the samples were fully dried (Figure 2.20). The weight of the crude (metallated) dried network after polymerization was corrected to account for the loss in metal and counterion ($Zn(NTf_2)_2$)

mass during demetallation (Figure 2.22, squares); the weight of $Zn(NTf_2)_2$ in each metallated SR-PCN was calculated from $X_{MC,met}$, and then subtracted from the mass of the crude (metallated) network.

2.4.3 Doubly-Threaded SR-PCN Characterization

2.4.3.1 UV-Vis Spectrometry

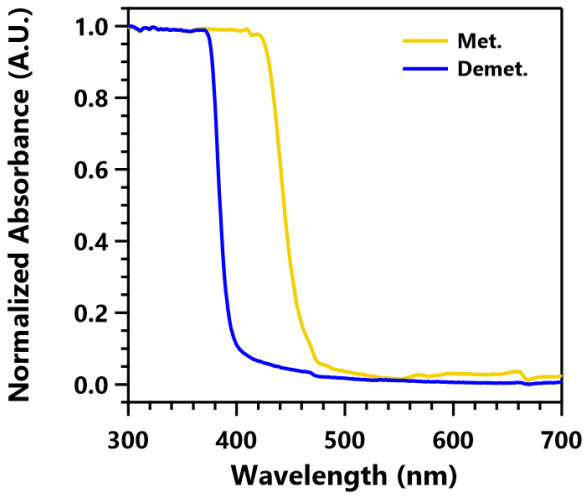

Figure 2.18. UV-Vis spectra of the metallated and demetallated (utilizing a dilute solution of tetrabutylammonium hydroxide (TBAOH)) SR-PCN (**2.8**$_{90/10}$). Gels were swollen in ethyl benzoate, cut into squares (~1mm/1mm), and placed onto a quartz glass slide for the measurement.

2.4.3.2 Quantitative NMR

The final number of rings incorporated within the network after demetallation was determined from the molar ratio of a reference molecule (thymol), with a known structure and mass, to the macrocycle (MC **2.1**) in the metallated and demetallated soluble fractions. The relationship between the number (moles) of MC in the soluble fraction and thymol is related to the integral of the diagnostic proton peak and the number of protons contributing to the peak, Equation 2.2:

$$X_{MC} \times \frac{N_{MC}}{I_{MC}} = X_{thymol} \times \frac{N_{thymol}}{I_{thymol}} \tag{2.2}$$

where X_{MC} is the number of moles of MC in the soluble fraction, X_{thymol} is the number of moles of thymol (known), I is the integrated area of the diagnostic proton peak, and N is the number of protons contributing to the peak. X_{thymol} is known, the integrals are measured via quantitative ^{1}H-NMR (qNMR), and N corresponding to those integrals are known. The doublet on the macrocycle pyridine ring (N=4) at 8.08 ppm was used as the diagnostic signal for the soluble fractions. Thymol was chosen for its diagnostic singlet (N=1) at 6.58 ppm that does not overlap with any other signals in the soluble fractions (Figure 2.19).

Rearranging Equation 2.2 and incorporating the relationship between moles and mass ($X_{thymol} = W_{thymol}/MW_{thymol}$) provides a simple relationship between the mass of the standard and the moles of MC in the soluble fraction, Equation 2.3:

$$X_{MC} = \frac{1}{4}\left(\frac{I_{MC}}{I_{thymol}}\right) \times \frac{W_{thymol}}{MW_{thymol}} \tag{2.3}$$

The average number (moles) of macrocycle (X_{MC}) present in each metallated and demetallated soluble fractions of three SR-PCN series is listed in Table 2.2 and plotted in Figure 2.3b. The metallated soluble fraction from washing the crude metallated gels, and the demetallated soluble fraction from washing the demetallated gels were used to calculate X_{MC} in each sol, i.e., $X_{MC,met}$ and $X_{MC,demet}$. Demetallating the metallated soluble fractions provided cleaner NMR spectra with more reliable MC integrations. To do this the metallated soluble fractions were dissolved in 3 mL of DCM, and 3 µL of TBAOH solution (1M in MeOH) was added to each sample. Each soluble fraction was washed with 15 mL of DI water and then the organic layer was dried under high vacuum. Each (metallated and demetallated) soluble fraction was dissolved in 600 µL of $CDCl_3$ and added to an NMR tube. An external standard was used to prevent molecular interactions with the soluble fractions. A thymol standard for quantitative NMR *Trace*CERT® (0.00050 g,

150.22 g/mol) was dissolved in 200 µL of $CDCl_3$ to make the reference solution that was added to a Wilmad® coaxial insert. The same coaxial insert was added to each NMR tube containing the (metallated or demetallated) soluble fraction and the outside of the insert was wiped with isopropyl alcohol between samples to prevent contamination. The soluble fractions from three SR-PCN series were used to calculate the average I_{MC} for each X/Y. The integral of the thymol singlet (N=1)

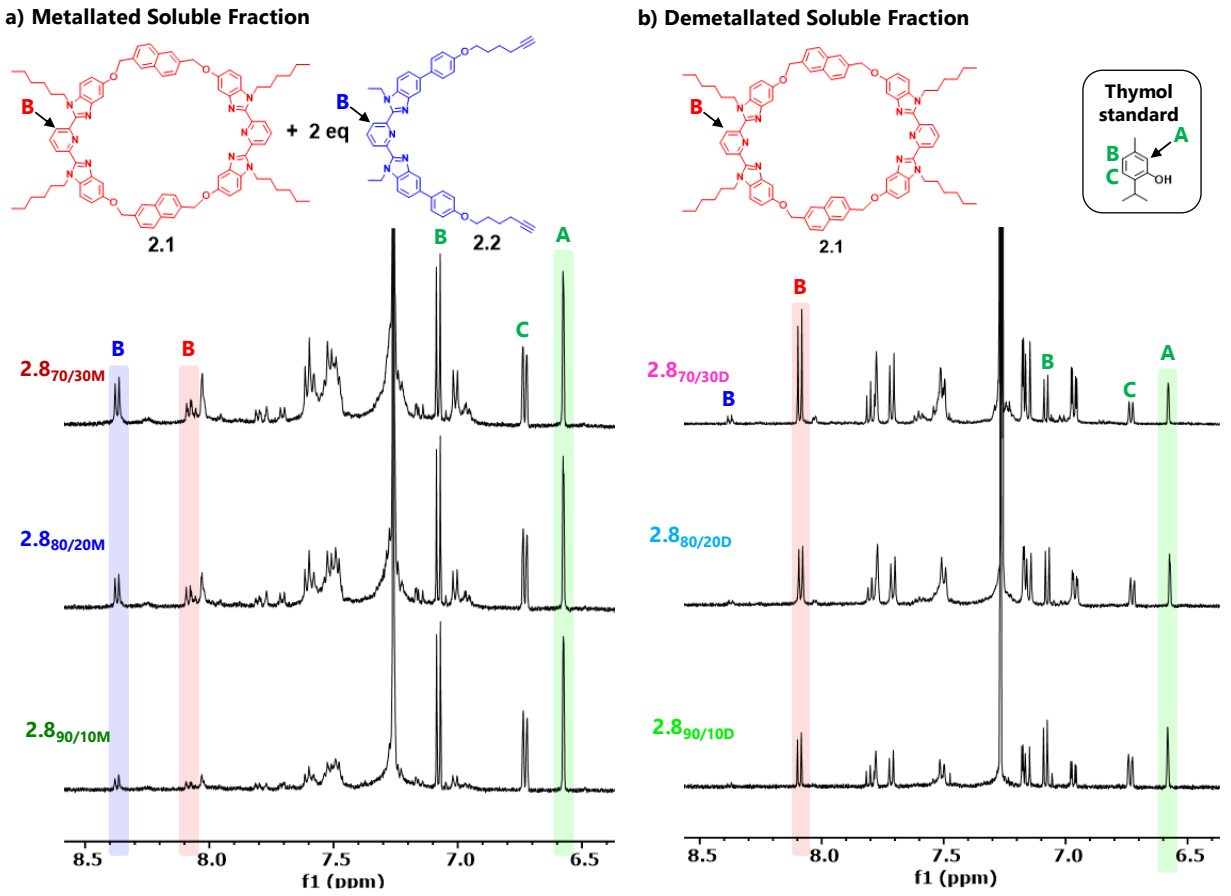

Figure 2.19. Partial ^{1}H-NMR overlay (500 MHz, 25°C, $CDCl_3$) of a) the metallated soluble fractions (after demetallation to remove metal ions) and b) the demetallated soluble fractions of a SR-PCN series **2.8**$_{X/Y}$ containing thymol as an external qNMR standard. The integrals of the doublet at 8.08 ppm (B, red) for MC **2.1** (N=4), I_{MC}, and the singlet at 6.58 ppm (A, green) for thymol (N=1), I_{thymol}, were used to calculate the moles of macrocycle **2.1** (X_{MC}) in each soluble fraction, i.e., $X_{MC,met}$ and $X_{MC,demet}$. The doublet at 8.37 ppm (B, blue) corresponds to the pyridine ring on thread **2.2** (N=4 for 2 eq of **2.2**). The doublets for **2.1** (red B) and **2.2** (blue B) integrate 1:1 (as in Figure 2.10 before metallation); therefore, the integration of **2.2** was used to verify I_{MC} at 8.08 ppm. All spectra were referenced to the thymol singlet at 6.58 ppm.

at 6.58 ppm was set to I_{thymol} =1, and the average integrals of the MC doublet (N=4) at 8.08 ppm (I_{MC}) for each soluble fraction are listed in Table 2.2.

The total number (moles) of rings that were washed out of the network ($X_{MC,total}$) is determined by adding $X_{MC,sol}$ in the metallated (i.e., $X_{MC,met}$) and demetallated (i.e., $X_{MC,met}$) soluble fractions, Equation 2.4:

$$X_{MC,total} = X_{MC,met} + X_{MC,demet} \tag{2.4}$$

The total percentage of MC lost from the network was calculated using $X_{MC,total}$ and the total number of rings added to the polymerization as P3R crosslinker (n_{P3R}), Equation 2.5:

$$\text{Total percent MC lost } = \frac{X_{MC,total}}{n_{P3R}} \times 100 \tag{2.5}$$

The percent of MC lost during demetallation was determined from $X_{MC,met}$ and $X_{MC,demet}$ using Equation 2.6:

$$\text{Percent MC lost during demetallation} = \frac{X_{MC,demet}}{n_{P3R} - X_{MC,met}} \times 100 \tag{2.6}$$

To better understand the sample, a number percent of possible MC crosslinks is calculated using Equation 2.7, plotted in Figure 2.3c, to provide a sense of how the sample compares to an ideal MC content, which assumes 100% incorporation based on the crosslinker feed ratio (plotted as a solid red line in Figure 2.3c for comparison).

$$\text{Percent MC Crosslinks} = \frac{n_{P3R} - X_{MC,total}}{n_{P3R} - X_{MC,total} + n_{PEG}} \times 100 \tag{2.7}$$

where n_{PEG} is the total number (moles) of 4-arm PEG-Alkyne crosslinker (**2.6**) added to the polymerization.

Table 2.2. Quantitative NMR experiment parameters

SR-PCN	n_{P3R} (mol)	n_{PEG} (mol)	$I_{MC,met}$	$I_{MC,demet}$	$X_{MC,met}$ (mol)	$X_{MC,demet}$ (mol)	$X_{MC,total}$ (mol)
2.8$_{90/10}$	8.86E-07	7.97E-06	0.26	0.45	2.06E-07	3.85E-07	5.91E-07
2.8$_{80/20}$	1.77E-06	7.08E-06	0.40	1.13	3.13E-07	9.51E-07	1.26E-06
2.8$_{70/30}$	2.66E-06	6.20E-06	0.85	1.37	6.62E-07	1.16E-06	1.82E-06

2.4.3.3 Thermal Characterization

Changing the crosslinking topology by altering X/Y also influences the network's thermal transitions and thermal stability in the dry (unswollen) state. Thermal properties (Table 2.3) of the dry, SR-PCNs were extracted from the TGA curves in Figure 2.20 and the DSC thermograms in Figure 2.21. Glass transition temperature T_g was determined from the half-height midpoint of the thermal transition during the second heating cycle. The melting and crystallization temperatures T_m and T_c (°C) were determined from the peak maxima obtained during the second heating/cooling cycle, and the enthalpies of fusion ΔH_f (J/g) (defined as the melting enthalpy per gram) and crystallization ΔH_c were calculated from the peak areas. The final plateau of the TGA curve determined the residual mass percentage for each sample.

The degree of crystallinity (DC) for the dry, demetallated SR-PCNs was calculated from ΔH_f using Equation 2.8:

$$\text{DC}\ (\%) = \frac{\Delta H_f}{\Delta H_f^0} \times 100 \tag{2.8}$$

where ΔH_f is the enthalpy of fusion per gram of PEG in the network and ΔH_f^0 is the enthalpy of fusion of perfectly crystalline poly(ethylene oxide) that is calculated from T_m using Equation 2.9:[78]

$$\Delta H_f^0 = 178.6 + 0.629\, T_m - 2.93 \times 10^{-3}\, T_m^2 \tag{2.9}$$

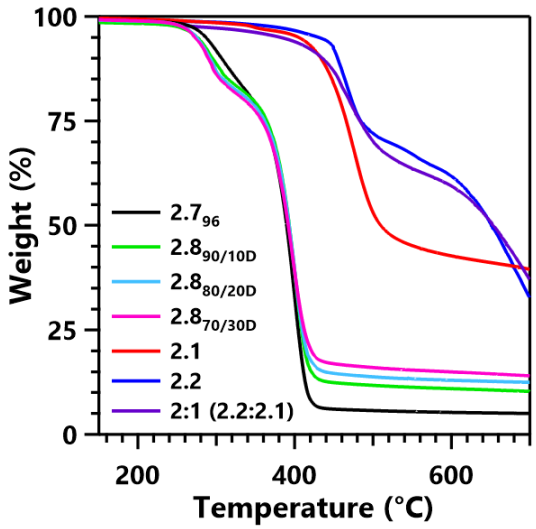

Figure 2.20. Thermogravimetric analysis (TGA) curves for dried covalent **2.7$_{96}$** and demetallated SR-PCNs **2.8$_{90/10D}$** (light green), **2.8$_{80/20D}$** (light blue), **2.8$_{70/30D}$** (pink), MC **2.1** (red), thread **2.2** (blue), and 2:1 stoichiometric mixture of **2.2:2.1** (dark purple) (ramp rate = 10°C/min).

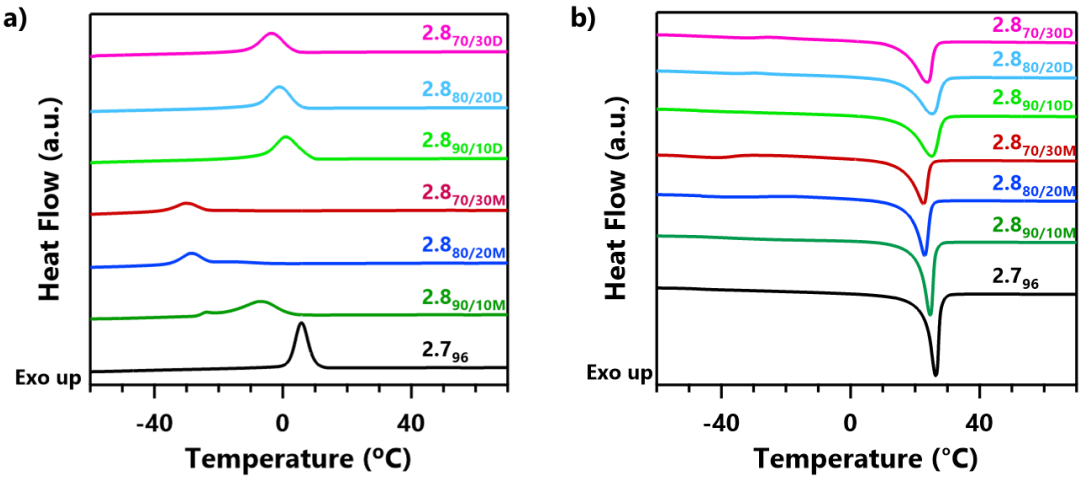

Figure 2.21. Differential scanning calorimetry (DSC) curves during a) cooling and b) second heating for the dried covalent **2.7$_{96}$** (black) and SR-PCNs: **2.8$_{90/10M}$** (green), **2.8$_{80/20M}$** (blue), **2.8$_{70/30M}$** (red), **2.8$_{90/10D}$** (light green), **2.8$_{80/20D}$** (light blue), and **2.8$_{70/30D}$** (pink), (exotherm up, ramp rate = 10°C/min, curves offset for ease of viewing).

Table 2.3. Thermal properties of dried covalent **2.7$_{96}$** and SR-PCNs **2.8$_{X/Y}$**

Covalent/ SR-PCN	T_g (°C)	T_m (°C)	ΔH_f (J/g)	DC (%)	T_c (°C)	ΔH_c (J/g)	Residual Mass (%) (from TGA)
2.7$_{96}$	-48	26	61	32	6	54	5
2.8$_{90/10M}$	-41	25	54	28	-7	51	-
2.8$_{90/10D}$	-52	25	53	28	0	47	9
2.8$_{80/20M}$	-46	23	53	27	-29	35	-
2.8$_{80/20D}$	-46	24	51	26	-3	44	12
2.8$_{70/30M}$	-53	23	51	27	-30	18	-
2.8$_{70/30D}$	-50	24	50	26	-4	43	18

2.4.3.4 Gel Fraction (GF)

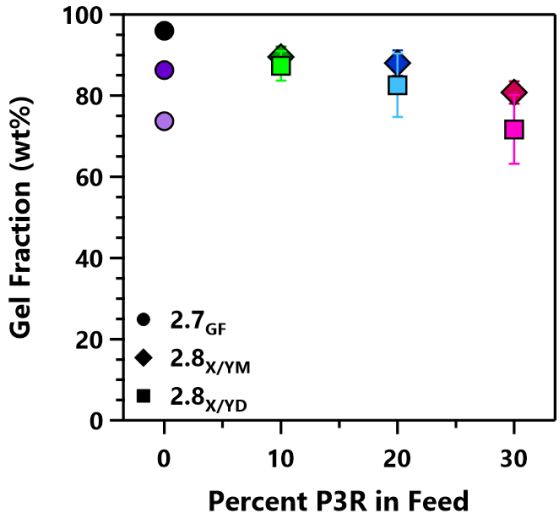

Figure 2.22. Gel fractions (GFs) for the covalent controls, **2.7$_{GF}$**: **2.7$_{96}$** (96%, black circle), **2.7$_{86}$** (86%, dark purple circle), **2.7$_{74}$** (74%, light purple circle), and SR-PCNs, **2.8$_{X/Y}$: 2.8$_{90/10M}$** (89.6%, green diamond), **2.8$_{90/10D}$** (87.3%, light green square), **2.8$_{80/20M}$** (88.1%, blue diamond), **2.8$_{80/20D}$** (82.6%, light blue square), **2.8$_{70/30M}$** (80.8%, red diamond), and **2.8$_{70/30D}$** (71.7%, pink square), calculated from Equation 2.1.

2.4.3.5 Swelling Ratio (wt%)

A sieve filtration method was employed to ensure repeatable, reproducible measurement of *N*-methyl-2-pyrrolidone (NMP) swelling, achieved via fast and complete removal of excess fluid from the gel on a wire mesh sieve using vacuum filtration.[79] The mass of a 316 stainless steel wire sieve (250 x 250 mesh size, 0.0024" opening size) was recorded as W_1. The metallated (or demetallated) gels were placed in a vacuum oven overnight at ~25°C, and their dry masses were recorded as W_0. The gels were then submerged in 15 mL of solvent for 24 hours at room temperature to allow gels to reach their swelling equilibrium. The swollen gels were poured onto the wire sieve under vacuum to remove excess solvent from the gel (and sieve), and the mass of the sieve with the gel on it was recorded as W_2. The average of three weight measurements W_2 was calculated for each sample (and multiple samples for each X/Y) and used to calculate the swelling ratio, Equation 2.10:

$$\text{Swelling Ratio (wt\%)} = \frac{W_2 - W_1 - W_0}{W_0} \times 100 \qquad (2.10)$$

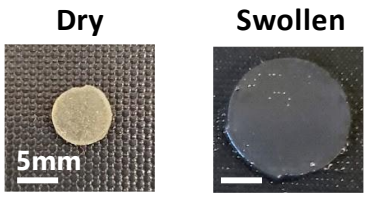

Figure 2.23. Pictures of **2.8$_{80/20D}$** dry (left) and swollen in NMP (right), 5mm scale bar.

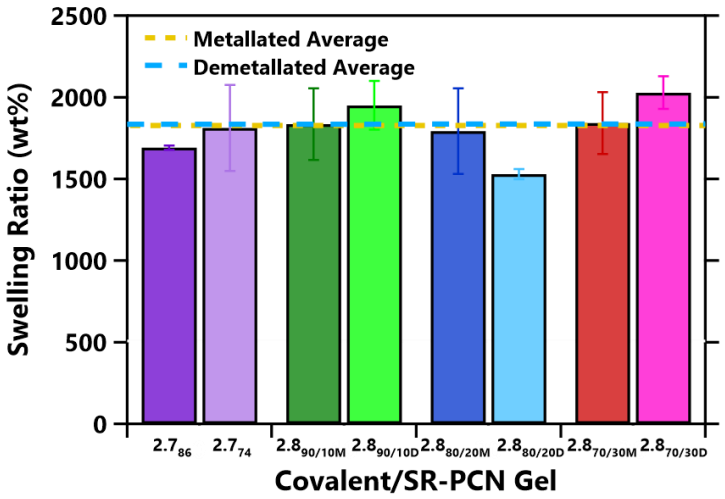

Figure 2.24. Weight-based swelling ratios calculated from Equation 2.10 for the SR-PCNs **2.8$_{90/10M}$** (dark green), **2.8$_{90/10D}$** (light green), **2.8$_{80/20M}$** (blue), **2.8$_{80/20D}$** (light blue), **2.8$_{70/30M}$** (red), and **2.8$_{70/30D}$** (pink) and the two covalent gels with comparable GF, **2.7$_{86}$** (dark purple) and **2.7$_{74}$** (light purple). All samples were swollen in NMP for at least 24 hours at ~20°C. The average swelling ratios for the metallated (~1823 wt%, yellow) and demetallated (~1836 wt%, light blue) SR-PCNs are indicated by the dashed lines, showing similar swelling with the lower GF control **2.7$_{74}$** (~1812 wt%).

2.4.3.6 Compressive Stress Relaxation

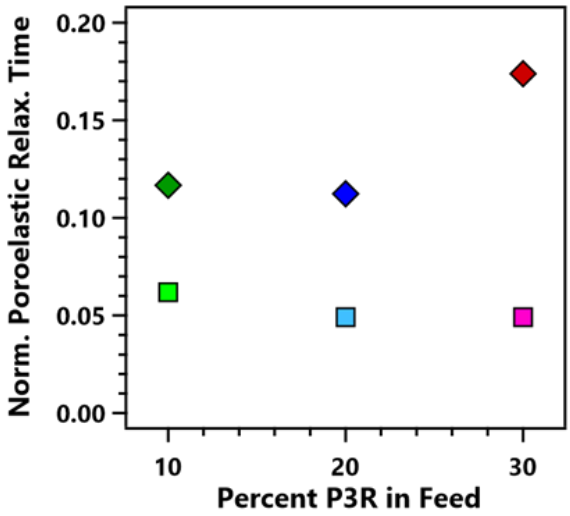

Figure 2.25. Normalized poroelastic relaxation times for SR-PCNs: **2.8$_{90/10M}$** (dark green diamond), **2.8$_{90/10D}$** (light green square), **2.8$_{80/20M}$** (blue diamond), **2.8$_{80/20D}$** (light blue square), **2.8$_{70/30M}$** (red diamond), and **2.8$_{70/30D}$** (pink square). The normalized poroelastic relaxation time is calculated by dividing the SR-PCN relaxation time by the relaxation time of the covalent gel with equivalent gel fraction (Table 2.4): SR-PCN **2.8$_{90/10M}$**, **2.8$_{90/10D}$**, and **2.8$_{80/20M}$** were normalized by **2.7$_{86}$** and **2.8$_{80/20D}$**, **2.8$_{70/30M}$**, and **2.8$_{70/30D}$** were normalized by **2.7$_{74}$**.

The additive model (Equation 2.12) and product model (Equation 2.13) used to fit the stress relaxation data assumes both relax from the same initial stress:

$$E(t)/\mathrm{E}_0 = exp\left(-\left(\frac{t}{\tau_1}\right)^{\beta_1}\right) + exp\left(-\left(\frac{\mathrm{t}}{\tau_2}\right)^{\beta_2}\right) \tag{2.12}$$

$$E(t)/\mathrm{E}_0 = \left[exp\left(-\left(\frac{t}{\tau_1}\right)^{\beta_1}\right)\right] \times \left[exp\left(-\left(\frac{\mathrm{t}}{\tau_2}\right)^{\beta_2}\right)\right] \tag{2.13}$$

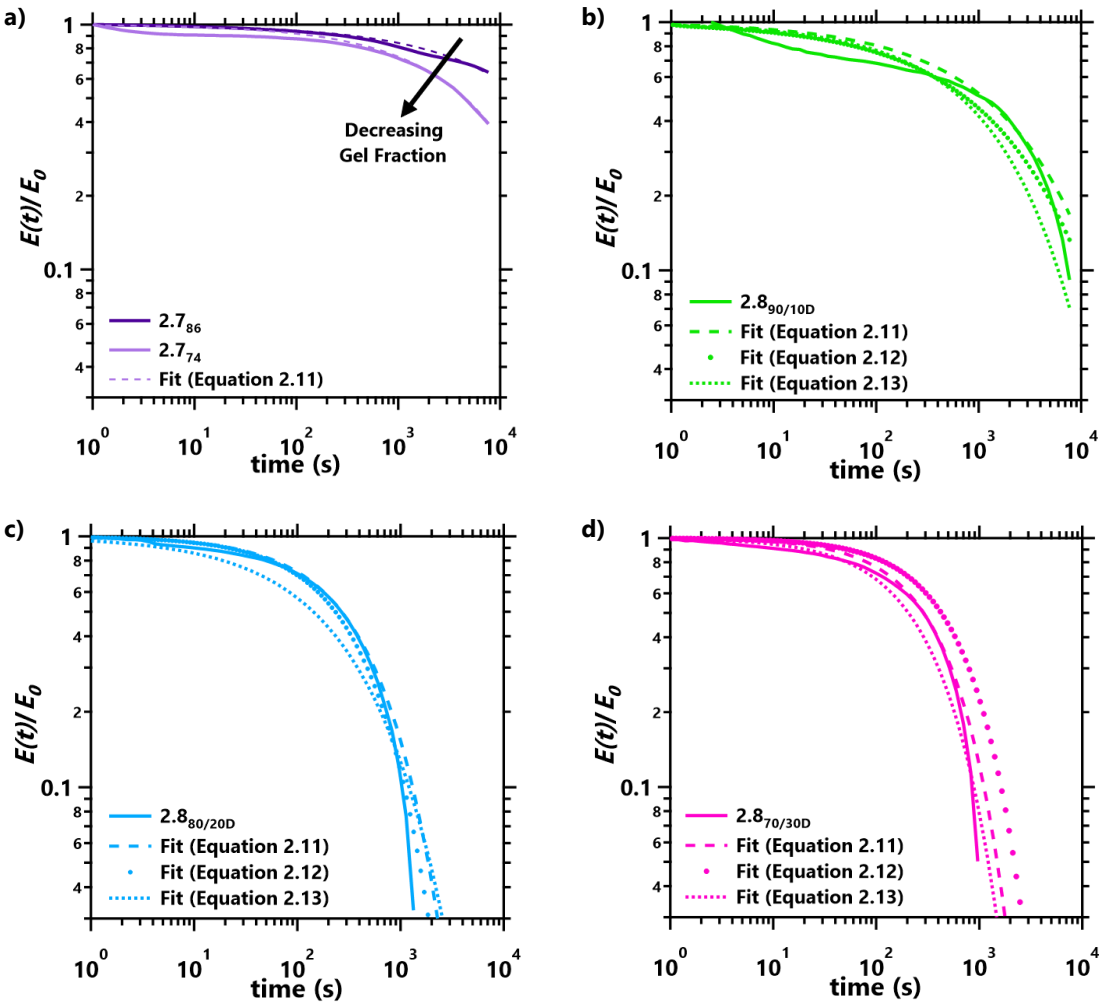

Figure 2.26. Normalized compressive stress relaxation responses (solid lines) for the a) covalent **2.7$_{86}$** (dark purple) and **2.7$_{74}$** (light purple), and demetallated SR-PCNs: b) **2.8$_{90/10D}$** (light green), c) **2.8$_{80/20D}$** (light blue), and d) **2.8$_{70/30D}$** (pink) gels swollen in NMP with fits from Equation 2.11 (long dashed lines), Equation 2.12 (dots), Equation 2.13 (short dashed lines).

Table 2.4. Stress relaxation parameters for covalent **2.7$_{GF}$** and SR-PCN **2.8$_{X/YM}$** and **2.8$_{X/YD}$** gels swollen in NMP.

Covalent/ SR-PCN	τ (s)	β
2.7$_{86}$	37710	0.484
2.7$_{74}$	8887	0.549
2.8$_{90/10M}$	4400	0.621
2.8$_{90/10D}$	2334	0.485
2.8$_{80/20M}$	4235	0.564
2.8$_{80/20D}$	436	0.758
2.8$_{70/30M}$	1545	0.555
2.8$_{70/30D}$	436	0.892

2.4.3.7 SAOC Rheology

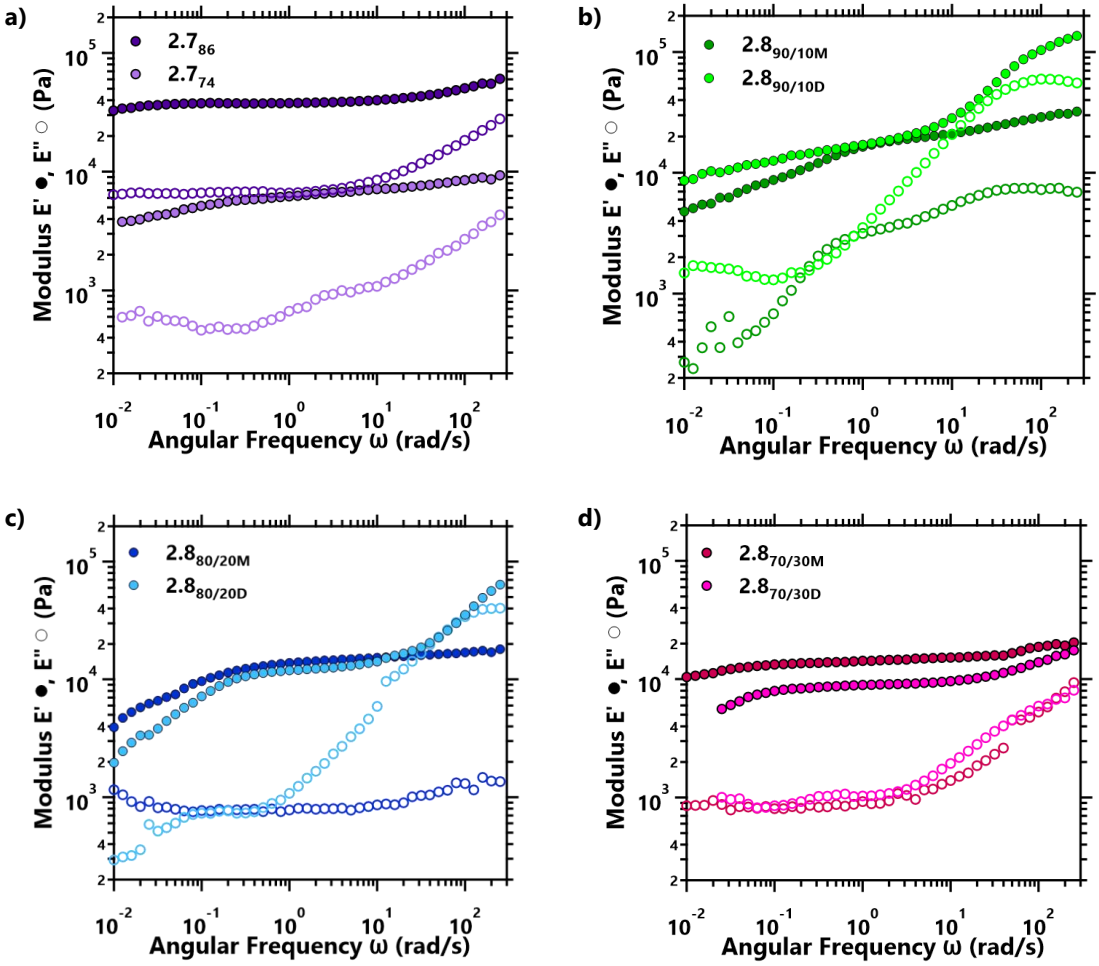

Figure 2.27. Small-amplitude oscillatory compression (SAOC) frequency sweeps showing E' (filled) and E" (open) for: a) **2.7$_{86}$** (dark purple) and **2.7$_{74}$** (light purple), b) **2.8$_{90/10M}$** (dark green) and **2.8$_{90/10D}$** (light green), c) **2.8$_{80/20M}$** (blue) and **2.8$_{80/20D}$** (light blue), and d) **2.8$_{70/30M}$** (red) and **2.8$_{70/30D}$** (pink) SR-PCN gels swollen in NMP. Samples were preloaded with 0.025 N to ensure uniform contact between the sample and plates. Frequency sweeps were performed from 1000 rad/s to 0.01 rad/s with a strain amplitude of 1%.

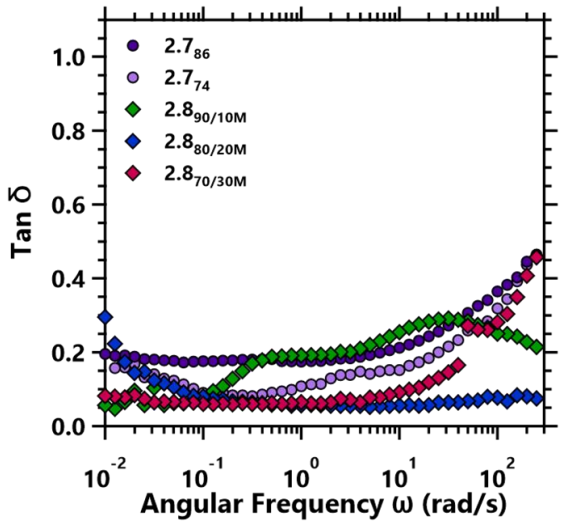

Figure 2.28. Tan δ vs. angular frequency for covalent (**2.7$_{86}$**, dark purple circles; **2.7$_{74}$**, light purple circles) and metallated SR-PCNs (**2.8$_{90/10M}$**, green diamonds; **2.8$_{80/20M}$,** blue diamonds; **2.8$_{70/30M}$,** red diamonds) swollen in NMP. Samples were preloaded with 0.025 N to ensure uniform contact between the sample and plates. Frequency sweeps were performed from 1000 rad/s to 0.01 rad/s with a strain amplitude of 1%.

2.5 References

(1) Whittaker, A. K. The Structure of Polymer Networks. In *Modern Magnetic Resonance*; Webb, G. A., Ed.; Springer Netherlands: Dordrecht, 2006; pp 583–589. https://doi.org/10.1007/1-4020-3910-7_74.

(2) Zhong, M.; Wang, R.; Kawamoto, K.; Olsen, B. D.; Johnson, J. A. Quantifying the Impact of Molecular Defects on Polymer Network Elasticity. *Science (80-.).* **2016**, *353* (6305), 1264–1268. https://doi.org/10.1126/science.aag0184.

(3) Gu, Y.; Zhao, J.; Johnson, J. A. A (Macro)Molecular-Level Understanding of Polymer Network Topology. *Trends Chem.* **2019**, *1* (3), 318–334. https://doi.org/10.1016/j.trechm.2019.02.017.

(4) Stepto, R. F. T. Fundamentals of the Formation, Structure and Properties of Polymer Networks. *Compr. Polym. Sci. Suppl.* **1989**, 199–226. https://doi.org/10.1016/b978-0-08-096701-1.00228-7.

(5) Shibayama, M. Structure-Mechanical Property Relationship of Tough Hydrogels. *Soft Matter* **2012**, *8* (31), 8030–8038. https://doi.org/10.1039/c2sm25325a.

(6) Hart, L. F.; Hertzog, J. E.; Rauscher, P. M.; Rawe, B. W.; Tranquilli, M. M.; Rowan, S. J. Material Properties and Applications of Mechanically Interlocked Polymers. *Nat. Rev. Mater.* **2021**, *6* (6), 508–530. https://doi.org/10.1038/s41578-021-00278-z.

(7) Gong, J. P. Why Are Double Network Hydrogels so Tough? *Soft Matter* **2010**, *6* (12), 2583–2590. https://doi.org/10.1039/b924290b.

(8) Chen, L.; Sheng, X.; Li, G.; Huang, F. Mechanically Interlocked Polymers Based on Rotaxanes. *Chem. Soc. Rev.* **2022**, *51* (16), 7046–7065. https://doi.org/10.1039/d2cs00202g.

(9) Okumura, Y.; Ito, K. The Polyrotaxane Gel: A Topological Gel by Figure-of-Eight Cross-Links. *Adv. Mater.* **2001**, *13* (7), 485–487. https://doi.org/10.1002/1521-4095(200104)13:7<485::AID-ADMA485>3.0.CO;2-T.

(10) Mayumi, K.; Ito, K.; Kato, K.; Mayumi, K. *Polyrotaxane and Slide-Ring Materials*; Monographs in Supramolecular Chemistry; Royal Society of Chemistry: Cambridge, 2015. https://doi.org/10.1039/9781782622284.

(11) Fleury, G.; Schlatter, G.; Brochon, C.; Travelet, C.; Lapp, A.; Lindner, P.; Hadziioannou, G. Topological Polymer Networks with Sliding Cross-Link Points: The "Sliding Gels". Relationship between Their Molecular Structure and the Viscoelastic as Well as the Swelling Properties. *Macromolecules* **2007**, *40* (3), 535–543. https://doi.org/10.1021/ma0605043.

(12) Kato, K.; Ito, K. Dynamic Transition between Rubber and Sliding States Attributed to Slidable Cross-Links. *Soft Matter* **2011**, *7* (19), 8737. https://doi.org/10.1039/c1sm06212c.

(13) Kato, K.; Yasuda, T.; Ito, K. Viscoelastic Properties of Slide-Ring Gels Reflecting Sliding Dynamics of Partial Chains and Entropy of Ring Components. *Macromolecules* **2013**, *46* (1), 310–316. https://doi.org/10.1021/ma3021135.

(14) Fleury, G.; Schlatter, G.; Brochon, C.; Hadziioannou, G. Unveiling the Sliding Motion in Topological Networks: Influence of the Swelling Solvent on the Relaxation Dynamics. *Adv. Mater.* **2006**, *18* (21), 2847–2851. https://doi.org/10.1002/adma.200600107.

(15) Kato, K.; Karube, K.; Nakamura, N.; Ito, K. The Effect of Ring Size on the Mechanical Relaxation Dynamics of Polyrotaxane Gels. *Polym. Chem.* **2015**. https://doi.org/10.1039/c4py01644k.

(16) Liu, C.; Kadono, H.; Yokoyama, H.; Mayumi, K.; Ito, K. Crack Propagation Resistance of Slide-Ring Gels. *Polymer (Guildf).* **2019**, *181*. https://doi.org/10.1016/j.polymer.2019.121782.

(17) Liu, C.; Kadono, H.; Mayumi, K.; Kato, K.; Yokoyama, H.; Ito, K. Unusual Fracture Behavior of Slide-Ring Gels with Movable Cross-Links. *ACS Macro Lett.* **2017**, *6* (12), 1409–1413. https://doi.org/10.1021/acsmacrolett.7b00729.

(18) Liu, C.; Mayumi, K.; Hayashi, K.; Jiang, L.; Yokoyama, H.; Ito, K. Direct Observation of Large Deformation and Fracture Behavior at the Crack Tip of Slide-Ring Gel. *J. Electrochem. Soc.* **2019**, *166* (9), B3143–B3147. https://doi.org/10.1149/2.0241909jes.

(19) Shinohara, Y.; Kayashima, K.; Okumura, Y.; Zhao, C.; Ito, K.; Amemiya, Y. Small-Angle X-Ray Scattering Study of the Pulley Effect of Slide-Ring Gels. *Macromolecules* **2006**, *39* (21), 7386–7391. https://doi.org/10.1021/ma061037s.

(20) Konda, A.; Mayumi, K.; Urayama, K.; Takigawa, T.; Ito, K. Influence of Structural Characteristics on Stretching-Driven Swelling of Polyrotaxane Gels with Movable Cross Links. *Macromolecules* **2012**, *45* (16), 6733–6740. https://doi.org/10.1021/ma301089k.

(21) Noda, Y.; Hayashi, Y.; Ito, K. From Topological Gels to Slide-ring Materials. *J. Appl. Polym. Sci.* **2014**, *131* (15), app.40509. https://doi.org/10.1002/app.40509.

(22) Pang, C.; Wang, H.; Zhang, F.; Patel, A. K.; Lee, H. P.; Wooley, K. L. Glucose-derived Superabsorbent Hydrogel Materials Based on Mechanically-interlocked Slide-ring and Triblock Copolymer Topologies. *J. Polym. Sci.* **2023**. https://doi.org/10.1002/pol.20220639.

(23) Choi, S.; Kwon, T.; Coskun, A.; Choi, J. W. Highly Elastic Binders Integrating Polyrotaxanes for Silicon Microparticle Anodes in Lithium Ion Batteries. *Science (80-.).* **2017**, *357* (6348), 279–283. https://doi.org/10.1126/science.aal4373.

(24) Noda, Y.; Hayashi, Y.; Ito, K. From Topological Gels to Slide-Ring Materials. *J. Appl. Polym. Sci.* **2014**, *131* (15), app.40509. https://doi.org/10.1002/app.40509.

(25) Zhuo, Y.; Li, T.; Wang, F.; Håkonsen, V.; Xiao, S.; He, J.; Zhang, Z. An Ultra-Durable

Icephobic Coating by a Molecular Pulley. *Soft Matter* **2019**, *15* (17), 3607–3611. https://doi.org/10.1039/c9sm00162j.

(26) Nakahata, M.; Mori, S.; Takashima, Y.; Yamaguchi, H.; Harada, A. Self-Healing Materials Formed by Cross-Linked Polyrotaxanes with Reversible Bonds. *Chem* **2016**. https://doi.org/10.1016/j.chempr.2016.09.013.

(27) De Bo, G. Combining Mobile and Dynamic Bonds for Rapid and Efficient Self-Healing Materials. *Chem* **2016**, *1* (5), 672–673. https://doi.org/10.1016/j.chempr.2016.10.013.

(28) Cho, I. S.; Ooya, T. Cell-Encapsulating Hydrogel Puzzle: Polyrotaxane-Based Self-Healing Hydrogels. *Chem. – A Eur. J.* **2020**, *26* (4), 913–920. https://doi.org/10.1002/chem.201904446.

(29) Kobayashi, Y.; Zheng, Y.; Takashima, Y.; Yamaguchi, H.; Harada, A. Physical and Adhesion Properties of Supramolecular Hydrogels Cross-Linked by Movable Cross-Linking Molecule and Host-Guest Interactions. *Chem. Lett.* **2018**, *47* (11), 1387–1390. https://doi.org/10.1246/cl.180646.

(30) Sakai, T.; Murayama, H.; Nagano, S.; Takeoka, Y.; Kidowaki, M.; Ito, K.; Seki, T. Photoresponsive Slide-Ring Gel. *Adv. Mater.* **2007**, *19* (15), 2023+. https://doi.org/10.1002/adma.200700457.

(31) Bin Imran, A.; Esaki, K.; Gotoh, H.; Seki, T.; Ito, K.; Sakai, Y.; Takeoka, Y. Extremely Stretchable Thermosensitive Hydrogels by Introducing Slide-Ring Polyrotaxane Cross-Linkers and Ionic Groups into the Polymer Network. *Nat. Commun.* **2014**, *5* (1), 5124. https://doi.org/10.1038/ncomms6124.

(32) Yasumoto, A.; Gotoh, H.; Gotoh, Y.; Imran, A. Bin; Hara, M.; Seki, T.; Sakai, Y.; Ito, K.; Takeoka, Y. Highly Responsive Hydrogel Prepared Using Poly(N -Isopropylacrylamide)-Grafted Polyrotaxane as a Building Block Designed by Reversible Deactivation Radical Polymerization and Click Chemistry. *Macromolecules* **2017**, *50* (1), 364–374. https://doi.org/10.1021/acs.macromol.6b01955.

(33) Ma, W.; Fang, H.; Tian, D.; Zheng, L.; Xie, M.; Sun, R. Solvent-Free Stretchable Photo-Responsive Supramolecular Actuator Topologically Cross-Linked by Azobenzene-Cyclodextrin Based Slide-Ring System. *Dye. Pigment.* **2022**, *200*, 110120. https://doi.org/10.1016/j.dyepig.2022.110120.

(34) Zhang, K.; Lackey, M. A.; Cui, J.; Tew, G. N. Gels Based on Cyclic Polymers. *J. Am. Chem. Soc.* **2011**, *133* (11), 4140–4148. https://doi.org/10.1021/ja111391z.

(35) Oike, H.; Mouri, T.; Tezuka, Y. A Cyclic Macromonomer Designed for a Novel Polymer Network Architecture Having Both Covalent and Physical Linkages. *Macromolecules* **2001**, *34* (18), 6229–6234. https://doi.org/10.1021/ma010291b.

(36) Xing, H.; Li, Z.; Wu, Z. L.; Huang, F. Catenane Crosslinked Mechanically Adaptive Polymer Gel. *Macromol. Rapid Commun.* **2018**, *39* (1), 1–6.

https://doi.org/10.1002/marc.201700361.

(37) Nosiglia, M. A.; Colley, N. D.; Danielson, M. K.; Palmquist, M. S.; Delawder, A. O.; Tran, S. L.; Harlan, G. H.; Barnes, J. C. Metalation/Demetalation as a Postgelation Strategy To Tune the Mechanical Properties of Catenane-Crosslinked Gels. *J. Am. Chem. Soc.* **2022**, *144* (22), 9990–9996. https://doi.org/10.1021/jacs.2c03166.

(38) Hu, P.; Madsen, J.; Huang, Q.; Skov, A. L. Elastomers without Covalent Cross-Linking: Concatenated Rings Giving Rise to Elasticity. *ACS Macro Lett.* **2020**, *9* (10), 1458–1463. https://doi.org/10.1021/acsmacrolett.0c00635.

(39) Jiang, L.; Liu, C.; Mayumi, K.; Kato, K.; Yokoyama, H.; Ito, K. Highly Stretchable and Instantly Recoverable Slide-Ring Gels Consisting of Enzymatically Synthesized Polyrotaxane with Low Host Coverage. *Chem. Mater.* **2018**, *30* (15), 5013–5019. https://doi.org/10.1021/acs.chemmater.8b01208.

(40) Xing, Z.; Shu, D. W.; Lu, H.; Fu, Y. Q. Untangling the Mechanics of Entanglements in Slide-Ring Gels towards Both Super-Deformability and Toughness. *Soft Matter* **2022**, *18* (6), 1302–1309. https://doi.org/10.1039/d1sm01737c.

(41) Yamamoto, K.; Nameki, R.; Sogawa, H.; Takata, T. Macrocyclic Dinuclear Palladium Complex as a Novel Doubly Threaded [3]Rotaxane Scaffold and Its Application as a Rotaxane Cross-Linker. *Angew. Chemie Int. Ed.* **2020**, *59* (41), 18023–18028. https://doi.org/10.1002/anie.202007866.

(42) Jang, K.; Iijima, K.; Koyama, Y.; Uchida, S.; Asai, S.; Takata, T. Synthesis and Properties of Rotaxane-Cross-Linked Polymers Using a Double-Stranded γ-CD-Based Inclusion Complex as a Supramolecular Cross-Linker. *Polymer (Guildf).* **2017**, *128*, 379–385. https://doi.org/10.1016/j.polymer.2017.01.062.

(43) Iijima, K.; Aoki, D.; Otsuka, H.; Takata, T. Synthesis of Rotaxane Cross-Linked Polymers with Supramolecular Cross-Linkers Based on γ-CD and PTHF Macromonomers: The Effect of the Macromonomer Structure on the Polymer Properties. *Polymer (Guildf).* **2017**, *128*, 392–396. https://doi.org/10.1016/j.polymer.2017.01.024.

(44) Harada, A. Design and Construction of Supramolecular Architectures Consisting of Cyclodextrins and Polymers. In *Metal Complex Catalysts Supercritical Fluid Polymerization Supramolecular Architecture*; Springer Berlin Heidelberg: Berlin, Heidelberg, 2017; pp 141–191. https://doi.org/10.1007/3-540-68442-5_4.

(45) Lewis, J. E. M.; Beer, P. D.; Loeb, S. J.; Goldup, S. M. Metal Ions in the Synthesis of Interlocked Molecules and Materials. *Chem. Soc. Rev.* **2017**, *46* (9), 2577–2591. https://doi.org/10.1039/C7CS00199A.

(46) Denis, M.; Goldup, S. M. The Active Template Approach to Interlocked Molecules. *Nat. Rev. Chem.* **2017**, *1* (8). https://doi.org/10.1038/s41570-017-0061.

(47) Hubin, T. J.; Busch, D. H. Template Routes to Interlocked Molecular Structures and Orderly

Molecular Entanglements. *Coord. Chem. Rev.* **2000**, *200–202*, 5–52. https://doi.org/10.1016/S0010-8545(99)00242-8.

(48) McKenzie, B. M.; Miller, A. K.; Wojtecki, R. J.; Johnson, J. C.; Burke, K. A.; Tzeng, K. A.; Mather, P. T.; Rowan, S. J. Improved Synthesis of Functionalized Mesogenic 2,6-Bisbenzimidazolylpyridine Ligands. *Tetrahedron* **2008**, *64* (36), 8488–8495. https://doi.org/10.1016/j.tet.2008.05.075.

(49) Piguet, C.; Bernardinelli, G.; Williams, A. F.; Bocquet, B. Formation of the First Isomeric [2]Catenates by Self-Assembly about Two Different Metal Ions. *Angew. Chemie Int. Ed. 6(11), 951–952.* **1995**, *34* (5), 582–584.

(50) Wojtecki, R. J.; Wu, Q.; Johnson, J. C.; Ray, D. G.; Korley, L. T. J.; Rowan, S. J. Optimizing the Formation of 2,6-Bis(N-Alkyl-Benzimidazolyl)Pyridine-Containing [3]Catenates through Component Design. *Chem. Sci.* **2013**, *4* (12), 4440. https://doi.org/10.1039/c3sc52082j.

(51) Wu, Q.; Rauscher, P. M.; Lang, X.; Wojtecki, R. J.; De Pablo, J. J.; Hore, M. J. A. A.; Rowan, S. J.; Wu, Q.; De Pablo, J. J.; Wojtecki, R. J.; Rowan, S. J.; Rauscher, P. M. Poly[n]Catenanes: Synthesis of Molecular Interlocked Chains. *Science (80-.).* **2017**, *358* (6369), 1434–1439. https://doi.org/10.1126/science.aap7675.

(52) Tranquilli, M. M.; Wu, Q.; Rowan, S. J. Effect of Metallosupramolecular Polymer Concentration on the Synthesis of Poly[n]Catenanes. *Chem. Sci.* **2021**, *12* (25), 8722–8730. https://doi.org/10.1039/d1sc02450g.

(53) Hertzog, J. E.; Maddi, V. J.; Hart, L. F.; Rawe, B. W.; Rauscher, P. M.; Herbert, K. M.; Bruckner, E. P.; de Pablo, J. J.; Rowan, S. J. Metastable Doubly Threaded [3]Rotaxanes with a Large Macrocycle. *Chem. Sci.* **2022**, *00*, 1–12. https://doi.org/10.1039/d2sc01486f.

(54) Lee, Y. G.; Yonekawa, M.; Koyama, Y.; Takata, T. Synthesis of a Kinetically Stabilized Homoditopic Nitrile N-Oxide Directed toward Catalyst-Free Click Polymerization. *Chem. Lett.* **2010**, *39* (4), 420–421. https://doi.org/10.1246/cl.2010.420.

(55) Sogawa, H.; Monjiyama, S.; Wang, C.-G.; Tsutsuba, T.; Takata, T. New Synthetic Route to OH-Functionalized Nitrile N -Oxide and Polyfunctional Nitrile N -Oxides for Click Crosslinking and Decrosslinking of Natural Rubber. *Polym. Chem.* **2018**, *9* (34), 4382–4385. https://doi.org/10.1039/C8PY00904J.

(56) Wang, C. G.; Koyama, Y.; Yonekawa, M.; Uchida, S.; Takata, T. Polymer Nitrile N-Oxides Directed toward Catalyst- and Solvent-Free Click Grafting. *Chem. Commun.* **2013**, *49* (70), 7723–7725. https://doi.org/10.1039/c3cc42992j.

(57) Tsutsuba, T.; Sogawa, H.; Takata, T. Preparation of a Highly Reactive Polymer Click Reagent, PEG Nitrile: N -Oxide, and Its Application in Block and Star Polymer Synthesis. *Polym. Chem.* **2017**, *8* (9), 1445–1448. https://doi.org/10.1039/c7py00100b.

(58) Singh, I.; Zarafshani, Z.; Lutz, J.-F.; Heaney, F. Metal-Free “Click” Chemistry: Efficient

Polymer Modification via 1,3-Dipolar Cycloaddition of Nitrile Oxides and Alkynes. *Macromolecules* **2009**, *42* (15), 5411–5413. https://doi.org/10.1021/ma9013912.

(59) Matsumura, T.; Ishiwari, F.; Koyama, Y.; Takata, T. C−C Bond-Forming Click Synthesis of Rotaxanes Exploiting Nitrile N -Oxide. *Org. Lett.* **2010**, *12* (17), 3828–3831. https://doi.org/10.1021/ol101543x.

(60) Yuki, T.; Koyama, Y.; Matsumura, T.; Takata, T. Click Annulation of Pseudo[2]Rotaxane to [2]Catenane Exploiting Homoditopic Nitrile N -Oxide. *Org. Lett.* **2013**, *15* (17), 4438–4441. https://doi.org/10.1021/ol401986u.

(61) Lee, Y. G.; Koyama, Y.; Yonekawa, M.; Takata, T. Synthesis of Main-Chain-Type Polyrotaxanes by New Click Polymerization Using Homoditopic Nitrile N -Oxides via Rotaxanation-Polymerization Protocol. *Macromolecules* **2010**, *43* (9), 4070–4080. https://doi.org/10.1021/ma100262g.

(62) Tsutsuba, T.; Sogawa, H.; Kuwata, S.; Takata, T. Kinetically Stabilized Aliphatic Nitrile *N* -Oxides as Click Agents: Synthesis, Structure, and Reactivity. *Chem. Lett.* **2017**, *46* (3), 315–318. https://doi.org/10.1246/cl.161098.

(63) Ahmad, Z.; Salman, S.; Khan, S. A.; Amin, A.; Rahman, Z. U.; Al-Ghamdi, Y. O.; Akhtar, K.; Bakhsh, E. M.; Khan, S. B. Versatility of Hydrogels: From Synthetic Strategies, Classification, and Properties to Biomedical Applications. *Gels* **2022**, *8* (3). https://doi.org/10.3390/gels8030167.

(64) Zhang, K.; Feng, W.; Jin, C. Protocol Efficiently Measuring the Swelling Rate of Hydrogels. *MethodsX* **2020**, *7* (December 2019), 100779. https://doi.org/10.1016/j.mex.2019.100779.

(65) Dey, K.; Agnelli, S.; Borsani, E.; Sartore, L. Degradation-Dependent Stress Relaxing Semi-Interpenetrating Networks of Hydroxyethyl Cellulose in Gelatin-Peg Hydrogel with Good Mechanical Stability and Reversibility. *Gels* **2021**, *7* (4). https://doi.org/10.3390/gels7040277.

(66) Chan, E. P.; Deeyaa, B.; Johnson, P. M.; Stafford, C. M. Poroelastic Relaxation of Polymer-Loaded Hydrogels. *Soft Matter* **2012**, *8* (31), 8234–8240. https://doi.org/10.1039/c2sm25363a.

(67) Kingsbury, H. B. On the Dynamic Behavior of Poroelastic Materials. *J. Acoust. Soc. Am.* **1979**, *65* (1), 90–95. https://doi.org/10.1121/1.382273.

(68) Cuccia, N. L.; Pothineni, S.; Wu, B.; Méndez Harper, J.; Burton, J. C. Pore-Size Dependence and Slow Relaxation of Hydrogel Friction on Smooth Surfaces. *Proc. Natl. Acad. Sci.* **2020**, *117* (21), 11247–11256. https://doi.org/10.1073/pnas.1922364117.

(69) Peppas, N. A.; Bures, P.; Leobandung, W.; Ichikawa, H. Hydrogels in Pharmaceutical Formulations. *Eur. J. Pharm. Biopharm.* **2000**, *50* (1), 27–46. https://doi.org/10.1016/S0939-6411(00)00090-4.

(70) Kuang, X.; Liu, G.; Dong, X.; Wang, D. Correlation between Stress Relaxation Dynamics and Thermochemistry for Covalent Adaptive Networks Polymers. *Mater. Chem. Front.* **2017**, *1* (1), 111–118. https://doi.org/10.1039/C6QM00094K.

(71) Yasuda, Y.; Hidaka, Y.; Mayumi, K.; Yamada, T.; Fujimoto, K.; Okazaki, S.; Yokoyama, H.; Ito, K. Molecular Dynamics of Polyrotaxane in Solution Investigated by Quasi-Elastic Neutron Scattering and Molecular Dynamics Simulation: Sliding Motion of Rings on Polymer. *J. Am. Chem. Soc.* **2019**, *141* (24), 9655–9663. https://doi.org/10.1021/jacs.9b03792.

(72) Mayumi, K.; Nagao, M.; Endo, H.; Osaka, N.; Shibayama, M.; Ito, K. Dynamics of Polyrotaxane Investigated by Neutron Spin Echo. *Phys. B Condens. Matter* **2009**, *404* (17), 2600–2602. https://doi.org/10.1016/j.physb.2009.06.035.

(73) Berberan-Santos, M. N.; Bodunov, E. N.; Valeur, B. Mathematical Functions for the Analysis of Luminescence Decays with Underlying Distributions 1. Kohlrausch Decay Function (Stretched Exponential). *Chem. Phys.* **2005**, *315* (1–2), 171–182. https://doi.org/10.1016/j.chemphys.2005.04.006.

(74) Galli, M.; Comley, K. S. C.; Shean, T. A. V.; Oyen, M. L. Viscoelastic and Poroelastic Mechanical Characterization of Hydrated Gels. *J. Mater. Res.* **2009**, *24* (3), 973–979. https://doi.org/10.1557/jmr.2009.0129.

(75) Syed, I. H.; Stratmann, P.; Hempel, G.; Klüppel, M.; Saalwächter, K. Entanglements, Defects, and Inhomogeneities in Nitrile Butadiene Rubbers: Macroscopic versus Microscopic Properties. *Macromolecules* **2016**, *49* (23), 9004–9016. https://doi.org/10.1021/acs.macromol.6b01802.

(76) Łukasik, B.; Milczarek, J.; Pawlowska, R.; Żurawiński, R.; Chworos, A. Facile Synthesis of Fluorescent Distyrylnaphthalene Derivatives for Bioapplications. *New J. Chem.* **2017**, *41* (15), 6977–6980. https://doi.org/10.1039/C7NJ00004A.

(77) Hsieh, T. H. H.; Dong, V. M. Indole Synthesis: Palladium-Catalyzed C-H Bond Amination via Reduction of Nitroalkenes with Carbon Monoxide. *Tetrahedron* **2009**, *65* (16), 3062–3068. https://doi.org/10.1016/j.tet.2008.11.034.

(78) Domszy, R. C.; Mobbs, R. H.; Leung, Y. K.; Heatley, F.; Booth, C. Crystallinity and Fusion of Low Molecular Weight α,ω-Alkoxy-Poly (Ethylene Oxide): Octadecoxy to Triacontanoxy End-Groups. *Polymer (Guildf).* **1979**, *20* (10), 1204–1214. https://doi.org/10.1016/0032-3861(79)90144-7.

(79) Zhang, K.; Feng, W.; Jin, C. Protocol Efficiently Measuring the Swelling Rate of Hydrogels. *MethodsX* **2020**, *7* (September 2019), 100779. https://doi.org/10.1016/j.mex.2019.100779.

3 Improving Structural Understanding of Relaxations in Doubly-Threaded Slide-Ring Polycatenane Networks

3.1 Introduction

Copolymerization of doubly-threaded pseudo[3]rotaxanes and covalent crosslinkers in Chapter 2 presented a simple way to include complex catenane moieties into a network structure, providing a platform for deeper investigations of the structure-property relationships in these SR-PCNs. SR-PCNs contain two primary molecular structures – the chain and the ring – where the diffusion of doubly-threaded rings influences the conformation and mesh size of the network. Connections between polymer chains dictate the conformational changes that result in viscoelastic relaxations. These relaxations are influenced by the flexibility and molecular weight of the chains, which can be systematically controlled in the SR-PCN system by adding different monomers into the click polymerization. Furthermore, pseudo[3]rotaxanes (P3Rs) can be assembled from different types of rings to determine how the ring's size, flexibility, and solubility influence the conformation of chains between crosslinks.

Determining how the doubly-threaded crosslink behaves in this system and what variables interact with that behavior is the first step to unlocking the potential of these SR-PCNs as a major platform for studying interlocked systems. Crosslinking topology influences the coupled network relaxations between ring mobility and chain diffusion[1] during deformation and is frequency-dependent. Ring diffusion, by the nature of the chain, is on a longer length scale than the local segmental relaxations of the polymer chain. Therefore, ring diffusion along the chain will always be limited by the relaxation time of the polymer chain unless the chain is very stiff (i.e., high persistence length). Rheology experiments on CD/PEG-based SRNs swollen in DMSO[2–6] reveal a second modulus plateau at a low frequency with a pronounced tan(δ) peak that marks the (sliding)

transition between two different viscoelastic regimes. The second-order relaxation dynamics of the glass transition are related to the reptation model with a relaxation time, $\tau = M^3$, and the sliding transition has a similar molecular weight dependence and influence on the modulus. The rate-determining process for the relaxation is the reptation-like local diffusion of partial chains through the crosslink, where the sliding motion produces a change in the distribution of partial strand lengths between mobile crosslinks.

Swelling solvents that favor ring aggregation suppress ring sliding, leading to similar structural inhomogeneities typical of covalently crosslinked systems.[7–9] Fixed crosslinks restrain polymer chains in typical networks, preventing these inhomogeneities from being resolved. However, the lack of constraining covalent crosslinks in SRNs allows for faster, facile network relaxations when rings become mobile. SRNs show viscoelastic behavior highly dependent on the swelling solvent because of the different inter- and intramolecular interactions between CD rings and the type of solvent.[5] For example, the long α-CD transient tubes formed by intramolecular hydrogen bonds increase the persistence length of the sliding chains in DMSO (Figure 3.1a). This increased stiffness leads to limited mobility of the SRN in DMSO vs. the same SRN in water. However, higher modulus values are observed for SRNs in water due to the high number of intermolecular physical bonds in water that form chemical (permanent) and physical (transient) crosslinks between CDs (Figure 3.1b). The overall shape of the storage modulus (E', Figure 3.1c) curve is similar for SRNs in DMSO and water: the effective relaxation of PEG chains through α-CD figure-of-eight crosslinks is possible at low frequencies, and at higher frequencies, these relaxations slow down due to the presence of CD tubes that increase the persistence length of the polymer chains, leading to a higher modulus plateau.[2] In contrast, the shape of the loss modulus (E") curve depends on the solvent: the more elastic behavior of the chains in DMSO leads to

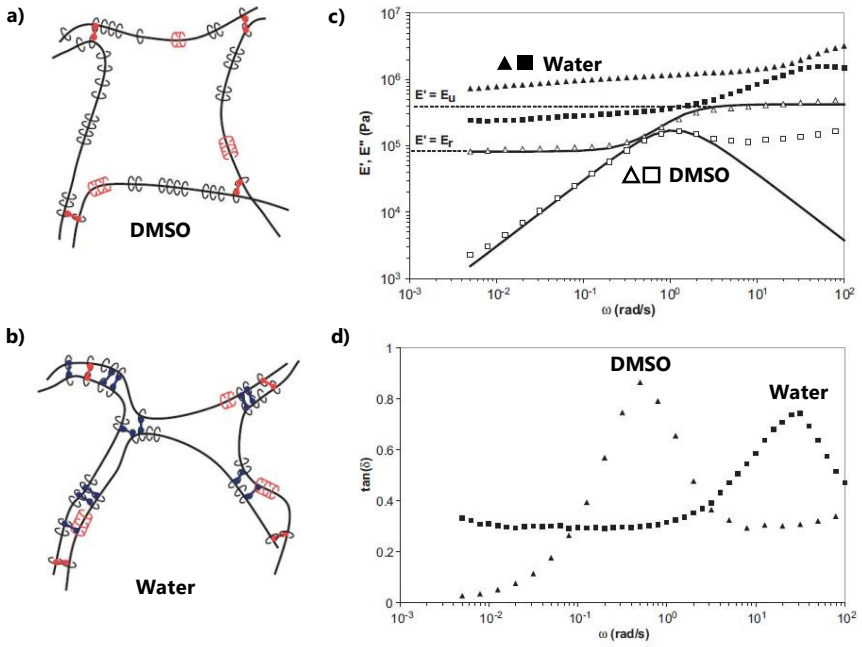

Figure 3.1. Effect of DMSO and water on CD-based SRN viscoelasticity.[5] a) SRN in DMSO with permanent CD tubes due to intramolecular reaction during crosslinking (red) and the transient CD tubes that form in DMSO. b) SRN in water with topological chemical (red) and physical (blue) crosslinking points between rings on different polyrotaxanes. c) Change in viscoelastic properties (E' triangles, E" squares for SRN in water (filled points) and DMSO (open points). d) Tan δ for DMSO (triangles) and water (squares) SRNs. Adapted from Ref. 5 with permission from John Wiley and Sons.

variations in E" at low frequencies, whereas E" plateaus in water. The swelling solvent changes the effective network chains' length and rigidity, leading to higher relaxation times in DMSO than in water (Figure 3.1d). The shift in tan δ results from the higher persistence length of the network strands in DMSO and their persistence in time compared to those in water.[5]

The co-inclusion of solvent in ring cavities can also influence gel mechanics.[6] The figure-of-eight topology is one type of ring crosslink; polymer chains can also come together inside a single ring cavity where the friction and repulsion between two chains contribute to the mechanics and rate of ring sliding. Though γ-CD rings are large enough to thread two polymer chains, the co-inclusion of solvent is known to occur in the extra cavity of a complex between γ-CD and a thin

polymer, leading SRNs with larger γ-CD figure-of-eights to show relaxation times five times slower than those with smaller (α-CD) rings.[6]

The mechanical deformation of swollen networks involves two molecular processes of energy dissipation and time-dependent behavior: the conformational change of the polymer chains and the mass transport of solvent through the network, known as poroelasticity.[10] As discussed above, viscoelastic dissipation is related to the network relaxation and reconfiguration of polymer chains. Poroelastic energy dissipation originates from the frictional interactions between the solvent and solid structure due to fluid pressurization and viscous drag through the porous matrix. At lower frequencies, covalent gels show a distinct relaxation as solvent molecules migrate out of the gel matrix. When a covalent gel is subject to constant strain, the stress relaxes as solvent migrates out of the gel, so the network undergoes elastic deformation.[11] Polymer gels can absorb (and expel) a large amount of solvent, resulting in volume deformation that contributes to network relaxations. The specifics of this relaxation depend on the mechanics of the polymer chains in the network and how the swelling solvent interacts with those chains.[10–13] Furthermore, the specific nature of the relaxation will be influenced by how the measurement is performed and the limitations of that measurement. The test conditions, material, process conditions, etc., all determine whether the viscoelastic or poroelastic response (or both) might be dominant.[14]

As discussed in Chapter 2, the existence of a second independent relaxation (likely attributed to ring sliding) capable of interacting with the poroelastic relaxation observed under compressive strain may account for the inability of a single stretched exponential to capture SR-PCN behavior. Generally, polymer gels with high liquid content exhibit poroviscoelastic behavior, and the network relaxations attributed to ring sliding will undoubtedly impact solvent migration in SRNs. The gel structure, particularly the mesh size of the percolating covalent network that

changes with ring sliding, likely drives the solvent transport in the SR-PCNs. This hypothesis warrants further investigation into the frequency response of SR-PCNs using different techniques to decouple poroviscoelastic relaxations and achieve a better structural understanding of the SR-PCN system under deformation.

Previous studies on the rheological properties of gels[11,15] focus on measuring the modulus and complex modulus of gels by compression testing,[16–19] cavitation rheology,[20] particle-tracking microrheology,[21,22] and indentation,[29–33,35,36] to name a few (Figure 3.2).[23] Hydrated, compliant specimens can be difficult to grip for tensile or compressive mechanical testing, making

method	Advantage	disadvantage
Tensile test	• Modulus and Poisson's ratio can be measured. • Simple geometry for analysis	• Difficult to clamp sample • Sample requires uniform cross-section. • Only applicable to relatively stiff gels (modulus > 100kPa) • Local property cannot be measured.
Compression test	• Modulus, Poisson's ratio and diffusivity can be measured • Simple geometry for analysis	• For transport measurements, sample needs to be small to reduce measurement time. • Local property cannot be measured
Beam bending	• Modulus, Poisson's ratio and diffusivity can be measured • Boundary value problem is simple	• Only applicable to stiff gels (modulus > MPa) • Local property cannot be measured
Shear	• Shear modulus can be measured	• Not possible to measure transport properties
Cavitation	• Modulus can be measured • Set-up and handling are simple • Local property can be measured	• Only instantaneous modulus is measured • Diffusivity cannot be measured
Microbead rheology	• Modulus can be measured • Viscoelasticity can be characterized	• Only used for uncross-linked polymer solutions or lightly cross-linked gels (modulus<100 Pa). • Data interpretation is difficult
Nano-scale indentation	• Modulus can be measured • Viscoelasticity can be characterized • Local property can be measured	• Equipment is expensive • Contact point is hard to detect
Macro-scale indentation	• Modulus, Poisson's ratio and diffusivity can be measured • Simple experimental set-up • Minimum specimen preparation	• Viscoelasticity cannot be characterized • Large sample is required (>5mm)
Swelling kinetics	• Diffusivity can be measured	• For small samples, tracing of fluorescent particles may be required • Local property cannot be measured • Modulus cannot be measured.
Transport through membrane	• Diffusivity can be measured.	• Very difficult measurement • Local property cannot be measured • Modulus cannot be measured • Specific transport model is required

Figure 3.2. Advantages and disadvantages of existing techniques for studying the mechanical properties of polymer gels.[23] Adapted from Ref. 23 with permission from Springer Nature.

probe-based testing more ideal. The difficulty in synthesizing ditopic macrocycles on a larger scale requires synthesizing multiple batches and arduous purification. Nanoindentation requires minimal sample and preparation, overcoming the challenges of making hydrogels into regular specimen geometries that require large amounts of sample.[24–26]

The combination of interlocked and fixed crosslinks results in a unique mesh structure in SR-PCNs that warrants further investigation. This chapter explores the nature and timescale of the relaxations in SR-PCNs and whether and how they may interact. The same SR-PCN materials from Chapter 2 (i.e., **2.8$_{90/10}$**, **2.8$_{80/20}$**, **2.8$_{70/30}$**) were swollen in different solvents to look for changes in stress relaxation and frequency-dependent behavior using bulk DMA. This knowledge will lay the groundwork for developing hypotheses of structure-property relationships in SR-PCNs that would require studying local inhomogeneities in the network structure using indentation techniques.

3.2 Results and Discussion

Metallated SR-PCNs **2.8$_{X/YM}$** and demetallated **2.8$_{X/YD}$** synthesized in Chapter 2 from P3R **2.1:2.2$_2$:Zn(II)$_2$** (Y mol%) nitrile-oxide monomer **2.5** and tetra-PEG **2.6** (5.3 kg mol^{-1} X mol%), were used for the following studies (see Experimental). The covalent gel **2.7$_{GF}$** (gel fraction, GF = 80 wt%, Equation 2.1) was made by reacting **2.5** and **2.6** for 18 hours. The gels were swollen in three high boiling point solvents for mechanical testing to limit solvent evaporation: *N*-methyl-2-pyrrolidone (NMP) (**2.8$_{X/YM}$-NMP** and **2.8$_{X/YD}$-NMP**), dimethyl sulfoxide (DMSO) (**2.8$_{X/YM}$-DMSO** and **2.8$_{X/YD}$-DMSO**), and deionized water (**2.8$_{X/YM}$-H$_2$O** and **2.8$_{X/YD}$- H$_2$O**).

3.2.1 Swelling

The swelling ratio describes how polymer chains interact with the solvent and is one of the most significant properties of polymer gels.[11,15] When a polymer is dissolved in a good solvent, it will swell more, and in a poor solvent will swell less, with the molecular weight between crosslinks acting as the upper limit. The swelling ratio of polymer gels is typically reported as a weight ratio (Equation 2.10), and a sieve-filtration method[27] (see Experimental) can be used to ensure accurate and repeatable swelling measurements.

Metallated SR-PCNs (i.e., **2.8$_{90/10M}$**, **2.8$_{80/20M}$**, **2.8$_{70/30M}$**) and the covalent control **2.7$_{80}$** were submerged in deionized water and *N*-methyl-2-pyrrolidone (NMP) for 48 hours at room temperature to allow gels to swell to equilibrium before recording masses to calculate their weight-based swelling ratio (wt%). The SR-PCN gels were demetallated (**2.8$_{90/10D}$**, **2.8$_{80/20D}$**, **2.8$_{70/30D}$**) and then swollen in water, NMP, and DMSO to determine the swelling ratio, as described in the Experimental section.

Swelling studies show that the average weight-based swelling ratios for **2.7$_{80}$, 2.8$_{X/YM}$** and **2.8$_{X/YD}$** (Figure 3.3)[28] in NMP (green) and water (pink) are consistent across all X/Y with the percolating covalent network dominating the swelling behavior in SR-PCNs. SR-PCNs appear to swell as much as the covalent PEG controls, although higher swelling ratios were calculated for the NMP gels. The limiting factor is likely the contour length measured along fixed crosslinks from one surface to another, which does not change much with the varying network topology (i.e., X/Y). **2.8$_{X/YM}$-NMP** and **2.8$_{X/YD}$-NMP** have the highest weight-based swelling ratio because the molar mass of NMP (99.13 g/mol) is higher than water (18.02 g/mol) and DMSO (78.13 g/mol).

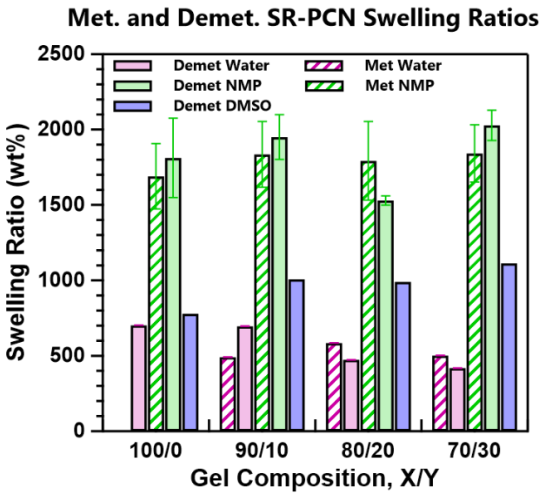

Figure 3.3. SR-PCN swelling in NMP (**2.8$_{X/YM}$-NMP** and **2.8$_{X/YD}$-NMP**), DI water (**2.8$_{X/YM}$-H2O** and **2.8$_{X/YD}$-H2O**), and DMSO (**2.8$_{X/YM}$-DMSO** and **2.8$_{X/YD}$-DMSO**). a) Demetallated SR-PCNs swelling in water (pink), NMP (green), and DMSO (blue). b) Comparison with the metallated samples (dashed bars) reveals similar swelling as the demetallated gels.

SR-PCNs **2.8$_{80/20M}$-NMP** appear homogeneous and fluoresce yellow-green under 365 nm UV light regardless of the amount of P3R in the network (Figure 3.4a shows **2.8$_{80/20M}$-NMP** as an example). However, the **2.8$_{X/YM}$-H$_2$O** gels are less transparent in water and fluoresce a stronger yellow color under UV, likely due to solubility and aggregation of the P3R, or metal and counterion, in poor solvents such as water. The polarity of the solvent and whether the solvent is protic or aprotic influences the color of the metal-ligand complex. When the demetallated SR-PCN

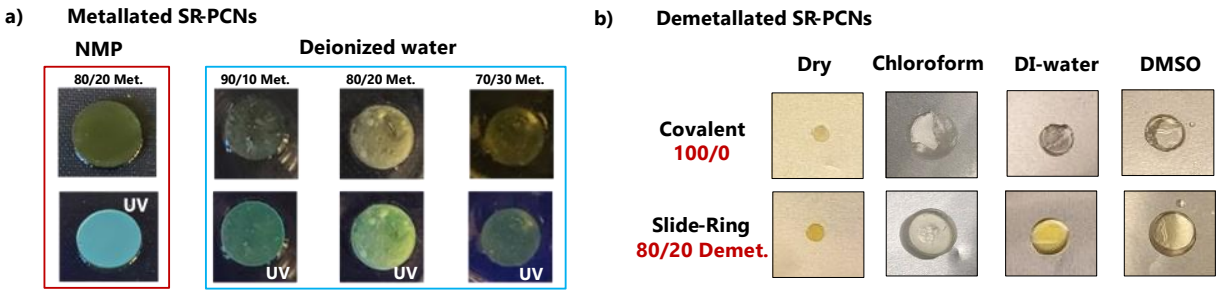

Figure 3.4. a) Pictures of metallated SR-PCNs in NMP (15mm diameter) and DI water (13-15mm diameters). The metallated gels appear more opaque in water than NMP, with slight differences for each SR-PCN composition. The 80/20 sample is the most noticeable, appearing more yellow under 365 nm light, with inhomogeneities likely due to the precipitation of metal and counterion (i.e., $Zn(NTf_2)_2$) in water. b) Pictures of a demetallated SR-PCN and covalent network: dry and swollen in chloroform, DI water, and DMSO.

is swollen in different solvents (Figure 3.4b), the color changes based on the solubility of the macrocycle in the network, appearing colorless in the best solvent (chloroform) and yellow in the worst solvent (DI water). In contrast, the swollen covalent network appears colorless in all solvents.

Indentation experiments on SR-PCN gels with different metals and counterions (e.g., $Fe(NTf_2)_2$ vs. $Zn(NTf_2)_2$ vs. $ZnCl_2$) should provide insight into how the strength of the metal-ligand complex affects polymer chain and mobility of different solvents in the gel. For example, changing to a stronger metal-ligand bond using Fe(II) would decrease network mobility compared to the more labile Zn(II) system. Improving the solubility of the counterion by using $ZnCl_2$ should decrease network inhomogeneity caused by P3R aggregation.

Due to the inhomogeneity of these metallated gels, indentation experiments would allow for localized probing of the system to determine complex moduli and relaxation times at specific locations. Nanoindentation techniques are commonly used to quantify solvent transport and tune the poroelastic response in polymer gels using a combination of stress relaxation and dynamic mechanical analysis (DMA).[29–31,38–41] A variety of tip sizes would need to be tested to extract relaxation modes from the poroelastic behavior, and this will be discussed in more detail in the nanoindentation section.

3.2.2 Stress Relaxation

As discussed in the previous chapter, the demetallated SR-PCNs **2.8$_{X/YD}$-NMP** relax faster than the stretched exponential model for relaxation (Equation 2.11)[34] predicts (Figure 3.5a). While this function can capture a distribution of relaxation times around a single primary relaxation, it fails when multiple distinct relaxation modes contribute to the stress relaxation, resulting in a

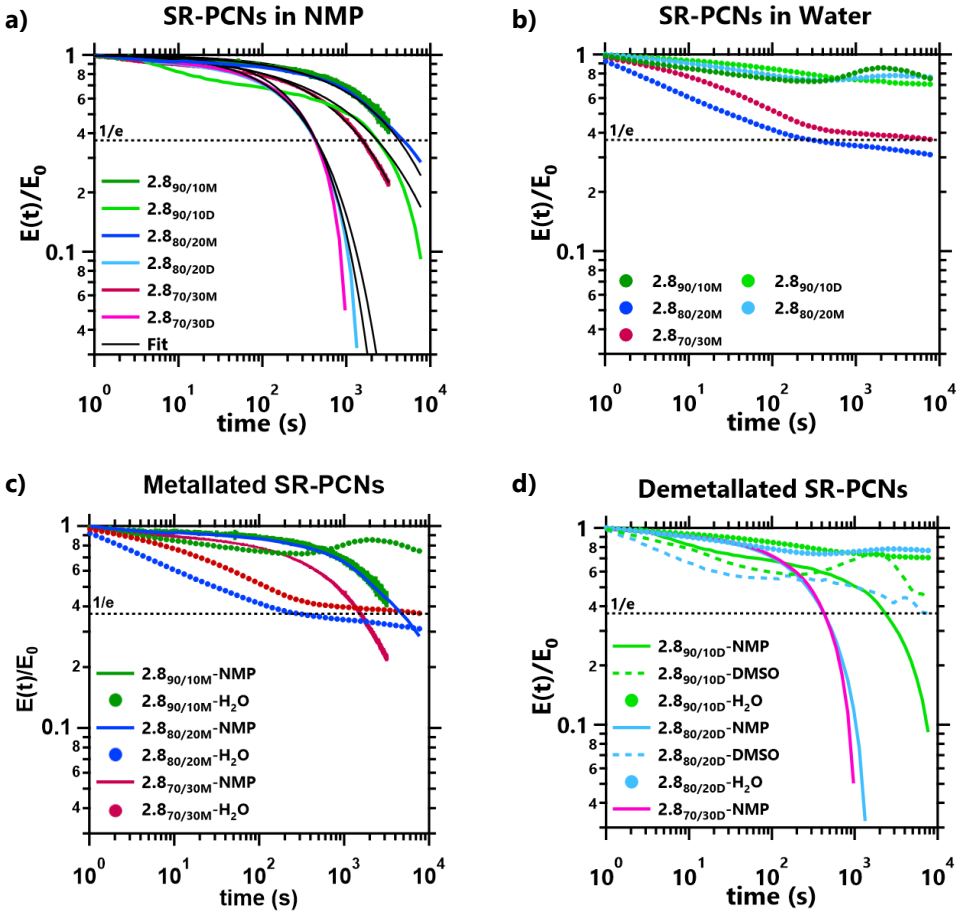

Figure 3.5. Normalized compressive stress relaxation response of metallated (**2.8$_{90/10M}$**, green; **2.8$_{80/20M}$**, blue; **2.8$_{70/30M}$**, red) and demetallated (**2.8$_{90/10D}$**, light green; **2.8$_{80/20D}$**, light blue; **2.8$_{70/30M}$**, pink) SR-PCNs swollen in a) NMP (i.e., **2.8$_{X/Y}$-NMP**) data with fits from Chapter 2) and b) DI water (**2.8$_{X/Y}$-H$_2$O**). c) Comparison between **2.8$_{X/YM}$-H$_2$O** show different trends in relaxation than **2.8$_{X/YM}$-NMP**. d) Comparison between **2.8$_{X/YD}$** swollen in different solvents show the fastest relaxation for **2.8$_{X/YD}$-DMSO** vs. **2.8$_{X/YD}$-H$_2$O**; however, the fastest relaxation is observed in **2.8$_{X/YD}$-NMP**. An instantaneous strain of 7% was applied to gel samples swollen in NMP, DI water, or DMSO ~20°C.

multimodal distribution. In contrast, the covalent (**2.7$_{80}$-NMP**) and metallated (**2.8$_{X/YM}$-NMP**) networks assembled from $Zn(NTf_2)_2$ follow the fitted exponential function, with faster relaxations occurring for gels with the higher ring content. The difference in relaxation time is also attributed to the variation in the PEG network structure resulting from the decrease in gel fraction (GF, Equation 2.1) as P3R is added to the polymerization, which also decreases the amount of PEG in the network and, therefore, the molecular weight between crosslinks.[12,35] This suggests the rings

metallated with Zn(II) effectively act as fixed crosslinks, causing metallated SRNs to behave similarly to covalent networks when swollen in NMP. Demetallation frees the rings, maintaining the relaxation properties of the covalent gel while adding another distinct relaxation mode due to ring mobility.

In the covalent gel **2.7$_{80}$-NMP** and metallated (with Zn(II)) SR-PCNs (**2.8$_{X/YM}$-NMP**), the stretched exponential fits well, indicating the crosslinks are fixed over the time scale of the solvent draining. However, the stress relaxation response of SR-PCNs swollen in water (**2.8$_{X/YM}$-H$_2$O**) does not follow the same trend, likely indicating a slower relaxation process (Figure 3.5b). Incorporating metallated (with $Zn(NTf_2)_2$) crosslinks decreases the relaxation time of NMP gels by about half relative to the equivalent covalent gel of similar GF. While it is clear the incorporation of metallated rings increases solvent draining, the specific cause is uncertain. It is likely related to specific features of the defects in the network or how the specific solvent interacts with the P3R; for example, the slower relaxations for SR-PCNs in water likely result from poor solubility of the metallated P3R crosslink and the bistriflimide (NTf_2) counterions.

After treating the SR-PCNs with base (see Experimental), there is a substantial decrease in the relaxation time of the demetallated **2.8$_{X/YD}$-NMP** gels, with a decrease of about an order of magnitude for the gels with the higher ring content. While some of this change can be accounted for by the decrease in gel fraction, as discussed in the previous chapter, comparing it to the covalent controls shows that gel fraction cannot entirely account for this phenomenon. A possible explanation for this effect is that the average mesh size is increasing as the rings can slide to accommodate the stress on the network, facilitating the faster flow of the solvent. Small angle neutron and X-ray scattering (SANS and SAXS) can measure this and will be discussed in Chapter 7. The slower relaxations in **2.8$_{X/YD}$-H$_2$O** and **2.8$_{X/YD}$-DMSO** (Figure 3.5d) could also directly

result from swelling or ring aggregation. Compared to water or DMSO, an enhanced swelling ratio is observed for the NMP gels, and the expanded network could facilitate faster and more facile solvent transport.

Poroelastic Relaxation Indentation (PRI)[23,30] would be a more suitable technique for probing SR-PCN relaxation times in different solvents as it measures the diffusivity of a polymer gel at a particular solvent concentration. This technique will require a large range of indentation tips sizes and a confocal microscope to watch the contact area during the experiment, and will be discussed in a later section.

3.2.3 Small-Amplitude Oscillatory Compression (SAOC) DMA

The demetallated SR-PCN **2.8$_{90/10D}$** was remetallated to see if the ring mobility can be switched off. Therefore, **2.8$_{90/10D}$** was submerged in an aqueous solution of $Zn(NTf_2)_2$ (1.76E-4 M) for 48 hours, resulting in the remetallated gel **2.8$_{90/10R}$**. The storage and loss moduli frequency dependence of **2.8$_{90/10D}$** (light blue, Figure 3.6a) swollen in DI water shows a transition at 10 rad/s. A prominent peak in the phase angle δ corresponds to this transition (Figure 3.6b). After remetallation, **2.8$_{90/10R}$** (yellow, Figure 3.6a) stays in the rubbery transition even at low frequency,

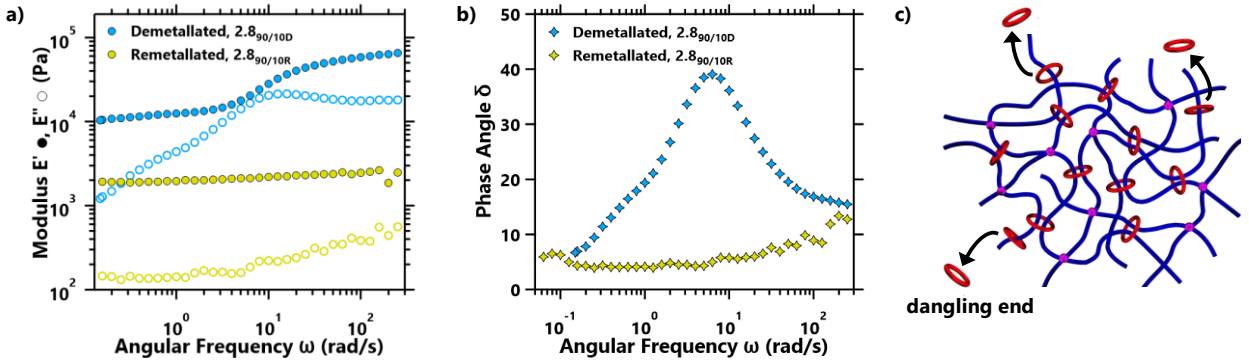

Figure 3.6. a) Small-amplitude oscillatory compression (SAOC) frequency sweeps for demetallated SR-PCN **2.8$_{90/10D}$** (light blue) and the remetallated SR-PCN **2.8$_{90/10R}$** (yellow) swollen in DI water. b) Phase angle δ vs. angular frequency for **2.8$_{90/10D}$** (light blue) and **2.8$_{90/10R}$** (yellow) swollen in DI water. Samples were preloaded with 0.025 N to ensure uniform contact between the sample and plates. Frequency sweeps were performed from 1000 rad/s to 0.05 rad/s with a strain amplitude of 1%.

and there is no longer a peak in the phase angle δ (Figure 3.6b). The metallated SR-PCN is likely softer than the original metallated sample (after polymerization) because of the rings that fall off dangling ends during the first demetallation process (Figure 3.6c). This remetallation experiment proves that ring sliding can be turned off in the network by adding metal ions.

Demetallated SR-PCNs swollen in DMSO (**2.8$_{X/YD}$-DMSO**) were compared to the frequency response of the same gels in NMP (**2.8$_{X/YD}$-NMP**). Figure 3.7 shows the frequency dependence of the storage modulus *E'* and the loss modulus *E''* of SR-PCNs swollen in DMSO with those in NMP. The storage moduli of the covalent control **2.7$_{80}$-NMP** and metallated samples **2.8$_{X/YM}$-NMP** display minimal angular frequency dependence above 1 rad/s with typical poroelastic behavior below this frequency. [24] The frequency response of the covalent **2.7$_{80}$-NMP** and **2.7$_{80}$-DMSO** (Figure 3.7a) shows stiffer gels in NMP than in DMSO. After demetallation, the higher frequency relaxation in DMSO (Figure 3.7a) and the peaks in the phase angle (Figure 3.7b) occur at a similar angular frequency as **2.8$_{X/YD}$-NMP** (Figure 3.7c). The phase angle peak intensity and frequency increase with the amount of P3R crosslinks, where the increasing peak height

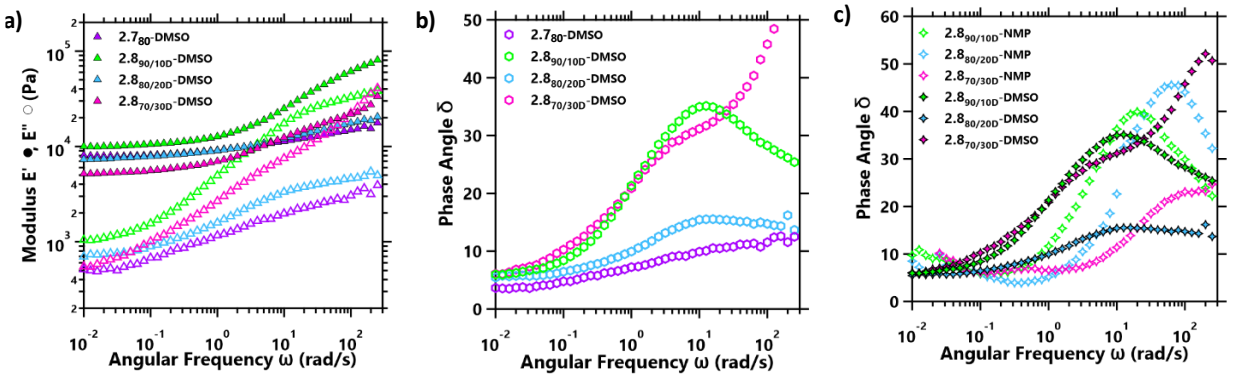

Figure 3.7. Small-amplitude oscillatory compression (SAOC) frequency sweeps for a) covalent (**2.7$_{80}$-DMSO**, purple) and demetallated SR-PCNs in DMSO (**2.8$_{X/YD}$-DMSO**), and b) the phase angle δ evolution observed in the **2.8$_{X/YD}$-DMSO** gel series. c) Comparison of δ for **2.8$_{X/YD}$-NMP** (open diamonds) and **2.8$_{X/YD}$-DMSO** (filled diamonds). Samples were preloaded with 0.025 N to ensure uniform contact between the sample and plates. Frequency sweeps were performed from 1000 rad/s to 0.01 rad/s with a strain amplitude of 1%.

suggests more energy dissipation at that frequency. As previous work has shown,[2–6] the effective molecular weight between the mobile crosslinks decreases when the number of rings on a chain increases. This molecular weight dictates the relaxation time of the chain moving through the ring. At higher frequencies, polymer chains can no longer slide through rings and behave more like trapped entanglements, resulting in more elastically effective chains in the network and a higher modulus.[36] Chains can slide through rings at lower frequencies to relax stress, resulting in fewer elastically effective chains and a lower modulus.

Demetallated SR-PCNs exhibit higher weight-based swelling ratios in NMP than DMSO, which could account for the higher moduli at high frequency and the lower moduli at low frequency. The solvent's viscosity also plays a role in solvent flow through the network. The more drastic drop in the viscoelastic relaxation (and the presence of a poroelastic relaxation) in NMP is likely a result of the more expanded polymer chains that would facilitate solvent transport through the network.

The frequency response of the covalent **2.7$_{80}$-NMP** and **2.7$_{80}$-DMSO** (Figure 3.8a) shows stiffer gels in NMP than in DMSO. SR-PCN **2.8$_{X/YD}$-NMP** gels show limited poroelastic response at low frequency during the timescale of this experiment (Figures 3.8b-d). Poroelastic relaxation indentation and dynamic micro-indentation tests[37] with different probe radii would help decouple the poroelastic and viscoelastic responses in these SR-PCN systems, which may or may not occur at the same timescale in different solvents.

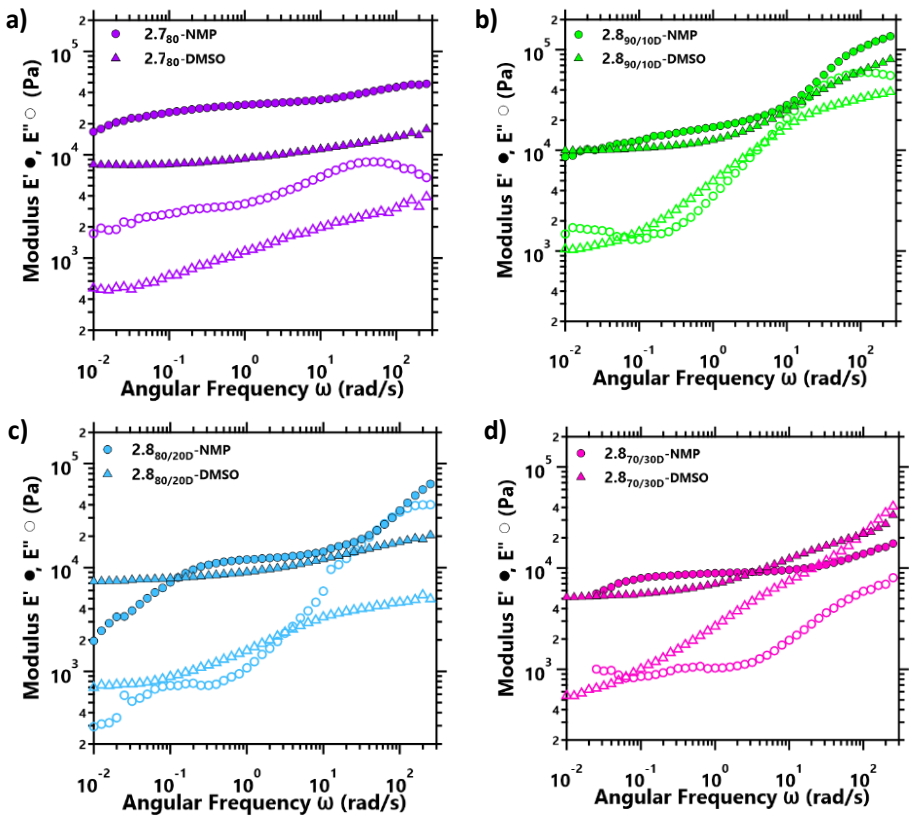

Figure 3.8. Small-amplitude oscillatory compression (SAOC) frequency sweeps in NMP (circles) and DMSO (triangles) for a) covalent **2.7$_{80}$** (purple), b) **2.8$_{90/10D}$** (light green), c) **2.8$_{80/20D}$** (light blue), and d) **2.8$_{70/30D}$** (pink). Samples were preloaded with 0.025 N to ensure uniform contact between the sample and plates. Frequency sweeps were performed from 1000 rad/s to 0.01 rad/s with a strain amplitude of 1%.

It is worth noting that shear rheology was also explored for these SR-PCNs. Shear measurements on **2.8$_{X/YD}$-DMSO** (Figure 3.9a) revealed a decrease in the storage modulus (G') and a slight increase in loss behavior (G") with the addition of rings. However, the sandblasted upper plate geometry could not prevent slippage at higher frequencies (> 50 Hz) during the experiment, which is also seen in the phase angle (Figure 3.9b).

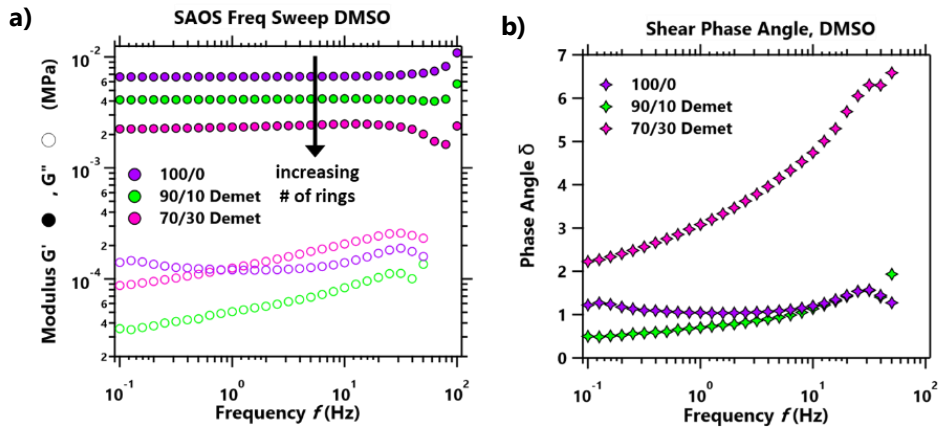

Figure 3.9. Shear rheology on **2.7$_{80}$-DMSO** (purple), **2.8$_{90/10D}$-DMSO** (light green), and **2.8$_{70/30D}$-DMSO** (pink) swollen at ~20°C showing slippage at high-frequency a) in the storage and loss moduli, and b) phase angle. Discovery Hybrid Rheometer, 0.5 N axial force, 1% strain amplitude, Peltier plate with solvent trap, 20mm sandblasted upper plate.

While testing the gels in DMSO, there were problems with the material crystallizing as the DMSO solvent left the gel during the experiment, which hampers the investigation of ring sliding.

3.2.4 Nanoindentation

Nanoindenting allows for mechanical testing of the dried SR-PCNs that are too small and irregular for bulk mechanical testing and serves as a good starting point for basic troubleshooting on the nanoindenter before moving on to the swollen samples. Preliminary nanoindentation was performed using an FT-104 Femto-Indenter from FemtoTools (see Experimental). Dry gels were cut into strips and superglued (cyanoacrylate) directly onto the surface of a 30 mm diameter aluminum puck supplied by FemtoTools for testing (Figure 3.10a). Sample prep is critical for accurate data acquisition because inconsistent sample thickness and roughness can increase the probability of encountering the experimental challenges shown in Figure 3.10b.[38] Variations in sample roughness increase the risk of running the tip into the sample laterally when trying to take many measurements.

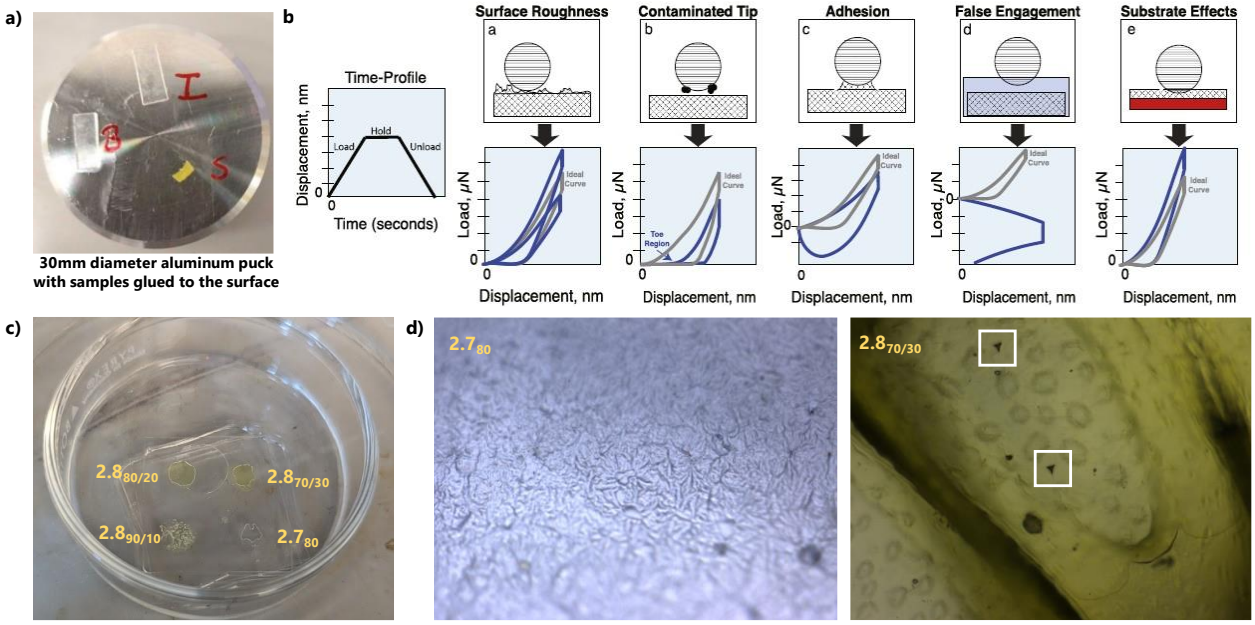

Figure 3.10. Investigating nanoindentation techniques and sample preparation. a) Dry gel samples were cut using a razor blade and superglued with cyanoacrylate to an aluminum sample puck (30 mm diameter). b) Load-displacement behavior of common indentation challenges: surface roughness, contaminated tip, adhesion, false engagement, and substrate effects are the most common.[38] c) Preparation of indentation samples by dropping the gel mixture (directly after adding the covalent crosslink **2.6**) onto a coated glass slide to crosslink directly onto the glass surface. d) Snapshots of covalent **2.7**$_{80}$ (colorless) and metallated SR-PCN **2.8**$_{70/30M}$ (yellow) under the Femto-Indenter microscope (20x lens) after indentation. The white boxes show the indentation marks left by the Berkovich tip. Adapted from Ref. 38 with permission from Elsevier.

Preparing gel samples directly onto glass slides (Figure 3.10c, see Experimental) resulted in the desired thin, more consistent sample height than the gel samples prepared in vials, which provided better focus under the microscope. Figure 3.10d shows the covalent **2.7**$_{80}$ (colorless) and metallated SR-PCN **2.8**$_{70/30M}$ (yellow) under the Femto-Indenter microscope (20x lens) after indentation with the Berkovich tip. Indentation marks are visible on the surface of SR-PCN **2.8**$_{70/30M}$ (white boxes) but not the covalent **2.7**$_{80}$.

Even though sample preparation was improved, there were issues during data collection related to surface roughness and other challenges, including adhesion and substrate effects. Improvements in sample preparation will further limit these defects for reliable data collection. Circular glass slides with the same 30mm diameter as the sample puck should guarantee a more

consistent glue settling between the glass slide and the aluminum surface. Storing the slides in a desiccator during crosslinking will better prevent solvent evaporation during gelation, which can lead to surface roughness. After troubleshooting sample preparation and troubleshooting simple indentation techniques with the Berkovich tip on the dry SR-PCNs, the samples can be swollen in different solvents to compare the nanoindentation DMA results with those from the bulk DMA experiments. Testing wet samples via indentation requires supergluing (cyanoacrylate) the glass slide (with the samples adhered to the surface) to a low-wall Pyrex petri dish that is then glued to the aluminum sample puck. The petri dish allows a small amount of solvent to be added to keep gels submerged during testing, which will be the key to investigating relaxations in the SR-PCNS swollen in different solvents.

3.2.4.1 Proposed Studies

Nanoindentation may yield higher absolute moduli values than bulk DMA testing because it probes a smaller volume with a different constraint; however, the technique captures the same trends in mechanical behavior with frequency. There is good agreement between nanoindentation and rheometry for stiffer samples, but these values are typically higher for compliant samples because when a sample is locally compressed, it pushes against the other molecules in the bulk.[24–26] In the bulk measurement, the sample can bulge out into the air, resulting in a change in the Poisson's ratio of the gel. However, the nanoindentation loss factor is independent of the contact area because the loss and storage moduli rely similarly on the contact area. A potential experimental factor in overestimating elastic modulus values is the indentation depth relative to the gel layer thickness; there is a trend toward decreasing modulus values with increasing indentation depth for thinner gels.

Poroelastic Relaxation Indentation (PRI) experiments measure the diffusivity of a polymer gel at a particular solvent concentration after it reaches chemical equilibrium with the environment (Figure 3.11a).[23,30,33] Before indentation, the gel (typically disk-shaped) takes up the solvent and swells to equilibrium. Compressing the gel at a fixed displacement (δ) causes the solvent to migrate in the gel so that the force (F) on the indenter decreases as a function of time until the gel reaches a new state of equilibrium.[30] This results in a relaxation in load (P) that is characterized by a relaxation time (τ) (Figure 3.11b)

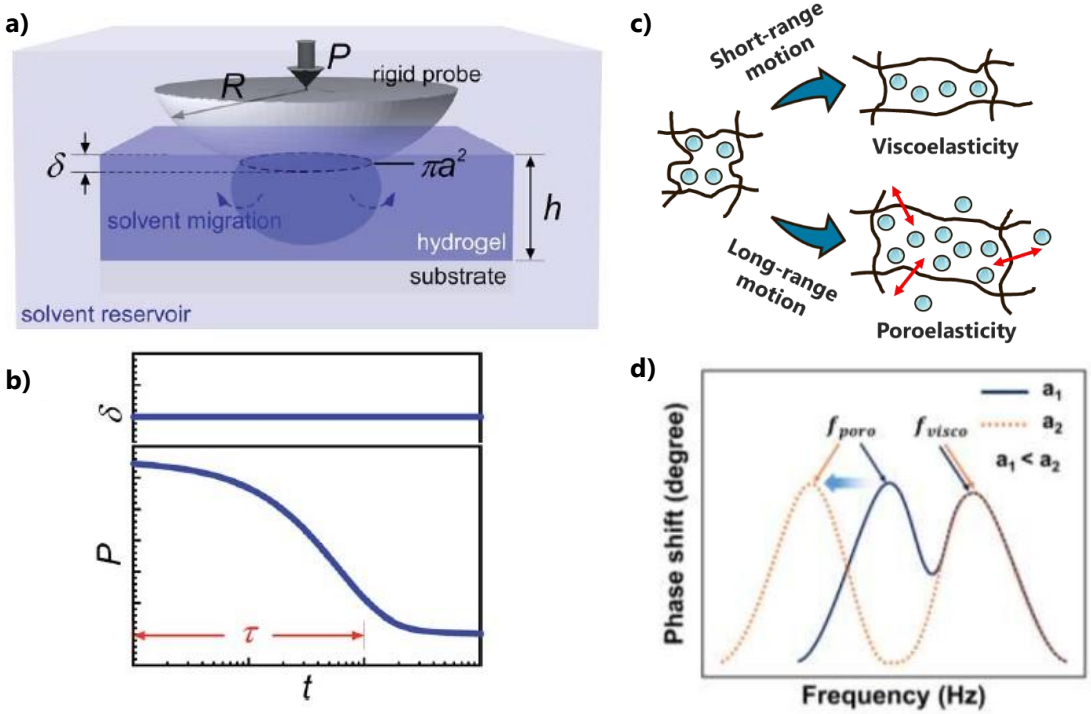

Figure 3.11. Poroelastic relaxation indentation (PRI) testing of polymer gels. a) A spherical probe encounters the gel surface, and the volume directly beneath the probe represents the region where solvent migration occurs. The interface between the probe and gel, and the gel and substrate, are considered frictionless. The poroelastic relaxation process is associated with the fluid phase transport out of the region as defined by the contact area (πa^2).[33] b) The poroelastic force is a function of the indentation rate and is space-dependent because it is a function of the size of the contact area between the indenter and gel. c) In viscoelasticity, polymer molecules move relative to the network over short-range motion. In poroelasticity, solvent molecules move relative to the network over a long-range motion. d) Dynamic micro-indentation decouples the viscoelastic and poroelastic time responses by performing dynamic testing with different contact radii.[37] Adapted from Ref. 33 with permission from Royal Society of Chemistry and Ref. 37 with permission from Elsevier.

Indentation of poroelastic gels at a high strain rate or frequency can generate resistive forces that are functions (linear or nonlinear) of strain rate or frequency of indentation and size of the contact between the indenter and gel.[14] The crosslinked polymer network of the gel resists strains, resulting in the viscoelastic response. The shear viscosity and the shear modulus are independent of the contact radius, and their ratio determines the viscoelastic time scale. At the same time, applied strain pushes the mobile molecules of the solvents of the gel (fluid phase) through the porous, crosslinked network (solid phase) (Figure 3.11c). The energy loss incurred in moving the fluid through the solid phase results in the poroelastic (also called bi-phasic) response. Dynamic micro-indentation tests[37] on hydrated cartilage measured the dynamic modulus and phase shift at different contact radii. The phase shift at small radii was governed by poroelasticity, while the phase shift at large radii was dominantly governed by intrinsic viscoelasticity (Figure 3.11d). Because the poroelastic peak frequency is inversely proportional to the square of the contact radius, the effects of the two mechanisms can be uncoupled by performing dynamic testing at different contact radii.

3.3 Conclusions

Utilizing a metal-template approach for rotaxane synthesis has allowed us to design a route to access doubly-threaded interlocked materials. The SR-PCN synthesis is highly adaptable in controlling the number and type of ring (and polymer) components added to the crosslinking reaction. The ability to control every handle in the system makes this system an infinitely better platform for the general study of SRNs. In contrast, Ito's SRN synthesis affords limited control over the number of crosslinked and uncrosslinked rings in the network. Although these studies use a tetra-PEG **2.6** and triethylene glycol-based monomer **2.5**, the SR-PCN backbone can be changed

by incorporating different monomers into the NOAC click polymerization. The molecular weight of the polymer chains, ring size, and the number of doubly-threaded and singly-threaded rings are all design parameters that will influence the flow of solvent and poroelastic draining in these SR-PCNs. Future nanoindentation studies on SR-PCNs in different solvents would provide a way to probe the network locally without worrying about solvent expelling from the gel, like in bulk DMA testing. The whole suite of testing can be done without handling or changing the sample in any way, as required for the bulk DMA experiments.

3.4 Experimental

3.4.1 Materials and Methods

All chemicals were purchased from Sigma-Aldrich and used without further purification unless otherwise mentioned. Benzophenone imine was purchased from Oakwood Chemical. Zinc di[bis(trifluoromethylsulfonyl)imide] was purchased from Strem Chemicals and stored in a nitrogen desiccator. Sodium hydride, dry powder, was purchased from Sigma-Aldrich and stored in a nitrogen desiccator. 4-arm PEG-Alkyne (5.0 kg/mol) was purchased from Creative PEGWorks. Solvents for chromatography were purchased from Fisher-Scientific. Deuterated solvents and nitromethane were purchased from ACROS Organics. Nitrile-oxide monomer **2.5**[39] and 2,6-bisbenzimidazolylpyridine ligands[40] were prepared following literature procedures. Tetrahydrofuran (THF) was dried over sodium and benzophenone. Dichloromethane was distilled over calcium hydride before use. Dimethylformamide (DMF) was dried with activated 4Å molecular sieves before use. All synthesized components were stored in a freezer at -8°C before use.

Compressive Stress Relaxation was performed using a TA Instruments RSA GS2 with the 25 mm compression plate geometry operating in compression. Gel samples (swollen in NMP, DMSO, or DI water) were cut using a die punch of 16 mm, and an instantaneous strain of 7% was applied.

Small Amplitude Oscillatory Compression (SAOC) Rheology was performed using a TA Instruments RSA GS2 with the 25 mm compression plate geometry. Gel samples (swollen in NMP, DMSO, or DI water) were cut using a die punch of 16 mm and preloaded with 0.025 N to ensure uniform contact between the sample and plates. Frequency sweeps were performed from 1000 rad/s to 0.01 rad/s with a strain amplitude of 1%.

Shear Rheology was performed using a Discovery Hybrid Rheometer with the Peltier plate and solvent trap using the 20 mm sandblasted upper plate. Samples were cut using a die punch of 20 mm. A 0.5 N axial force and 1% strain amplitude were applied.

3.4.2 Synthesis of SR-PCNs **2.8$_{X/YM}$** and **2.8$_{X/YD}$**

The polymerization procedure from Chapter 2 was used to create the SR-PCNs used in this Chapter: P3R **1:2$_2$:Zn(II)$_2$** (Y mol, Table 2.1) and nitrile-oxide **2.5** (0.010 g, 0.0177 mmol) were dissolved in 95:5 $CHCl_3$:MeCN (~250 µL) and added to a glass shell vial with a stir bar and capped. The solution was left to stir at room temperature for 4 hours. During the first step, the ditopic nitrile-oxide monomer **2.5** (2.0 eq) reacts with terminal alkynes on **2.1:2.2$_2$:Zn(II)$_2$**, (Y mol) to form isoxazole prepolymers/oligomers in the presence of the excess monomer (Figure 3.15, top). The covalent gel **2.7** was made by reacting **2.5** and **2.6**.

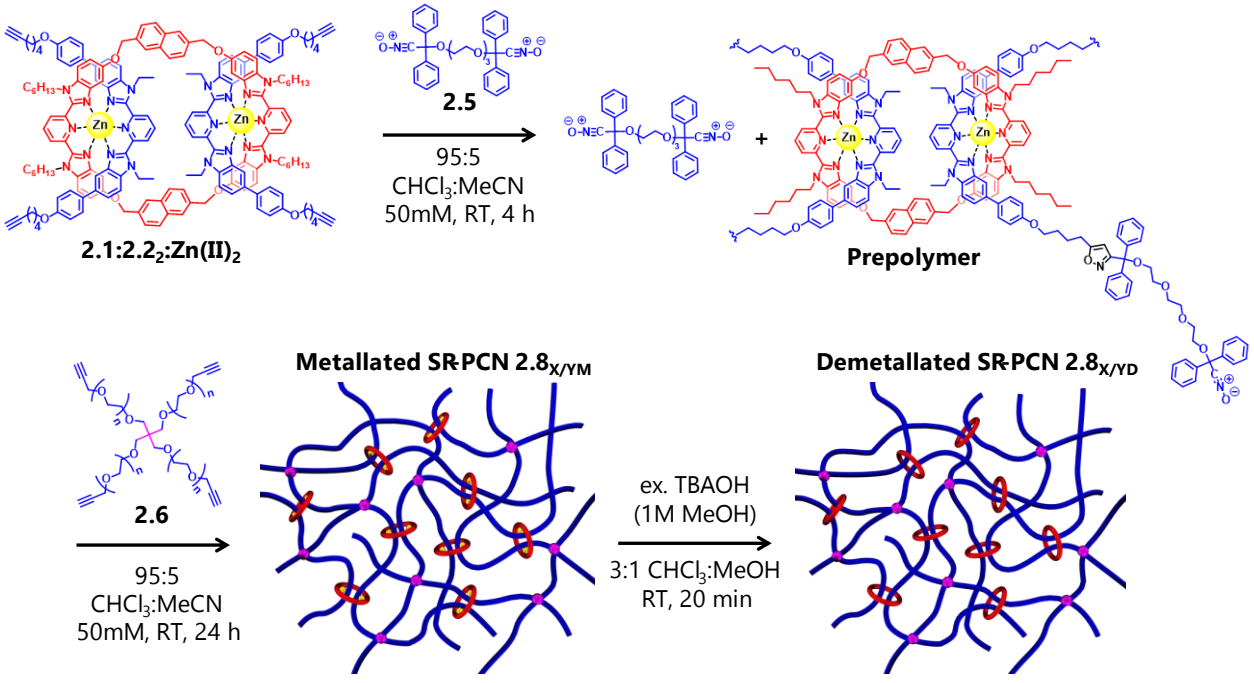

Figure 3.12. NOAC polymerization of metallated SR-PCNs **2.8$_{X/YM}$** (top) and demetallation with a dilute solution of tetrabutylammonium hydroxide (TBAOH) to the demetallated SR-PCNs **2.8$_{X/YD}$** (bottom).

The 4-arm PEG-Alkyne **2.6** (M_n = 5 kgmol^{-1}, X mol) was dissolved in 95:5 $CHCl_3$:MeCN (~100 µL) then added to the vial. A viscous solution formed within minutes; the stir bar was removed, and then the vial was capped and left to gel at room temperature for ~48 hours. The gels dried in a fume hood overnight. The covalent gel **2.7** and the metallated SR-PCNs **2.8$_{X/YM}$** were washed by submerged in a large beaker full of ~200 mL of chloroform at 48°C on a hot plate. A watch glass was placed on top of the beaker, and the gels were left heating for 4 hours to ensure the complete extraction of lower molecular weight components (including unreacted P3R and prepolymers) into the soluble fraction.

3.4.3 Demetallation Procedure

To demetallate, the washed, metallated SR-PCNs **2.8$_{X/YM}$** were submerged in 35 mL of chloroform and 5 mL of methanol in a Teflon dish. 10 µL of tetrabutylammonium hydroxide solution (1M in MeOH) was added dropwise to demetallate the rings (Figure 3.15, bottom). After 20 minutes, the SR-PCNs were transferred to a second Teflon dish containing 40 mL of 50/50 chloroform/methanol for 2-3 hours, changing the solvent every 30 minutes. Then the gels were submerged in a large beaker full of ~200 mL of chloroform at 48°C on a hot plate. A watch glass was placed on top of the beaker, and the gels were left heating for 4 hours to ensure the complete extraction of metal, salts, and any soluble fractions of the network.

3.4.4 Swelling Tests

Metallated SR-PCNs (i.e., **2.8$_{90/10M}$**, **2.8$_{80/20M}$**, **2.8$_{70/30M}$**) and the covalent control **2.7$_{96}$** were submerged in deionized water and *N*-methyl-2-pyrrolidone (NMP) for 48 hours at room temperature to allow gels to swell to equilibrium before recording masses to calculate their weight-based swelling ratio (wt%). The SR-PCN gels were demetallated (**2.8$_{90/10D}$**, **2.8$_{80/20D}$**, **2.8$_{70/30D}$**) and then swollen in water, NMP, and DMSO to determine the swelling ratio, as described below.

A sieve filtration method was employed to ensure repeatable, reproducible measurement of swelling, achieved via fast and complete removal of excess fluid from the gel on a wire mesh sieve using vacuum filtration.[27] The mass of a 316 stainless steel wire sieve (250 x 250 mesh size, 0.0024" opening size) was recorded as W_1. The metallated (or demetallated) gels were placed in a vacuum oven overnight at ~25°C, and their dry masses were recorded as W_0. The gels were then submerged in 15 mL of solvent for 48 hours at room temperature to allow gels to reach their swelling equilibrium. The swollen gels were poured onto the wire sieve under vacuum to remove excess solvent from the gel (and sieve), and the mass of the sieve with the gel on it was recorded as W_2. The average of three weight measurements W_2 was calculated for each sample (and multiple samples for each X/Y) and used to calculate the swelling ratio from Equation 2.10:

$$\text{Swelling Ratio (wt\%)} = \frac{W_2 - W_1 - W_0}{W_0} \times 100\% \tag{2.10}$$

which is based on the weight of the dry gel (W_0) and that of a wire mesh (W_1).

3.4.5 Nanoindentation

Preliminary nanoindentation was performed using an FT-104 Femto-Indenter from FemtoTools, a brand-new instrument of the Materials Research Science and Engineering Center (MRSEC) at the University of Chicago. Preparing gel samples in vials leads to thicker samples with varying surface heights and roughness on the dried surface, and gluing the sample strips to the aluminum can lead to worsening effects. No cryo-microtome is available at the University of Chicago, which would help achieve reliable sample thickness with smooth surfaces. However, changing the SR-PCN sample preparation did provide more consistent samples. Gelation was performed by dropping the SR-PCN gel mixture (directly after adding the covalent crosslink) onto an alkyne-functionalized glass slide to fix it directly to the surface. Glass slides were dipped into a solution of nitric acid and washed with deionized water, then dried at room temperature under

nitrogen. The surface was treated with a drop of O-(propargyl)-N-(triethoxysilylpropyl) carbamate (OPTC) and left to react for ~2 hours. A second glass slide was coated with a drop of Teflon solution (from Dr. Joe Dennis) and put into the oven for 20 minutes at 90°C. This second glass slide was placed on top of the drops, which helped ensure a smoother sample surface after crosslinking and placed in a petri dish with a small chloroform bath to prevent solvent evaporation during gelation (~48 hours) (Figure 3.11c). The top slide was removed, and the bottom slide with the samples was left to dry at room temperature. The bottom slide was glued onto the aluminum sample puck with cyanoacrylate for indentation testing.

3.5 References

(1) Xing, Z.; Shu, D. W.; Lu, H.; Fu, Y. Q. Untangling the Mechanics of Entanglements in Slide-Ring Gels towards Both Super-Deformability and Toughness. *Soft Matter* **2022**, *18* (6), 1302–1309. https://doi.org/10.1039/d1sm01737c.

(2) Fleury, G.; Schlatter, G.; Brochon, C.; Travelet, C.; Lapp, A.; Lindner, P.; Hadziioannou, G. Topological Polymer Networks with Sliding Cross-Link Points: The "Sliding Gels". Relationship between Their Molecular Structure and the Viscoelastic as Well as the Swelling Properties. *Macromolecules* **2007**, *40* (3), 535–543. https://doi.org/10.1021/ma0605043.

(3) Kato, K.; Ito, K. Dynamic Transition between Rubber and Sliding States Attributed to Slidable Cross-Links. *Soft Matter* **2011**, *7* (19), 8737. https://doi.org/10.1039/c1sm06212c.

(4) Kato, K.; Yasuda, T.; Ito, K. Viscoelastic Properties of Slide-Ring Gels Reflecting Sliding Dynamics of Partial Chains and Entropy of Ring Components. *Macromolecules* **2013**, *46* (1), 310–316. https://doi.org/10.1021/ma3021135.

(5) Fleury, G.; Schlatter, G.; Brochon, C.; Hadziioannou, G. Unveiling the Sliding Motion in Topological Networks: Influence of the Swelling Solvent on the Relaxation Dynamics. *Adv. Mater.* **2006**, *18* (21), 2847–2851. https://doi.org/10.1002/adma.200600107.

(6) Kato, K.; Karube, K.; Nakamura, N.; Ito, K. The Effect of Ring Size on the Mechanical Relaxation Dynamics of Polyrotaxane Gels. *Polym. Chem.* **2015**, *6* (12), 2241–2248. https://doi.org/10.1039/C4PY01644K.

(7) Karino, T.; Shibayama, M.; Okumura, Y.; Ito, K. SANS Study on Pulley Effect of Slide-Ring Gel. *Phys. B Condens. Matter* **2006**, *385–386* (December 2014), 807–809. https://doi.org/10.1016/j.physb.2006.06.095.

(8) Karino, T.; Okumura, Y.; Ito, K.; Shibayama, M. SANS Studies on Spatial Inhomogeneities of Slide-Ring Gels. *Macromolecules* **2004**, *37* (16), 6177–6182. https://doi.org/10.1021/ma049598b.

(9) Karino, T.; Shibayama, M.; Okumura, Y.; Ito, K. SANS Study on Pulley Effect of Slide-Ring Gel. *Phys. B Condens. Matter* **2006**, *385–386*, 807–809. https://doi.org/10.1016/j.physb.2006.06.095.

(10) Chan, E. P.; Deeyaa, B.; Johnson, P. M.; Stafford, C. M. Poroelastic Relaxation of Polymer-Loaded Hydrogels. *Soft Matter* **2012**, *8* (31), 8234–8240. https://doi.org/10.1039/c2sm25363a.

(11) Zhao, X.; Huebsch, N.; Mooney, D. J.; Suo, Z. Stress-Relaxation Behavior in Gels with Ionic and Covalent Crosslinks. *J. Appl. Phys.* **2010**, *107* (6), 063509. https://doi.org/10.1063/1.3343265.

(12) Dey, K.; Agnelli, S.; Borsani, E.; Sartore, L. Degradation-Dependent Stress Relaxing Semi-Interpenetrating Networks of Hydroxyethyl Cellulose in Gelatin-Peg Hydrogel with Good Mechanical Stability and Reversibility. *Gels* **2021**, *7* (4). https://doi.org/10.3390/gels7040277.

(13) Kingsbury, H. B. On the Dynamic Behavior of Poroelastic Materials. *J. Acoust. Soc. Am.* **1979**, *65* (1), 90–95. https://doi.org/10.1121/1.382273.

(14) Maningding, A.; Azadi, M. The Interrelated Mechanics of Poroelastic Gels in Time- and Frequency-Domain Detected by Indentation. *Int. J. Appl. Mech.* **2020**, *12* (09), 2050103. https://doi.org/10.1142/S1758825120501033.

(15) Ahmad, Z.; Salman, S.; Khan, S. A.; Amin, A.; Rahman, Z. U.; Al-Ghamdi, Y. O.; Akhtar, K.; Bakhsh, E. M.; Khan, S. B. Versatility of Hydrogels: From Synthetic Strategies, Classification, and Properties to Biomedical Applications. *Gels* **2022**, *8* (3). https://doi.org/10.3390/gels8030167.

(16) Bhattacharyya, A.; O'Bryan, C.; Ni, Y.; Morley, C. D.; Taylor, C. R.; Angelini, T. E. Hydrogel Compression and Polymer Osmotic Pressure. *Biotribology* **2020**, *22* (August 2019), 100125. https://doi.org/10.1016/j.biotri.2020.100125.

(17) Sleeboom, J. J. F.; Voudouris, P.; Punter, M. T. J. J. M.; Aangenendt, F. J.; Florea, D.; Van Der Schoot, P.; Wyss, H. M. Compression and Reswelling of Microgel Particles after an Osmotic Shock. *Phys. Rev. Lett.* **2017**, *119* (9), 1–5. https://doi.org/10.1103/PhysRevLett.119.098001.

(18) Schulze, K. D.; Hart, S. M.; Marshall, S. L.; O'Bryan, C. S.; Urueña, J. M.; Pitenis, A. A.; Sawyer, W. G.; Angelini, T. E. Polymer Osmotic Pressure in Hydrogel Contact Mechanics. *Biotribology* **2017**, *11* (March), 3–7. https://doi.org/10.1016/j.biotri.2017.03.004.

(19) Cai, S.; Hu, Y.; Zhao, X.; Suo, Z. Poroelasticity of a Covalently Crosslinked Alginate Hydrogel under Compression. *J. Appl. Phys.* **2010**, *108* (11). https://doi.org/10.1063/1.3517146.

(20) Zimberlin, J. A.; Sanabria-DeLong, N.; Tew, G. N.; Crosby, A. J. Cavitation Rheology for Soft Materials. *Soft Matter* **2007**, *3* (6), 763. https://doi.org/10.1039/b617050a.

(21) Mason, T. G.; Ganesan, K.; Van Zanten, J. H.; Wirtz, D.; Kuo, S. C. Particle Tracking Microrheology of Complex Fluids. *Phys. Rev. Lett.* **1997**, *79* (17), 3282–3285. https://doi.org/10.1103/PhysRevLett.79.3282.

(22) McGlynn, J. A.; Wu, N.; Schultz, K. M. Multiple Particle Tracking Microrheological Characterization: Fundamentals, Emerging Techniques and Applications. *J. Appl. Phys.* **2020**, *127* (20), 201101. https://doi.org/10.1063/5.0006122.

(23) Hu, Y.; You, J.-O.; Auguste, D. T.; Suo, Z.; Vlassak, J. J. Indentation: A Simple,

Nondestructive Method for Characterizing the Mechanical and Transport Properties of PH-Sensitive Hydrogels. *J. Mater. Res.* **2012**, *27* (1), 152–160. https://doi.org/10.1557/jmr.2011.368.

(24) Galli, M.; Comley, K. S. C.; Shean, T. A. V.; Oyen, M. L. Viscoelastic and Poroelastic Mechanical Characterization of Hydrated Gels. *J. Mater. Res.* **2009**, *24* (3), 973–979. https://doi.org/10.1557/jmr.2009.0129.

(25) Akhtar, R.; Draper, E. R.; Adams, D. J.; Hay, J. Oscillatory Nanoindentation of Highly Compliant Hydrogels: A Critical Comparative Analysis with Rheometry. *J. Mater. Res.* **2018**, *33* (8), 873–883. https://doi.org/10.1557/jmr.2018.62.

(26) Oyen, M. L. Mechanical Characterisation of Hydrogel Materials. *Int. Mater. Rev.* **2014**, *59* (1), 44–59. https://doi.org/10.1179/1743280413Y.0000000022.

(27) Zhang, K.; Feng, W.; Jin, C. Protocol Efficiently Measuring the Swelling Rate of Hydrogels. *MethodsX* **2020**, *7* (September 2019), 100779. https://doi.org/10.1016/j.mex.2019.100779.

(28) Zhang, K.; Feng, W.; Jin, C. Protocol Efficiently Measuring the Swelling Rate of Hydrogels. *MethodsX* **2020**, *7* (December 2019), 100779. https://doi.org/10.1016/j.mex.2019.100779.

(29) Tiwari, A. Nanomechanical Analysis of Hybrid Silicones and Hybrid Epoxy Coatings—A Brief Review. *Adv. Chem. Eng. Sci.* **2012**, *02* (01), 34–44. https://doi.org/10.4236/aces.2012.21005.

(30) Hu, Y.; Chen, X.; Whitesides, G. M.; Vlassak, J. J.; Suo, Z. Indentation of Polydimethylsiloxane Submerged in Organic Solvents. *J. Mater. Res.* **2011**, *26* (6), 785–795. https://doi.org/10.1557/jmr.2010.35.

(31) Delavoipière, J.; Tran, Y.; Verneuil, E.; Chateauminois, A. Poroelastic Indentation of Mechanically Confined Hydrogel Layers. *Soft Matter* **2016**, *12* (38), 8049–8058. https://doi.org/10.1039/c6sm01448h.

(32) Lai, Y.; Hu, Y. Probing the Swelling-Dependent Mechanical and Transport Properties of Polyacrylamide Hydrogels through AFM-Based Dynamic Nanoindentation. *Soft Matter* **2018**, *14* (14), 2619–2627. https://doi.org/10.1039/c7sm02351k.

(33) Chan, E. P.; Hu, Y.; Johnson, P. M.; Suo, Z.; Stafford, C. M. Spherical Indentation Testing of Poroelastic Relaxations in Thin Hydrogel Layers. *Soft Matter* **2012**, *8* (5), 1492–1498. https://doi.org/10.1039/C1SM06514A.

(34) Mishra, S.; Badani Prado, R. M.; Lacy, T. E.; Kundu, S. Investigation of Failure Behavior of a Thermoplastic Elastomer Gel. *Soft Matter* **2018**, *14* (39), 7958–7969. https://doi.org/10.1039/C8SM01397G.

(35) Kuang, X.; Liu, G.; Dong, X.; Wang, D. Correlation between Stress Relaxation Dynamics and Thermochemistry for Covalent Adaptive Networks Polymers. *Mater. Chem. Front.* **2017**, *1* (1), 111–118. https://doi.org/10.1039/C6QM00094K.

(36) Syed, I. H.; Stratmann, P.; Hempel, G.; Klüppel, M.; Saalwächter, K. Entanglements, Defects, and Inhomogeneities in Nitrile Butadiene Rubbers: Macroscopic versus Microscopic Properties. *Macromolecules* **2016**, *49* (23), 9004–9016. https://doi.org/10.1021/acs.macromol.6b01802.

(37) Han, G.; Hess, C.; Eriten, M.; Henak, C. R. Uncoupled Poroelastic and Intrinsic Viscoelastic Dissipation in Cartilage. *J. Mech. Behav. Biomed. Mater.* **2018**, *84*, 28–34. https://doi.org/10.1016/j.jmbbm.2018.04.024.

(38) Arevalo, S. E.; Ebenstein, D. M.; Pruitt, L. A. A Methodological Framework for Nanomechanical Characterization of Soft Biomaterials and Polymers. *J. Mech. Behav. Biomed. Mater.* **2022**, *134*, 105384. https://doi.org/10.1016/j.jmbbm.2022.105384.

(39) Tsutsuba, T.; Sogawa, H.; Kuwata, S.; Takata, T. Kinetically Stabilized Aliphatic Nitrile *N* -Oxides as Click Agents: Synthesis, Structure, and Reactivity. *Chem. Lett.* **2017**, *46* (3), 315–318. https://doi.org/10.1246/cl.161098.

(40) McKenzie, B. M.; Miller, A. K.; Wojtecki, R. J.; Johnson, J. C.; Burke, K. A.; Tzeng, K. A.; Mather, P. T.; Rowan, S. J. Improved Synthesis of Functionalized Mesogenic 2,6-Bisbenzimidazolylpyridine Ligands. *Tetrahedron* **2008**, *64* (36), 8488–8495. https://doi.org/10.1016/j.tet.2008.05.075.

4 Optimizing Nitrile-Oxide/Alkyne Cycloaddition (NAOC) Polymerization of Main-Chain Polyrotaxanes

4.1 Introduction

Singly-threaded [2]rotaxanes have been synthesized in the literature via metal-templating using triaryl stopper groups.[1,2] It has been shown that it is important to match the size of the ring with the size of the stopper groups. For example, a 33-membered phenanthroline ring was found to form a stable [2]rotaxane at 60°C in chloroform-d with tris(biphenyl)methyl stopper moieties (Figure 4.1). However, a slight increase in ring size from 33 to 37 atoms resulted in a dissociation of the rotaxane at 60°C in a process that has been termed slippage, and the 41-atom ring resulted in no interlocked product. Increasing the temperature (e.g., 130°C in 1,1,2,2,-tetrachloroethane-*d2*) results in faster slippage of the rotaxanes. Adding substituents (R) to the biphenyl moiety provided a series of different stopper sizes to probe the dissociation of the [2]rotaxane further. The half-life of the original tris(biphenyl)methyl stoppered rotaxane (R = H) was less than 30 minutes, however adding ethyl to the biphenyls slowed the half-life to 1.1 hours. Attaching cyclohexyl moieties to the stopper slowed [2]rotaxane dissociation to 35 hours.[3]

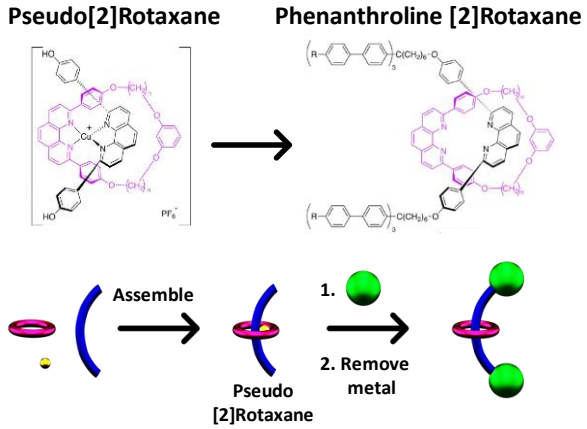

Ring Size	Stopper "R"	Rotaxane Yield	Half-life (130°C)
33 (n = 6)	H	62%	< 0.5 h
37 (n = 8)	H	34%	Unstable at 60°C
41 (n = 10)	H	Not isolated	---
45 (n = 12)	H	Not isolated	---
33	Et	60%	20% dissoc. after 240h
37	Et	64%	1.1 h
41	Et	Not isolated	---
33	Cy	51%	No dissoc. after 240h
37	Cy	54%	35 h
41	Cy	Not isolated	---

Figure 4.1. Synthesis of [2]rotaxanes through metal-ligand binding and the relationship between the size of the stopper and ring components that affect the interlocked rotaxane's stability. Adapted from Ref. 3 with permission from American Chemical Society.

The Nitrile-Oxide/Alkyne Cycloaddition (NAOC) stoppering chemistry has been utilized by Takata to synthesize [2]rotaxanes[4] and [2]catenanes[5] by reacting a variety of pseudo[2]rotaxanes with nitrile-oxide moieties to generate chemically stable isoxazoline, isoxazole, and oxadiazole units in the absence of any catalyst. The pseudo[2]rotaxanes were assembled from dibenzo-24-crown-8-ether (DB24C8) and sec-ammonium salt axle molecules that possess alkene, alkyne, or nitrile terminal groups which react with nitrile-oxide. Benzohydroxamoyl chloride moieties can form nitrile-oxide moieties in situ; however, this process requires a catalyst such as triethylamine, silver triflate, or 4Å mol sieves that limits interlocked yield. Employing a stable nitrile-oxide end-capping agent provided rotaxane yields of up to 97% without requiring a catalyst. Increasing the reaction temperature resulted in faster reaction times but a decrease in yield on account on the entropy-driven dissociation of the pseudorotaxane.[4]

The reactivity of the terminal group on the pseudo[2]rotaxane affects the bond formation with the nitrile-oxide stopper. Adding a phenyl extension between the ring complex and terminal

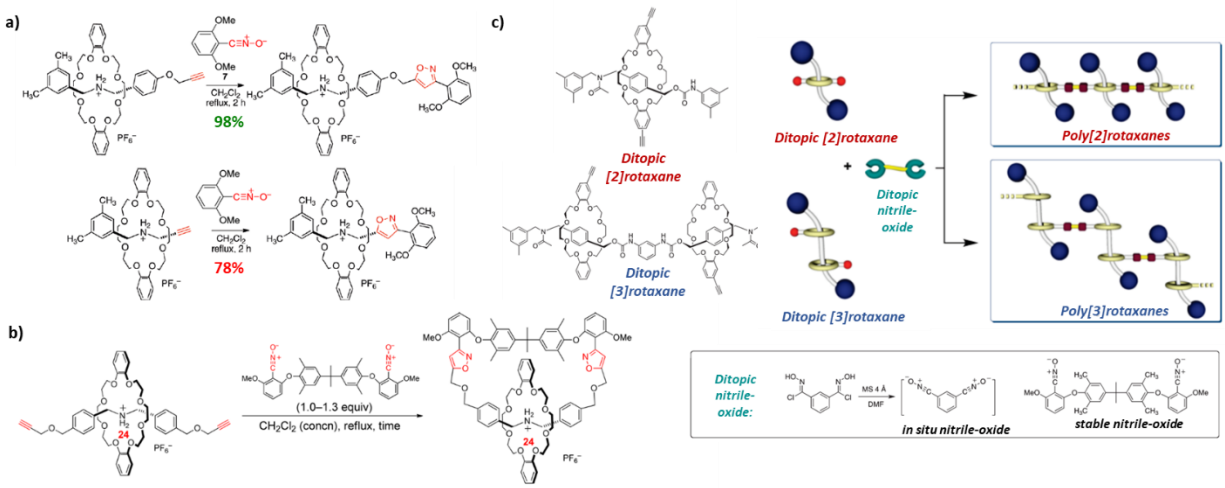

Figure 4.2. a) Optimizing NOAC stoppering of [2]rotaxanes by extending an alkyne group away from the pseudorotaxane complex to limit steric hindrance and produce chemically stable isoxazole linkages.[4] b) Click annulation of a pseudo[2]rotaxane to a [2]catenane with stable nitrile-oxide monomer.[5] c) NOAC click polymerization of poly[2]- and poly[3]rotaxanes from ditopic acetylene [2]- and [3]rotaxanes and (in situ or stable) ditopic nitrile N-oxide monomers.[6] Adapted from Refs. 4, 5, and 6 with permission from American Chemical Society.

alkyne (or alkene) increased rotaxane yield from 78% to 98% (Figure 4.2a). The stability of the cycloadduct also influences the interlocked yield. Isoxazoles and isoxazolines form stable carbon-carbon bonds between pseudorotaxanes and stoppers; however, the basicity of the oxadiazoles formed from terminal nitriles causes decomposition of the pseudorotaxanes, accounting for the lower 24% yield.

The double end-capping reaction of two terminal alkynes on a similar complex formed [2]rotaxanes with nitrile-oxide stoppers in high (86%) yield. A click annulation reaction of the same pseudo[2]rotaxane with a homoditopic nitrile-oxide generated [2]catenanes under more dilute conditions.[5] A central *gem*-dialkyl group induces steric hindrance that favors ring closure and intramolecular reactions, making this particular homoditopic nitrile-oxide attractive for ring-closing polycatenane materials (Figure 4.2b). Various interlocked architectures, including main-chain poly[2]-and poly[3]rotaxanes,[6] have been accessed using NAOC click chemistry, highlighting its ability to assemble topologically intricate materials from complex monomers without side reactions (Figure 4.2c). NAOC click is a high-yielding reaction, multi-arm star polymers have been reported with conversions over 99%,[7] making it ideal for accessing enough material to investigate the unique properties and functions resulting from the nature of the mechanical bond.

This chapter explores the use of the catalyst-free nitrile-oxide/alkyne cycloaddition (NOAC) in the synthesis of [2]rotaxanes by reacting a metal-coordinated bis-alkyne pseudo[2]rotaxane (P2R) and a nitrile-oxide-containing stopper group (Figure 4.3).

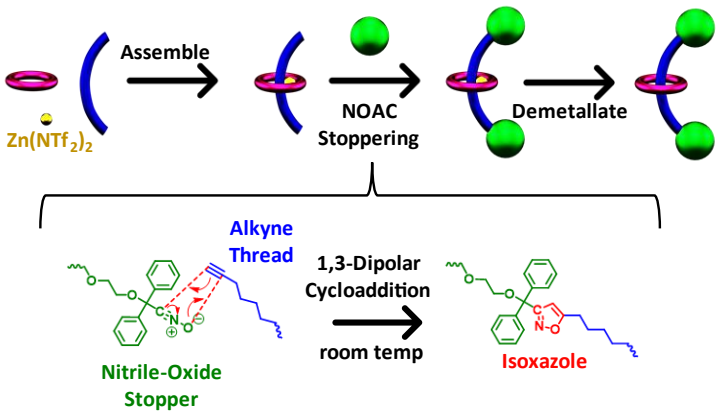

Figure 4.3. Pseudo[2]rotaxane metal-template assembly from a bis-alkyne thread and 36-atom monotopic ring, and NOAC stoppering with a stable nitrile-oxide triaryl stopper group to form the [2]rotaxane after demetallation.

Following the [2]rotaxane proof-of-concept studies, the same stoppering conditions were exploited for the NOAC polymerization of main-chain polyrotaxanes with the nitrile-oxide monomer (**2.5**) used to develop SR-PCNs in Chapter 2. The work detailed in this chapter will guide current and future Rowan Group members in synthesizing new SR-PCN architectures using stoppers (instead of covalent crosslinks used in Chapter 2) to keep rings threaded in the network.

4.2 Results and Discussion

4.2.1 Design of [2]Rotaxane Components

A ligand-based [2]rotaxane system optimized the reaction between alkyne-terminated thread components with a nitrile-oxide stopper. The diagnostic ^{1}H-NMR singlet for a terminal alkyne and the singlet on the corresponding isoxazole cycloadduct allows for facile monitoring of the stoppering step. Bis-alkyne Bip thread **2.2** (Figure 4.4a, left) and a bis-alkyne 2’2-bipyridyl (Bipy) thread **4.1** Figure 4.4a, right) were synthesized for preliminary dumbbell (thread + stopper) and [2]rotaxane (P2R + stopper) stoppering experiments. [2]Rotaxanes were also assembled from the smaller Bipy thread in anticipation of smaller ring cavities that might not be able to thread the

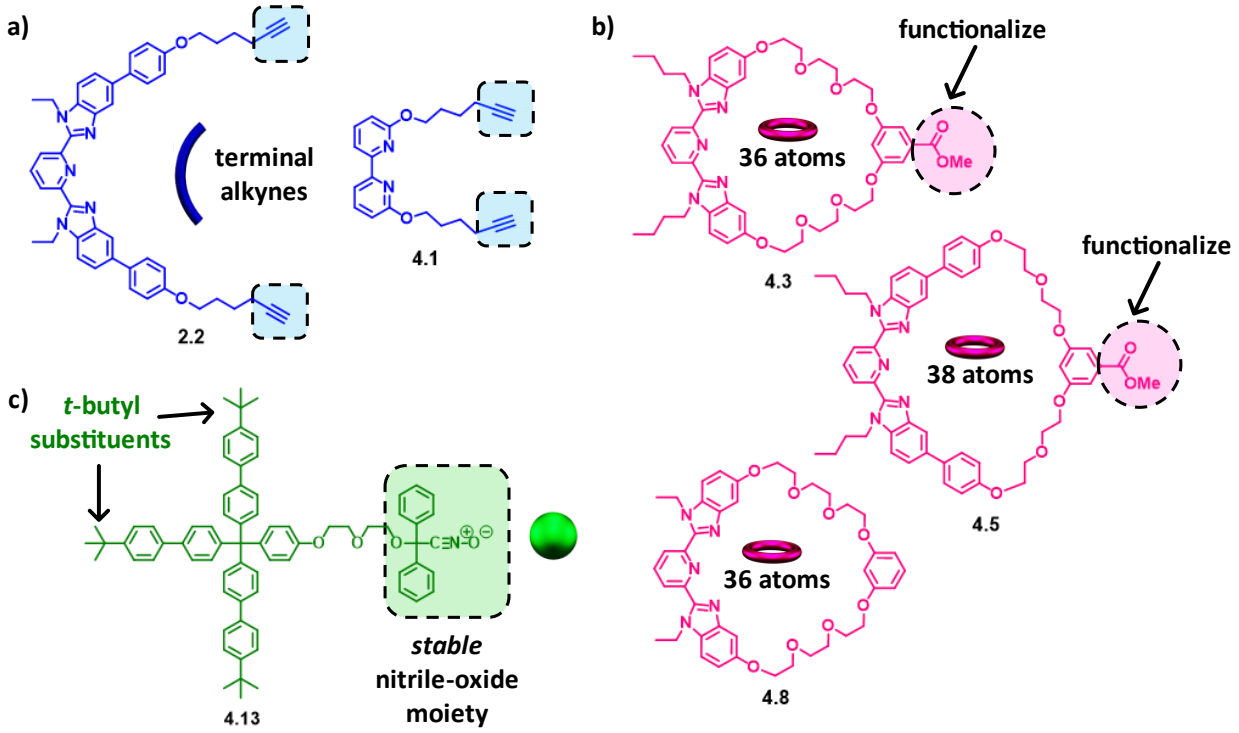

Figure 4.4. [2]Rotaxane Components: a) bis-alkyne threads **2.2** (Bip) and **4.1** (Bipy), b) 36-atom (**4.3** and **4.8**) and 38-atom (**4.5**) monotopic rings, and c) stable nitrile-oxide triaryl stopper **4.13** See Experimental for synthetic details of each component.

bulkier Bip moiety. Extending the terminal alkynes away from the ligand site with (six carbon) alkyl chains ensures minimal interference with the metallated ring complex.

The flexible nature of the macrocycle synthesis is advantageous as we can change the number of ligand sites to access singly-threaded and doubly-threaded rings. Smaller, monotopic rings can be synthesized using Bip and a shorter ethylene glycol linker by adapting a standard crown ether literature procedure.[8] Previous [3]catenane work in the Rowan Group[9] employed a 62-atom macrocycle ligated with one (phenyl-extended) Bip moiety and an ethylene glycol linker. Similarly, 36-atom **4.3** (Figure 4.4b, top) was synthesized from non-extended Bip and a benzoate linker with six total ethylene glycol units. The benzoate moiety provides a reactive site that can functionalize monotopic rings to react together or be incorporated into different dynamic and interlocked systems. Phenyl-extended Bip and a similar benzoate linker with four total ethylene

glycol units did not form the 38-atom **4.5** (Figure 4.4b, middle) as expected. Based on the MALDI-TOF of the column fractions, **4.5** was predominately dimer. Furthermore, a more significant shift in the NMR spectrum would be expected for the monotopic vs. ditopic (dimer) ring (see Experimental). The 38-MC is too strained because the benzoate linker is too short, preventing the formation of **4.5** during the ring-closing reaction. Therefore, the 36-atom synthesis was further optimized by removing the benzoate group susceptible to transesterification during the linker synthesis and replacing it with benzene (Paul Jokinen, a previous member of the Rowan Lab, successfully performed the reverse transesterification process by simply refluxing the product in methanol to regenerate the desired methyl benzoate group). Shortening the alkyl tails on Bip from butyl to ethyl improved purification significantly, permitting recrystallization of the oily product **4.8** (Figure 4.4b, bottom).

A stable nitrile-oxide moiety was chosen for stopper **4.13** (Figure 4.4c) to promote better yields over the *in situ* approaches that use benzohydroxamoyl chloride to form the nitrile-oxide.[209] Generally, nitrile-oxides are labile and dimerize easily to form furoxans if not sufficiently hindered by bulky substituents. For example, benzonitrile oxide dimerizes quickly to diphenyl furoxan, whereas *ortho*-disubstituted benzonitrile-oxides are highly stable and reactive. Biphenyl groups have been proven sufficient for stabilizing nitrile-oxides, commonly achieved by reacting nitro groups with phenyl isocyanate under basic conditions to generate nitrile-oxides (Figure 4.5).[11,12] As such, nitrile-oxide **4.13** was synthesized through the SN2 reaction of 1,1-diphenylnitroethene[13] (**2.3**) with hydroxy chain ends on the stopper moiety to provide a nitro group for the nitrile-oxide forming reaction (see Experimental).

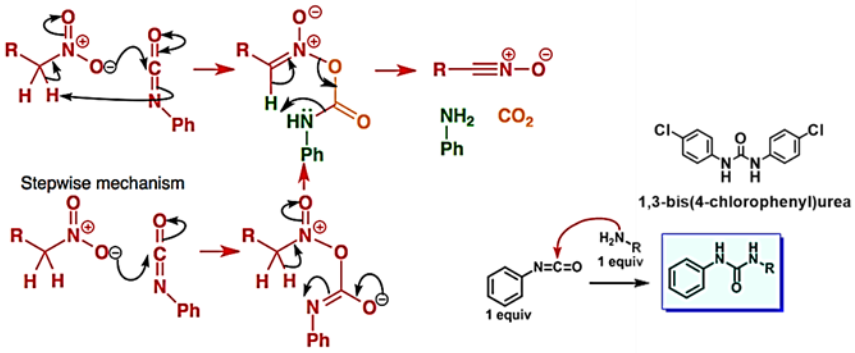

Figure 4.5. The final nitrile-oxide forming step[12] is a reaction of aliphatic nitro compounds with phenyl isocyanate to give aniline and carbon dioxide; two slightly different mechanisms are proposed, and the last step might not be concerted. When 4-chlorophenyl isocyanate is employed, the reaction forms a 1,3-bis(4-chlorophenyl)urea byproduct that crashes out as the reaction proceeds. Adapted from ChemTube3D by Nick Greeves licensed under a Creative Commons Attribution-Noncommercial-Share Alike 2.0 UK: England & Wales License.

Bip (**4.14**) and Bipy (**4.15**) dumbbells (Figure 4.6) were synthesized from the alkyne-terminated threads **2.2** and **4.1** and excess nitrile-oxide stopper **4.13**. The diagnostic ^{1}H-NMR singlet for a terminal alkyne at ~2.0 ppm and the singlet on the corresponding isoxazole dumbbell cycloadduct at ~6.0 ppm allows for facile monitoring of the stoppering step (see Experimental).

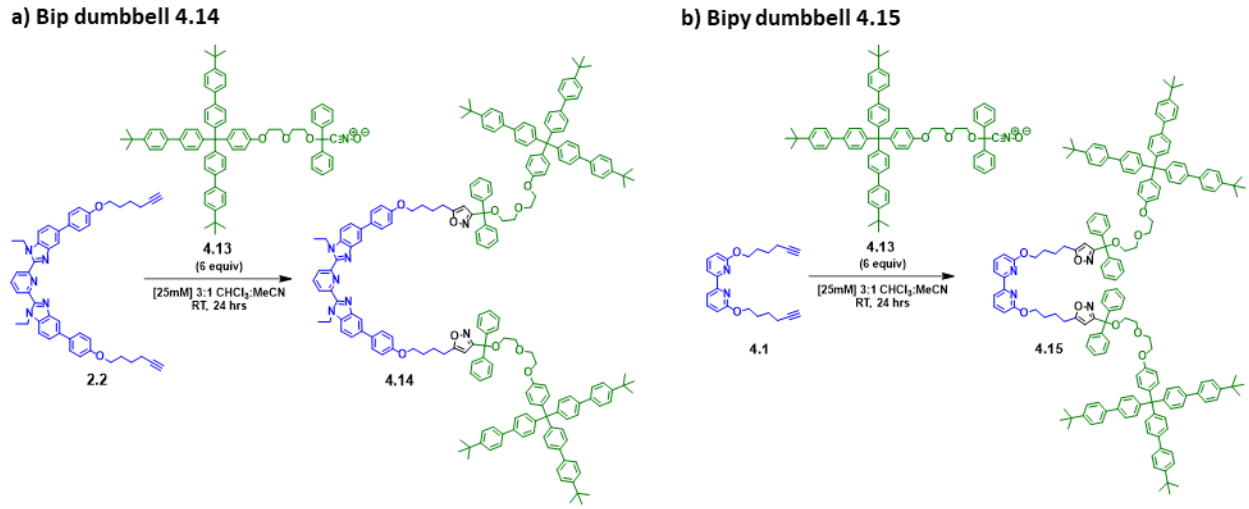

Figure 4.6. Synthesis of a) Bip (**4.14**) and b) Bipy (**4.15**) dumbbells from threads **2.2** and **4.1** using an excess of nitrile-oxide stopper **4.13**. Components are dissolved in 3:1 chloroform:acetonitrile at [25mM] and left to stir at room temperature for 24 hours.

4.2.2 Synthesis of [2]Rotaxanes

A Bip-based [2]rotaxane **4.16** (Figure 4.7a) and Bipy-based [2]rotaxane **4.17** (Figure 4.7b) were synthesized by reacting P2Rs with stopper **4.13** and then demetallating with a dilute base solution to remove the metal. Pseudo[2]rotaxanes were assembled by titrating a solution of $Zn(NTf_2)_2$ into a 1:1 solution of **4.8:2.2** or **4.8:4.1** to form Bip-P2R **4.8:2.2:Zn(II)** (Figure 4.7) or Bipy-P2R **4.8:4.1:Zn(II)** (Figure 4.8). The template-directed assembly of the desired P2R was confirmed by the downfield shift of the aromatic Bip protons on **4.8** and **2.2** and the Bipy protons on **4.1** in the NMR spectrum after adding one equivalent of Zn^{2+} (see Experimental).

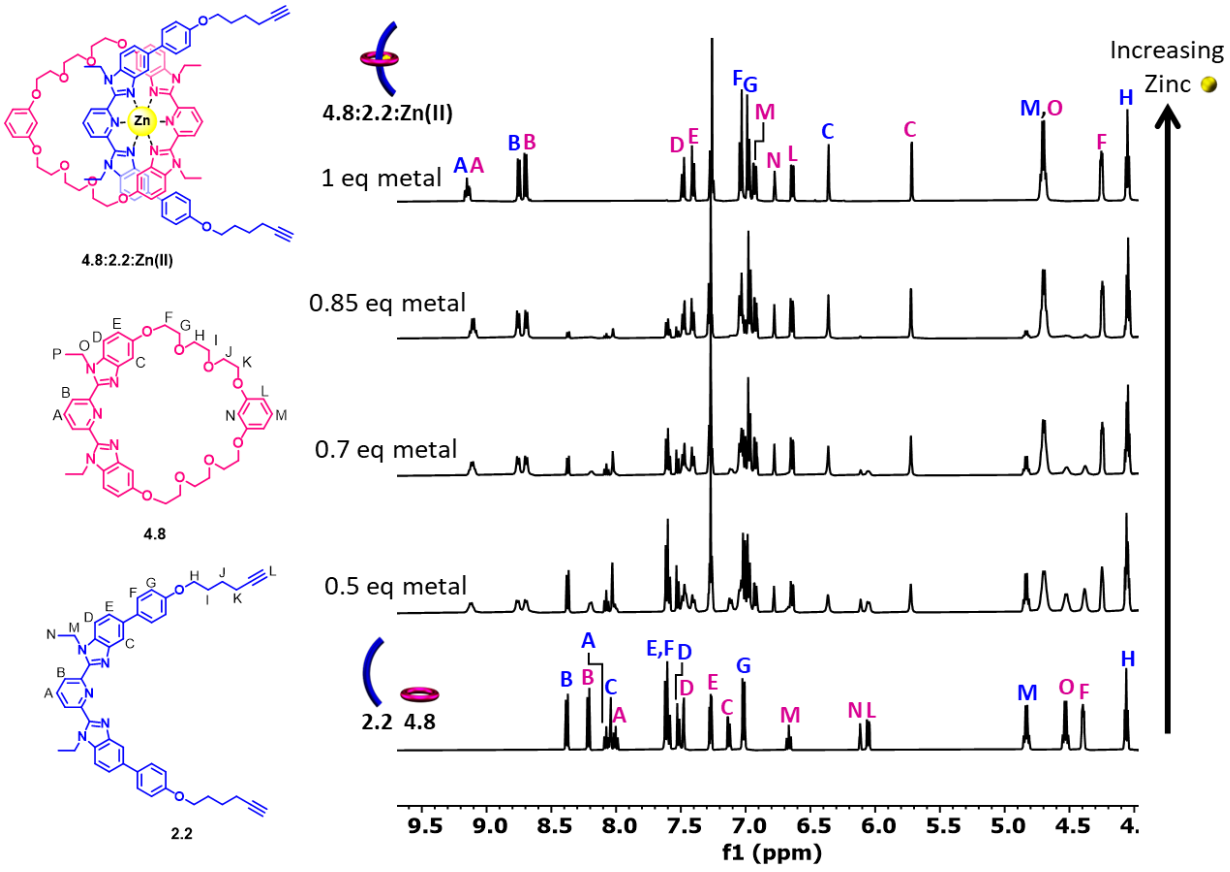

Figure 4.7. Partial ^{1}H-NMR overlay (500 MHz, 25°C, Solvent: 0, 7.5, 10.5, 12.75, 15% d_3-MeCN in $CDCl_3$ increasing upwards) of metal addition to form **4.8:2.2:Zn(II)**.

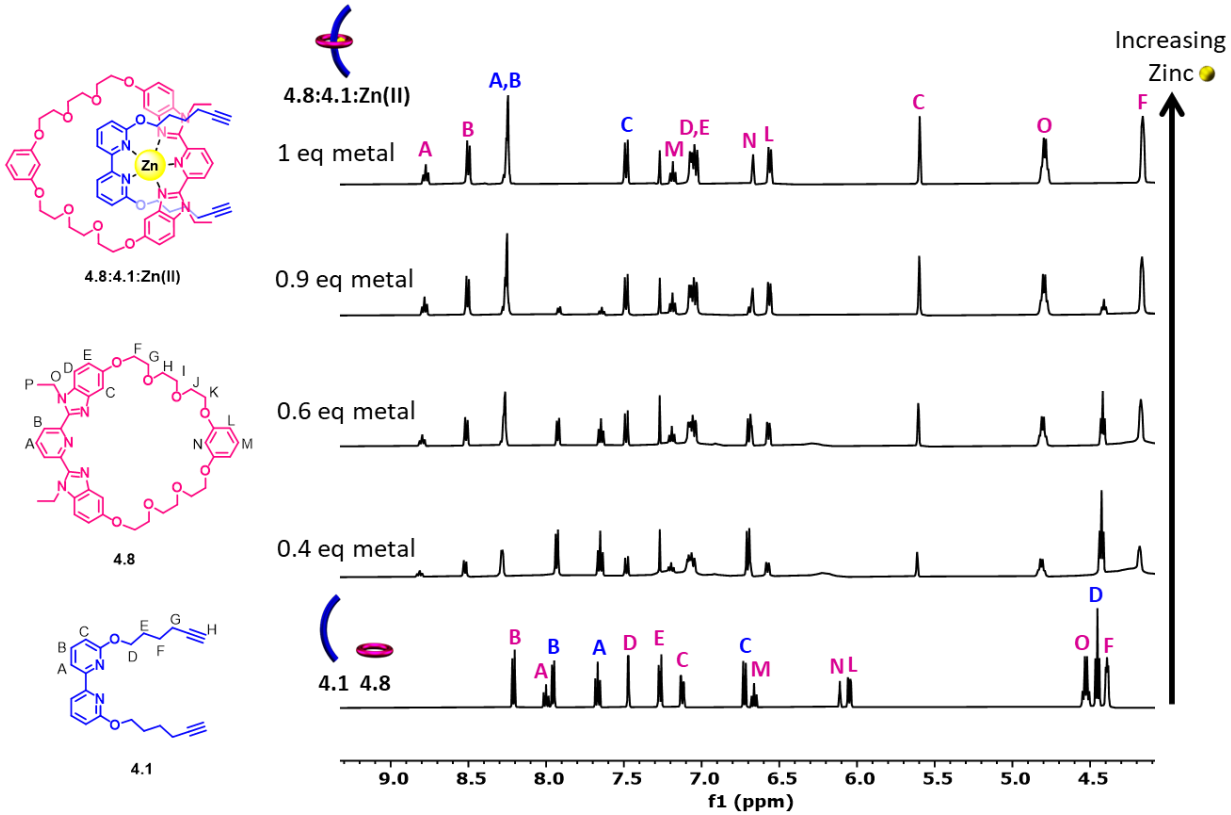

Figure 4.8. Partial ^{1}H-NMR overlay (500 MHz, 25°C, Solvent: 0, 6, 9, 13.5, 15% d_3-MeCN in $CDCl_3$ increasing upwards) of metal addition to form **4.8:4.1:Zn(II)**.

NOAC stoppering of the bis-alkyne P2Rs followed by demetallation was carried to target the [2]rotaxanes **4.16** (Figure 4.9a) and **4.17** (Figure 4.9b) resulting in products in good (~82% crude, interlocked) yield. Shifts in the Bip [2]rotaxane **4.16** arise from the ring current of aromatic groups, resulting in upfield-shifted peaks in the interlocked product (Figures 4.10). MALDI-TOF further confirms the interlocked [2]rotaxane structure, showing a strong peak at 3615 m/z as expected for **4.16** (Figure 4.11).

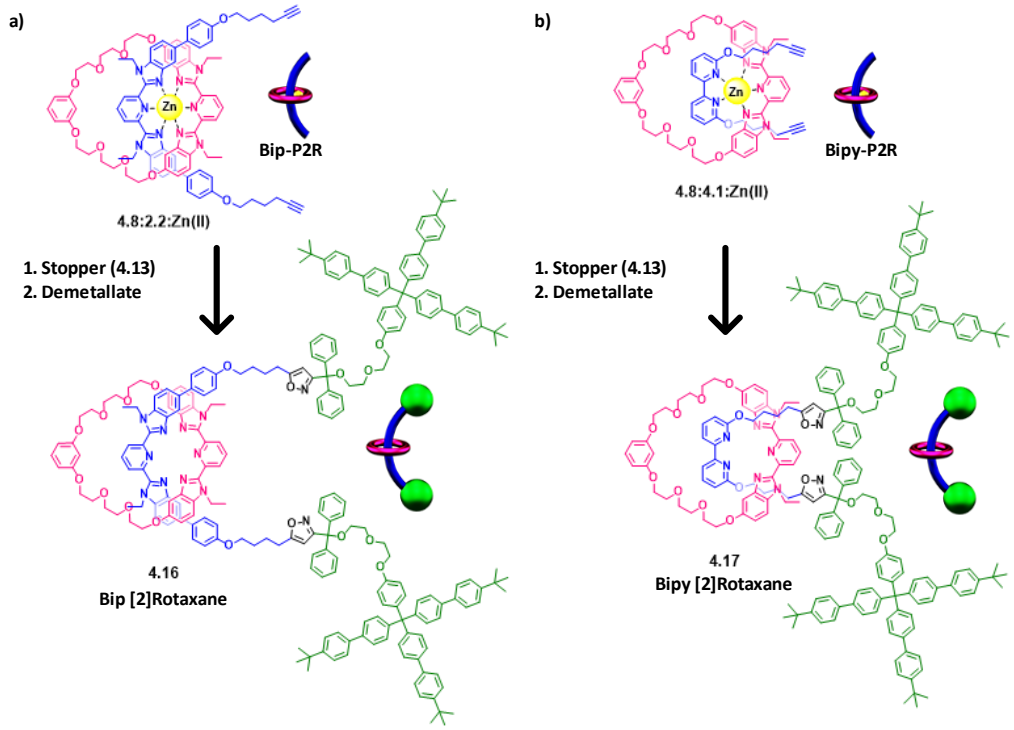

Figure 4.9. Stoppering of a) Bip-P2R (**4.8:2.2:Zn(II)**) and b) Bipy-P2R (**4.8:4.1:Zn(II)**) with nitrile-oxide **4.13** results in Bip [2]rotaxane **4.16** and Bipy [2]rotaxane **4.17** after demetallation.

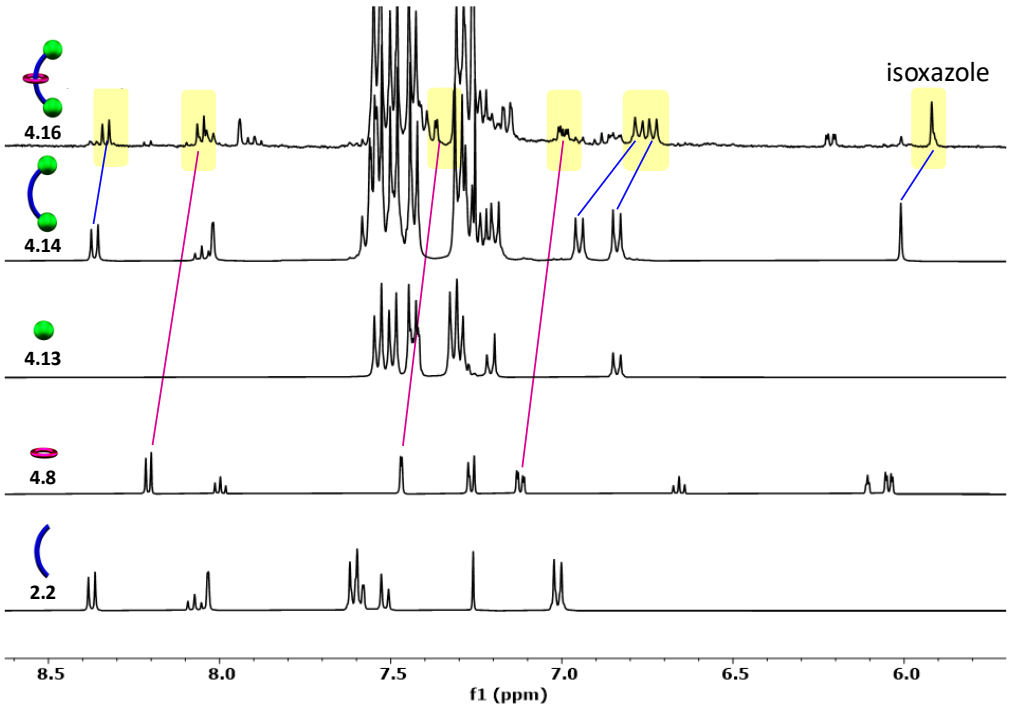

Figure 4.10. Partial ^{1}H-NMR overlay (500 MHz, 25°C, $CDCl_3$) of Bip [2]rotaxane **4.16**. The top NMR spectrum corresponds to the crude, demetallated **4.16**. The bottom four spectra correspond to indicated components and starting materials for comparison. Upfield shifted peaks from the interlocked product are highlighted in yellow.

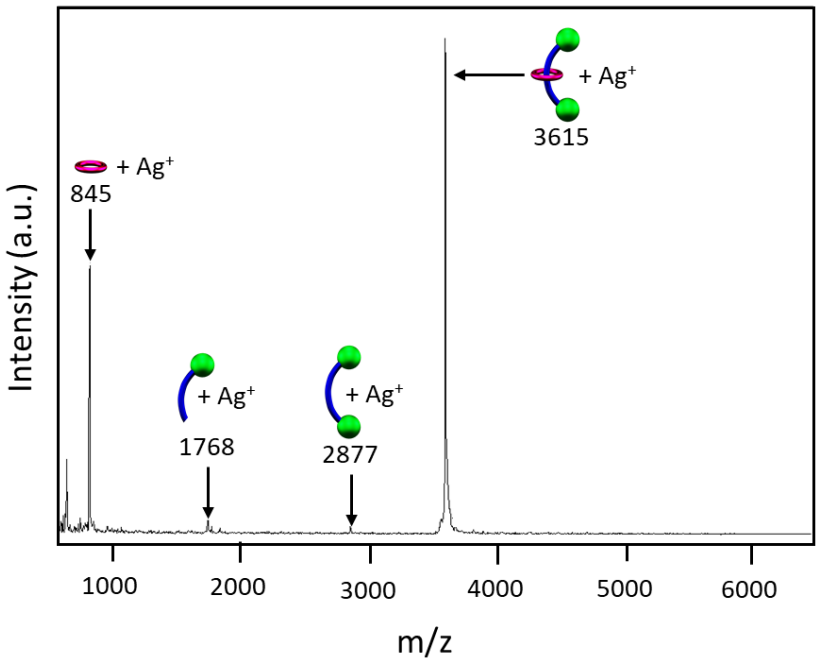

Figure 4.11. MALDI-TOF MS (Dithranol, silver trifluoroacetate) of Bip [2]rotaxane **4.16**.

The upfield shifted NMR peaks in the Bipy [2]rotaxane **4.17** spectrum also suggest [2]rotaxane formation (Figure 4.12). The meta-Bip protons on the macrocycle in **4.17** (i.e., **4.8**) undergo the same chemical shift from 8.20 – 8.04 ppm as in **4.16**. MALDI-TOF also confirms the formation of interlocked **4.17** (Figure 4.13). The successful formation of **4.16** and **4.17** shows that different bis-alkyne ligands (i.e., thread **2.2** and **4.1**) can be employed in this system.

Although the stoppering reaction appears quantitative via NMR, the overall interlocked yield for Bip **4.16** was found to be ca. 82%, consistent with the poly[*n*]catenanes[14] and [3]rotaxanes[15] that have been reported using the same Bip ligand moiety. The stability of the [2]rotaxane architecture was tested by heating (crude) **4.16** in $CDCl_3$ (50mM, 50°C) and monitoring the aromatic Bip peaks via ^{1}H-NMR over 45 days (Figure 4.14). A slow increase in the aromatic peaks of ring **4.8** (pink) and thread **2.2** (blue) and the corresponding decrease in the interlocked peaks suggests slow slippage of 36-atom **4.8** over stopper **4.13,** resulting in 53%

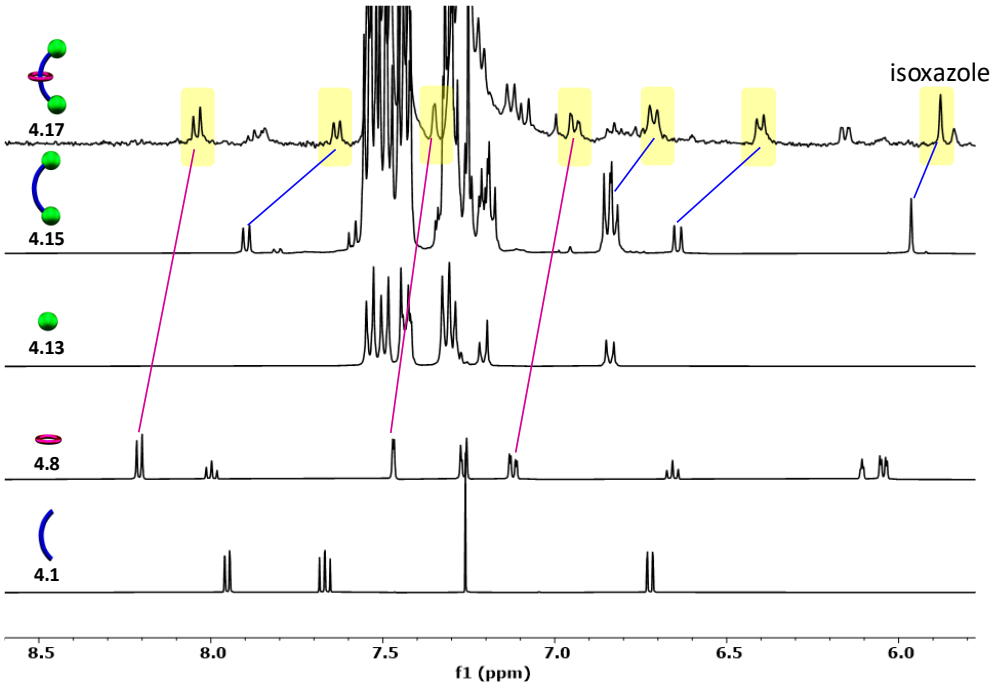

Figure 4.12. Partial ^{1}H-NMR overlay (500 MHz, 25°C, $CDCl_3$) of Bipy [2]rotaxane **4.17**. The top NMR spectrum corresponds to the crude, demetallated **4.17**. The bottom four spectra correspond to indicated components and starting materials for comparison. Upfield shifted peaks from the interlocked product are highlighted in yellow.

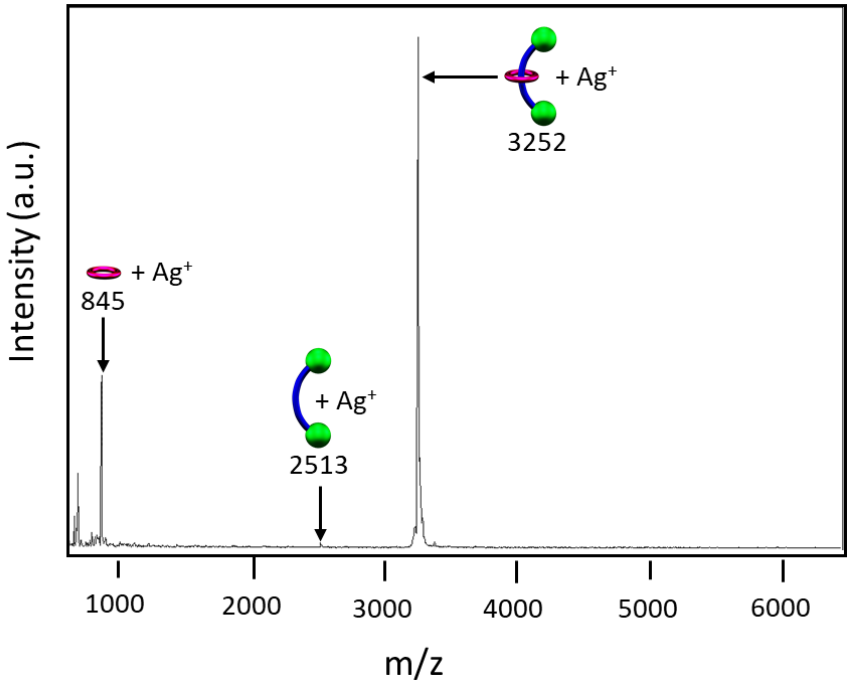

Figure 4.13. MALDI-TOF MS (Dithranol, silver trifluoroacetate) of Bipy [2]rotaxane **4.17**.

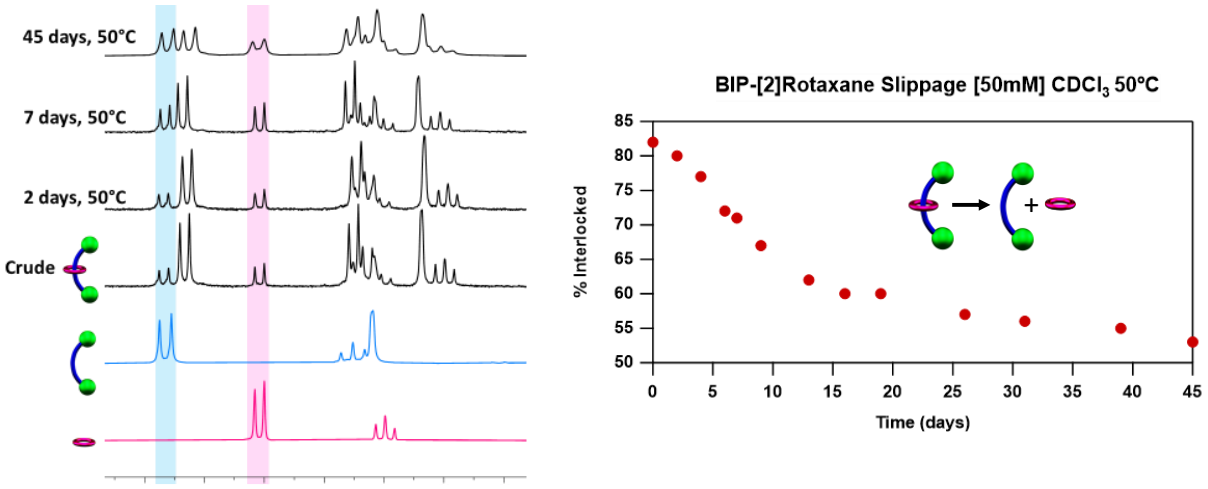

Figure 4.14. Partial ^{1}H-NMR overlay (500 MHz, 25°C, $CDCl_3$, d1=5s) of crude **4.16** (82% interlocked) slippage experiment with **4.8** (pink) and **4.14** (blue) for comparison (left). Slippage data was plotted after heating for 45 days at 50°C, showing 53% interlocked **4.16** (right). The experiment was stopped after 45 days.

interlocked **4.16** after 45 days (the slippage was not monitored past 45 days). A larger stopper will be discussed in Chapter 7 for accessing fully interlocked MIPs with doubly-threaded rings.

The [2]rotaxane stoppering experiments discussed here show that [2]rotaxanes can be made from 36-atom **4.8** and triaryl stopper **4.13**, thus serving as a proof-of-concept for the NOAC polymerization of main-chain polyrotaxanes from P2R.

4.2.3 Synthesis of Main-Chain Polyrotaxanes

Polyrotaxanes have a variety of attractive material properties but continue to be synthetically challenging. Catalyst-free NOAC click polymerization overcomes these challenges by assembling main-chain polyrotaxanes from a simple mixture of components. The [2]rotaxane experiments discussed above verified NOAC as a viable approach for stoppering; the subsequent click polymerization studies will help optimize the polymerization conditions used to assemble doubly-threaded MIPs using stoppers and singly-threaded (monotopic) rings. Template synthesis affords control over the number of rings on the polymer backbone, achieved simply by controlling the feed ratio of bis-alkyne P2R **4.8:2.2:Zn(II)** (Z mol%) and thread **2.2** (Y mol%) with a

poly(ethylene glycol) (PEG) based macromonomer (X mol%) and nitrile-oxide monomer **2.5** (1.0 mol) to form polyrotaxanes (Figure 4.15).

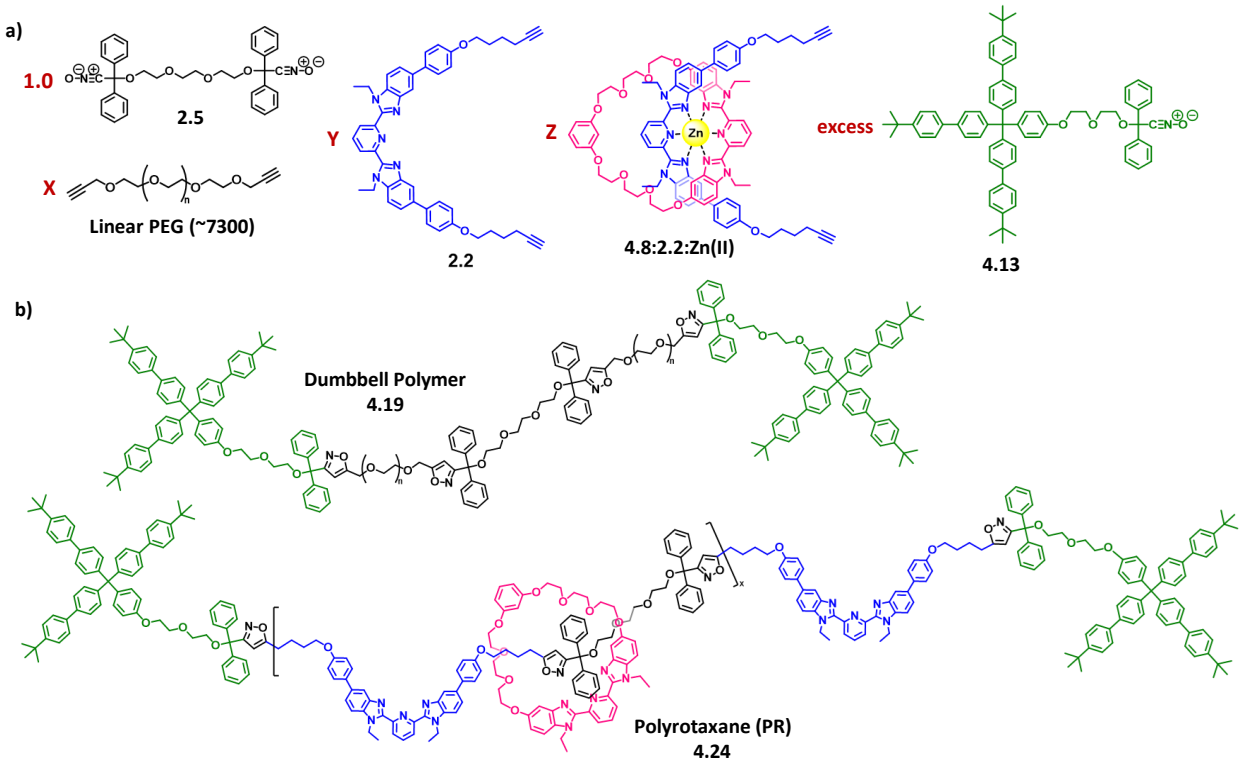

Figure 4.15. a) NOAC polymerization of difunctional monomer **2.5** (1.0 eq.) with varying amounts of linear PEG (7300 g/mol, X mol%), bis-alkyne Bip **2.2** (Y mol%), and P2R (**4.8:2.2:Zn(II)**, Z mol%) and excess stopper **4.13** affords b) dumbbell polymers (i.e., **4.19**) when **4.8:2.2:Zn(II)** and **2.2** are omitted, and main-chain polyrotaxanes (PRs) (i.e., **4.24**) from varying amounts of thread **2.2** and P2R **4.8:2.2:Zn(II)**.

NMR was used to monitor the NOAC polymerization by tracking the decrease in alkyne peaks and the growth of isoxazole peaks with the addition of components. Low ring density (**4.23-PR25**) and higher ring density (**4.23-PR50**) metallated polyrotaxanes were made by varying the molar ratio of components (Table 4.1).

The broadening of peaks in Figure 4.16 associated with P2R and thread in the aromatic (yellow) and upfield alkyl (dark blue) region verifies polymer formation. The broader alkyl peaks share the same chemical shifts as those in the Bip dumbbell **4.14**, consistent with the

Table 4.1. Feed ratio of components for NOAC polymerization of metallated Bip pseudopolyrotaxanes.

Sample	Monomer **2.5**	Alkyne-PEG-alkyne (X mol%)	Bip thread **2.2** (Y mol%)	P2R **4.8:2.2:Zn(II)** (Z mol%)
4.23-PR0	0.0050 g 0.0089 mmol	0.0377 g 0.0052 mmol X = 0.583	0.0032 g 0.0044 mmol Y = 0.500	0
4.23-PR25	0.0050 g 0.0089 mmol	0.0377 g 0.0052 mmol X = 0.583	0.0024 g 0.0033 mmol Y = 0.375	0.0023 g 0.0011 mmol Z = 0.125
4.23-PR50	0.0050 g 0.0089 mmol	0.0377 g 0.0052 mmol X = 0.583	0.0016 g 0.0022 mmol Y = 0.250	0.0046 g 0.0022 mmol Z = 0.250

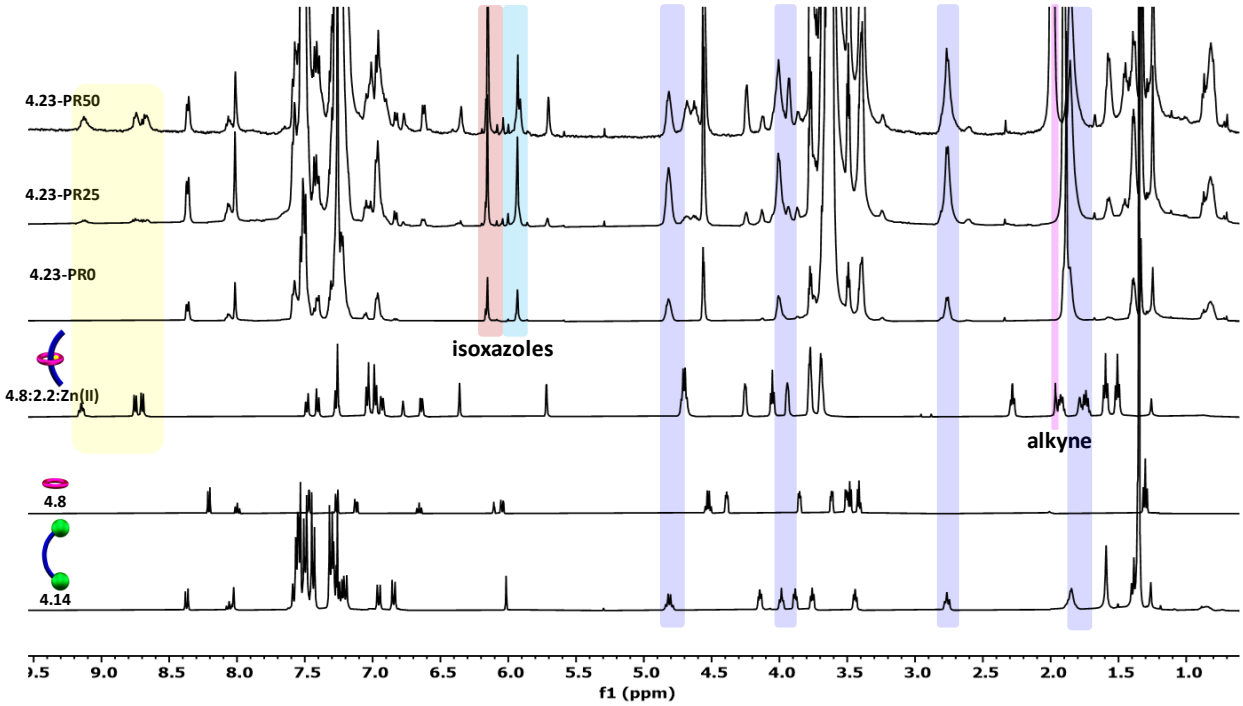

Figure 4.16. ^{1}H-NMR (500 MHz, d_1=5s, 25°C, $CDCl_3$) overlay of **4.23-PR0** (precipitated) and metallated Bip polyrotaxanes, **4.23-PR25** and **4.23-PR50**, (precipitated) with indicated components for comparison. The metallated Bip region is highlighted in yellow, the isoxazoles in red (closer to stopper) and light blue (between monomer and P2R), polymeric Bip thread **2.2** components in dark blue, and the alkyne singlet in purple.

polymerization of Bip components **2.2** and **4.8:2.2:Zn(II)**. Prominent isoxazole singlets at 6.15 and 5.93 ppm, and the disappearance of alkyne peaks at 1.9 ppm (**4.8:2.2:Zn(II)**) and 2.00 ppm (**2.2**), also prove successful NOAC click. The growth of new signals at 6.00, 6.04, and 6.08 as the amount of pseudo[2]rotaxane increases indicates multiple isoxazole environments along the backbone, as expected from NOAC polymerization of different components.

Precipitation removed excess stopper **4.13**, a small amount of macrocycle **4.8** and lower molecular weight products from **4.23-PR25** and **4.23-PR50** before demetallation (see Experimental). Gratifyingly, we see the retention of isoxazole (red and light blue) and polymeric Bip peaks (dark blue) after demetallation (Figure 4.17), although the smaller isoxazole signals are now buried under the (demetallated) macrocycle peaks (~6.1 ppm, pink).

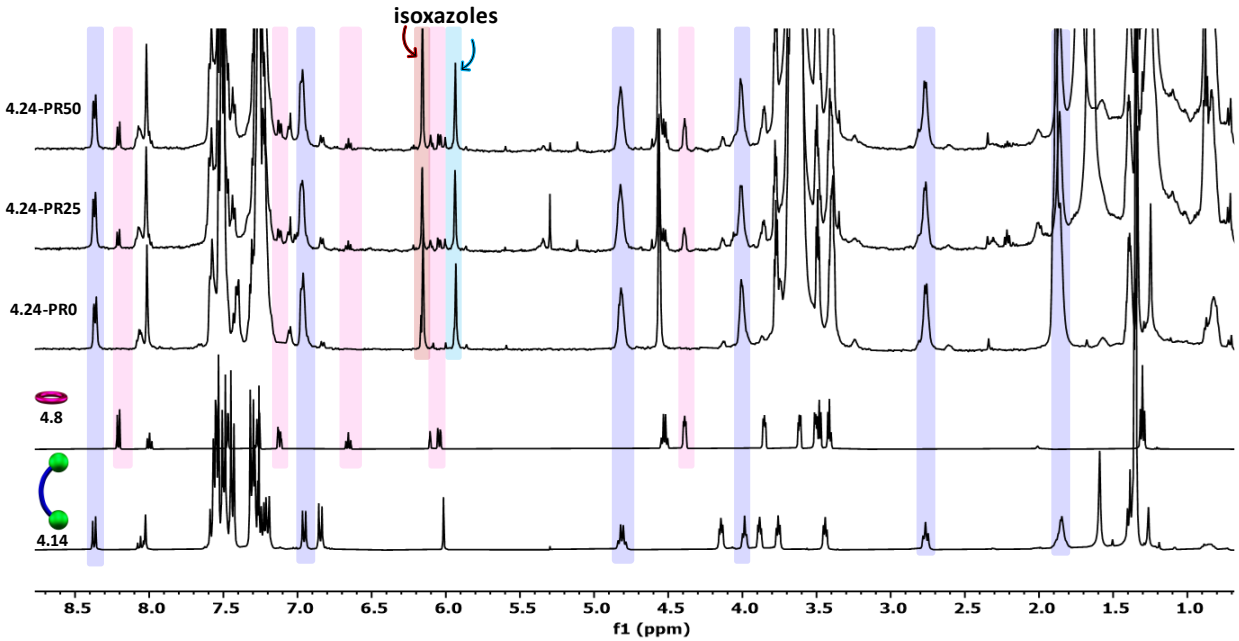

Figure 4.17. ^{1}H-NMR (500 MHz, d_1=5s, 25°C, $CDCl_3$) of demetallated Bip polyrotaxane, **4.24-PR25** and **4.24-PR50** (and **4.24-PR0**), with indicated components for comparison. Peaks corresponding to the macrocycle **4.8** are highlighted in pink, polymeric Bip peaks in dark blue, and the metallated aromatic region in yellow. The isoxazole units closer to the stopper are in red, and the isoxazoles in the backbone are in light blue.

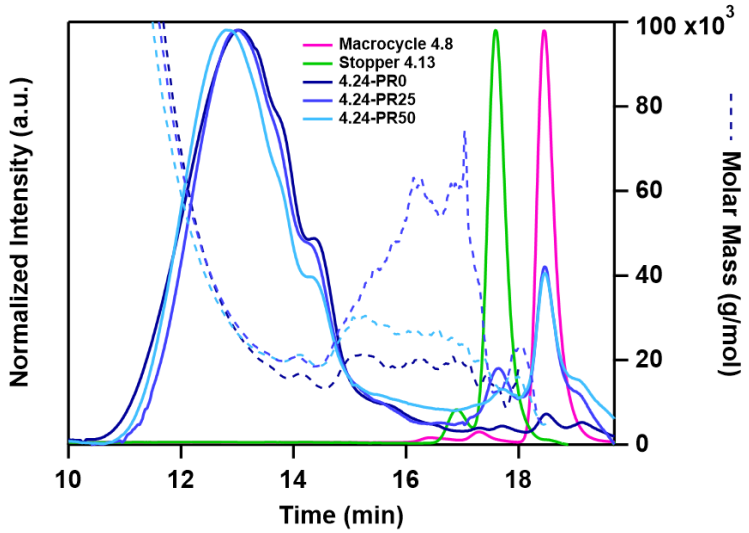

Figure 4.18. GPC traces of demetallated **4.24** polyrotaxanes.

The GPC traces in Figure 4.18 confirm the presence of a higher molecular weight product for **4.24-PR50**. There is also free macrocycle (**4.8**) which suggests some dethreading because of the small stopper size.

Although full retention of rings was not achieved for the demetallated PRs, a series of metallated polyrotaxanes with different ring densities was successfully prepared. One possible explanation is the stability of the pseudo[2]rotaxane complex in excess bis-alkyne Bip thread **2.2**; there is an increased likelihood of forming 2:1 Bip:Zn^{2+} complexes, i.e., **2.2$_2$:Zn(II)**, and the free (unbound) macrocycle **4.8** in solution. As such, metallated PR **4.25** was made by polymerizing the pseudorotaxane complex **4.8:2.2:Zn(II)** and the bis-nitrile-oxide monomer (**2.5**) without bis-alkyne Bip thread **2.2**, to combat the potential formation of **2.2$_2$:Zn(II)** and free **4.8** during the polymerization. The expected broadening of peaks, the disappearance of alkyne signals, and the growth of singlets in the isoxazole region of the NMR spectrum (Figure 4.19) confirm the formation of **4.25**. The more prominent isoxazole peak at 5.93 ppm likely corresponds to the isoxazole linkage between the P2R and monomer units. The metallated polyrotaxane was successfully precipitated from a mixture of cold hexanes/chloroform (6/1 v/v); the NMR spectrum

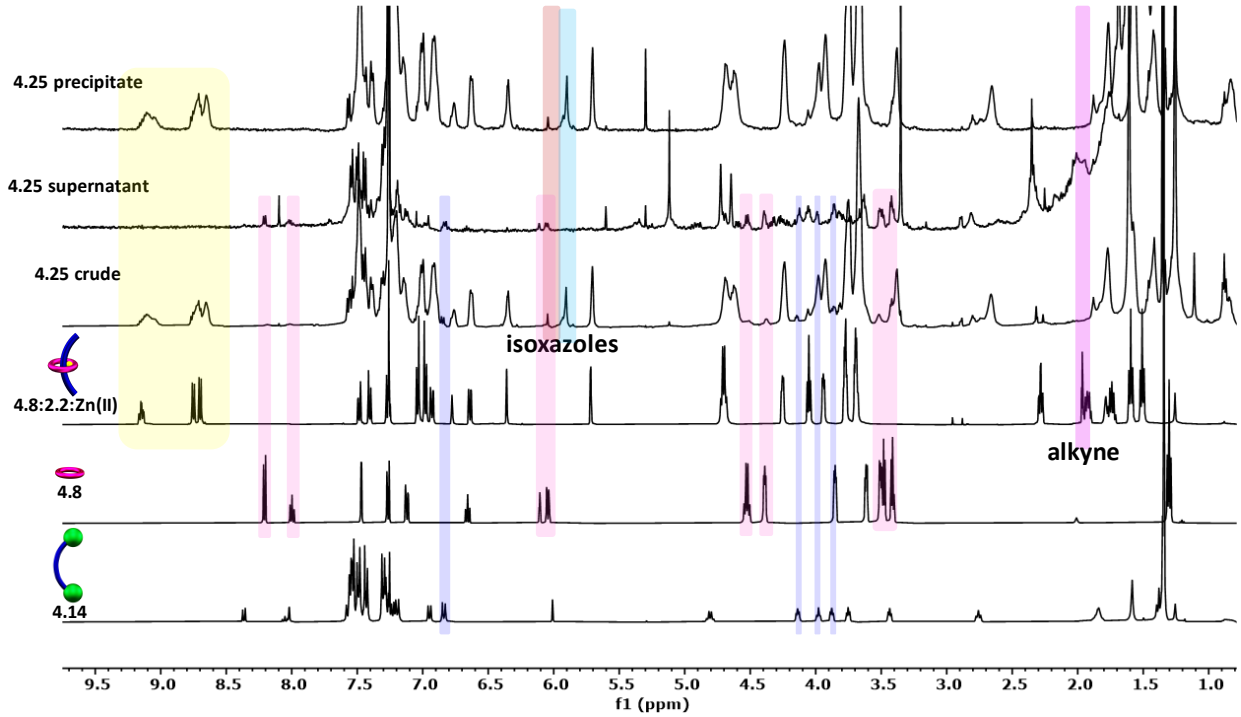

Figure 4.19. ^{1}H-NMR (500 MHz, d_1=5s, 25°C, $CDCl_3$) overlay of metallated Bip polyrotaxane **4.25** (crude, supernatant, precipitate) with indicated components for comparison. Peaks corresponding to the macrocycle **4.8** are highlighted in pink, polymeric Bip in dark blue, and the metallated aromatic region in yellow. The alkyne peak is highlighted in purple to show the full disappearance upon stoppering **4.8:2.2:Zn(II)**. The isoxazole units closer to the stopper are in red, and the isoxazoles in the backbone are in light blue.

for the supernatant solution shows a mixture of components and lower molecular weight compounds (Figure 4.19).

PR **4.25** was demetallated to form PR **4.26**, precipitated in cold methanol, and analyzed via NMR (Figure 4.20). The supernatant was predominately macrocycle **4.8** (pink) and other lower molecular weight Bip products (blue). The free (unbound) thread was exempt from this reaction to ensure the stability of the P2R complex in the solution. Integrating the *meta*-pyridyl Bip peaks in **4.26** reveals a similar ratio of components as that calculated for **4.24-PR25**. The low ring retention resulting from this experiment suggests the system needs further optimization. Ring size is one potential issue, but this can also be combatted with a larger stopper group that will be discussed in Chapter 7.

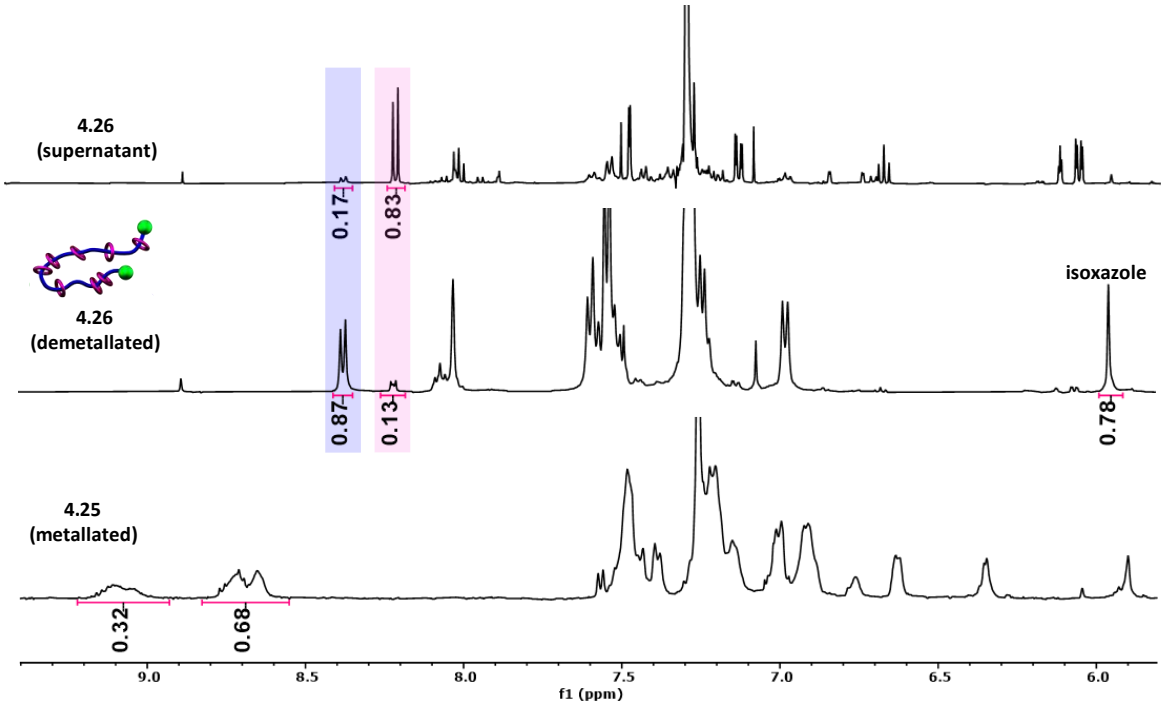

Figure 4.20. Partial ^{1}H-NMR (500 MHz, d_1=5s, 25°C, $CDCl_3$) overlay of demetallated Bip polyrotaxane **4.26** (middle spectrum) with metallated **4.25** (bottom spectrum) and the demetallated wash (top spectrum). Polymeric *meta*-pyridyl Bip peaks are in dark blue, and the *meta*-pyridyl Bip peaks on 36-atom macrocycle **4.8** is in pink.

The different binding geometry in Bip:Bipy:Zn(II) and Bip:Bip:Zn(II) could affect how the ring binds to the thread. The smaller Bipy ligand also has a better chance of threading through the tighter rings required for this triaryl stopper size. Investigating the polymerization of **4.8:4.1:Zn(II)** with nitrile-oxide monomer **2.5** and assessing the extent of dethreading will help determine if the Bipy complex should be used to synthesize polyrotaxanes moving forward. This experiment used a slight excess of P2R (1:1.09 **2.5: 4.8:4.1:Zn(II)**) to ensure alkyne end groups; further increasing the stopper amount added should also encourage complete stoppering of all polymer products.

The metallated region in the polyrotaxane **4.27** NMR spectrum cleans up nicely like the metallated [2]rotaxane **4.17** (8.9 - 8.1 ppm, Figure 4.21); the macrocycle shifts upfield as seen in the [2]rotaxane system, suggesting a more interlocked environment. The *para*- and *meta*-pyridyl

Bip protons on **4.8** shift upfield to the same region as the metallated pyridyl peaks on Bipy thread **4.1**, suggesting the stoppering of the ring as it is more confined to the Bipy environment. The shift also hints at a high ring density for the polymer; rings held closer along the backbone are more confined to the Bipy backbone. As expected for PR, there are more isoxazole peaks in the range (5.55 – 5.95 ppm) because there are more isoxazole sites along the polymer backbone. **4.27** has similar chemical shifts as the metallated [2]rotaxane **4.17**; however, the peaks are broader, indicating the formation of polymer products.

The crude metallated [2]rotaxane and polyrotaxane contain doublets corresponding to the bipyridyl peaks of **4.1**, hinting at the formation of free (unbound) thread during the polymerization (dark blue, Figure 4.21). Free Bipy could result from the formation of **4.1$_2$:Zn(II)** in solution or the instability of the Bipy:Bip pseudo[2]rotaxane complex. Stronger metal-ligand interactions

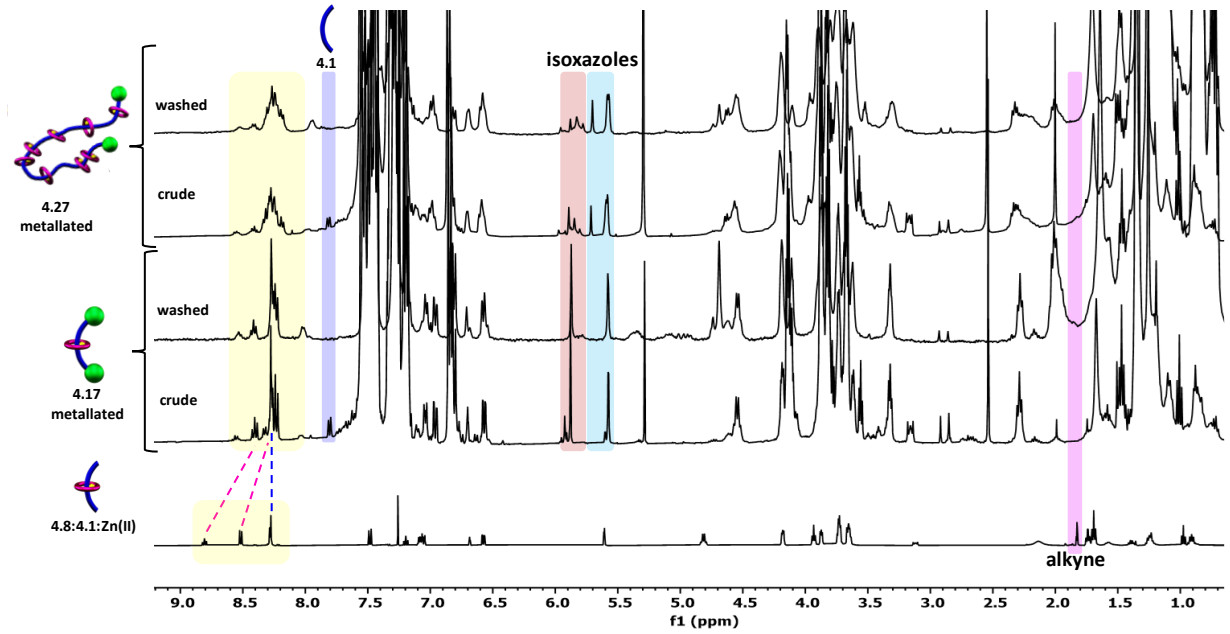

Figure 4.21. ^{1}H-NMR (500 MHz, d_1=5s, 25°C, $CDCl_3$) overlay of pseudo[2]rotaxane **4.8:4.1:Zn(II)** with metallated **4.17** (crude and washed) and metallated Bipy polyrotaxane **4.27** (crude and washed). The alkyne peak is highlighted in purple to show the full disappearance upon stoppering **4.8:4.1:Zn(II)**. The metallated aromatic region is highlighted in yellow, the isoxazole units closer to the stopper in red, and the isoxazoles in the backbone in light blue. The *meta*-pyridyl peaks on free (unbound) Bipy thread **4.1** are highlighted in dark blue.

could solve this issue, perhaps with a different metal ion (i.e., Fe^{2+}) that demetallates under the same conditions as Zn^{2+}.

The demetallated (crude) **4.28** has similar chemical shifts as the demetallated [2]rotaxane **4.17**, suggesting retention of macrocycles on the backbone (Figure 4.22). However, there is also evidence of free **4.8** in the NMR spectrum, so full ring retention was not achieved, likely because of the small stopper size.

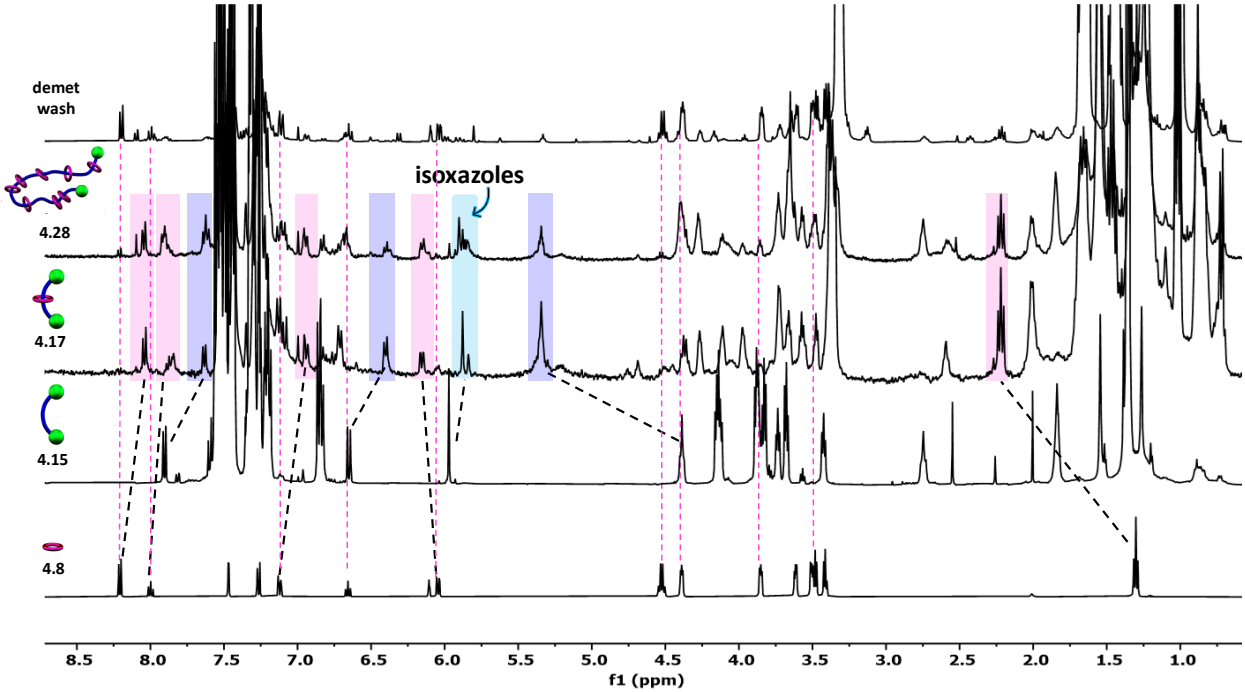

Figure 4.22. ^{1}H-NMR (500 MHz, d_1=5s, 25°C, $CDCl_3$) overlay of the crude demetallated Bipy polyrotaxane **4.28** with the demetallated wash (top spectrum) and indicated components for comparison. The dashed pink lines correspond to free (unbound) macrocycle **4.8,** and the black dashed lines show the expected shift in peaks for the interlocked ring (highlighted in pink) and the Bipy polymer backbone (dark blue). The isoxazoles in the polymer backbone are highlighted in light blue, showing a shift compared to the non-interlocked dumbbell product **4.15**.

GPC traces confirm the formation of a higher molecular weight **4.28** product (black) compared to the stopper (green) and ring (pink) components (Figure 4.23). Evidence of unbound (free) macrocycle **4.8** in the crude **4.28** confirms what was observed in the NMR spectrum. The molecular weight is less than 10,000 g/mol; however, ring slippage is expected based on the

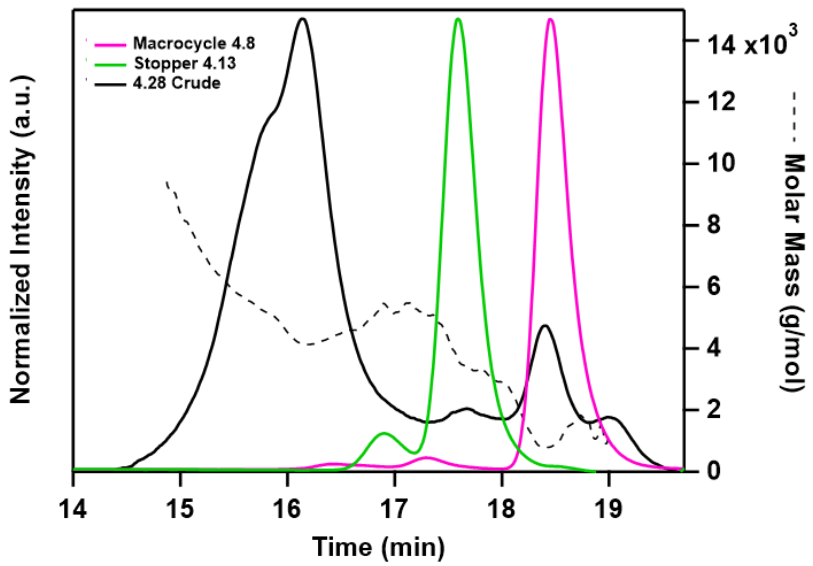

Figure 4.23. GPC (3:1 THF:DMF) of the crude demetallated Bipy polyrotaxane **4.28** (black) with stopper **4.13** (green) and macrocycle **4.8** (pink) for comparison.

metastability of the [2]rotaxane, which accounts for the free macrocycle. The crude **4.28** was precipitated and analyzed via GPC; there was a significant decrease in molecular weight and an increase in **4.8** ~18.5 minutes, indicating ring slippage (Figure 4.24).

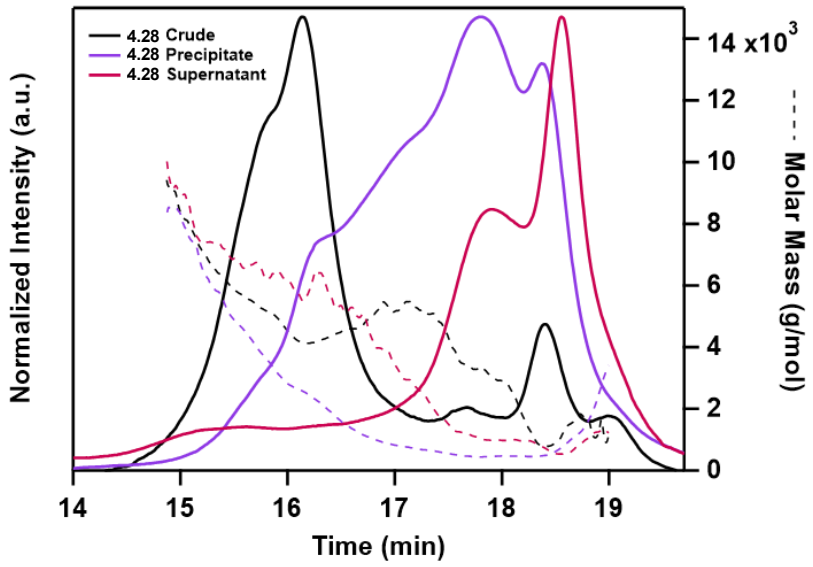

Figure 4.24. GPC (3:1 THF:DMF) of the crude demetallated Bipy polyrotaxane **4.28** (black) and **4.28** precipitate (purple) and **4.28** supernatant (dark red).

4.3 Conclusions

Nitrile-oxide/alkyne cycloaddition (NOAC) provides optimal stoppering conditions for assembling [2]rotaxanes from bis-alkyne P2R and nitrile-oxide stoppers. A series of polyrotaxanes with different ring densities was synthesized by alternating the ratio of thread (**2.2**) and P2R (**4.8:2.2:Zn(II)**); However, there is evidence of unbound macrocycle **4.8** in the NMR spectrum. These Bip-based PRs did not show an interlocked shift in the NMR spectrum. In contrast, the crude Bipy PR **4.28** has similar chemical shifts as the demetallated [2]rotaxane **4.17**, suggesting ring retention along the backbone. The bulkier Bip ligand in **2.2** could slow down or hinder the formation of the desired pseudo[2]rotaxane. In addition to size, the synthesis of rotaxanes relies on the conformation of the stopper and macrocycle that influences the stability of the fully interlocked [2]rotaxane.[2,16] For example, it has been postulated that the efficiency of the threading reaction might decrease due to the flexibility of the macrocyclic component. Thus, the flexible ethylene glycols in **4.8** could adopt a bent (folded) conformation, and larger, more flexible rings should be avoided to ensure the stoppering reaction proceeds with the threaded ring.

This chapter focused on designing a highly variable NOAC polymerization of main-chain polyrotaxanes; altering the ratio of P2R and other components added to the reaction results in polyrotaxanes with varying amounts of rings (Figure 4.25a). This system can also target doubly-threaded SRNs by introducing a pseudo[3]rotaxane into the polymerization to form **1.29** after stoppering and demetallation to remove metal ions from the interlocked network (Figure 4.25b). The protocols developed here are already being implemented in the Rowan Group to form **1.29** using bis-alkyne components and nitrile-oxide stoppers, to be discussed in Chapter 7.

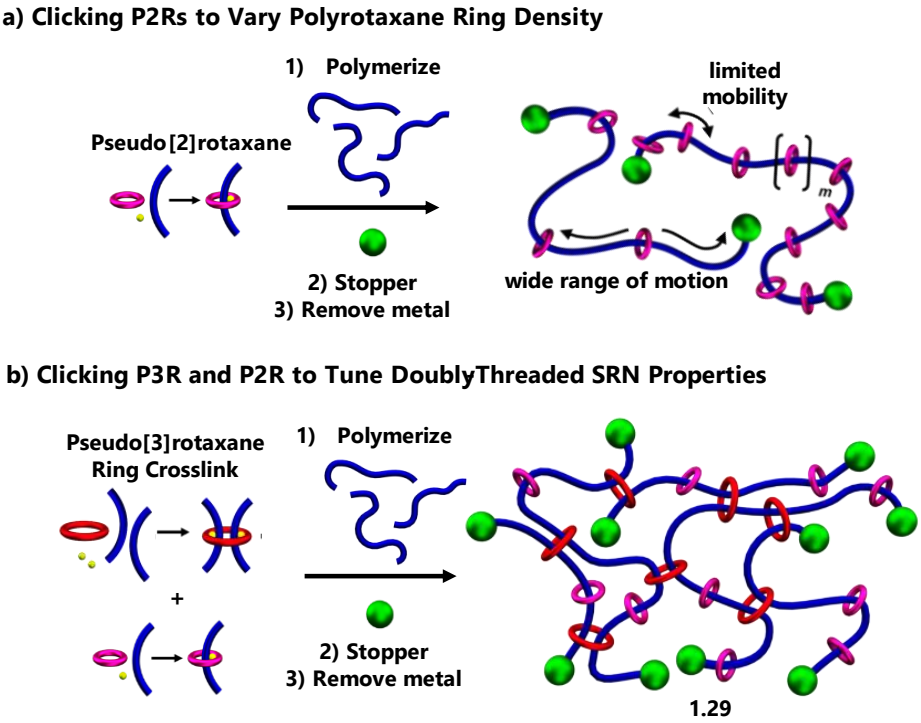

Figure 4.25. Extending NOAC polymerization of P2R to SRN **1.29** with free rings. a) Optimizing the synthesis of main-chain polyrotaxanes from NOAC polymerization of P2Rs will serve as a model for b) synthesizing fully interlocked SRNs with varying amounts of free rings to study the effect of ring density on mechanical properties.

4.4 Experimental

4.4.1 Materials and Methods

All chemicals were purchased from Sigma-Aldrich and used without further purification unless otherwise mentioned. Benzophenone imine was purchased from Oakwood Chemical. Zinc di[bis(trifluoromethylsulfonyl)imide] was purchased from Strem Chemicals and stored in a nitrogen desiccator. Sodium hydride, dry powder, was purchased from Sigma-Aldrich and stored in a nitrogen desiccator. Alkyne-PEG-Alkyne, MW 5K was purchased from Creative PEGWorks and characterized via ^{1}H-NMR and MALDI-TOF to determine a more accurate molecular weight, approximating 7300 g/mol. Solvents for chromatography were purchased from Fisher-Scientific. Deuterated solvents and nitromethane were purchased from ACROS Organics. 1,1-Diphenylnitroethene[13] and 2,6-bisbenzimidazolylpyridine ligands[17] were prepared following literature procedures. Tetrahydrofuran (THF) was dried over sodium and benzophenone. Dichloromethane was distilled over calcium hydride before use. Dimethylformamide (DMF) was dried with activated 4Å molecular sieves before use. All synthesized components were stored in a freezer at -8°C before use.

Matrix Assisted Laser Desorption/Ionization Mass Spectrometry (MALDI-TOF MS) was measured by a Bruker Ultraflextreme MALDI-TOF-TOF spectrometer in linear (or reflectance) mode using dithranol or trans-2-[3-(4-tert-butylphenyl)-2-methyl-2-propenylidene]malononitrile (DCTB) as matrix and sodium trifluoroacetate or silver trifluoroacetate as ionizer (or no ionizer).

Room Temperature Nuclear Magnetic Resonance Spectroscopy was performed using a Bruker Ascend AVANCE III 500 MHz spectrometer, a Bruker AVANCE II+ 500 MHz spectrometer, or a Bruker DRX 400 MHz spectrometer at the University of Chicago NMR

facilities. ^{1}H NMR spectra were referenced to the residual protonated solvent signal and ^{13}C{^{1}H} NMR spectra were referenced to the deuterated solvent carbon resonance signal.

Gel Permeation Chromatography (GPC) measurements were performed using a Shimadzu autosampler, Shimadzu HPLC LC20-AD pump, 2 Agilent PLgel 5 um MIXED-D + guard SEC columns, and a Wyatt Optilab TrEX differential refractive index detector at the University of Chicago Soft Matter Characterization Facility. Measurements were conducted at 25ºC using THF or 3:1 THF:DMF as eluent (flow rate = 1 mL/min).

4.4.2 Synthetic Procedures

4.4.2.1 Synthesis of bis-alkyne Bipy **4.1**

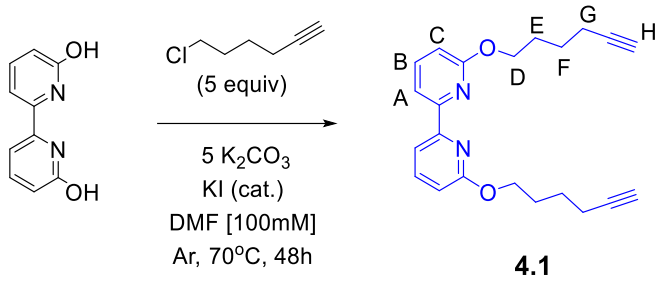

4.1

2,2'-Bipyridine-6,6'-diol (1.0 g, 8.46 mmol), K_2CO_3 (5.85 g, 42.31 mmol), and KI (catalytic amount) were added to a 100 mL round bottom flask under argon. Dry DMF (33.85 mL) was injected, and the flask was placed into a heating block and heated to 70°C. Once the solution reached temperature, 6-chloro-1-hexyne (5.13 mL, 42.31 mmol) was injected dropwise. After 48 hours, the reaction was cooled to room temperature and then precipitated dropwise into cold DI water. The white solid was collected by filtration and subsequently recrystallized in a mixture of chloroform and methanol to yield 6,6'-bis(hex-5-yn-1-yloxy)-2,2'-bipyridine **4.1** in 95% yield by mass. ^{1}H NMR (500 MHz, $CDCl_3$) δ 7.95 (dd, *J* = 7.4, 0.8 Hz, 2H, A), 7.67 (dd, *J* = 8.2, 7.4 Hz, 2H, B), 6.72 (dd, *J* = 8.2, 0.8 Hz, 2H, C), 4.45 (t, *J* = 6.4 Hz, 4H, D), 2.30 (td, *J* = 7.1, 2.7 Hz, 4H, E), 2.00 – 1.91 (m, 6H, G+H), 1.80 – 1.70 (m, 4H, F). ^{13}C NMR (101 MHz, $CDCl_3$) δ 163.31,

153.58, 139.34, 113.66, 111.17, 84.41, 68.67, 65.21, 28.28, 25.38, 18.39. MS (MALDI, positive): *m/z* 347 ([M]).

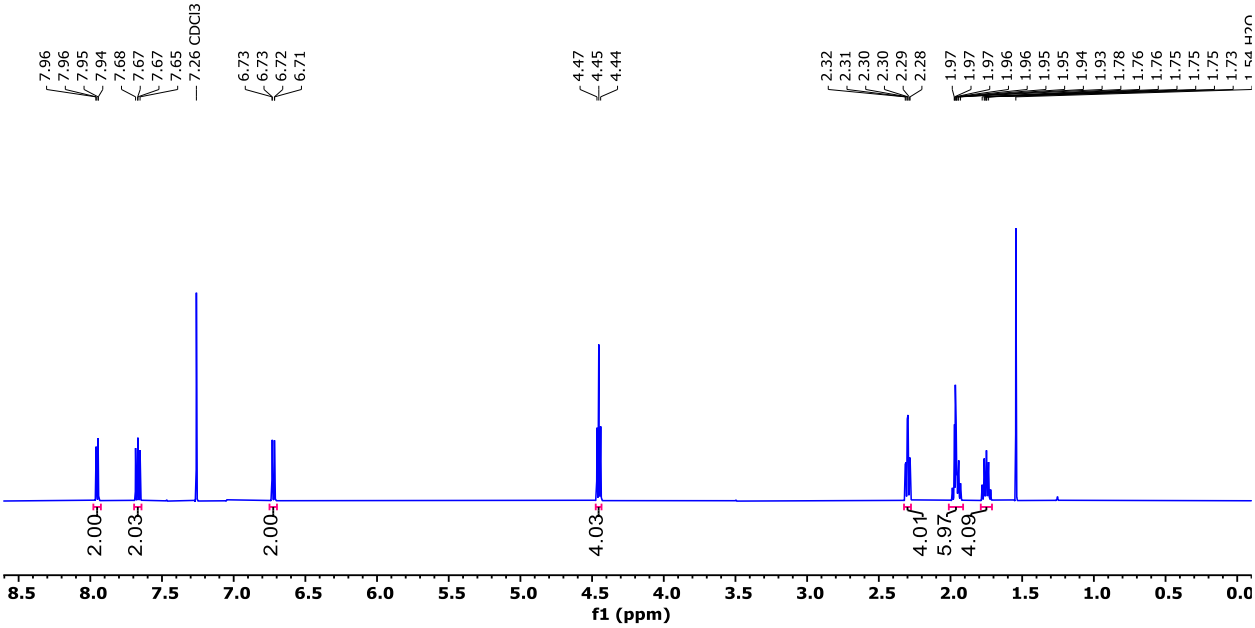

Figure 4.26. ^{1}H-NMR (400 MHz, 25°C, $CDCl_3$) of bis-alkyne Bipy **4.1**.

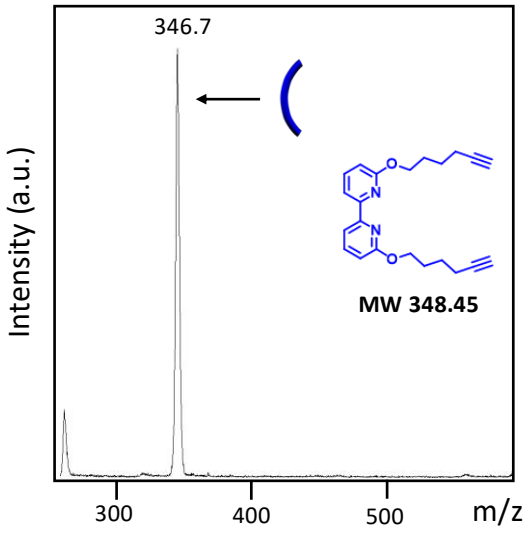

Figure 4.27. MALDI-TOF MS (Dithranol) of bis-alkyne Bipy **4.1**.

4.4.2.2 Synthesis of benzoate 36-atom macrocycle **4.3**

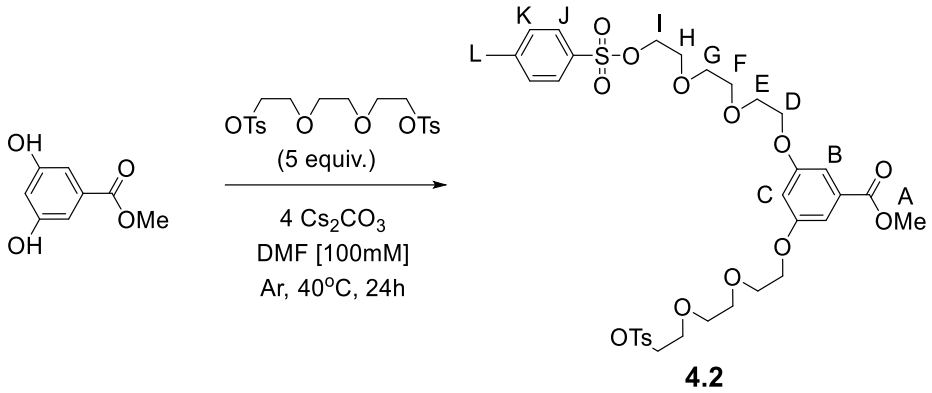

4.2

Triethylene glycol di(*p*-toluenesulfonate) (13.6 g, 29.7 mmol), Cs_2CO_3 (7.75 g, 23.8 mmol), and dry DMF (30 mL) were added to a 250 mL round bottom flask equipped with an addition funnel. The reaction was placed under argon flow and heated at 40°C. Once the solution reached temperature, a solution of methyl 3,5-dihydroxybenzoate (1.0 g, 5.95 mmol) in 30 mL dry DMF was added to the addition funnel and slowly added dropwise. After 24 hours, the reaction was cooled to room temperature and DMF was removed in vacuo. The remaining residue was triturated with chloroform, and the filtrate was collected after vacuum filtration. The solvent was removed in vacuo and the resulting oil was purified using column chromatography (silica gel, 3:1 hexanes:ethyl acetate), resulting in **4.2** as a colorless oil in 55% yield. ^{1}H NMR (500 MHz, $CDCl_3$) δ 7.82 – 7.76 (d, 4H, J), 7.36 – 7.30 (d, 4H, K), 7.18 (d, *J* = 2.3 Hz, 2H, B), 6.68 (t, *J* = 2.3 Hz, 1H, C), 4.17 – 4.14 (m, 4H, I), 4.13 – 4.09 (m, 4H, D), 3.89 (s, 3H, A), 3.84 – 3.78 (m, 4H, H), 3.70 – 3.67 (m, 4H, E), 3.66 – 3.63 (m, 4H, F), 3.62 – 3.58 (m, 4H, G), 2.42 (s, 6H, L).

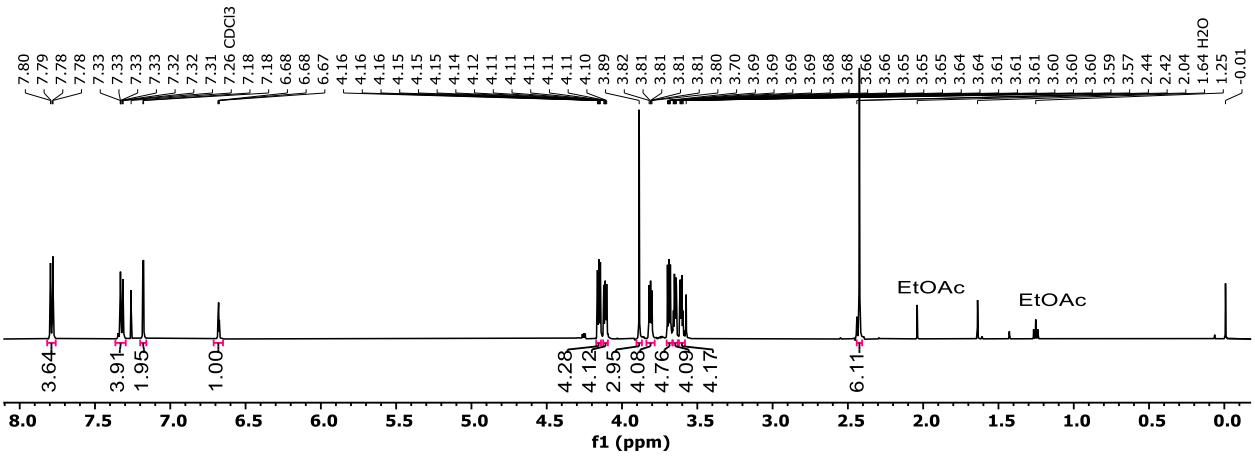

Figure 4.28. ^{1}H-NMR (400 MHz, 25°C, $CDCl_3$) of tosylated benzoate macrocycle precursor **4.2**.

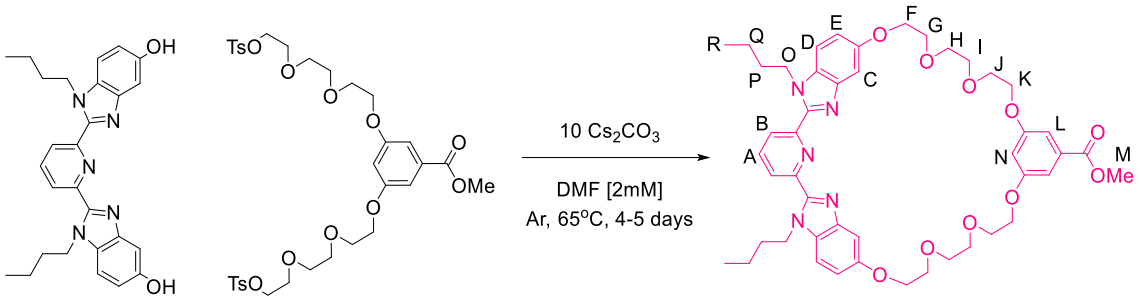

4.2 **4.3**

Macrocycle **4.3** was prepared by adapting a standard crown ether literature procedure.[8] A 500mL dropping funnel containing the ditosylate **4.2** (0.50 g, 0.675 mmol) and butyl non-extended Bip (0.31 g, 0.675 mmol)[17] in 450 mL anhydrous DMF was fitted to a 1L round bottom flask containing Cs_2CO_3 (2.20 g, 6.75 mmol) and stir bar. The reaction vessel was flushed with argon before anhydrous DMF (450 mL) was added by cannula. The reaction was placed into a heating block and heated to 65°C while rapidly stirring to create a suspension of Cs_2CO_3. Once the solution reached temperature, the dissolved mixture of components in the dropping funnel was slowly added dropwise over 3 days. The reaction was allowed to stir at 65°C for four more days, after which the solvent was removed, and the remaining residue triturated with chloroform. After vacuum filtration the filtrate was collected, and solvent removed in vacuo. The resulting oil was purified using column chromatography (triethylamine-treated silica gel, chloroform:methanol

gradient 100:0....97:3), resulting in **4.3** as a clear oil in ~50% yield by mass. ^{1}H NMR (500 MHz, $CDCl_3$) δ 8.08 (d, *J* = 7.8 Hz, 2H, B), 7.92 (t, *J* = 7.4 Hz, 1H, A), 7.48 (d, *J* = 2.3 Hz, 2H, D), 7.25 (d, 2H, E), 7.10 (dd, *J* = 8.8, 2.3 Hz, 2H, C), 6.98 (d, *J* = 2.4 Hz, 2H, L), 6.29 (t, *J* = 2.3 Hz, 1H, N), 4.44 (t, *J* = 7.4 Hz, 4H, O), 4.39 (t, *J* = 4.4 Hz, 4H, F), 3.87 – 3.81 (s, 3H, M), 3.68 (t, *J* = 5.4 Hz, 4H, G), 3.61 (dd, *J* = 6.1, 2.8 Hz, 4H, J), 3.53 (dd, *J* = 5.9, 3.1 Hz, 4H, H), 3.46 (t, *J* = 5.5 Hz, 4H, I), 1.70 – 1.61 (m, 4H, P), 1.10 (p, *J* = 7.4 Hz, 4H, Q), 0.72 (t, *J* = 7.3 Hz, 6H, R). MS (MALDI, positive): *m/z* 875 ([M]+Na^+), 1101 ([M]+Na^++dithranol).

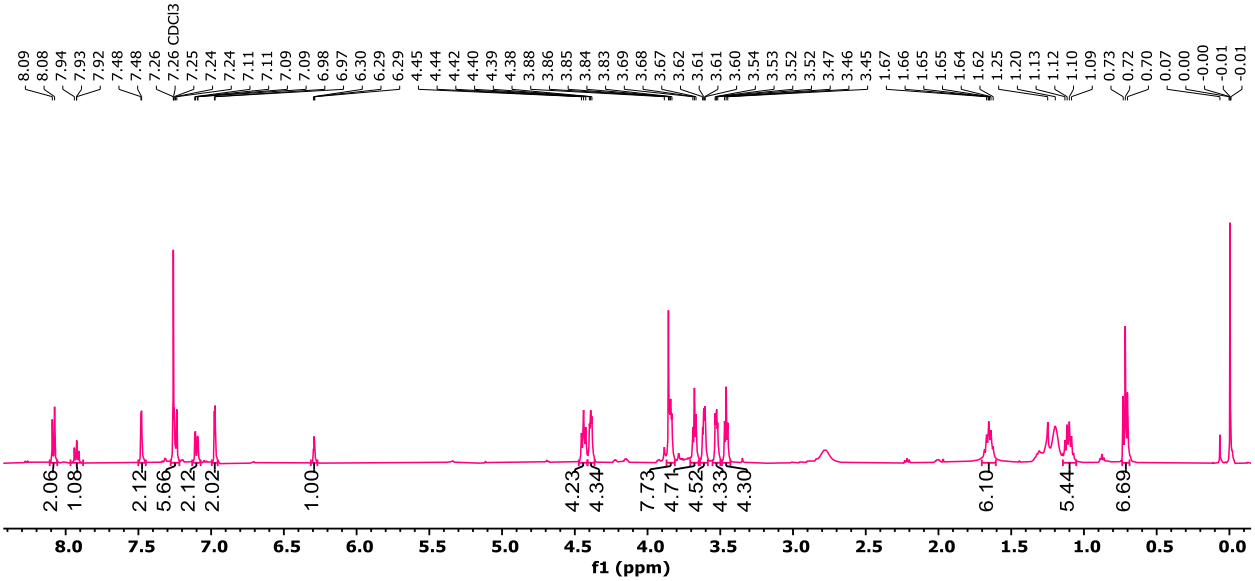

Figure 4.29. ^{1}H-NMR (500 MHz, 25°C, $CDCl_3$) of benzoate 36-atom **4.3**.

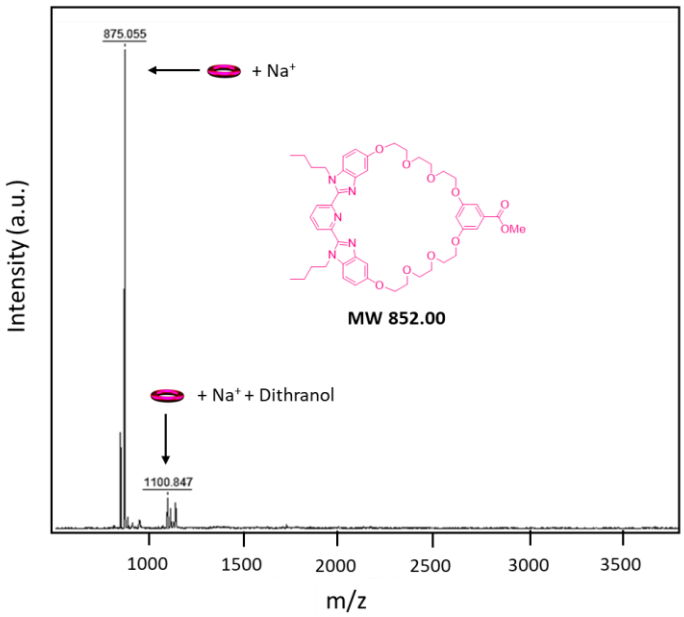

Figure 4.30. MALDI-TOF MS (Dithranol, sodium trifluoroacetate) of benzoate 36-atom **4.3**.

4.4.2.3 Synthesis of benzoate 38-atom macrocycle **4.5**

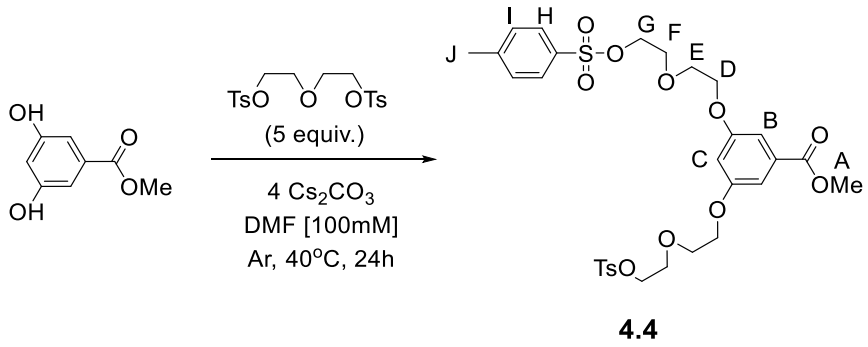

4.4

Diethylene glycol di(p-toluenesulfonate) (8.63 g, 20.8 mmol), Cs2CO3 (5.43 g, 16.7 mmol), and dry DMF (20 mL) were added to a 250 mL round bottom flask equipped with an addition funnel. The reaction was placed under argon flow and heated at 40°C. Once the solution reached temperature, a solution of methyl 3,5-dihydroxybenzoate (0.7 g, 4.16 mmol) in 20 mL dry DMF was added to the addition funnel and slowly added dropwise. After 24 hours, the reaction was cooled to room temperature and DMF was removed in vacuo. The remaining residue was triturated with chloroform, and after vacuum filtration, the filtrate was collected. The solvent was removed in vacuo and the resulting oil was purified using column chromatography (silica gel, hexanes:ethyl

acetate) resulting in **4.4** as a colorless oil in 55% yield. 1H NMR (500 MHz, CDCl3) δ 7.80 – 7.73 (m, 4H, H), 7.35 – 7.27 (m, 4H, I), 7.15 (d, J = 2.3 Hz, 2H, B), 6.63 (t, J = 2.3 Hz, 1H, C), 4.18 – 4.15 (m, 4H, G), 4.05 – 4.01 (m, 4H, D), 3.88 (s, 3H, A), 3.78 – 3.71 (m, 8H, F+E), 2.38 (s, 6H, J).

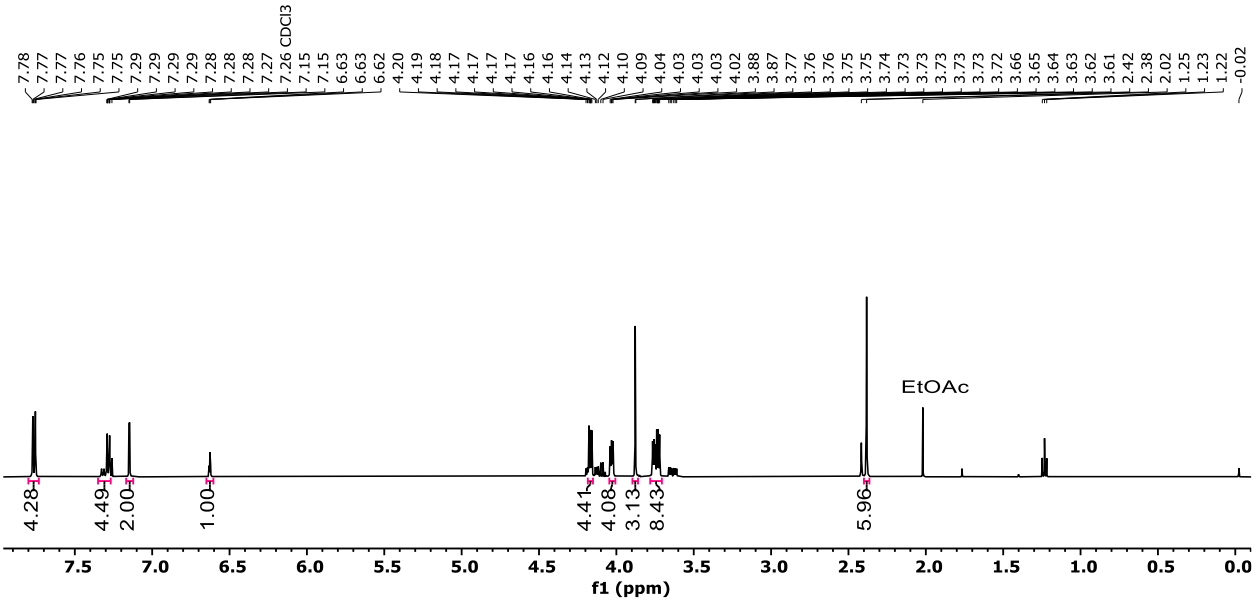

Figure 4.31. ^{1}H-NMR (400 MHz, 25°C, $CDCl_3$) of ditosylate **4.4**.

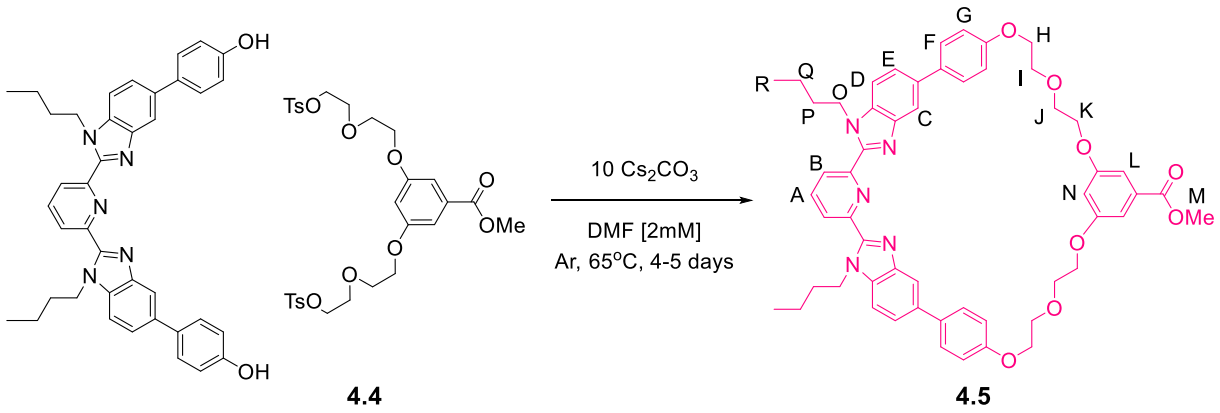

Macrocycle **4.5** was prepared by adapting a standard crown ether literature procedure.[8] A 500mL dropping funnel containing the ditosylate **4.4** (0.71 g, 1.09 mmol) and Butyl Bip (0.66 g, 1.09 mmol)[17] in 450 mL anhydrous DMF was fitted to a 1L round bottom flask containing Cs_2CO_3 (3.54 g, 10.9 mmol) and stir bar. The reaction vessel was flushed with argon before anhydrous

DMF (450 mL) was added by cannula. The reaction was placed into a heating block and heated to 65°C while rapidly stirring to create a suspension of Cs_2CO_3. Once the solution reached temperature, the dissolved mixture of components in the dropping funnel was slowly added dropwise over 3 days. The reaction was allowed to stir at 65°C for four more days, after which the solvent was removed, and the remaining residue was triturated with chloroform. After vacuum filtration, the filtrate was collected, and the solvent was removed in vacuo. The resulting oil was purified using column chromatography (triethylamine-treated silica gel, chloroform:methanol gradient 100:0....97:3), resulting in a mixture of products that was analyzed by NMR and MALDI-TOF (Figures 4.29 – 4.31).

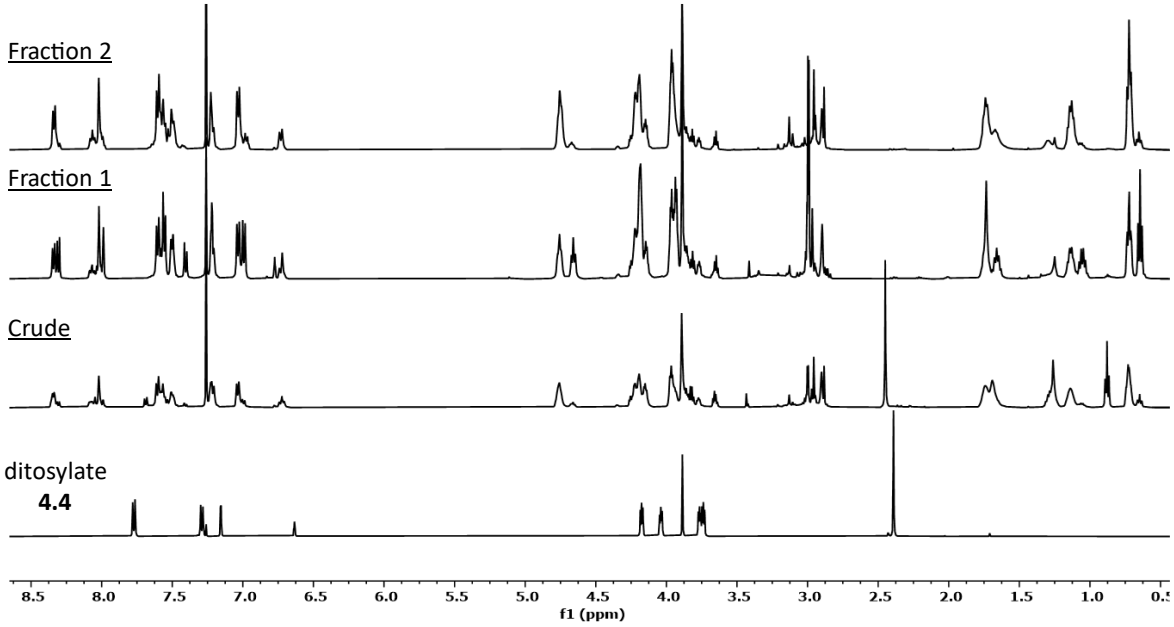

Figure 4.32. ^{1}H-NMR (500 MHz, 25°C, $CDCl_3$) analysis of benzoate 38-atom **4.5** product mixture.

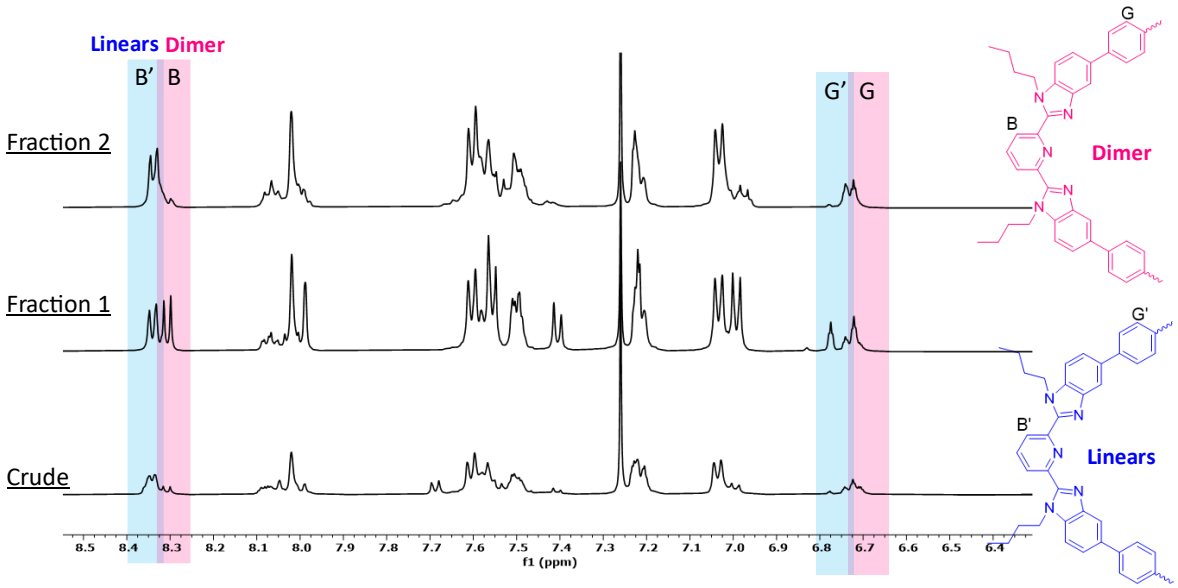

Figure 4.33. ^{1}H-NMR (500 MHz, 25°C, $CDCl_3$) analysis of benzoate 38-atom **4.5** linear and dimer products.

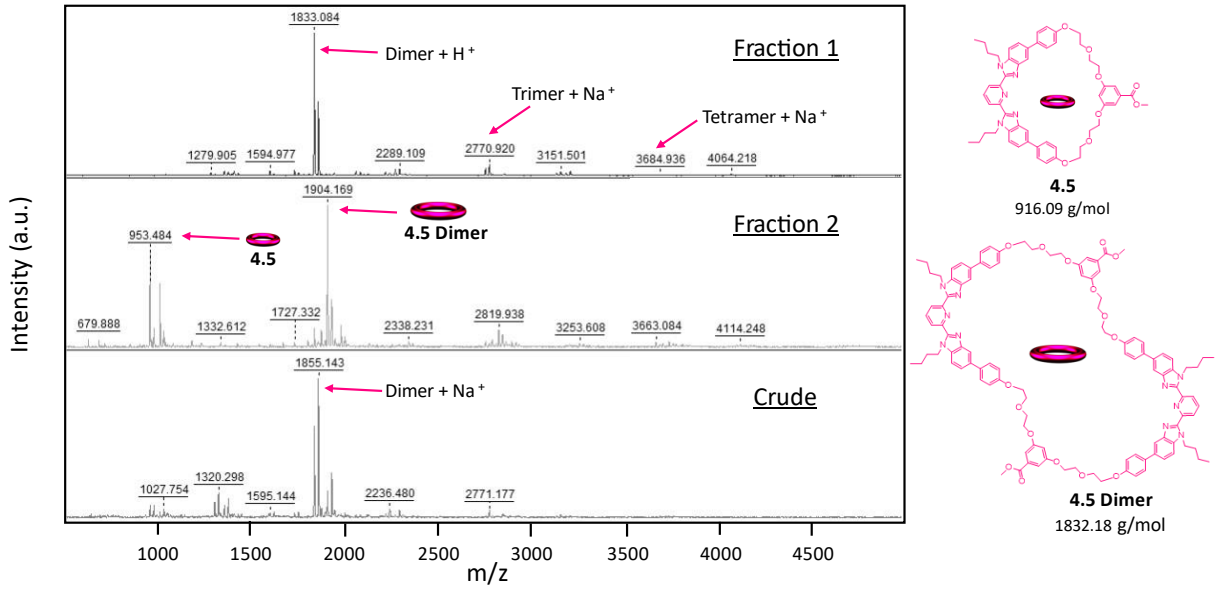

Figure 4.34. MALDI-TOF MS (Dithranol, sodium trifluoroacetate) analysis of **4.5** product mixture.

4.4.2.4 Synthesis of 36-atom macrocycle **4.8**

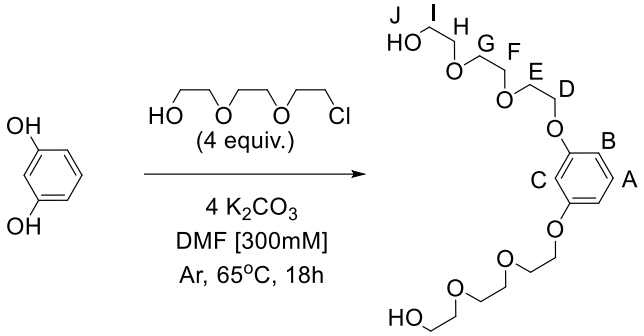

4.6

Resorcinol (5.0 g, 45.41 mmol) and K_2CO_3 (25.1 g, 181.64 mmol) were added to a 250 mL round bottom flask under argon. Anhydrous DMF (151 mL) was added, and the flask was placed into a heating block at 70°C. Once the solution reached temperature, 2-[2-(2-Chloroethoxy)ethoxy]ethanol (26.4 mL, 181.64 mmol) was injected dropwise. After 18 hours, the reaction was cooled to room temperature and DMF was removed in vacuo. The resulting material was dissolved in DCM and washed with DI-water/brine three times. The organic layer was isolated and dried over magnesium sulfate, and then the solvent was removed under vacuum. The remaining pale-yellow oil was purified using column chromatography (silica gel, chloroform:methanol gradient 100:0….) resulting in **4.6** as a colorless oil in 60% yield. ^{1}H NMR (400 MHz, $CDCl_3$) δ 7.20 – 7.11 (m, 1H, A), 6.56 – 6.48 (m, 3H, C, B), 4.19 – 4.08 (m, 4H, D), 3.95 – 3.79 (m, 4H, I), 3.77 – 3.64 (m, 12H, E, H, F), 3.64 – 3.58 (m, 4H, G), 2.61 (tb, 2H, J).

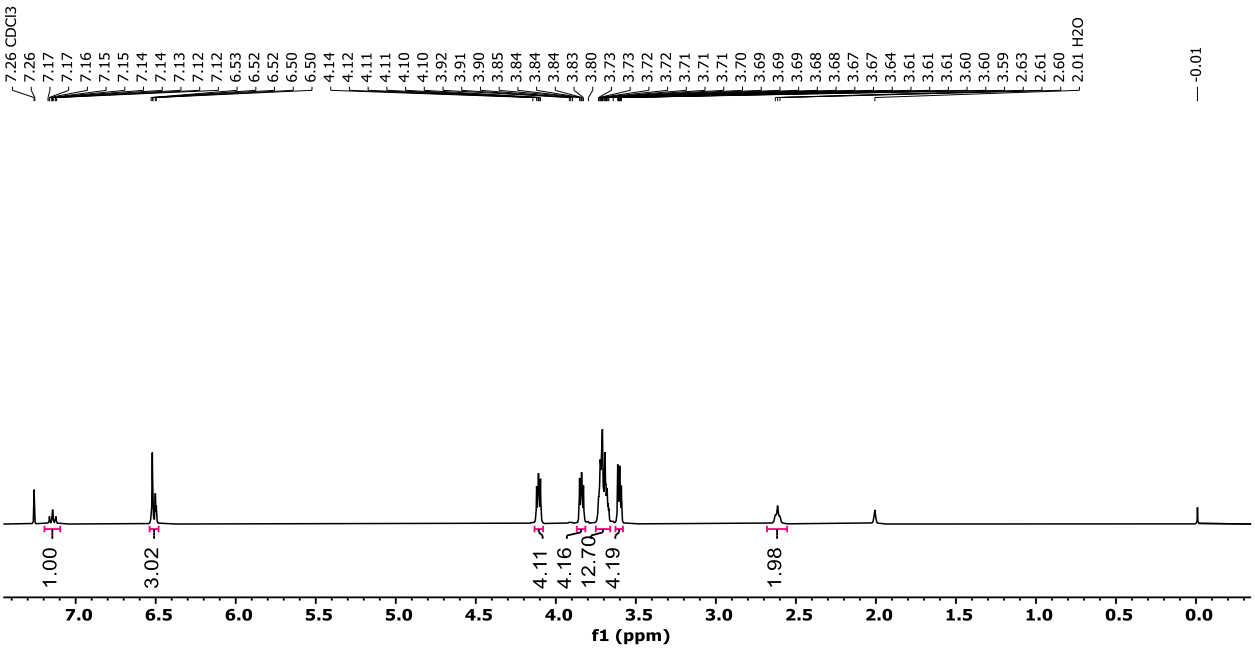

Figure 4.35. ^{1}H-NMR (400 MHz, 25°C, $CDCl_3$) of dihydroxy macrocycle precursor **4.6**.

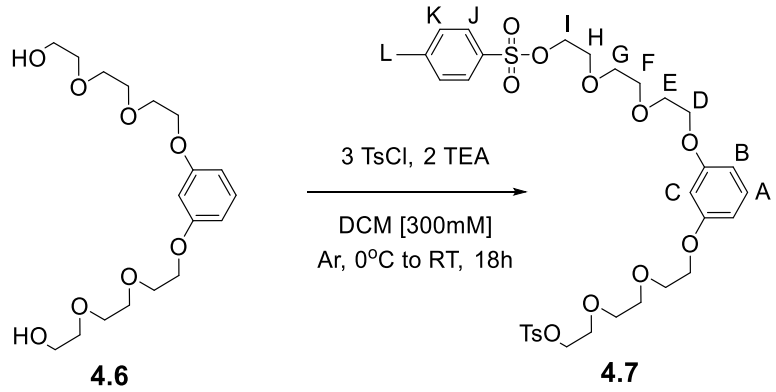

4.6 **4.7**

The dihydroxy precursor **4.6** (5.50 g, 14.68 mmol), *p*-toluenesulfonyl chloride (8.39 g, 44.03 mmol) were added to a 100mL oven-dried round bottom flask and put under argon. Anhydrous DCM (45 mL) was injected, and the reaction was placed into a 0°C ice bath. Triethylamine (3.12 g, 30.82 mmol) was added dropwise, and after 1 hour, the ice bath was removed to allow the reaction to reach room temperature. After 18 hours, the DCM was removed under vacuum, and the resulting residue dissolved in ethyl acetate and then filtered. The filtrate was collected, the solvent removed in vacuo, and purified using column chromatography (silica gel, 3:1 hexanes:ethyl acetate) to afford **4.7** as a colorless oil in 80% yield by mass. ^{1}H NMR (400 MHz,

$CDCl_3$) δ 7.81 – 7.74 (d, 4H, J), 7.35 – 7.28 (d, 4H, K), 7.13 (t, 1H, A), 6.53 – 6.45 (m, 3H, C+B), 4.18 – 4.12 (m, 4H, I), 4.09 – 4.03 (m, 4H, D), 3.82 – 3.75 (m, 4H, H), 3.70 – 3.65 (m, 4H, E), 3.65 – 3.61 (m, 4H, F), 3.61 – 3.56 (m, 4H, G), 2.41 (s, 6H, L). ^{13}C NMR (101 MHz, $CDCl_3$) δ 166.34, 151.21, 139.38, 136.22, 134.35, 113.46, 108.14, 83.80, 83.48, 83.16, 77.16, 77.12, 76.13, 75.67, 75.10, 73.77, 66.76, 59.87, 28.01, 27.43, 20.59. MS (MALDI, positive): *m/z* 705.0 ($[M]+Na^+$).

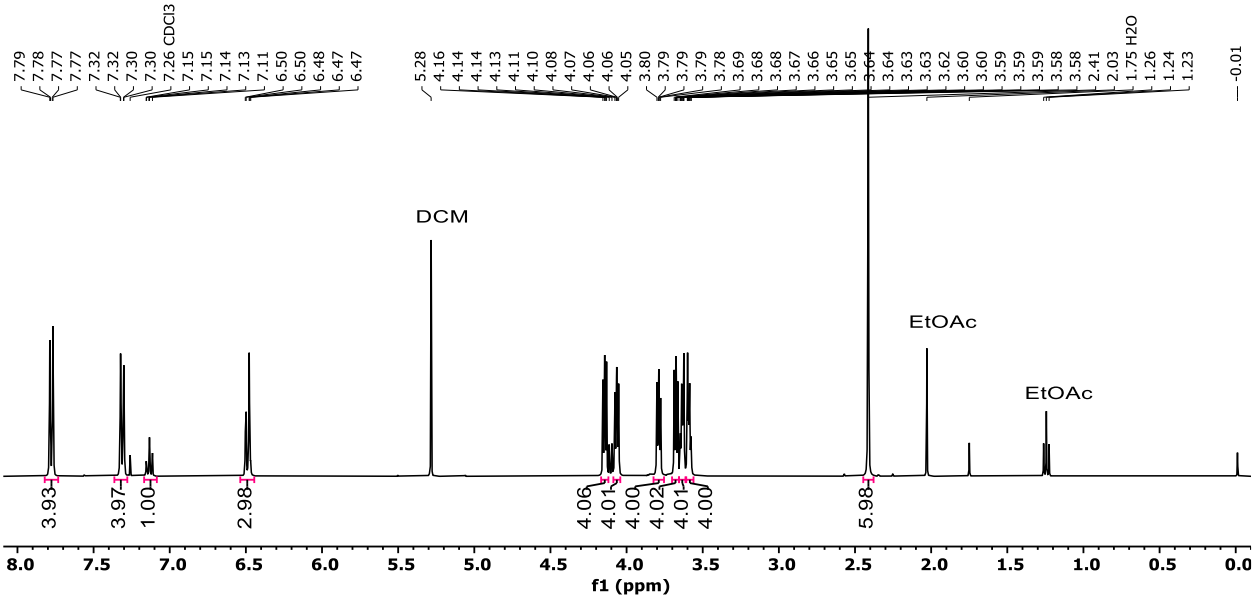

Figure 4.36. ^{1}H-NMR (400 MHz, 25°C, $CDCl_3$) of ditosylate **4.7**. Solvent peaks are still visible in the spectrum; this product was dried further under high vacuum before further use.

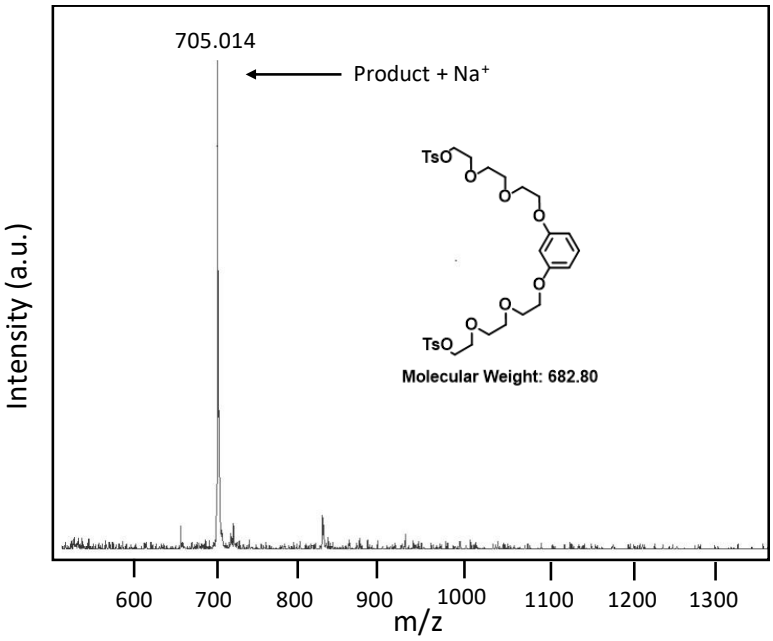

Figure 4.37. MALDI-TOF MS (Dithranol, sodium trifluoroacetate) of ditosylate **4.7**.

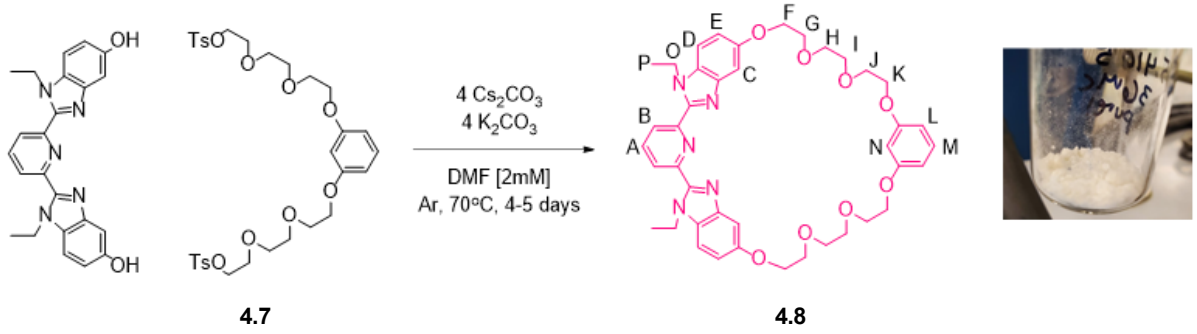

4.7 **4.8**

Macrocycle **4.8** was prepared by adapting a standard crown ether literature procedure.[8] A 500mL dropping funnel containing the ditosylate **4.7** (1.71g, 2.50 mmol) and ethyl non-extended Bip (1.00, 2.50mmol)[17] in 450 mL anhydrous DMF was fitted to a 1L round bottom flask containing Cs_2CO_3 (3.26g, 10.01 mmol) and K_2CO_3 (1.38g, 10.01 mmol) and stir bar. The reaction vessel was flushed with argon before anhydrous DMF (450 mL) was added by cannula. The reaction was placed into a heating block and heated to 70°C while rapidly stirring to create a suspension of Cs_2CO_3 and K_2CO_3. Once the solution reached temperature, the dissolved mixture of components in the dropping funnel was slowly added dropwise over the course of 3 days. After complete addition of components, the final concentration of the reaction was 2.65mM. The reaction was

allowed to stir at 70°C for four more days, after which the solvent was removed, and the remaining residue triturated with chloroform. After vacuum filtration the filtrate was collected, and solvent removed in vacuo. The resulting oil was purified using column chromatography (triethylamine-treated silica gel, chloroform:methanol gradient 100:0....97:3) and slow diffusion crystallization from methanol into diethyl ether, producing **4.8** as fluffy white crystals in ~50% yield by mass. ^{1}H NMR (500 MHz, $CDCl_3$) δ 8.21 (d, *J* = 7.8 Hz, 2H, B), 8.00 (t, *J* = 7.9 Hz, 1H, A), 7.48 (d, *J* = 2.3 Hz, 2H, D), 7.27 (d, *J* = 8.8 Hz, 2H, E), 7.13 (dd, *J* = 8.9, 2.3 Hz, 2H, C), 6.66 (t, *J* = 8.2 Hz, 1H, M), 6.11 (t, *J* = 2.4 Hz, 1H, N), 6.05 (dd, *J* = 8.2, 2.4 Hz, 2H, L), 4.53 (q, *J* = 7.2 Hz, 4H, O), 4.42 – 4.37 (m, 4H, F), 3.88 – 3.83 (m, 4H, K), 3.65 – 3.59 (m, 4H, G), 3.54 – 3.46 (m, 8H, J+H), 3.42 (t, *J* = 5.4 Hz, 4H, I), 1.31 (t, *J* = 7.2 Hz, 6H, P). ^{13}C NMR (101 MHz, $CDCl_3$) δ 159.67, 155.62, 150.27, 150.13, 143.59, 137.88, 130.93, 129.81, 124.81, 115.59, 110.41, 105.83, 105.59, 102.56, 77.36, 71.20, 70.99, 70.56, 69.53, 68.98, 66.63, 39.91, 30.08, 15.57. MS (MALDI, positive): *m/z* 738.5 ([M]+H^+).

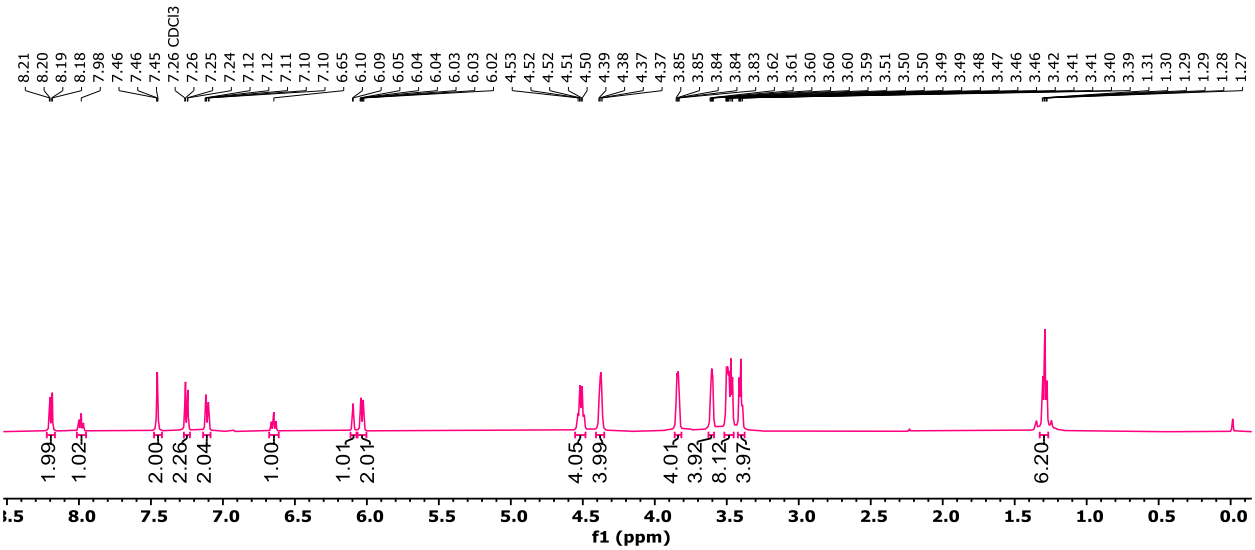

Figure 4.38. ^{1}H-NMR (500 MHz, 25°C, $CDCl_3$) of 36-atom macrocycle **4.8**.

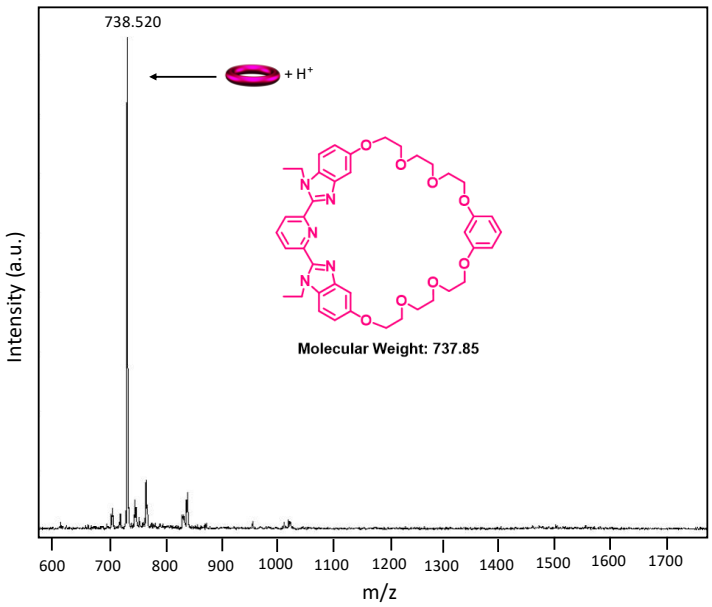

Figure 4.39. MALDI-TOF MS (Dithranol) of 36-atom macrocycle **4.8**.

4.4.2.5 Synthesis of Nitrile-Oxide Stopper Group **4.13**

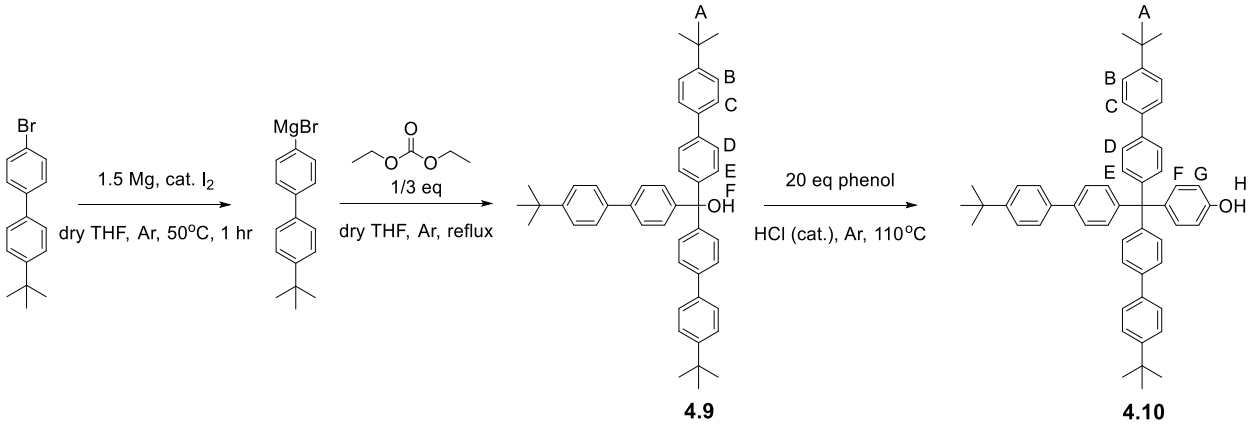

Phenol stopper **4.10** was synthesized from the literature procedure.[15] A 3-neck 500mL round bottom flask equipped with a 250 mL addition funnel and condenser was charged with Mg turnings (1.68 g, 69.2 mmol) and flame-dried under vacuum. The flask was put under argon and I_2 (15 mg) and 30 mL dry THF was added resulting in a brown color. The mixture was heated to 50°C. A solution of 4-bromo-4'-tert-butylbiphenyl (10 g, 34.6 mmol) in 50 mL THF was cannulated into the addition funnel and then added dropwise over 30 min which turned the reaction colorless. The reaction refluxed for another 90 minutes after which it was cooled to RT. A solution of diethyl

carbonate (1.24 g, 1.2 mL, 10.5 mmol) in 2 mL THF was added dropwise, turning the solution green in color, and the reaction was refluxed overnight. The dark green solution was cooled to RT the next day and quenched with 1M HCl. The resulting yellow mixture was filtered, and then hexanes and water were added to the filtrate. The organic layer was washed with brine, dried over magnesium sulfate, and concentrated in vacuo to give an off-white solid. This solid was boiled in hexanes overnight and filtered to yield the Grignard product **4.9** as a white powder in 75% yield by mass. ^{1}H NMR (500 MHz, $CDCl_3$) δ 7.60 – 7.53 (m, 12H), 7.48 – 7.45 (m, 6H), 7.44 – 7.40 (m, 6H), 1.37 (s, 27H). ^{13}C NMR (101 MHz, $CDCl_3$) δ 150.47, 145.70, 140.10, 137.86, 128.46, 126.87, 126.69, 125.86, 81.88, 34.68, 31.52. MALDI-TOF MS: 679.6 ([M]+Na^+) and 639.7 ([M] – OH^-).

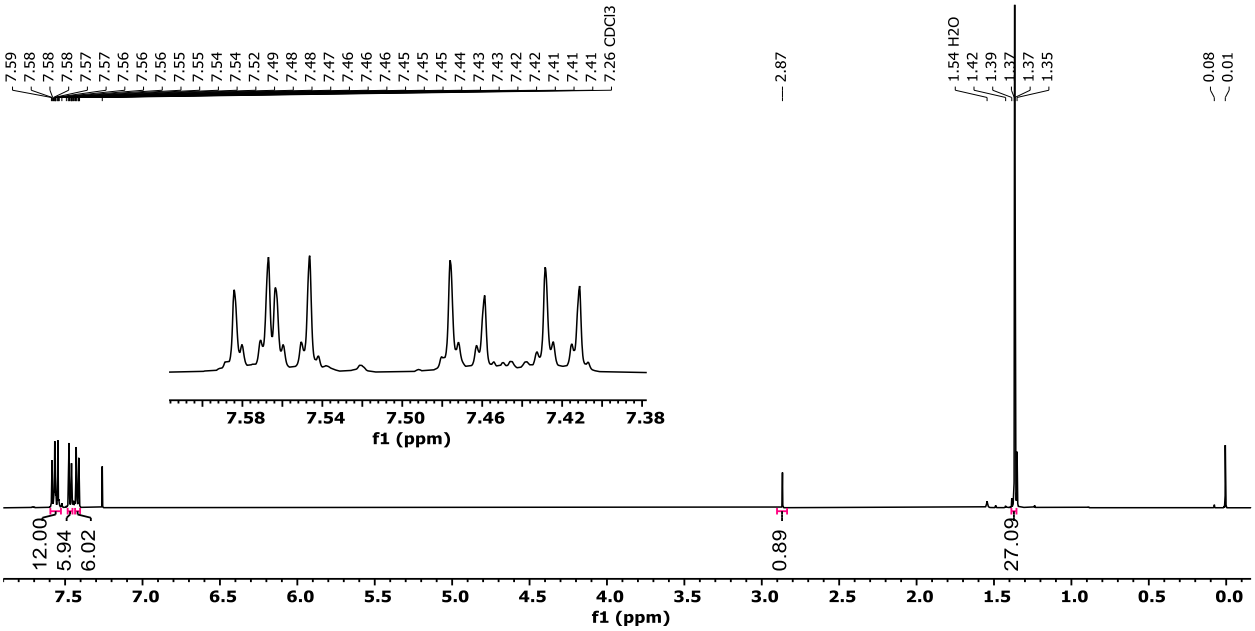

Figure 4.40. ^{1}H-NMR (500 MHz, 25°C, $CDCl_3$) of Grignard product **4.9**.

An oven-dried 50 mL round bottom flask equipped with a condenser was charged with **4.9** (5 g, 6.8 mmol) and put under argon. Phenol (20 mL of an 89% phenol solution in water) and 2 mL of conc. HCl was added. The reaction was heated to 110°C overnight. The reaction was cooled to RT the next day and diluted with 250 mL of toluene. The solution was washed with 1M NaOH until the aqueous layer was colorless and the organic layer was concentrated in vacuo. The resulting

orange solid was boiled in hexanes overnight and filtered, leaving phenol stopper **4.10** as a white powder in 83% yield by mass. ^{1}H NMR (400 MHz, $CDCl_3$) δ 7.55 (d, *J* = 8.4 Hz, 6H, B), 7.51 (d, *J* = 8.5 Hz, 6H, C), 7.45 (d, *J* = 8.4 Hz, 6H, D), 7.32 (d, *J* = 8.5 Hz, 6H, E), 7.18 (d, *J* = 8.8 Hz, 2H, F), 6.77 (d, *J* = 8.8 Hz, 2H, G), 4.66 (s, 1H, H), 1.36 (s, 27H, A).^{13}C NMR (101 MHz, $CDCl_3$) δ 153.56, 150.17, 145.78, 139.24, 138.39, 137.70, 132.46, 131.44, 126.59, 125.93, 125.68, 114.32, 63.64, 34.67, 31.36. MALDI-TOF MS: 841.1 ([M]+Ag^+).

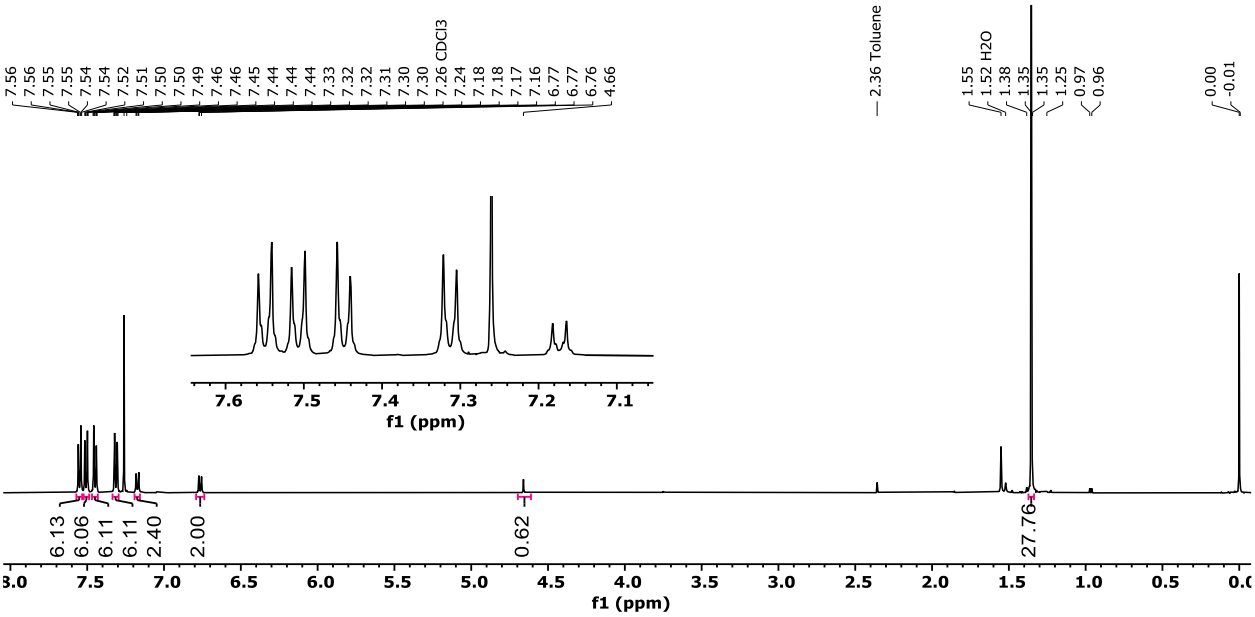

Figure 4.41. ^{1}H-NMR (400 MHz, 25°C, $CDCl_3$) of phenol stopper **4.10**.

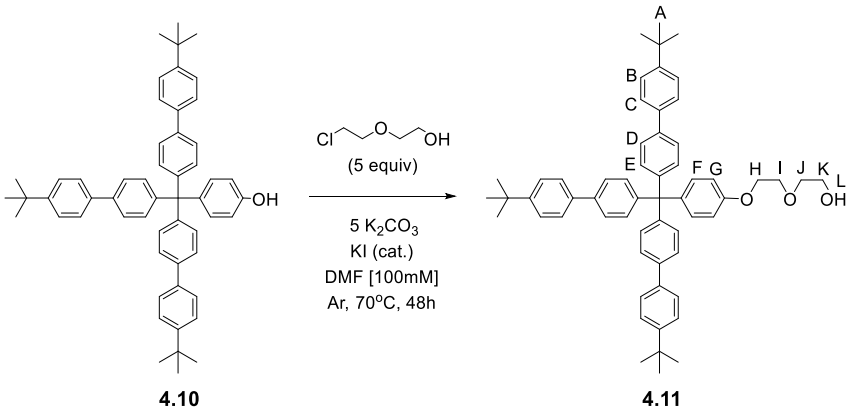

Phenol stopper **4.10** (2.0 g, 2.73 mmol),[17] K_2CO_3 (1.13 g, 8.18 mmol), and KI (catalytic amount) were added to a 100 mL round bottom flask under argon. Dry DMF (27.3 mL) was injected, and

the flask was placed into a heating block and heated to 70°C. Once the solution reached temperature, 2-(2-chloroethoxy)ethanol (0.87 mL, 8.18 mmol) was injected dropwise. After 48 hours, the reaction was cooled to room temperature, after which the solvent was removed, and the remaining residue was triturated with chloroform. After vacuum filtration, the filtrate was collected, and the solvent was removed under vacuum. The remaining white solid was recrystallized in a mixture of hexanes and chloroform to yield the desired stopper **4.11** as fluffy white crystals in 95% yield by mass. ^{1}H NMR (500 MHz, $CDCl_3$) δ 7.55 (d, *J* = 8.6 Hz, 6H, B), 7.51 (d, *J* = 8.5 Hz, 6H, C), 7.45 (d, *J* = 8.5 Hz, 6H, D), 7.35 – 7.28 (m, 6H, E), 7.25 – 7.18 (m, 2H, F), 6.88 – 6.82 (m, 2H, G), 4.17 – 4.12 (m, 2H, H), 3.90 – 3.85 (m, 2H, K), 3.80 – 3.73 (m, 2H, I), 3.71 – 3.65 (m, 2H, J), 2.13 (t, *J* = 6.2 Hz, 1H, L), 1.36 (s, 27H, A). ^{13}C NMR (101 MHz, $CDCl_3$) δ 156.81, 150.28, 145.90, 139.50, 138.52, 137.82, 132.39, 131.57, 126.72, 126.06, 125.80, 113.56, 72.68, 69.84, 67.40, 63.78, 61.94, 34.65, 31.50. MALDI-MS: 928.2 ([M]-H^++Ag^+), 1035.1 ([M]-H^++2Ag^+).

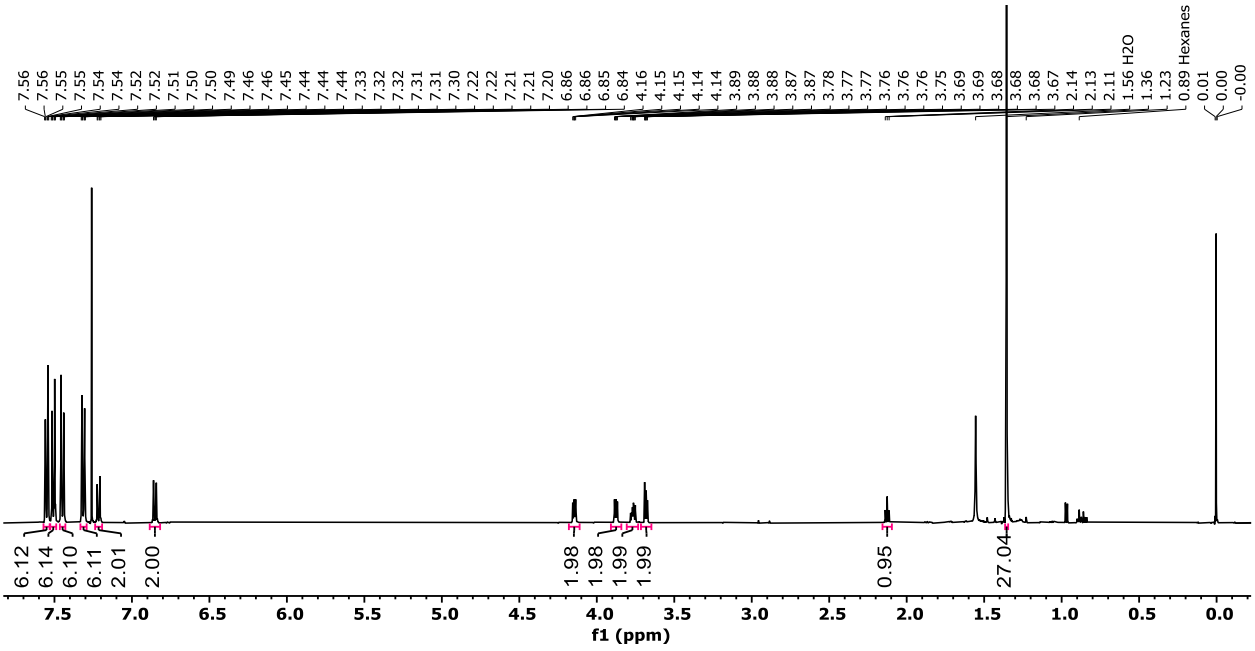

Figure 4.42. ^{1}H-NMR (400 MHz, 25°C, $CDCl_3$) of hydroxy stopper **4.11**.

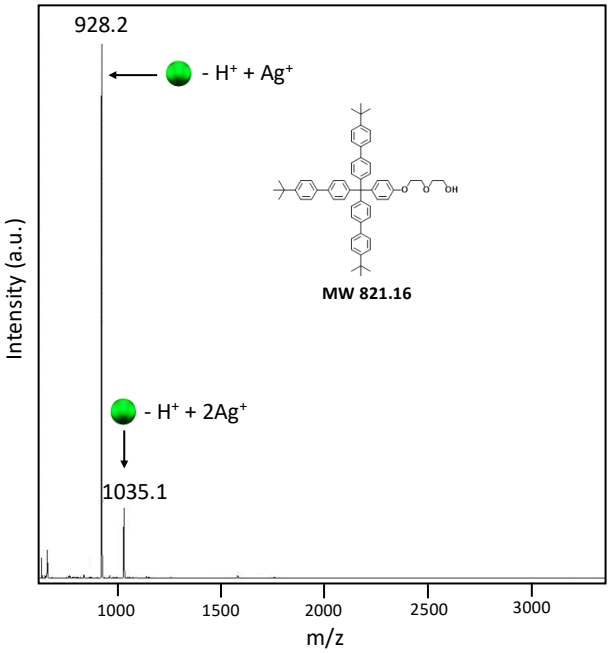

Figure 4.43. MALDI-TOF MS (Dithranol, silver trifluoroacetate) of hydroxy stopper **4.11**.

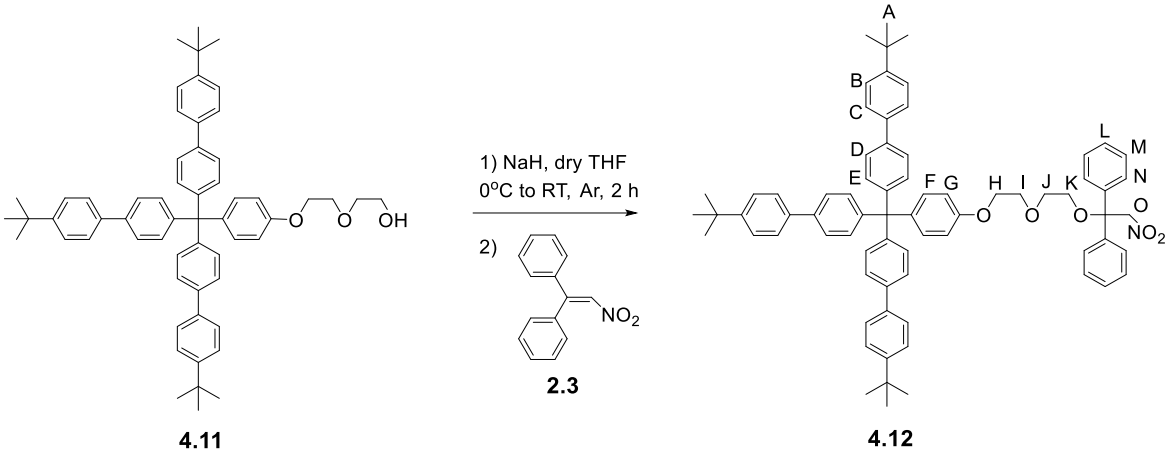

Based on the lit procedure.[11] All glassware was dried in the oven at 130°C overnight and then flame-dried under vacuum before use. Sodium hydride powder (0.071 g, 2.96 mmol) was weighed out and added immediately to a round bottom flask under argon. Anhydrous THF (1 mL) was injected and then the flask was placed in a 0°C ice bath. A solution of **4.11** (0.45 g, 0.55 mmol) in anhydrous THF (3 mL) was added dropwise. After one hour, the ice bath was removed, and the reaction mixture was stirred for one more hour at room temperature. A solution of 1,1-diphenylnitroethene (0.247 g, 1.10 mmol) in 1 mL anhydrous THF was then added dropwise at

room temperature. After 18 hours, the reaction was cooled to 0°C with an ice bath and then quenched with acetic acid. The mixture was diluted with DCM and washed three times with 1.0 M HCl and brine. The organic layer was collected and dried over magnesium sulfate, and the solvent was removed under vacuum. The resulting material was purified using column chromatography (silica gel, hexanes to ethyl acetate gradient) and recrystallized in a mixture of hexanes and chloroform to yield **4.12** as white crystals in 60% yield by mass. ^{1}H NMR (400 MHz, $CDCl_3$) δ 7.55 (dd, *J* = 18.1, 8.5 Hz, 12H, B, C), 7.47 (d, *J* = 8.4 Hz, 6H, D), 7.38 – 7.27 (m, 16H, E, L, M, N), 7.25 – 7.20 (m, 2H, F), 6.91 – 6.82 (m, 2H, G), 5.33 (s, 1H, O), 4.15 (dd, *J* = 5.7, 3.8 Hz, 2H, H), 3.90 (dd, *J* = 5.7, 3.8 Hz, 2H, K), 3.81 (t, *J* = 5.2 Hz, 2H, I), 3.56 (t, *J* = 5.2 Hz, 2H, J), 1.38 (s, 27H, A). ^{13}C NMR (101 MHz, $CDCl_3$) δ 156.99, 150.26, 145.96, 141.15, 139.27, 138.48, 137.82, 132.32, 131.58, 128.55, 128.23, 126.88, 126.72, 126.04, 125.80, 113.62, 81.82, 80.19, 70.36, 69.94, 67.54, 63.77, 63.12, 34.63, 31.50. MS (MALDI, positive): *m/z* 1154.2 ($[M]+Ag^+$).

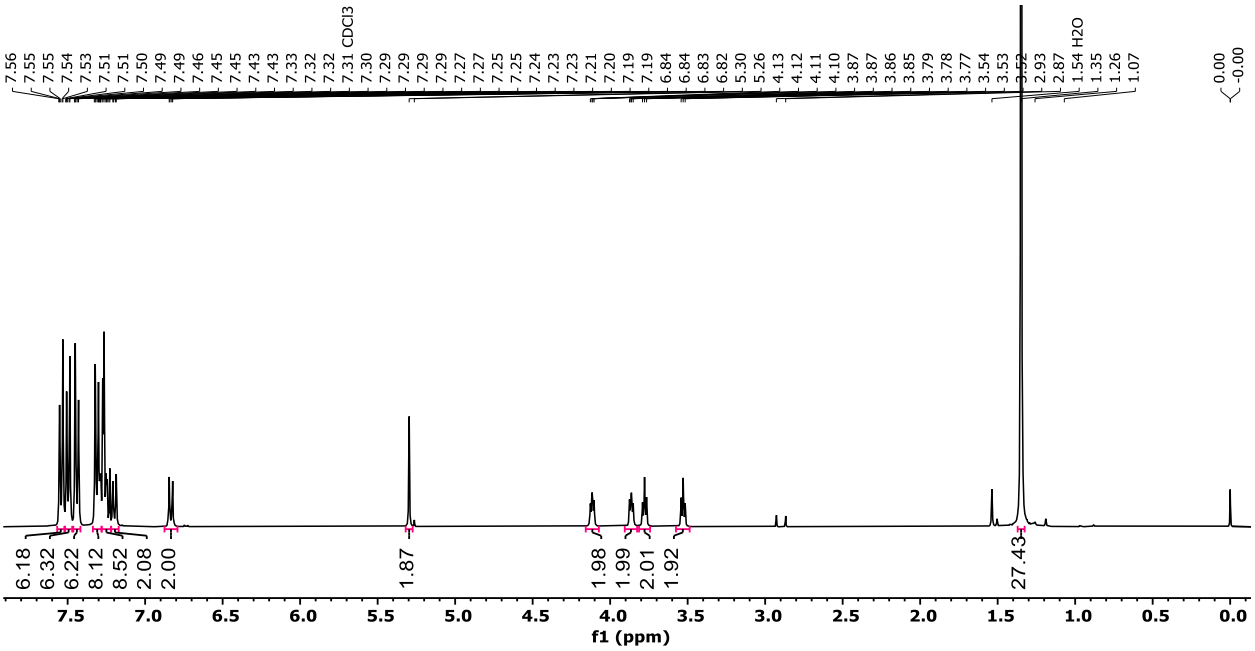

Figure 4.44. ^{1}H-NMR (400 MHz, 25°C, $CDCl_3$) of nitro stopper **4.12**.

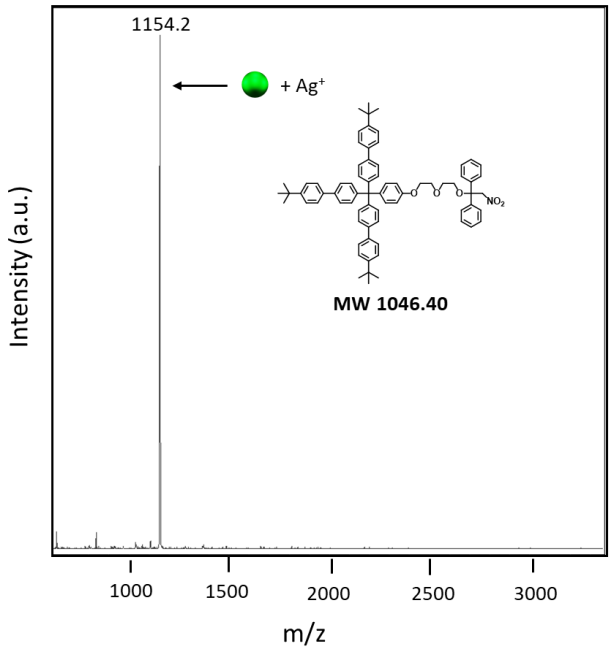

Figure 4.45. MALDI-TOF MS (Dithranol, silver trifluoroacetate) of nitro stopper **4.12**.

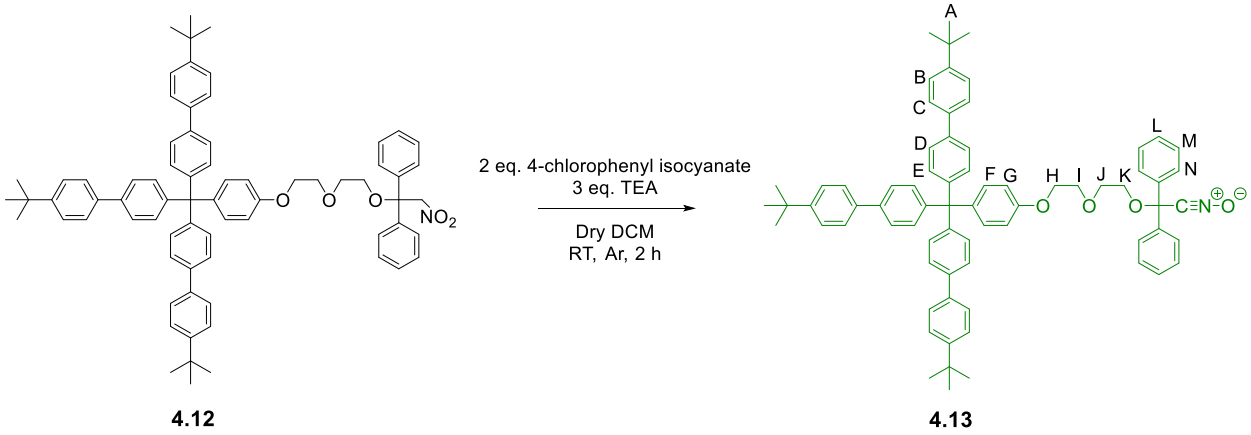

4.12 **4.13**

Nitro stopper **4.12** (0.863 g, 0.8247 mmol) and 4-chlorophenyl isocyanate (0.253 g, 1.65 mmol) were added to a round bottom flask under an argon atmosphere. Dry DCM (8.25 mL) and triethylamine (345 µL, 2.47 mmol) were injected, and a white precipitate formed within the first minute. After stirring at room temperature for 2 hours, the reaction solution was filtered to remove the urea byproduct, and the filtrate was dried under vacuum. The remaining residue was dissolved in chloroform and filtered. The filtrate was collected, and the solvent was removed under vacuum, leaving behind a yellow solid that was purified using column chromatography (silica gel, hexanes

to ethyl acetate gradient) to yield **4.13** as a white powder in 65% yield by mass. ^{1}H NMR (400 MHz, $CDCl_3$) δ 7.55 (d, *J* = 8.4 Hz, 6H, B), 7.50 (d, *J* = 8.5 Hz, 6H, C), 7.47 – 7.41 (m, 10H, D, N), 7.37 – 7.28 (m, 12H, E, L, M), 7.23 – 7.16 (m, 2H, F), 6.89 – 6.81 (m, 2H, G), 4.15 (dd, *J* = 5.7, 3.8 Hz, 2H, H), 3.88 (dd, *J* = 5.7, 3.8 Hz, 2H, K), 3.83 (dd, *J* = 5.6, 4.1 Hz, 2H, I), 3.68 (dd, *J* = 5.5, 4.1 Hz, 2H, J), 1.36 (s, 27H, A). ^{13}C NMR (101 MHz, $CDCl_3$) δ 156.83, 150.15, 145.80, 140.35, 139.22, 138.37, 137.71, 132.23, 131.45, 128.92, 128.71, 126.59, 126.43, 125.91, 125.67, 113.47, 84.25, 77.21, 70.02, 69.86, 67.44, 66.07, 63.64, 34.52, 31.36.

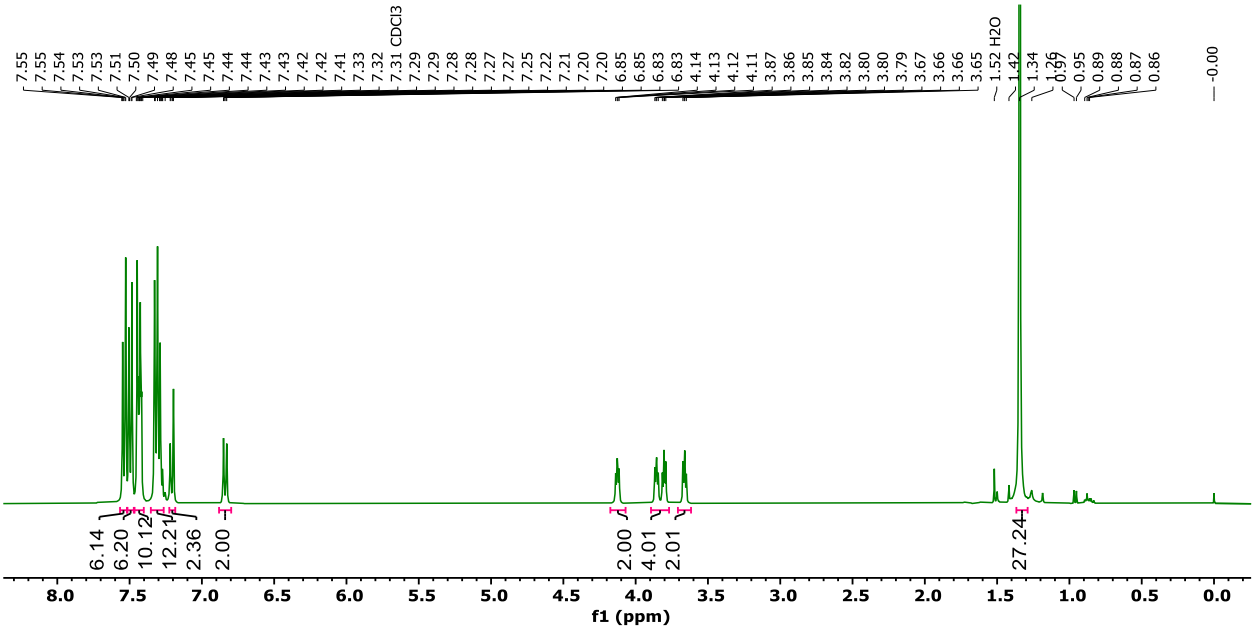

Figure 4.46. ^{1}H-NMR (400 MHz, 25°C, $CDCl_3$) of nitrile-oxide stopper **4.13**.

4.4.2.6 Synthesis of Bip dumbbell **4.14**.

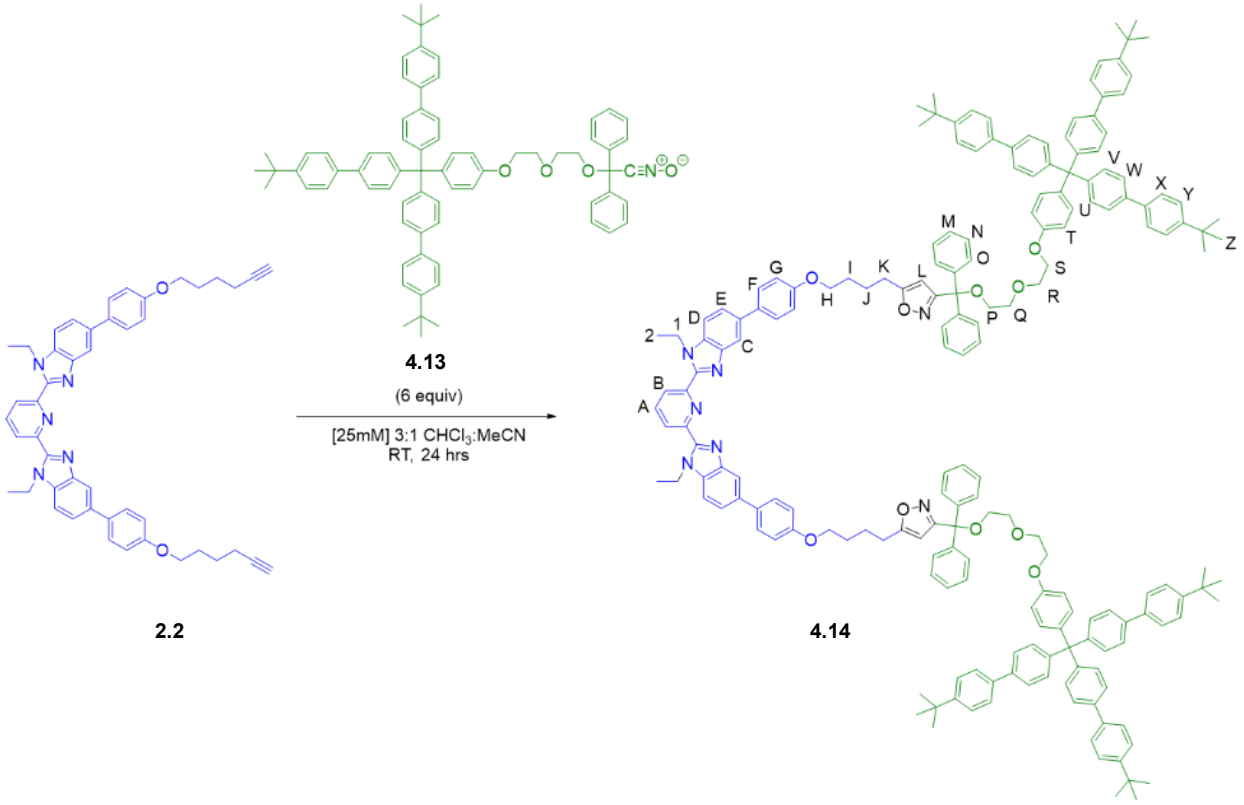

Bis-alkyne Bip **2.2** (0.005 g, 0.0070 mmol) and nitrile-oxide stopper **4.13** (0.0217 g, 0.0211 mmol) were added to a vial and dissolved in chloroform/acetonitrile (3/1 v/v, 280µL). The vial was capped, and the reaction stirred at room temperature for 24 hours after which the solvent was removed under vacuum. The crude mixture was precipitated into hexanes to remove the excess stopper, providing dumbbell product **4.14** in 94% yield by mass. ^{1}H NMR (400 MHz, $CDCl_3$) δ 8.37 (d, *J* = 7.8 Hz, 2H, B), 8.09 – 8.00 (m, 3H, A+C), 7.60 – 7.52 (m, 16H, D+E+Y), 7.49 (m, 12H, X), 7.46 – 7.41 (m, 20H, W+O), 7.33 – 7.27 (m, 24H, V+M+N), 7.27-7.17 (m, 8H, F+U), 6.97 – 6.92 (m, 4H, G), 6.86 – 6.81 (m, 4H, T), 6.01 (s, 2H, L), 4.81 (q, *J* = 7.1 Hz, 4H, 1), 4.14 (dd, *J* = 5.8, 3.8 Hz, 4H, S), 3.98 (t, *J* = 5.6 Hz, 4H, H), 3.88 (dd, *J* = 5.7, 3.8 Hz, 4H, R), 3.75 (t, *J* = 4.9 Hz, 4H, Q), 3.44 (t, *J* = 4.9 Hz, 4H, P), 2.76 (t, *J* = 7.1 Hz, 4H, I), 1.84 (s, 8H, K+J), 1.39 (t, *J* = 7.1 Hz, 6H, 2), 1.34 (s, 54H, Z).

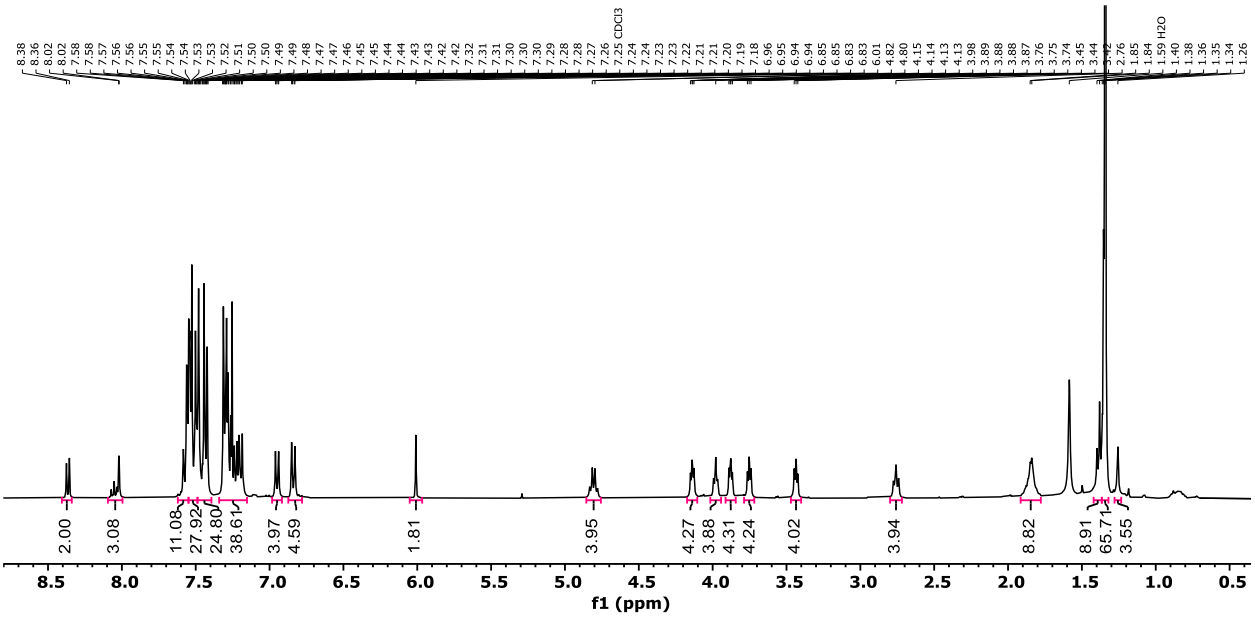

Figure 4.47. ^{1}H-NMR (500 MHz, d_1=5s, 25°C, $CDCl_3$) of Bip dumbbell **4.14**.

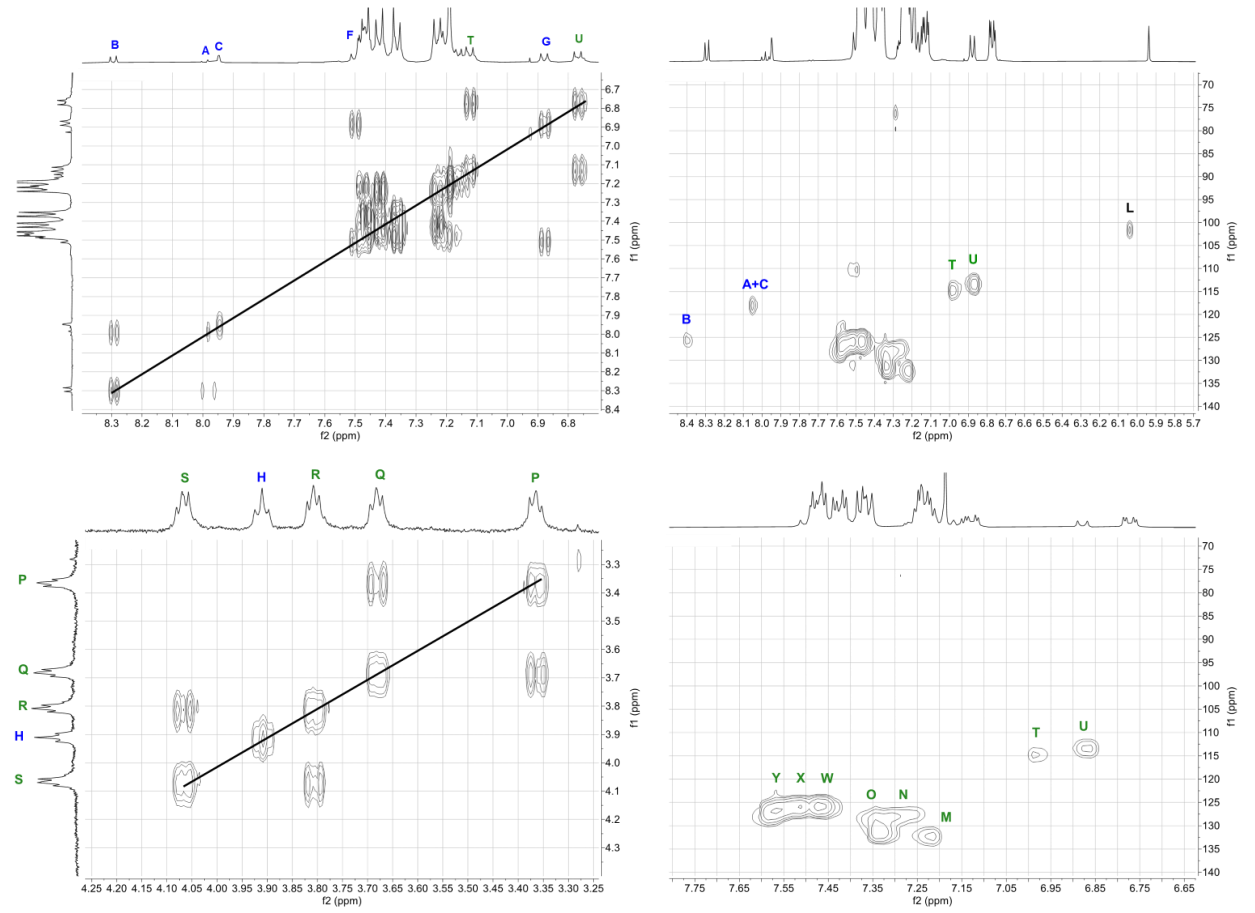

Figure 4.48. COSY NMR (400 MHz, 25°C, $CDCl_3$) of Bip dumbbell **4.14**.

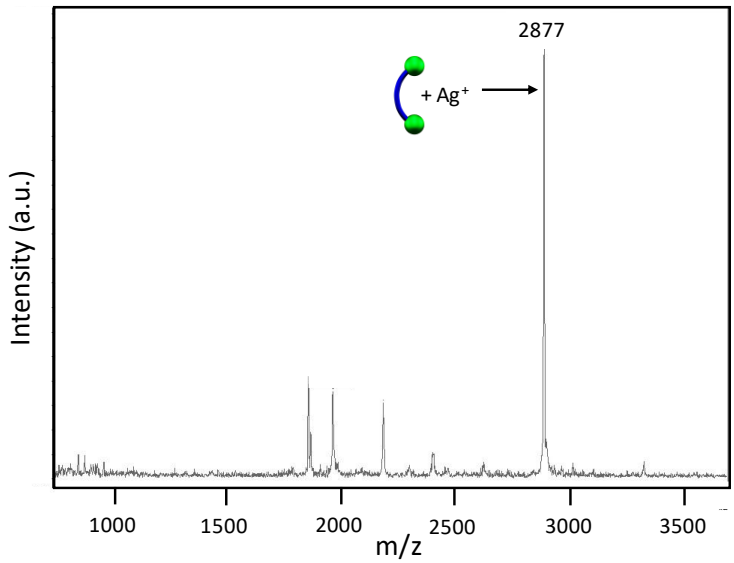

Figure 4.49. MALDI-TOF MS (Dithranol, silver trifluoroacetate) of Bip dumbbell **4.14**.

4.4.2.7 Synthesis of Bipy dumbbell **4.15**

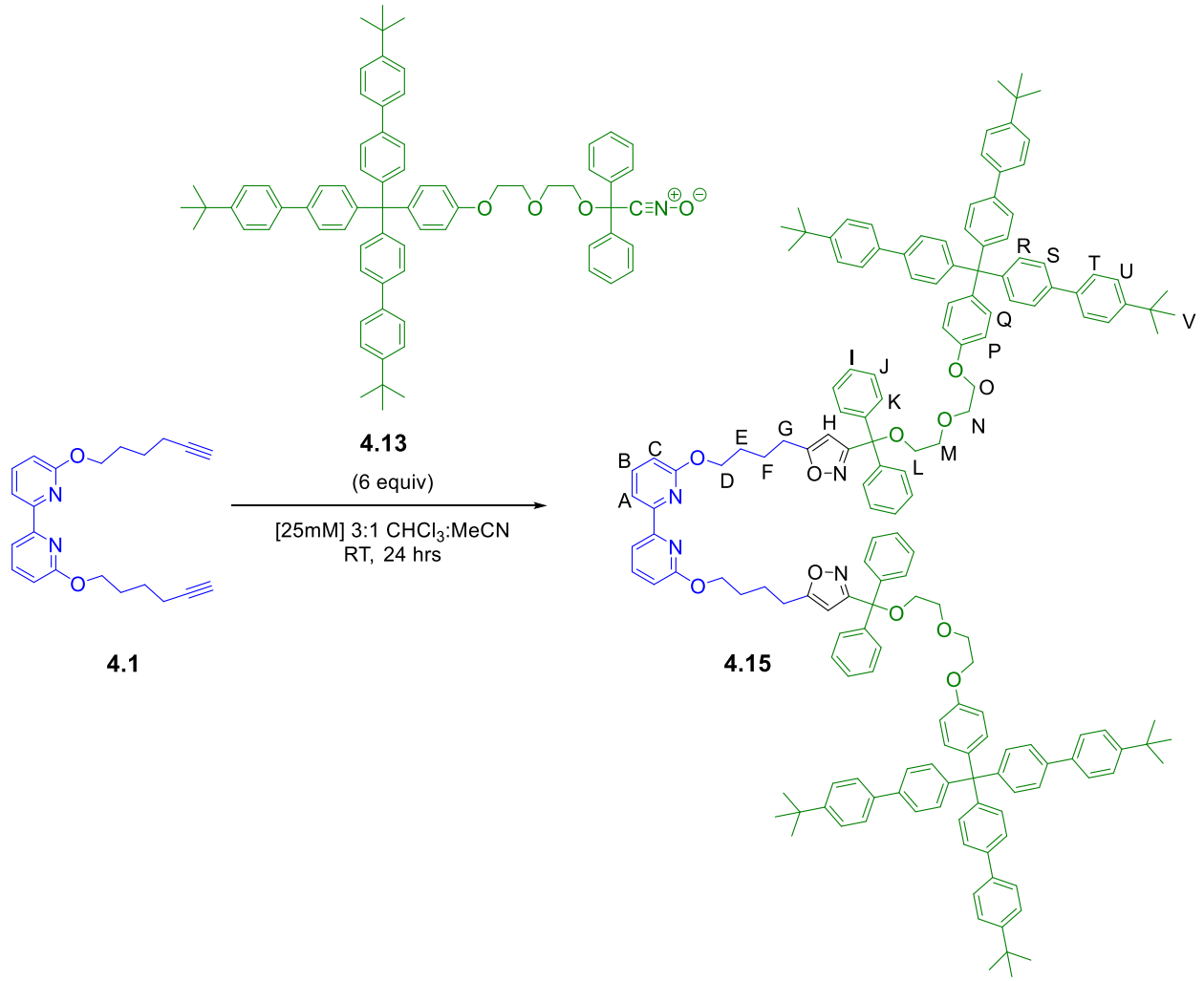

Bis-alkyne Bipy **4.1** (0.001 g, 0.0029 mmol) and nitrile-oxide stopper **4.13** (0.0089 g, 0.0086 mmol) were added to a vial and dissolved in chloroform/acetonitrile (3/1 v/v, 115 µL). The vial was capped, and the reaction stirred at room temperature for 24 hours after which the solvent was removed under vacuum. The crude mixture was precipitated into hexanes to remove the excess stopper, providing dumbbell **4.15** in 94% yield by mass. ^{1}H NMR (400 MHz, $CDCl_3$) δ 7.90 (dd, *J* = 7.5, 0.9 Hz, 2H, A), 7.59 (d, *J* = 7.9 Hz, 2H, B), 7.57 – 7.47 (m, 24H, U+T), 7.47 – 7.40 (m, 20H, S+K), 7.35 – 7.27 (m, 24H, R+I+J), 7.20 (m, 4H, Q), 6.89 – 6.79 (m, 4H, P), 6.64 (dd, *J* = 8.2, 0.8 Hz, 2H, C), 5.96 (s, 2H, H), 4.39 (t, 4H, D), 4.13 (dd, *J* = 5.8, 3.9 Hz, 4H, O), 3.91 – 3.85

(m, 4H, N), 3.73 (t, *J* = 5.0 Hz, 4H, M), 3.42 (t, 4H, L), 2.74 (t, 4H, E), 1.83 (s, 8H, G+F), 1.35 (s, 54H, V).

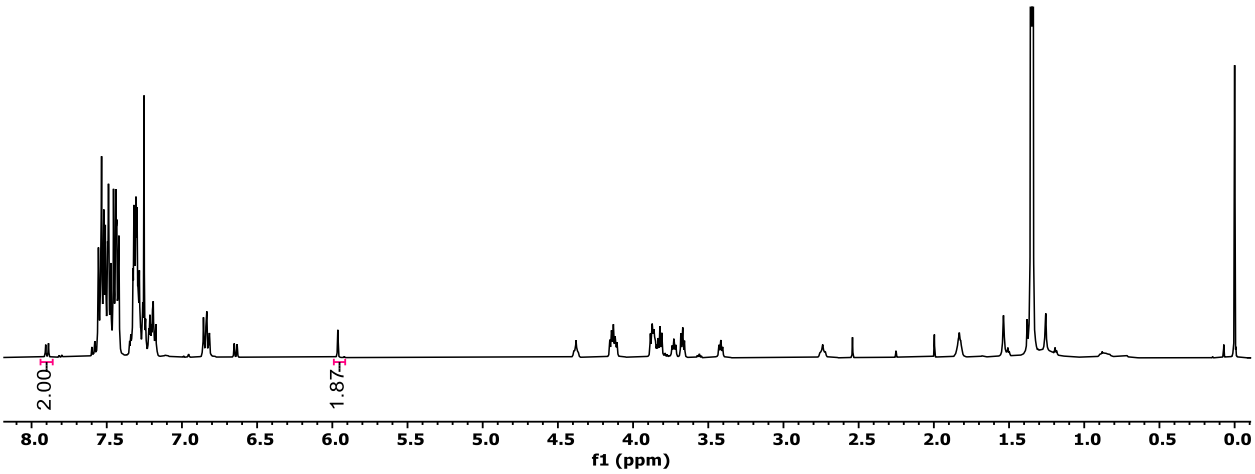

Figure 4.50. ^{1}H-NMR (500 MHz, d_1=5s, 25°C, $CDCl_3$) of Bipy dumbbell **4.15**.

4.4.2.8 Synthesis of Bip P2R **4.8:2.2:Zn(II)**

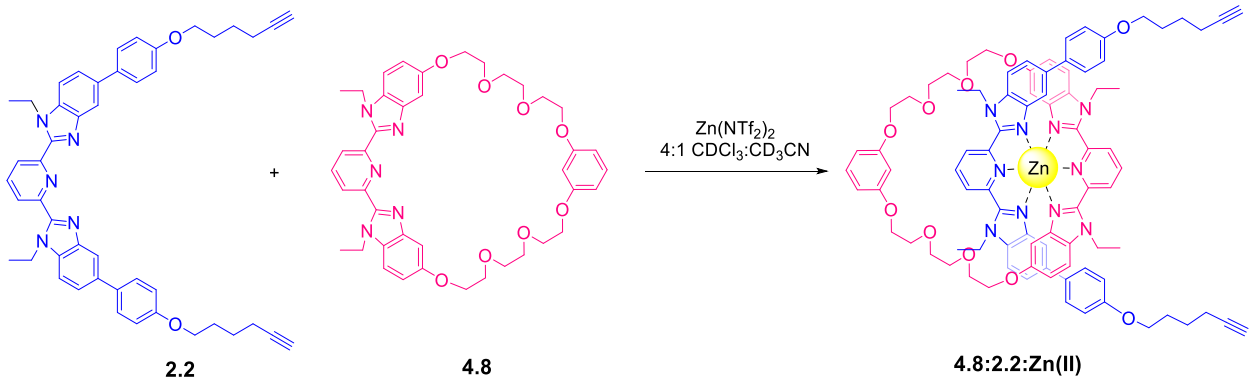

36-atom macrocycle **4.8** (40 mg, 0.054 mmol) was dissolved in 500 µL $CDCl_3$**.** A stock solution of **2.2** (30 mM) was titrated into the solution of **4.8** until an exact 1:1 (**4.8**:**2.2**) ratio was formed (done by monitoring both the N-CH_2 peaks on the alkyl groups of the Bip ligands). A stock solution of $Zn(NTf_2)_2$ (30 mM in 4:1 $CDCl_3$:CD_3CN) was added until no free Bip peak appeared at ~1 equiv. of the metal ion. The complete disappearance of the doublets at 8.38 and 8.21 ppm (and the corresponding growth of the peaks at 8.74 and 8.69 ppm) indicates that all Bip ligands are bound with zinc in a 2:1 Bip:metal ratio. The resulting pseudo[2]rotaxane solution **4.8:2.2:Zn(II)** was dried under vacuum to obtain a yellow powder that was stored in the freezer at -8°C before use.

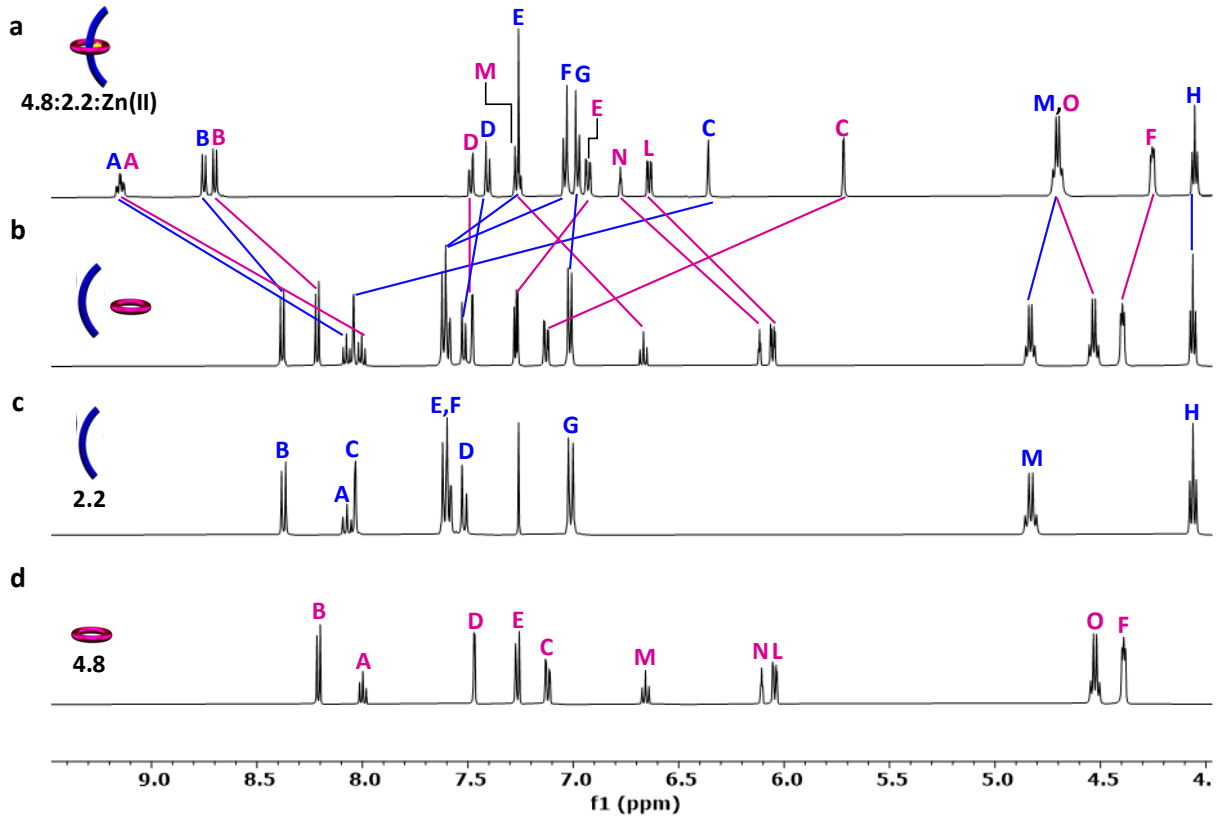

Figure 4.51. Partial ^{1}H-NMR overlay (500 MHz, 25°C, $CDCl_3$) of a) **4.8:2.2:Zn(II)** (b) 1:1 mixture of **4.8**:**2.2**, c) **2.2** and d) **4.8**.

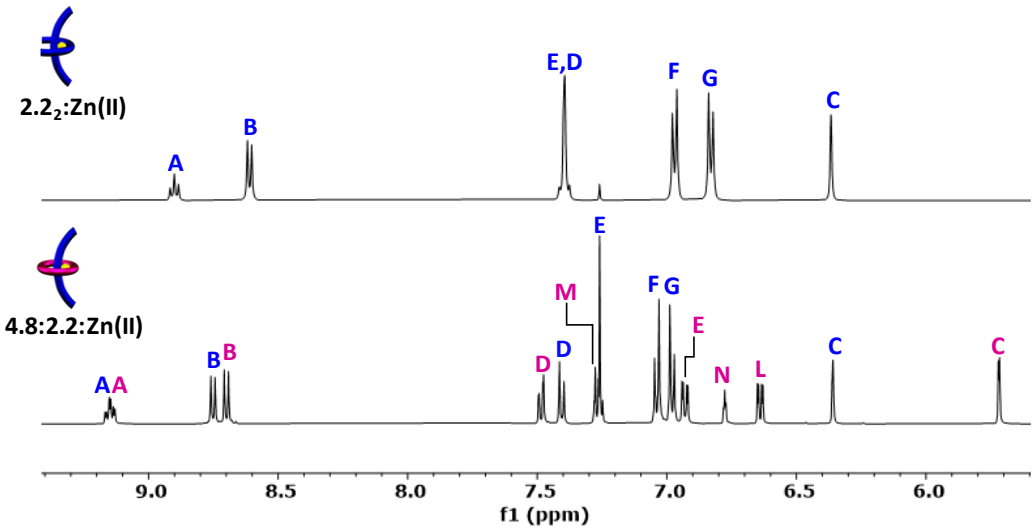

Figure 4.52. Partial ^{1}H-NMR overlay (500 MHz, 25°C, $CDCl_3$) of **2.2$_2$:Zn(II)** (top) and **4.8:2.2:Zn(II)** (bottom) shows diagnostic peaks.

4.4.2.9 Synthesis of Bipy P2R **4.8:4.1:Zn(II)**

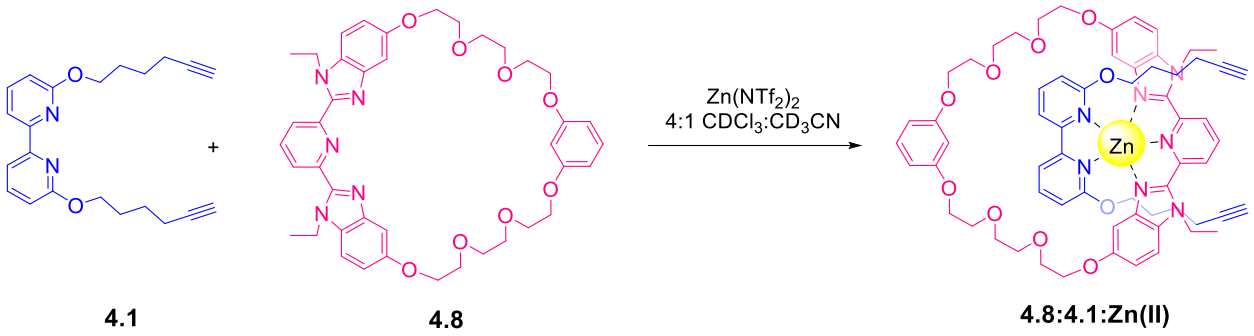

4.1 **4.8** **4.8:4.1:Zn(II)**

36-atom macrocycle **4.8** (40 mg, 0.054 mmol) was dissolved in 500 µL $CDCl_3$**.** A stock solution of Bipy thread **4.1** (30 mM) was titrated into the solution of **4.8** until an exact 1:1 (**4.8**:**4.1**) ratio was formed (done by monitoring the pyridyl peaks on the Bip ligand and the pyridyl peaks of Bipy). A stock solution of $Zn(NTf_2)_2$ (30 mM in 4:1 $CDCl_3$:CD_3CN) was added until no free Bipy peak appeared at ~1 equiv. of the metal ion. The complete disappearance of the doublet at 8.21 and the triplet at 7.66 ppm (and the corresponding growth of the peaks at 8.53 and 8.29 ppm) indicates that all Bip and Bipy ligands are bound with zinc in a 1:1:1 Bip:Bipy:metal ratio. The resulting pseudo[2]rotaxane solution **4.8:4.1:Zn(II)** was dried under vacuum to obtain a yellow powder that was stored in the freezer at -8°C before use.

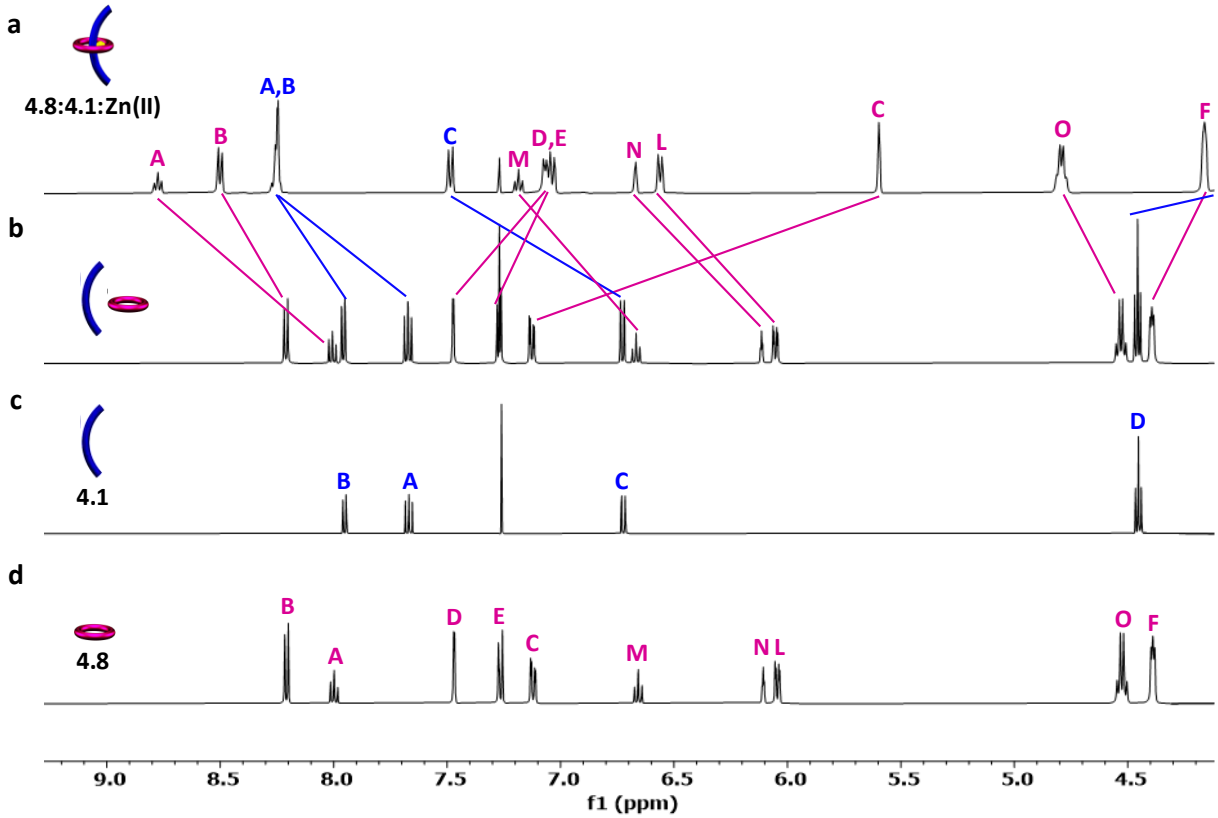

Figure 4.53. Partial ^{1}H-NMR overlay (500 MHz, 25°C) of a) **4.8:4.1:Zn(II)** (15% d_3-MeCN in $CDCl_3$), b) 1:1 mixture of **4.8**:**4.1** ($CDCl_3$), c) **4.1** ($CDCl_3$), and d) **4.8** ($CDCl_3$).

4.4.2.10 Synthesis of Bip [2]rotaxane **4.16**

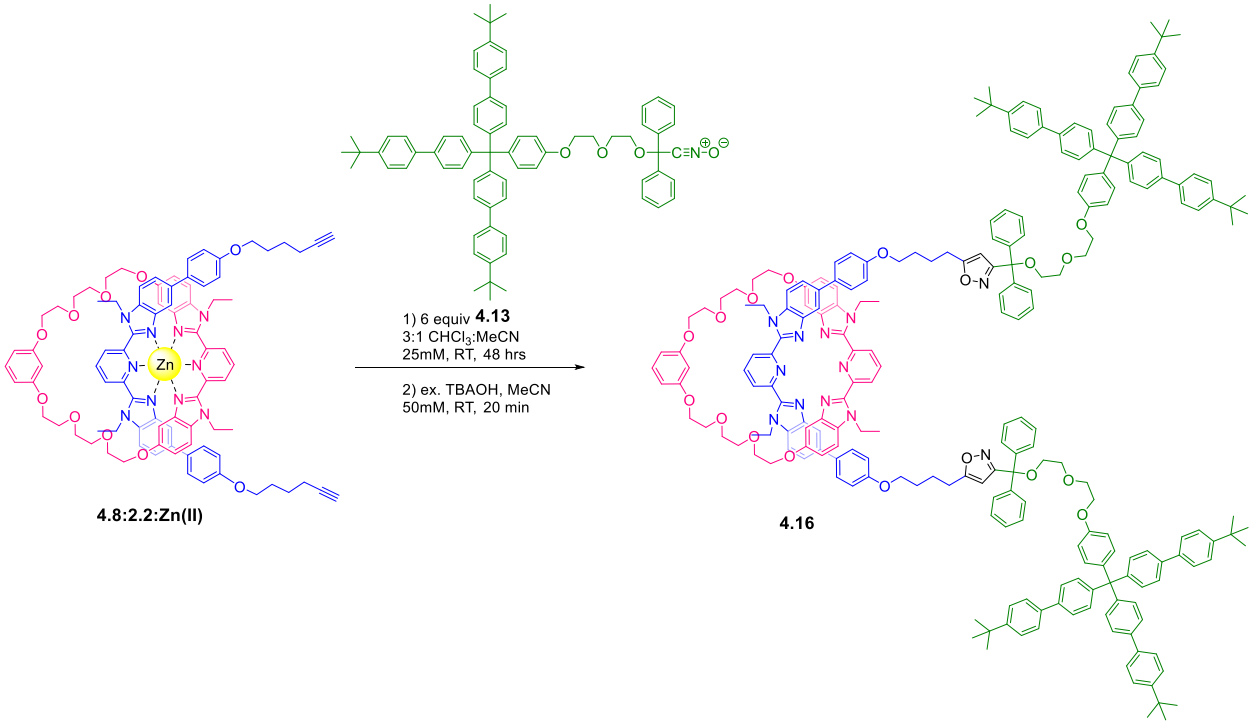

Bip pseudo[2]rotaxane **4.8:2.2:Zn(II)** (0.005 g, 0.0024 mmol) and nitrile-oxide stopper **4.13** (0.0149 g, 0.0145 mmol) were added to a vial and dissolved in chloroform/acetonitrile (3/1 v/v, 97 µL). The vial was capped, and the reaction stirred at room temperature for 48 hours, after which the solvent was removed under vacuum. The crude mixture was precipitated into a mixture of cold hexanes/chloroform (6/1 v/v, 35 mL) and centrifuged (8000 rpm, 15 min) 3x to remove the excess stopper. The metallated rotaxane was dissolved in acetonitrile, and 20 µL of tetrabutylammonium hydroxide solution (1M in MeOH) was added dropwise, resulting in a rapid color change from yellow to off-white, and precipitation of the demetallated product. After 20 minutes, the solid (**4.16**) was filtered, dried, and redissolved in $CDCl_3$ for NMR analysis. Acetonitrile was removed from the demetallated wash under vacuum, and the residue was also dissolved in $CDCl_3$ for NMR analysis. MALDI-TOF MS: 3615.2 ([M]+Ag^+), 2877.1 ([M]+ Ag^+-MC(**4.8**)), 1767.9 ([M]+Ag^+-MC(**4.8**)-SG(**4.13**)), 845.3 ([M]+Ag^+-DB(**4.14**)).

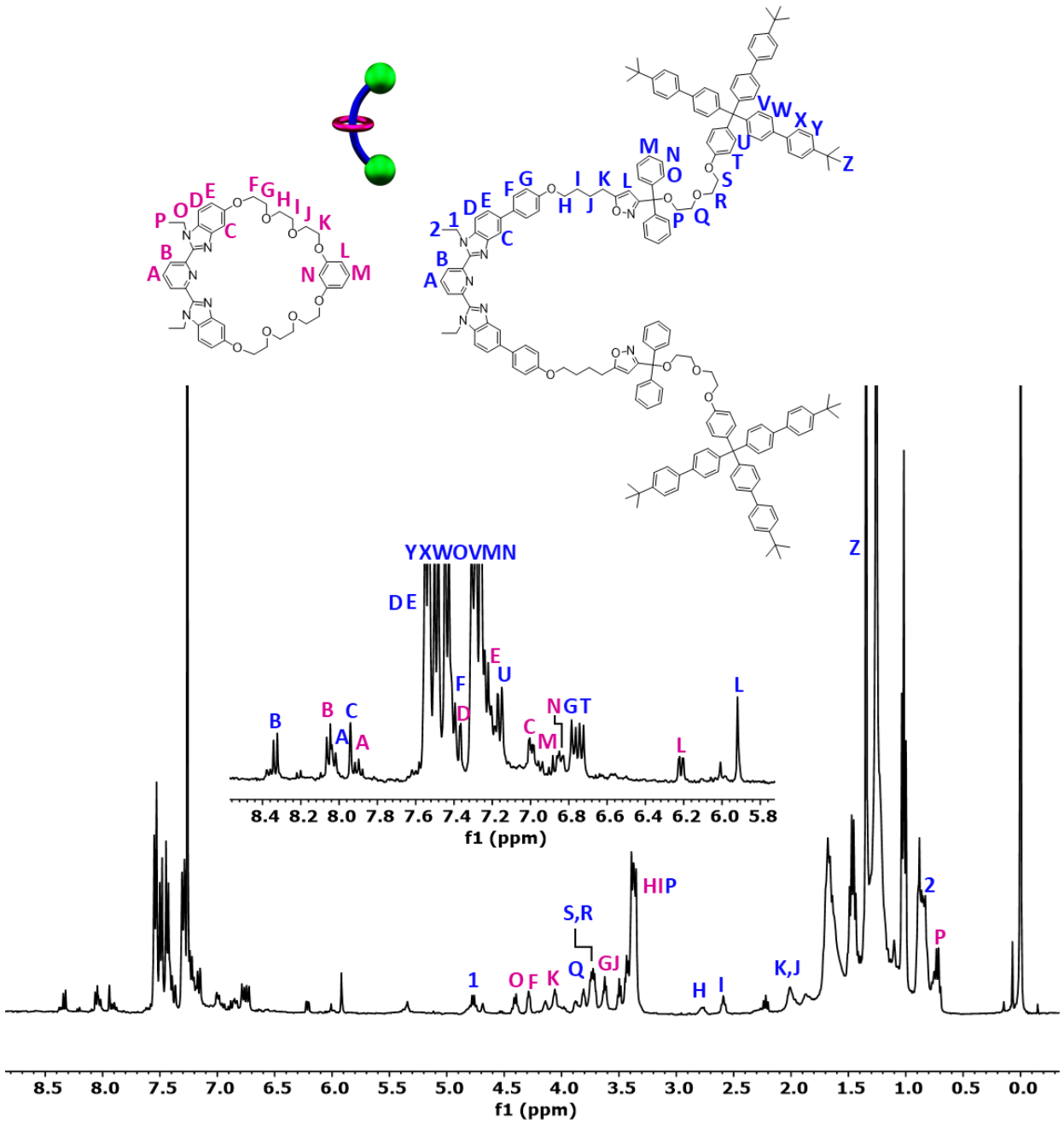

Figure 4.54. ^{1}H-NMR (500 MHz, 25°C, $CDCl_3$) of Bip [2]rotaxane **4.16**.

4.4.2.11 Synthesis of Bipy [2]rotaxane **4.17**

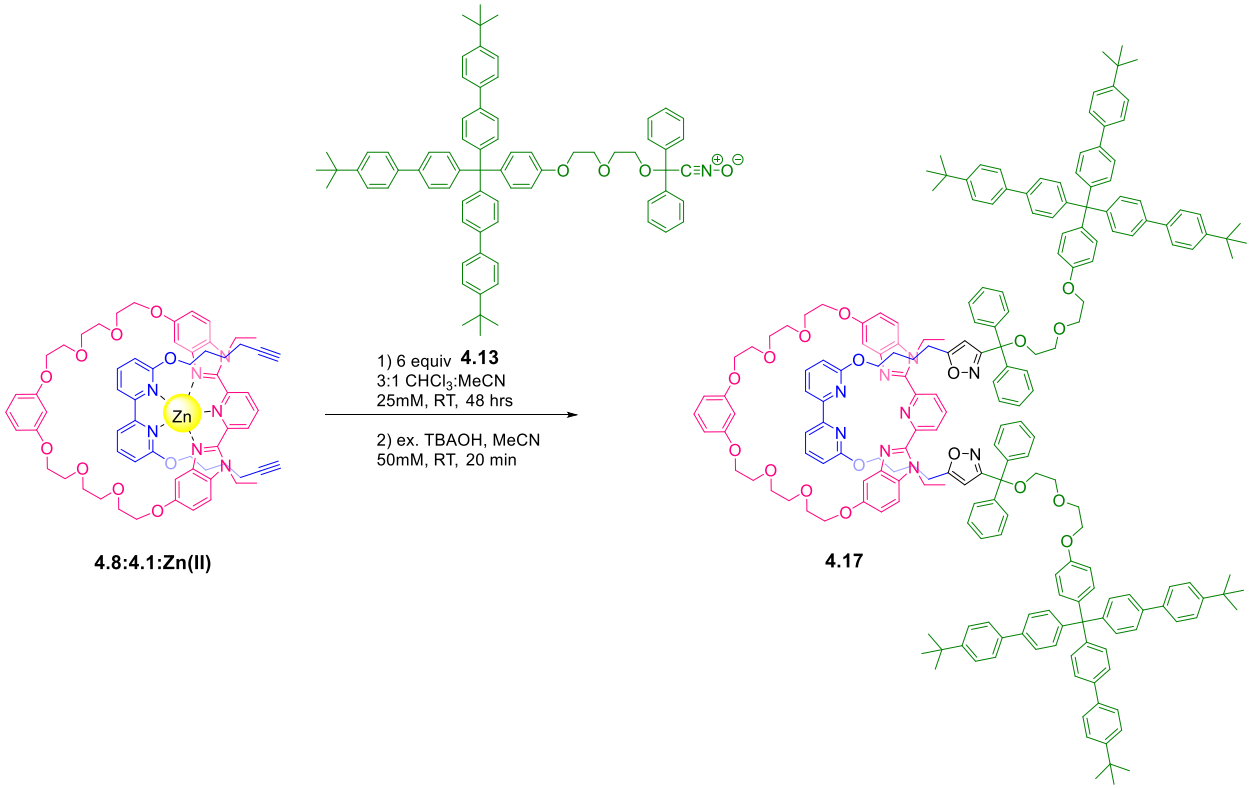

Bipy pseudo[2]rotaxane **4.8:4.1:Zn(II)** (0.005 g, 0.0029 mmol) and nitrile-oxide stopper **4.13** (0.0180 g, 0.0175 mmol) were added to a vial and dissolved in chloroform/acetonitrile (3/1 v/v, 117 µL). The vial was capped, and the reaction stirred at room temperature for 48 hours, after which the solvent was removed under vacuum. The crude mixture was precipitated into a mixture of cold hexanes/chloroform (6/1 v/v, 35 mL) and centrifuged (8000 rpm, 15 min) 3x to remove the excess stopper. The metallated rotaxane was dissolved in acetonitrile, and 20 µL of tetrabutylammonium hydroxide solution (1M in MeOH) was added dropwise, resulting in a rapid color change from yellow to off-white and precipitation of the demetallated product. After 20 minutes, the solid (**4.17**) was filtered, dried, and redissolved in $CDCl_3$ for NMR analysis. Acetonitrile was removed from the demetallated wash under vacuum, and the residue was also dissolved in $CDCl_3$ for NMR analysis. MALDI-TOF MS: 3251.6 ([M]+Ag^+), 2513.3 ([M]+ Ag^+-MC(**4.8**)), 845.4 ([M]+Ag^+-DB(**4.15**)).

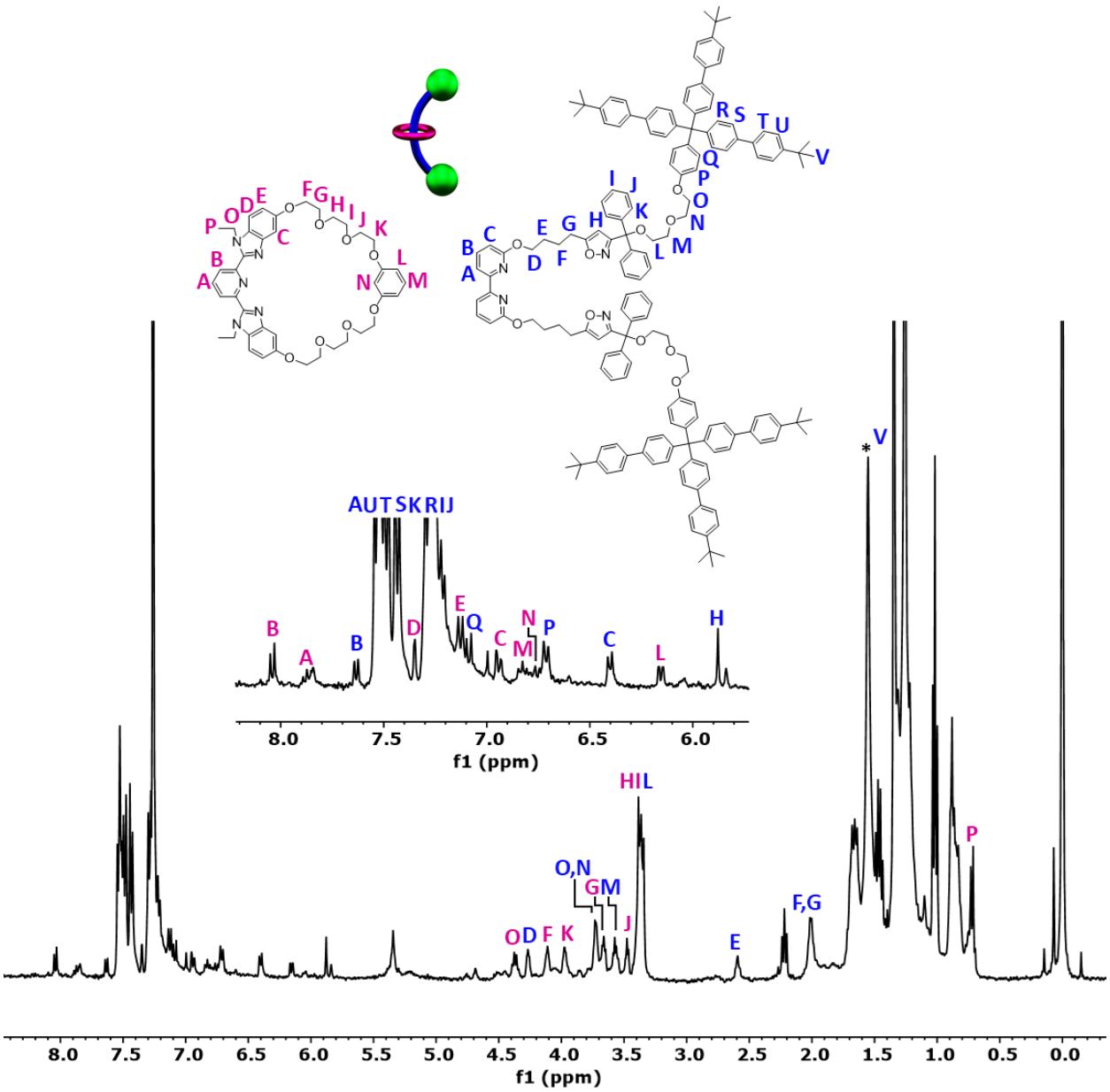

Figure 4.55. ^{1}H-NMR (500 MHz, 25°C, $CDCl_3$) of Bipy [2]rotaxane **4.17**.

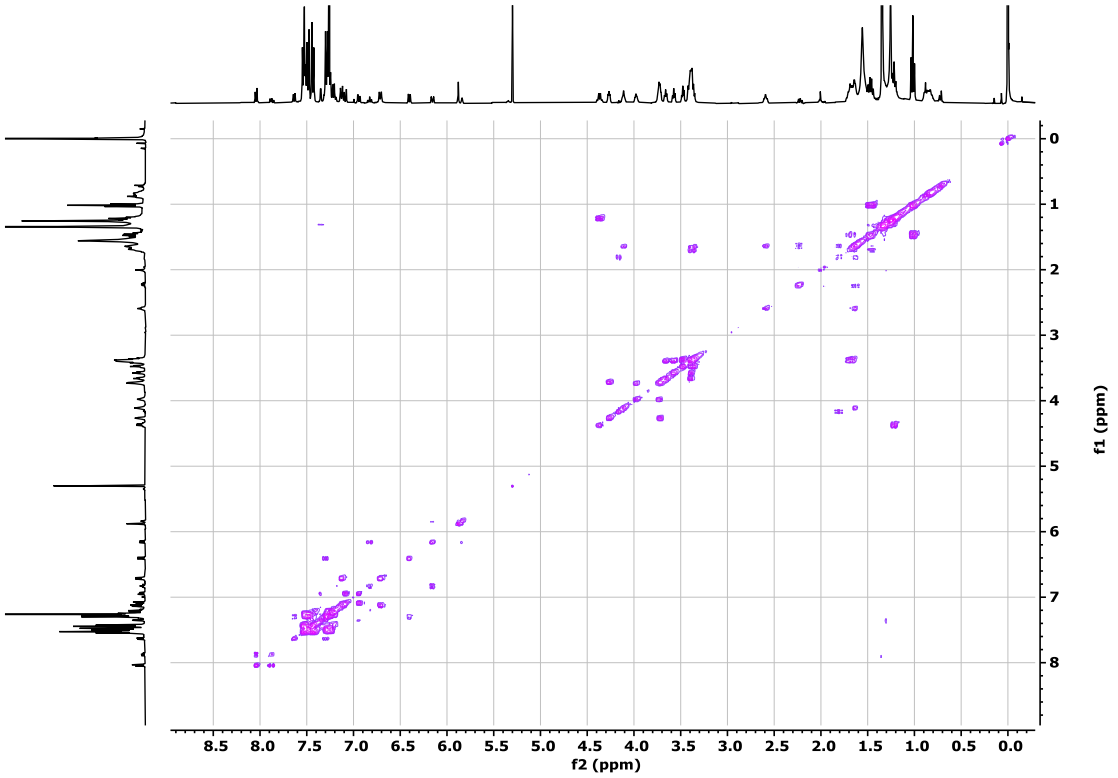

Figure 4.56. COSY NMR (400 MHz, 25°C, $CDCl_3$) of Bipy [2]rotaxane **4.17**.

4.4.2.12 Optimizing the synthesis of dumbbell polymer **4.19**.

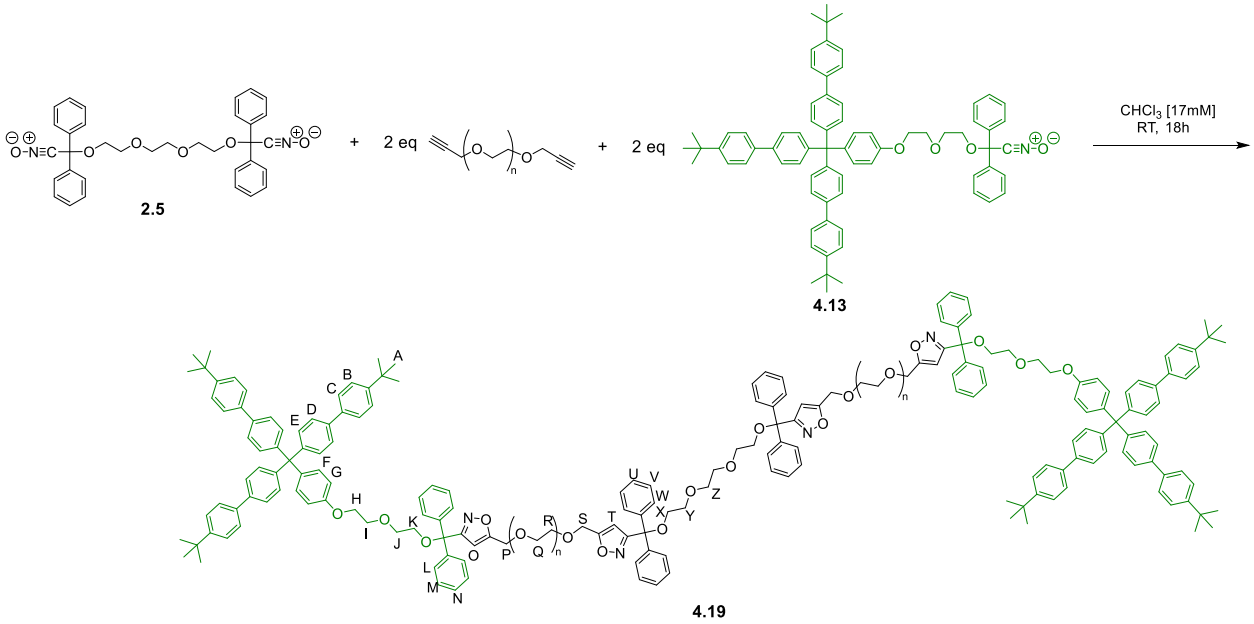

The alkyne-PEG-alkyne purchased from Creative PEGWorks was characterized by NMR end-group analysis and MALDI-TOF MS to confirm molecular weight before adding it to the NOAC

polymerization. ^{1}H NMR (400 MHz, $CDCl_3$) δ 4.20 (s, 4H, B), 3.81 (m, 4H, C), 3.64 (m, 166H, E), 3.46 (m, 4H, D), 2.43 (t, 2H, A).

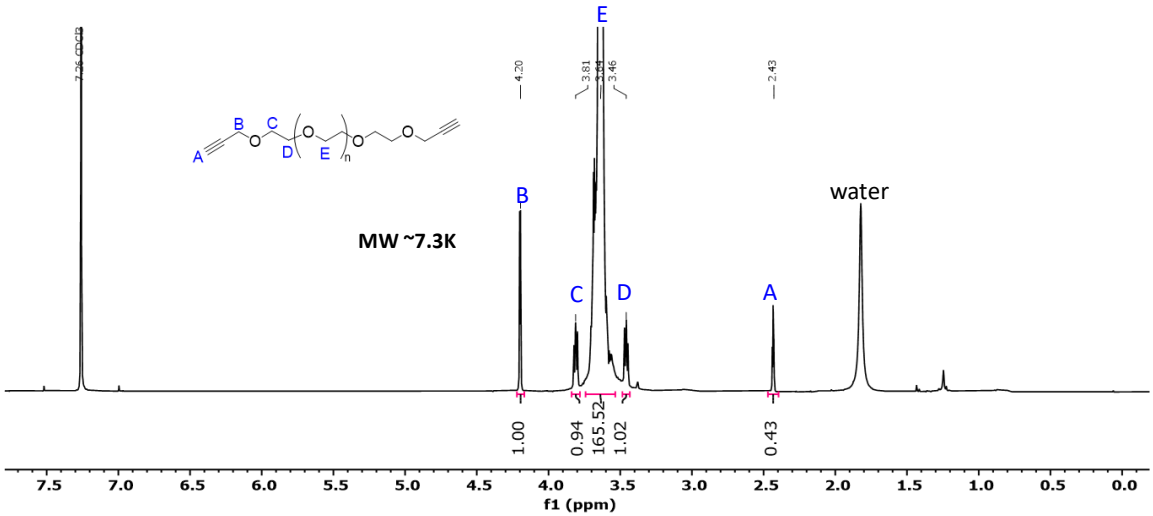

Figure 4.57. ^{1}H-NMR (500 MHz, d_1=5s, 25°C, $CDCl_3$) of alkyne-PEG-alkyne (Creative PEGWorks, 5K).

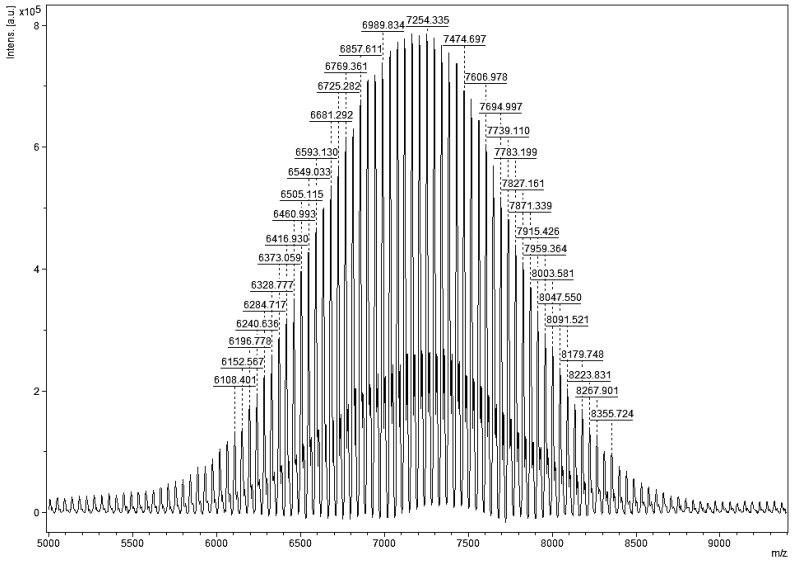

Figure 4.58. MALDI-TOF MS (DCTB: *trans*-2-[3-(4-*tert*-Butylphenyl)-2-methyl-2-propenylidene]malononitrile) of alkyne-PEG-alkyne (Creative PEGWorks, 5K).

The delay time for the NMR experiment was increased to 5 seconds to ensure a more accurate integration of alkyne chain-ends. The integration of the singlet at 4.20 ppm (B) was set to four protons and used as the end-group, providing a molecular weight closer to 7,300 g/mol.

The DCTB (*trans*-2-[3-(4-*tert*-Butylphenyl)-2-methyl-2-propenylidene]malononitrile) MALDI matrix provided the cleanest spectrum with two hedgehogs correlating to the polymer and the polymer flying with sodium ions. This alkyne-PEG-alkyne was purchased as a 5,000 g/mol polymer, but NMR (Figure 4.57) and MALDI-TOF (Figure 4.58) suggest a 7,300 g/mol molecular weight. Therefore, calculations for the following polymerizations used 7,300 g/mol for the alkyne-PEG-alkyne component.

Alkyne-PEG-alkyne (0.1293 g, 0.0177 mmol, Creative PEGWorks 7300 g/mol) and nitrile-oxide stopper **4.13** (0.0182 g, 0.0177 mmol) were added to a small vial with a stir bar. Nitrile-oxide monomer **2.5** (0.0050 g, 0.0089 mmol) was dissolved in 520 µL of chloroform and added to the vial. The polymerization was capped and left to stir at room temperature for 18 hours, after which the solvent was removed under vacuum. The resulting viscous oil was further dried under vacuum, and then dissolved in $CDCl_3$ for crude NMR to verify peak assignments: ^{1}H NMR (500 MHz, $CDCl_3$) δ 7.54 – 7.43 (m, 36H, B-D), 7.43 – 7.35 (m, 12H, E), 7.28 – 7.10 (m, 44H, F+L+M+N+U+V+W), 6.81 (d, *J* = 8.5 Hz, 4H, G), 6.18 (s, 2H, O), 6.14 (s, 2H, T) 4.54 (d, *J* = 6.3 Hz, 8H, H+K), 4.17 (d, *J* = 2.4 Hz, 4H, P), 4.13 – 4.09 (m, 4H, S), 3.62 (s, 1114H, I+J+Q+R+X+Y+Z), 1.31 (s, 54H, A).

Based on the molecular weight determined for the PEG, the polymer should be about 17,200 g/mol: **2.5** (564.64 g/mol), two equivalents of the alkyne-PEG-alkyne (7,300 g/mol), two equivalents of **4.13** (1028.39 g/mol). This first experiment combines all three components in a single step to make the dumbbell polymer **4.19**. A second approach proceeds step-wise, resulting in a click polymer **4.18** with alkyne chain ends that can react in the final stoppering step. NMR end-group analysis of crude **4.19** will determine the (crude) molecular weight for each experiment (Figure 4.59).

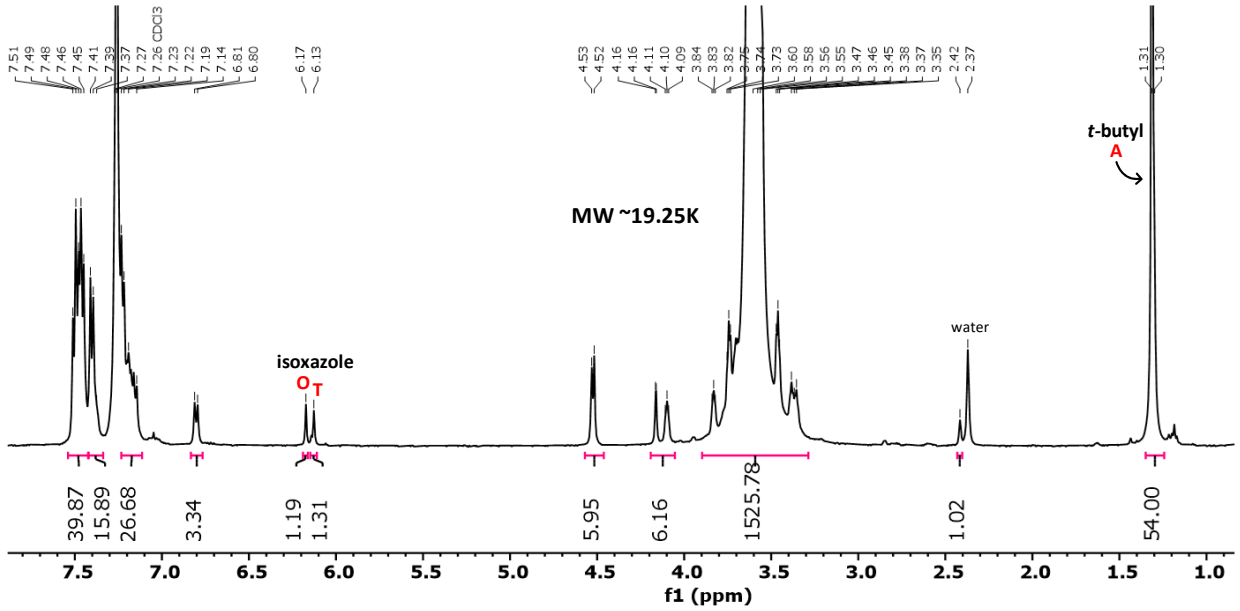

Figure 4.59. ^{1}H-NMR (500 MHz, d_1=5s, 25°C, $CDCl_3$) of crude **4.19** via one-pot polymerization.

There are two isoxazole peaks present in the crude NMR spectrum for **4.19**; the more downfield signal at 6.17 ppm (O) correlates to the isoxazole on the stoppered end group (O) because it is in a more aromatic environment (Figure 4.59). Therefore, the peak at 6.13 ppm (T) is the isoxazole proton between the monomer and linear PEG.

The *t*-butyl groups on **4.13** were used for end-group analysis because they appear as a strong singlet at 1.31 ppm (A). The peak integration was set to 54 protons because an exact 2.0 equivalents of **4.13** was added to the reaction. Integrating the PEG region (between 3.27 and 3.81 ppm; 1526 protons), dividing by four (protons in ethylene glycol), and multiplying by the molecular weight of the repeat unit (44.05 g/mol) gave the molecular weight of PEG in the dumbbell **4.19**. Adding the molecular weight of stoppers and biphenyl isoxazole linkages resulted in a 19,250 g/mol molecular weight.

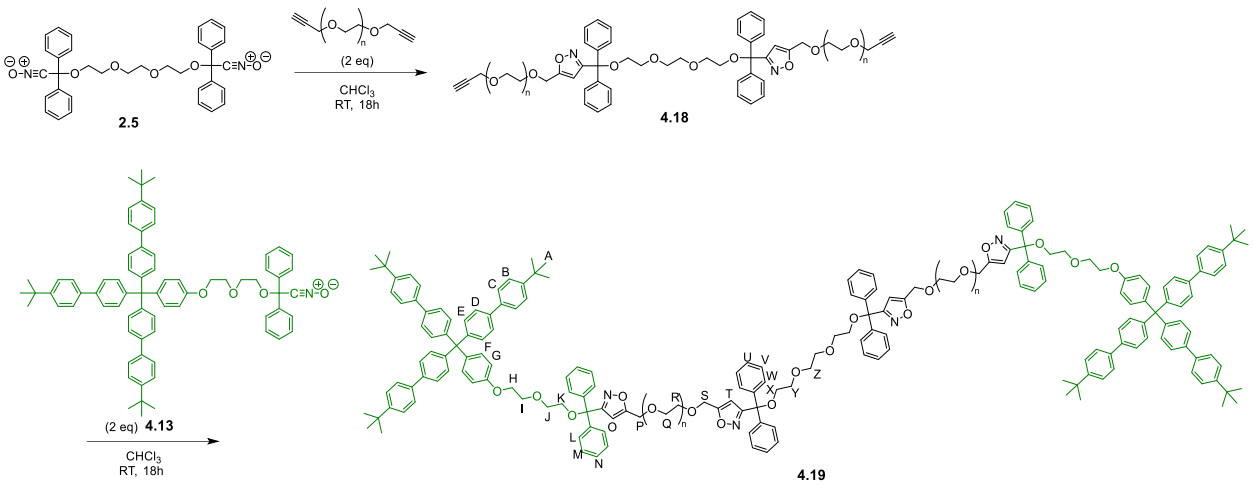

Alkyne-PEG-alkyne (0.1293 g, 0.0177 mmol, Creative PEGWorks 7300 g/mol) was added to a small vial with a stir bar. Nitrile-oxide monomer **2.5** (0.0050 g, 0.0089 mmol) was dissolved in 350 µL of chloroform and added to the vial. The polymerization was capped and left to stir at room temperature for 18 hours. Nitrile-oxide stopper **4.13** (0.0182 g, 0.0177 mmol) was dissolved in 170 µL of chloroform and added to the vial. The polymerization was left for 18 more hours, after which the solvent was removed under vacuum. The resulting viscous oil was further dried under vacuum, and then dissolved in $CDCl_3$ for crude NMR analysis to verify peak assignments: ^{1}H NMR (500 MHz, $CDCl_3$) δ 7.54 – 7.37 (m, 48H, B-E), 7.28 – 7.10 (m, 44H, F+L+M+N+U+V+W), 6.81 (d, *J* = 8.5 Hz, 4H, G), 6.18 (s, 2H, O), 6.14 (s, 2H, T) 4.54 (d, *J* = 6.3 Hz, 8H, H+K), 4.17 (d, *J* = 2.4 Hz, 4H, P), 4.13 – 4.09 (m, 4H, S), 3.62 (s, 1114H, I+J+Q+R+X+Y+Z), 1.31 (s, 54H, A).

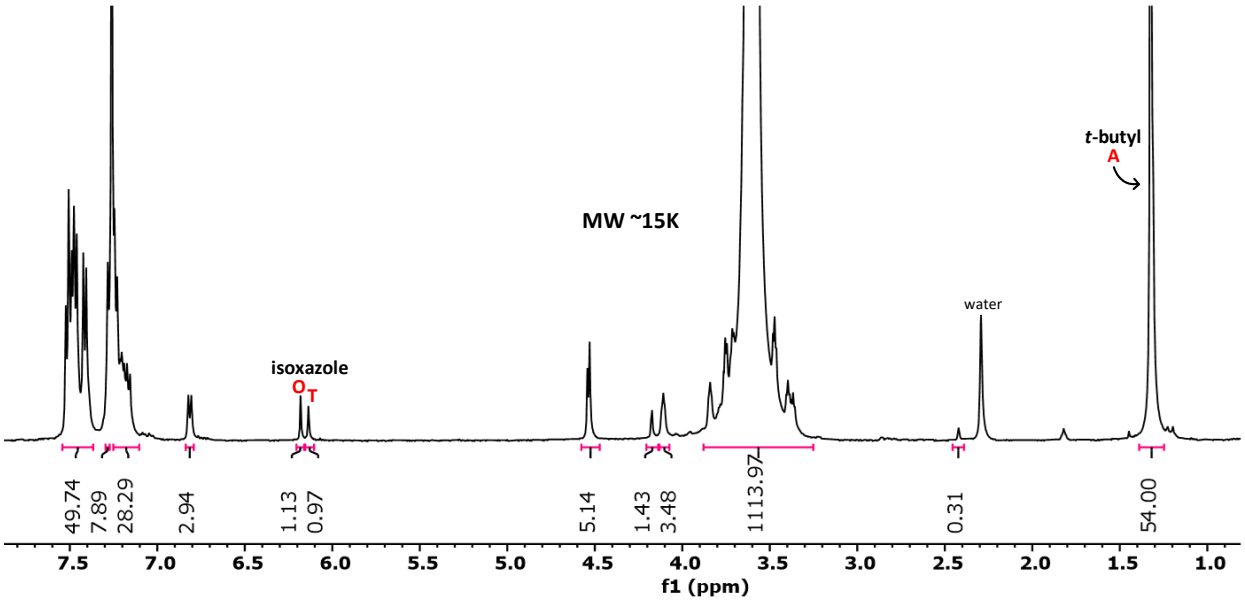

Figure 4.60. ^{1}H-NMR (500 MHz, d_1=5s, 25°C, $CDCl_3$) of crude **4.19** via two-step polymerization.

The crude NMR for the one-pot and step-wise polymerization of **4.19** are similar; however, the end-group analysis determined a molecular weight closer to 15,000 g/mol for the two-step procedure (Figure 4.60). While alkyne peaks (~2.43 ppm) are present in both polymerization products, the integration is much less for this two-step procedure (1.02 vs. 0.31). Adding more stopper in future polymerizations should lead to complete stoppering and increase the molecular weight closer to the expected value (17,200 g/mol).

The one-pot procedure was repeated at three concentrations (10, 20, and 50 mM), and the crude samples were analyzed via GPC (Figure 4.61). The two-step procedure was repeated at the higher concentration (50 mM) and compared to the preliminary results (17 mM).

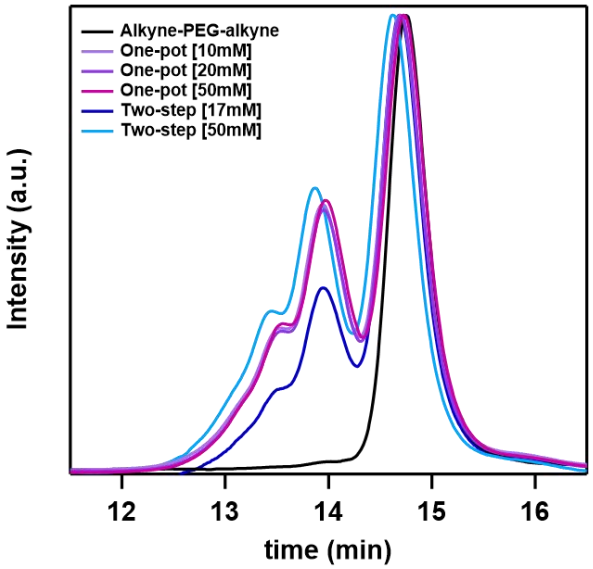

Figure 4.61. GPC (3:1 THF:DMF) traces of dumbbell polymer **4.19** (crude) formed in one-pot at three different concentrations compared with **4.19** (crude) prepared via two-step polymerization (light blue) and the alkyne-PEG-alkyne starting material (7300 g/mol, black).

The two-step process was concentration-dependent; the product molecular weight and distribution were constant at all concentrations. However, there is a shift to higher molecular weight for the two-step polymerization when the concentration was increased to 50 mM (light blue) compared to the sample prepared at 17 mM (dark blue). The one-step reaction has a greater chance of forming smaller dumbbells by capping the alkyne-PEG-alkyne polymer, which would also explain the increased residual alkynes in the crude NMR spectra mentioned above.

The step-wise synthesis of **4.19** was repeated on a larger scale (using 0.02 g of monomer **2.5**) and at a higher concentration (50mM vs. 17mM). An aliquot of the polymerization was taken to verify the formation of the pre-stoppered click polymer **4.18** via NMR.

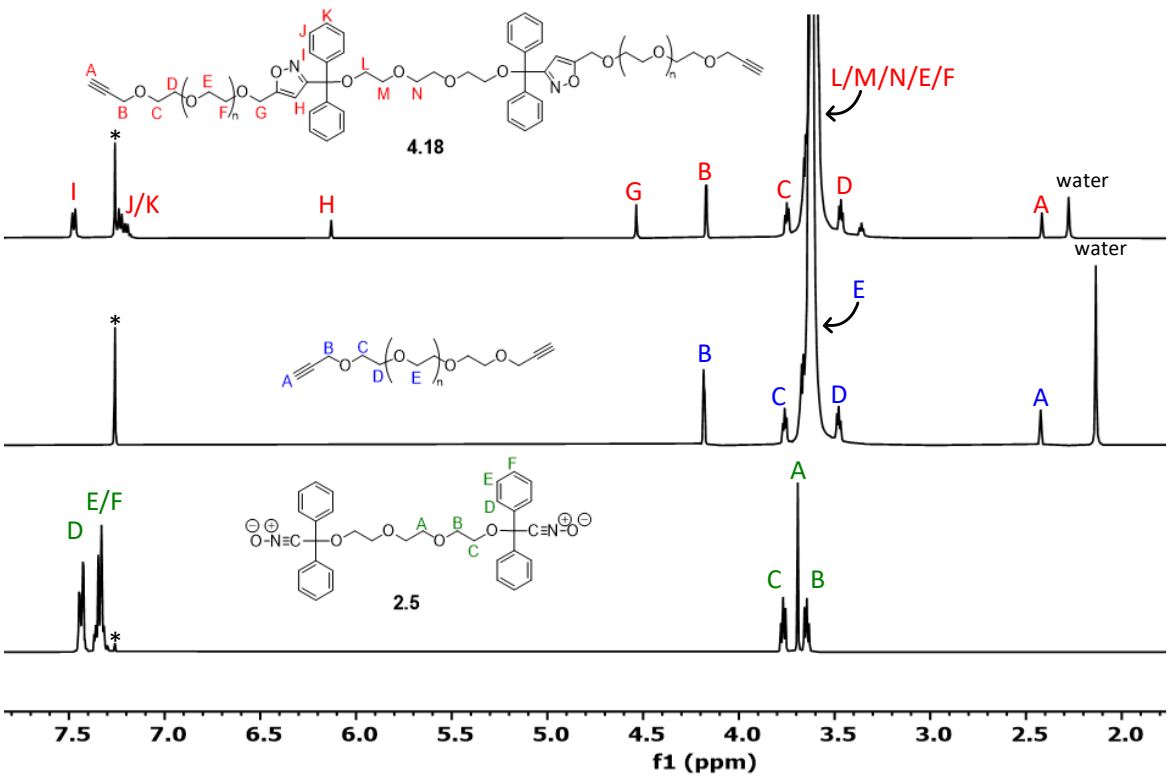

Figure 4.62. ^{1}H-NMR (500 MHz, d_1=5s, 25°C, $CDCl_3$) overlay of crude polymer **4.18** with alkyne-PEG-alkyne and monomer **2.5** for comparison.

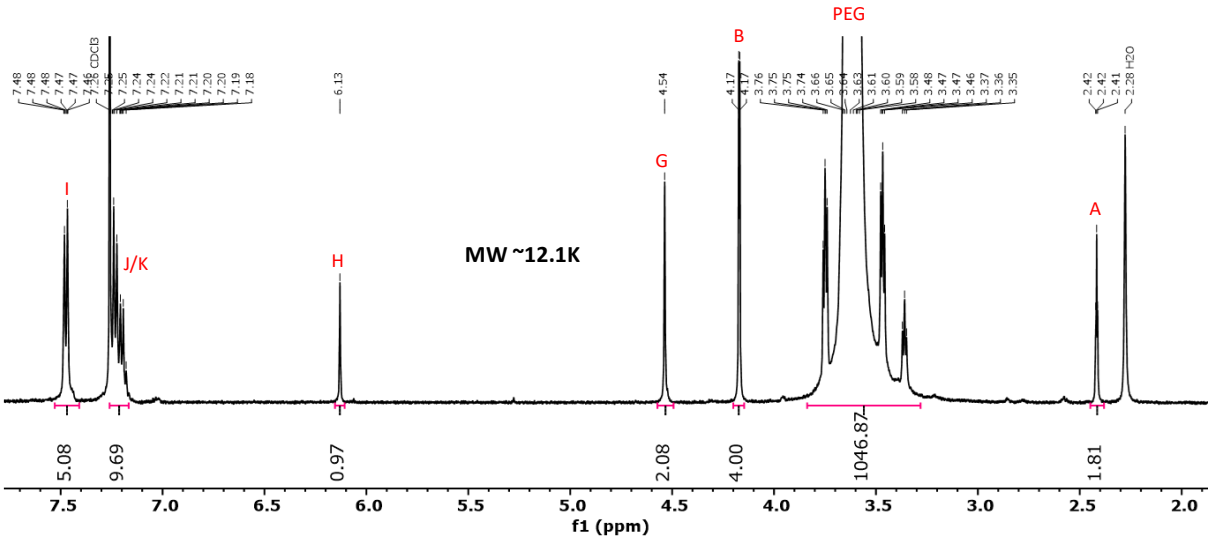

Figure 4.63. ^{1}H-NMR (500 MHz, d_1=5s, 25°C, $CDCl_3$) of crude **4.18**.

Similar to the end-group analysis for the alkyne-PEG-alkyne, the singlet at 4.20 (B) was used to determine the molecular weight of **4.18**. Setting this peak to four protons results in two protons at 2.42 ppm (A), as expected for the two alkyne end groups. The PEG region integrates to 1047 protons, which corresponds to (n=1047/4) 262 ethylene glycol units; the final molecular weight is about 12,000 g/mol.

After adding the stopper to **4.18**, the polymerization was left for 18 hours at room temperature. The solvent was removed under vacuum, leaving behind a viscous oil that was dissolved in $CDCl_3$ for crude NMR analysis. The sample was then precipitated into cold methanol and put into the freezer overnight. The solid was filtered, and the solvent was removed from the methanol filtrate; both samples were further dried under high vacuum for NMR analysis (Figure 4.64).

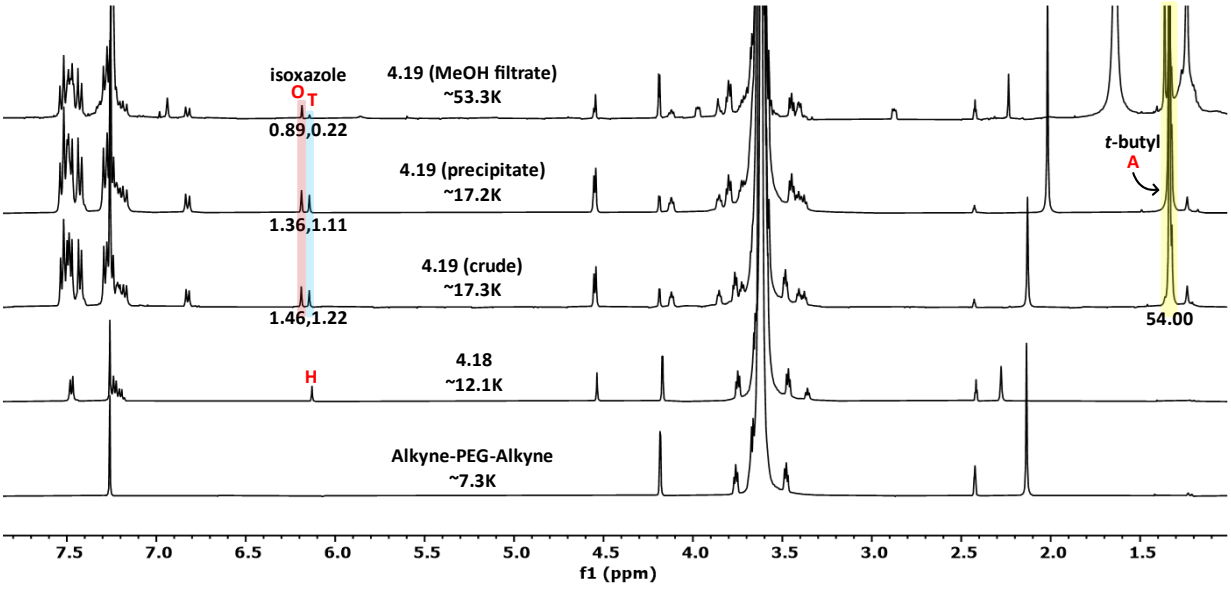

Figure 4.64. ^{1}H-NMR (500 MHz, d_1=5s, 25°C, $CDCl_3$) of **4.19** purification. t-butyl peak (1.31 ppm) set to 54H, and then isoxazole peaks (6.18 and 6.14 ppm) were integrated.

Gratifyingly, end-group analysis on the precipitate confirmed a molecular weight that matches the expected value of 17,200 g/mol for **4.19** (Figure 4.65). The crude sample is also close in molecular weight (17,300 g/mol); simple methanol precipitation successfully removed higher

molecular weight products. Increasing the amount of stopper moving forward should remove the small alkyne peak still present.

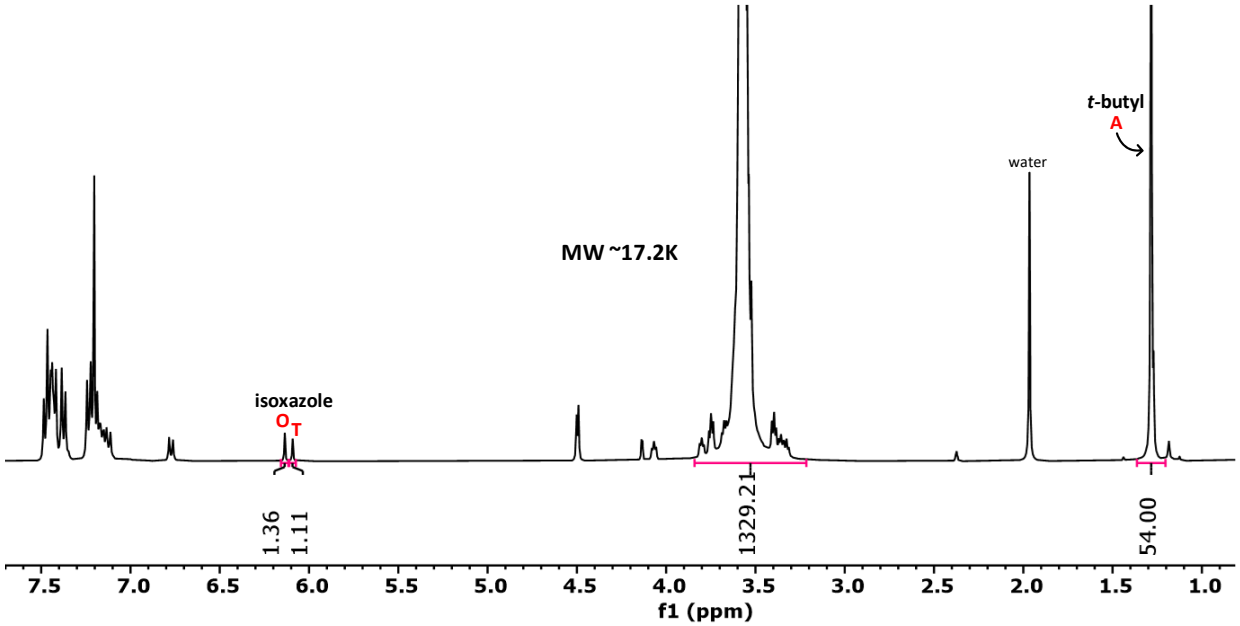

Figure 4.65. ^{1}H-NMR (500 MHz, d_1=5s, 25°C, $CDCl_3$) of dumbbell polymer precipitated in methanol **4.19**.

4.4.2.13 Synthesis of dumbbell polymer **4.21**.

The next step in optimizing the polyrotaxane synthesis involves adding bis-alkyne Bip **2.2** to the NOAC polymerization. The ratio of alkyne and nitrile-oxide end groups controls the molecular weight of the polymer, and a slight excess of alkyne-PEG-alkyne will provide the required alkyne chain ends for stoppering with nitrile-oxide **4.13**.

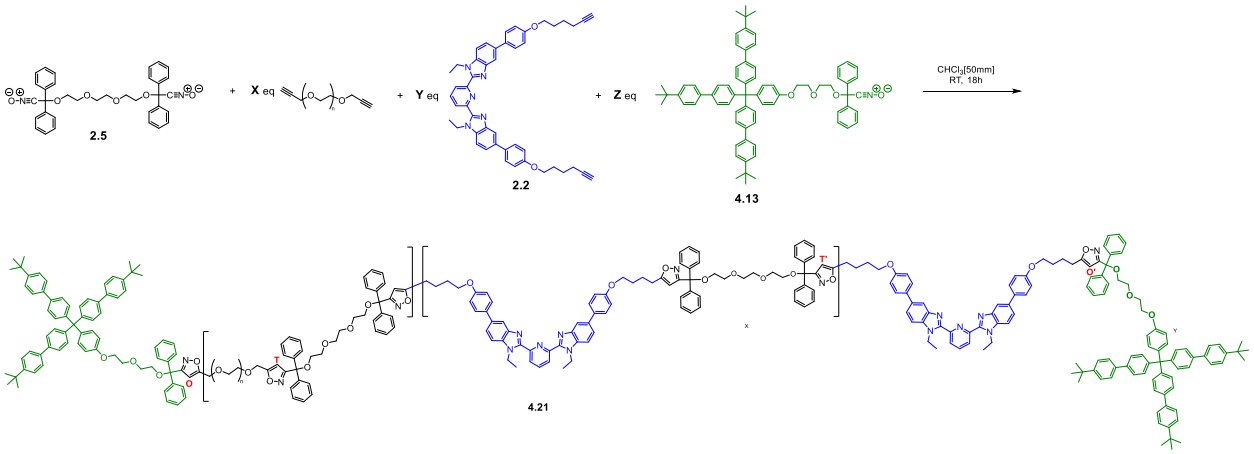

Alkyne-PEG-alkyne (0.0377 g, 0.0052 mmol, 7300 g/mol) and bis-alkyne **2.2** (0.0032 g, mmol) were added to a small vial with a stir bar. Nitrile-oxide **2.5** (0.0050 g, 0.0044 mmol) and **4.13** (0.0191 g, 0.0186 mmol) were dissolved in 177 µL chloroform and added to the reaction vial for a final concentration of 50 mM. The solution was left stirring for 18 hours, after which the solution was dried under vacuum. The crude residue was dissolved in $CDCl_3$ for NMR (Figure 4.66, bottom spectrum) and GPC (Figure 4.67, magenta) analysis.

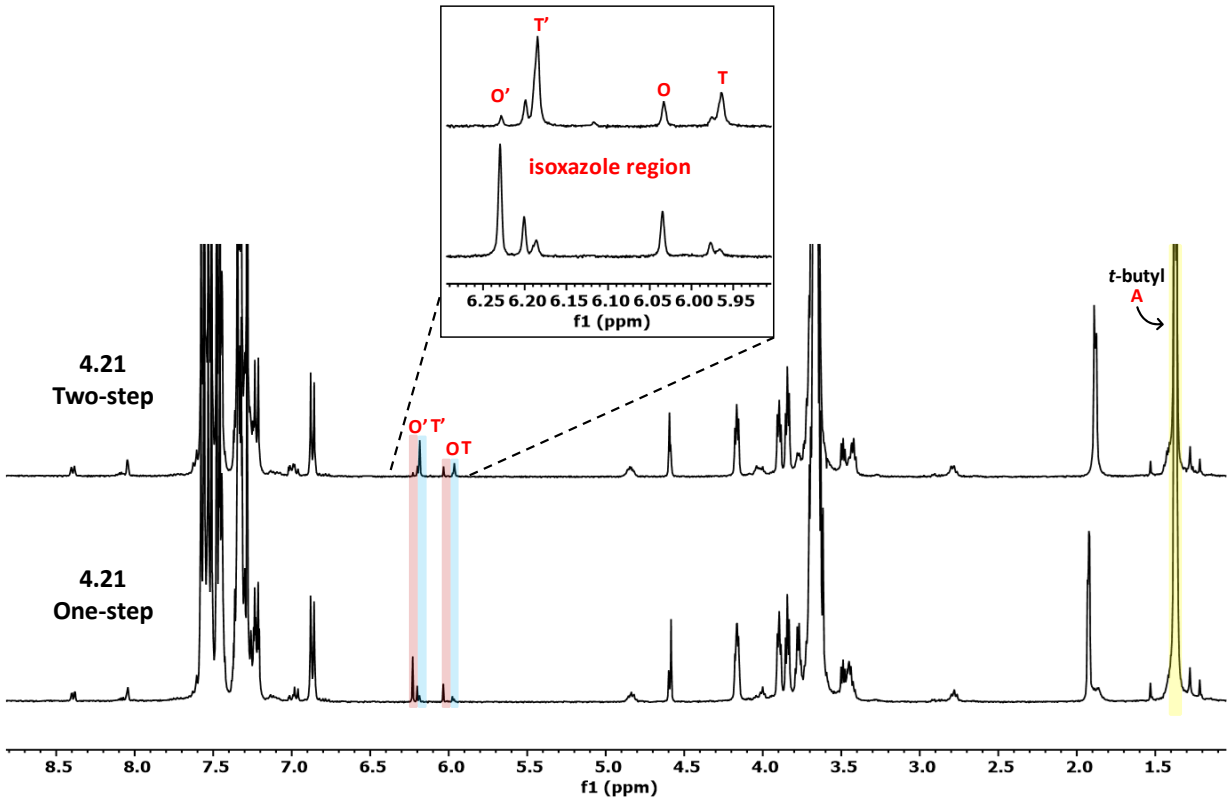

Figure 4.66. ^{1}H-NMR (500 MHz, d_1=5s, 25°C, $CDCl_3$) of Bip dumbbell polymer **4.21** (crude) prepared in one-pot (bottom spectrum; 2.1 eq **4.13**) and two-steps (top spectrum; 2.4 eq **4.13**).

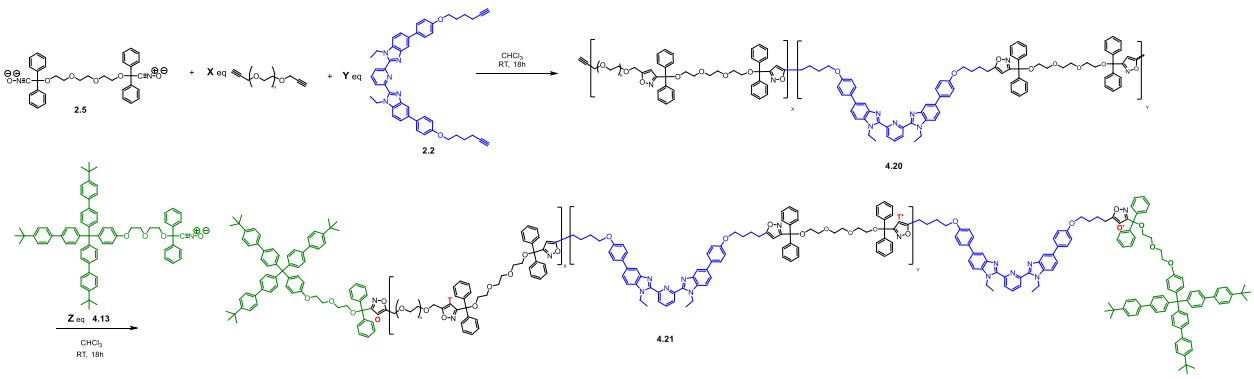

Alkyne-PEG-alkyne (0.0377 g, 0.0052 mmol, 7300 g/mol) and bis-alkyne **2.2** (0.0032 g, mmol) were added to a small vial with a stir bar. Nitrile-oxide **2.5** (0.0050 g, 0.0044 mmol) was dissolved in 118 µL chloroform and added to the reaction vial. The solution was left stirring for 18 hours, after which **4.13** (0.0219 g, 0.0213 mmol) was dissolved in 59 µL chloroform and added to the polymerization for a final concentration of 50mM. After 18 more hours, the solvent was removed under vacuum, and the crude residue was dissolved in $CDCl_3$ for NMR (Figure 4.66, top spectrum) and GPC (Figure 4.67, light blue) analysis.

The broader doublet at 6.95 ppm (corresponding to the phenyl protons on Bip) suggests a higher molecular weight backbone for the two-step method (Figure 4.66, top). The broadening of signals at 3.95 and 2.78 ppm on the alkyl chains of Bip also indicates the successful incorporation of Bip into the polymer. The presence of isoxazole peaks between 6.25 and 5.95 ppm confirms polymerization and stoppering of the alkyne chain ends. A slight excess of **4.13** was used for these experiments, helping the alkyne peak (2.54 ppm) disappear completely to form **4.21.**

Depending on the terminal alkyne from thread or PEG polymer, there are more than one possible end-group isoxazole proton environments. For consistency, the isoxazole peaks in Figure 4.53 are labeled O and T, like in the previous polymer **4.19**. There are two more isoxazole environments (O' and T') in **4.21** on either side of Bip; the more downfield signal corresponds to

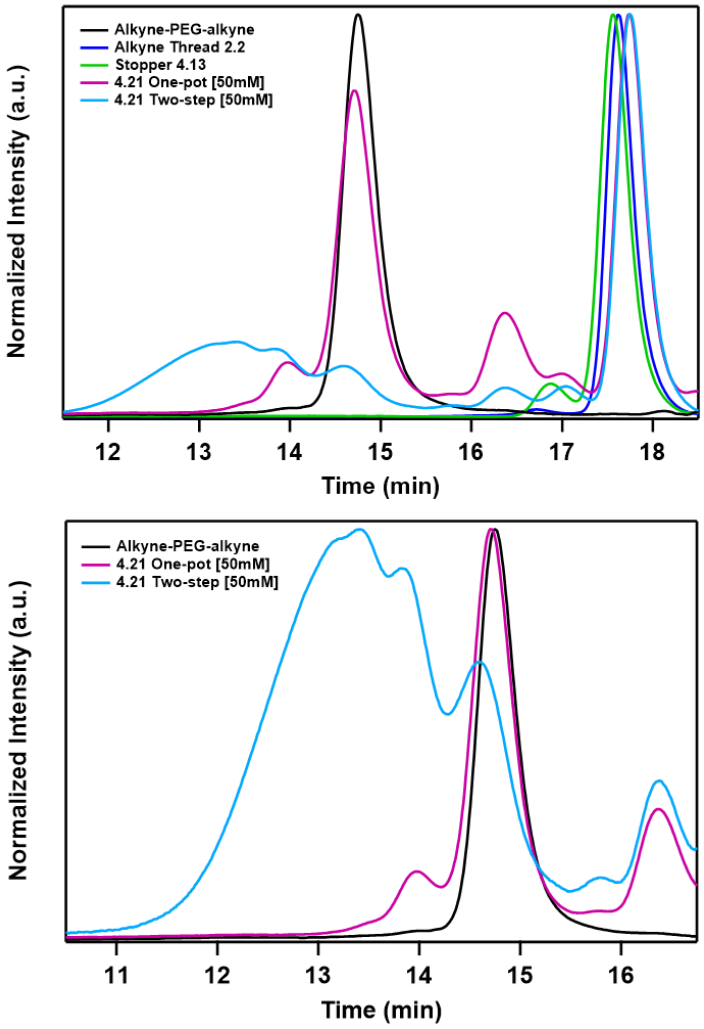

Figure 4.67. GPC (3:1 THF:DMF) traces of dumbbell polymer **4.21** (crude) formed in one-pot (magenta) and two-steps (light blue) at [50mM], compared with stopper **4.13** (green), alkyne thread **2.2** (dark blue), and alkyne-PEG-alkyne (7300 g/mol, black). The **4.21** traces in the top figure are normalized to the highest peak (excess **4.13**). Those in the bottom figure are normalized to the second-highest peak, revealing a much higher molecular weight distribution for the two-step method (light blue).

stoppered Bip chain ends (O'), and upfield the linkage between Bip and monomer units (T'). The more prominent O' peak for the one-step suggests stoppering of lower molecular weight products.

In contrast, two-step provides a larger signal for T', suggesting more monomer-Bip linkages and higher molecular weight polymer upon stoppering chain ends. Lower molecular weight products are more likely to form in the one-pot procedure because stoppers can react with both ends of the PEG macromonomer, limiting polymerization.

GPC confirmed the conclusions made from NMR (Figure 4.67); the **4.21** sample prepared in two steps (light blue) revealed a much higher molecular weight product distribution than that prepared in one pot (magenta). This two-step NOAC polymerization-stoppering procedure was applied to subsequent experiments to make metallated polyrotaxanes by substituting pseudo[2]rotaxane **4.8:2.2:Zn(II)** for thread **2.2**.

4.4.2.14 Synthesis of Bip polyrotaxane **4.23**

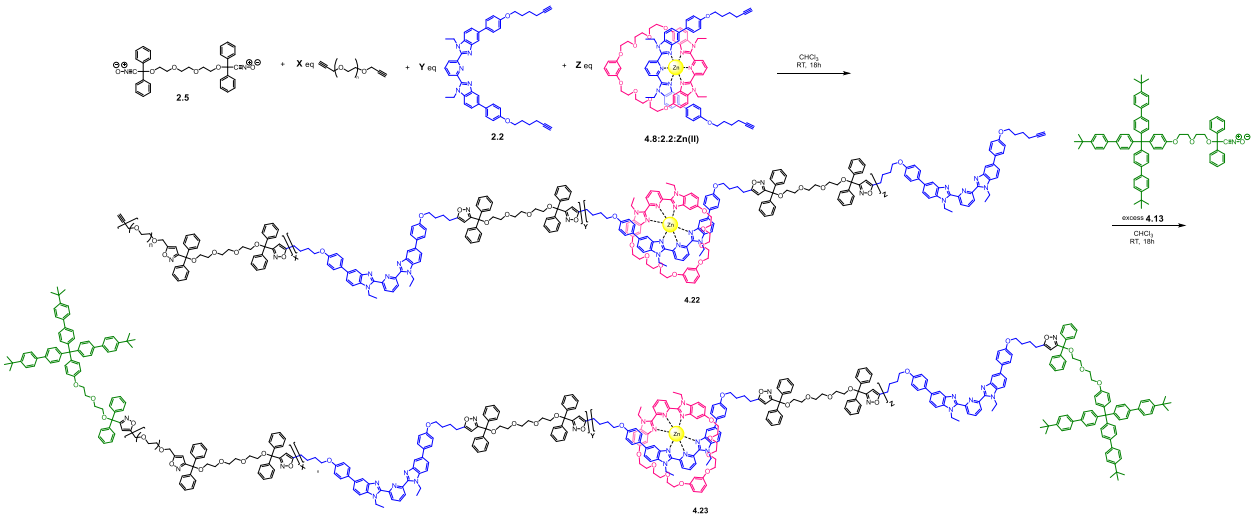

Alkyne-PEG-alkyne (X equiv., 7,300 g/mol), Bip thread **2.2** (Y equiv.), and pseudo[2]rotaxane (P2R) **4.8:2.2:Zn(II)** (Z equiv.) were weighed out (see Table 4.1) and added to a small vial with a stir bar. Nitrile-oxide monomer **2.5** (0.0050 g, 0.0089 mmol) was dissolved in 118 µL of chloroform and added to the reaction vial. The polymerization stirred for 18 hours, resulting in a viscous solution. **4.13** (0.0018 g, 0.0018 mmol) was dissolved in 59 µL chloroform and added to the polymerization for a final concentration of 50mM. After 18 more hours, the solvent was removed via rotary evaporation, and the crude samples were dried under high vacuum overnight. The crude mixture was precipitated into a mixture of cold hexanes/chloroform (6/1 v/v, 35 mL) and centrifuged (8000 rpm, 15 min) 3x to remove the excess stopper and lower molecular weight products.

Integrating the aromatic region confirms the systematic incorporation of pseudo[2]rotaxane into the polymer backbone (Figure 4.68). The *p*-pyridyl (A/A, 9.14 ppm) and *m*-pyridyl (B/B, 8.66 and 8.74 ppm) Bip peaks on **4.8:2.2:Zn(II)** were integrated with the *m*-pyridyl (B, 8.37 ppm) Bip peak on **2.2** to calculate the ratio of components. Therefore, a 2:4:2 (or 0.25:0.5:0.25) ratio of A/A:B/B:B would indicate the successful formation of PR50 containing equimolar amounts of thread and pseudo[2]rotaxane. Integrating the actual ratio gives 0.23:0.49:0.28, which is in good agreement with the expected 0.25:0.5:0.25 ratio. PR25 should have three threads for every pseudo[2]rotaxane, resulting in a 2:4:6 (0.167:0.33:0.50) ratio. Integration leads to 0.08:0.23:0.68 for A/A:B/B:B in PR25, which agrees well with the calculated ratio.

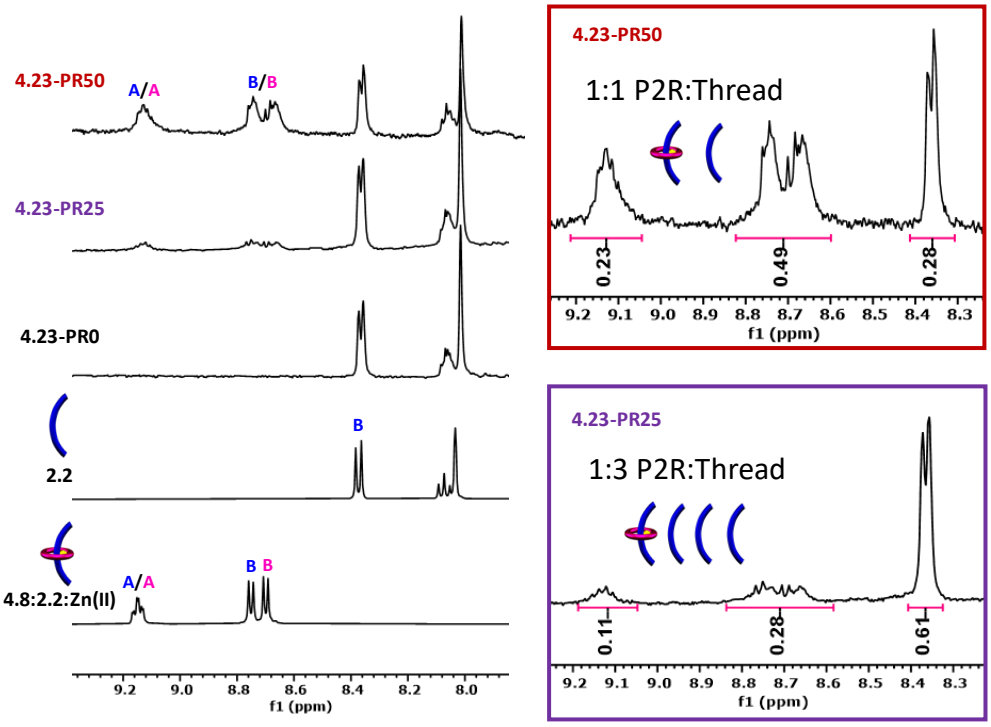

Figure 4.68. ^{1}H-NMR (500 MHz, d_1=5s, 25°C, $CDCl_3$) overlay of the aromatic region of **4.23-PR0** (precipitated) and metallated Bip polyrotaxanes, **4.23-PR25** and **4.23-PR50**, (precipitated) with indicated components for comparison.

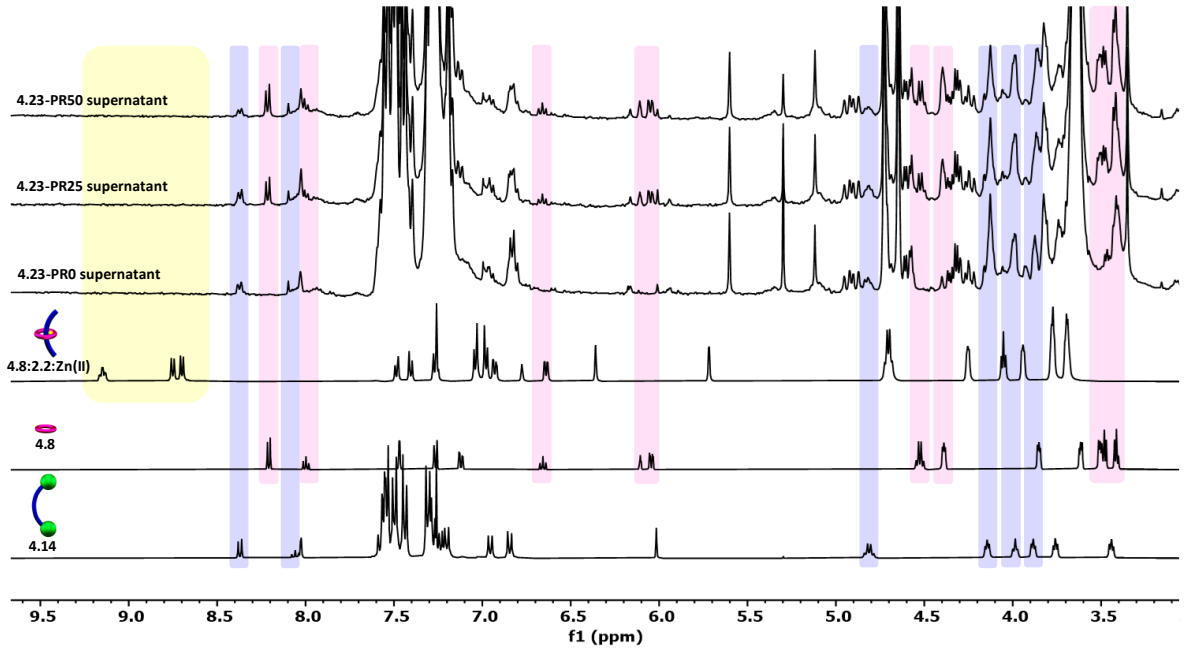

Figure 4.69. ^{1}H-NMR (500 MHz, d_1=5s, 25°C, $CDCl_3$) overlay of **4.23-PR0** supernatant and metallated Bip polyrotaxane, **4.23-PR25** and **4.23-PR50**, supernatants with indicated components for comparison.

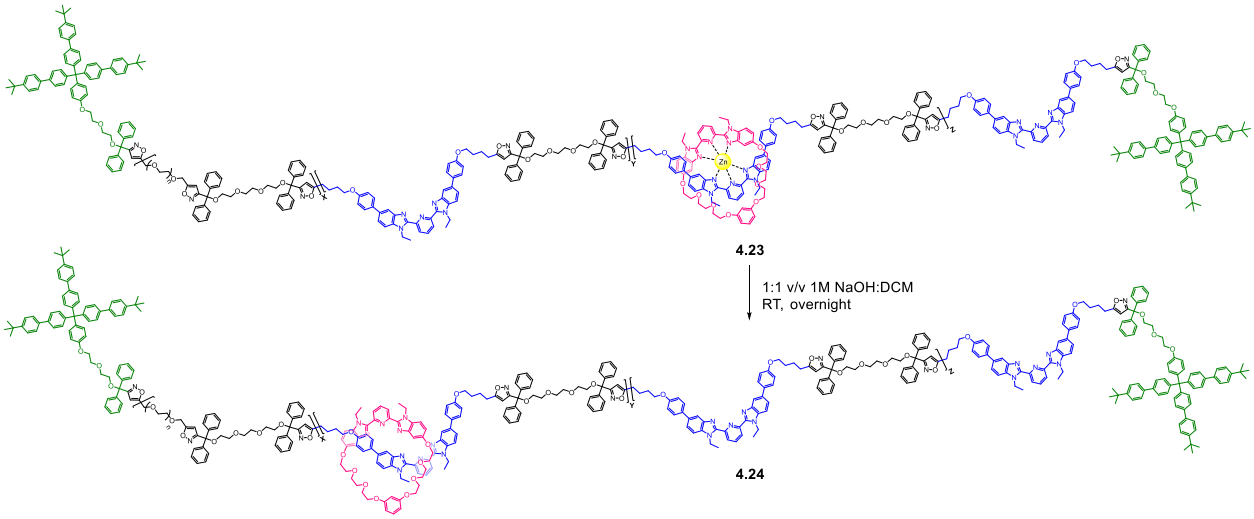

The metallated polyrotaxanes **4.23-PR25** and **4.23-PR50** (and **4.23-PR0**) were dissolved in 6 mL of DCM and added to separate vials with 6 mL of 1M NaOH and a stir bar. The solutions were stirred overnight at room temperature, and the organic (long wave UV-active) layers were collected and dried under vacuum (without heat). The crude mixtures were precipitated into a

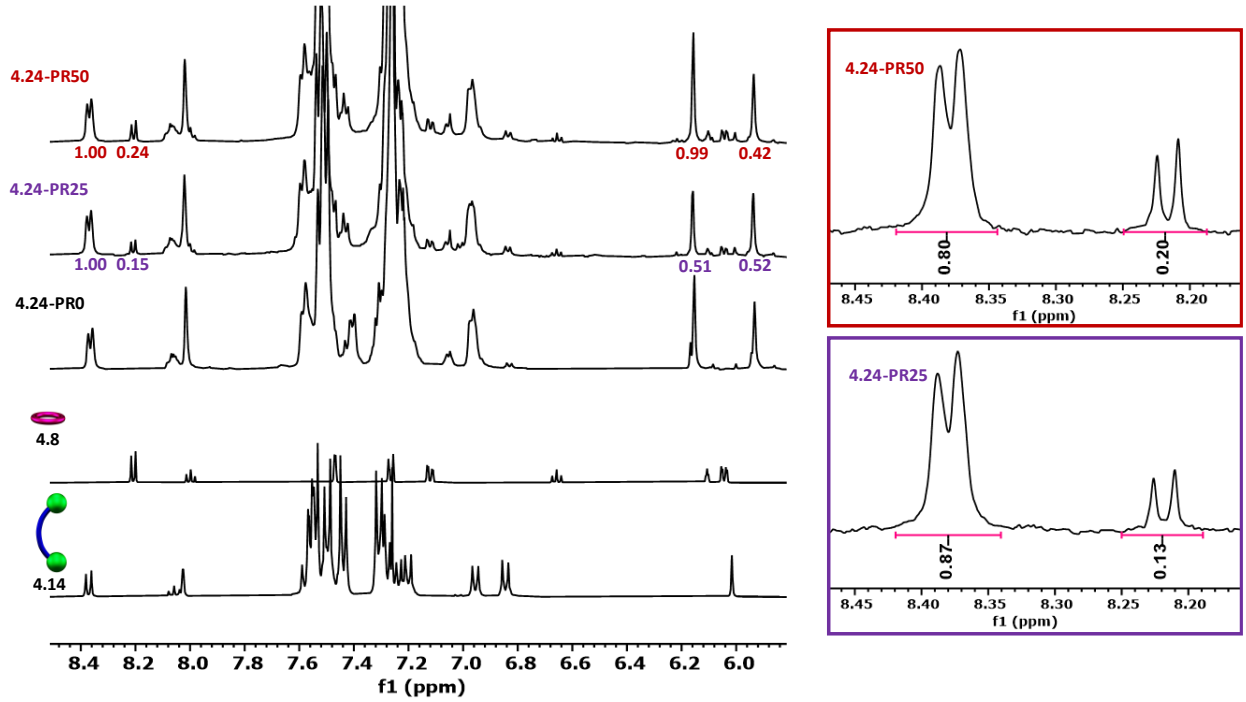

Figure 4.70. ^{1}H-NMR (500 MHz, d_1=5s, 25°C, $CDCl_3$) overlay of the aromatic region of **4.24-PR0** and demetallated Bip polyrotaxane, **4.24-PR25** and **4.24-PR50**, with indicated components for comparison (left). Integration of *para*-pyridine protons on Bip and isoxazoles for PR25 and PR50 (right).

mixture of cold hexanes/chloroform (6/1 v/v, 35 mL) and centrifuged (8000 rpm, 15 min) 3x to remove the excess stopper and lower molecular weight products.

4.4.2.15 Synthesis of Bip polyrotaxane **4.25**

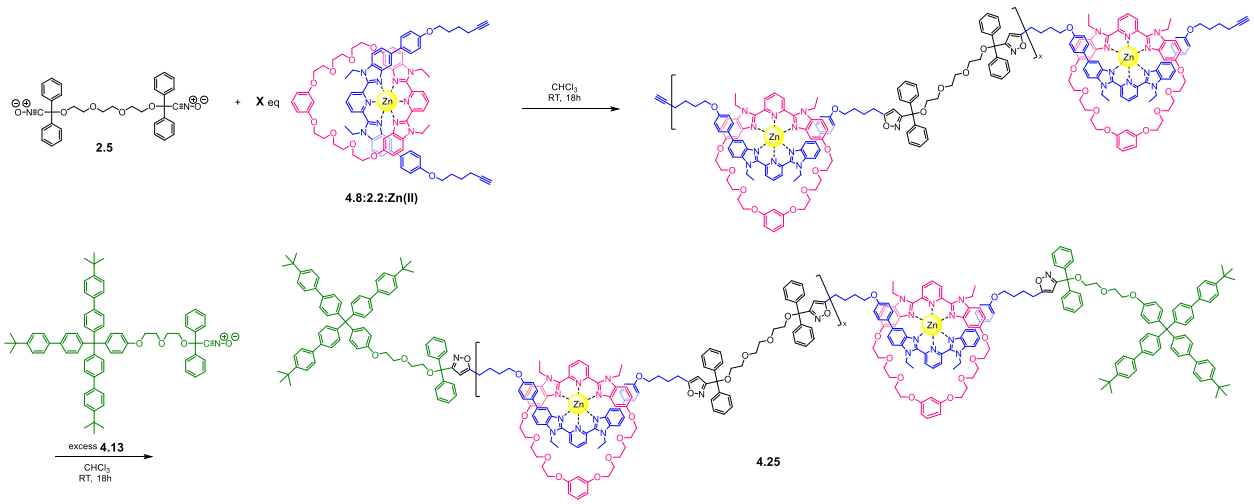

A slight excess (1:1.1) of P2R ensured alkyne chain-ends for stoppering with nitrile-oxide **4.13**. P2R **4.8:2.2:Zn(II)** (0.0040 g, 0.0019 mmol) was weighed out and added to a small vial with a stir bar. Nitrile-oxide monomer **2.5** (0.001 g, 0.0018 mmol) was dissolved in 24 µL of chloroform and added to the reaction vial. The polymerization stirred for 18 hours, resulting in a viscous solution. **4.13** (0.0004 g, 0.0004 mmol) was dissolved in 12 µL chloroform and added to the polymerization for a final concentration of 50mM. After 18 more hours, the solvent was removed via rotary evaporation, and the crude samples were dried under high vacuum overnight. The crude mixture was precipitated into a mixture of cold hexanes/chloroform (6/1 v/v, 35 mL) and centrifuged (8000 rpm, 15 min) 3x to remove the excess stopper and lower molecular weight products.

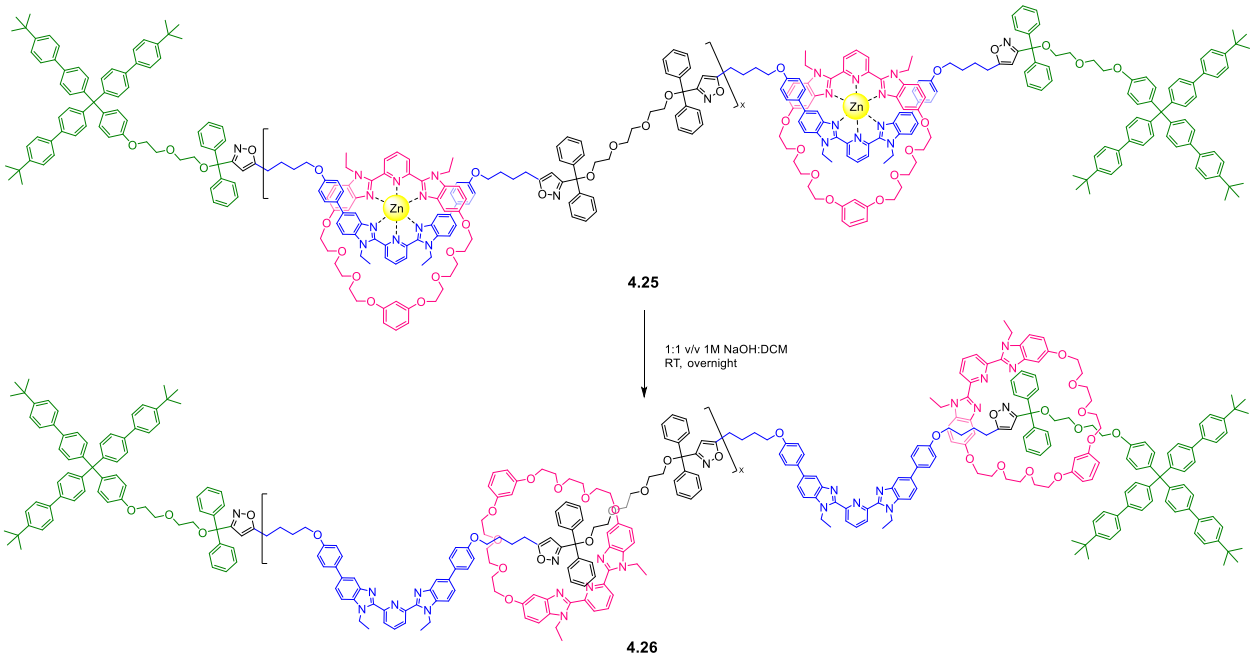

The metallated polyrotaxane was dissolved in 6 mL of DCM and added to a vial with 6 mL of 1M NaOH and a stir bar. The solution was stirred overnight at room temperature, and the organic (365 nm UV-active) layer was collected and dried under vacuum (without heat).

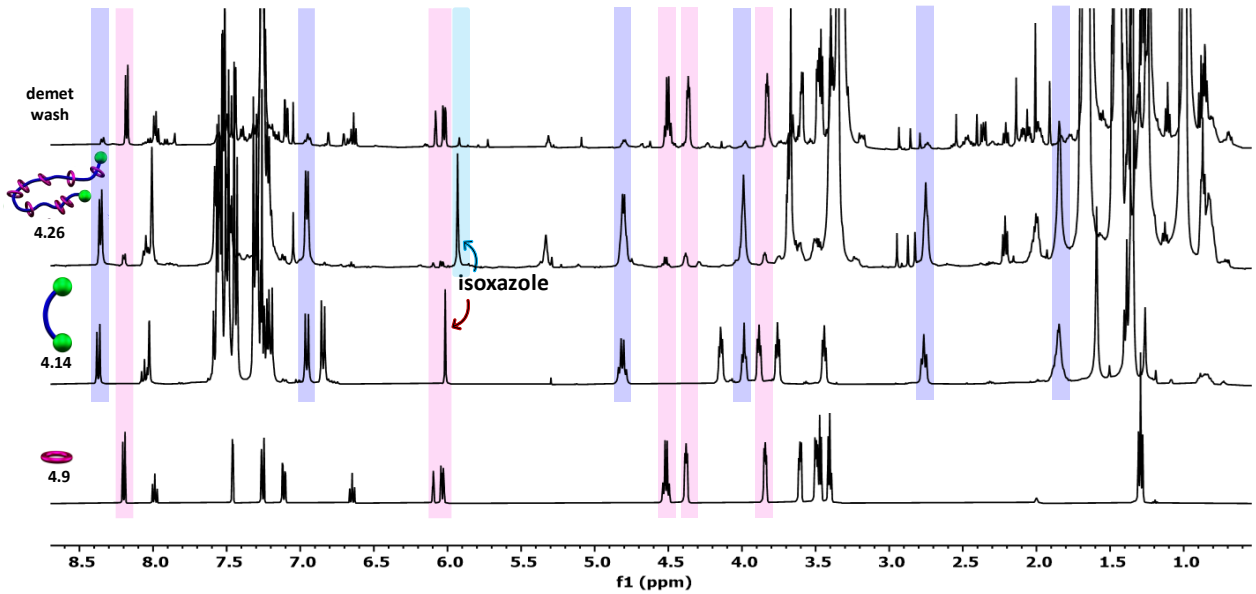

Figure 4.71. ^{1}H-NMR (500 MHz, d_1=5s, 25°C, $CDCl_3$) overlay of demetallated Bip polyrotaxane **4.26** with the demetallated wash (top spectrum) and indicated components for comparison.

4.4.2.16 Synthesis of Bipy polyrotaxane **4.27**

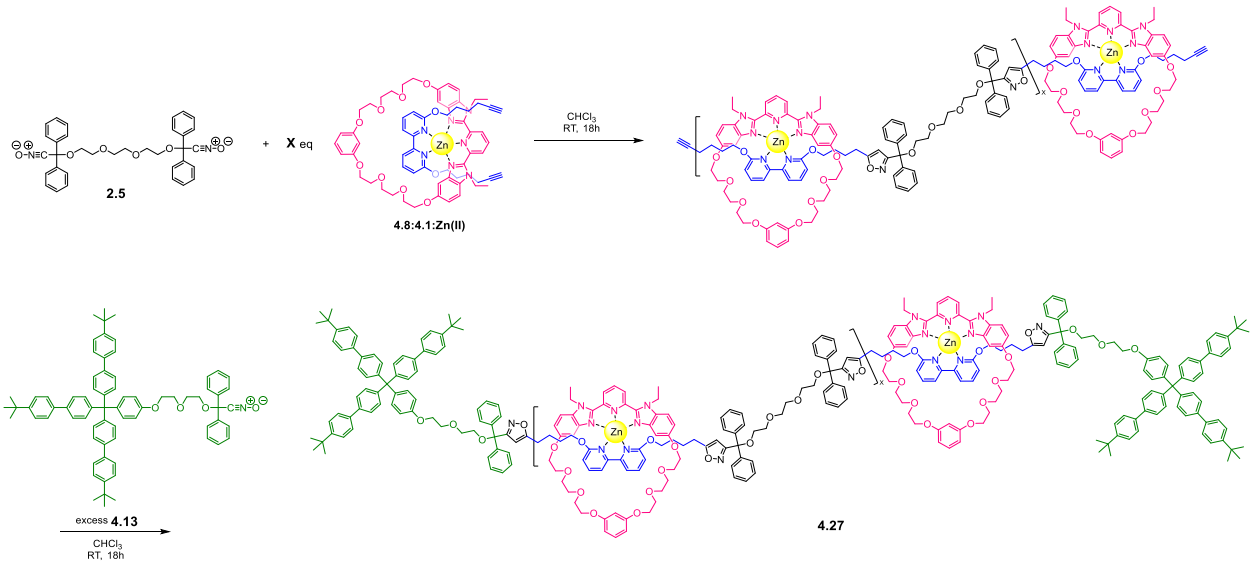

P2R **4.8:4.1:Zn(II)** (0.0033 g, 0.0019 mmol) was weighed out and added to a small vial with a stir bar. Nitrile-oxide monomer **2.5** (0.001 g, 0.0018 mmol) was dissolved in 24 µL of chloroform and added to the reaction vial. The polymerization stirred for 18 hours, resulting in a viscous solution. **4.13** (0.0018 g, 0.0018 mmol) was dissolved in 12 µL chloroform and added to the polymerization for a final concentration of 50mM. After 18 more hours, the solvent was removed via rotary

evaporation, and the crude samples dried under high vacuum overnight. The crude mixture was precipitated into a mixture of cold hexanes/chloroform (6/1 v/v, 35 mL) and centrifuged (8000 rpm, 15 min) 3x to remove the excess stopper and lower molecular weight products.

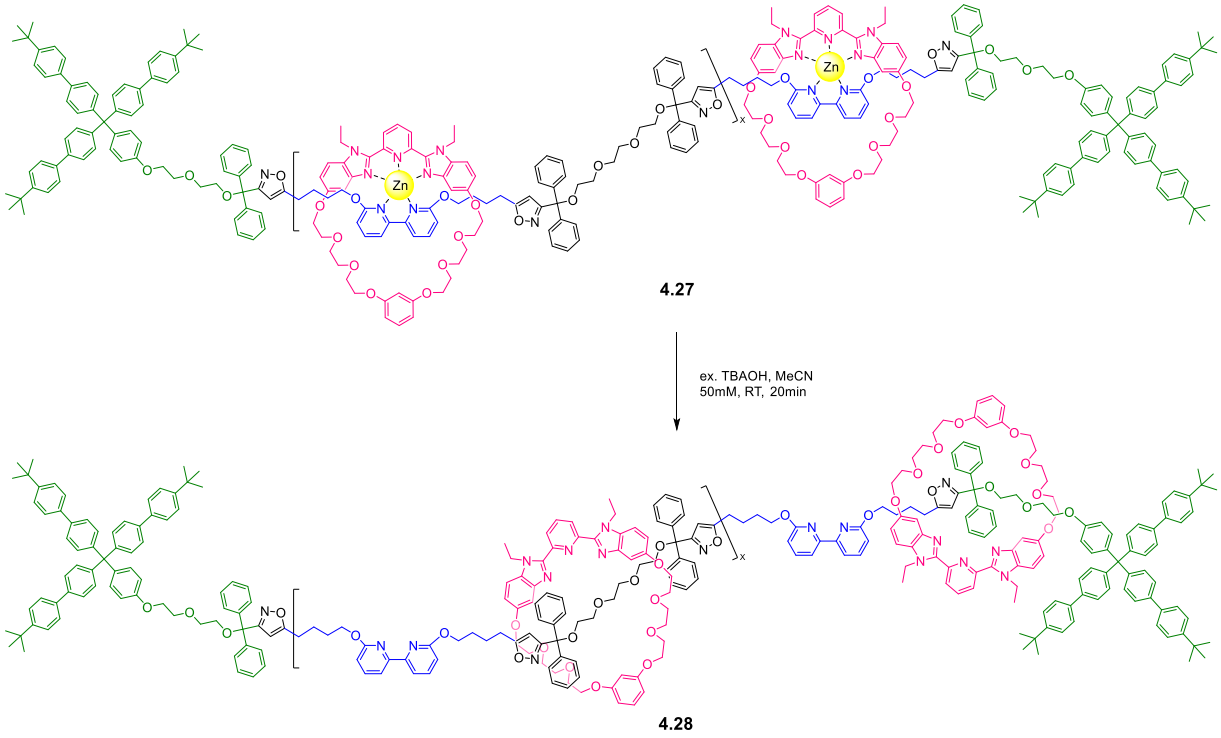

The same procedure used to demetallate **4.17** was used to demetallate polyrotaxane **4.27**. The metallated polyrotaxane **4.27** was dissolved in acetonitrile and 20 µL of tetrabutylammonium hydroxide solution (1M in MeOH) was added dropwise resulting in a rapid color change from yellow to off-white, and precipitation of the demetallated product. After 20 minutes, the solid (**4.28**) was filtered, dried, and redissolved in $CDCl_3$ for NMR analysis. Acetonitrile was removed from the demetallated wash under vacuum, and the residue was also dissolved in $CDCl_3$ for NMR analysis.

4.5 References

(1) Saito, S.; Nakazono, K.; Takahashi, E. Template Synthesis of [2]Rotaxanes with Large Ring Components and Tris(Biphenyl)Methyl Group as the Blocking Group. The Relationship between the Ring Size and the Stability of the Rotaxanes. *J. Org. Chem.* **2006**, *71* (19), 7477–7480. https://doi.org/10.1021/jo060829h.

(2) Saito, S.; Takahashi, E.; Wakatsuki, K.; Inoue, K.; Orikasa, T.; Sakai, K.; Yamasaki, R.; Mutoh, Y.; Kasama, T. Synthesis of Large [2]Rotaxanes. the Relationship between the Size of the Blocking Group and the Stability of the Rotaxane. *J. Org. Chem.* **2013**, *78* (8), 3553–3560. https://doi.org/10.1021/jo302800t.

(3) Saito, S.; Takahashi, E.; Wakatsuki, K.; Inoue, K.; Orikasa, T.; Sakai, K.; Yamasaki, R.; Mutoh, Y.; Kasama, T. Synthesis of Large [2]Rotaxanes. The Relationship between the Size of the Blocking Group and the Stability of the Rotaxane. *J. Org. Chem.* **2013**, *78* (8), 3553–3560. https://doi.org/10.1021/jo302800t.

(4) Matsumura, T.; Ishiwari, F.; Koyama, Y.; Takata, T. C−C Bond-Forming Click Synthesis of Rotaxanes Exploiting Nitrile N -Oxide. *Org. Lett.* **2010**, *12* (17), 3828–3831. https://doi.org/10.1021/ol101543x.

(5) Yuki, T.; Koyama, Y.; Matsumura, T.; Takata, T. Click Annulation of Pseudo[2]Rotaxane to [2]Catenane Exploiting Homoditopic Nitrile N -Oxide. *Org. Lett.* **2013**, *15* (17), 4438–4441. https://doi.org/10.1021/ol401986u.

(6) Lee, Y.-G.; Koyama, Y.; Yonekawa, M.; Takata, T. Synthesis of Main-Chain-Type Polyrotaxanes by New Click Polymerization Using Homoditopic Nitrile N -Oxides via Rotaxanation−Polymerization Protocol. *Macromolecules* **2010**, *43* (9), 4070–4080. https://doi.org/10.1021/ma100262g.

(7) Tsutsuba, T.; Sogawa, H.; Takata, T. Preparation of a Highly Reactive Polymer Click Reagent, PEG Nitrile N-Oxide, and Its Application in Block and Star Polymer Synthesis. *Polym. Chem.* **2017**, *8* (9), 1445–1448. https://doi.org/10.1039/C7PY00100B.

(8) Hamann, C.; Kern, J. M.; Sauvage, J. P. Zinc(II)-Templated Synthesis of a [2]-Catenane Consisting of a 2,2′,6′,2′-Terpyridine-Incorporating Cycle and a 1,10-Phenanthroline-Containing Ring. *Inorg. Chem.* **2003**, *42* (6), 1877–1883. https://doi.org/10.1021/ic020381c.

(9) Wojtecki, R. J.; Wu, Q.; Johnson, J. C.; Ray, D. G.; Korley, L. T. J.; Rowan, S. J. Optimizing the Formation of 2,6-Bis(N-Alkyl-Benzimidazolyl)Pyridine-Containing [3]Catenates through Component Design. *Chem. Sci.* **2013**, *4* (12), 4440. https://doi.org/10.1039/c3sc52082j.

(10) Beltrame, P.; Veglio, C.; Simonetta, M. Kinetics and Mechanism of 1,3-Cycloaddition of a Substituted Benzonitrile Oxide to a Series of Arylacetylenes. *J. Chem. Soc. B Phys. Org.* **1967**, No. 2416, 867–873. https://doi.org/10.1039/J29670000867.

(11) Tsutsuba, T.; Sogawa, H.; Kuwata, S.; Takata, T. Kinetically Stabilized Aliphatic Nitrile *N* -Oxides as Click Agents: Synthesis, Structure, and Reactivity. *Chem. Lett.* **2017**, *46* (3), 315–318. https://doi.org/10.1246/cl.161098.

(12) Mukaiyama, T.; Hoshino, T. The Reactions of Primary Nitroparaffins with Isocyanates 1. *J. Am. Chem. Soc.* **1960**, *82* (20), 5339–5342. https://doi.org/10.1021/ja01505a017.

(13) Wang, C. G.; Koyama, Y.; Yonekawa, M.; Uchida, S.; Takata, T. Polymer Nitrile N-Oxides Directed toward Catalyst- and Solvent-Free Click Grafting. *Chem. Commun.* **2013**, *49* (70), 7723–7725. https://doi.org/10.1039/c3cc42992j.

(14) Wu, Q.; Rauscher, P. M.; Lang, X.; Wojtecki, R. J.; de Pablo, J. J.; Hore, M. J. A.; Rowan, S. J. Poly[n]Catenanes: Synthesis of Molecular Interlocked Chains. *Science (80-.).* **2017**, *358* (6369), 1434–1439. https://doi.org/10.1126/science.aap7675.

(15) Hertzog, J. E.; Maddi, V. J.; Hart, L. F.; Rawe, B. W.; Rauscher, P. M.; Herbert, K. M.; Bruckner, E. P.; de Pablo, J. J.; Rowan, S. J. Metastable Doubly Threaded [3]Rotaxanes with a Large Macrocycle. *Chem. Sci.* **2022**, *00*, 1–12. https://doi.org/10.1039/d2sc01486f.

(16) Saito, S.; Nakazono, K.; Takahashi, E. Template Synthesis of [2]Rotaxanes with Large Ring Components and Tris(Biphenyl)Methyl Group as the Blocking Group. The Relationship between the Ring Size and the Stability of the Rotaxanes. *J. Org. Chem.* **2006**, *71* (19), 7477–7480. https://doi.org/10.1021/jo060829h.

(17) McKenzie, B. M.; Miller, A. K.; Wojtecki, R. J.; Johnson, J. C.; Burke, K. A.; Tzeng, K. A.; Mather, P. T.; Rowan, S. J. Improved Synthesis of Functionalized Mesogenic 2,6-Bisbenzimidazolylpyridine Ligands. *Tetrahedron* **2008**, *64* (36), 8488–8495. https://doi.org/10.1016/j.tet.2008.05.075.

5 Exploring Thiol-Maleimide Stoppering of Doubly-Threaded Pseudo[3]Rotaxanes

5.1 Introduction

Rotaxanes consisting of one ring threaded have been synthesized in myriad ways; however, increasing the number of interlocked components in the rotaxane is far from trivial.[1] Finding the correct ring size and stoppering conditions are vital for accessing rotaxanes in high yield. Metal-ligand coordination has been widely employed for its efficient and facile approach to rotaxane assembly; ligands gather around a metal ion to form a pseudorotaxane that can be subsequently stoppered to afford the interlocked product after demetallation. Current template strategies for synthesizing rotaxanes have focused on utilizing one metal center to assemble rotaxane components and typically use monovalent rings. This chapter focuses on synthesizing ditopic macrocycles and the metal-templated assembly of doubly-threaded [3]rotaxanes using click chemistry to stopper a metallated pseudo[3]rotaxane complex (Figure 5.1).

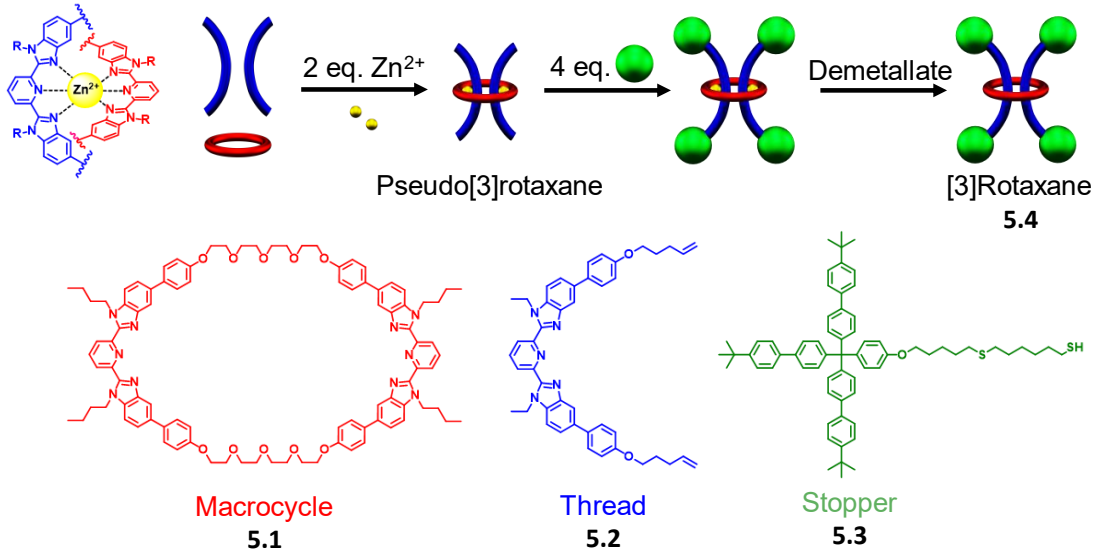

Figure 5.1. Metal-template approach for doubly-threading. Coordination of Bip (2,6-bis(N-alkyl-benzimidazolyl)pyridine) ligands with Zn^{2+} in a 2:1 fashion and the original components used in preliminary rotaxane experiments by Dr. Katie Herbert. A ditopic macrocycle (**5.1**, red, 68-atom) and two threads (**5.2**, blue) self-assemble in the presence of Zn^{2+} to form a doubly-threaded pseudo[3]rotaxane. A thiol-terminated stopper group (**5.3**, green) was used to cap the reactive alkene chain ends on the thread, which should form the doubly-threaded [3]rotaxane **5.4** after demetallation with a dilute solution of base.

A similar synthetic design employing two coordination sites per ring has been successfully applied to the synthesis of [3]catenanes (comprised of 3 interlocking rings)[2] and linear poly[*n*]catenanes[3] to create the longest interlocked molecular chain to date. Zn^{2+} ions facilitate the threading of two linear components through a single ditopic ring in a thermodynamically driven process. Forming the doubly-threaded architecture depends on the coordination of 2,6-bis(N-alkyl-benzimidazolyl)pyridine (Bip) ligands with transition metals such as Zn^{2+} or ions Fe^{2+} in a 2:1 fashion (Figure 5.1, top left).[4] The resulting pseudo[3]rotaxane (P3R) is a consequence of the exact stoichiometry employed and the principle of maximum site occupancy.[5] The two ligands in the macrocycle cannot bind to the same metal ion (as confirmed by UV-Vis studies on the ditopic 68-atom macrocycle);[3] thus, the only way for the system to maximize its enthalpic gain is for all Bip ligands to form a 2:1 Bip:Zn^{2+} complex in the formation of a thermodynamically stable pseudo[3]rotaxane assembly.[6]

The stability of the metal complex is vital for keeping the ring interlocked during stoppering, or rotaxanes will not form, so avoiding difficult reaction conditions is critical. Accessing interlocked products also requires complete conversion; if only three of the four thread ends are stoppered, the entire [3]rotaxane will fall apart after demetallation if the ring is too big to stabilize the resulting [2]rotaxane. Prior work on this project used P3R assembled from a 68-atom ditopic macrocycle **5.1** (Figure 5.1, bottom left) with two Bip-containing bis-alkene rotaxane threads **5.2** (Figure 5.1, bottom center) upon the addition of Zn^{2+} ions. The reactive chain ends on the rotaxane thread were designed to react with thiols on triaryl stopper **5.3** (Figure 5.1, bottom right) to form the doubly-threaded [3]rotaxane product **5.4** after demetallation (Figure 5.1, top right). Thiol-ene click chemistry was the first reaction explored for stoppering the P3R complex assembled from Bip, but it consistently led to an incomplete reaction between stopper **5.3** and the

chain ends of **5.3**. UV and thermal initiation did not lead to quantitative conversion using either AIBN or V-70, respectively, concluding that the Bip:metal complex acts as a radical trap to inhibit the thiol-ene stoppering reaction.

Click polymerizations have widened the scope of materials science, providing high reaction rates at a lower temperature and an easy route to bioconjugation and other post-polymerization modifications. Various well-defined hydrogels and polymer architectures have been accessed using different click chemistries.[7,8] For example, the Michael Addition reaction between thiol and maleimide has been highly successful for bioconjugation reactions with cysteine, a thiol-functionalized amino acid.[9–11]

Maleimides are the most reactive vinyl groups in thiol-Michael reactions; the Michael addition between maleimide and thiol requires only a catalytic amount of base and does not require light or heat to initiate the reaction (Figure 5.2).[9] This chapter tests the Michael Addition between a maleimide thread component and the thiol stopper **5.3**. The advantages and disadvantages of this click chemistry for stoppering the P3R metal complex will also be discussed.

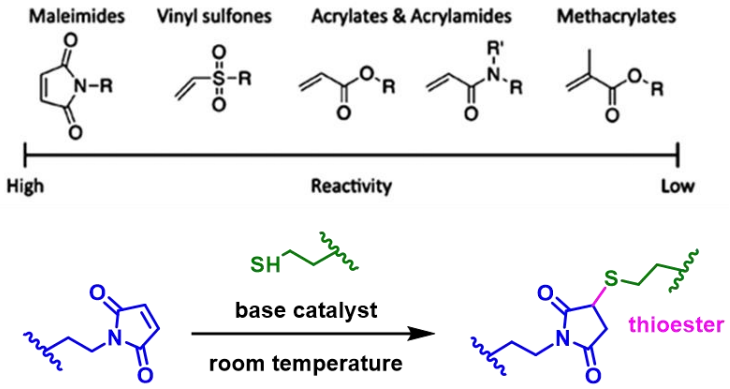

Figure 5.2. Thia-Michael addition with maleimide. Reactivity of commonly used vinyl groups in thiol-Michael addition reactions (top). N-alkylation of maleimide provides highly reactive rotaxane threads that can react with the thiol stopper in the presence of a catalytic amount of base to form a thioester bond. This reaction proceeds at room temperature and can be performed in a variety of solvents. Adapted from Ref. 9 with permission from American Chemical Society.

5.2 Results and Discussion

5.2.1 Finding a Compatible Stoppering Catalyst

The vinyl group on maleimide is extremely electron deficient, which makes it highly reactive with thiols in the presence of a base catalyst (Figure 5.3).[9] Metallosupramolecular polymers comprised of similar Bip ligands coordinated with transition metal ions demetallate under basic conditions such as diethylenetriamine or tetrabutylammonium hydroxide. DBU (1,8-diazabicycloundec-7-ene) is a viable option for the stoppering catalyst because it is sterically hindered and non-nucleophilic. This decreases the chance of DBU interfering with the complex and increases the likelihood of it reacting with the thiol to perform the Michael Addition instead. Mechanistically, DBU extracts a proton from the thiol to form the conjugate acid and thiolate anion that reacts readily with the maleimide vinyl group; an intermediate anion then reacts with the conjugate acid to create the thioester product and regenerates the catalyst (Figure 5.3). To determine DBU's reactivity and potential as a stoppering catalyst, the stability of the metal

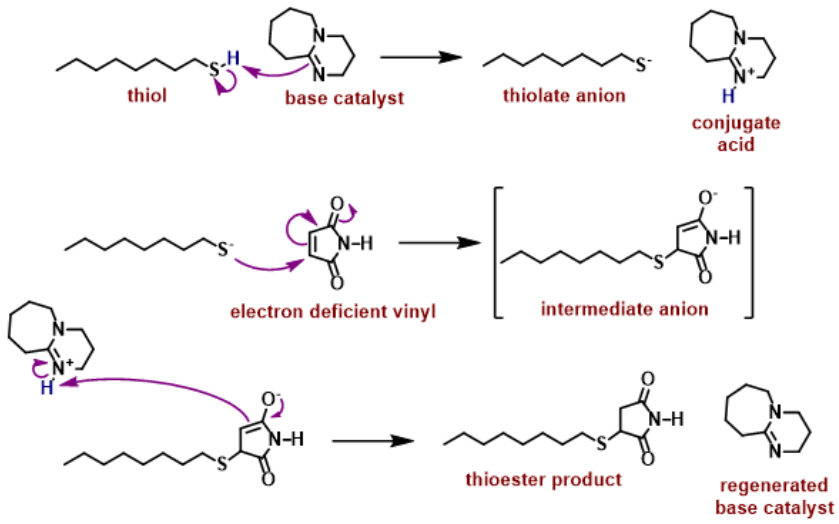

Figure 5.3. Base-catalyzed Michael Addition between a thiol and the electron-deficient vinyl group (such as maleimide) yields the thioester product and the regenerated base catalyst. DBU (1,8-diazabicycloundec-7-ene) is a sterically hindered, non-nucleophilic base that was chosen to limit interactions with the 2:1 Bip:Zn(II) metal complex.

complex must be investigated, and reaction conditions need to be optimized to guarantee stoppering of the P3R without dethreading.

5.2.2 Testing Metal Complex Stability

Making a doubly-threaded complex starts with a 1 to 2 stoichiometric ratio of the ring-to-thread components, verified via NMR integration. ^{1}H Nuclear Magnetic Resonance (NMR) titrations provide a systematic way to monitor the metallation of Bip. A solution of $Zn(NTf_2)_2$ was titrated into an NMR tube containing the Bip ligand to form an octahedral metal complex. Signals corresponding to aromatic hydrogens on the central pyridine of the Bip ligand (8.33 ppm) will shift downfield (8.75 ppm) with metal binding because of electron deshielding (Figure 5.4).

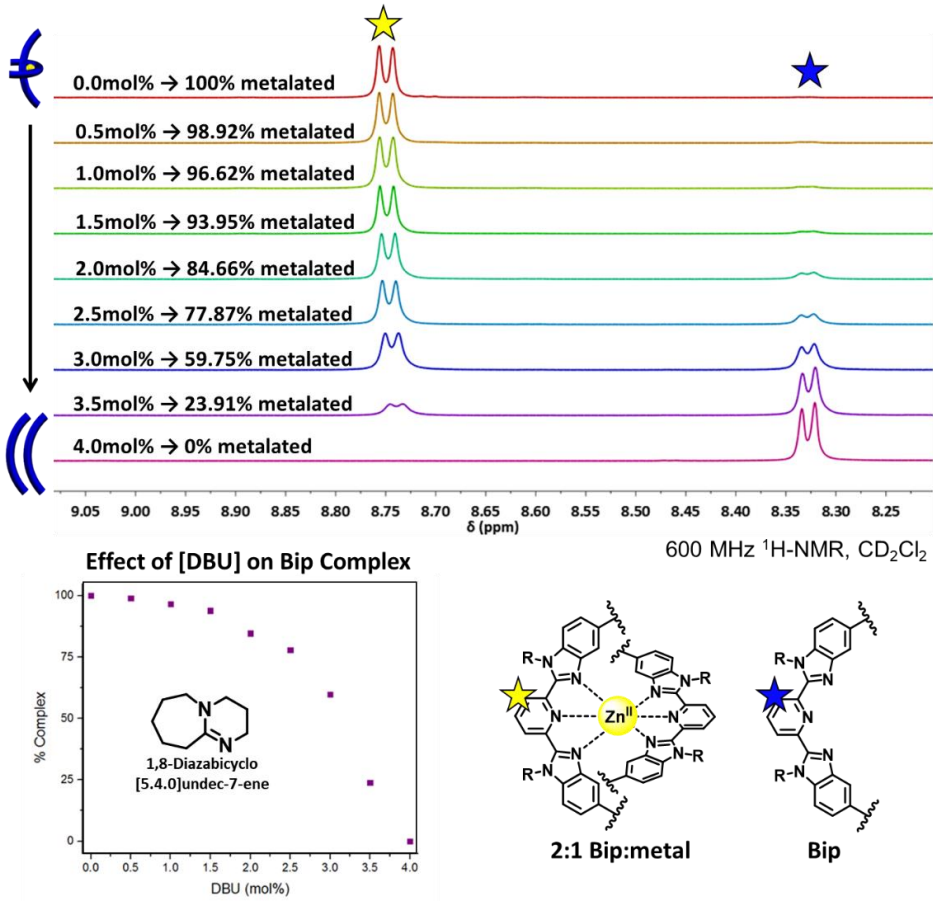

Figure 5.4. Effect of DBU Concentration on 2:1 Bip:metal. 1H-NMR (600 MHz, 25°C, CD2Cl2) titration of DBU to 2:1 Bip:metal complex (top). Plot showing the decrease in the percentage of the metal complex as DBU is added during the titration (bottom left). Doublets correspond to the meta-proton on the inner pyridine ring of the Bip ligand (bottom right).

^{1}H NMR titration experiments confirmed 1,8-diazabicyclo[5.4.0]undec-7-ene (DBU) to be a viable option for our catalyst as it is a sterically hindered, non-nucleophilic base. Small increments of DBU were titrated into the metal complex (dissolved in CD_2Cl_2), confirming its stability below 1.0 mol% DBU, thus providing a ceiling concentration under which to investigate reaction progress at even lower amounts of DBU. Full demetallation of the 2:1 complex was observed at 4.0 mol% DBU.

5.2.3 Optimizing Reaction Conditions

After verifying Bip complex stability at DBU concentrations below 1.0 mol%, the maleimide-thiol conditions were further investigated to determine the minimum DBU required for the reaction. A test reaction between maleimide and 1-octanethiol was performed at room temperature in the presence of 0.1 mol% of DBU in DCM (200 mM concentration) and was found to react instantaneously and quantitatively. The vinyl hydrogens on maleimide appear as a strong, sharp singlet at 6.7 ppm in ^{1}H-NMR, which makes it the ideal diagnostic peak for reaction monitoring; the peak completely disappears upon the addition of base, indicating complete conversion (Figure 5.5). Conjugation between the thiol and maleimide results in a new region of peaks forming between 3.8 and 2.4 ppm. The click reaction also proceeds in DMF, which acts as a Lewis basic solvent and catalyst for the Michael Addition.

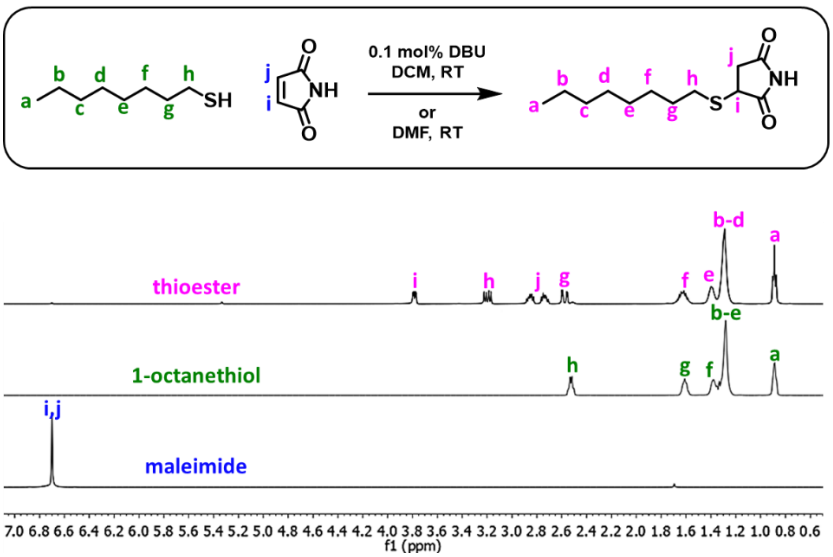

Figure 5.5. Thiol-maleimide click proof-of-concept. ^{1}H-NMR spectra (600 MHz, $CDCl_3$) showing maleimide reacting with 1-octane thiol in the presence of 0.1 mol% DBU in CD_2Cl_2 to form the thioester product. Similar results are seen when DMF is used as the reaction solvent, wherein the amines can catalyze the click reaction with thiol.

5.2.4 Designing Maleimide Rotaxane Thread

Maleimides are known to react with thiols readily;[9] therefore, a maleimide-functionalized thread component was designed to react with the thiol on triaryl stopper **5.3**. N-alkylation of maleimides from hydroxy chain ends is a common technique for attaching maleimide groups to polymers and other molecules for bioconjugation reactions.[9–11] Attaching extended hydroxy groups on Bip (**5.5**) allows the thread to undergo Mitsunobu conditions[12] to form the desired thread component **5.6** with the exposed, highly reactive vinyl group (Figure 5.6).

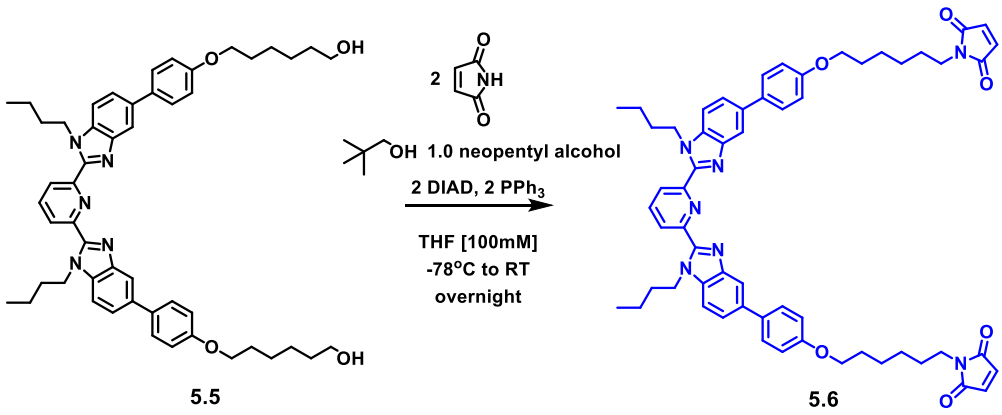

Figure 5.6. Mitsunobu synthesis of maleimide thread **5.6** (see Experimental).

The key to creating the maleimide thread in high yields is the addition of neopentyl alcohol (Figure 5.7) which acts as a non-reacting ligand to push the reaction forward to the final SN2 displacement. Without the neopentyl alcohol, a dark red color was observed, corresponding to the maleimide reaction with a quaternary phosphonium salt intermediate that inhibits the reaction.

Dr. Qiong Wu was interested in forming pseudo[3]rotaxanes from smaller ligands to thread through tighter macrocycles, leading to the alkene-functionalized Bipy thread **5.11** (Figure 5.8). Like the functionalization of phenolic Bip derivatives, Williamson ether conditions attach brominated alkyl chains to the 2,2'-bipyridine-6,6'-diol (Bipy) ligand. Similar reaction conditions were employed to access the dihydroxy Bipy derivatives required for functionalizing chain-ends with maleimide to form **5.13**. The hydroxy chains were extended even further (using 11-bromo-1-

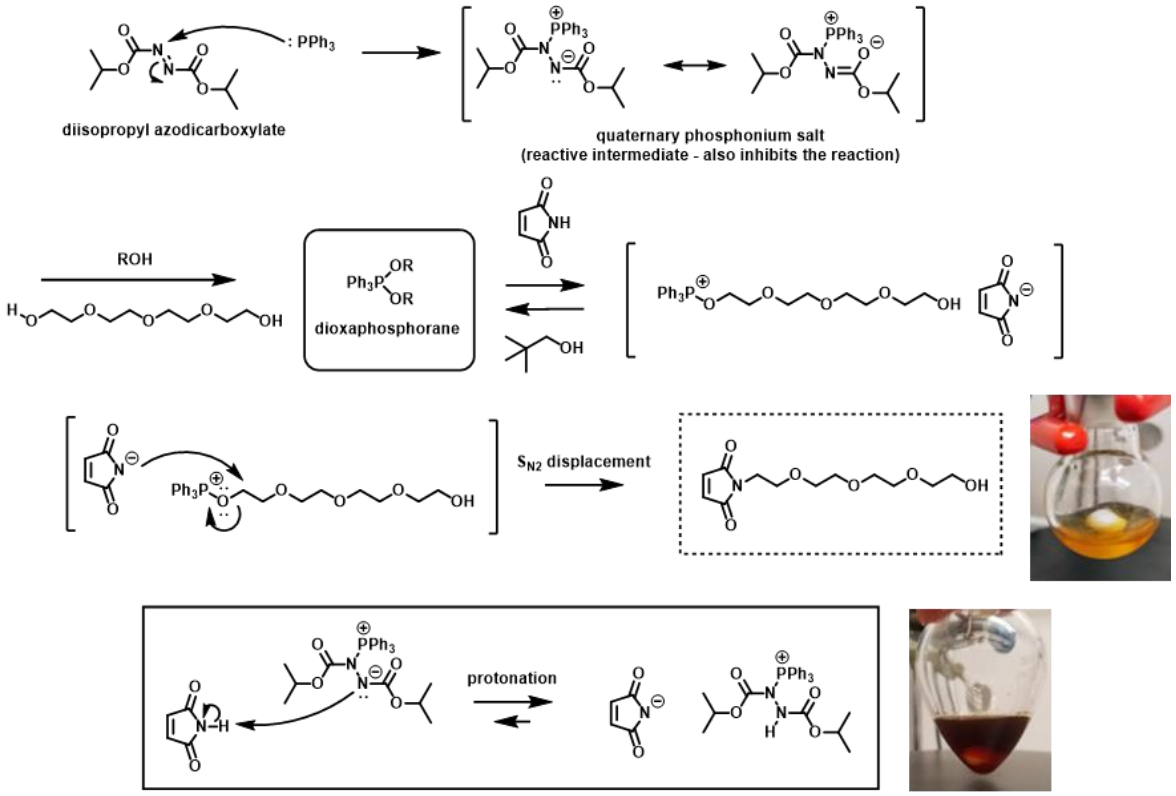

Figure 5.7. Modified Mitsunobu reaction mechanism. Neopentyl alcohol acts as a non-reacting ligand for phosphorus to drive the reaction forward. Without the ligand, maleimide can protonate the reactive intermediate, hindering the reaction and turning the color dark red. The successful N-alkylation of the maleimide group results in a yellow-orange crude mixture.

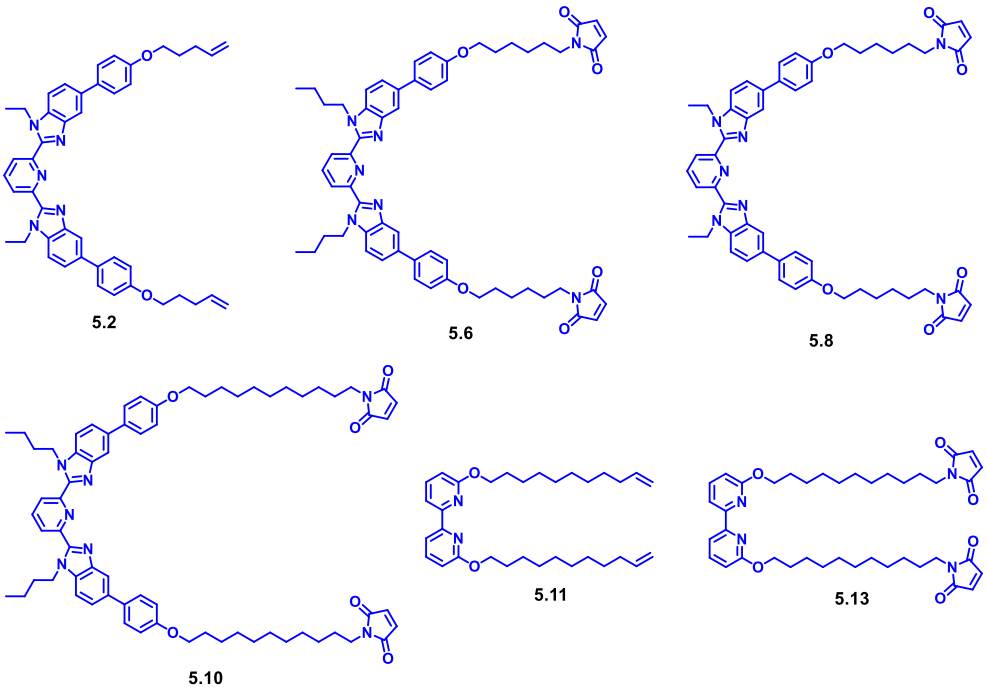

Figure 5.8. Different thread derivatives discussed in this chapter (see Experimental).

undecanol) with the idea that keeping the maleimide moiety farther from the pseudo[3]rotaxane would limit potential interactions with the metal template. Figure 5.8 shows the library of thread components discussed in this chapter.

5.2.5 Thiol-Maleimide Dumbbell Experiments

After successfully synthesizing maleimide threads and thiol stopper, ^{1}H-NMR titration experiments evaluated the reactivity of the two components under base-catalyzed conditions. Testing both Bip- and Bipy-based maleimide threads determined whether the type of ligand changes the efficiency of this stoppering chemistry. Monitoring the disappearance of the maleimide singlet (corresponding to the reactive vinyl group) at 6.7 ppm while adding small increments of the DBU catalyst determined reaction progress (see Experimental); new peaks formed a conjugation region, corresponding to the thioester dumbbell product between 3.7 and 2.4 ppm (Figure 5.9).

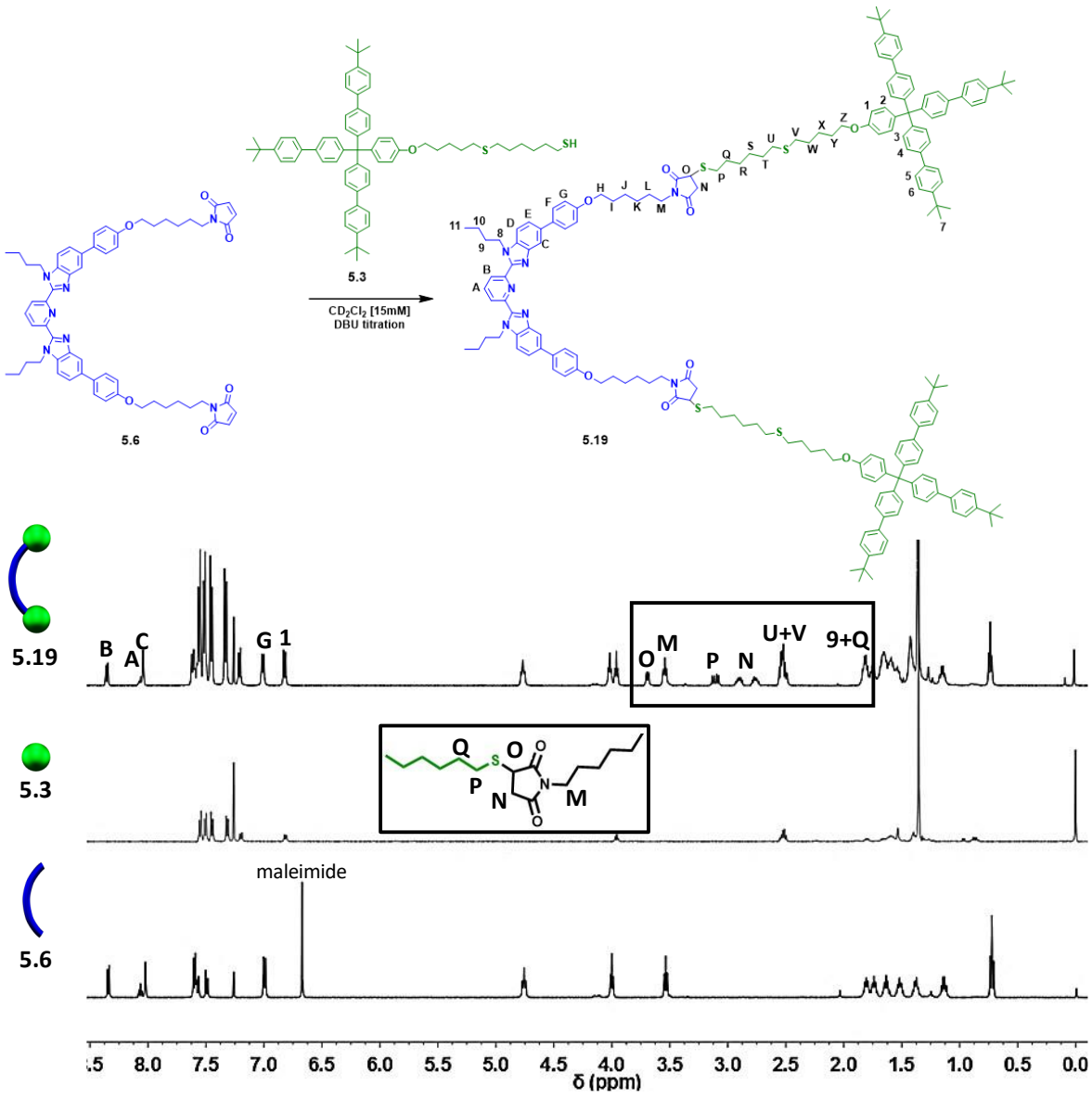

Figure 5.9. Synthesis of thioester Bip dumbbell **5.19** (top). ^{1}H-NMR (500 MHz, 25°C, CD_2Cl_2) of **5.19** with indicated components for comparison (bottom).

The Bipy system **5.20** required less DBU (0.2 mol%) to drive the Michael addition to completion (Figure 5.10); the Bip dumbbell **5.19** required more than 2.5 mol% DBU to reduce the maleimide singlet significantly. This result is likely due to the more significant number of nitrogen atoms in the Bip framework that could interfere with the thiolate anion and thioester bond formation under basic conditions.

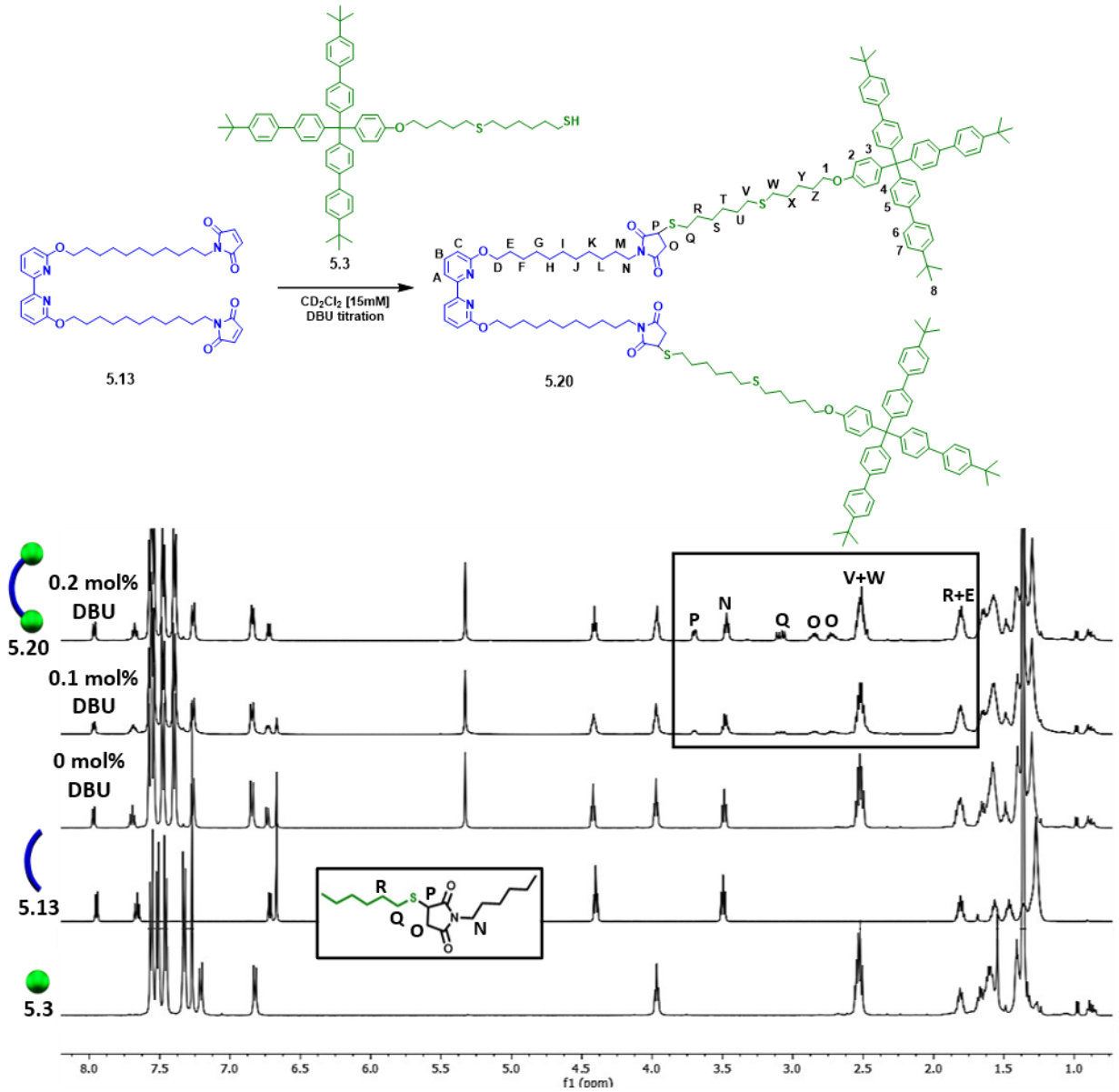

Figure 5.10. Synthesis of thioester Bipy dumbbell **5.20** (top). ^{1}H-NMR (500 MHz, 25°C, CD_2Cl_2) of Bipy dumbbell **5.20** titration with indicated components for comparison (bottom).

Highly polar solvents such as dimethyl sulfoxide (DMSO) and dimethylformamide (DMF) allow the thiol-maleimide reaction to proceed without the addition of a catalyst. The polarity of the solvent helps facilitate the formation of the active thiolate ion, acting as a catalyst for the Michael Addition.[9] This approach was also tested on **5.6** to determine if DMF could be used to

attach thiol stoppers to the pseudo[3]rotaxane complex (see Experimental). The stoppering reaction to form **5.21** was unsuccessful in DMF, a nitrogen-rich solvent.

5.2.6 Synthesizing Smaller Rings

Through collaboration with Dr. Phillip Rauscher in the de Pablo Research Group, computational studies were performed on the 68-membered macrocycle.[3] Molecular simulations provide valuable information on the macrocycle by plotting three eigenvalues vs. simulation time (Figure 5.11, top center). This plot shows how the shape of the macrocycle changes during the simulation. The ring tends to have one large eigenvalue and two smaller, similar ones. When one eigenvalue differs from two slightly similar values, it indicates a cylindrical shape: this correlates to a macrocycle in a collapsed conformation due to π-π stacking (Figure 5.11, top left). Occasionally, the second eigenvalue drifts upwards, and the macrocycle will take up a disk shape

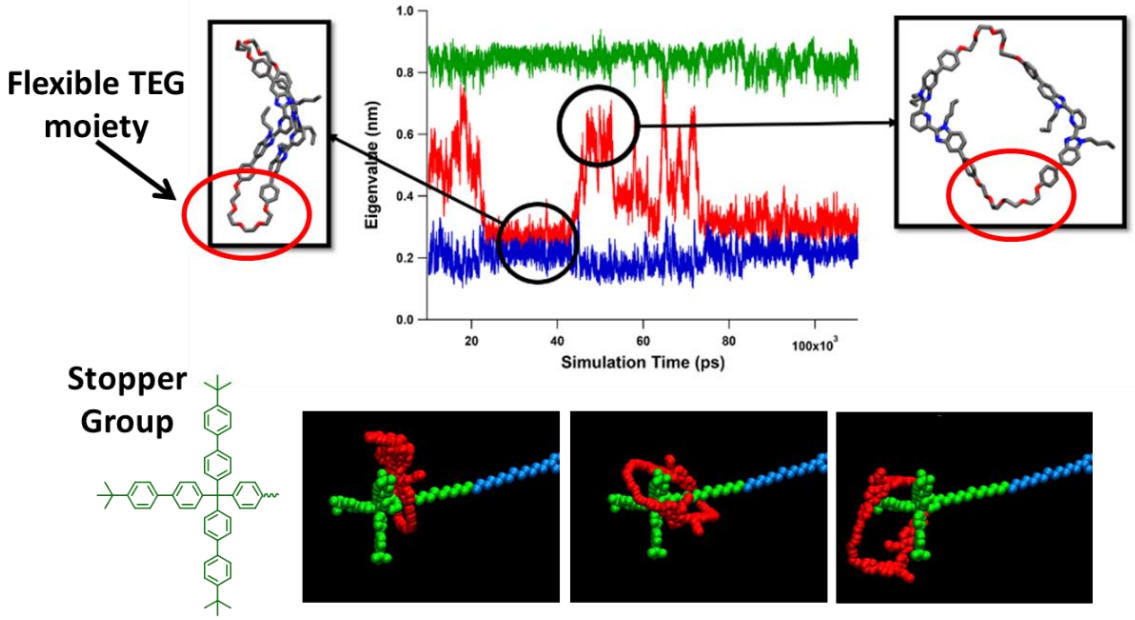

Figure 5.11. Molecular Simulation of 68-atom Ring **5.1**. Molecular simulations provide us with valuable information on how the shape of the macrocycle changes in the form of a plot of three eigenvalues vs. simulation time. The ring can form a cylindrical shape consistent with the collapsed conformation because of π-π stacking which can disengage occasionally, and the molecule obtains a disc-like shape. These changes in conformation were shown to help facilitate dethreading from a molecule stoppered with a bulky triaryl moiety (green); the molecular simulation shows the ring looping around the three biphenyl arms of the stopper group.

when the π-π interactions are disengaged (although the fact that the three values are quite different means that there is no real symmetry in the molecule) (Figure 5.11, top right).

These changes in conformation facilitate the dethreading of the ring over the triaryl stopper group (used in previous [3]rotaxane studies by Dr. Katie Herbert) during the simulation. When the ring is threaded on a polymer chain, the flexible tetraethylene glycol moiety allows it to change conformation as it slides along the chain; when the macrocycle is in its collapsed, cylindrical shape, it can loop around all three biphenyl arms on the stopper group (Figure 5.11, bottom).

A defining characteristic of a rotaxane molecule is the ability of the ring to slide along the axis molecule without falling off. The size matching of macrocycle and stopper groups is one of the essential design parameters for designing components and assembling rotaxanes; the end groups must be bulky enough to stopper the ring, and the macrocycle cavity big enough for threading and ring sliding. A triaryl component (i.e., **5.3**) was synthesized to provide a rigid stopper group to prevent the macrocycle from slipping. Synthesizing macrocycles of different sizes will determine how many atoms the ring cavity needs to hold two thread components without slipping off stoppers.

The macrocycle design controls the number of ligand sites introduced to access singly-threaded and doubly-threaded rings. This synthesis can be modified to incorporate different linker groups to access different ring sizes and conformations (Figure 5.12). Ring size is tailored by shortening (or lengthening) the Bip moieties by taking out (or including) the terminal phenol units or designing shorter linkages, the two main components in the ring synthesis. Using non-extended Bip moieties[4] connected via shorter linkages leads to the smaller rings desired for forming stable rotaxanes. Different ring conformations can be accessed through more flexible (ethylene glycol) or rigid (aromatic) linkages; triethylene glycol and naphthalene form 46-membered rings with non-

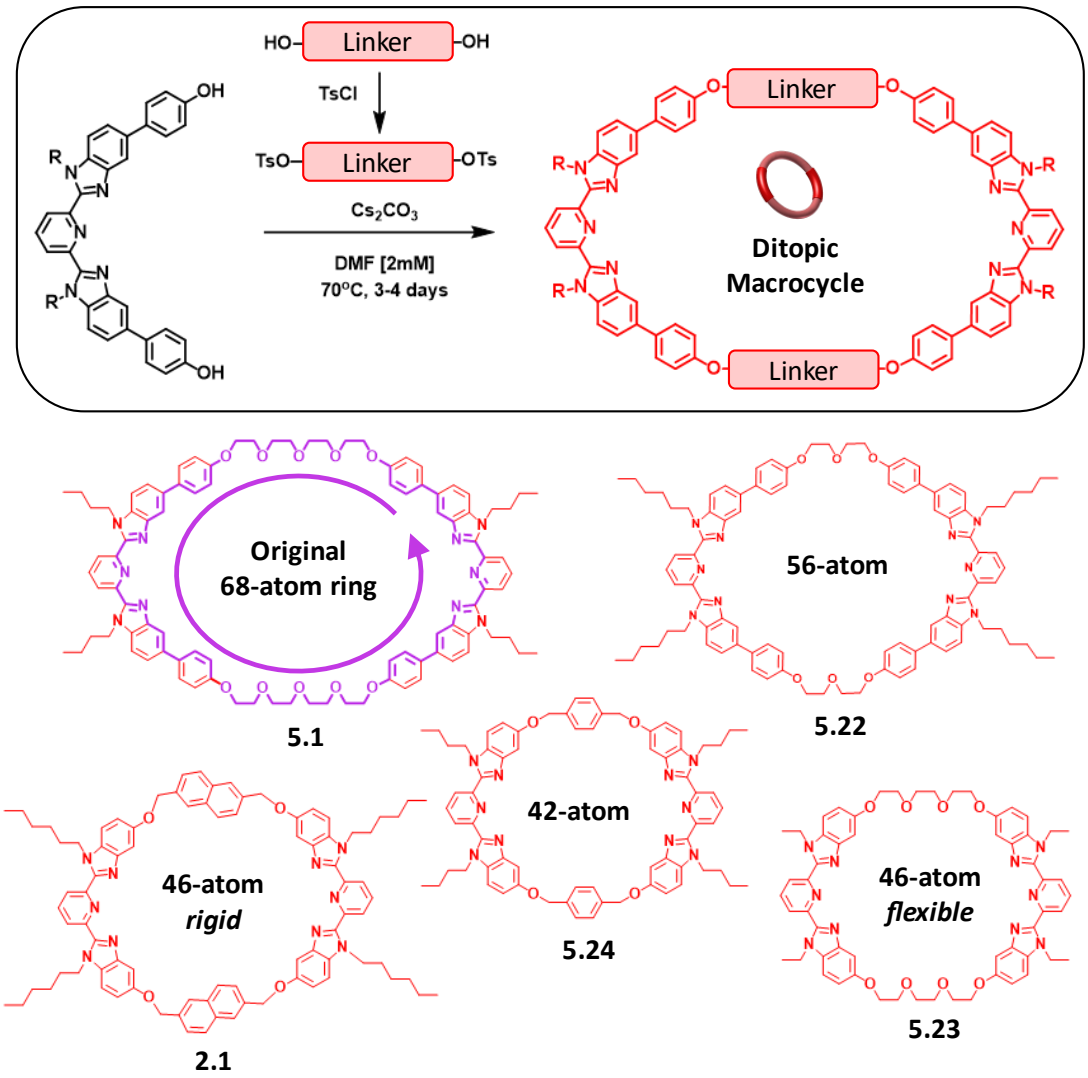

Figure 5.12. Controlling Ditopic Ring Size. The design of our macrocycle synthesis allows us to change the size and flexibility of the ring with different linker moieties. The length of the alkyl R groups on the 2,6-bis(N-alkyl-benzimidazolyl) pyridine (Bip) ligand (top left) helps with the solubility of the highly aromatic rings. Smaller rings can be accessed by removing the phenol extension on Bip. Aromatic linkers result in more rigid macrocycles, while the ethylene glycol linkages impart flexibility to the ring.

extended Bip moieties allowing us to investigate ring flexibility between rings of similar size.

As mentioned above, the 68-atom rings **5.1** are too big for our triaryl stopper size, necessitating the synthesis of smaller rings by shortening the tetraethylene glycol linkage between the two Bip units. Tosylation of diethylene glycol provided a slightly smaller 56-atom ring **5.22**

but it was still too big (confirmed by Dr. Jerry Hertzog). Accessing even tighter rings requires removing the phenol extension on the Bip ligand (see Experimental).

5.2.7 Assembling Pseudo[3]rotaxanes from Maleimide Thread

All pseudo[3]rotaxane titration experiments followed the same procedure outlined below. Two equivalents of the maleimide thread were added slowly for every macrocycle until an exact 2:1 ratio of components was verified using ^{1}H-NMR integration. Then, metal ions are slowly added, and the metallation is tracked via NMR. Zn^{2+} (with bistriflimide as a noncoordinating counterion) was chosen as the metal ion for the pseudo[3]rotaxane because it forms a labile bond with tridentate ligands but still has a relatively high overall binding constant ($\beta_n > 10^8\ M^{-n}$; n=2)[13] that keeps the ring bound during the stoppering process. The downfield shift in aromatic Bip protons upon adding Zn^{2+} ions confirms the formation of pseudo[3]rotaxanes from the smaller ditopic macrocycles and maleimide-functionalized thread components (see Experimental). Figure 5.13 shows the assembly of P3R **5.22:5.6:Zn(II)$_2$** from 56-atom **5.22** and maleimide thread **5.6** using $Zn(NTf_2)_2$ as an example.

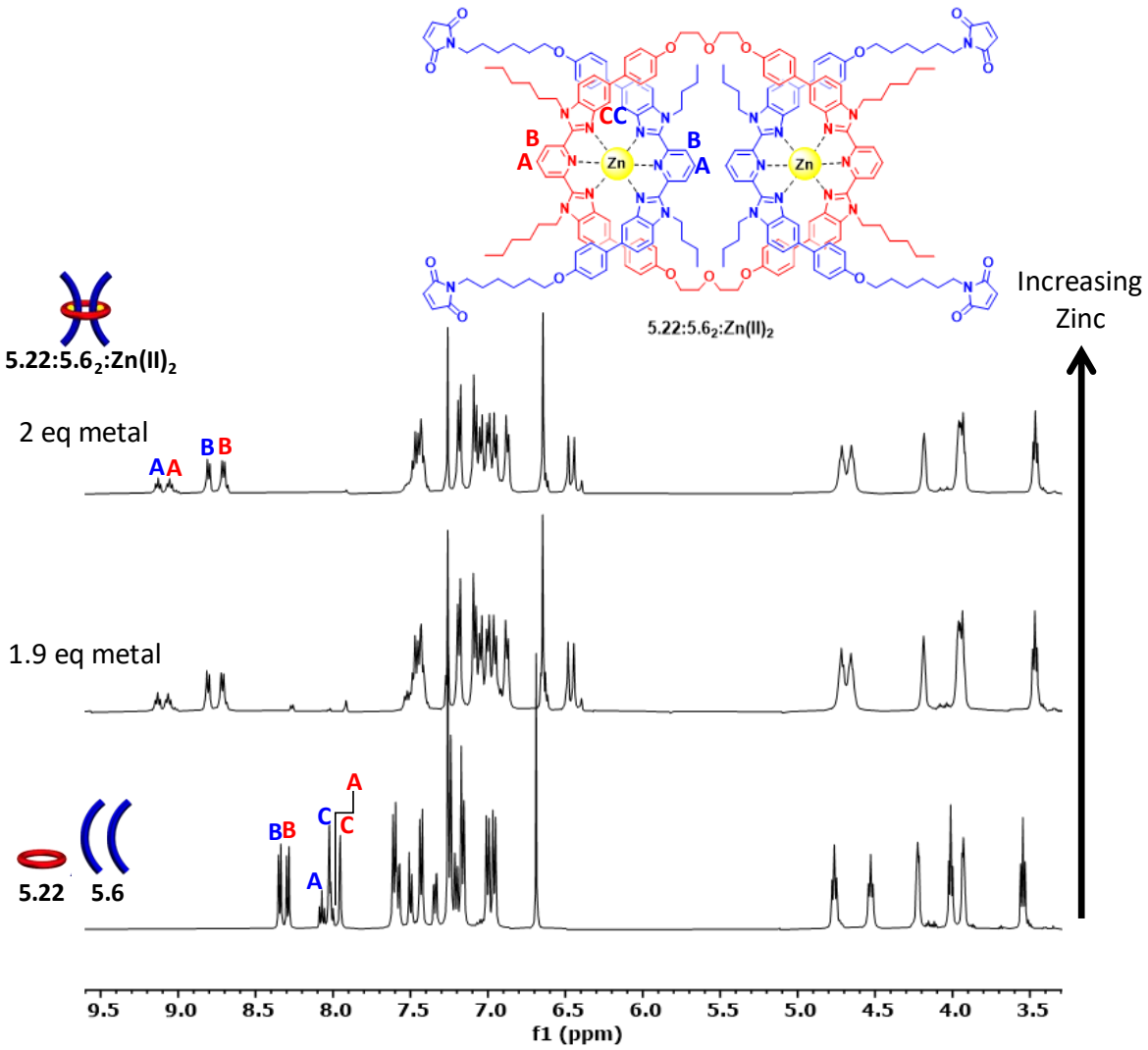

Figure 5.13. Partial ^{1}H-NMR overlay (500 MHz, 25°C, Solvent: 0, 14.25, 15% d_3-MeCN in $CDCl_3$ increasing upwards) of metal addition to form **5.22:5.6$_2$:Zn(II)$_2$**.

The 2,2'-bipyridine (Bipy) ligand was explored in Chapter 4 as an alternative to the larger Bip ligand. Smaller ligands have a better chance of threading through the tighter rings (i.e., 42-atoms) required to prevent dethreading from the triaryl stopper group employed here. Figure 5.14 shows the assembly of **5.24** and **5.13** as an example.

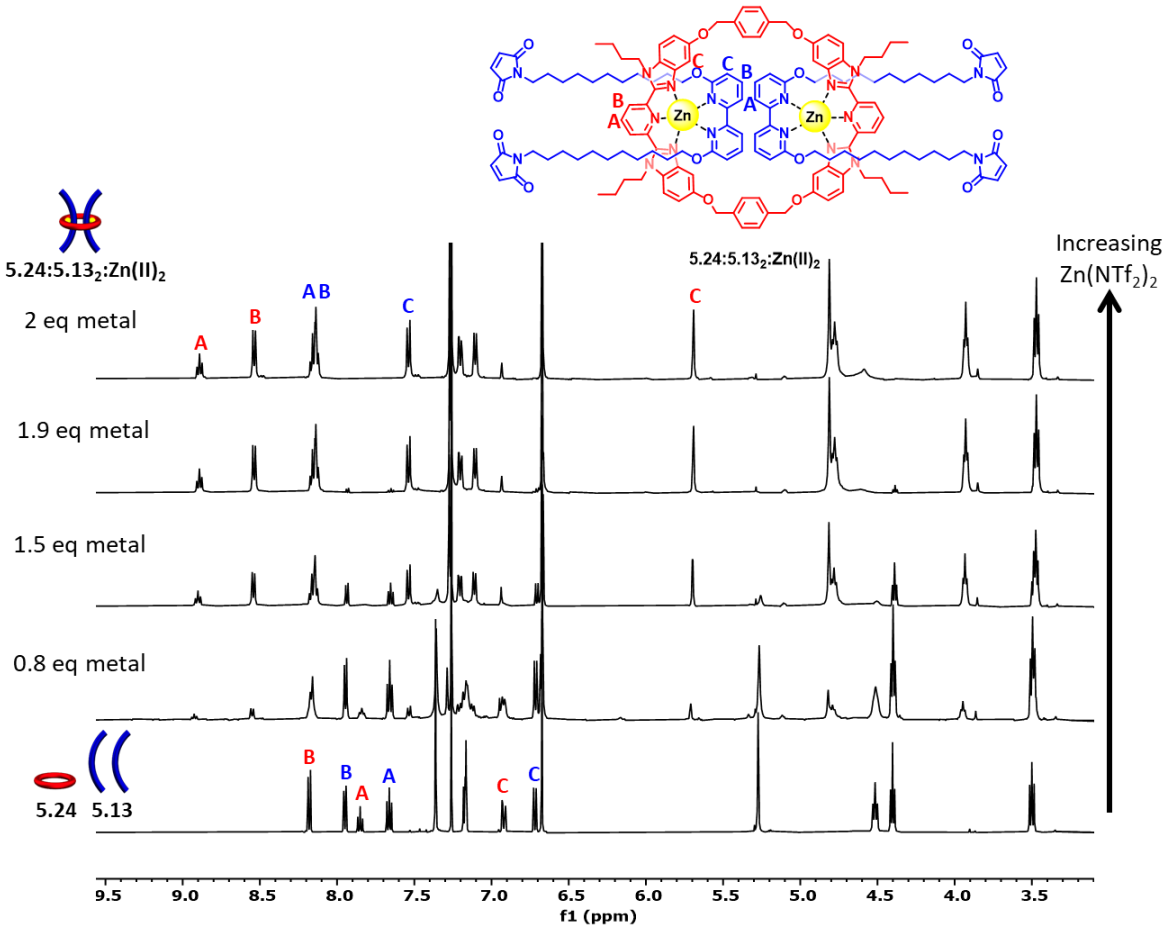

Figure 5.14. Partial ^{1}H-NMR overlay (500 MHz, 25°C, Solvent: 0, 6, 11.25, 14.25, 15% d_3-MeCN in $CDCl_3$ increasing upwards) of metal addition to form **5.24:5.13$_2$:Zn(II)$_2$**.

Instead of the bistriflimide counterion typically used to assemble Bip complexes for its noncoordinating nature, Dr. Wu chose a triflate (i.e., $Zn(OTf)_2$) to see if coordination with a counterion could help stabilize the pentacoordinate complex that forms from a 1:1:1 stoichiometric mixture of Bip:Bipy:Zn^{2+}. NMR signals between the metallated Bipy peaks (~8.15 – 8.40ppm) suggest zinc exchanging between Bipy ligands (see Experimental). Comparisons between the bistriflimide and triflate titration experiments reveal cleaner and more stable pseudo[3]rotaxane complexes when the noncoordinating bistriflimide counterion is employed.

5.2.8 Stoppering Pseudo[3]rotaxanes

Keeping the interlocked moiety intact during stoppering requires reaction conditions that do not interact with the pseudo[3]rotaxane metal complex; harsh reaction conditions requiring thermal- or photo-initiators or metal complexes will promote dethreading of the ring before the stoppering reaction can occur. In collaboration with Dr. Qiong Wu, a V-70 thermal initiated thiol-ene reaction between the thiol stopper and a pseudo[3]rotaxane showed promising preliminary results; however, repeating the click reaction was unsuccessful (see Experimental).

Successful thiol-maleimide conjugation would be indicated by a decrease in the integration of the 6.7 ppm maleimide singlet and growth of peaks corresponding to the thioester product, as seen in the dumbbell experiments. Furthermore, complete retention of the metallated complex peaks would indicate successful stoppering of the interlocked pseudo[3]rotaxane. Thiol-maleimide stoppering of P3R **5.1:5.6$_2$:Zn(II)$_2$** with thiol stopper **5.3** was used to target [3]rotaxane **5.27** after demetallation (Figure 5.15, top) (see Experimental). A ^{1}H-NMR spectrum was acquired after each DBU addition to monitor reaction progress and watch for demetallation caused by DBU displacing thread and complexing with Zn^{2+} ions (see Experimental). The maleimide singlet from the pseudo[3]rotaxane **5.1:5.6$_2$:Zn(II)$_2$** at 6.72 ppm in CD_2Cl_2 (6.70 in $CDCl_3$) did not decrease even after adding 1.0 mol% DBU (Figure 5.15, bottom). However, at 0.75 mol% DBU, peaks grew between 8.35 ppm and 8.0 ppm, corresponding to the Bip thread no longer bound to the metal ion (Figure 5.16). The same result was observed for P3Rs assembled from Bipy thread **5.13** and the smaller 42-atom ring **5.24** (Figure 5.17).

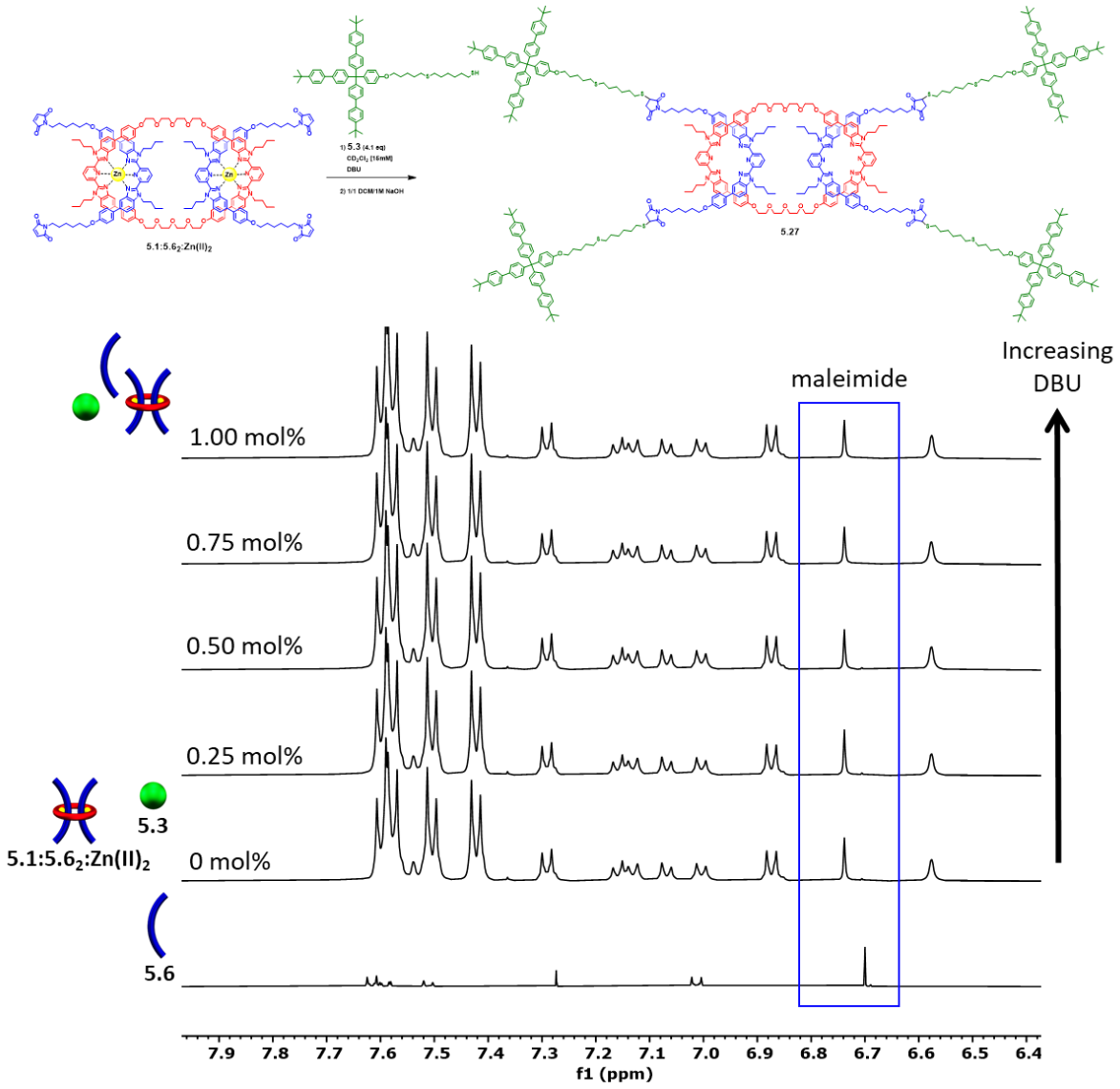

Figure 5.15. Synthesis attempt of [3]rotaxane **5.27** (top). Partial ^{1}H-NMR overlay (500 MHz, 25°C, CD_2Cl_2) of DBU titration showing the lack of decreasing P3R maleimide singlet in **5.1:5.6$_2$:Zn(II)$_2$** at 6.72 ppm (bottom).

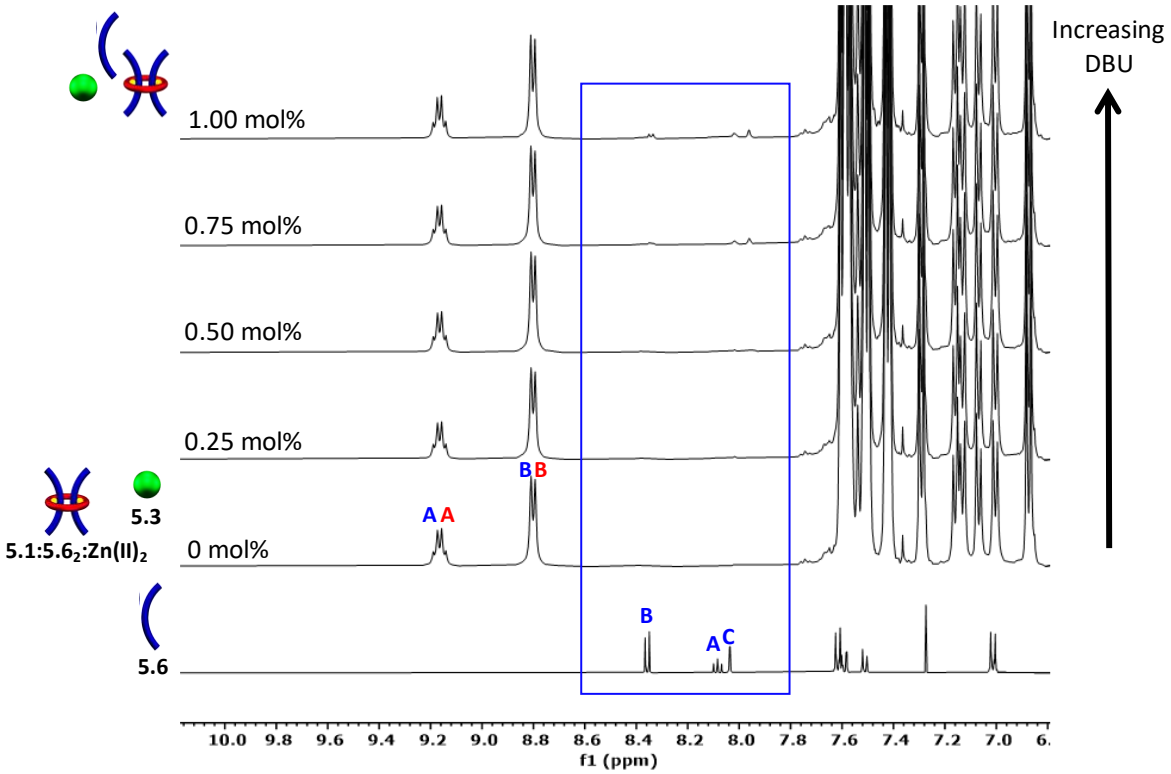

Figure 5.16. Partial ^{1}H-NMR overlay (500 MHz, 25°C, CD_2Cl_2) of DBU titration (aromatic region) showing demetallation of **5.1:5.6$_2$:Zn(II)$_2$** and reappearance of the Bip peaks from demetallated **5.6**.

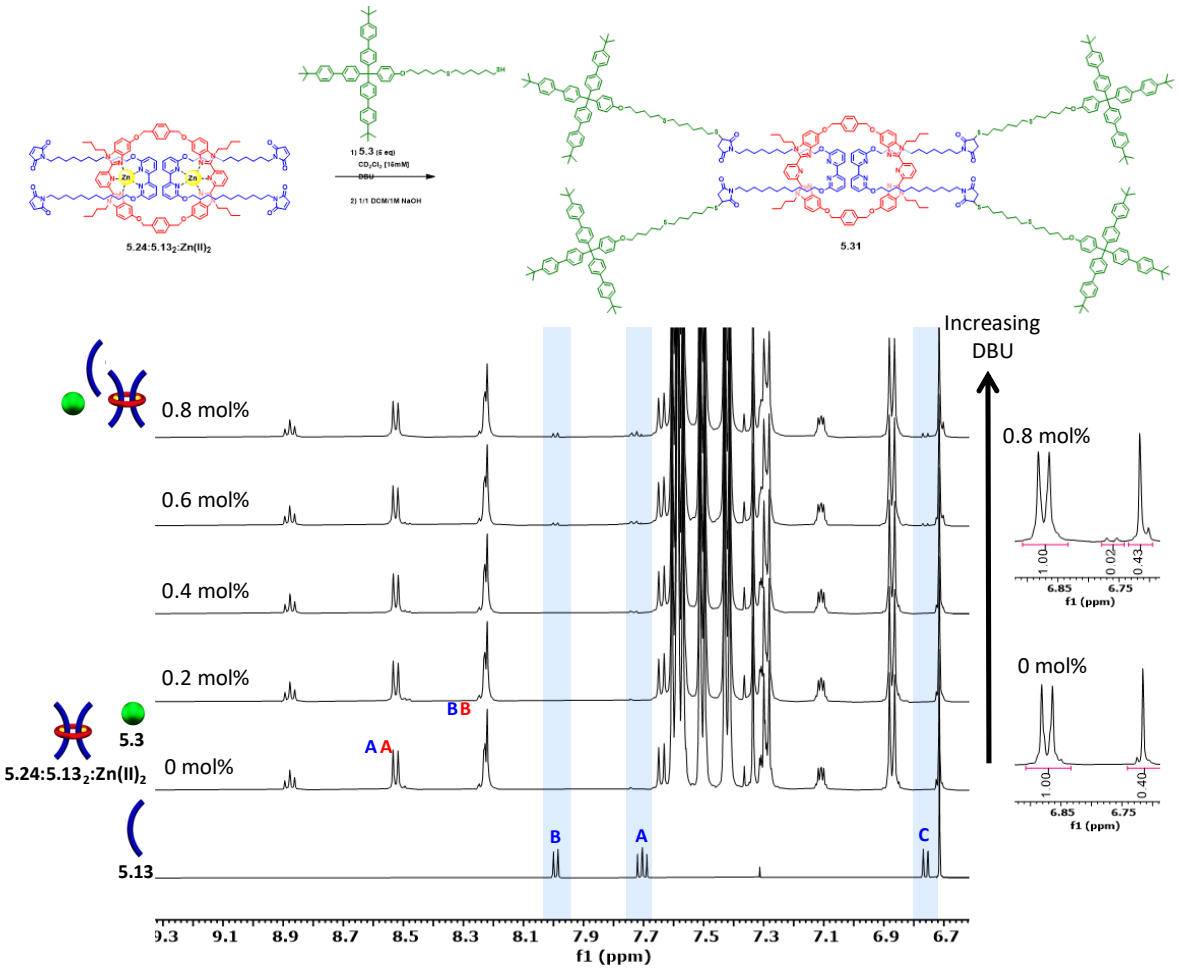

Figure 5.17. a) Synthesis attempt of [3]rotaxane **5.31** (top). b) Partial ^{1}H-NMR overlay (500 MHz, 25°C, CD_2Cl_2) of **5.24:5.13$_2$:Zn(II)$_2$** DBU titration showing complex demetallation and reappearance of the Bipy peaks from demetallated thread **5.13** (bottom). The maleimide singlet in **5.24:5.13$_2$:Zn(II)$_2$** did not decrease during the titration (integrations shown on the right).

The sterically hindered and noncoordinating nature of DBU should minimize the likelihood of interfering with the metal complex, making it an attractive choice for the stoppering catalyst. Unfortunately, even at low concentrations, DBU prefers to bind to the Zn^{2+} ions before performing the Thia-Michael reaction between thread and stopper. The poor stability of the pseudo[3]rotaxane under base-catalyzed Thia-Michael conditions necessitates a catalyst-free approach to remove any potential interaction with the metal, ensuring that the only components capable of reacting are the rotaxane thread and stopper end groups to form the desired interlocked product.

5.3 Conclusions

The N-alkylation of maleimide using a modified Mitsunobu approach was used to optimize the synthesis of maleimide threads **5.6** and **5.13** from Bip and Bipy ligands used to react with thiol stopper group **5.3**. DBU was chosen as a sterically hindered, non-nucleophilic base to facilitate the Michael addition before interacting with the metal complex. Smaller rings were synthesized and titrated with maleimide thread components and Zn^{2+} ions to form pseudo[3]rotaxanes. Small amounts of DBU were titrated into an NMR tube containing a mixture of rotaxane components, and the formation of the thioester product was monitored via ^{1}H-NMR. During NMR experiments, stoppering P3R with DBU revealed no interlocked product even after the complete disappearance of the maleimide singlet at 6.7 ppm (and the corresponding growth in upfield conjugation peaks). These results suggest that dumbbells form outside the ring cavity; DBU catalyzes the thiol-maleimide reaction, but only after it interferes with the metal complex and the pseudo[3]rotaxane falls apart.

Maleimide is highly reactive and susceptible to hydrolysis under basic conditions, limiting the scope of compatible reactions; however, protecting groups prevent hydrolysis, allowing harsher reaction conditions. Furan derivatives, specifically 2,5-disubstituted furans, are commonly used to protect maleimide because Diels-Alder adducts form at room temperature without a catalyst. A simple retro-reaction at elevated temperatures unmasks the reactive maleimide vinyl group, making this chemistry ideal for thermoreversible polymer networks that can decrosslink at high temperatures. Chapter 6 discusses the synthesis of a furan-functionalized stopper and assesses its ability to stopper pseudo[3]rotaxanes using Diels-Alder chemistry.

Accessing larger stoppers to prevent slippage of ditopic rings is limited by synthetic challenges, such as the poor solubility of bulky aromatics and expensive starting materials.

Therefore, the smaller ring complex (i.e., **5.24:5.13$_2$:Zn(II)$_2$**) will be used in the following chapter for stoppering experiments because it has the best chance of successfully forming a stable, doubly-threaded topology. Further investigations into the thermal limitations of these reversible bicyclic adducts should lead to possible solutions for stabilizing interlocked products.

5.4 Experimental

5.4.1 Materials and Methods

All chemicals were purchased from Sigma-Aldrich and used without further purification unless otherwise mentioned. Zinc di[bis(trifluoromethyl sulfonyl)imide] was purchased from Strem Chemicals and stored in a nitrogen desiccator. Maleimide and 2,2'-bipyridine-6,6'-diol were purchased from TCI America. Solvents for chromatography were purchased from Fisher-Scientific. 2,6-bisbenzimidazolylpyridine ligands[4] were prepared following literature procedures. Deuterated solvents and diisopropyl azodicarboxylate were purchased from ACROS Organics. Tetrahydrofuran (THF) was dried over sodium and benzophenone. Dichloromethane was distilled over calcium hydride before use. Dimethylformamide (DMF) was dried with activated 4Å molecular sieves before use. All synthesized components were stored in a freezer at -8°C before use.

Matrix Assisted Laser Desorption/Ionization Mass Spectrometry (MALDI-TOF MS) was measured by a Bruker AutoFlex III or Bruker Ultraflextreme MALDI-TOF-TOF spectrometer in linear (or reflectance) mode using dithranol as matrix and silver or sodium trifluoroacetate as ionizer (or no ionizer).

Room Temperature Nuclear Magnetic Resonance Spectroscopy was performed using a Varian Inova 600 MHz spectrometer (at Case Western Reserve University), Bruker Ascend AVANCE III 500 MHz spectrometer, a Bruker AVANCE II+ 500 MHz spectrometer, or a Bruker DRX 400 MHz spectrometer at the University of Chicago NMR facilities. ^{1}H NMR spectra were referenced to the residual protonated solvent signal and ^{13}C NMR spectra were referenced to the deuterated solvent carbon resonance signal.

5.4.2 Synthetic Procedures

5.4.2.1 Synthesis of alkene thread **5.2**

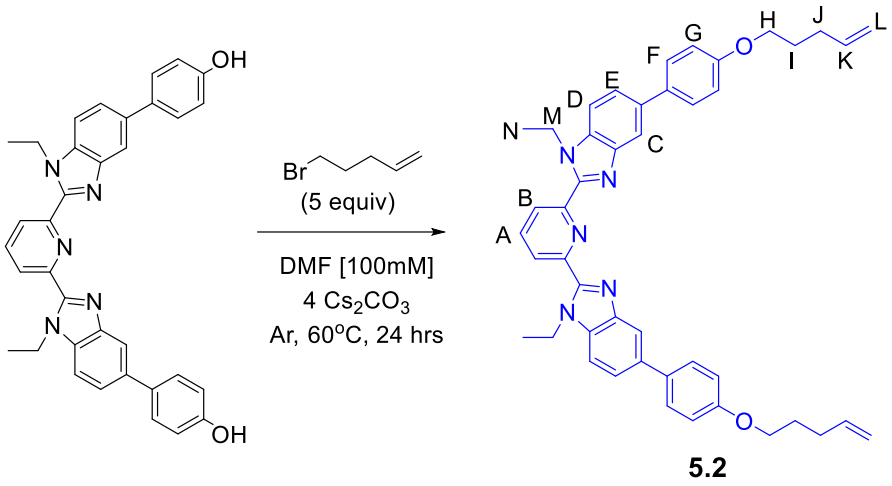

5.2

Ethyl Bip-OH[3] (0.5 g, 0.91 mmol) and Cs_2CO_3 (1.2 g, 3.6 mmol) were added to a 50mL RBF purged with Ar. Dry DMF (9 mL) and 5-bromo-1-pentene (0.675 g, 0.536 mL, 4.5 mmol) were added to the mixture. The reaction was stirred at 60°C overnight, after which the reaction mixture was cooled to room temperature, and the solvent was removed under reduced pressure. The residue was dissolved in $CHCl_3$, and the insoluble material (salts) was removed by filtration. The filtrate was collected, and the solvent was removed under reduced pressure. The resulting material was purified using column chromatography (TEA-treated silica gel, chloroform/methanol gradient as eluent) followed by recrystallization (chloroform/acetonitrile mixture) to yield white crystals of **5.2** in 72% yield by mass. ^{1}H NMR (500 MHz, $CDCl_3$) δ 8.38 (d, *J* = 7.9 Hz, 2H, B), 8.11 – 8.03 (m, 3H, A+C), 7.65 – 7.57 (m, 6H, E+F), 7.51 (d, *J* = 8.4 Hz, 2H, D), 7.05 – 6.99 (m, 4H, G), 5.89 (ddt, *J* = 16.9, 10.2, 6.6 Hz, 2H, K), 5.10 (dq, *J* = 17.2, 1.7 Hz, 2H, L), 5.03 (dq, *J* = 10.2, 1.5 Hz, 2H, L), 4.83 (q, *J* = 7.2 Hz, 4H, M), 4.04 (t, *J* = 6.4 Hz, 4H, H), 2.32 – 2.24 (m, 4H, J), 1.97 – 1.90 (m, 4H, I), 1.40 (t, *J* = 7.2 Hz, 6H, N).

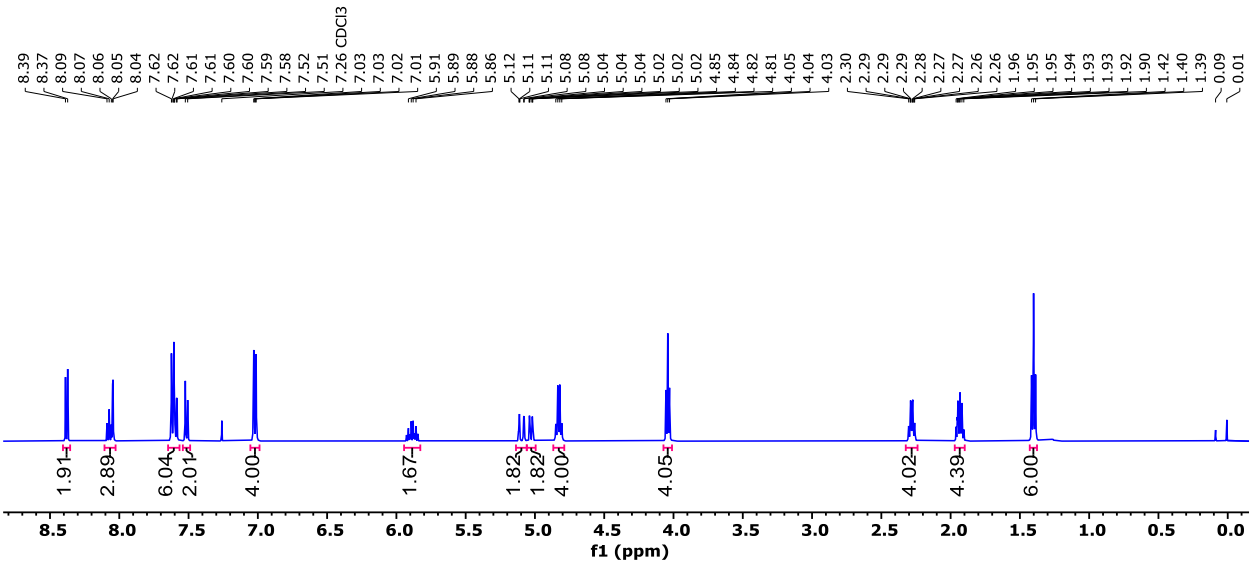

Figure 5.18. ^{1}H-NMR (500 MHz, 25°C, $CDCl_3$) of ethyl Bip alkene thread **5.2**.

5.4.2.2 Synthesis of maleimide thread **5.6**

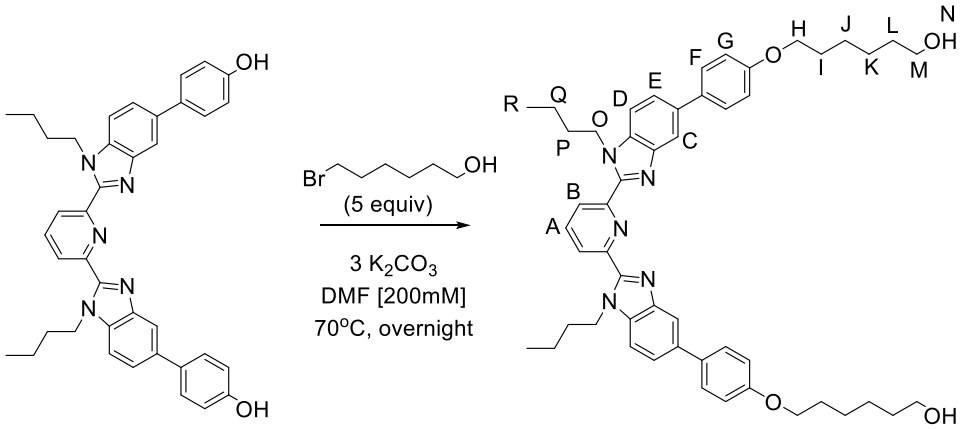

Butyl Bip-OH[3] (1.5 g, 2.47 mmol) and K_2CO_3 (1.02 g, 7.4 mmol) were added to a 100mL RBF purged with Ar. To this mixture was added dry DMF (12.5 mL) and 6-bromo-1-hexanol (2.23 g, 1.61 mL, 12.34 mmol.). The reaction was stirred at 70°C overnight, after which the reaction mixture was cooled to room temperature, and the solvent was removed under reduced pressure. The residue was dissolved in $CHCl_3$, and the insoluble material (salts) was removed by filtration. The filtrate was collected, and the solvent was removed under reduced pressure. The resulting material was purified using column chromatography (TEA-treated silica gel, chloroform/methanol

gradient as eluent) followed by recrystallization (chloroform/methanol mixture) to yield white crystals of **5.5** in 80% yield by mass. ^{1}H NMR (500 MHz, $CDCl_3$) δ 8.35 (d, *J* = 7.9 Hz, 2H, B), 8.11 – 8.00 (m, 3H, A+C), 7.64 – 7.55 (m, 6H, F+E), 7.50 (d, *J* = 8.5 Hz, 2H, D), 7.03 – 6.99 (m, 4H, G), 4.76 (t, *J* = 7.3 Hz, 4H, O), 4.03 (t, *J* = 6.5 Hz, 4H, H), 3.68 (q, *J* = 6.5 Hz, 4H, M), 1.85 (dt, *J* = 14.2, 6.6 Hz, 4H, P), 1.75 (p, *J* = 7.5 Hz, 4H, I), 1.63 (dt, *J* = 14.0, 6.8 Hz, 4H, L), 1.56 – 1.51 (m, 4H, J), 1.51 – 1.42 (m, 4H, K), 1.25 (t, *J* = 5.4 Hz, 2H, N), 1.14 (h, *J* = 7.4 Hz, 4H, Q), 0.73 (t, *J* = 7.4 Hz, 6H, R). MALDI-TOF MS: 810.3 ([M]+H^+).

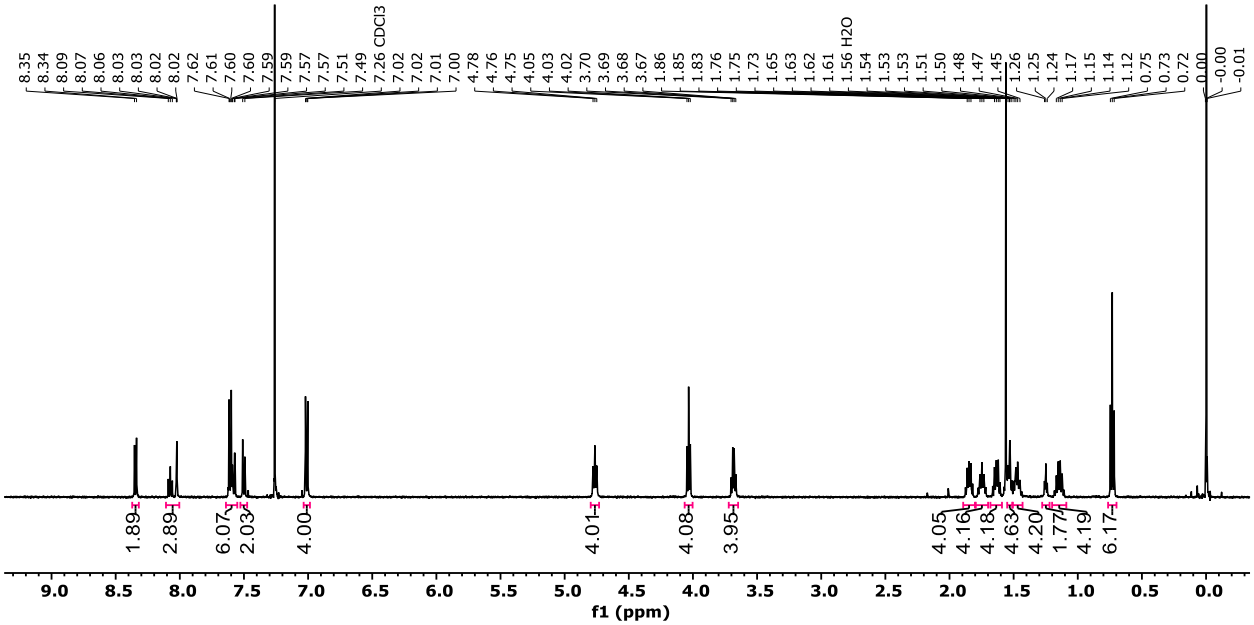

Figure 5.19. ^{1}H-NMR (500 MHz, 25°C, $CDCl_3$) of dihydroxy butyl Bip thread **5.5**.

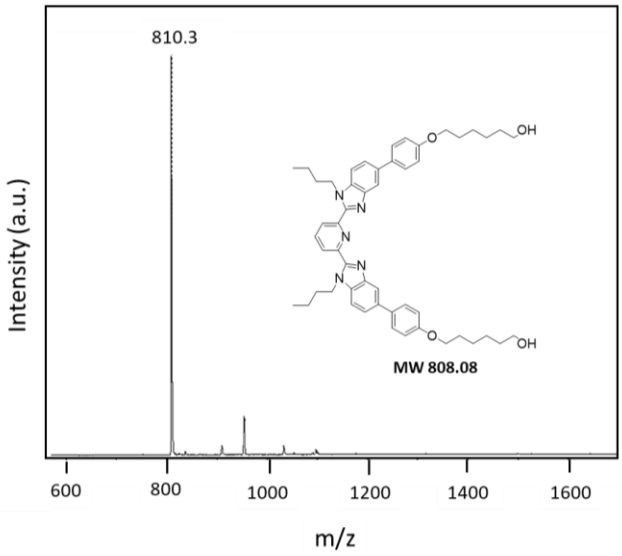

Figure 5.20. MALDI-TOF MS (Dithranol) of dihydroxy butyl Bip thread **5.5**.

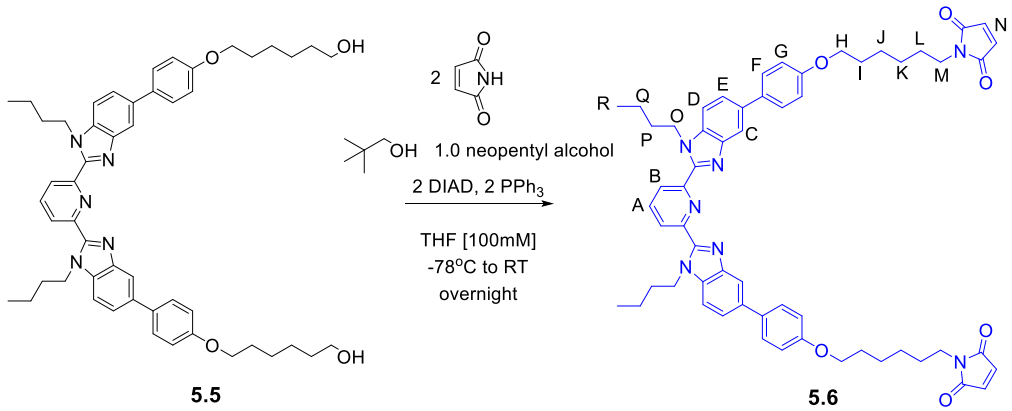

N-alkylation of maleimide to form thread **1** was based on Walker's modified Mitsunobu procedure.[14,15] Triphenylphosphine (0.487 g, 1.86 mmol) was added to an oven-dried, 25 mL round bottom flask and put under argon flow. Dry THF (1 mL) was added to the flask and cooled to -78°C using a dry ice/acetone bath. DIAD (0.375 g, 0.365 mL, 1.86 mmol) was dissolved in 1 mL dry THF and added dropwise via syringe and the resulting light-yellow solution was stirred for 5 minutes. **5.5** (0.75 g, 0.93 mmol) was dissolved in 7.3 mL of dry THF and added in ~0.2 mL increments via syringe over 10 minutes. Neopentyl alcohol (0.082 g, 0.93 mmol) and maleimide (0.18 g, 1.86 mmol) were added sequentially as solids. The reaction flask was removed from the dry ice/acetone bath and allowed to stir overnight at room temperature. The solvent was removed

via rotary evaporation and the resulting material was purified using column chromatography (silica gel, hexanes/ethyl acetate gradient as eluent) to yield **5.6** as a white powder in 50% yield by mass. ^{1}H NMR (500 MHz, $CDCl_3$) δ 8.34 (d, *J* = 7.9 Hz, 2H, B), 8.10 – 8.00 (m, 3H, A+C), 7.64 – 7.55 (m, 6H, F+E), 7.50 (dd, *J* = 8.5, 0.7 Hz, 2H, D), 7.03 – 6.97 (m, 4H, G), 6.67 (s, 4H, N), 4.76 (t, *J* = 7.3 Hz, 4H, O), 4.01 (t, *J* = 6.4 Hz, 4H, H), 3.55 (t, 4H, M), 1.81 (dt, *J* = 14.5, 6.5 Hz, 4H, P), 1.75 (tt, *J* = 6.8, 1.7 Hz, 4H, I), 1.69 – 1.60 (m, 4H, L), 1.53 (dtd, *J* = 9.6, 7.5, 5.6 Hz, 4H, J), 1.43 – 1.33 (m, 4H, K), 1.20 – 1.09 (m, 4H, Q), 0.73 (t, *J* = 7.4 Hz, 6H, R). MALDI-TOF MS: 967.39 ([M]+H^+).

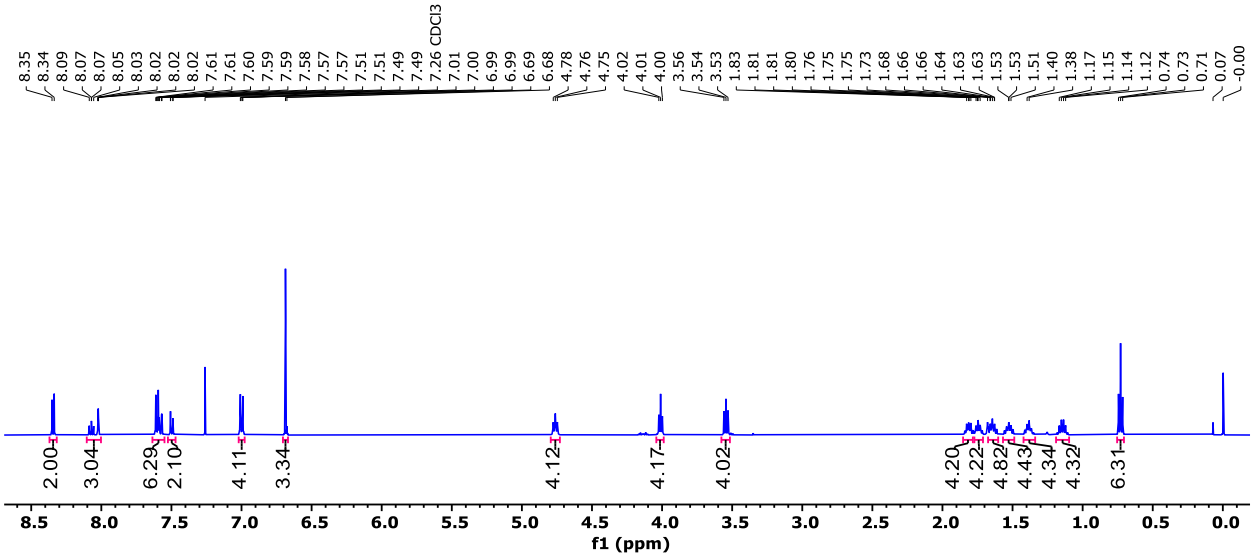

Figure 5.21. ^{1}H-NMR (500 MHz, 25°C, $CDCl_3$) of butyl Bip maleimide thread **5.6**. The quartet at 3.68 from the protons next to the hydroxy group on the precursor changes to a triplet and moves to 3.53 ppm after functionalizing with maleimide.

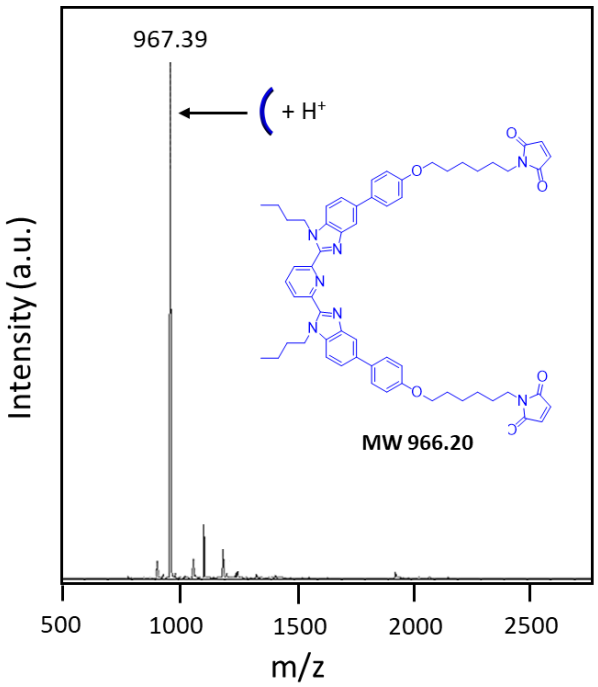

Figure 5.22. MALDI-TOF MS (Dithranol) of butyl Bip maleimide thread **5.6**.

5.4.2.3 Synthesis of maleimide thread **5.8**

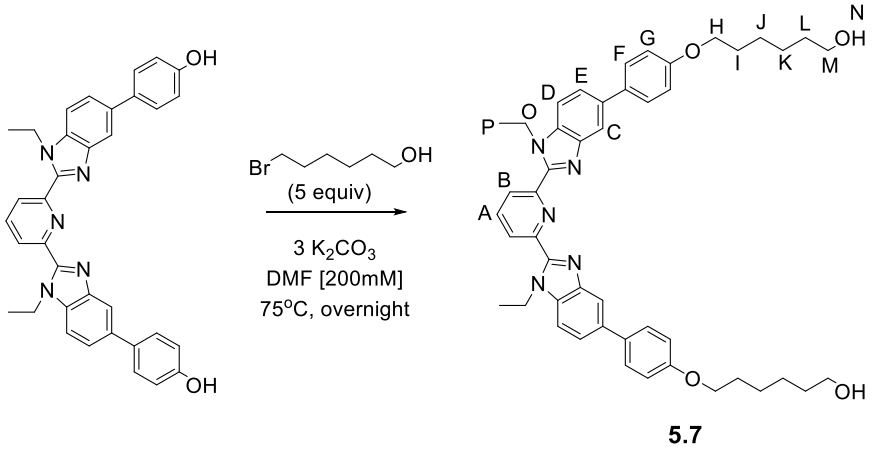

Ethyl Bip-OH[3] (1.5 g, 2.72 mmol) and K_2CO_3 (1.13 g, 8.16 mmol) were added to a 100 mL RBF which was purged with Ar. To this mixture was added dry DMF (13.6 mL) and 6-bromo-1-hexanol (2.46 g, 1.78 mL, 13.6 mmol.). The reaction was stirred at 75°C overnight, after which the reaction mixture was cooled to RT and the solvent was removed under reduced pressure. The residue was dissolved in $CHCl_3$, and the insoluble material (salts) was removed by filtration. The filtrate was collected, and the solvent was removed under reduced pressure. The resulting material was purified

using column chromatography (silica gel, chloroform/methanol gradient as eluent) followed by recrystallization (chloroform/acetonitrile mixture) to yield white crystals of 5.7 in 83% yield by mass. ^{1}H NMR (500 MHz, $CDCl_3$) δ 8.37 (d, *J* = 7.8 Hz, 2H, B), 8.11 – 8.01 (m, 3H, A+C), 7.64 – 7.56 (m, 6H, F+E), 7.52 (d, *J* = 8.4 Hz, 2H, D), 7.03 – 6.99 (m, 4H, G), 4.83 (q, *J* = 7.2 Hz, 4H, O), 4.03 (t, *J* = 6.5 Hz, 4H, H), 3.68 (dd, *J* = 6.9, 5.4 Hz, 4H, M), 1.85 (dt, *J* = 14.1, 6.6 Hz, 4H, I), 1.63 (dt, *J* = 14.0, 6.7 Hz, 4H, L), 1.55 – 1.52 (m, 4H, J), 1.47 (q, *J* = 8.1 Hz, 4H, K), 1.40 (t, *J* = 7.2 Hz, 6H, P), 1.24 (t, *J* = 5.8 Hz, 2H, N). MALDI-TOF MS: 753.0 ([M]+H^+).

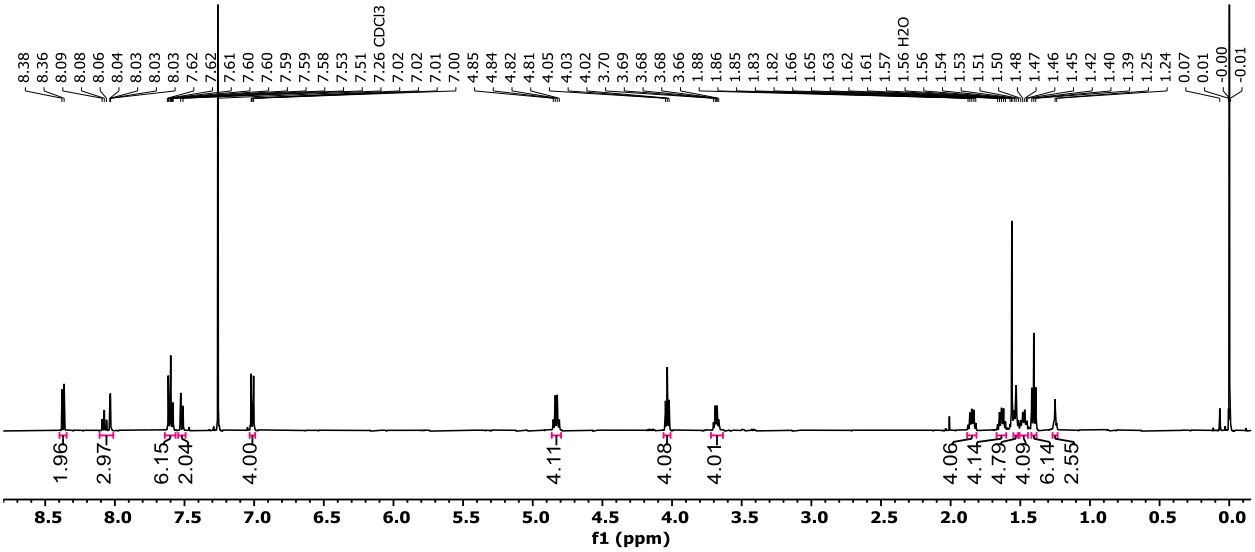

Figure 5.23. ^{1}H-NMR (500 MHz, 25°C, $CDCl_3$) of dihydroxy ethyl Bip thread **5.7**.

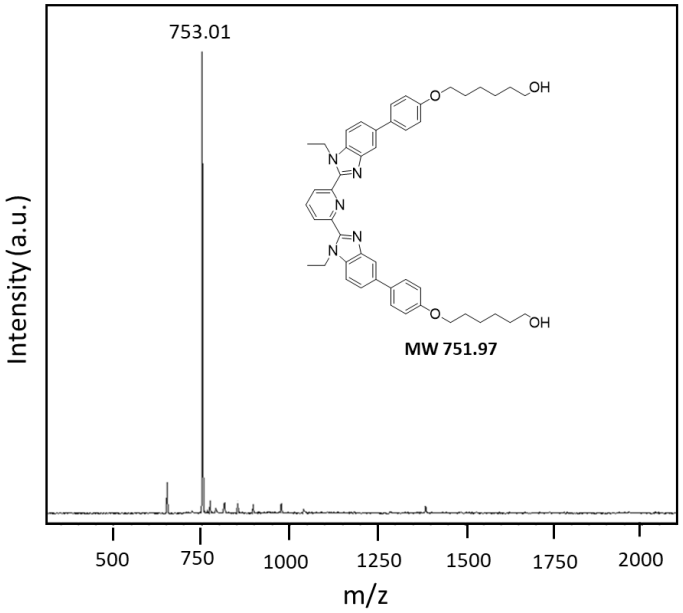

Figure 5.24. MALDI-TOF MS (Dithranol) of dihydroxy ethyl Bip thread **5.7**.

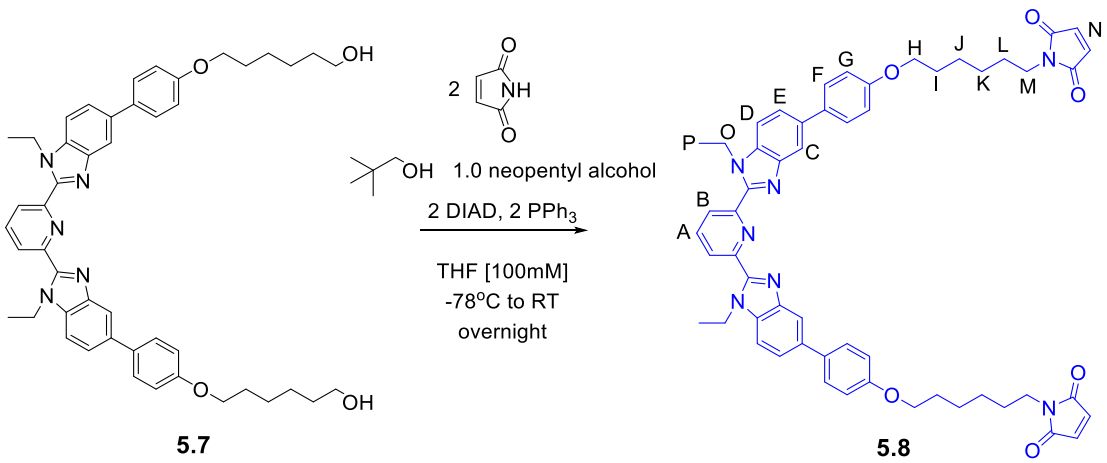

N-alkylation of maleimide to form thread **5.8** was based on Walker's modified Mitsunobu procedure.[14,15] Triphenylphosphine (0.35 g, 1.33 mmol) was added to an oven-dried, 25 mL round bottom flask and put under argon flow. Dry THF (1 mL) was added to the flask and cooled to -78°C using a dry ice/acetone bath. DIAD (0.27 g, 0.262 mL, 1.33 mmol) was dissolved in 1 mL dry THF and added dropwise via syringe and the resulting light-yellow solution was stirred for 5 minutes. **5.7** (0.5 g, 0.665 mmol) was dissolved in 4.7 mL of dry THF and added in ~0.2 mL increments via syringe over 10 minutes. Neopentyl alcohol (0.059 g, 0.665 mmol) and maleimide (0.13 g, 1.33 mmol) were added sequentially as solids. The reaction flask was removed from the

dry ice/acetone bath and allowed to stir overnight at room temperature. The solvent was removed via rotary evaporation and the resulting material was purified using column chromatography (silica gel, hexanes/ethyl acetate gradient as eluent) to yield **5.8** as a white powder in 50% yield by mass. ^{1}H NMR (500 MHz, $CDCl_3$) δ 8.37 (d, *J* = 7.9 Hz, 2H, B), 8.11 – 8.01 (m, 3H, A+C), 7.64 – 7.56 (m, 6H, F+E), 7.52 (dd, *J* = 8.6, 0.7 Hz, 2H, D), 7.03 – 6.98 (m, 4H, G), 6.69 (s, 4H, N), 4.83 (q, *J* = 7.2 Hz, 4H, O), 4.01 (t, *J* = 6.4 Hz, 4H, H), 3.55 (t, *J* = 7.2 Hz, 4H, M), 1.81 (dt, *J* = 14.3, 6.5 Hz, 4H, I), 1.65 (p, *J* = 7.4 Hz, 4H, L), 1.55 – 1.50 (m, 8H, J+K), 1.39 (t, *J* = 7.6 Hz, 6H, P). MALDI-TOF MS: 911.3 ([M]+H^+), 1137.1 ([M]+ H^++Dithranol).

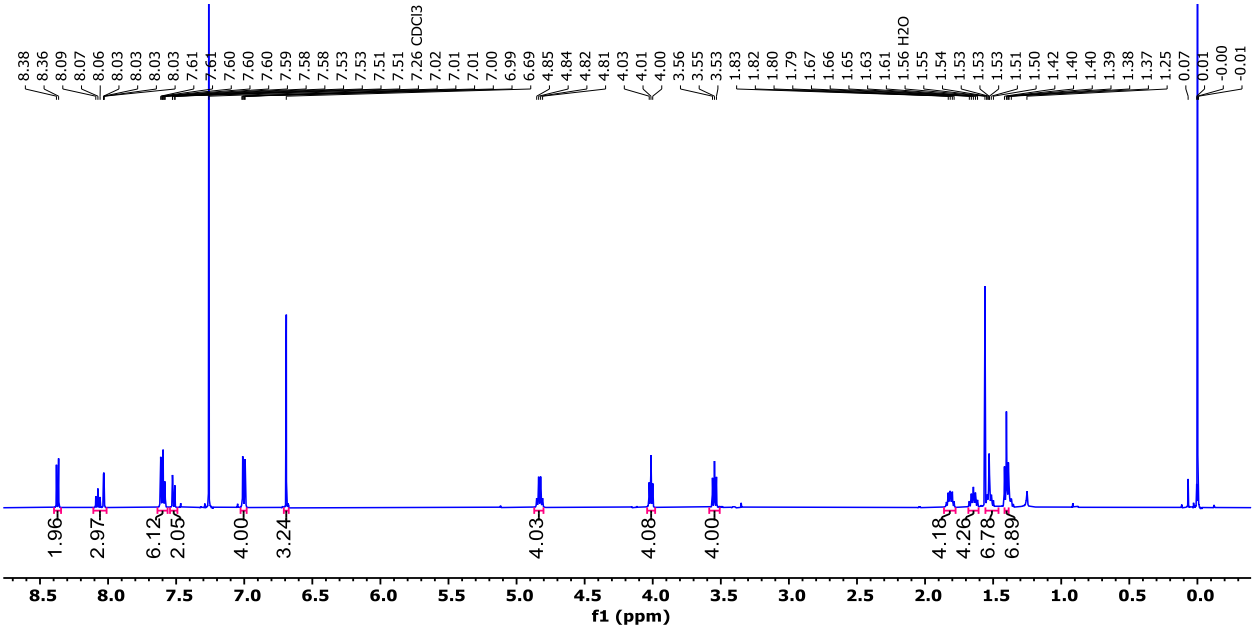

Figure 5.25. ^{1}H-NMR (500 MHz, 25°C, $CDCl_3$) of ethyl Bip maleimide thread **5.8**. The quartet at 3.68 from the protons next to the hydroxy group on the precursor changes to a triplet and moves to 3.55 ppm after functionalizing with maleimide.

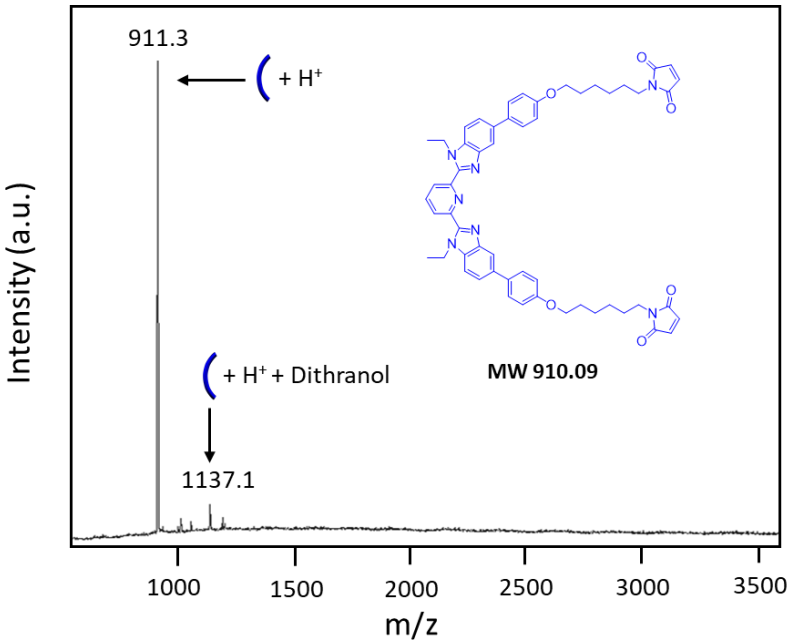

Figure 5.26. MALDI-TOF MS (Dithranol) of ethyl Bip maleimide thread **5.8**.

5.4.2.4 Synthesis of maleimide thread **5.10**

The hydroxy chains were extended even further (using 11-bromo-1-undecanol) with the idea that keeping the maleimide moiety farther from the pseudo[3]rotaxane would limit potential interactions with the metal template

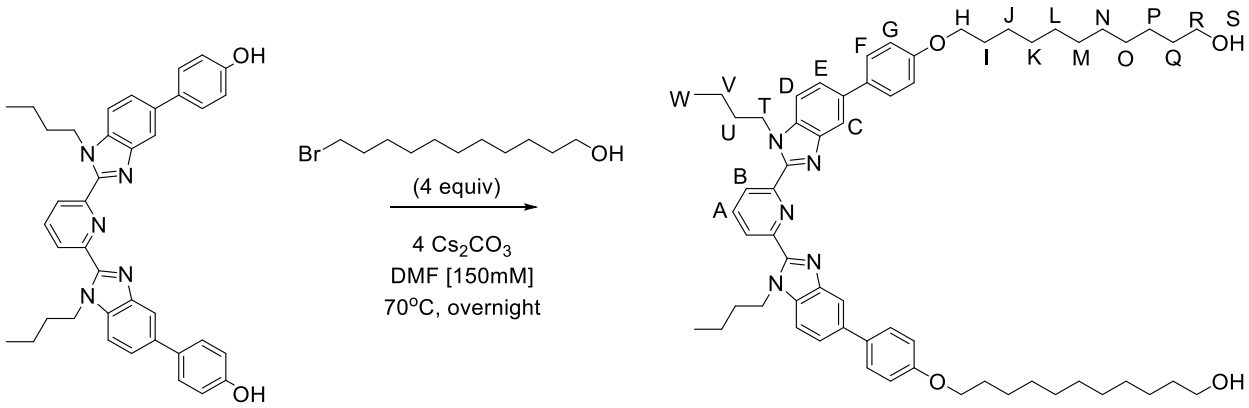

5.9

Butyl Bip-OH[3] (1.0 g, 1.65 mmol) and Cs_2CO_3 (2.14 g, 6.58 mmol) were added to a 50 mL RBF which was purged with Ar. To this mixture was added dry DMF (11 mL) and 11-bromo-1-undecanol (1.65 g, 6.58 mmol.). The reaction was stirred at 70°C overnight, after which the

reaction mixture was cooled to RT and the solvent was removed under reduced pressure. The residue was dissolved in $CHCl_3$, and the insoluble material (salts) was removed by filtration. The filtrate was collected, and the solvent was removed under reduced pressure. The resulting material was purified using column chromatography (silica gel, chloroform/methanol gradient as eluent) followed by recrystallization (chloroform/acetonitrile mixture) and precipitation into ether to yield white crystals of 5.9 in 86% yield by mass. ^{1}H NMR (500 MHz, $CDCl_3$) δ 8.34 (d, *J* = 7.9 Hz, 2H, B), 8.07 (t, *J* = 7.6 Hz, 1H, A), 8.02 (s, 2H, C), 7.63 – 7.55 (m, 6H, F+E), 7.50 (dd, *J* = 8.5, 0.7 Hz, 2H, D), 7.01 (d, 4H, G), 4.76 (t, *J* = 7.3 Hz, 4H, T), 4.02 (t, *J* = 6.5 Hz, 4H, H), 3.69 – 3.61 (m, 4H, R), 1.82 (dt, *J* = 14.3, 6.7 Hz, 4H, I), 1.75 (p, *J* = 7.3 Hz, 4H, Q), 1.63 – 1.53 (m, 4H, J), 1.48 (q, *J* = 7.5 Hz, 4H, P), 1.42 – 1.24 (m, 28H, K+L+M+N+O+S+U), 1.14 (h, *J* = 7.5 Hz, 4H, V), 0.73 (t, *J* = 7.4 Hz, 6H, W). MALDI-TOF MS: 949.85 ([M]+H^+), 1173.28 ([M]+H^++Dithranol).

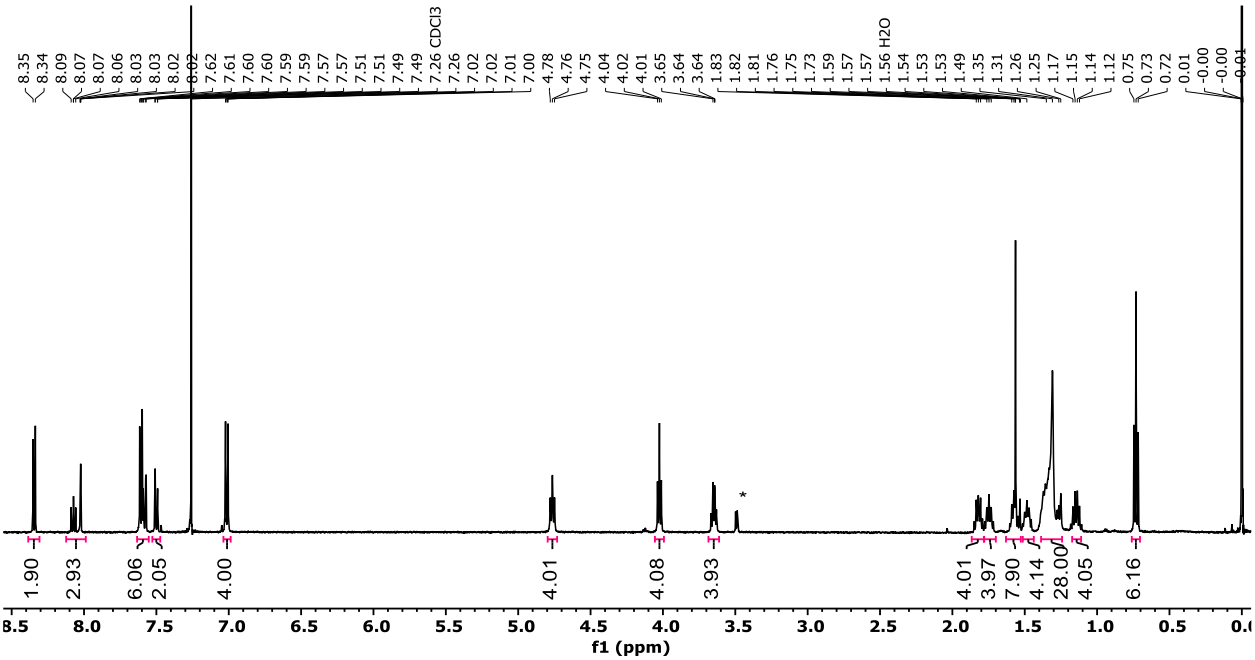

Figure 5.27. ^{1}H-NMR (500 MHz, 25°C, $CDCl_3$) of dihydroxy butyl C11 Bip thread **5.9**.

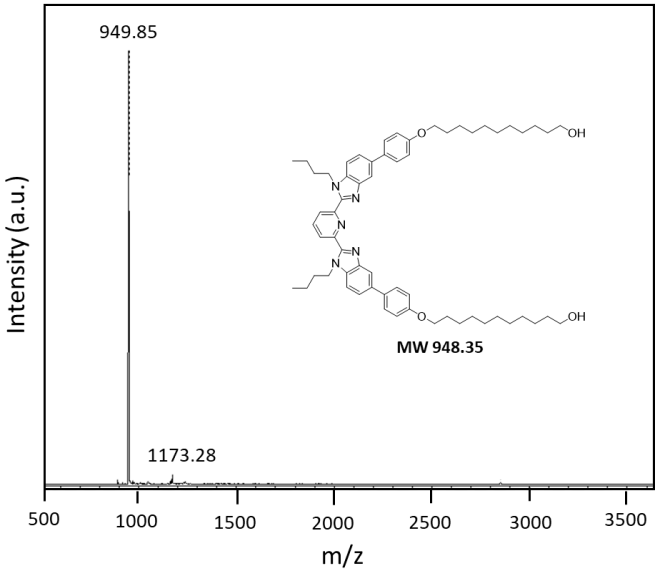

Figure 5.28. MALDI-TOF MS (Dithranol) of dihydroxy butyl C11 Bip thread **5.9**.

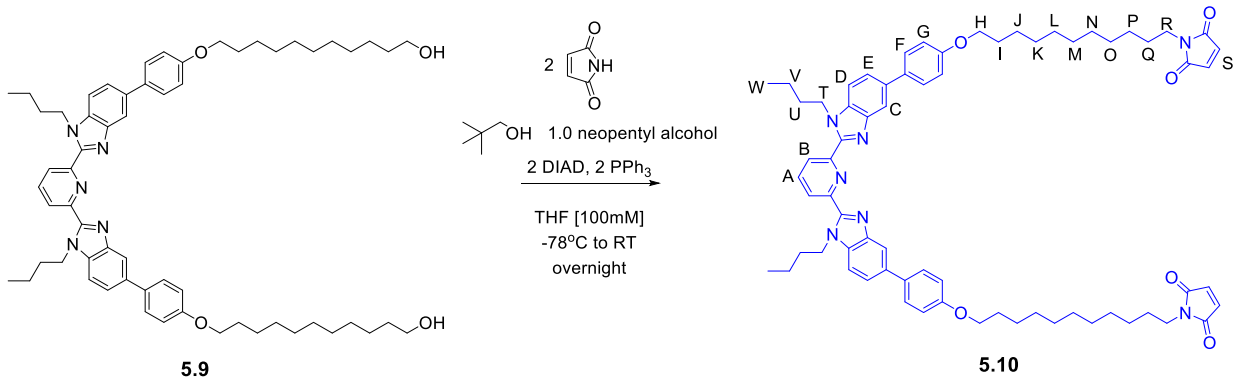

N-alkylation of maleimide to form thread **5.10** was based on Walker's modified Mitsunobu procedure.[14,15] Triphenylphosphine (0.055 g, 0.21 mmol) was added to an oven-dried, 25 mL round bottom flask and put under argon flow. Dry THF (200 µL) was added to the flask and cooled to -78°C using a dry ice/acetone bath. DIAD (0.043 g, 41.5 µL, 0.21 mmol) was dissolved in 200 µL dry THF and added dropwise via syringe and the resulting light-yellow solution was stirred for 5 minutes. **5.9** (0.1 g, 0.105 mmol) was dissolved in 600 µL of dry THF and added in ~100 µL increments via syringe over 10 minutes. Neopentyl alcohol (0.009 g, 0.11 mmol) and maleimide (0.020 g, 0.21 mmol) were added sequentially as solids. The reaction flask was removed from the dry ice/acetone bath and allowed to stir overnight at room temperature. The solvent was removed

via rotary evaporation and the resulting material was purified using column chromatography (silica gel, hexanes/ethyl acetate gradient as eluent) to yield **5.10** as a white powder in 55% yield by mass. ^{1}H NMR (500 MHz, $CDCl_3$) δ 8.34 (d, *J* = 7.9 Hz, 2H, B), 8.07 (t, *J* = 7.8 Hz, 1H, A), 8.02 (s, 2H, C), 7.63 – 7.55 (m, 6H, F+E), 7.50 (d, *J* = 8.5 Hz, 2H, D), 7.01 (d, 4H, G), 6.68 (s, 4H, S), 4.76 (t, *J* = 7.3 Hz, 4H, T), 4.02 (t, *J* = 6.6 Hz, 4H, H), 3.51 (t, 4H, R), 1.82 (p, *J* = 6.7 Hz, 4H, I), 1.78 – 1.71 (m, 4H, Q), 1.64 – 1.54 (m, 4H, J), 1.48 (p, *J* = 7.2 Hz, 4H, P), 1.42 – 1.19 (m, 24H, K+L+M+N+O+U), 1.18 – 1.10 (m, 4H, V), 0.73 (t, *J* = 7.3 Hz, 6H, W).

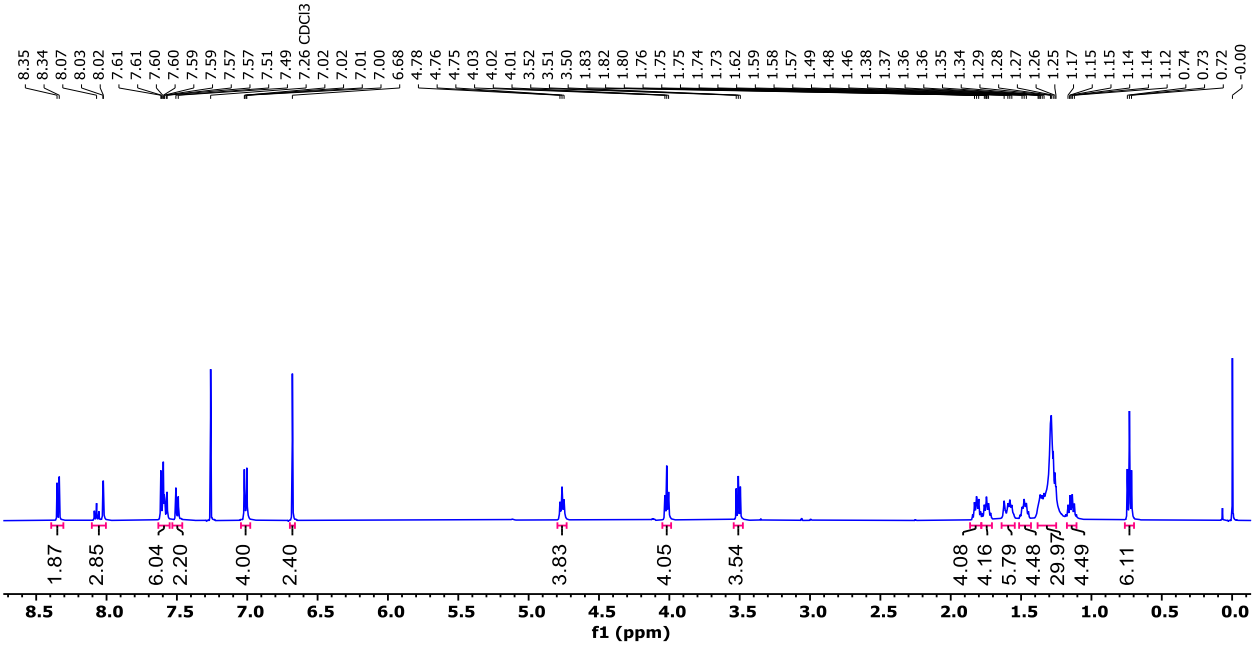

Figure 5.29. ^{1}H-NMR (500 MHz, 25°C, $CDCl_3$) of Butyl C11 Bip maleimide thread **5.10**.

5.4.2.5 Synthesis of maleimide thread **5.13**

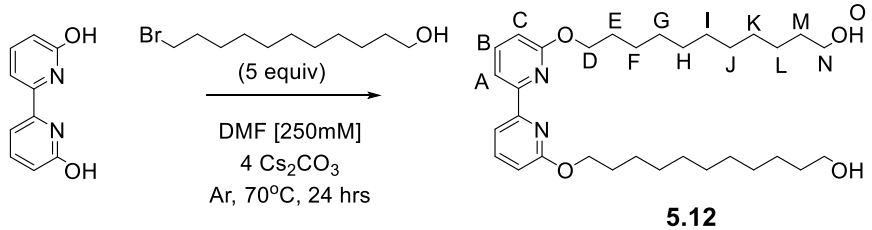

5.12

2,2'-Bipyridine-6,6'-diol **5.11** (1.0 g, 1.81 mmol), Cs_2CO_3 (2.36 g, 7.25 mmol), and 11-bromo-1-undecanol (2.28 g, 9.06 mmol) were added to a 25 mL oven-dried round bottom flask under argon.

Dry DMF (7.25 mL) was injected, and the flask was placed into a heating block and heated to 70°C. The reaction was stirred at 70°C for 24 hours, after which the reaction mixture was cooled to room temperature, and the solvent was removed under reduced pressure. The residue was dissolved in $CHCl_3$, and the insoluble material (salts) was removed by filtration. The filtrate was collected, and the solvent was removed under reduced pressure. The resulting material was purified using column chromatography (TEA-treated silica gel, chloroform/methanol gradient as eluent) followed by recrystallization (chloroform/acetonitrile mixture) to yield white crystals of **5.12** in 73% yield by mass. ^{1}H NMR (500 MHz, $CDCl_3$) δ 7.95 (dd, *J* = 7.4, 0.8 Hz, 2H, A), 7.70 – 7.63 (m, 2H, B), 6.72 (dd, *J* = 8.2, 0.8 Hz, 2H, C), 4.41 (t, *J* = 6.7 Hz, 4H, D), 3.63 (td, *J* = 6.5, 4.2 Hz, 4H, N), 1.86 – 1.77 (m, 4H, E), 1.55 (dt, *J* = 8.0, 6.5 Hz, 4H, F), 1.52 – 1.42 (m, 4H, M), 1.42 – 1.28 (m, 24H, G-L), 1.28 – 1.22 (t, 2H, O). MALDI-TOF MS: 534.6 ([M]-OH^-+Na^+), 759.5 ([M]-OH^-+Dithranol).

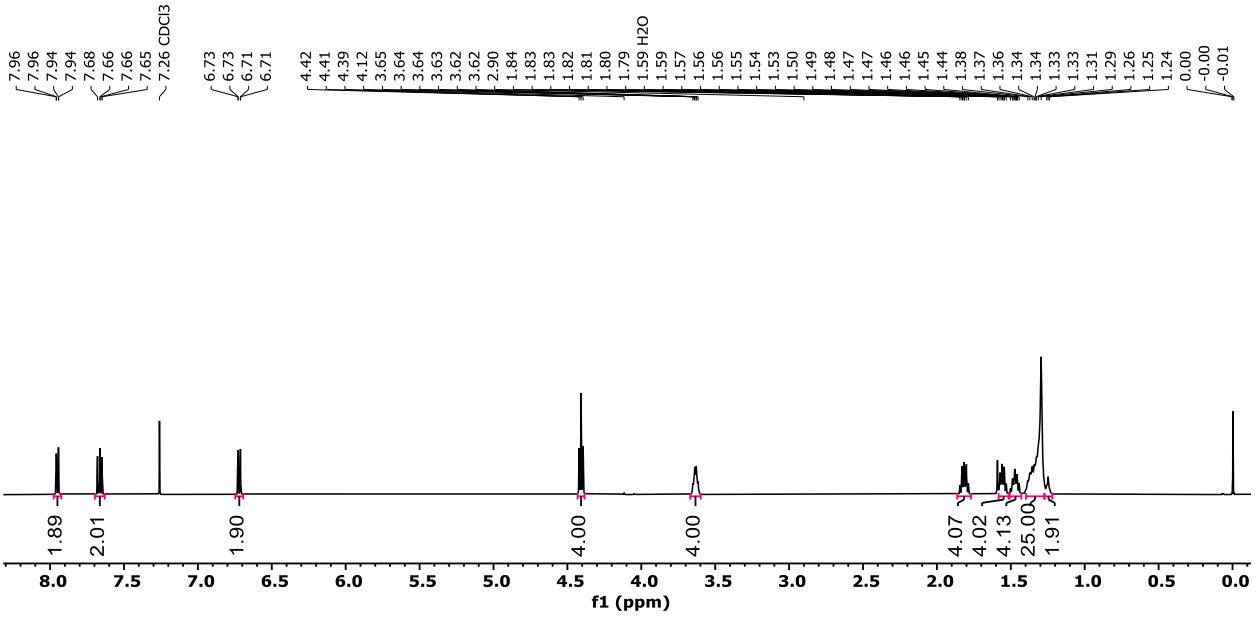

Figure 5.30. ^{1}H-NMR (500 MHz, 25°C, $CDCl_3$) of dihydroxy Bipy thread **5.12**.

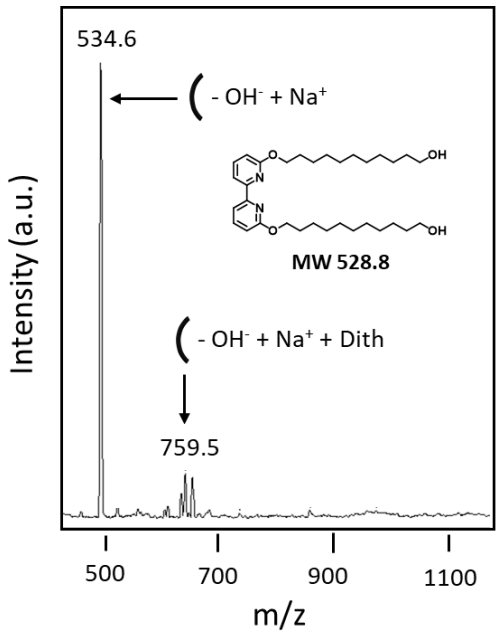

Figure 5.31. MALDI-TOF MS (Dithranol, sodium trifluoroacetate) of dihydroxy Bipy thread **5.12**.

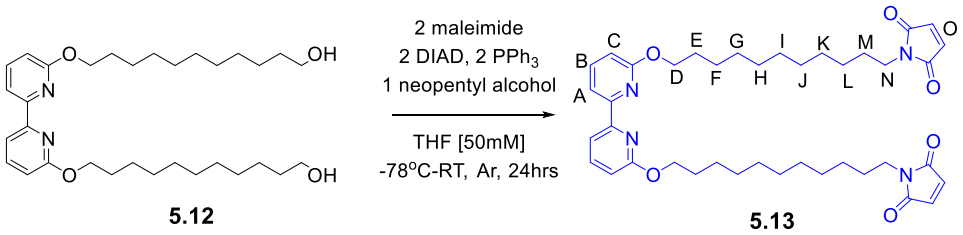

N-alkylation of maleimide to form **5.13** was based on Walker's modified Mitsunobu procedure.[14,15] Triphenylphosphine (0.248 g, 0.95 mmol) was added to an oven-dried, 25 mL round bottom flask under argon flow. Dry THF (1 mL) was added to the flask and cooled to -78°C using a dry ice/acetone bath. DIAD (0.191 g, 0.186 mL, 0.95 mmol) was dissolved in 1 mL dry THF and added dropwise via syringe, and the resulting light-yellow solution was stirred for 5 minutes. **5.12** (0.25 g, 0.47 mmol) was dissolved in 7.4 mL of dry THF and added in ~0.2 mL increments via syringe over 10 minutes. Neopentyl alcohol (0.042 g, 0.47 mmol) and maleimide (0.092 g, 0.95 mmol) were added sequentially as solids. The reaction flask was removed from the dry ice/acetone bath and stirred overnight at room temperature. The solvent was removed via rotary evaporation, and the resulting material was purified using column chromatography (silica gel, hexanes/ethyl

acetate gradient as eluent) to yield **5.13** as a white powder in 52% yield by mass. ^{1}H NMR (500 MHz, $CDCl_3$) δ 7.94 (dd, *J* = 7.4, 0.8 Hz, 2H, A), 7.65 (dd, *J* = 8.2, 7.4 Hz, 2H, B), 6.71 (dd, *J* = 8.2, 0.8 Hz, 2H, C), 6.67 (s, 2H, O), 4.39 (t, *J* = 6.7 Hz, 4H, D), 3.52 – 3.45 (m, 4H, N), 1.85 – 1.75 (m, 4H, E), 1.56 (p, *J* = 7.6 Hz, 4H, F), 1.50 – 1.41 (m, 4H, M), 1.40 – 1.31 (m, 4H, G), 1.31 – 1.23 (m, 20H, H-L). MALDI-TOF MS: 687.8 ([M]+H^+), 709.8 ([M]+Na^+).

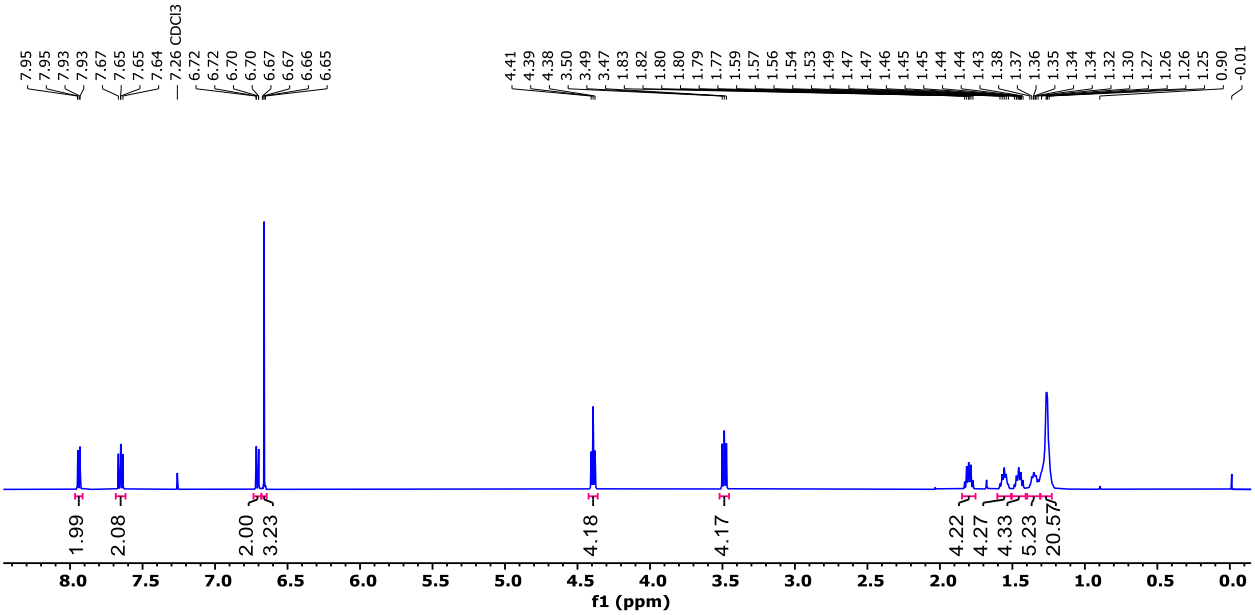

Figure 5.32. ^{1}H-NMR (500 MHz, 25°C, $CDCl_3$) of Bipy maleimide thread **5.13**.

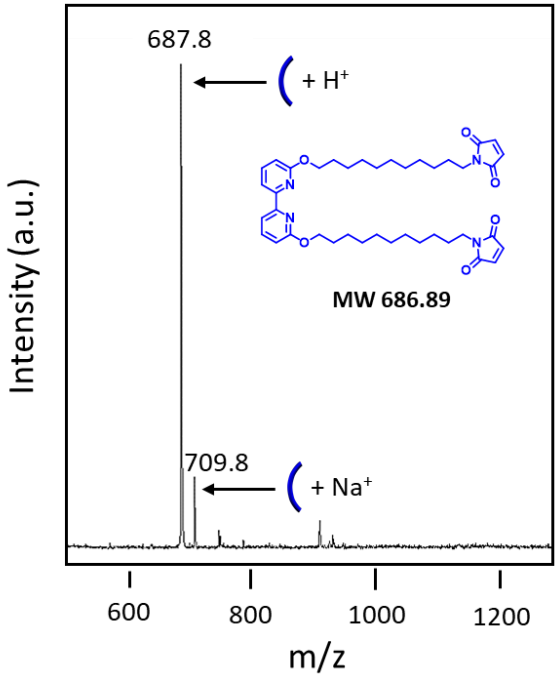

Figure 5.33. MALDI-TOF MS (Dithranol, sodium trifluoroacetate) of Bipy maleimide thread **5.13**.

5.4.2.6 Synthesis of thiol stopper **5.3**

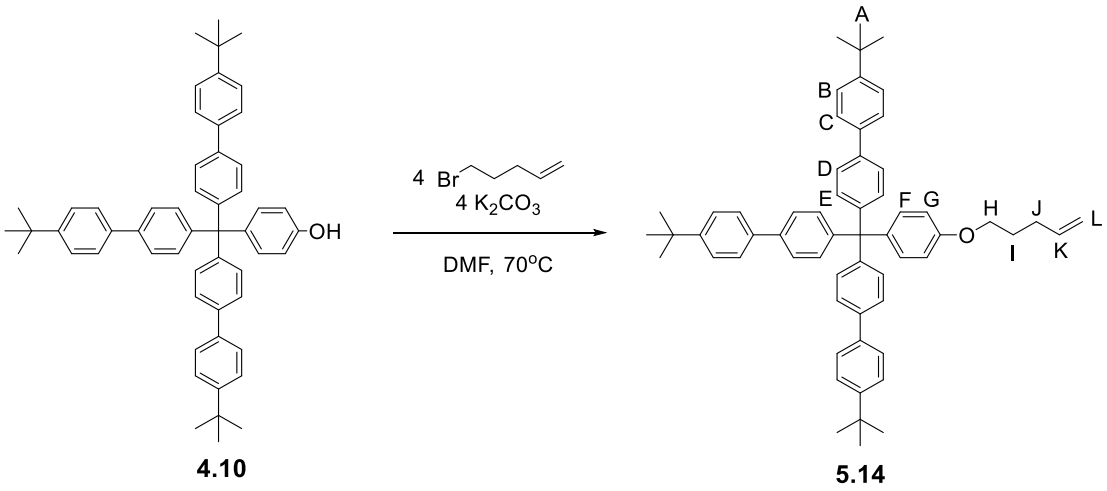

4.10 **5.14**

Phenol stopper **4.10**[6] (1.5 g, 2.05 mmol) and K_2CO_3 (1.13 g, 8.18 mmol) were added to a 50 mL oven-dried round bottom flask under argon flow. Dry DMF (20 mL) was injected, and the flask was placed into a heating block and heated to 70°C. Once the solution reached temperature, 5-bromo-1-pentene (1.22 g, 0.97 mL, 8.18 mmol) was injected dropwise. After 24 hours, the reaction was cooled to room temperature, after which the solvent was removed under vacuum. The residue

was dissolved in $CHCl_3$, and the insoluble material (salts) was removed by filtration. After vacuum filtration, the filtrate was collected, and the solvent was removed in vacuo. The resulting material was purified using column chromatography (silica gel, hexanes/chloroform gradient as eluent) to yield the desired product **5.14** in 57% yield by mass. ^{1}H NMR (500 MHz, $CDCl_3$) δ 7.57 – 7.53 (m, 6H, B), 7.52 – 7.48 (m, 6H, C), 7.47 – 7.43 (m, 6H, D), 7.34 – 7.29 (m, 6H, E), 7.22 – 7.17 (m, 2HF), 6.84 – 6.80 (m, 2H, G), 5.86 (ddt, *J* = 16.9, 10.1, 6.6 Hz, 1H, K), 5.07 (dq, *J* = 17.1, 1.7 Hz, 1H, L), 5.00 (ddt, *J* = 10.2, 2.1, 1.2 Hz, 1H, L), 3.97 (t, *J* = 6.5 Hz, 2H, H), 2.24 (dt, *J* = 7.9, 6.7 Hz, 2H, J), 1.96 – 1.81 (m, 2H, I), 1.35 (s, 27H, A).

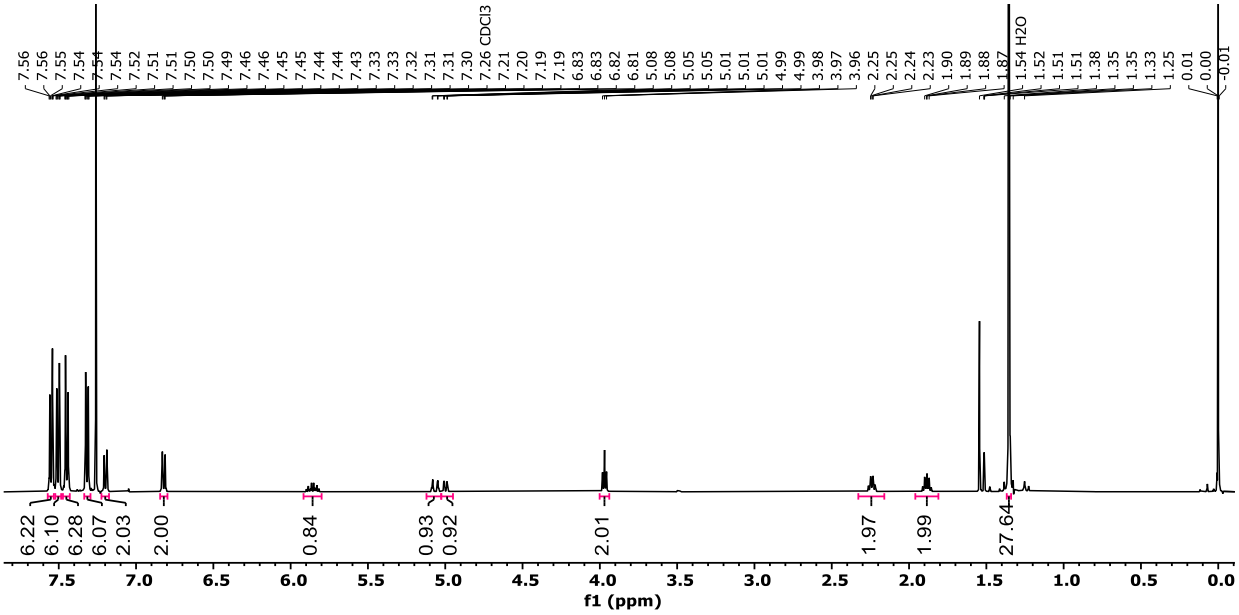

Figure 5.34. ^{1}H-NMR (500 MHz, 25°C, $CDCl_3$) of alkene stopper **5.14**.

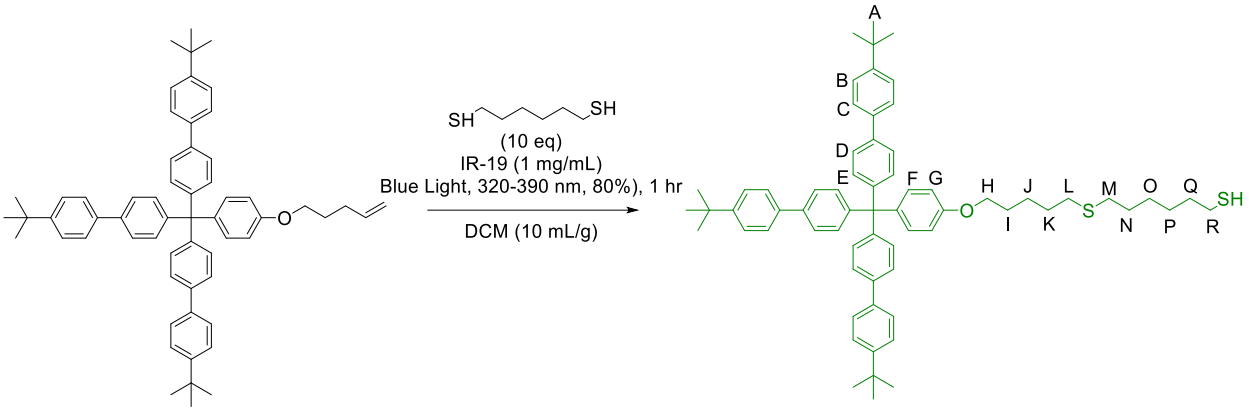

5.14 **5.3**

Alkene stopper **5.14** (0.82 g, mmol), 1.567 mL of 1,6-hexanedithiol, and 8 mg of Irgacure photocatalyst (IR-19) were added to a vial; after 8 mL of dichloromethane was added, resulting in a cloudy solution. The vial was exposed to UV light (320-390 nm, 80%) for one hour, turning the solution transparent. The reaction mixture was then concentrated to ~2mL DCM in vacuo. 100 mL of hexane was added, and the mixture was put into the freezer at 0°C overnight. The solution was filtered under vacuum, leaving behind thiol stopper **5.3** as a white powder in 80% yield by mass. ^{1}H NMR (500 MHz, $CDCl_3$) δ 7.57 – 7.53 (m, 6H, B), 7.52 – 7.48 (m, 6H, C), 7.47 – 7.43 (m, 6H, D), 7.34 – 7.30 (m, 6H, E), 7.22 – 7.18 (m, 2H, F), 6.82 (dd, *J* = 9.0, 3.8 Hz, 2H, G), 3.96 (q, *J* = 6.3 Hz, 2H, H), 2.52 (dt, *J* = 12.4, 7.3 Hz, 6H, L+M+R), 1.80 (p, *J* = 6.6 Hz, 2H, I), 1.70 – 1.54 (m, 8H, J+K+N+Q), 1.43 – 1.37 (m, 4H, O+P), 1.35 (s, 27H, A).

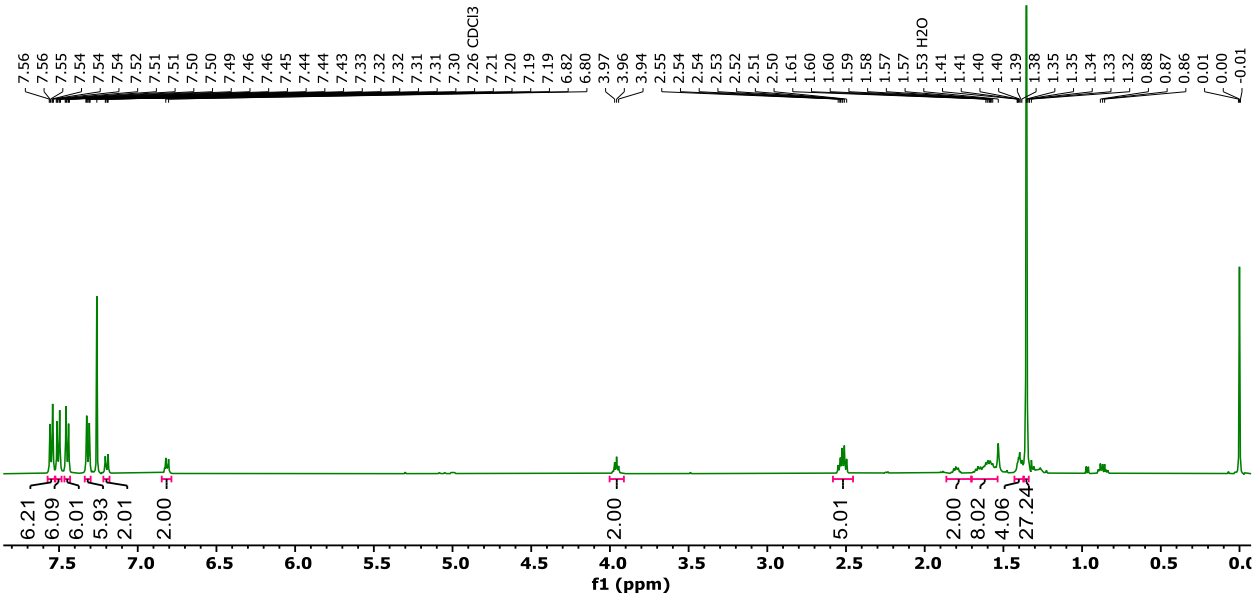

Figure 5.35. ^{1}H-NMR (500 MHz, 25°C, $CDCl_3$) of thiol stopper **5.3**.

5.4.2.7 Synthesis of polymer stopper **5.18**

A polymer stopper extends the thiol farther away from the bulky triaryl moiety to reduce steric hindrance during the stoppering step. Therefore, a stopper chain-transfer agent (CTA) was synthesized for the reversible addition-fragmentation chain-transfer (RAFT) polymerization (Figure 5.36) of *n*-butyl acrylate, chosen for its low glass transition temperature (about -50°C). The phenol on stopper **4.10** reacts with 3-bromo-1-propanol under basic conditions to provide terminal hydroxy groups; Steglich Esterification[16] attaches 2-(dodecylthiocarbonothioylthio)-2-methylpropionic acid (DDMAT), a CTA commonly used for the polymerization of acrylates. The resulting stopper CTA **5.16** was polymerized using AIBN as the initiator to target a 5K molecular weight of **5.17**, and then aminolysis with excess n-butylamine uncovered the reactive thiol moiety on polymer stopper **5.18**.[17–19]

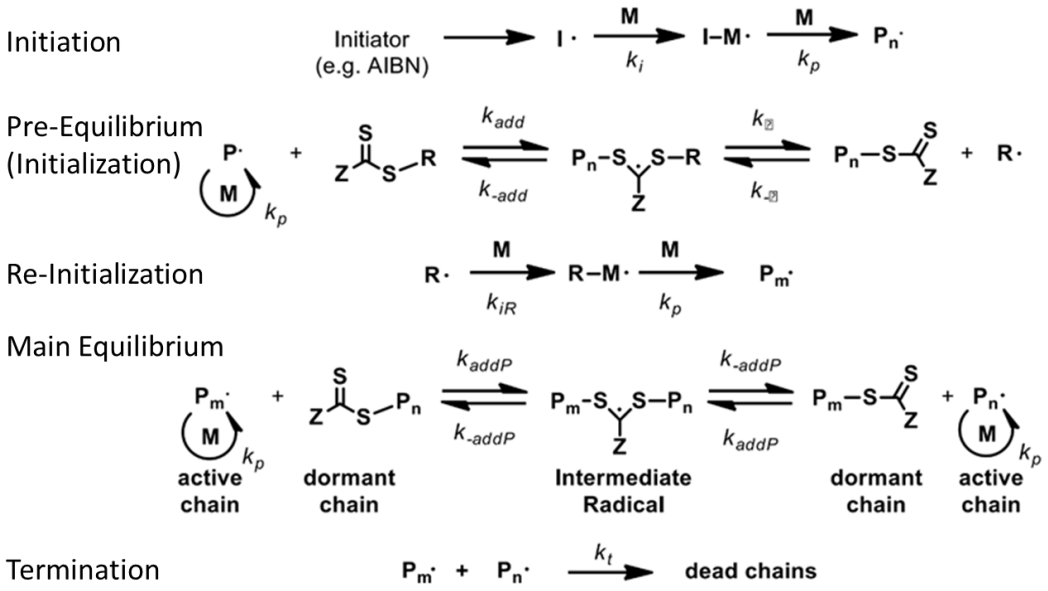

Figure 5.36. RAFT mechanism.

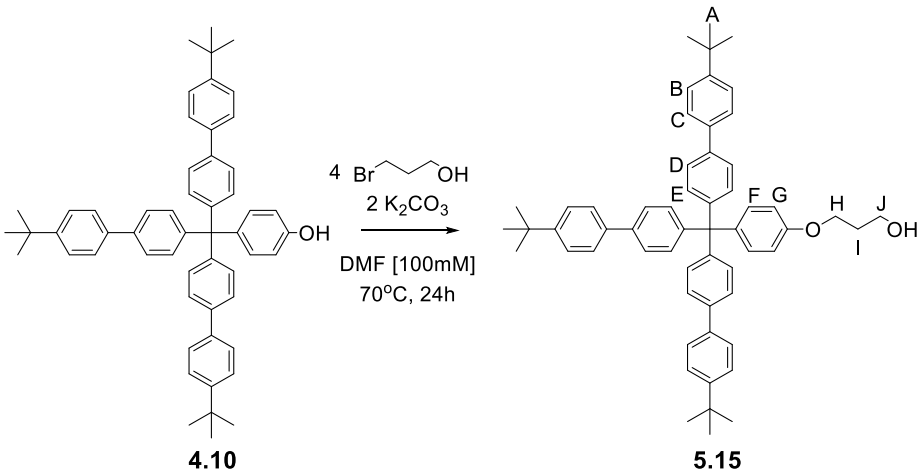

4.10 **5.15**

Phenol stopper **4.10**[6] (1.0 g, 1.36 mmol) and K_2CO_3 (0.377 g, 2.37 mmol) were added to a 25 mL oven-dried round bottom flask under argon flow. Dry DMF (13.6 mL) was injected, and the flask was placed into a heating block and heated to 70°C. Once the solution reached temperature, 3-bromo-1-propanol (0.758 g, 0.474 mL, 5.46 mmol) was injected dropwise. After 24 hours, the reaction was cooled to room temperature, after which the solvent was removed under vacuum. The residue was dissolved in $CHCl_3$, and the insoluble material (salts) was removed by filtration. After vacuum filtration, the filtrate was collected, and the solvent was removed in vacuo. The resulting

material was purified using column chromatography (silica gel, hexanes/chloroform gradient as eluent) to yield the desired product **5.15** in 50% yield by mass. ^{1}H NMR (500 MHz, $CDCl_3$) δ 7.56 (dq, *J* = 8.8, 2.2 Hz, 6H, B), 7.51 (dq, *J* = 9.0, 2.3 Hz, 6H, C), 7.48 – 7.43 (m, 6H, D), 7.32 (dq, *J* = 8.9, 2.3 Hz, 6H, E), 7.24 – 7.20 (m, 2H, F), 6.87 – 6.82 (m, 2H, G), 4.14 (td, *J* = 5.9, 1.8 Hz, 2H, H), 3.88 (t, *J* = 5.9 Hz, 2H, J), 2.05 (tt, *J* = 7.7, 4.9 Hz, 2H, I), 1.36 (d, *J* = 1.8 Hz, 27H, A).

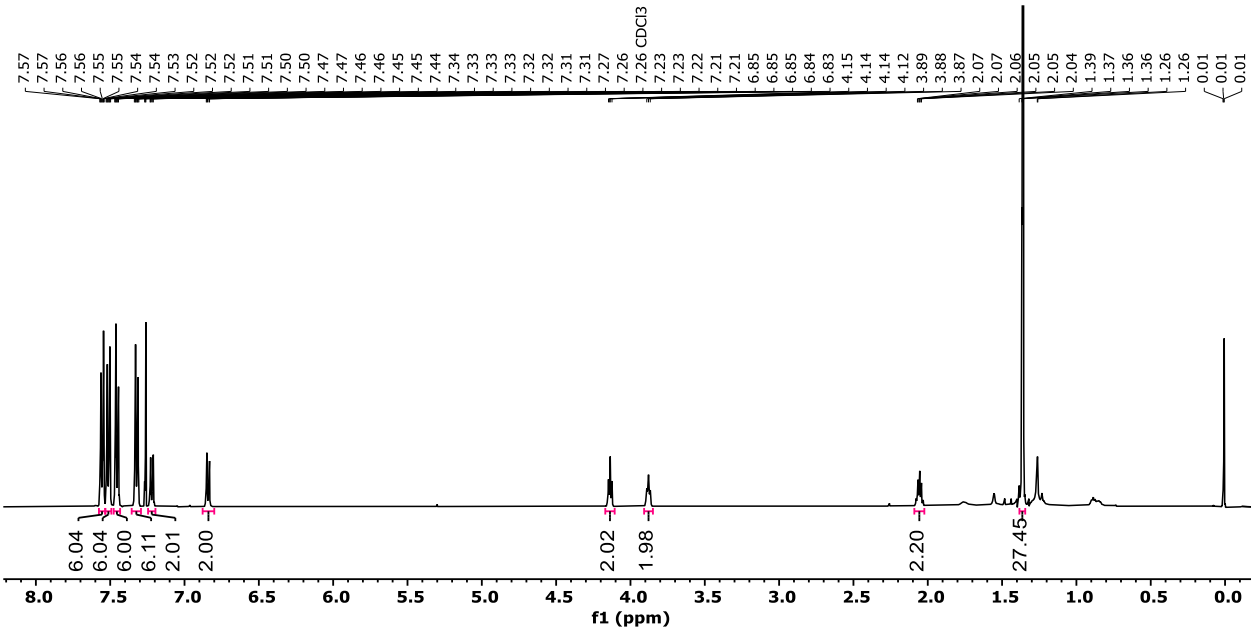

Figure 5.37. ^{1}H-NMR (500 MHz, 25°C, $CDCl_3$) of propanol stopper **5.15**.

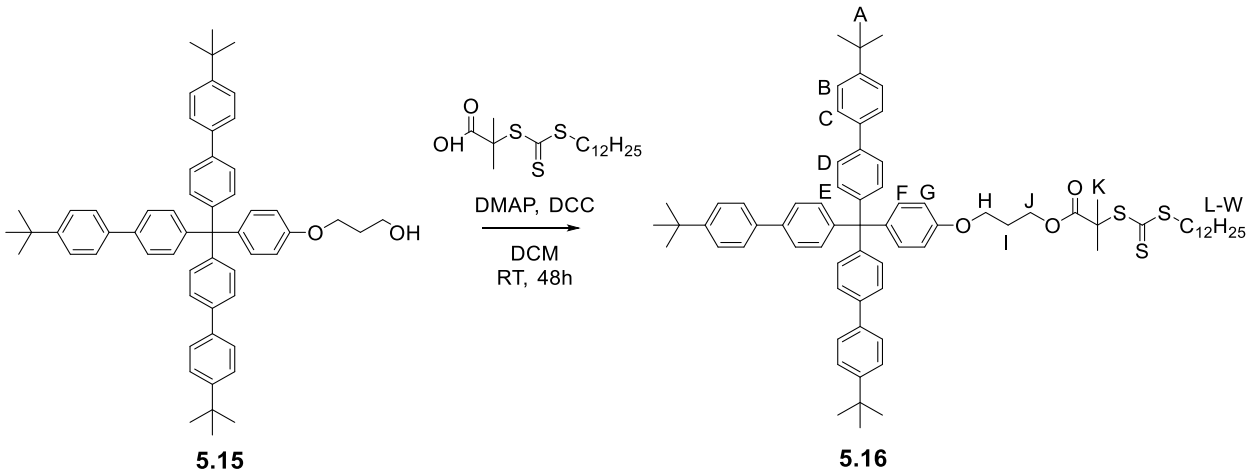

Stopper CTA **5.16** was prepared via Steglich Esterification.[16] **5.15** (0.25 g, 0.32 mmol), 2-(dodecylthiocarbonothioylthio)-2-methylpropionic acid (DDMAT, 0.127 g, 0.35 mmol, 1.1

equiv), N, N′-dicyclohexylcarbodiimide (0.072 g, 0.35 mmol, 1.1 equiv), and 4-dimethylaminopyridine (0.0077 g, 0.06 mmol) were added to a 25 mL oven-dried round bottom flask with a stir bar. The flask was put under argon flow, and dry DCM (3.2 mL) was injected. The reaction was left to stir at RT for 48 hours, after which the solution was filtered, and the filtrate was dried under vacuum. The resulting material was purified using column chromatography (silica gel, 15% hexanes in ethyl acetate as eluent) to yield the desired CTA **5.16** in 80% yield by mass. ^{1}H NMR (500 MHz, $CDCl_3$) δ 7.59 – 7.54 (m, 6H, B), 7.53 – 7.49 (m, 6H, C), 7.49 – 7.42 (m, 6H, D), 7.32 (dt, *J* = 9.8, 3.7 Hz, 6H, E), 7.20 (d, 2H, F), 6.81 (d, 2H, G), 4.30 (t, *J* = 6.0 Hz, 2H, H), 4.00 (t, *J* = 5.9 Hz, 2H, J), 3.19 (t, 2H, L), 2.15 – 2.07 (m, 2H, I), 1.69 (s, 6H, K), 1.60 (q, *J* = 7.2 Hz, 2H, M), 1.36 (s, 27H, A), 1.24 (dd, *J* = 14.6, 8.5 Hz, 18H, N-V), 0.87 (t, 3H, W). MALDI-TOF MS: 1159.8 ([M]+Na^+).

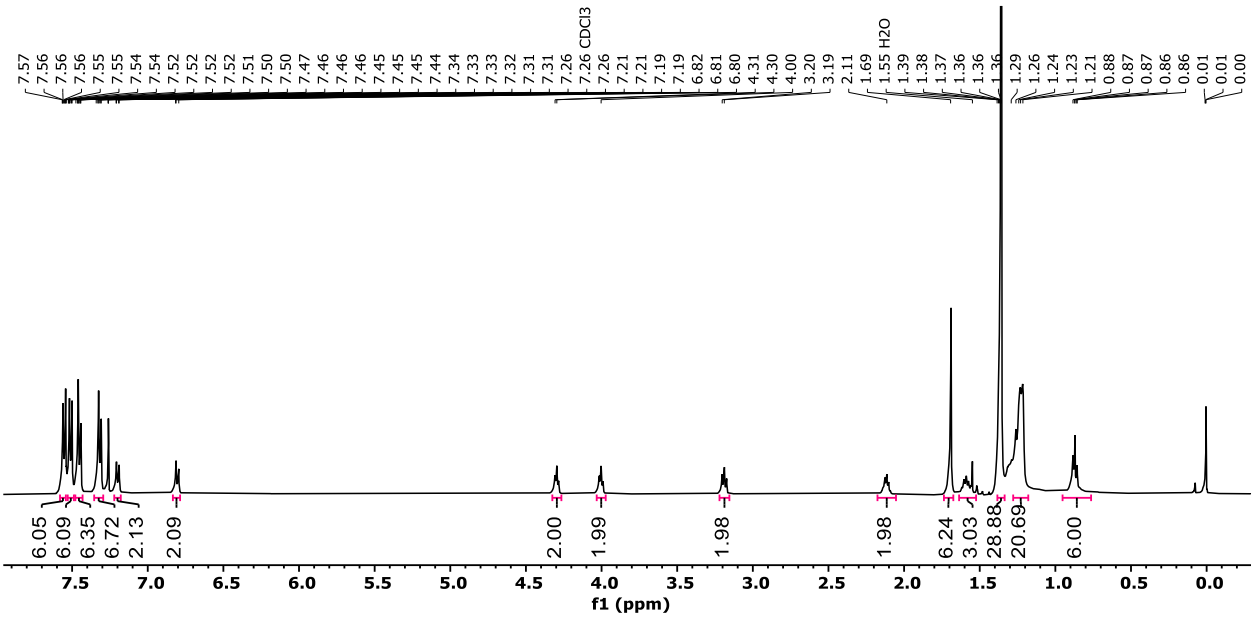

Figure 5.38. ^{1}H-NMR (500 MHz, 25°C, $CDCl_3$) of stopper CTA **5.16**.

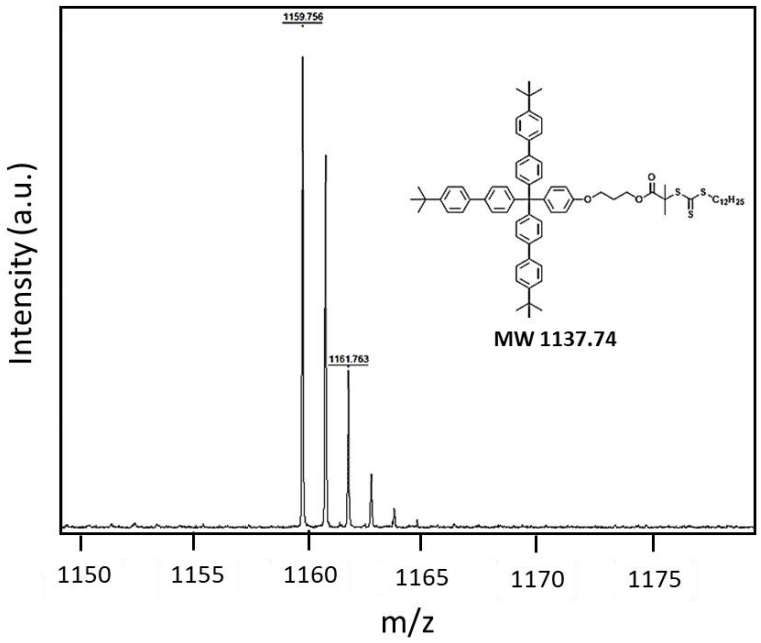

Figure 5.39. MALDI-TOF MS (Dithranol, sodium trifluoroacetate) of stopper CTA **5.16**.

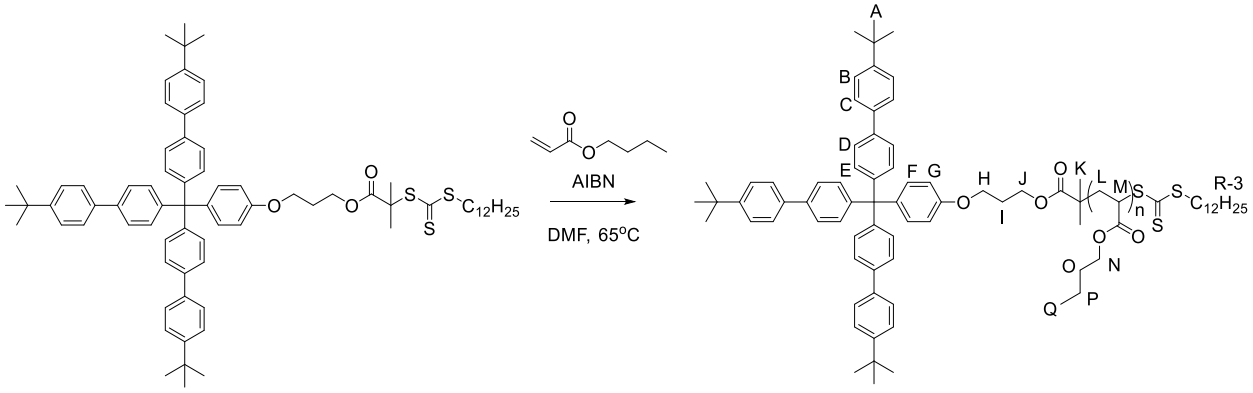

5.16 **5.17**

The RAFT polymerization and end-group modification procedures described below were based off literature protocols.[17–19] *N*-butyl acrylate was passed through an alumina column with a top layer of K_2CO_3 to remove the inhibitor before use. Stopper CTA **5.16** (0.046 g, 0.040 mmol), AIBN (0.00066 g, 0.004 mmol), and *n*-butyl acrylate monomer (0.518 g, 0.580 mL, 4.04 mmol) were added to a 20 mL vial with stir bar and flushed with argon. Dry DMF (4 mL) was injected, and the solution was bubbled with nitrogen for 1 hour, after which the vial was placed in a pre-heated oil bath at 65°C. After 3 hours, the vial was placed into an ice bath to cool. The crude

mixture was pipetted dropwise into cold methanol (200 mL) and the yellow product **5.17** was dried under vacuum.

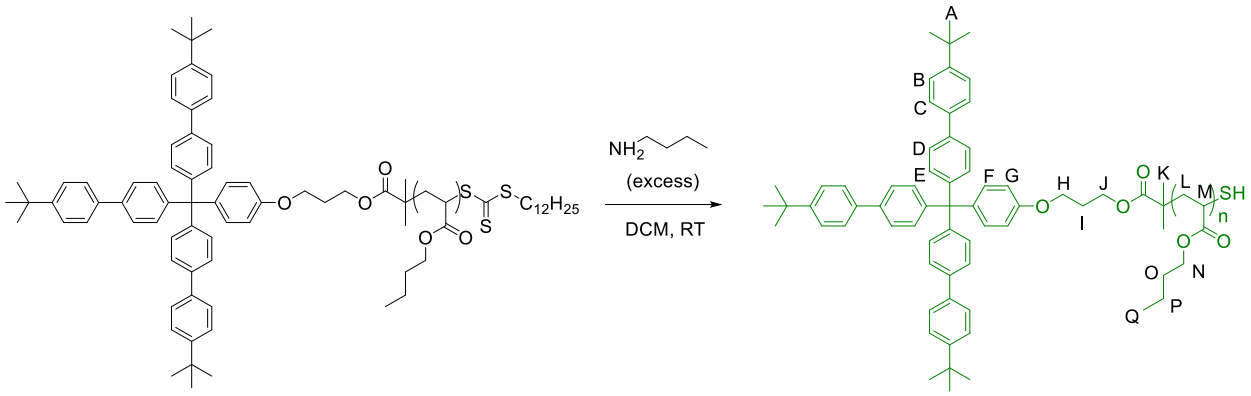

5.17 **5.18**

Polymer stopper **5.17** was added to a vial with excess butyl amine and DCM. The mixture was stirred at room temperature overnight, after which the product was precipitated into cold methanol and dried under vacuum to afford the thiol-terminated derivative **5.18**. ^{1}H NMR (500 MHz, $CDCl_3$) δ 7.55 (d, *J* = 8.2 Hz, 6H, B), 7.50 (d, *J* = 8.3 Hz, 6H, C), 7.45 (d, *J* = 8.3 Hz, 6H, D), 7.31 (d, *J* = 8.3 Hz, 6H, E), 7.20 (d, 2H, F), 6.81 (d, 2H, G), 4.20 (t, *J* = 6.0 Hz, 2H, H), 4.17 – 3.84 (m, 102H, J+N), 2.43 – 2.19 (m, 50H, L), 2.15 – 2.07 (m, 2H, I), 1.99 – 1.81 (m, 25H, M), 1.71 – 1.54 (m, 100H, O), 1.42 – 1.32 (m, 100H, P), 0.93 (t, *J* = 7.5 Hz, 150H, Q).

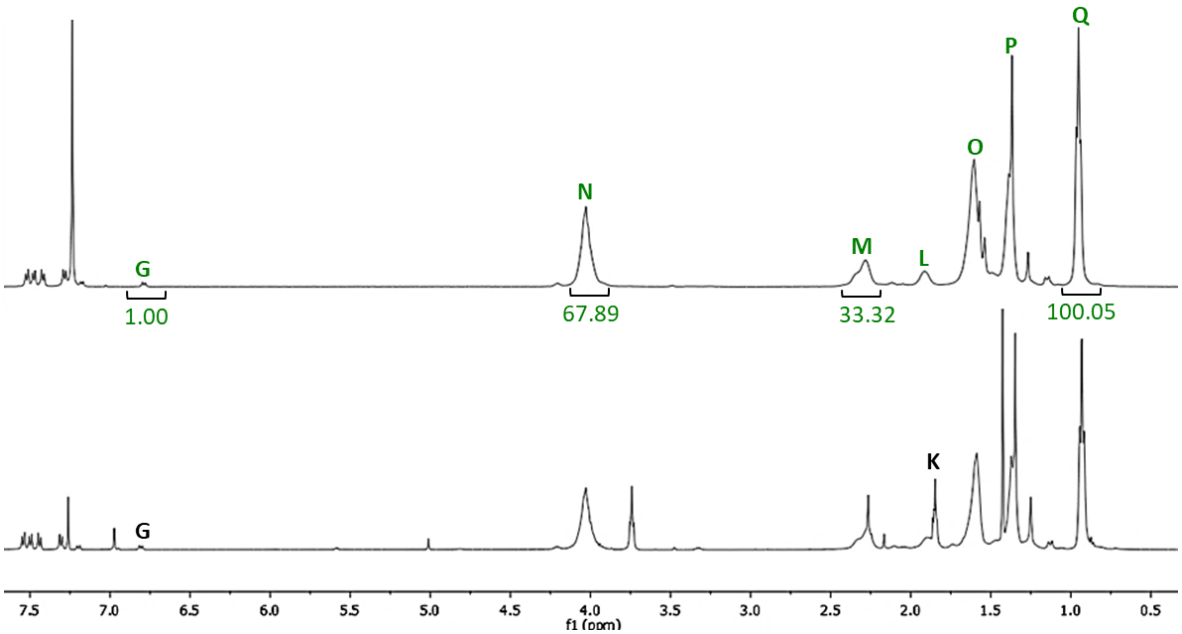

Figure 5.40. ^{1}H-NMR (500 MHz, 25°C, $CDCl_3$) of polymer stopper before (**5.17**, bottom) and after (**5.18**, top) aminolysis to uncover the thiol end group.

^{1}H-NMR end-group analysis determined the molecular weight of polymer **5.18** based on the terminal methyl group on the butyl acrylate chain (Q). Integrations are based off the stopper doublet at 6.8 ppm, which serves as a good end-group for this molecule; based on these integrations, the number of monomers incorporated in the backbone is ~33-34 (n = 100/3), which corresponds to a molecular weight of about 4300 g/mol when multiplied by the molecular weight of the butyl acrylate repeat unit:

$$\left(n = \frac{100}{3}\right) \times 128.17\ g/mol = \ 4272.33\ g/mol$$

Adding the mass of the triaryl stopper component (894.29 g/mol) to the polymer (4272.33 g/mol) gives 5166.62 g/mol, which is not far from the 5,000 g/mol target molecular weight. The number-average molecular weight from MALDI-TOF is 5260 g/mol (Figure 5.30; data collected and plotted by Dr. Debbie Schneiderman), which is in good agreement with the 5166.62 g/mol calculated from ^{1}H-NMR end-group analysis.

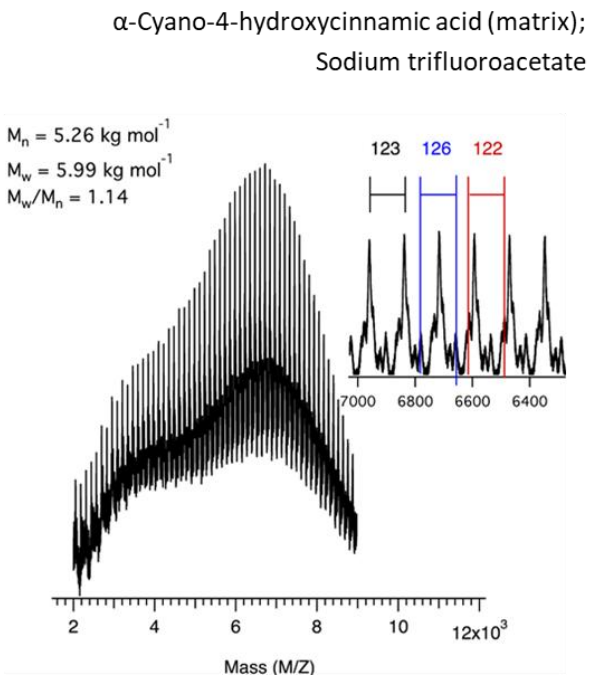

Figure 5.41. MALDI-TOF MS (α-Cyano-4-hydroxycinnamic acid, sodium trifluoroacetate) of thiol polymer stopper **5.18**. Special thank you to Dr. Debbie Schneiderman for collecting and plotting this data.

5.4.2.8 Synthesis of dumbbell **5.19**

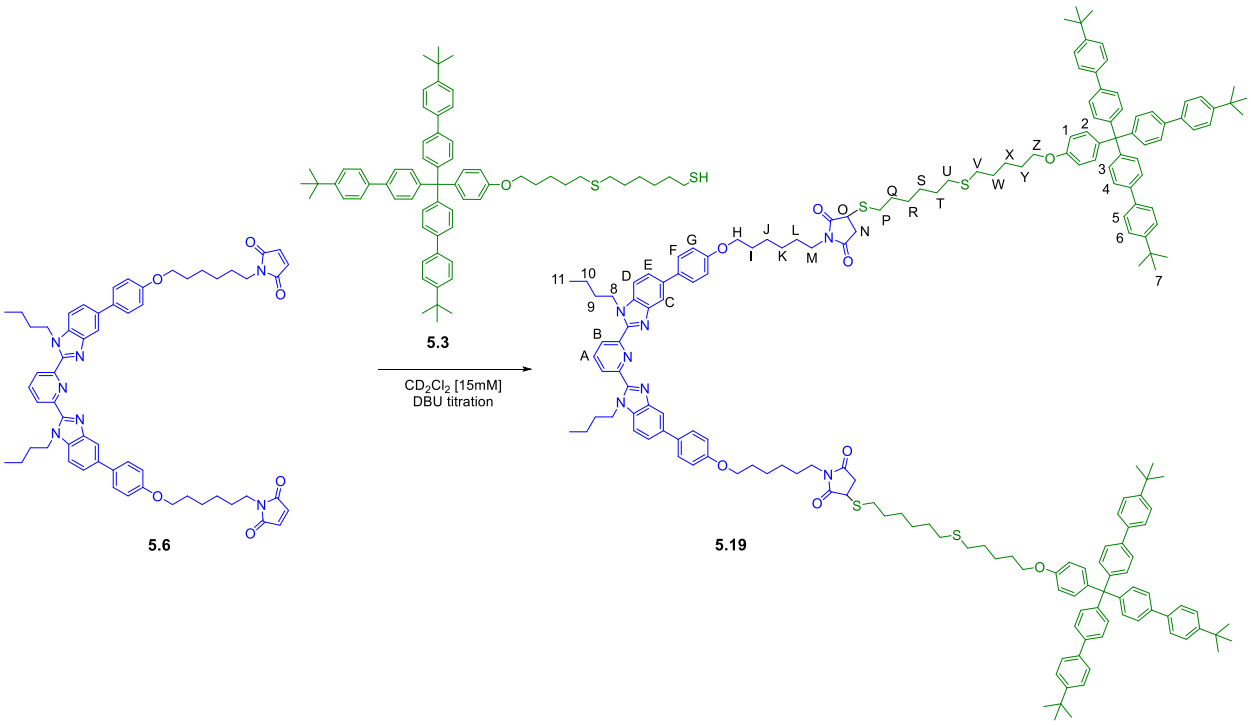

Maleimide thread **5.6** (0.005 g, 0.0052 mmol) and stopper **5.3** (0.010 g, 0.0103 mmol) were dissolved in 0.5 mL of CD_2Cl_2 and added to an NMR tube. A stock solution of 1,8-diazabicyclo[5.4.0]undec-7-ene (0.387 µL DBU in 0.5 mL CD_2Cl_2) was prepared and added in 0.5 mol% increments (0.003875 µL DBU in 5 µL CD_2Cl_2) with an NMR spectrum taken after every addition. DBU was added until the maleimide singlet at 6.7 ppm disappeared completely (4.0 mol% DBU). The solvent was removed under reduced pressure and then the resulting material was purified using column chromatography (TEA treated silica gel, chloroform/methanol gradient as eluent) to yield dumbbell **5.19** in 93% yield by mass. ^{1}H NMR (500 MHz, CD_2Cl_2) δ 8.35 (d, 2H, B), 8.07 (t, *J* = 7.9 Hz, 1H, A), 7.98 (s, 2H, C), 7.65 – 7.58 (m, 6H, F+E), 7.55 (ddt, *J* = 10.7, 9.0, 2.1 Hz, 26H, D+6+5), 7.47 (dd, 12H, 4), 7.39 (dd, *J* = 8.7, 2.3 Hz, 12H, 3), 7.29 – 7.23 (m, 4H, 2), 7.00 (d, 4H, G), 6.84 (d, 4H, 1), 4.80 (t, *J* = 7.3 Hz, 4H, H), 4.02 (t, *J* = 6.5 Hz, 4H, 8), 4.00 – 3.93 (t, 4H, Z), 3.70 (m, 2H, O), 3.52 (t, *J* = 7.3 Hz, 4H, M), 3.10 (m, 4H, P), 2.86 (m, 2H, N), 2.73 (m, 2H, N), 2.56 – 2.47 (m, 8H, U+V), 1.86 – 1.74 (m, 8H, 9+Q), 1.69 – 1.46 (m, 28H, I+J+K+L+T+W+X), 1.47 – 1.38 (m, 12H, R+S+Y), 1.36 (s, 54H, 7), 1.21 – 1.10 (m, 4H, 10), 0.74 (t, 6H, 11). MALDI-TOF MS: 2870 ([M]+H^+).

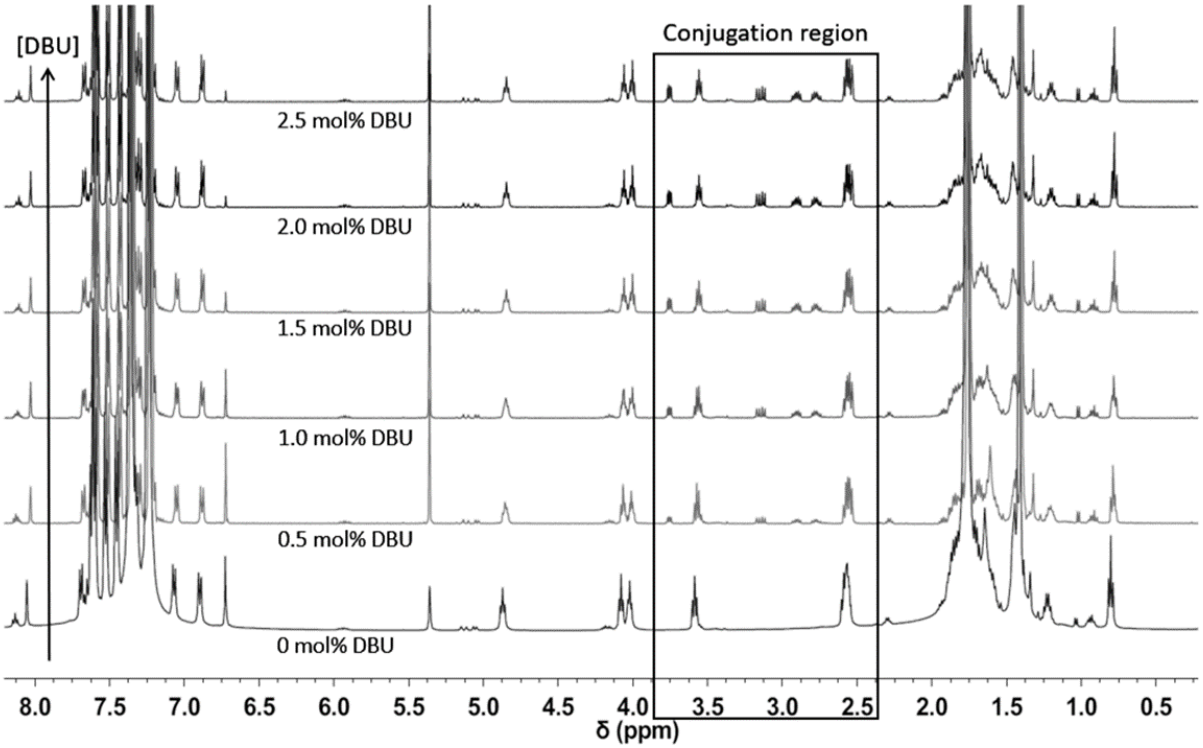

Figure 5.42. ^{1}H-NMR (500 MHz, 25°C, CD_2Cl_2) of Bip dumbbell **5.19** titration. Bottom NMR spectrum corresponds to maleimide thread **5.6** (0.005 g) and 2 equivalents of thiol stopper **5.3** (0.010 g) in 0.5 mL CD_2Cl_2 (0 mol% DBU). DBU was added in 0.5 mol% increments (0.003875 µL DBU in 5 µL CD_2Cl_2).

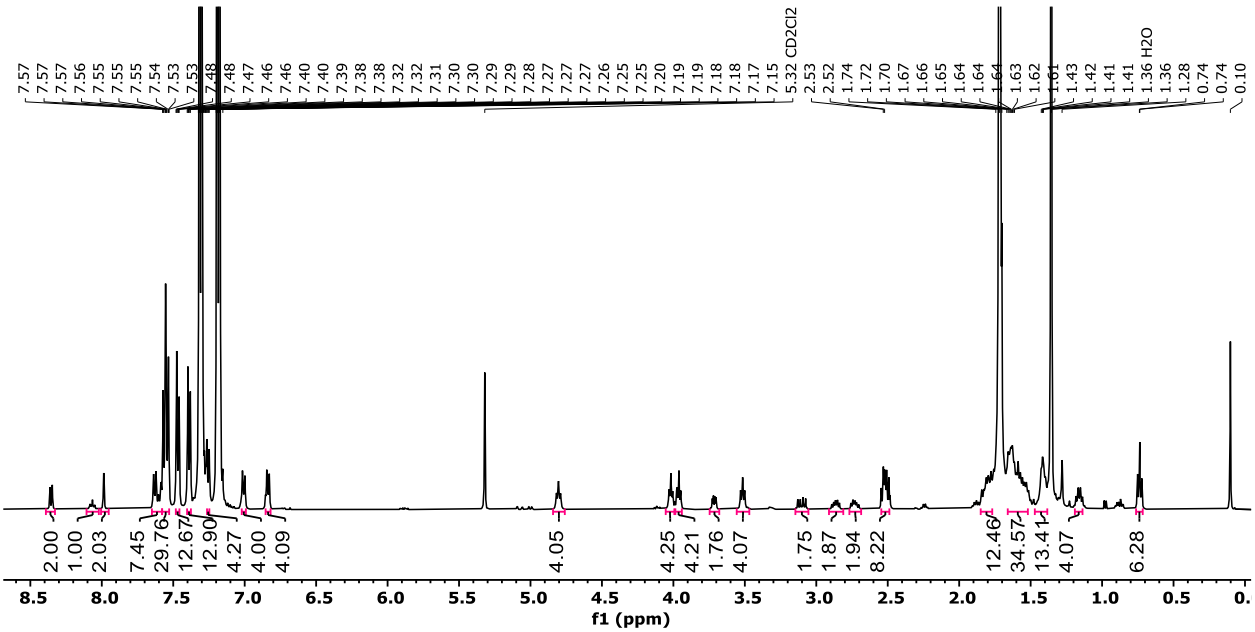

Figure 5.43. ^{1}H-NMR (500 MHz, 25°C, CD_2Cl_2) of thioester Bip dumbbell **5.19**.

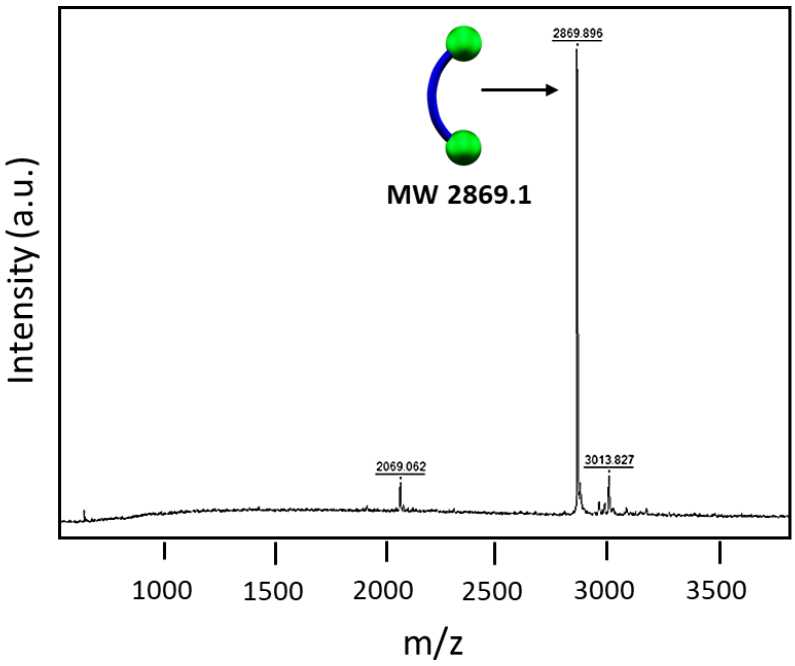

Figure 5.44. MALDI-TOF MS (Dithranol) of thioester Bip dumbbell **5.19**.

5.4.2.9 Synthesis of dumbbell **5.20**

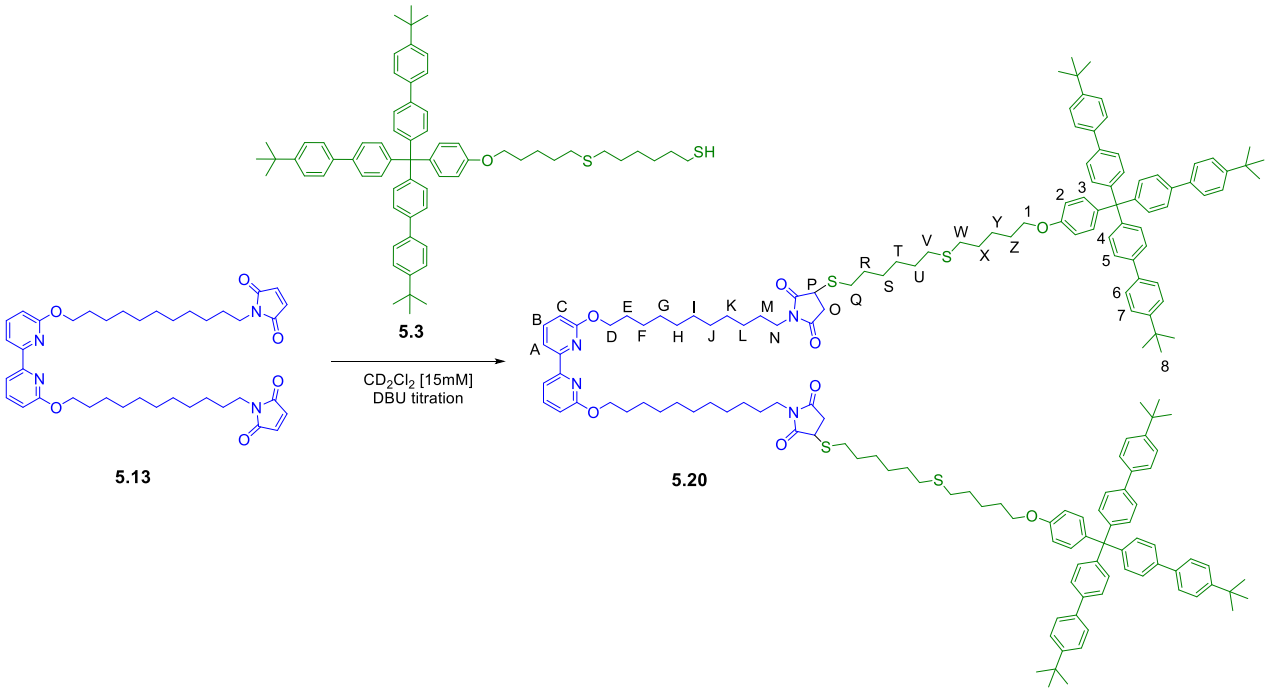

Bipy maleimide thread **5.13** (0.005 g, 0.007 mmol) and stopper **5.3** (0.014 g, 0.015 mmol) were dissolved in 0.4 mL of CD_2Cl_2 and added to an NMR tube. A stock solution of 1,8-

diazabicyclo[5.4.0]undec-7-ene (0.011 µL DBU in 100 µL CD_2Cl_2 was prepared and added in 0.1 mol% increments (10 µL) with NMR taken after every addition. DBU was added until the maleimide singlet at 6.7 ppm disappeared completely (0.2 mol% DBU), resulting in dumbbell **5.20**. ^{1}H NMR (500 MHz, CD_2Cl_2) δ 7.95 (d, 2H, A), 7.67 (t, 2H, B), 7.55 (ddt, *J* = 10.9, 9.0, 2.2 Hz, 24H, 6+7), 7.47 (dd, *J* = 8.3, 2.0 Hz, 12H, 5), 7.41 – 7.36 (m, 12H, 4), 7.25 (d, *J* = 1.7 Hz, 4H, 3), 6.83 (d, *J* = 3.0 Hz, 4H, 2), 6.71 (d, *J* = 8.2 Hz, 2H, C), 4.40 (t, *J* = 6.7 Hz, 4H, D), 3.96 (td, *J* = 6.4, 3.9 Hz, 4H, 1), 3.69 (dd, *J* = 9.2, 3.6 Hz, 2H, P), 3.46 (t, *J* = 7.3 Hz, 4H, N), 3.08 (dd, *J* = 18.6, 9.0 Hz, 4H, Q), 2.84 (ddd, *J* = 12.3, 8.2, 6.1 Hz, 2H, O), 2.71 (ddd, *J* = 12.4, 8.4, 6.7 Hz, 2H, O), 2.51 (dtd, *J* = 15.5, 8.6, 6.5 Hz, 8H, V+W), 1.85 – 1.74 (m, 8H, R+E), 1.69 – 1.51 (m, 16H, F+U+X+Y), 1.47 (q, *J* = 7.1 Hz, 4H, M), 1.42 – 1.36 (m, 16H, G+S+T+Z), 1.35 (s, 54H, 8). 1.31 – 1.23 (m, 20H, H-L).

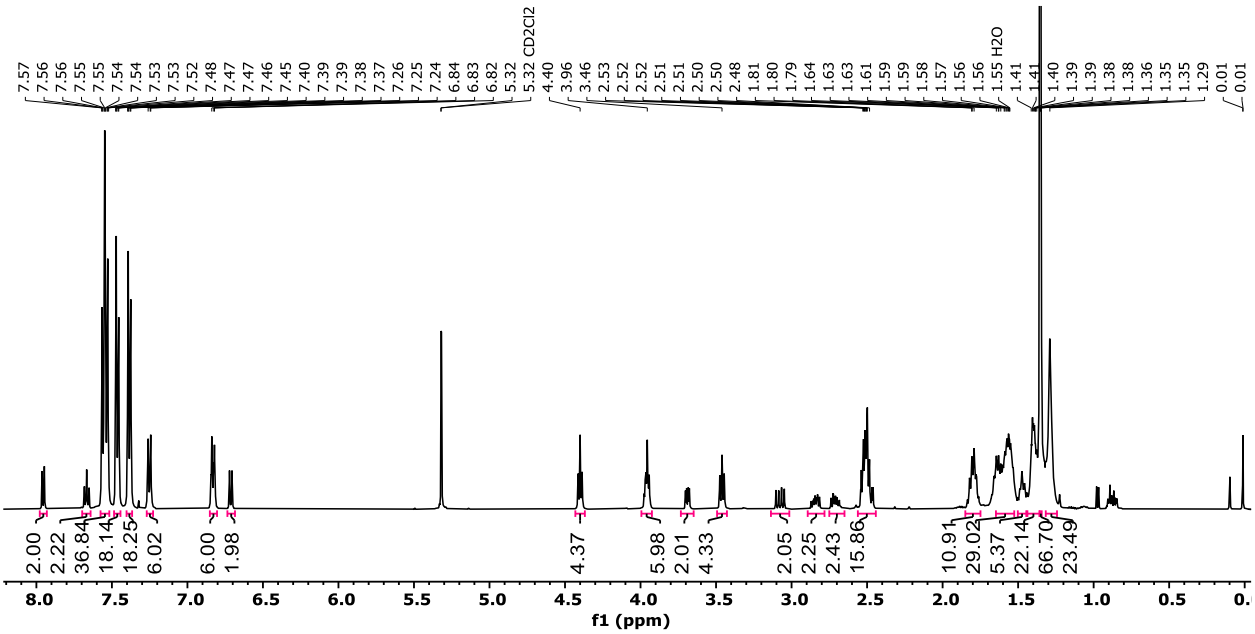

Figure 5.45. ^{1}H-NMR (500 MHz, 25°C, CD_2Cl_2) of thioester Bipy dumbbell **5.20**.

5.4.2.10 Synthesis of dumbbell **5.21**

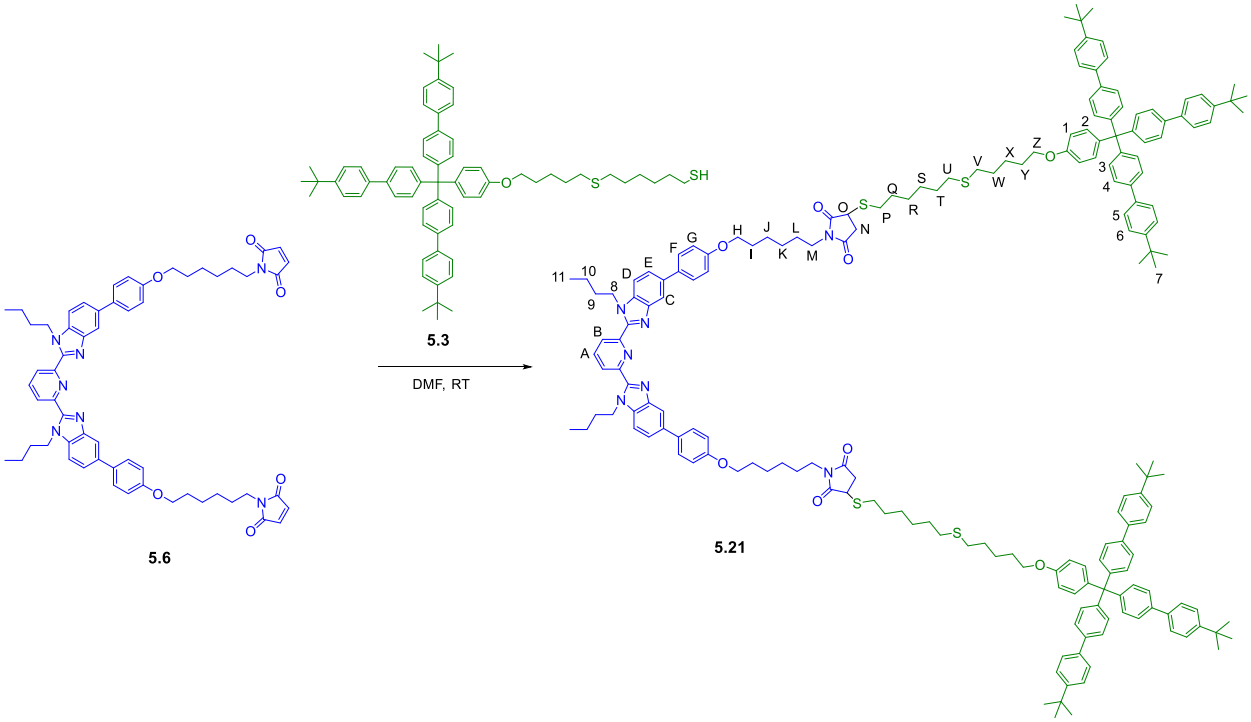

Maleimide thread **5.6** (0.005 g, 0.052 mmol) was dissolved in 0.5 mL of d_7-DMF and added to an NMR tube. Stopper **5.3** (0.010 g, 0.0103 mmol) was also dissolved in 1.0 mL of d_7-DMF and added in 0.5 mL increments with an NMR spectrum taken after each addition. No change was observed, so the NMR tube was left at RT overnight; however, no change was observed the next day (Figure 5.37). Dry DMF and argon flow were used in a second experiment to eliminate any potential interactions with water or oxygen that could account for the lack of reaction in the deuterated solvent. Maleimide thread **5.6** (0.010 g, 0.010 mmol) and stopper **5.3** (0.020 g, 0.0207 mmol) were dissolved in 0.5 mL of dry DMF (dried over 4Å mol sieves) and added to a vial under argon flow. The components were left to stir at RT overnight, after which the solvent was removed under vacuum and the crude mixture dissolved in $CDCl_3$ for NMR analysis; no reaction was observed.

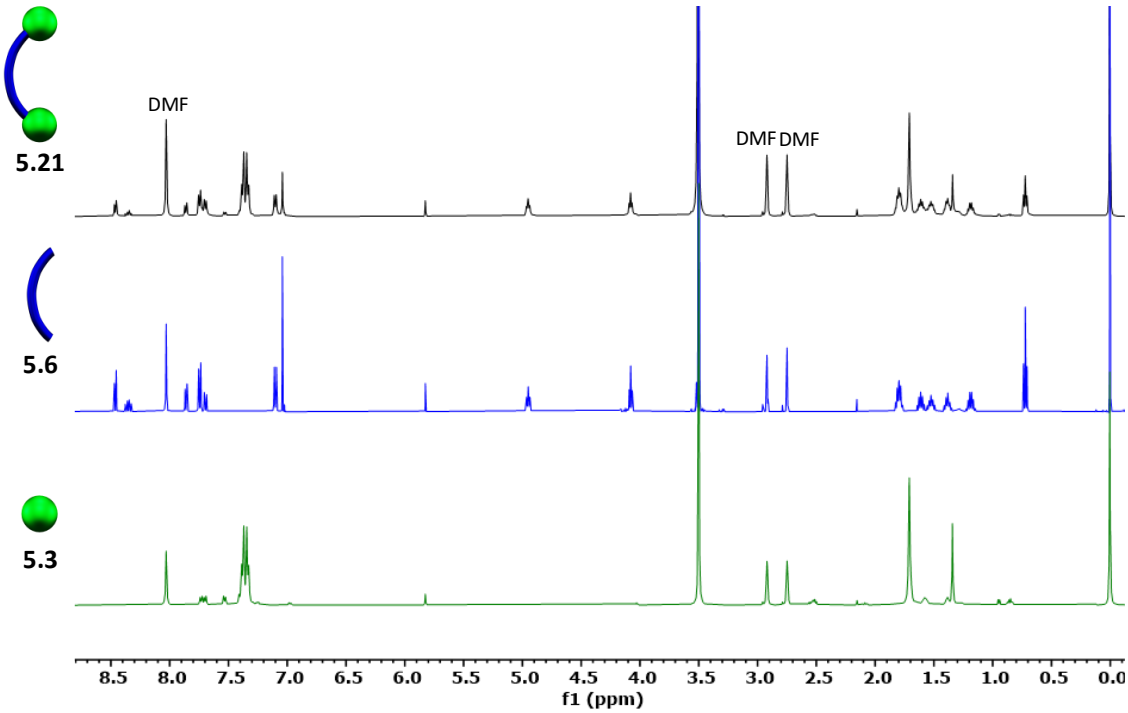

Figure 5.46. ^{1}H-NMR (500 MHz, 25°C, d_7-DMF) of DMF dumbbell **5.21** NMR experiment with starting materials, stopper **5.3** and thread **5.6**, for comparison.

5.4.2.11 Synthesis of 68-atom ring **5.1**

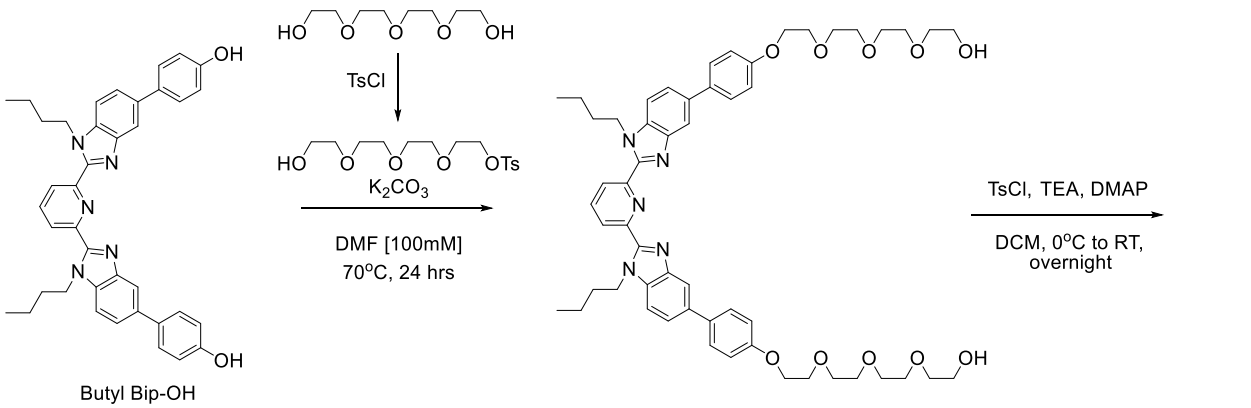

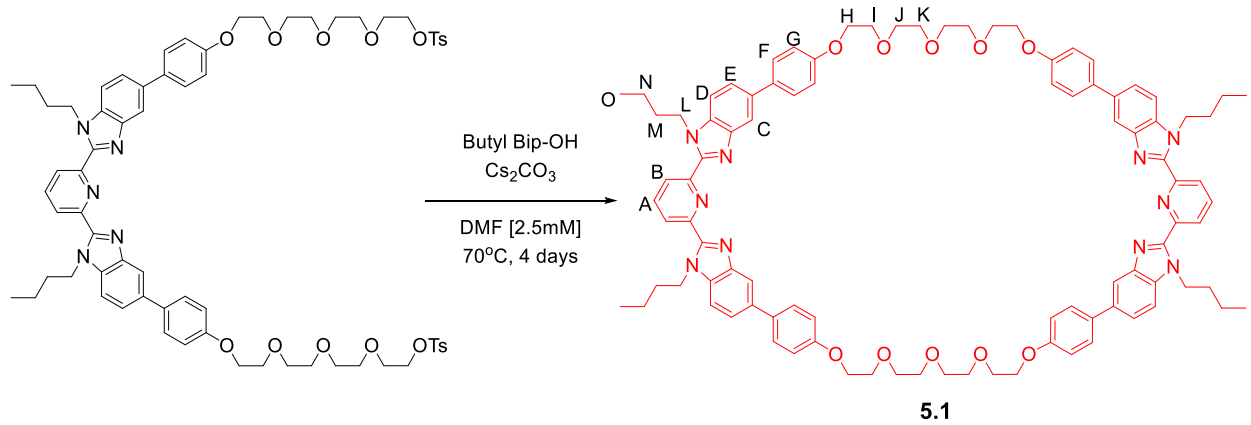

5.1

The 68-atom macrocycle **5.1** was synthesized from butyl Bip-OH using the literature procedure.[3] ^{1}H NMR (500 MHz, $CDCl_3$) δ 8.30 (d, *J* = 7.9 Hz, 4H, B), 8.04 – 7.93 (m, 6H, A+C), 7.54 – 7.46 (m, 8H, F), 7.39 (dd, *J* = 8.4, 1.7 Hz, 4H, E), 7.26 (dd, *J* = 8.5, 0.6 Hz, 4H, D), 7.00 – 6.94 (m, 8H, G), 4.56 (t, *J* = 7.3 Hz, 8H, L), 4.17 – 4.09 (m, 8H, H), 3.94 – 3.89 (m, 8H, I), 3.80 – 3.76 (m, 8H, J), 3.76 – 3.72 (m, 8H, K), 1.60 – 1.51 (m, 8H, M), 1.01 – 0.90 (m, 8H, N), 0.59 (t, *J* = 7.4 Hz, 12H, O). ^{13}C NMR (126 MHz, $CDCl_3$) δ 158.16, 150.49, 150.01, 143.35, 138.05, 135.97, 135.40, 134.18, 128.26, 125.50, 123.11, 117.86, 115.02, 110.45, 70.91, 69.79, 67.65, 44.58, 32.07, 19.74, 13.54, 13.45. MALDI-TOF MS: 1553.1 ([M]+Na^+).

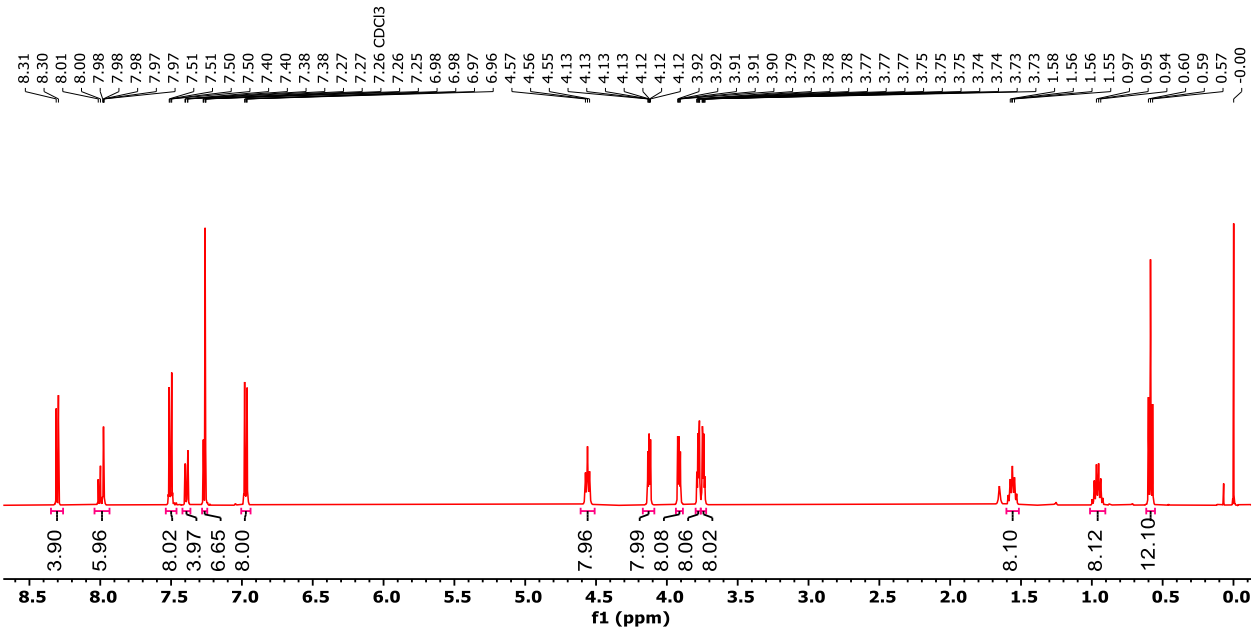

Figure 5.47. ^{1}H-NMR (500 MHz, 25°C, $CDCl_3$) of 4PEG 68-atom macrocycle **5.1**.

5.4.2.12 Synthesis 56-atom ring **5.22**

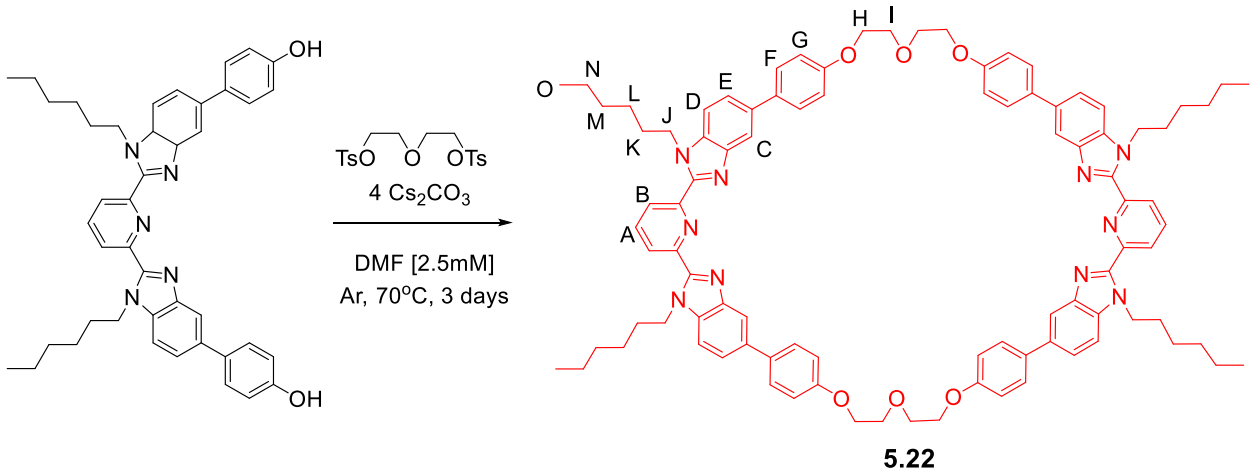

5.22

Macrocycle **5.22** was synthesized by Dr. Katie Herbert from hexyl Bip-OH and was then purified using column chromatography (TEA treated silica gel, 1.8-3% methanol in chloroform gradient as eluent) followed by recrystallization (chloroform/methanol mixture) to yield white crystals of **5.22**. ^{1}H NMR (500 MHz, $CDCl_3$) δ 8.29 (d, *J* = 7.8 Hz, 4H, B), 8.01 (t, *J* = 7.8 Hz, 2H, A), 7.95 (s, 4H, C), 7.43 (d, *J* = 8.2 Hz, 8H, F), 7.34 (dd, *J* = 8.4, 1.7 Hz, 4H, E), 7.28 – 7.19 (m, 24H, D), 7.17 (d, *J* = 8.4 Hz, 8H, F), 6.96 (d, *J* = 8.1 Hz, 8H, G), 4.53 (t, *J* = 7.3 Hz, 8H, J), 4.23 (t, *J* = 4.5 Hz, 8H,

H), 3.93 (t, *J* = 4.4 Hz, 8H, I), 1.65 – 1.55 (m, 8H, K), 0.99 – 0.88 (m, 24H, L+M+N), 0.57 (t, *J* = 6.1 Hz, 12H, O). MALDI-TOF MS: 1469.3 ([M]+H^+), 1693.6 ([M]+H^++Dithranol).

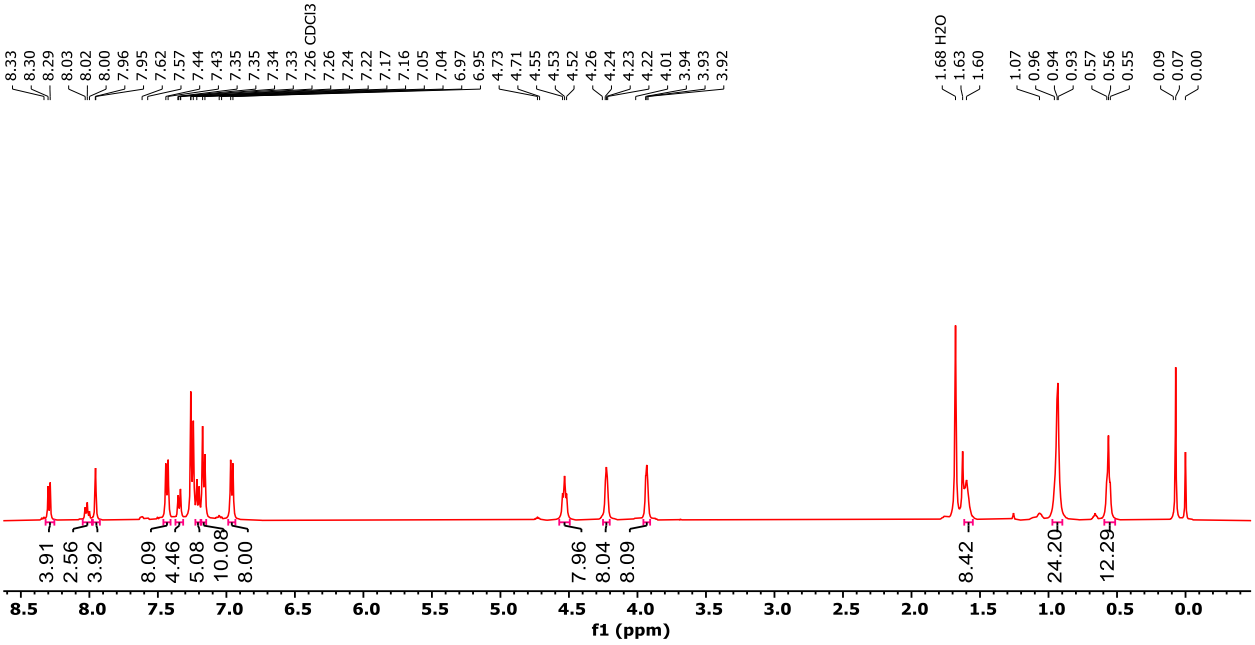

Figure 5.48. ^{1}H-NMR (500 MHz, 25°C, $CDCl_3$) of 2PEG 56-atom macrocycle **5.22**.

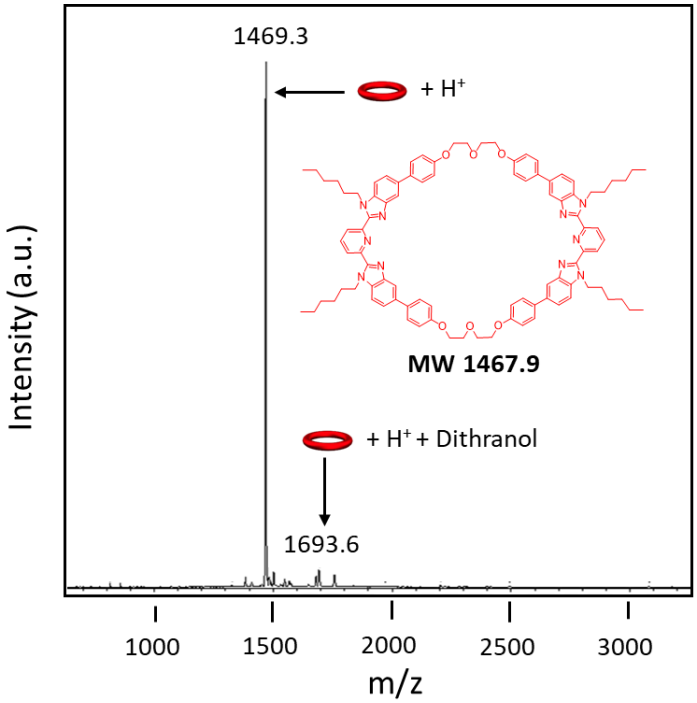

Figure 5.49. MALDI-TOF MS (Dithranol) of 56-atom macrocycle **5.22**.

5.4.2.13 Synthesis 46-atom ring **5.23**

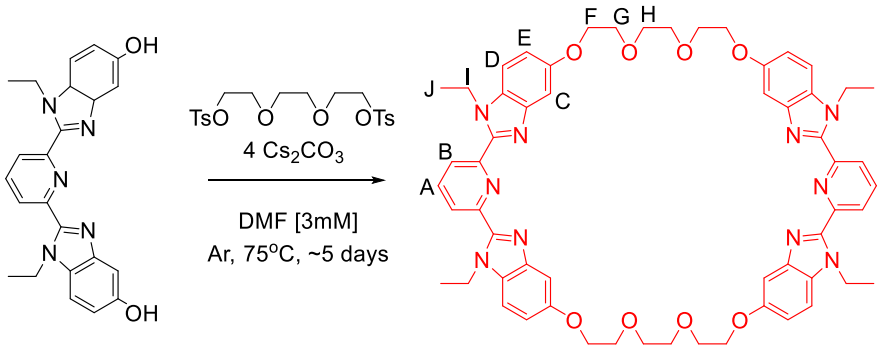

5.23

A 3-neck 1 L RBF was charged with Cs_2CO_3 (3.26 g, 10.0 mmol), non-extended ethyl Bip-OH[6] (1.0 g, 2.5 mmol, synthesized by Dr. Forrest Etheridge), and dry DMF (415 mL) under an Ar atmosphere. The mixture was heated to 70°C and stirred while a DMF (420 mL) solution of triethylene glycol di(p-toluenesulfonate) (1.15 g, 2.5 mmol, synthesized by Dr. Katie Herbert) was added dropwise (at an approximate rate of one drop every 20 seconds) over 3 days. After the complete addition of components, the final concentration of the reaction was 3mM. The reaction was allowed to stir at 70°C for one more day, after which the reaction mixture was cooled to RT and the solvent was removed under reduced pressure. The residue was dissolved in $CHCl_3$, and the insoluble material (salts) was removed by filtration. The filtrate was collected, and the solvent was removed under reduced pressure. The resulting material was purified using column chromatography (TEA treated silica gel, 1-4% methanol in chloroform gradient as eluent) followed by recrystallization (chloroform/methanol mixture) to yield white crystals of **5.23** in 42% yield by mass. ^{1}H NMR (500 MHz, $CDCl_3$) δ 8.24 (d, *J* = 7.8 Hz, 4H, B), 7.94 (t, *J* = 7.9 Hz, 2H, A), 7.25 (s, 4H, C), 7.05 – 6.96 (m, 8H, D+E), 4.41 (q, *J* = 7.2 Hz, 8H, I), 4.17 (dd, *J* = 5.7, 3.7 Hz, 8H, F), 3.95 – 3.91 (m, 8H, G), 3.82 (s, 8H, H), 1.05 (t, *J* = 7.2 Hz, 12H, J). MALDI-TOF MS: 1028.6 ([M]+H^+), 1251.6 ([M]+H^++Dithranol).

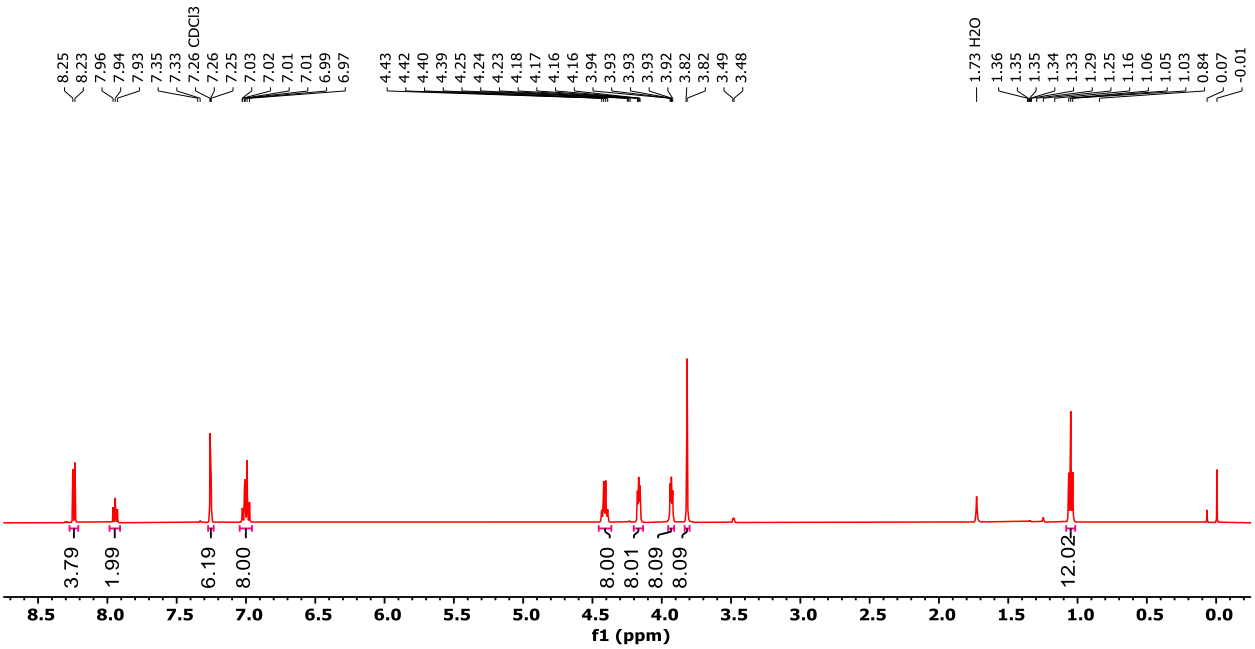

Figure 5.50. ^{1}H-NMR (500 MHz, 25°C, $CDCl_3$) of 3PEG 46-atom macrocycle **5.23**.

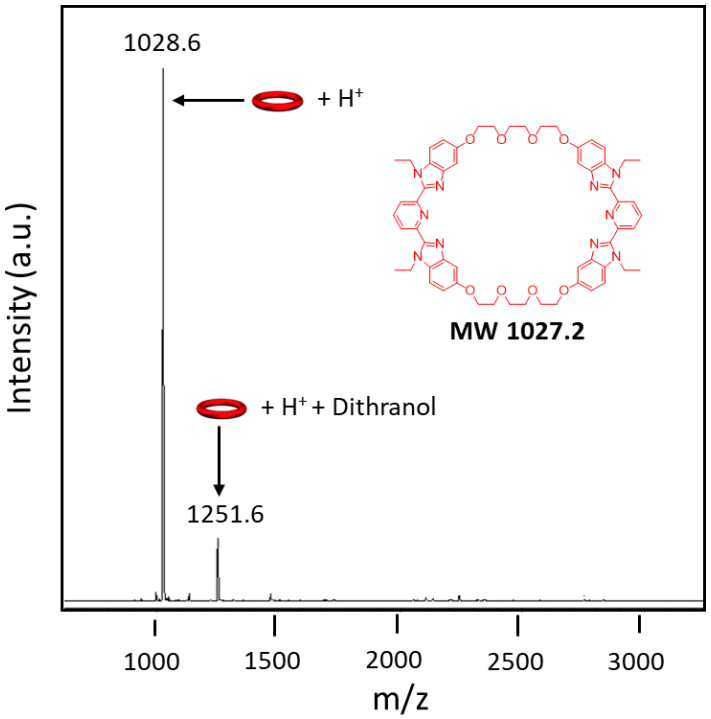

Figure 5.51. MALDI-TOF MS (Dithranol) of 46-atom macrocycle **5.23**.

5.4.2.14 Synthesis of 42-atom ring **5.24**

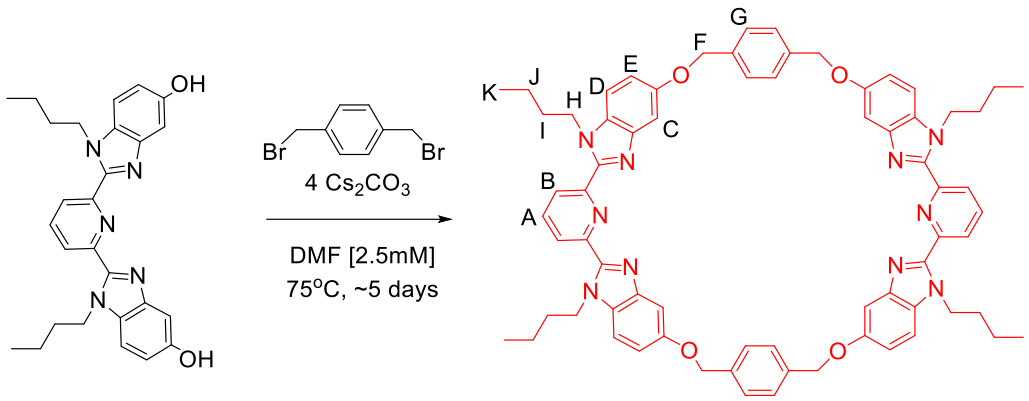

5.24

A 3-neck 1 L RBF was charged with Cs_2CO_3 (2.86 g, 8.78 mmol), non-extended butyl Bip-OH[6] (1.0 g, 2.20 mmol), and dry DMF (450 mL) under an Ar atmosphere. The mixture was heated to 75°C and stirred while a DMF (430 mL) solution of α,α'-dibromo-p-xylene (0.579 g, 2.20 mmol) was added dropwise (at an approximate rate of one drop every 20 seconds) over 4 days. After the complete addition of components, the final concentration of the reaction was 2.5mM. The reaction was allowed to stir at 75°C for one more day, after which the reaction mixture was cooled to RT and the solvent was removed under reduced pressure. The residue was dissolved in $CHCl_3$, and the insoluble material (salts) was removed by filtration. The filtrate was collected, and the solvent was removed under reduced pressure. The resulting material was purified using column chromatography (TEA treated silica gel, 1.8-2.3% methanol in chloroform gradient as eluent) followed by recrystallization (chloroform/methanol mixture) to yield white crystals of **5.24** in 45% yield by mass. ^{1}H NMR (500 MHz, $CDCl_3$) δ 8.18 (d, *J* = 7.9 Hz, 4H, B), 7.85 (t, *J* = 7.9 Hz, 2H, A), 7.36 (s, 8H, G), 7.20 – 7.15 (m, 8H, D+E), 6.92 (dd, *J* = 8.9, 2.2 Hz, 4H, C), 5.27 (s, 8H, F), 4.52 (t, *J* = 7.3 Hz, 8H, H), 1.51 (q, *J* = 7.5 Hz, 8H, I), 0.93 (dt, *J* = 14.8, 7.4 Hz, 8H, J), 0.54 (t, *J* = 7.4 Hz, 12H, K). MALDI-TOF MS: 1123.7.3 ([M]+Na^+), 1348.7 ([M]+Na^++Dithranol).

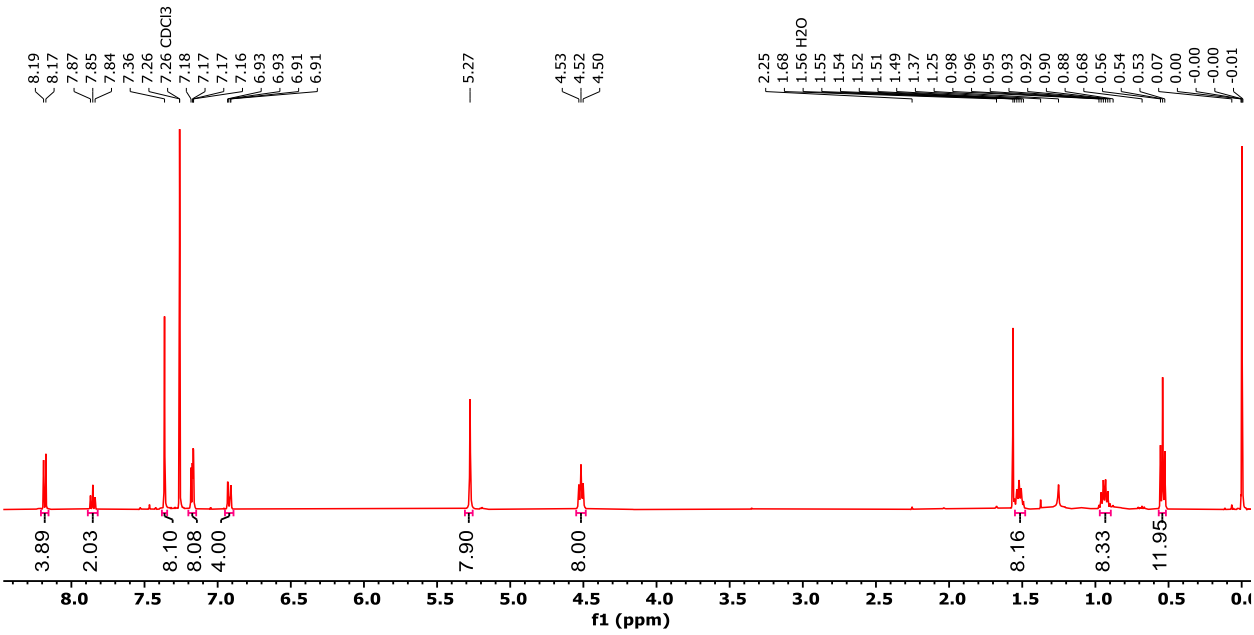

Figure 5.52. ^{1}H-NMR (500 MHz, 25°C, $CDCl_3$) of 42-atom macrocycle **5.24**.

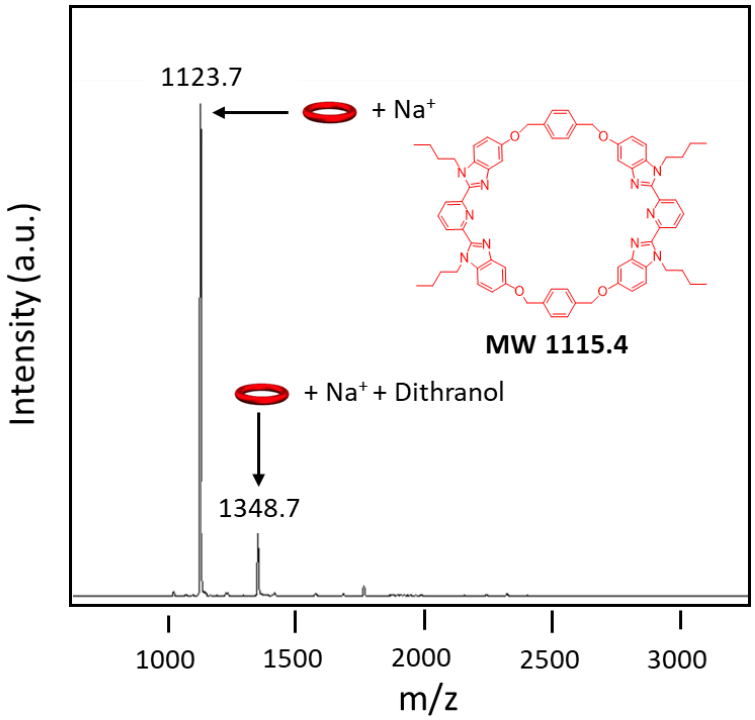

Figure 5.53. MALDI-TOF MS (Dithranol, sodium trifluoroacetate) of 42-atom macrocycle **5.24**.

5.4.2.15 Synthesis of P3R **5.1:5.6$_2$:Zn(II)$_2$** with Zn(NTf$_2$)$_2$

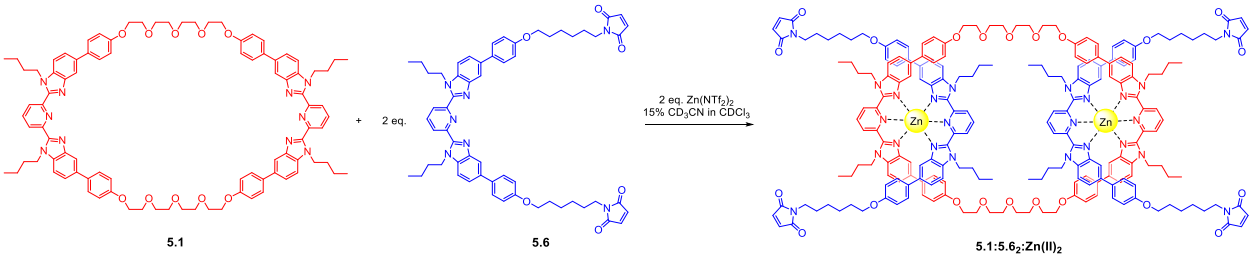

Macrocycle **5.1** (10mg, 0.0065mmol) was dissolved in 1mL $CDCl_3$**.** A stock solution of thread **5.6** (30mM) was titrated into the solution of **5.1** until an exact 2:1 (**5.6**:**5.1**) ratio was formed (done by monitoring both the N-CH_2 peaks on the alkyl groups of the Bip ligands). The mixture was then diluted to a total volume of 3mL $CDCl_3$ (5 mM **5.6**). A stock solution of Zn(NTf$_2$)$_2$ (30mM in 2:1 $CDCl_3$:CD_3CN) was added until no free Bip peak appeared at ~2 equiv. of the metal ion. The complete disappearance of the doublets at 8.30 and 8.35 ppm (and the corresponding growth of the peaks at 8.74 and 9.03 ppm) indicates that all Bip ligands are bound with zinc in a 2:1 Bip:metal ratio. The resulting pseudo[3]rotaxane solution was dried under vacuum to obtain a yellow powder that was stored in the freezer at -8°C before use.

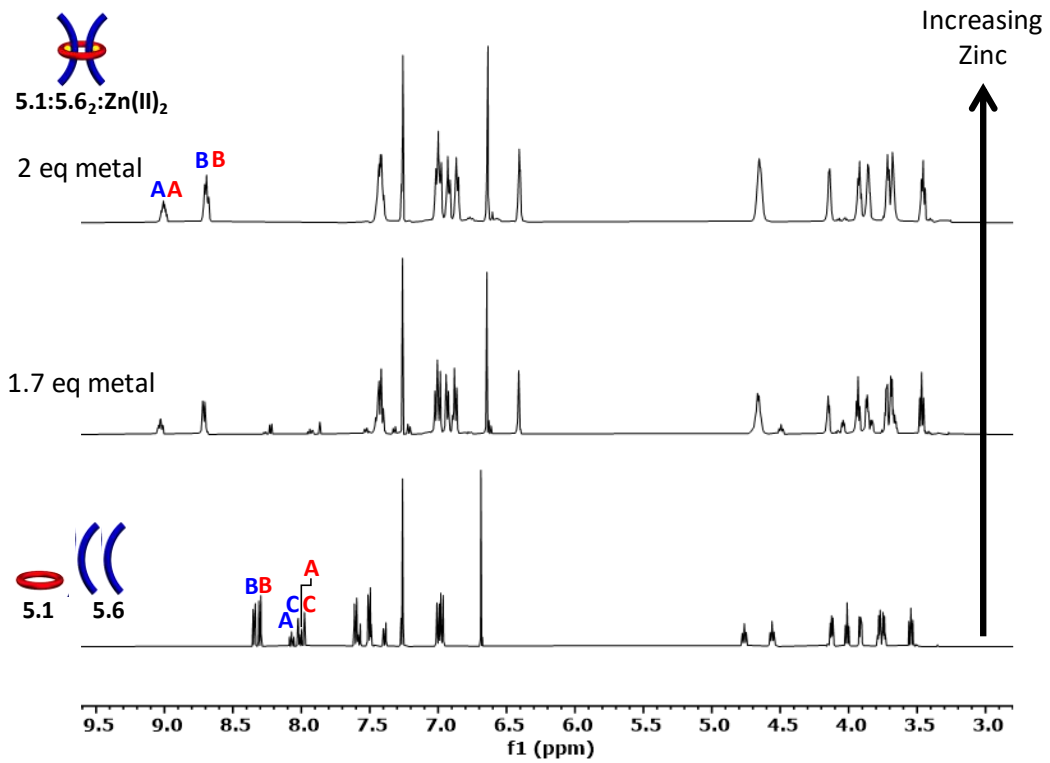

Figure 5.54. Partial ^{1}H-NMR overlay (500 MHz, 25°C, Solvent: 0, 12.75, 15% d_3-MeCN in $CDCl_3$ increasing upwards) of metal addition to form **5.1:5.6$_2$:Zn(II)$_2$**.

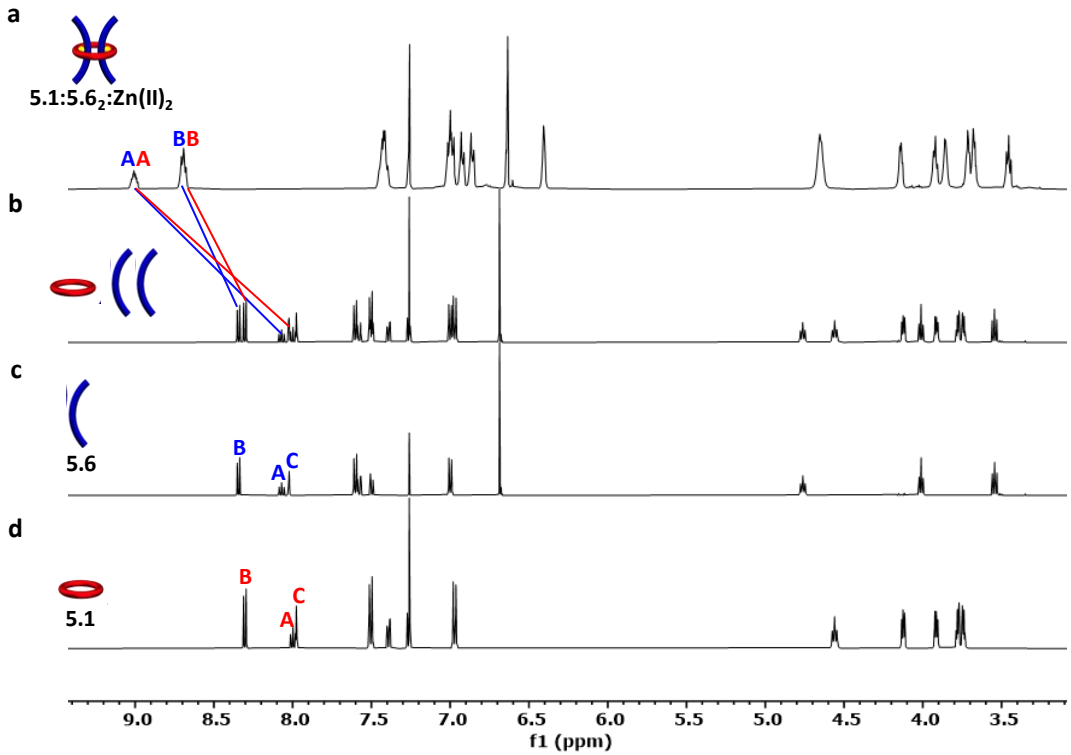

Figure 5.55. Partial ^{1}H-NMR overlay (500 MHz, 25°C) of a) **5.1:5.6$_2$:Zn(II)$_2$** (15% d_3-MeCN in $CDCl_3$), b) 2:1 mixture of **5.6**:**5.1** ($CDCl_3$), c) **5.6** ($CDCl_3$) and d) **5.1** ($CDCl_3$).

5.4.2.16 Synthesis of P3R **5.22:5.6$_2$:Zn(II)$_2$** with $Zn(NTf_2)_2$

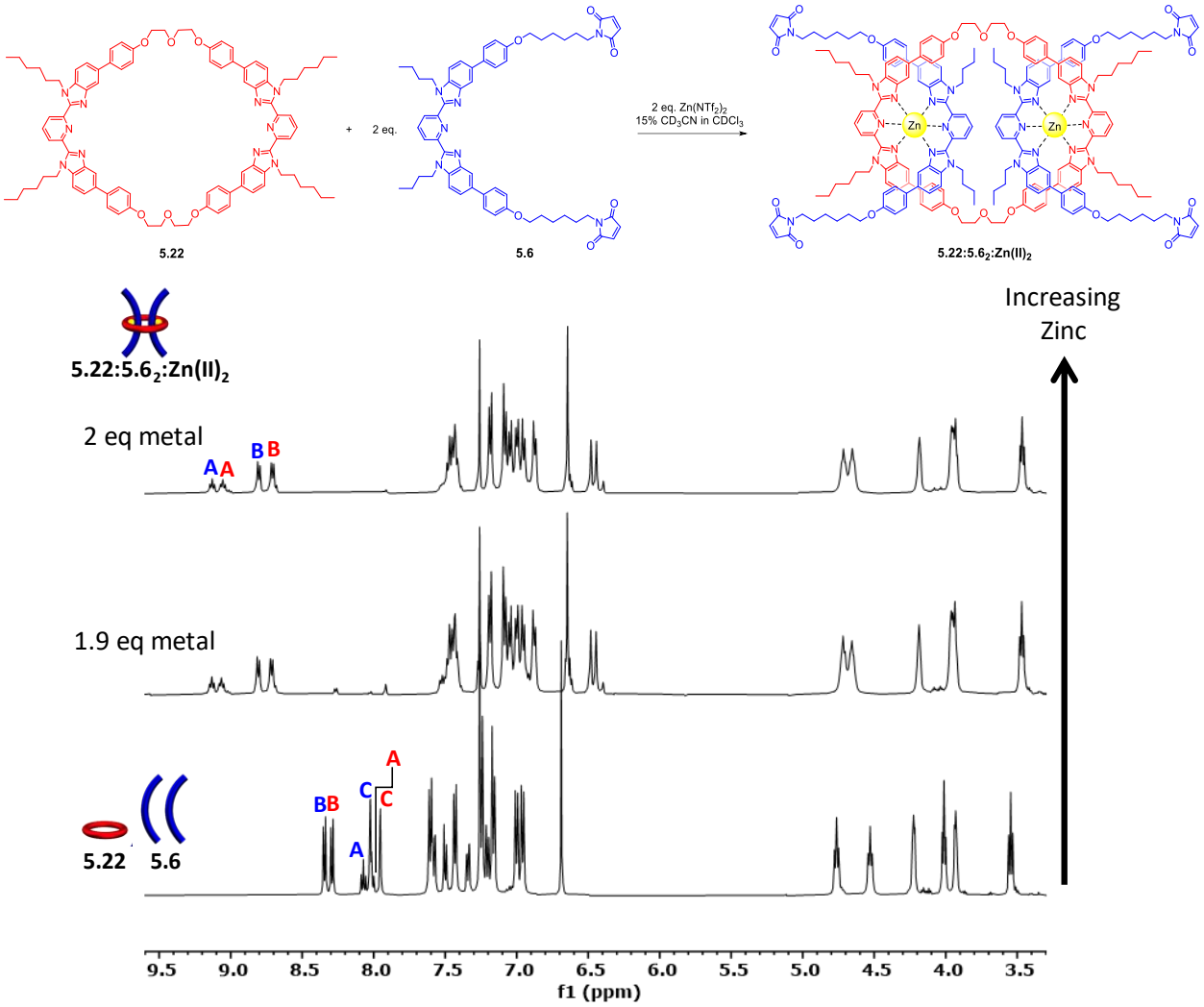

Figure 5.56. Partial ^{1}H-NMR overlay (500 MHz, 25°C, Solvent: 0, 14.25, 15% d_3-MeCN in $CDCl_3$ increasing upwards) of metal addition to form **5.22:5.6$_2$:Zn(II)$_2$**.

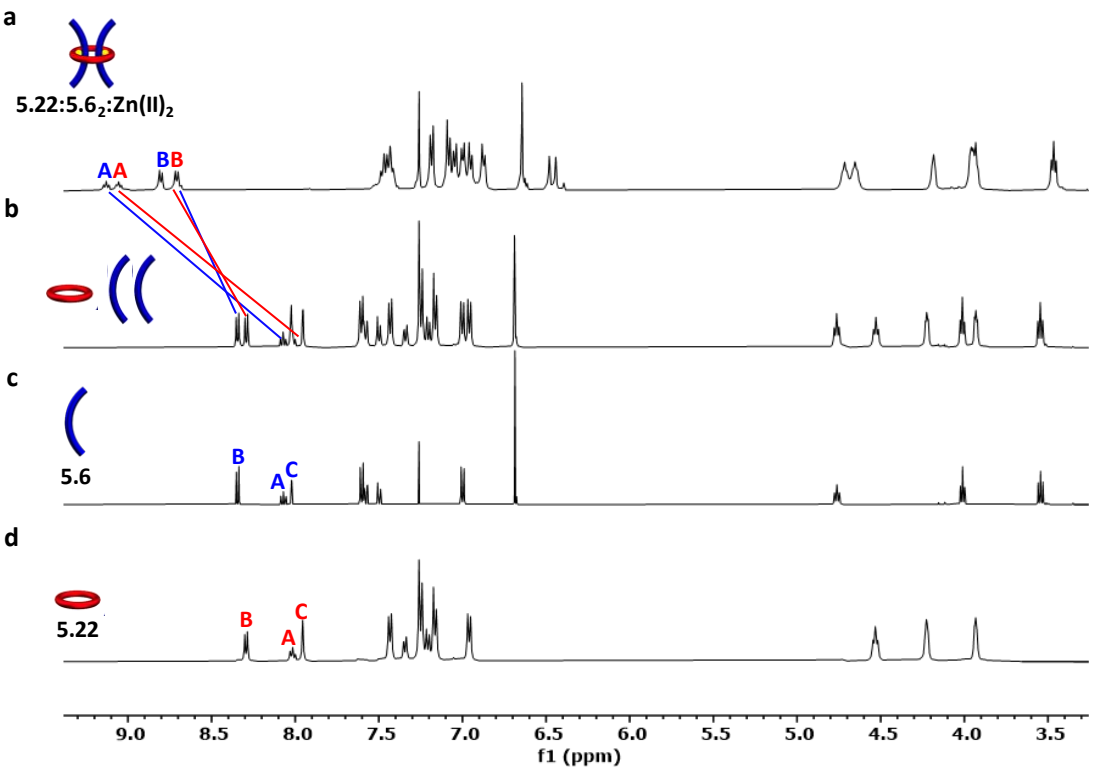

Figure 5.57. Partial ^{1}H-NMR overlay (500 MHz, 25°C) of a) **5.22:5.6$_2$:Zn(II)$_2$** (15% d$_3$-MeCN in $CDCl_3$), b) 2:1 mixture of **5.6**:**5.22** ($CDCl_3$), c) **5.6** ($CDCl_3$) and d) **5.22** ($CDCl_3$).

5.4.2.17 Synthesis of P3R **5.23:5.6$_2$:Zn(II)$_2$** with $Zn(NTf_2)_2$

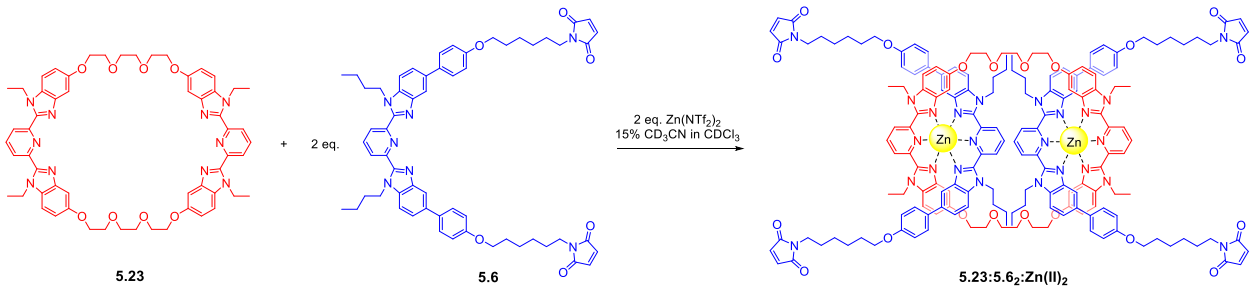

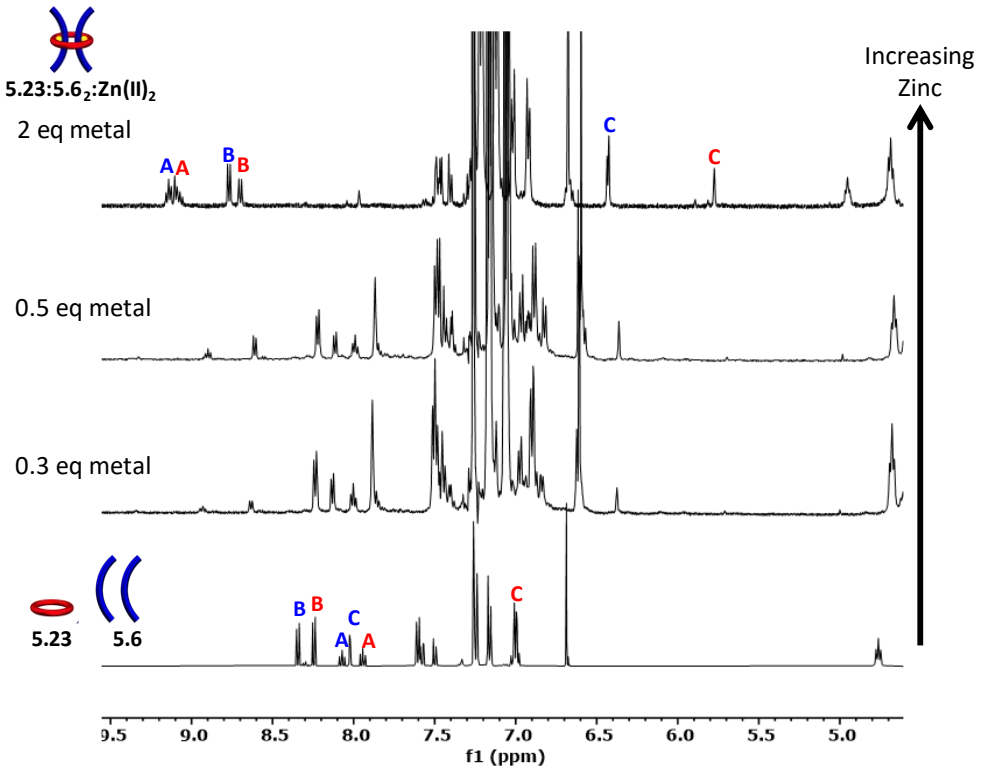

Figure 5.58. Partial ^{1}H-NMR overlay (500 MHz, 25°C, Solvent: 0, 2.25, 3.75, 15% d$_3$-MeCN in $CDCl_3$ increasing upwards) of metal addition to form **5.23:5.6$_2$:Zn(II)$_2$**.

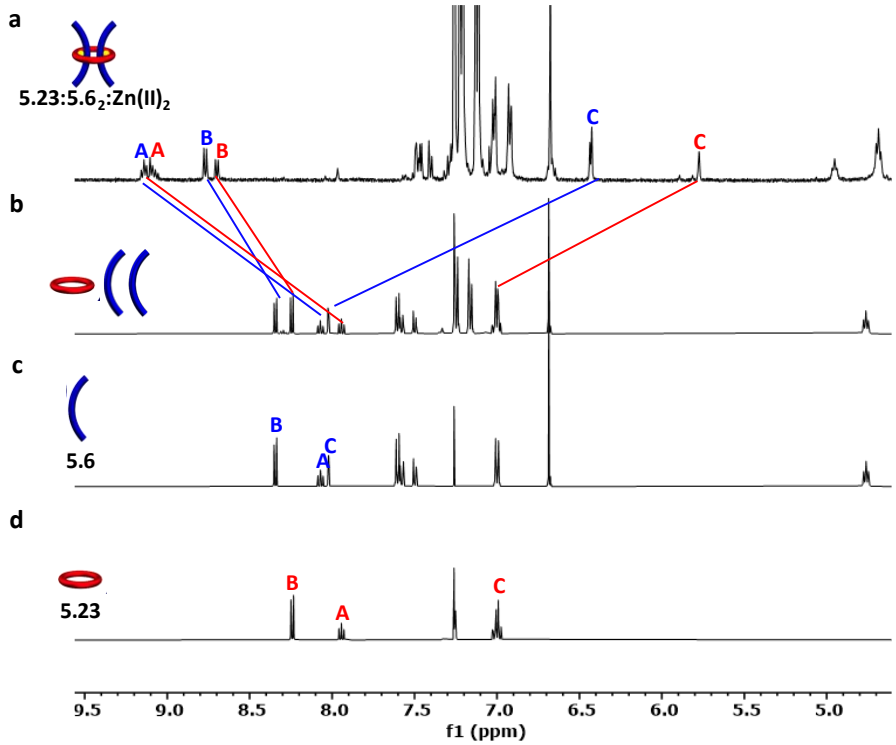

Figure 5.59. Partial ^{1}H-NMR overlay (500 MHz, 25°C) of a) **5.23:5.6$_2$:Zn(II)$_2$** (15% d$_3$-MeCN in $CDCl_3$), b) 2:1 mixture of **5.6**:**5.23** ($CDCl_3$), c) **5.6** ($CDCl_3$) and d) **5.23** ($CDCl_3$).

5.4.2.18 Synthesis of P3R **5.23:5.8$_2$:Zn(II)$_2$** with Zn(NTf$_2$)$_2$

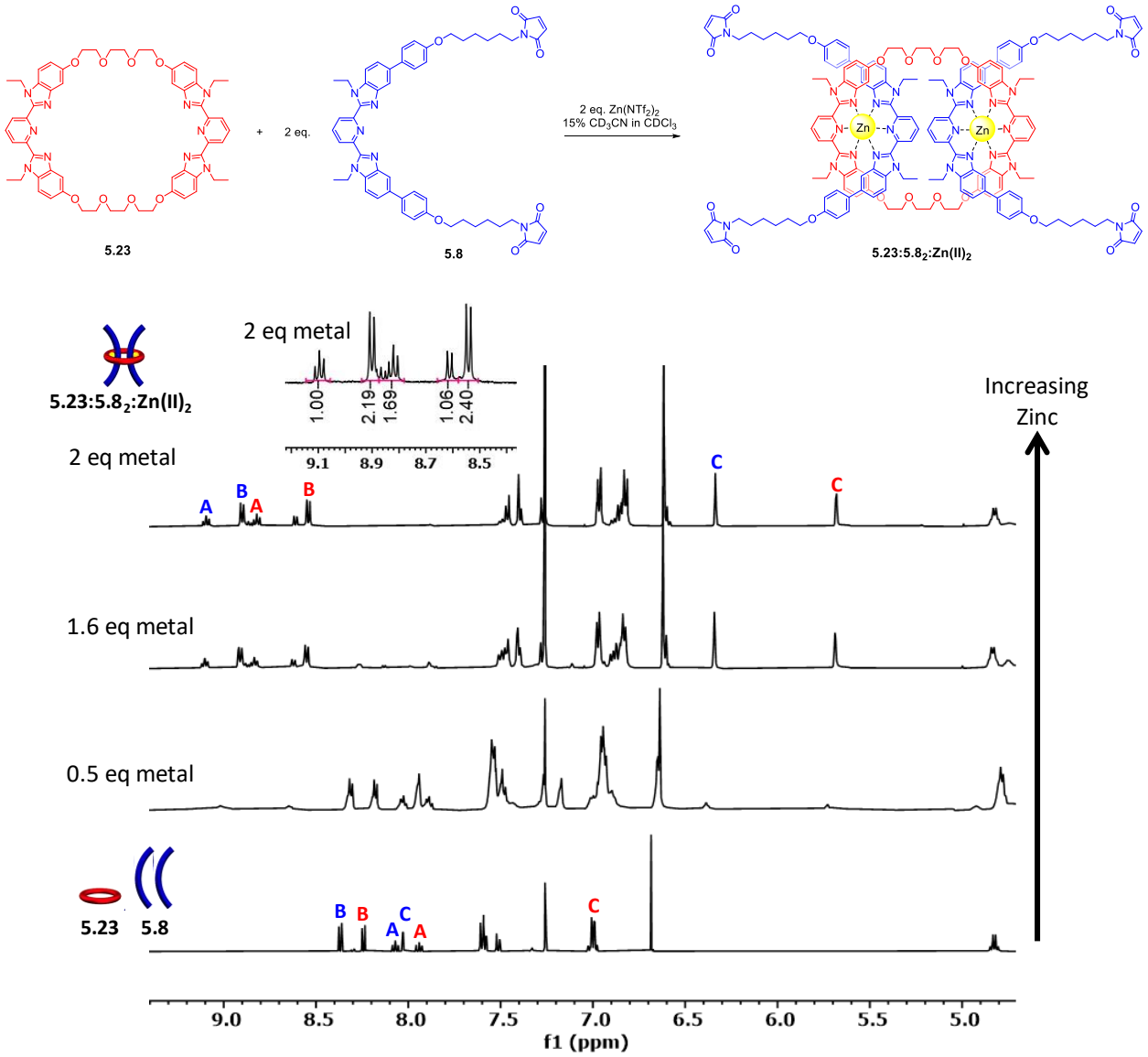

Figure 5.60. Partial ^{1}H-NMR overlay (500 MHz, 25°C, Solvent: 0, 3.75, 12, 15% d$_3$-MeCN in CDCl$_3$ increasing upwards) of metal addition to form **5.23:5.8$_2$:Zn(II)$_2$**.

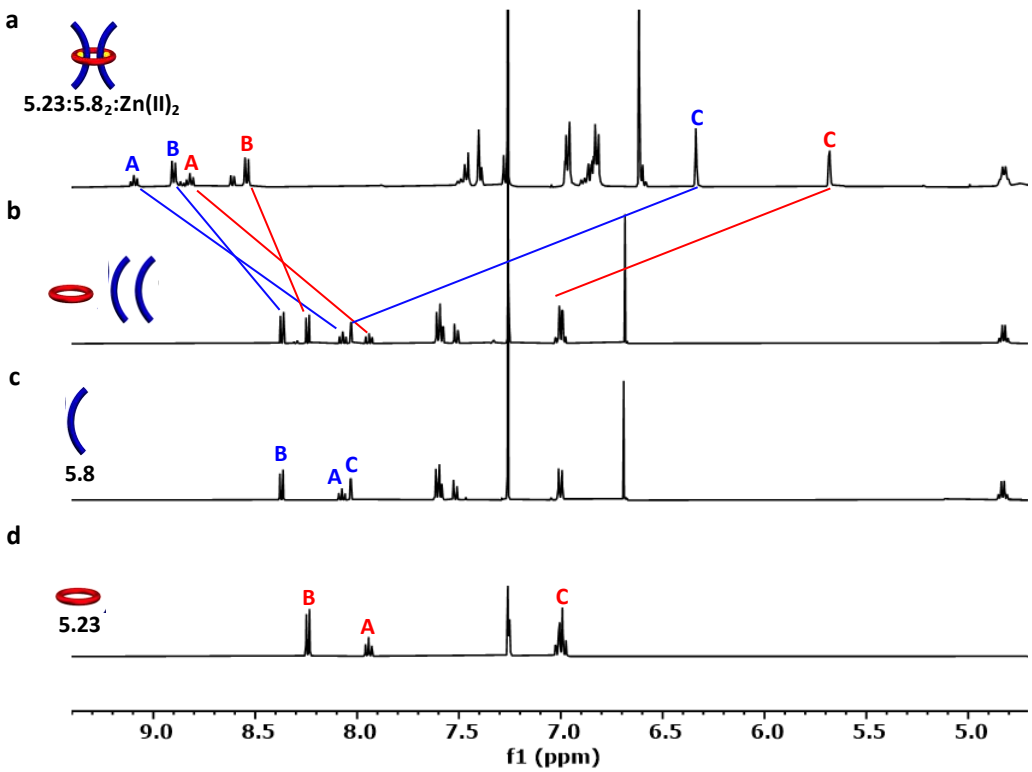

Figure 5.61. Partial ^{1}H-NMR overlay (500 MHz, 25°C) of a) **5.23:5.8$_2$:Zn(II)$_2$** (15% d$_3$-MeCN in $CDCl_3$), b) 2:1 mixture of **5.8**:**5.23** ($CDCl_3$), c) **5.8** ($CDCl_3$) and d) **5.23** ($CDCl_3$).

5.4.2.19 Synthesis of P3R **5.23:5.2$_2$:Zn(II)$_2$** with $Zn(OTf)_2$

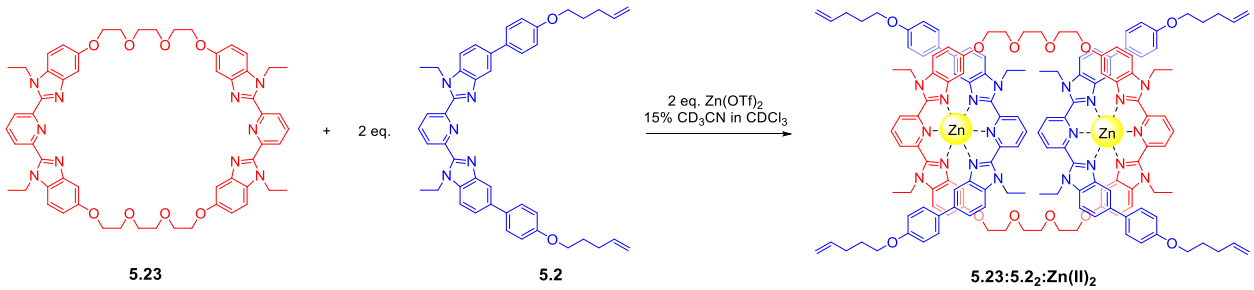

5.23 5.2 5.23:5.2$_2$:Zn(II)$_2$

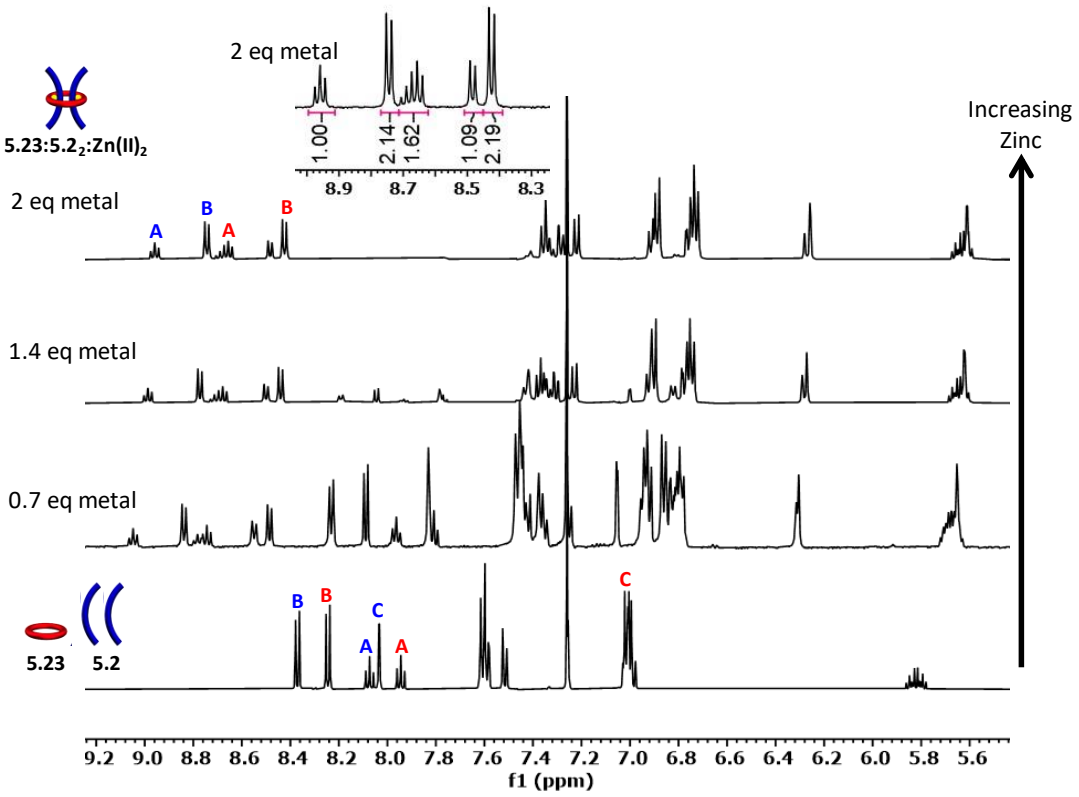

Figure 5.62. Partial ^{1}H-NMR overlay (500 MHz, 25°C, Solvent: 0, 5.25, 10.5, 15% d_3-MeCN in $CDCl_3$ increasing upwards) of metal addition to form **5.23:5.2$_2$:Zn(II)$_2$**.

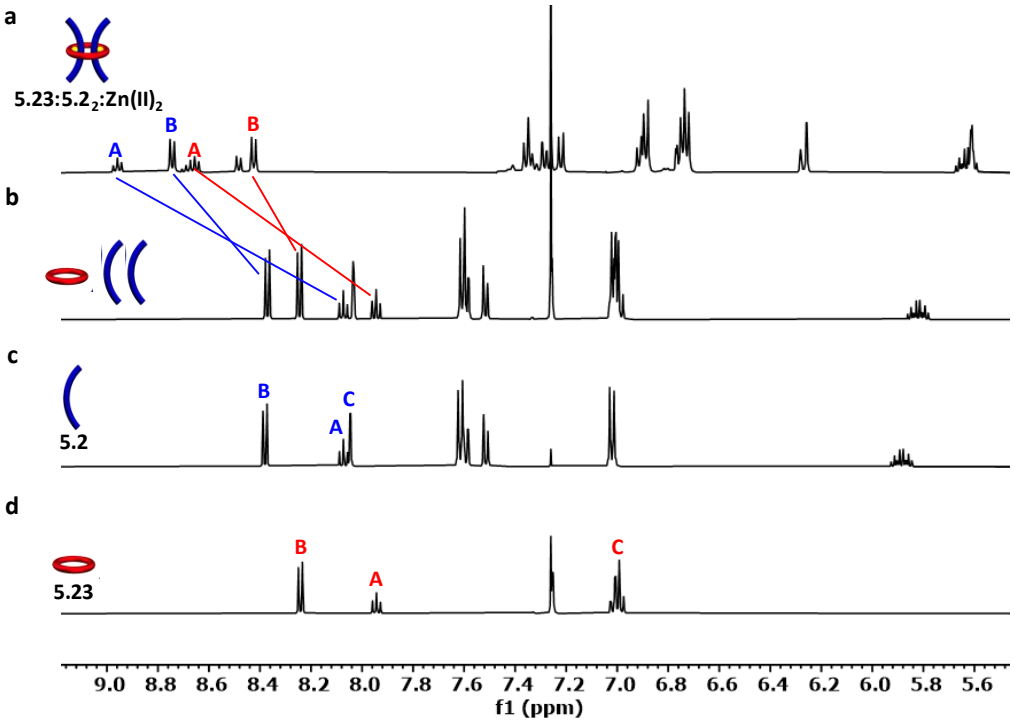

Figure 5.63. Partial ^{1}H-NMR overlay (500 MHz, 25°C) of a) **5.23:5.2$_2$:Zn(II)$_2$** (15% d_3-MeCN in $CDCl_3$), b) 2:1 mixture of **5.2**:**5.23** ($CDCl_3$), c) **5.2** ($CDCl_3$) and d) **5.23** ($CDCl_3$).

The flexibility of the 46-atom ditopic ring likely inhibits its ability to form exact 2:1 Bip:metal ratios in solution and could account for the extra metallated peaks encountered in the titrations above. Heating the P3R in solution shifted some of the signals into a single multiplet, which suggests the flexible ring could be preventing formation of the doubly-threaded complex required for making the [3]rotaxanes (Figure 5.57). Through collaboration with Dr. Jerry Hertzog on the synthesis of these smaller rotaxane rings, a successful pseudo[3]rotaxane formed when a more rigid 46-atom macrocycle (i.e., **2.1**) was employed and ultimately led to the successful preparation of the doubly-threaded slide-ring polycatenane networks (SR-PCNs) explored in Chapters 2 and 3.

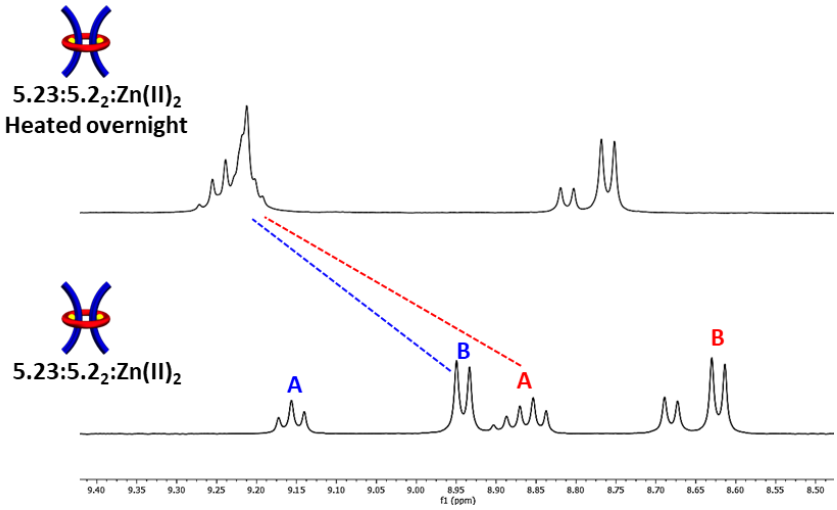

Figure 5.64. Partial ^{1}H-NMR overlay (500 MHz, 25°C) of **5.23:5.2$_2$:Zn(II)$_2$** (15% d$_3$-MeCN in $CDCl_3$) after titration (bottom), and after heating in a solution of $CDCl_3$ at 40°C overnight. Slight shifts on account of small amount of d$_3$-MeCN in the top spectrum.

5.4.2.20 Synthesis of P3R **5.24:5.13$_2$:Zn(II)$_2$** with $Zn(NTf_2)_2$

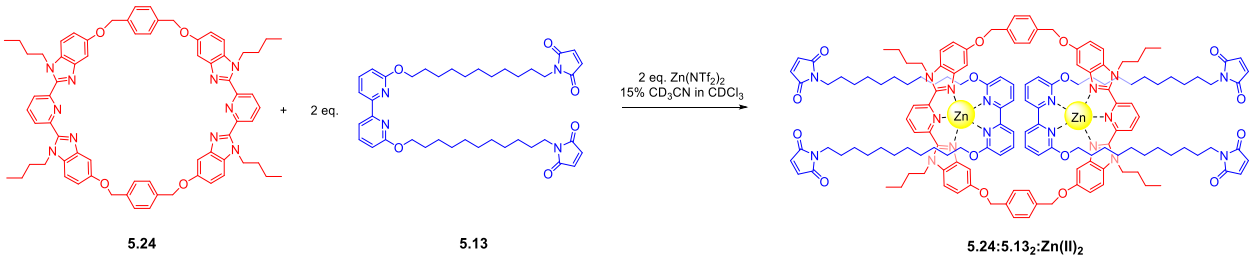

Macrocycle **5.24** (8mg, 0.0065mmol) was dissolved in 1mL $CDCl_3$**.** A stock solution of thread **5.13** (30mM) was titrated into the solution of **5.24** until an exact 2:1 (**5.13**:**5.24**) ratio was formed (done by monitoring both the N-CH_2 peaks on the alkyl groups of the Bip ligands). The mixture was then diluted to a total volume of 3mL $CDCl_3$ (5 mM **5.13**). A stock solution of $Zn(NTf_2)_2$ (30mM in 2:1 $CDCl_3$:CD_3CN) was added until no free Bip or Bipy peaks appeared at ~2 equiv. of the metal ion. The complete disappearance of the doublets at 8.30 and 8.35 ppm (and the corresponding growth of the peaks at 8.74 and 9.03 ppm) indicates that all Bip ligands are bound with zinc and Bipy in a 1:1:1 Bip:Bipy:metal ratio. The resulting pseudo[3]rotaxane solution was dried under vacuum to obtain a yellow powder that was stored in the freezer at -8°C before use.

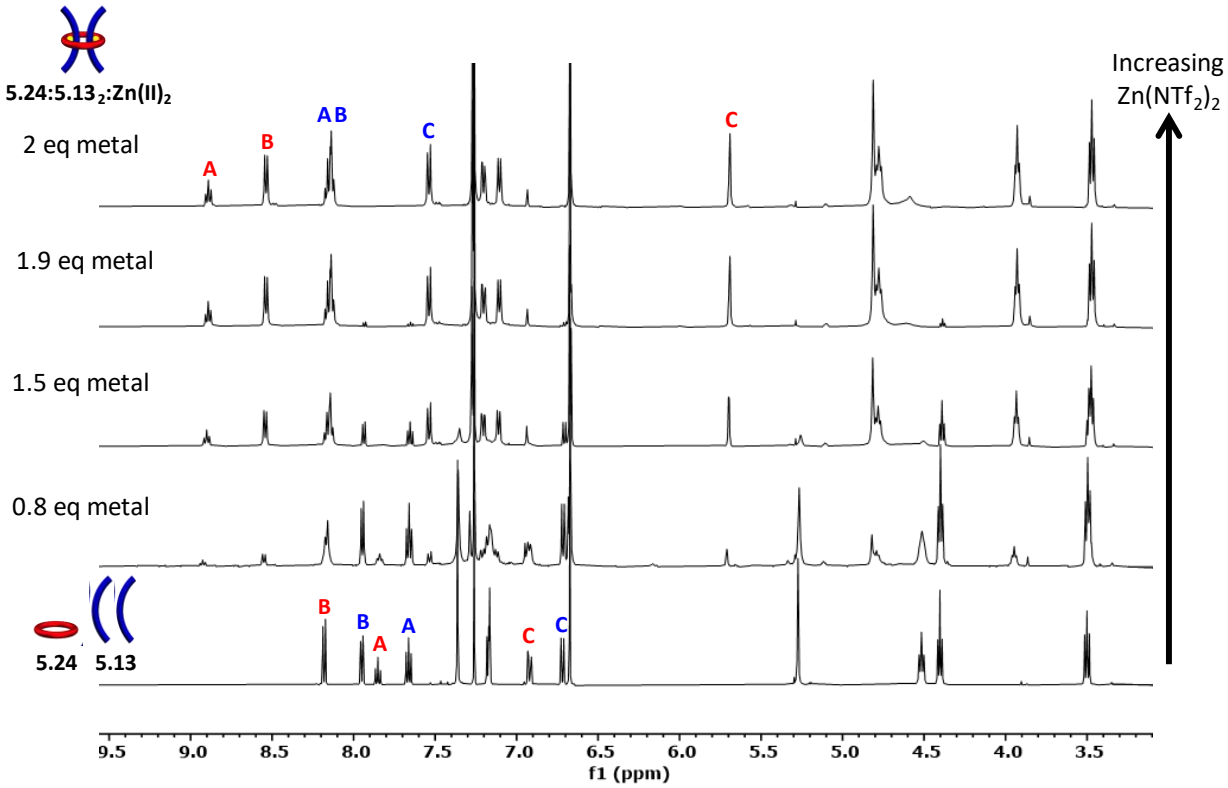

Figure 5.65. Partial ^{1}H-NMR overlay (500 MHz, 25°C, Solvent: 0, 6, 11.25, 14.25, 15% d_3-MeCN in $CDCl_3$ increasing upwards) of metal addition to form **5.24:5.13$_2$:Zn(II)$_2$**.

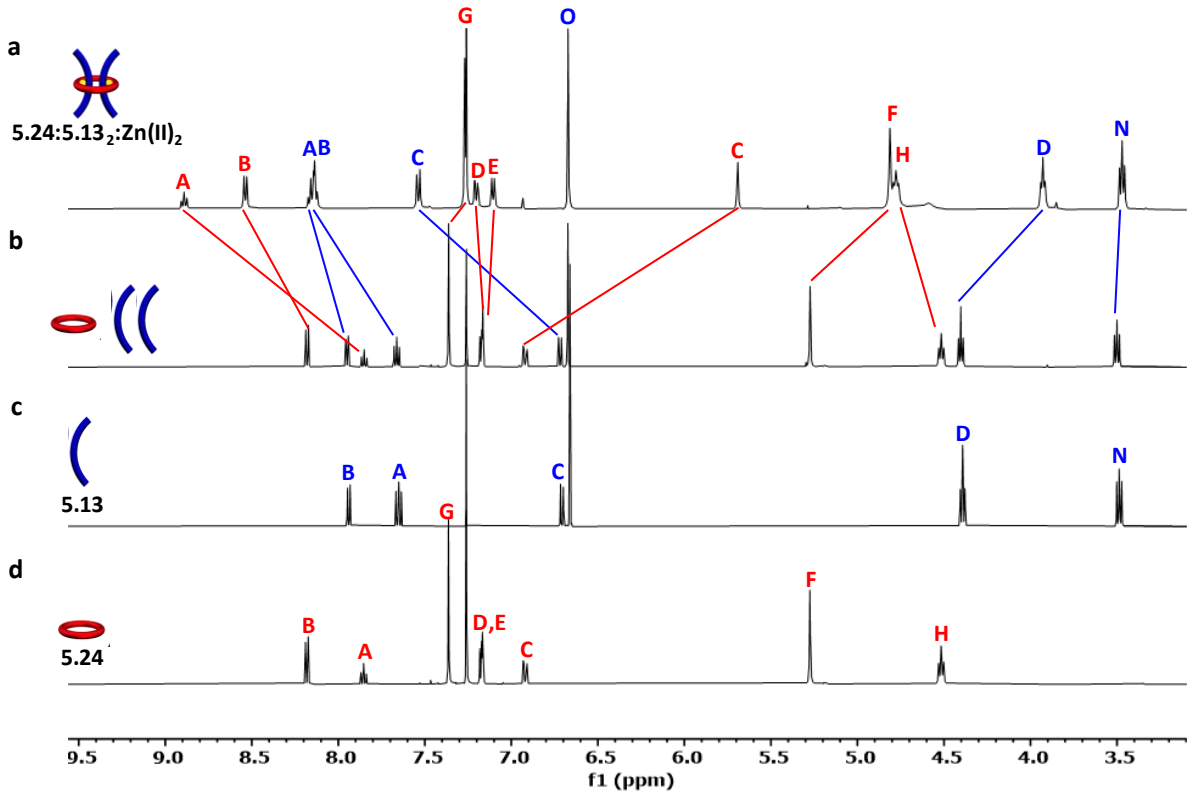

Figure 5.66. Partial ^{1}H-NMR overlay (500 MHz, 25°C) of a) **5.24:5.13$_2$:Zn(II)$_2$** (15% d$_3$-MeCN in $CDCl_3$), b) 2:1 mixture of **5.13**:**5.24** ($CDCl_3$), c) **5.13** ($CDCl_3$) and d) **5.24** ($CDCl_3$).

5.4.2.21 Synthesis of P3R **5.24:5.11$_2$:Zn(II)$_2$** with $Zn(OTf)_2$

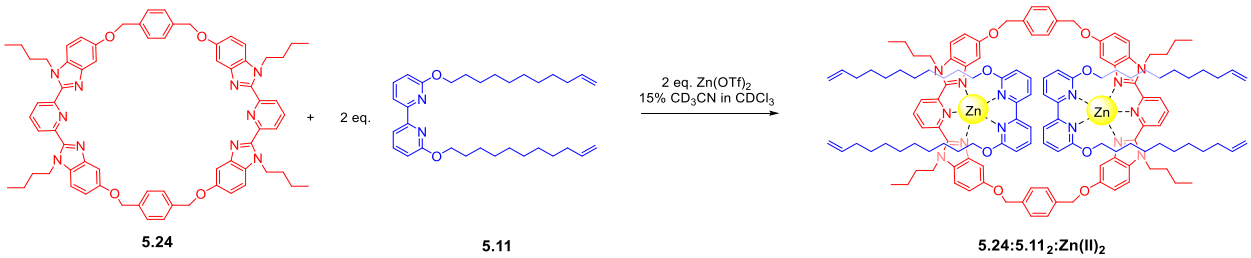

Pseudo[3]rotaxane **5.24:5.11$_2$:Zn(II)$_2$** was formed from 42-atom macrocycle **5.24** with 2 equivalents of alkene terminated Bipy thread **5.11** and 2 equivalents of zinc triflate (zinc trifluoromethanesulfonate, $Zn(OTf)_2$). Synthesis of the Bipy alkyne thread **5.11**, and NMR titration with **5.24** was performed by Dr. Qiong Wu.

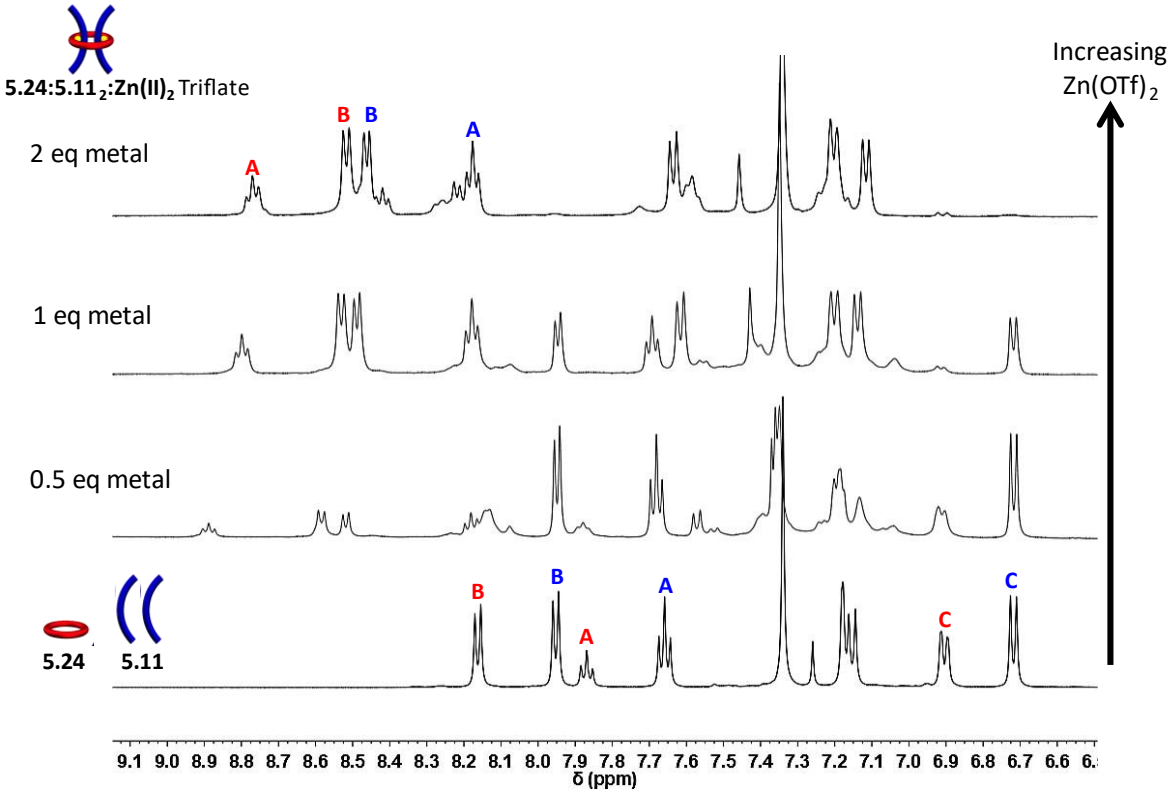

Figure 5.67. Partial ^{1}H-NMR overlay (500 MHz, 25°C, Solvent: 0, 3.75, 7.5, 15% d_3-MeCN in $CDCl_3$ increasing upwards) of $Zn(OTf)_2$ addition to form **5.24:5.11$_2$:Zn(II)$_2$** from a 2:1 mixture of **5.11**:**5.24**. Data obtained from Dr. Qiong Wu.

5.4.2.22 Synthesis of P3R **5.24:5.13$_2$:Zn(II)$_2$** with $Zn(OTf)_2$

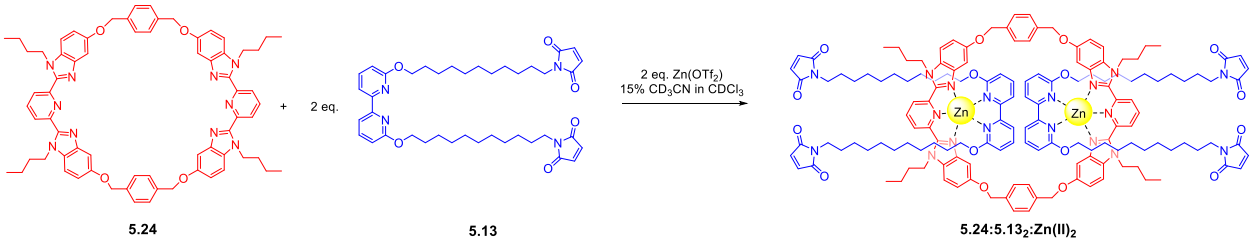

Macrocycle **5.24** (8mg, 0.0065mmol) was dissolved in 1mL $CDCl_3$**.** A stock solution of thread **5.13** (30mM) was titrated into the solution of **5.24** until an exact 2:1 (**5.13**:**5.24**) ratio was formed (done by monitoring both the N-CH_2 peaks on the alkyl groups of the Bip ligands). The mixture was then diluted to a total volume to 3mL $CDCl_3$ (5 mM **5.13**). A stock solution of $Zn(OTf)_2$ (30mM in 2:1 $CDCl_3$:CD_3CN) was added until no free Bip or Bipy peaks appeared at ~2 equiv. of the metal ion. The complete disappearance of the doublets at 8.30 and 8.35 ppm (and the

corresponding growth of the peaks at 8.74 and 9.03 ppm) indicates that all Bip and Bipy ligands are bound with zinc in a 1:1:1 Bip:Bipy:metal ratio. The resulting pseudo[3]rotaxane solution was dried under vacuum to obtain a yellow powder that was stored in the freezer at -8°C before use.

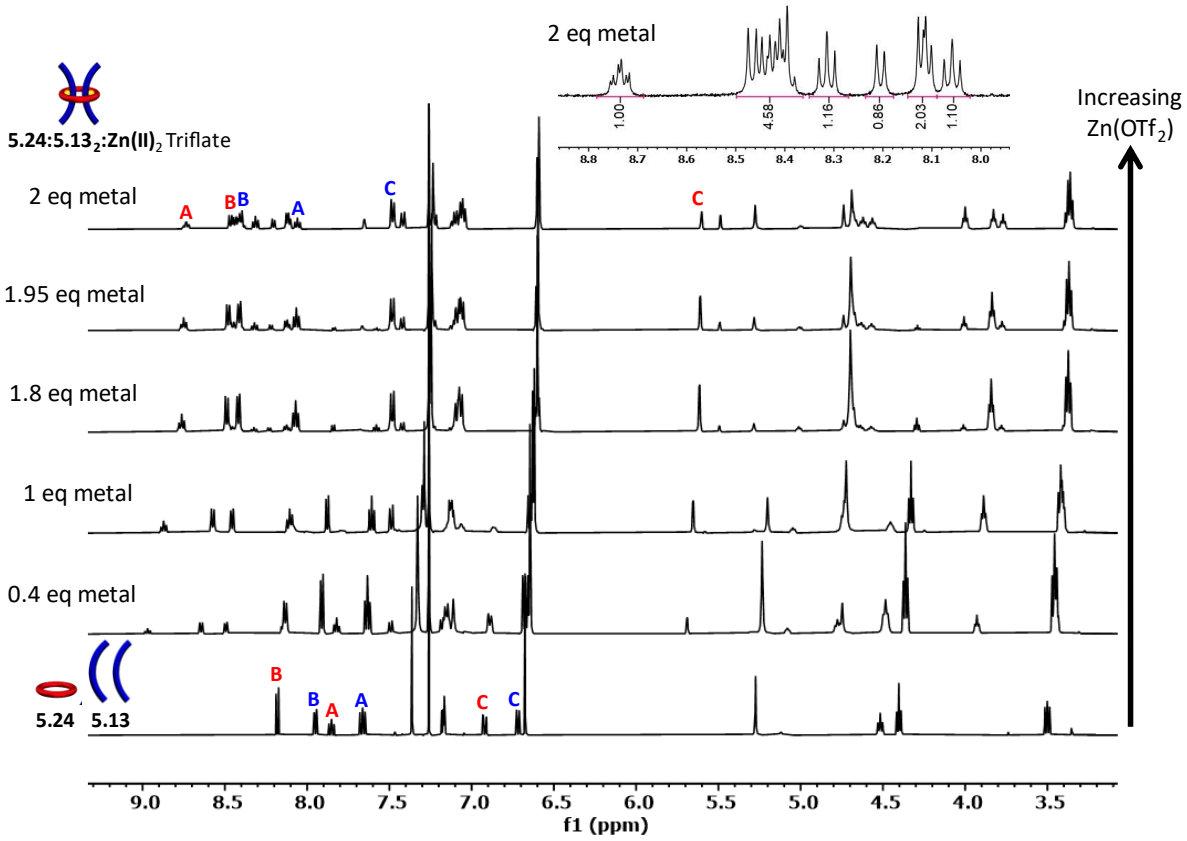

Figure 5.68. Titration A Partial ^{1}H-NMR overlay (500 MHz, 25°C, Solvent: 0, 3, 7.5, 13.5, 14.625, 15% d_3-MeCN in $CDCl_3$ increasing upwards) of $Zn(OTf)_2$ addition to form **5.24:5.13$_2$:Zn(II)$_2$**.

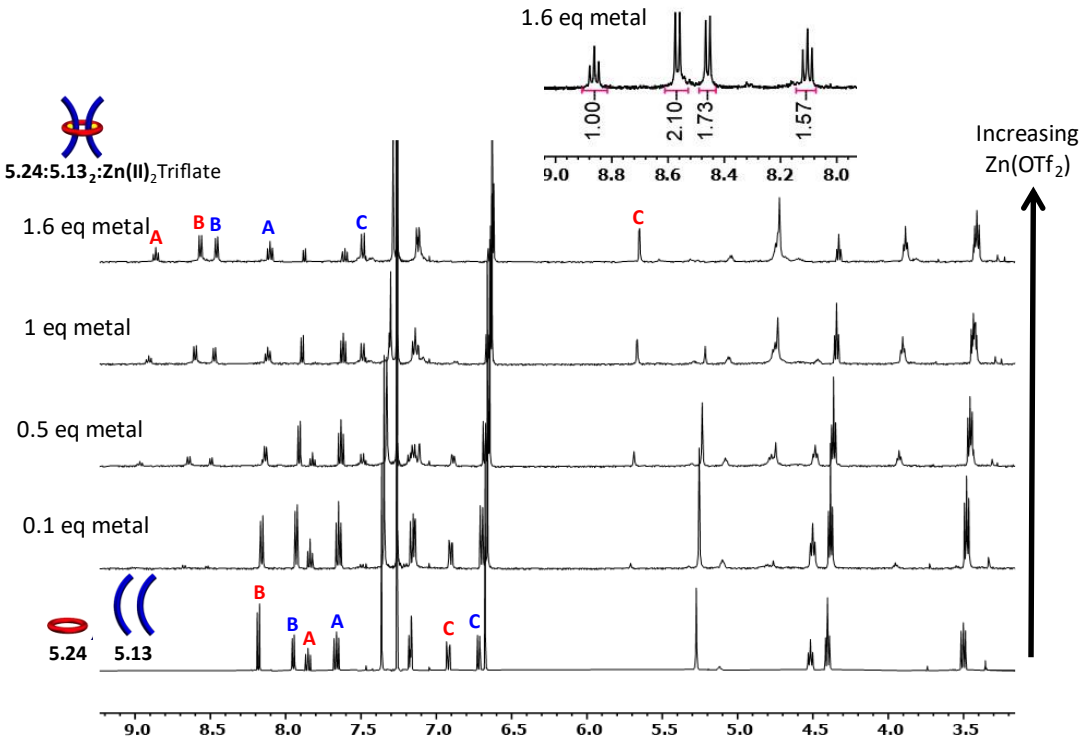

Figure 5.69. Titration B Partial ^{1}H-NMR overlay (500 MHz, 25°C, Solvent: 0, 0.75, 3.75, 7.5, 12% d_3-MeCN in $CDCl_3$ increasing upwards) of $Zn(OTf)_2$ addition to form **5.24:5.13$_2$:Zn(II)$_2$**.

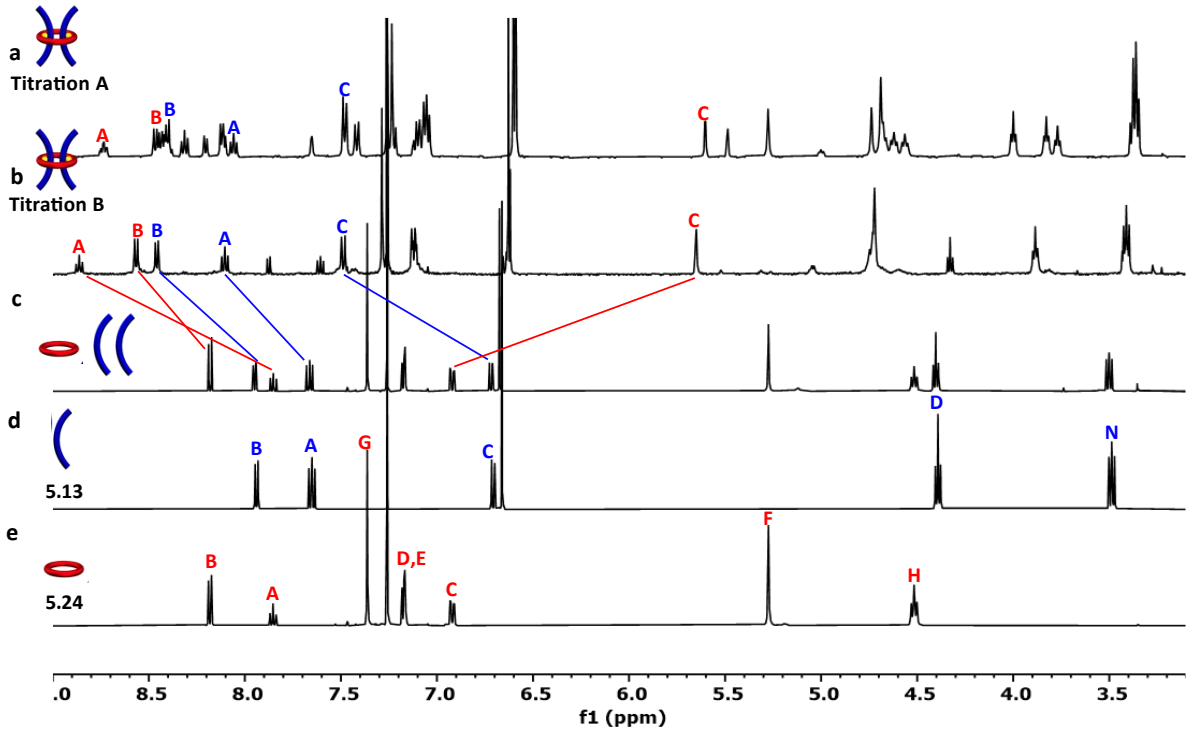

Figure 5.70. Partial ^{1}H-NMR overlay (500 MHz, 25°C) of a) **5.24:5.13$_2$:Zn(II)$_2$** (15% d_3-MeCN in $CDCl_3$) from Titration A. b) **5.24:5.13$_2$:Zn(II)** (12% d_3-MeCN in $CDCl_3$) from Titration B. c) 2:1 mixture of **5.13**:**5.24** ($CDCl_3$), d) **5.13** ($CDCl_3$) and e) **5.24** ($CDCl_3$).

5.4.2.23 Synthesis of [3]rotaxane **5.25**

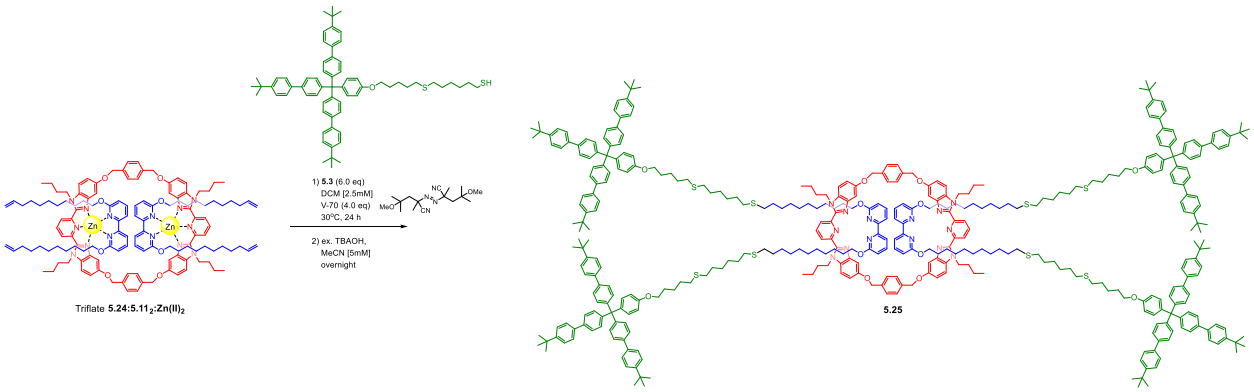

Triflate **5.24:5.11$_2$:Zn(II)$_2$** (0.0064 g, 0.0022 mmol; prepared by Dr. Qiong Wu using Zn(OTf)$_2$) was dissolved in 895 µL dry DCM. Thiol stopper **5.3** (0.0128 g, 0.0135 mmol) and 2,2'-azobis(4-methoxy-2,4-dimethylvaleronitrile azo initiator (V-70, 0.0028 g, 0.0090 mmol) were added to a 4 mL conical reaction vial with stir bar equipped with a water condenser and put under argon flow. After adding the pseudo[3]rotaxane solution to the reaction vial, the solution was bubbled with argon using a long needle for 5 minutes at RT. The reaction was then heated to 30°C and left for 24 hours with sufficient water flow through the condenser. After 24 hours, the reaction was cooled to room temperature, precipitated into a mixture of 1:20 DCM:hexanes (30 mL) then sonicated at 10,000 rpm at 4°C for 40 minutes. The liquid was decanted, leaving behind a yellow solid that was precipitated in a 3:1 mixture of hexanes:chloroform (30 mL) and sonicated again using the same conditions (x2). To demetallate, the yellow solid was dissolved in 1 mL of DCM and added to 20 mL of MeCN, and then 1 mL of tetrabutylammonium hydroxide (1M TBAOH in methanol) solution was injected. The sample was capped and stored in the freezer overnight and centrifuged the following day. The remaining off-white solid **5.25** was washed with 20 mL MeCN and centrifuged (x2) before drying under vacuum for analysis.

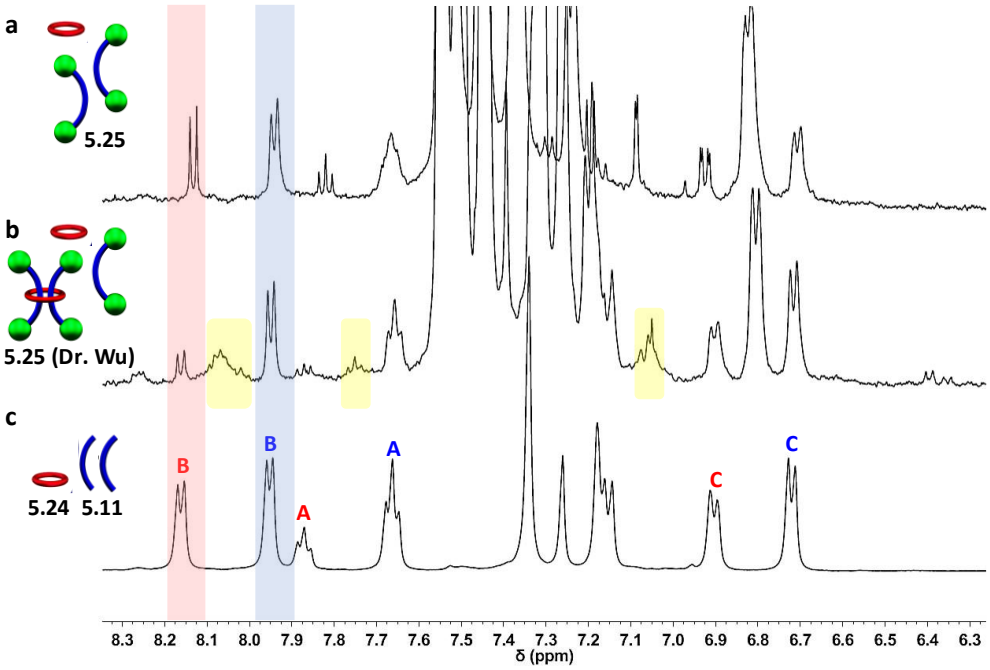

Figure 5.71. Partial ^{1}H-NMR overlay (500 MHz, 25°C, $CDCl_3$) of a) Demetallated **5.25** reaction mixture of dumbbell and macrocycle, b) Demetallated **5.25** reaction mixture from Dr. Qiong Wu, and c) 2:1 mixture of **5.11**:**5.24**. Upfield shifted peaks that likely indicate interlocked product highlighted in yellow.

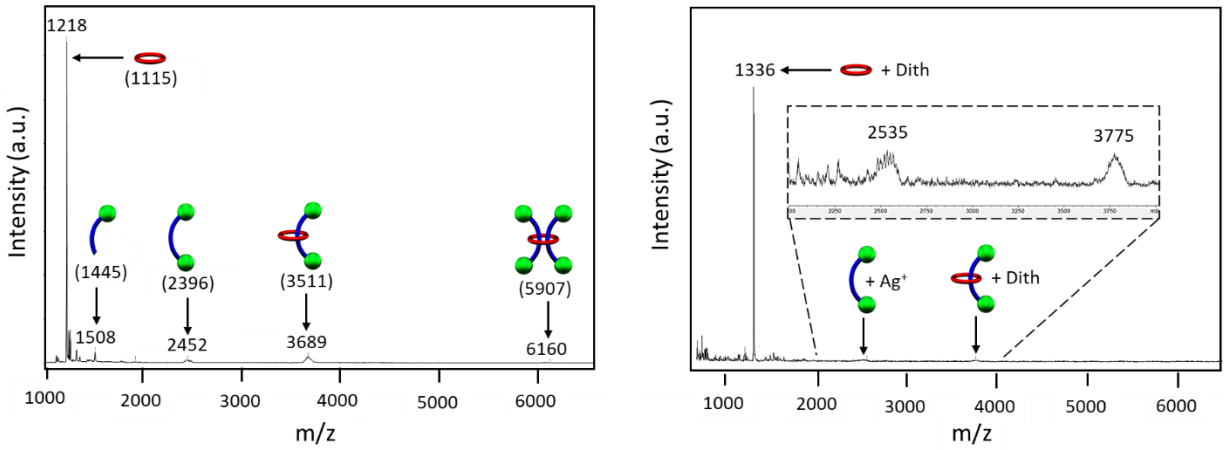

Figure 5.72. MALDI-TOF MS of [3]rotaxane **5.25** a) Dithranol (preliminary data collected by Dr. Wu, left) and b) Dithranol, silver trifluoroacetate (repeated experiment, right).

5.4.2.24 Synthesis of [3]rotaxane **5.26**

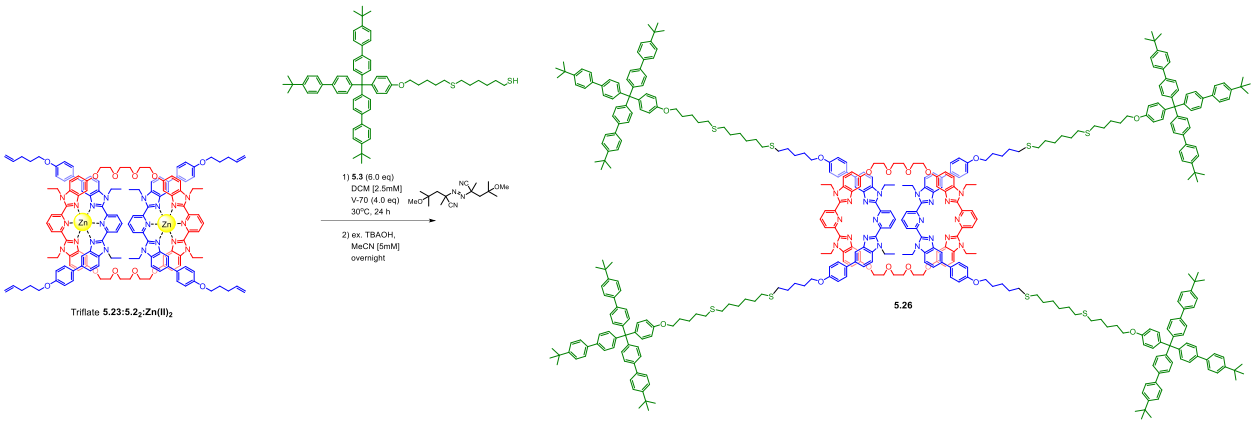

Triflate **5.23:5.2$_2$:Zn(II)$_2$** (0.004 g, 0.0012 mmol, prepared with $Zn(OTf)_2$), thiol stopper **5.3** (0.0066 g, 0.0069 mmol), and V-70 (0.0014 g, 0.0046 mmol) were dissolved in 490 µL of DCM and added to a vial equipped with a water condenser under argon flow. The reaction was heated to 30°C and left for 24 hours after which the reaction was cooled to RT and concentrated under vacuum. The sample was dissolved in $CDCl_3$ for NMR analysis, then pipetted into 35 mL of hexanes and sonicated at 10,000 rpm at 4°C for 40 minutes. The liquid was decanted, leaving behind a yellow solid that was precipitated in a 3:1 mixture of hexanes:chloroform (30 mL) and sonicated again using the same conditions (x3). To demetallate, the yellow solid was dissolved in 1 mL of DCM, and 0.3 mL of tetrabutylammonium hydroxide (1M TBAOH in methanol) solution was added. The **5.26** mixture was washed with DI water, and the organic layer was collected and dried under vacuum for analysis.

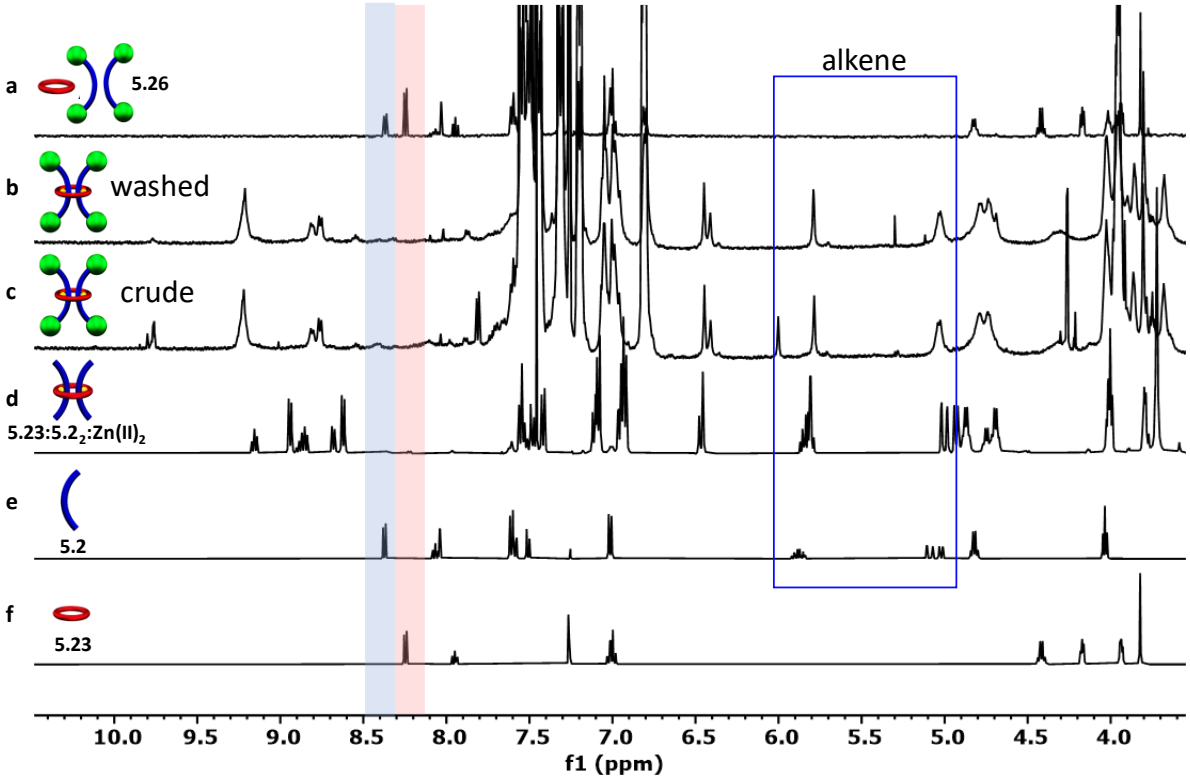

Figure 5.73. Partial ^{1}H-NMR overlay (500 MHz, 25°C, $CDCl_3$) of a) Demetallated **5.26** reaction mixture of dumbbell and macrocycle, b) washed, metallated **5.26** reaction mixture, c) crude, metallated **5.26** reaction mixture, d) **5.23:5.2$_2$:Zn(II)$_2$** (15% d_3-MeCN in $CDCl_3$), e) alkene thread **5.2**, and f) 46-atom macrocycle **5.23**.

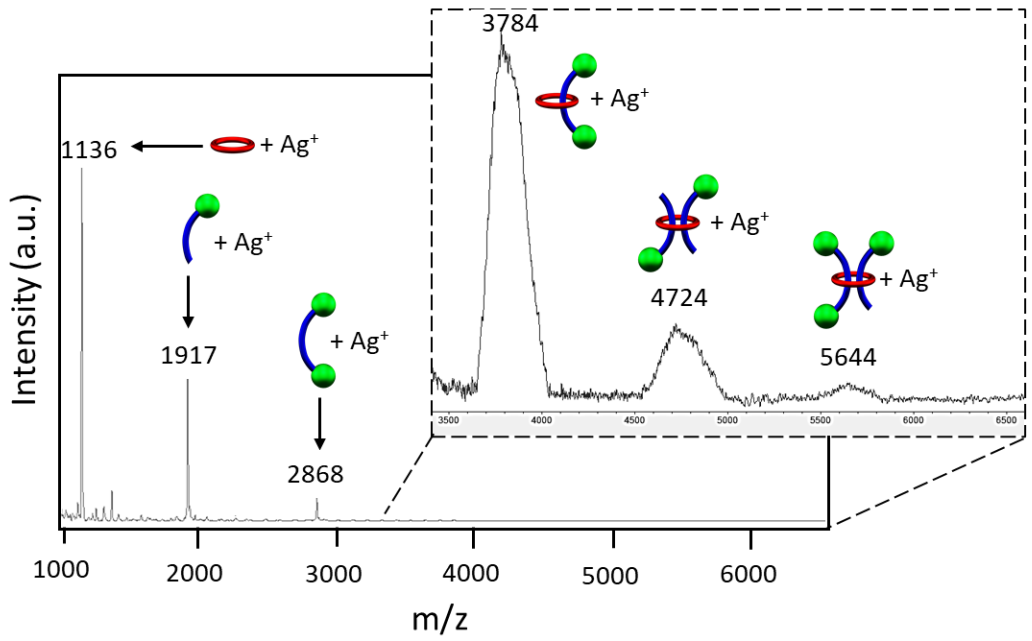

Figure 5.74. MALDI-TOF MS (Dithranol, silver trifluoroacetate) of [3]rotaxane **5.26** mixture.

5.4.2.25 Synthesis of [3]rotaxane **5.27**

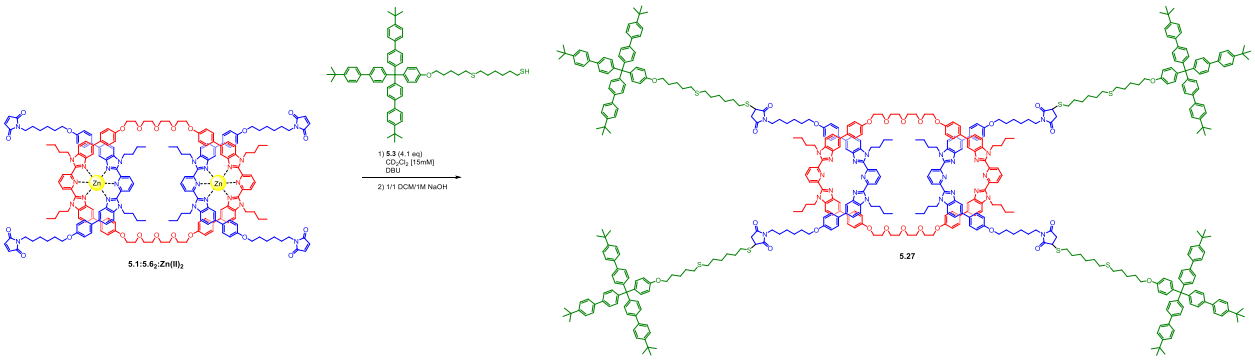

5.1:5.6$_2$:Zn(II)$_2$ (0.010 g, 0.0028 mmol) and thiol stopper **5.3** (0.011 g, 0.0115 mmol) were dissolved in 0.5 mL CD_2Cl_2 and added to an NMR tube. A stock solution of DBU (2.0 µL in 4 mL CD_2Cl_2) was prepared and added to the NMR tube in 2 µL (0.25 mol%) increments. A ^{1}H-NMR spectrum was acquired after each DBU addition to monitor reaction progress and watch for demetallation caused by DBU displacing thread and complexing with Zn^{2+} ions. The maleimide singlet from the pseudo[3]rotaxane at 6.72 ppm in CD_2Cl_2 (6.70 in $CDCl_3$) did not decrease even after adding 1.0 mol% DBU. However, at 0.75 mol% DBU, peaks started to grow between 8.35 ppm and 8.0 ppm corresponding to Bip thread no longer bound to the metal ion.

5.4.2.26 Synthesis of [3]rotaxane **5.28**

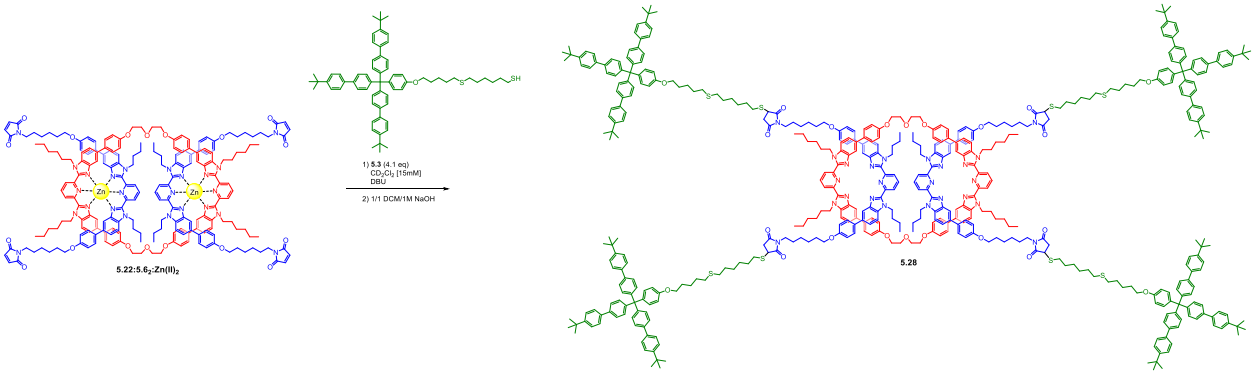

The 68-atom ring is too large for the current stopper size, as confirmed by simulations of the ring discussed above (Figure 5.38); thus, the 56-atom ring was used to repeat the thiol-maleimide stoppering experiment: **5.22:5.6$_2$:Zn(II)$_2$** (0.005 g, 0.0014 mmol) and thiol stopper **5.3** (0.006 g,

0.058 mmol) were dissolved in 0.5 mL CD_2Cl_2 and added to an NMR tube. A stock solution of DBU (0.2 µL in 200 µL CD_2Cl_2) was prepared, and 2 µL (1.0 mol%) was added to the NMR tube. After the spectrum was obtained, the metallated sample was demetallated by stirring rapidly in a 15 mL solution of 1/1 DCM/1M NaOH overnight. NMR on the demetallated mixture **5.28** revealed signals corresponding to the macrocycle and dumbbell only. The DBU in the sample facilitated the Michael addition to form the dumbbell product outside the ditopic ring cavity. Another explanation for the quantitative conversion to dumbbell is the base used to demetallate the ring, which could also complete the maleimide-thiol conjugation.

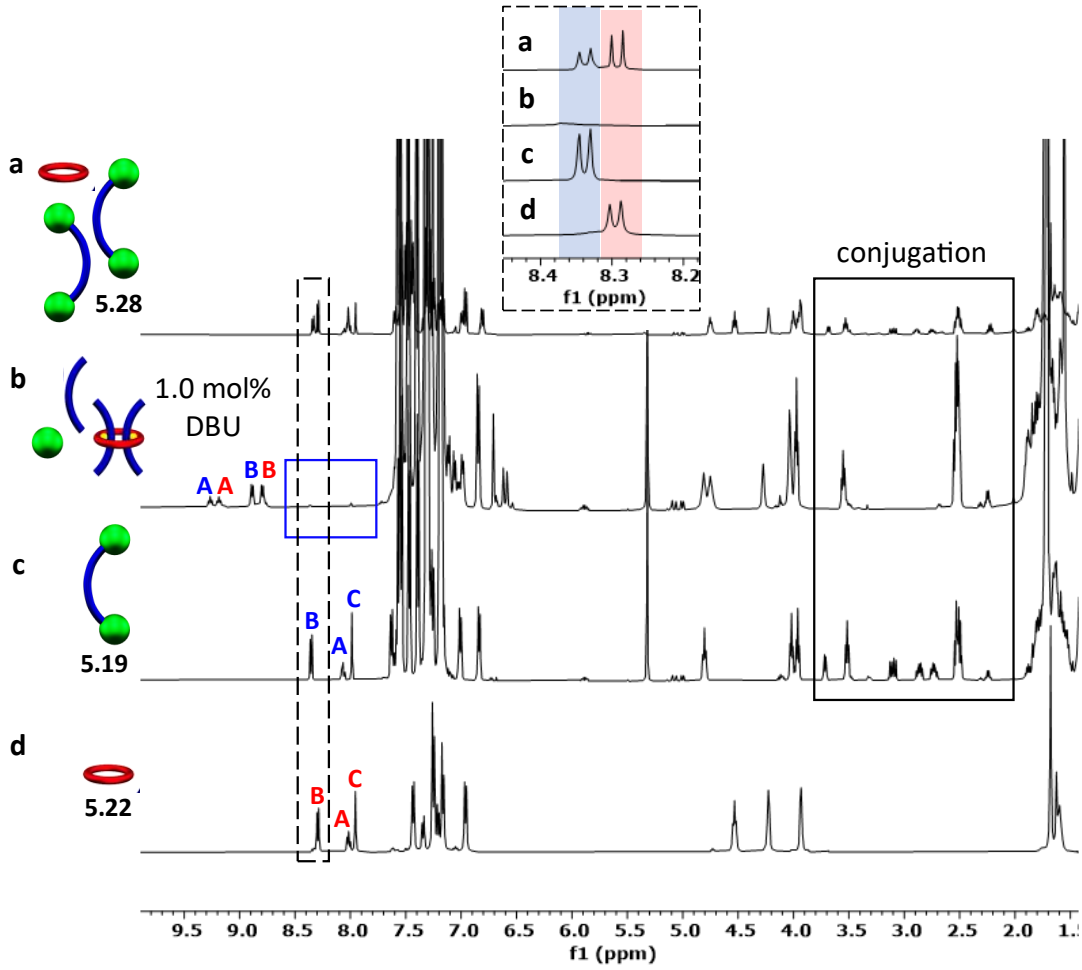

Figure 5.75. Partial ^{1}H-NMR overlay (500 MHz, 25°C) of a) Demetallated **5.28** reaction mixture of dumbbell and macrocycle ($CDCl_3$), b) mixture of **5.3**, **5.22:5.6$_2$:Zn(II)$_2$**, and **5.6** (Bip peaks of demetallated **5.6** in blue box) with 1.0 mol% DBU (CD_2Cl_2), c) **5.19** with thioester conjugation

region in black box (CD_2Cl_2), and d) 56-atom macrocycle **5.22** ($CDCl_3$). The dashed box and insert correspond to the meta-pyridyl peaks on Bip.

5.4.2.27 Synthesis of [3]rotaxane **5.29**

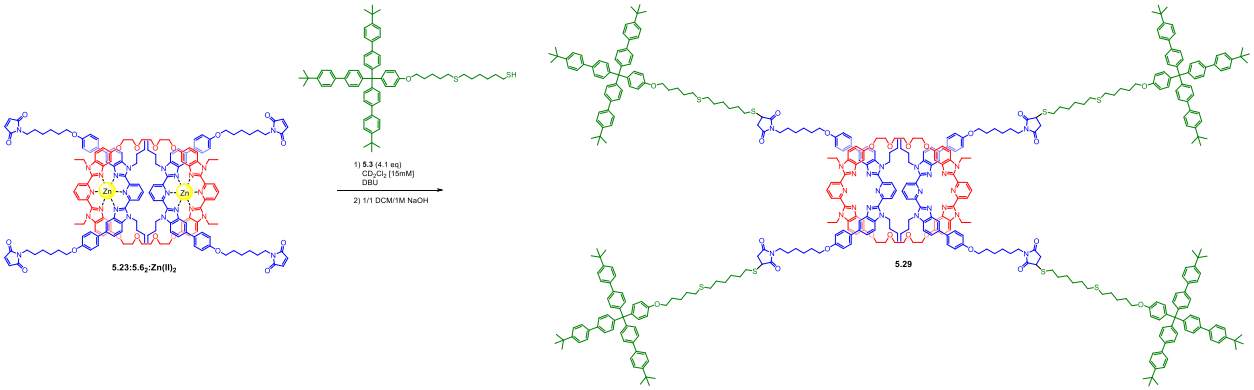

A smaller ring was accessed by removing the phenyl extensions on Bip and connecting the ligands via triethylene glycol linkages: **5.23:5.6$_2$:Zn(II)$_2$** (0.0085 g, 0.0028 mmol) and thiol stopper 5.3 (0.0107 g, 0.011 mmol) were dissolved in 0.5 mL CD_2Cl_2 and added to an NMR tube. A stock solution of DBU (0.165 µL in 1 mL CD_2Cl_2) was prepared, 0.1 mL (0.4 mol% used) was added to the NMR tube, and a spectrum was recorded. The decrease in metallated macrocycle and increase in unbound Bip peaks suggest that even at 0.4mol%, DBU chooses to bind with the metal ion instead of catalyzing the reaction between the stopper and metallated thread. The sample was demetallated by adding the NMR sample to a 20 mL vial with a stir bar with DCM (~9 mL) and 1M NaOH (~9 mL); the sample was left to stir rapidly overnight. The DCM layer was collected, washed with DI water, and dried under vacuum for NMR and MALDI-TOF analysis. NMR and MALDI-TOF confirmed a mixture of macrocycle and dumbbell; the higher molecular weight peaks (ca. 6650-6790 m/z) suggest a small amount of doubly-threaded[3]rotaxane may have formed, but not significantly enough.

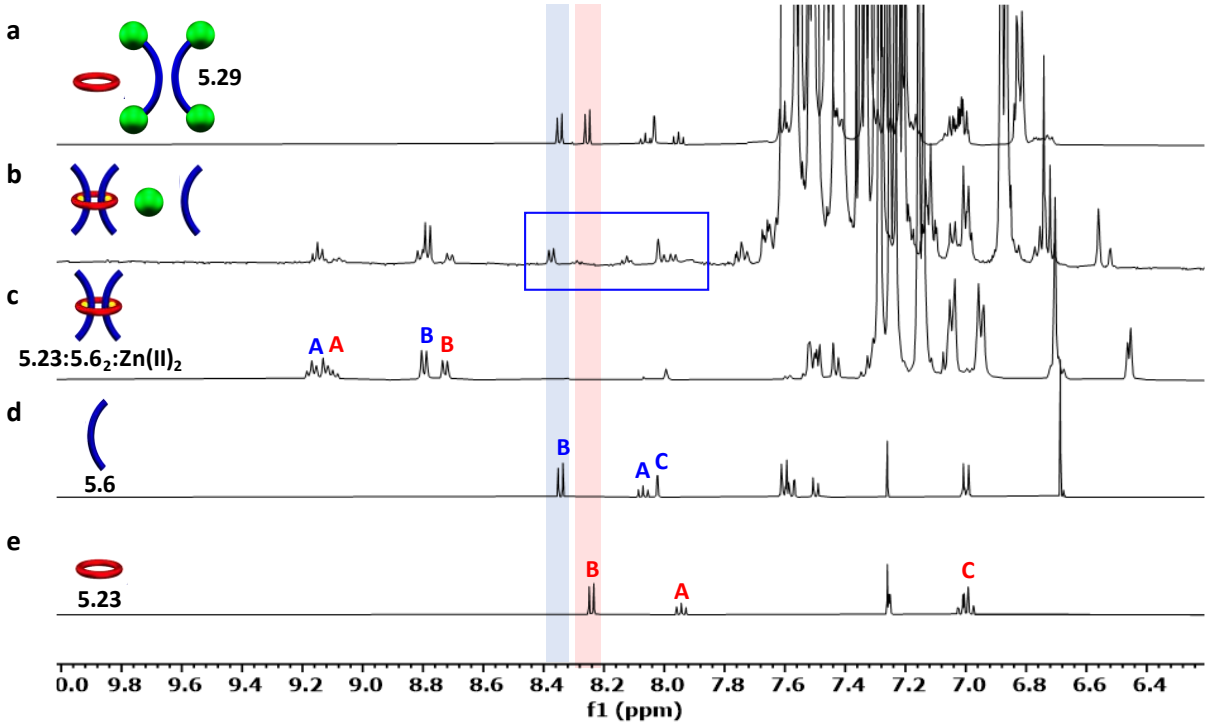

Figure 5.76. Partial ^{1}H-NMR overlay (500 MHz, 25°C, $CDCl_3$) of a) Demetallated **5.29** reaction mixture of dumbbell **5.19** and macrocycle **5.23**, b) mixture of **5.3**, **5.23:5.6$_2$:Zn(II)$_2$**, and **5.6** (Bip peaks of demetallated thread in blue box) with 0.4 mol% DBU (CD_2Cl_2), c) **5.23:5.6$_2$:Zn(II)$_2$** (15% d_3-MeCN in $CDCl_3$), d) **5.6**, and e) 46-atom macrocycle **5.23**.

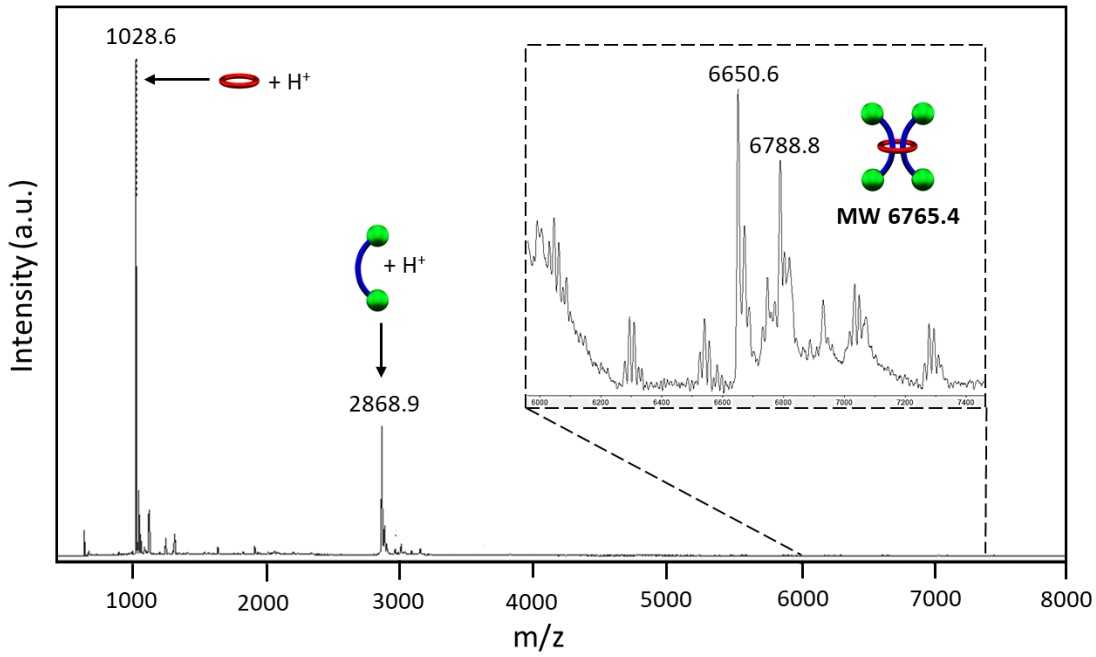

Figure 5.77. MALDI-TOF MS (Dithranol, silver trifluoroacetate) of [3]rotaxane **5.29** mixture.

5.4.2.28 Synthesis of [3]rotaxane **5.30**

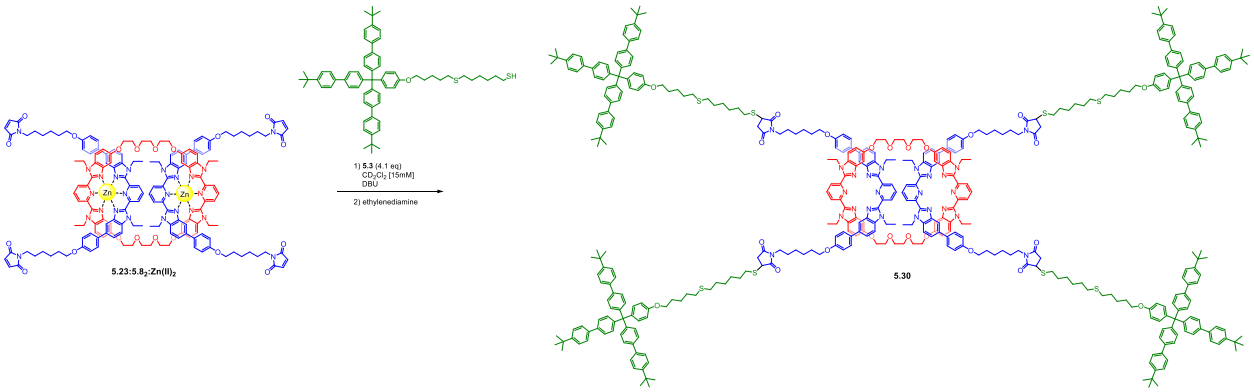

The same stoppering procedure was employed but with maleimide threads synthesized from ethyl-Bip; the shorter N-ethyl substituted Bip ligand to minimize steric repulsion between the thread molecules when both threaded within the same ring cavity. **5.23:5.6$_2$:Zn(II)$_2$** (0.010 g, 0.0034 mmol) and thiol stopper **5.3** (0.013 g, 0.014 mmol) were added to a vial and dissolved in 500 µL DCM. A DBU stock solution was prepared from 0.2 µL DBU in 1 mL DCM and 0.02 µL (1.0 mol%) was added to the vial. After 2 hours, 30 µL of ethylenediamine was added to the vial. Ethylenediamine was chosen over the prior demetallation conditions (1M NaOH) because it instantly removes metal ions from the Bip complex. The reaction mixture **5.30** was washed with DI water and extracted with DCM for analysis; NMR shows a mixture of macrocycle and dumbbell components and no interlocked product.

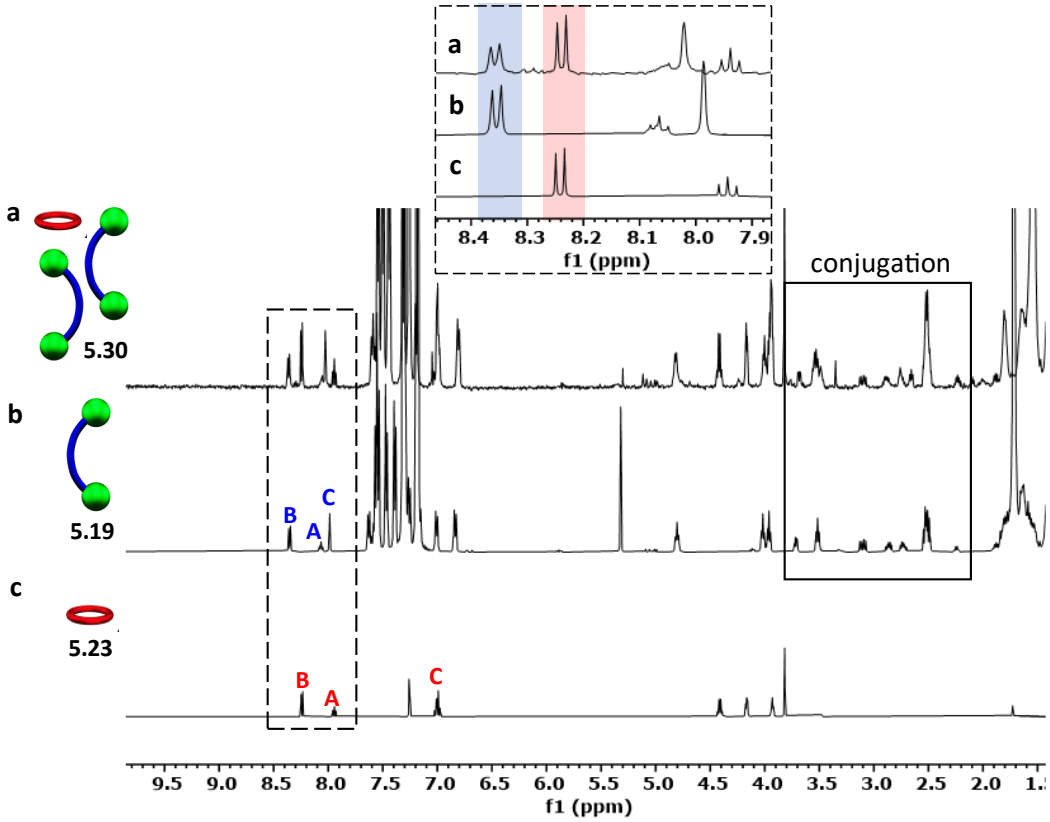

Figure 5.78. Partial ^{1}H-NMR overlay (500 MHz, 25°C) of a) Demetallated **5.30** reaction mixture of dumbbell and macrocycle ($CDCl_3$), (b) Bip dumbbell **5.19** with thioester conjugation region in the black box (CD_2Cl_2), and c) 46-atom macrocycle **5.23** ($CDCl_3$). The dashed box and insert correspond to Bip's meta- and para-pyridyl peaks.

5.4.2.29 Synthesis of [3]rotaxane **5.31**

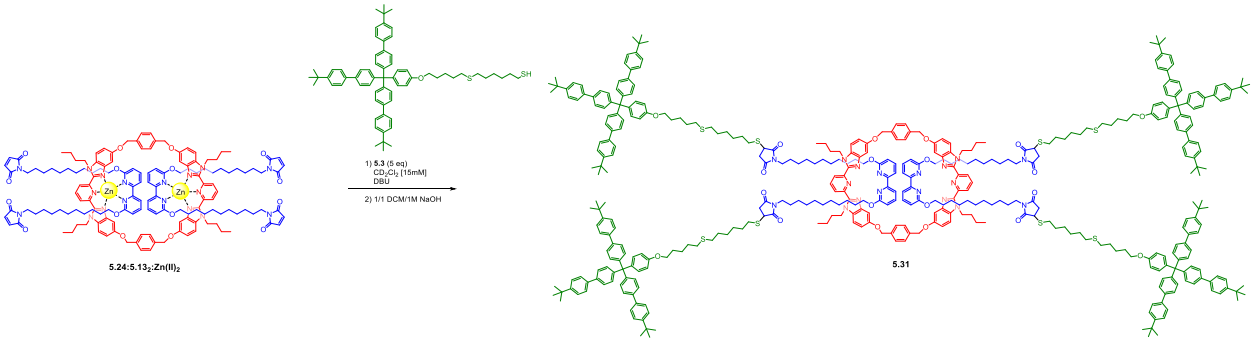

5.24:5.13$_2$:Zn(II)$_2$ (0.005 g, 0.0013 mmol) and thiol stopper **5.3** (0.0064 g, 0.0067 mmol) were dissolved in CD_2Cl_2 at [15mM]. A stock solution of DBU (0.01 µL in 500 µL CD_2Cl_2) was added in 10 µL (0.1 mol%) increments, and a spectrum was taken after each addition to monitor the maleimide singlet.

5.4.2.30 Synthesis of [3]rotaxane **5.32**

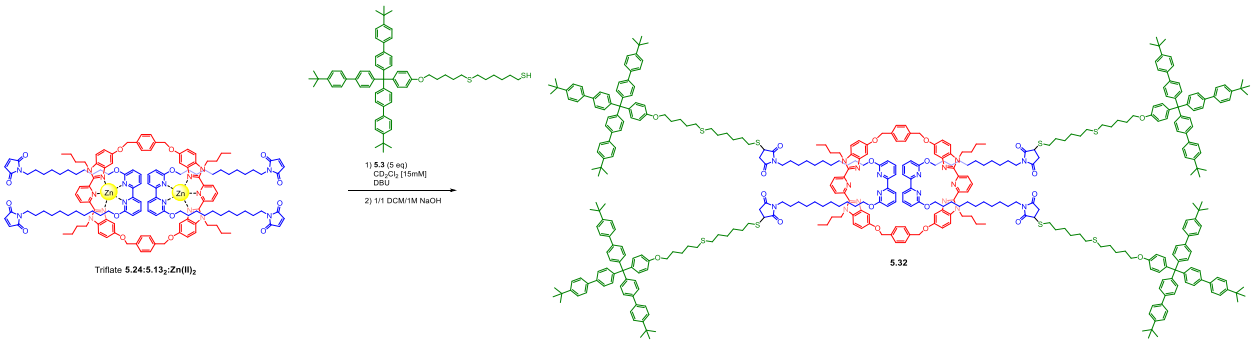

Triflate **5.24:5.13$_2$:Zn(II)$_2$** (Titration B, 0.0025 g, 0.0008 mmol, prepared with $Zn(OTf)_2$ and thiol stopper **5.3** (0.0037 g, 0.0039 mmol) were dissolved in CD_2Cl_2 at [15mM]. A stock solution of DBU (0.012 µL in 200 µL CD_2Cl_2) added in 2 µL (0.1 mol%) increments.

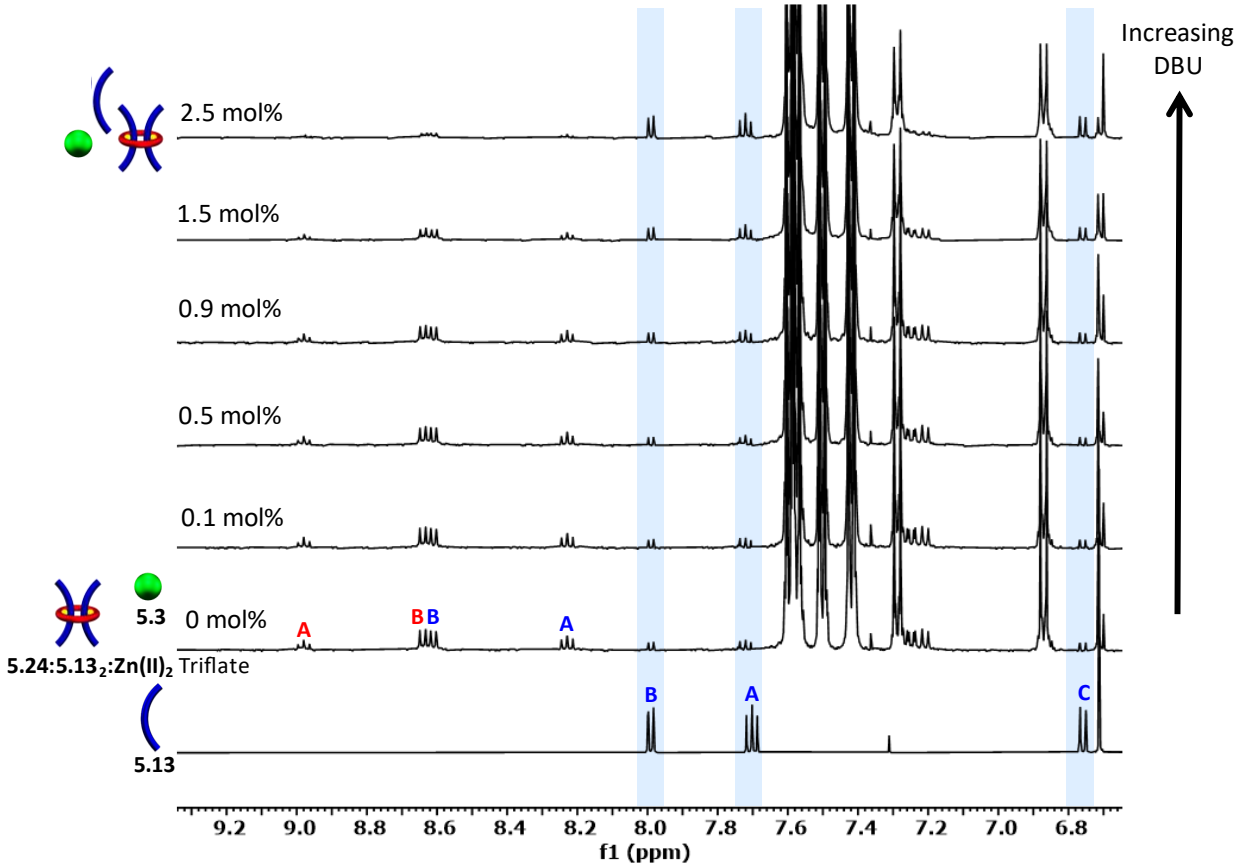

Figure 5.79. Partial ^{1}H-NMR overlay (500 MHz, 25°C, CD_2Cl_2) of triflate **5.24:5.13$_2$:Zn(II)** DBU titration showing complex demetallation and reappearance of the Bipy peaks from demetallated thread **5.13**.

5.5 References

(1) McGonigal, P. R. Multiply Threaded Rotaxanes. *Supramol. Chem.* **2018**, *30* (9), 782–794. https://doi.org/10.1080/10610278.2018.1433832.

(2) Wojtecki, R. J.; Wu, Q.; Johnson, J. C.; Ray, D. G.; Korley, L. T. J.; Rowan, S. J. Optimizing the Formation of 2,6-Bis(N-Alkyl-Benzimidazolyl)Pyridine-Containing [3]Catenates through Component Design. *Chem. Sci.* **2013**, *4* (12), 4440. https://doi.org/10.1039/c3sc52082j.

(3) Wu, Q.; Rauscher, P. M.; Lang, X.; Wojtecki, R. J.; De Pablo, J. J.; Hore, M. J. A.; Rowan, S. J. Poly[n]Catenanes: Synthesis of Molecular Interlocked Chains. *Science (80-.).* **2017**, *358* (6369), 1434–1439. https://doi.org/10.1126/science.aap7675.

(4) McKenzie, B. M.; Miller, A. K.; Wojtecki, R. J.; Johnson, J. C.; Burke, K. A.; Tzeng, K. A.; Mather, P. T.; Rowan, S. J. Improved Synthesis of Functionalized Mesogenic 2,6-Bisbenzimidazolylpyridine Ligands. *Tetrahedron* **2008**, *64* (36), 8488–8495. https://doi.org/10.1016/j.tet.2008.05.075.

(5) Kramer, R.; Lehn, J. M.; Marquis-Rigault, A. Self-Recognition in Helicate Self-Assembly: Spontaneous Formation of Helical Metal Complexes from Mixtures of Ligands and Metal Ions. *Proc. Natl. Acad. Sci. U. S. A.* **1993**, *90* (12), 5394–5398. https://doi.org/10.1073/pnas.90.12.5394.

(6) Hertzog, J. E.; Maddi, V. J.; Hart, L. F.; Rawe, B. W.; Rauscher, P. M.; Herbert, K. M.; Bruckner, E. P.; de Pablo, J. J.; Rowan, S. J. Metastable Doubly Threaded [3]Rotaxanes with a Large Macrocycle. *Chem. Sci.* **2022**, *00*, 1–12. https://doi.org/10.1039/d2sc01486f.

(7) Malkoch, M.; Vestberg, R.; Gupta, N.; Mespouille, L.; Dubois, P.; Mason, A. F.; Hedrick, J. L.; Liao, Q.; Frank, C. W.; Kingsbury, K.; Hawker, C. J. Synthesis of Well-Defined Hydrogel Networks Using Click Chemistry. *Chem. Commun.* **2006**, No. 26, 2774–2776. https://doi.org/10.1039/b603438a.

(8) Uliniuc, A.; Popa, M.; Hamaide, T.; Dobromir, M. New Approaches in Hydrogel Synthesis - Click Chemistry: A Review. *Cellul. Chem. Technol.* **2012**, *46* (1–2), 1–11.

(9) Nair, D. P.; Podgórski, M.; Chatani, S.; Gong, T.; Xi, W.; Fenoli, C. R.; Bowman, C. N. The Thiol-Michael Addition Click Reaction: A Powerful and Widely Used Tool in Materials Chemistry. *Chemistry of Materials*. 2014, pp 724–744. https://doi.org/10.1021/cm402180t.

(10) Perera, A. S.; Subbaiyan, N. K.; Kalita, M.; Wendel, S. O.; Samarakoon, T. N.; D'Souza, F.; Bossmann, S. H. A Hybrid Soft Solar Cell Based on the Mycobacterial Porin MspA Linked to a Sensitizer-Viologen Diad. *J. Am. Chem. Soc.* **2013**, *135* (18), 6842–6845. https://doi.org/10.1021/ja403090x.

(11) Ravasco, J. M. J. M.; Faustino, H.; Trindade, A.; Gois, P. M. P. Bioconjugation with Maleimides: A Useful Tool for Chemical Biology. *Chem. - A Eur. J.* **2019**, *25* (1), 43–59.

https://doi.org/10.1002/chem.201803174.

(12) Walker, M. A. A High Yielding Synthesis of N-Alkyl Maleimides Using a Novel Modification of the Mitsunobu Reaction. *J. Org. Chem.* **1995**, *60* (16), 5352–5355. https://doi.org/10.1021/jo00121a070.

(13) Dobrawa, R.; Würthner, F. Metallosupramolecular Approach toward Functional Coordination Polymers. *J. Polym. Sci. Part A Polym. Chem.* **2005**. https://doi.org/10.1002/pola.20997.

(14) Walker, M. A. A High Yielding Synthesis of N-Alkyl Maleimides Using a Novel Modification of the Mitsunobu Reaction. *J. Org. Chem.* **1995**, *60* (16), 5352–5355. https://doi.org/10.1021/jo00121a070.

(15) King, H. D.; Dubowchik, G. M.; Walker, M. A. Facile Synthesis of Maleimide Bifunctional Linkers. *Tetrahedron Lett.* **2002**, *43* (11), 1987–1990. https://doi.org/10.1016/S0040-4039(02)00192-2.

(16) Neises, B.; Steglich, W. Simple Method for the Esterification of Carboxylic Acids. *Angew. Chemie Int. Ed. English* **1978**, *17* (7), 522–524. https://doi.org/10.1002/anie.197805221.

(17) Li, M.; De, P.; Gondi, S. R.; Sumerlin, B. S. End Group Transformations of RAFT-generated Polymers with Bismaleimides: Functional Telechelics and Modular Block Copolymers. *J. Polym. Sci. Part A Polym. Chem.* **2008**, *46* (15), 5093–5100. https://doi.org/10.1002/pola.22837.

(18) Willcock, H.; O'Reilly, R. K. End Group Removal and Modification of RAFT Polymers. *Polym. Chem.* **2010**, *1* (2), 149–157. https://doi.org/10.1039/b9py00340a.

(19) Moehrke, J.; Vana, P. The Kinetics of Surface-Initiated RAFT Polymerization of Butyl Acrylate Mediated by Trithiocarbonates. *Macromol. Chem. Phys.* **2017**, *218* (6), 1–11. https://doi.org/10.1002/macp.201600506.

6 Accessing Thermodynamically Stable Doubly-Threaded [3]Rotaxane Diels-Alder Adducts

6.1 Introduction

Accessing doubly-threaded [3]rotaxanes relies on forming a stable intermediate that keeps the ring bound and maintains the doubly-threaded topology during the final end-capping reaction. Catalyst-free click chemistry is attractive for stoppering metal complexes susceptible to disassembly under basic (or acidic) conditions. Diels-Alder reactions of five-membered heterocycles are well-established and have been a valuable tool in organic synthesis for decades owing to their dynamic nature and facile reaction conditions; temperature changes promote the exchange and switching between molecules (e.g., maleimide and furan) with negligible side reactions. The thermoreversible equilibrium in maleimide-furan conjugation is commonly employed in protecting groups to synthesize oligonucleotide conjugates[1] and crosslinks for thermal self-healing materials (Figure 6.1).[2,3]

The cycloaddition between a highly reactive (diene) and furan (dienophile) proceeds via a concerted mechanism at room temperature.[1–3] The forward reaction dominates up to 60°C, forming a mixture of bicyclic compounds. The position of the bridgehead protons alpha to the

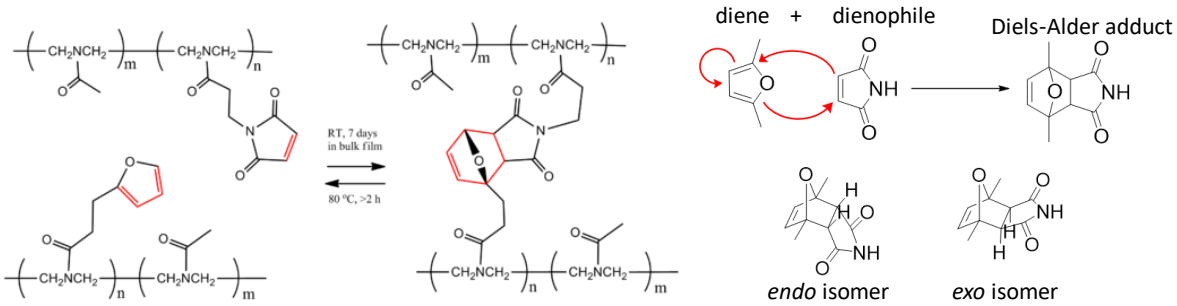

Figure 6.1. Thermoreversible Diels-Alder crosslinking for self-healing materials proceeds via a concerted mechanism at room temperature to form a mixture of *endo* (kinetically favored) and *exo* (thermodynamically favored) conjugation products. Adapted from Ref. 3 with permission from American Chemical Society.

carbonyl groups helps distinguish the regiochemistries in the different isomers. The *endo* adduct forms faster because the overlap of secondary orbitals lowers the energy of the transition state, making it the kinetic product. The oxygen-containing bridge in the *exo* adduct eclipses the anhydride so that substituents on the dienophile point away from the bicyclic ring. This conformation reduces steric hindrance in the cycloadduct, making the *exo* isomer thermodynamically favored under reversible conditions because it is more stable and lower in energy. Running reactions at room temperature and keeping them in the dark helps target the *endo* adduct, while higher temperatures produce the *exo* product.

Converting thermodynamic maleimide-furan conjugates into thermally stable counterparts is achieved through chemical modification, such as aromatization to a phthalimide moiety (Figure 6.2).[4,5] Heat is required to convert *endo* adducts into thermodynamically stable *exo* isomers that can undergo dehydrative rearrangement. A small amount of acid catalyzes aromatization by protonating the oxygen bridge, and the bridgehead protons help facilitate the loss of a water molecule to form the phthalimide derivative. Aromatization with *p*-toluenesulfonic acid (*p*-TsOH)

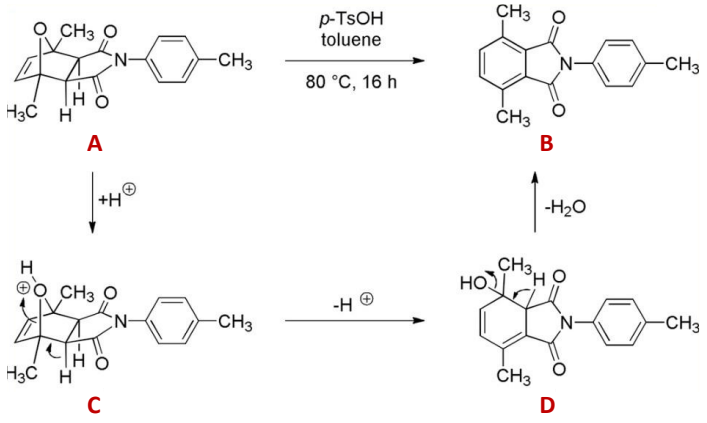

Figure 6.2. The acid-catalyzed reaction mechanism for the rearrangement of bicyclic Diels-Alder adduct **A**, with loss of water, when treated with *p*-TsOH in toluene at 80°C to give **B**.[4] Adapted from Ref. 4 with permission from Elsevier.

in toluene is a common approach for converting furan-maleimide conjugates to phthalimides;[233] other methods employ Brønsted and Lewis acid catalysts, such as metal triflates, for tandem Diels-Alder and dehydration reactions.[234]

This chapter explores maleimide-furan chemistry for the Diels-Alder stoppering and acid-catalyzed rearrangement of rotaxane components into thermally stable and functional doubly-threaded [3]rotaxane products. Dynamic bonding between polyrotaxane components could lead to networks with reversible crosslinking or assembly, typically desired for recyclable and degradable materials.[6] Rearrangement reactions of Diels-Alder adducts will be explored to determine their efficacy in creating stable [3]rotaxane products. This conversion would prevent decomposition over time and at elevated temperatures, providing a way to access stable and more robust materials from preassembled dynamic networks.

6.2 Results and Discussion

6.2.1 Diels-Alder Cycloadducts

A two-step maleimide-furan stoppering approach was devised to make doubly-threaded rotaxanes that will not fall apart when heated. Catalyst-free conditions should promote the

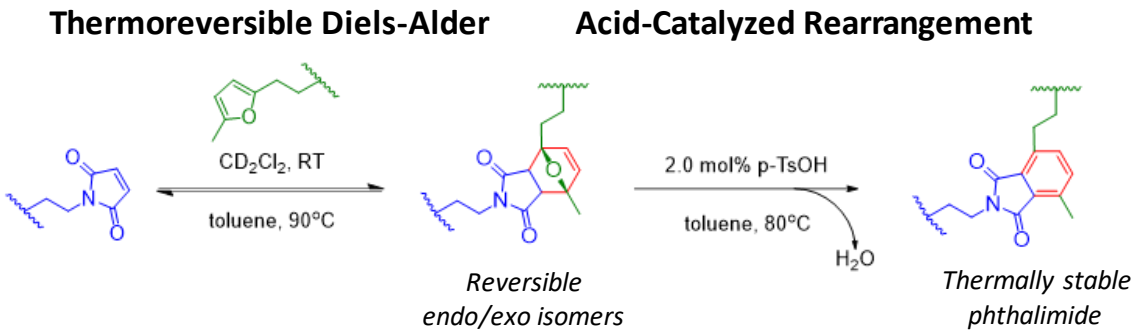

Figure 6.3. Maleimide-Furan Stoppering Approach. Diels-alder click reaction between N-alkylated maleimide and furan-terminated molecule, and subsequent acid-catalyzed (e.g., *p*-TsOH) dehydration of furan-maleimide cyclo-adducts in toluene to form a stable phthalimide linkage between components.

formation of reversible Diels-Alder adducts between the metal complexes and stopper, which would permit the aromatization of the reversible bicyclics to thermally stable phthalimides (Figure 6.3).

Small molecule reactions between maleimide and 2,5-dimethylfuran determined how the formation of a mixture of isomers looks on the NMR spectrum (see Experimental). Determining which peaks to monitor in NMR during the Diels-Alder cycloaddition and after the acid-catalyzed rearrangement will help determine what shifts to anticipate when forming the dumbbell component and confirm the rearrangement. The combination of *exo* and *endo* cycloadducts in the crude NMR spectrum shown in Figure 6.4 results from the reversibility of the Diels-Alder reaction. The bridgehead protons show up as a singlet at 2.9 ppm on the *exo* adduct (i.e., C') and 3.3 ppm for the *endo* adduct (C). These results are consistent with literature values for maleimide adducts with 2,5-dimethylfuran, where the *exo* bridgehead protons are consistently 0.40 ppm upfield for the *endo* adduct.[7]

The Diels-Alder reaction between furan and maleimide has been widely employed as a click-unclick tool in polymer synthesis.[1,8] As mentioned in Chapter 5, maleimides are highly reactive and hydrolyze under basic conditions without a protecting group. A protected maleimide

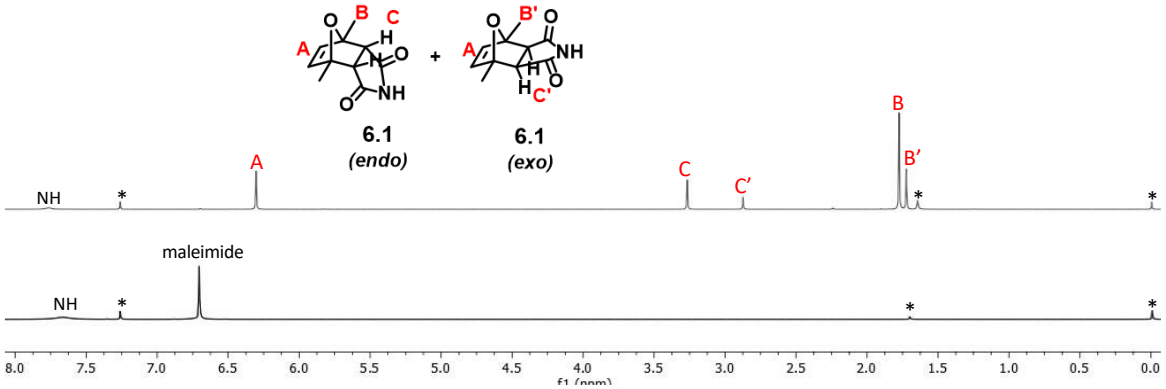

Figure 6.4. ^{1}H-NMR (500 MHz, 25°C, $CDCl_3$) of crude **6.1**, showing a mixture of *endo* and *exo* (prime) cycloadducts (top spectrum) formed from maleimide (bottom spectrum) and 2,5-dimethylfuran.

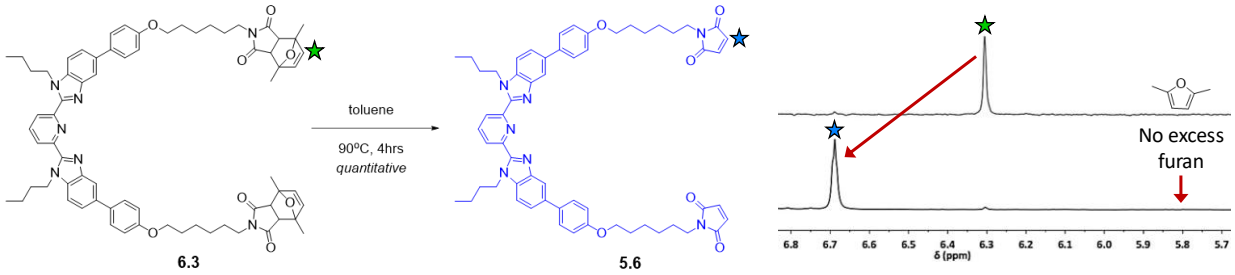

Figure 6.5. Refluxing **6.3** in toluene removes the furan (6.3 ppm) moiety, unmasking the reactive maleimide groups (~6.7 ppm) on **5.6** with complete removal of 2,5-dimethylfuran (5.8 ppm).

thread was synthesized to test the thermostability of the maleimide-furan cycloadducts in the Bip-containing thread (see Experimental). Heating **6.3** in solution sparks the retro Diels-Alder, which recovers the reactive maleimides on **5.6** (Figure 6.5, left). Refluxing the thread in toluene for four hours completely removes the furan; toluene extracts the 2,5-dimethylfuran, resulting in a clean thread product after removing the solvent. Diagnostic peaks in the ^{1}H-NMR spectrum help monitor the forward and reverse reactions; the signal at 6.7 ppm shifts to 6.3 ppm upon furan conjugation. The maleimide peak is recovered at elevated temperatures, and toluene helps extract 2,5-dimethylfuran from the product mixture. The ^{1}H-NMR spectrum confirms the clean conversion of **5.6**; the maleimide singlet at 6.7 ppm is recovered, and no signal at 5.8 ppm that would correspond to the aromatic protons on 2,5-dimethylfuran (Figure 6.5, right).

This experiment confirms 2,5-dimethylfuran as a sufficient maleimide-protecting group to prevent hydrolysis of maleimides under basic reaction conditions. Furthermore, the formation of the furan-maleimide adducts proceeds under catalyst-free conditions, and extending this concept to stopper P3R should lead to metallated [3]rotaxanes with high conversion.

6.2.2 Acid-Catalyzed Rearrangement

Accessing stable interlocked products requires stabilizing the thermoreversible Diels-Alder adducts; a common approach uses a catalytic amount of *p*-TsOH in toluene at elevated temperatures to rearrange furan-maleimide conjugates, such as the conversion of **6.1** to

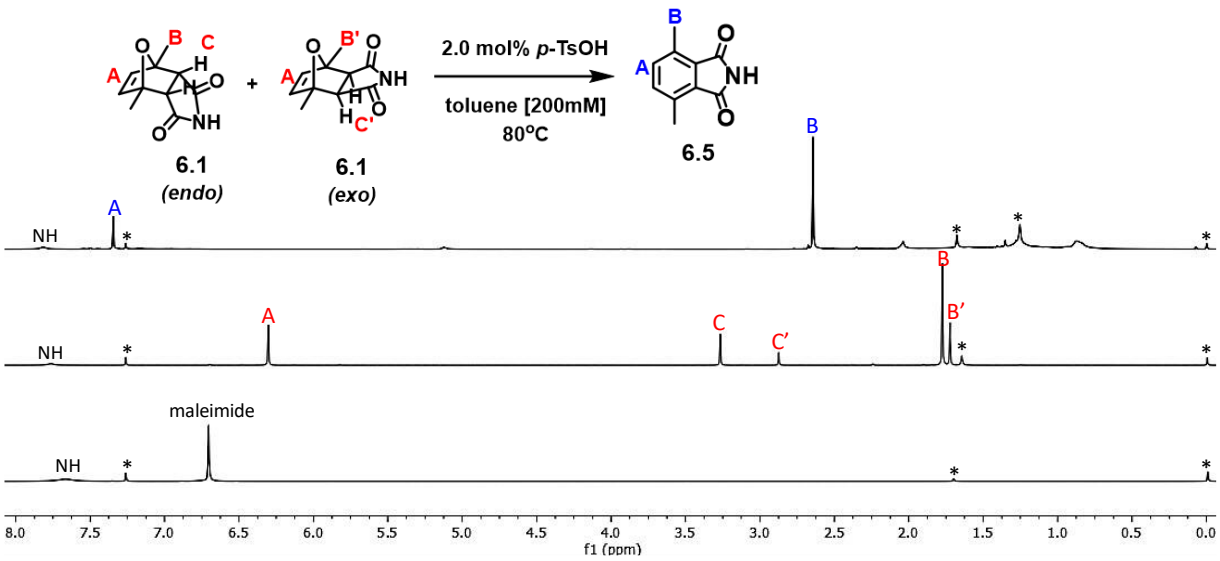

Figure 6.6. ^{1}H-NMR overlay (600 MHz, 25°C, $CDCl_3$) of crude phthalimide **6.5** (top spectrum), **6.1** isomers (middle spectrum) and maleimide (bottom spectrum). *Solvent

phthalimide **6.5** (see Experimental) shown in Figure 6.6.[7] The disappearance of signals corresponding to the conjugate bridgehead protons at 3.3 and 2.9 ppm (C, C') indicates successful aromatization; after the oxygen-bridge is protonated, these bridgehead protons remove the water molecule, facilitating rearrangement to phthalimide **6.5**. The methyl protons now show up as a single peak (B) at 2.7 ppm, and a downfield shift in the vinyl bond (A) from 6.3 to 7.3 ppm suggests a more aromatic environment, as expected for the phthalimide.

6.2.3 Dumbbell Stoppering Experiments

Investigating the maleimide-furan click as potential stoppering chemistry required synthesizing a furan-functionalized stopper group **6.7** (see Experimental) to react with maleimide thread **5.13** synthesized in Chapter 5 (Figure 6.7). Acid-catalyzed rearrangement conditions using *p*-toluenesulfonic acid (*p*-TsOH) at elevated temperatures were tested to convert reversible Diels-Alder adducts in 6.11 into stable units between components like the phthalimides in **6.12**. Heating the adducts during the rearrangement should help form more *exo* adducts in situ that can partake in the rearrangement reaction.

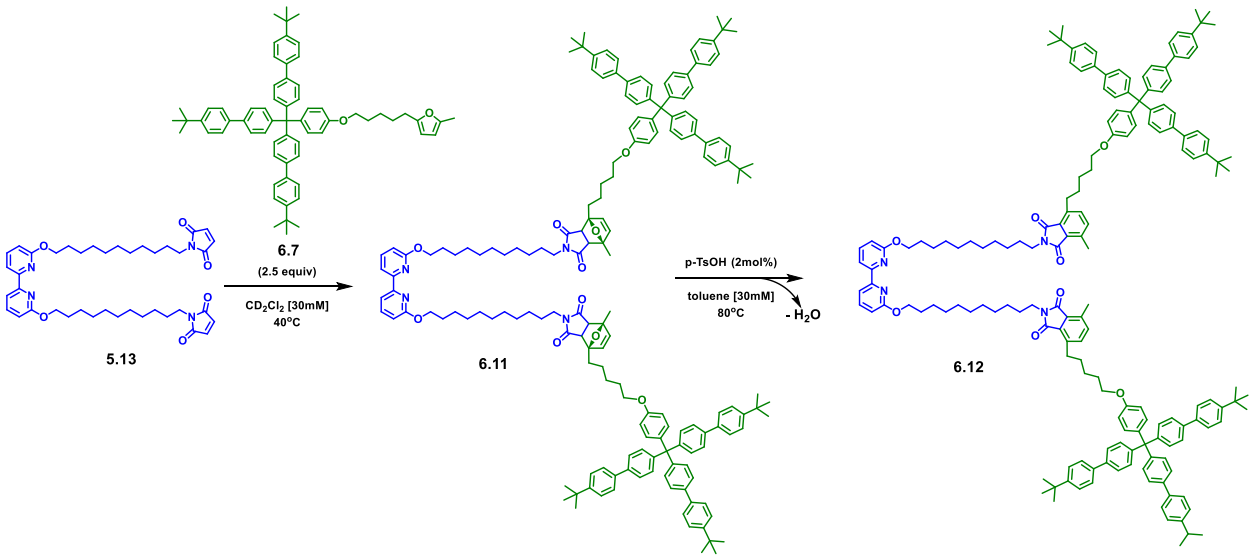

Figure 6.7. Dumbbell synthesis. Maleimide thread **5.13** and furan stopper **6.7** react at 40°C to form Diels-Alder dumbbell **6.11** as a mixture of *endo* and *exo* isomers (see Experimental). A catalytic amount of *p*-toluenesulfonic acid (*p*-TsOH) at 80°C results in the rearrangement of **6.11** to phthalimide **6.12** with dehydration.

NMR integrations and MALDI-TOF analysis of **6.11** confirm the formation of the Diels-Alder dumbbell. Integrating *exo* and *endo* isomers between 6.0 and 6.5 ppm (see Experimental) suggests a 1:2 ratio of *exo:endo* isomers for **6.11**. A small maleimide (6.7 ppm) and furan (5.8 ppm) peaks suggest unreacted components in the mixture, potentially resulting from retro Diels-Alder of the reversible cycloadducts. MALDI-TOF also confirmed the formation of Diels-Alder dumbbell **6.11** (see Experimental).

The Diels-Alder dumbbell **6.11** was converted to phthalimide **6.12** using toluene and a catalytic amount of *p*-TsOH. The NMR in Figure 6.8 shows a reduction in the *endo* and *exo* signals between 6.4 – 6.1 ppm (furan protons), 3.5 – 2.7 ppm (bridgehead protons), and 1.8 – 1.6 ppm (methyl protons) for **6.12**, suggesting that the dehydration mechanism observed in the small molecule studies also works on the dumbbell. However, the peaks corresponding to the Bipy ligand are also significantly reduced. This is likely due to the protonation of the nitrogen atoms with *p*-TsOH, and is worth further investigation. MALDI-TOF further confirms the rearrangement with

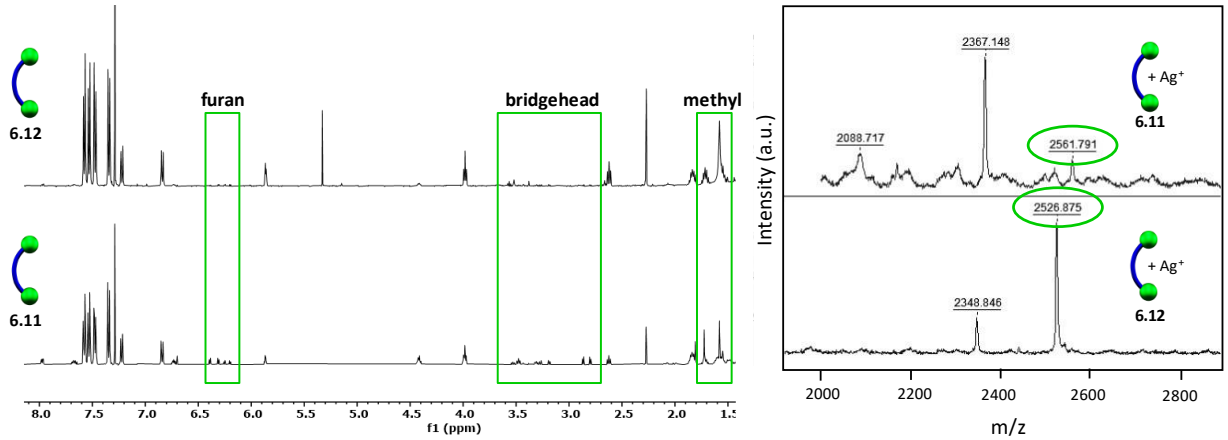

Figure 6.8. ^{1}H-NMR (500 MHz, 25°C, $CDCl_3$) of **6.12** (top) and **6.11** (bottom). b) MALDI-TOF MS (dithranol, silver trifluoroacetate) of **6.11** (top left) and **6.12** (bottom left). The difference between the two products (green circles, right) is ~35 which is close to the expected ~36 mass loss with (2*H_2O). The lower molecular weight signals correspond to the fragmented dumbbell products (loss of biphenyl arm, see Experimental).

a 34.9 (2561.791 - 2526.875 g/mol) reduction in molecular weight; a ~36.03 difference corresponds to the loss of two water molecules from the same dumbbell molecule (Figure 6.8, right).

Lewis acid catalysts should also trigger the dehydration of the maleimide-furan conjugates, such as metal triflates;[5] therefore, the dehydration of Diels-Alder dumbbell **6.11** was also tested using scandium triflate ($Sc(OTf)_3$) to evaluate its potential as a catalyst for stabilizing thermoreversible furan-maleimide adducts. Reacting **6.11** with scandium triflate ($Sc(OTf)_3$) in toluene instead of *p*-TsOH also resulted in the disappearance of bridgehead protons in the NMR spectrum (see Experimental). These results are promising because they show that other catalysts can trigger the rearrangement of furan-maleimide adducts.

6.2.4 Pseudo[3]Rotaxane Stoppering Experiments

P3R **5.24:5.13$_2$:Zn(II)$_2$** was chosen for these experiments because it is assembled from the small, 42-atom ring, which has the best chance of forming stable, interlocked [3]rotaxanes with the current triaryl stopper size in **6.7** (Figure 6.9, top). Gratifyingly, the *endo* and *exo* isomers of the

crude metallated [3]rotaxane **6.16** and the metallated Diels-Alder dumbbell **6.11$_2$:Zn(II)** show the same chemical shift in the NMR spectrum (Figure 6.9, bottom). After purification to remove the unreacted stopper (see Experimental), the metallated **6.16** exhibited a 1:4 integration of protons in the NMR spectrum for the ring **5.24** (A) and dumbbell **6.11** (W) components, suggesting full Diels-Alder stoppering of **5.24:5.13$_2$:Zn(II)$_2$** (Figure 6.10).

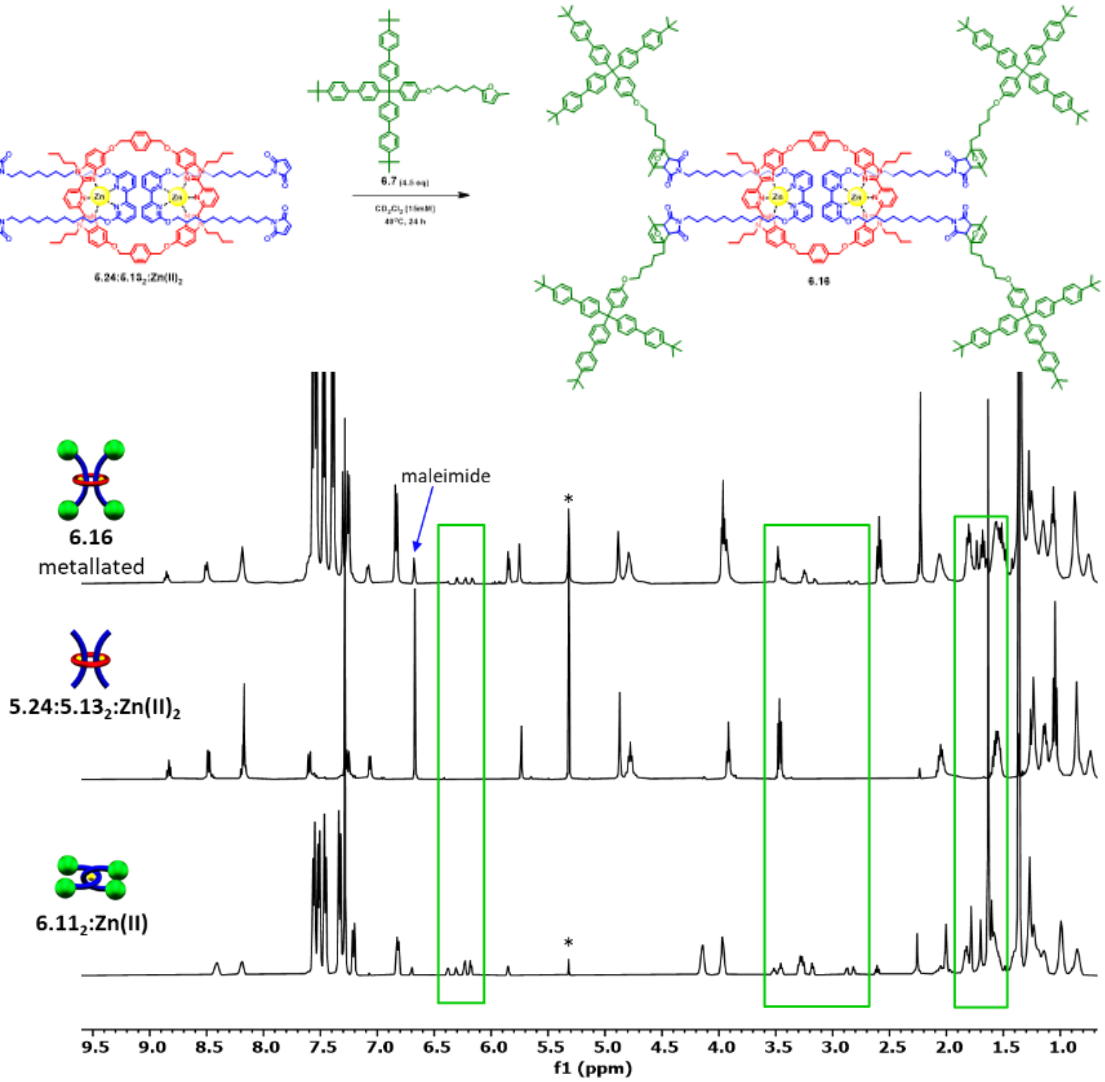

Figure 6.9. Stoppering of P3R **5.24:5.13$_2$:Zn(II)$_2$** with furan stopper **6.7** to form the metallated Diels-Alder [3]rotaxane **6.16** (top). ^{1}H-NMR overlay (500 MHz, 25°C, CD_2Cl_2) of the crude metallated Diels-Alder rotaxane **6.16** with **5.24:5.13$_2$:Zn(II)$_2$** shows a decrease in the maleimide singlet and the formation of *endo* and *exo* adducts (green boxes) upon stoppering. Diels-Alder adduct peaks in **6.16** match those on **6.11$_2$:Zn(II)**.

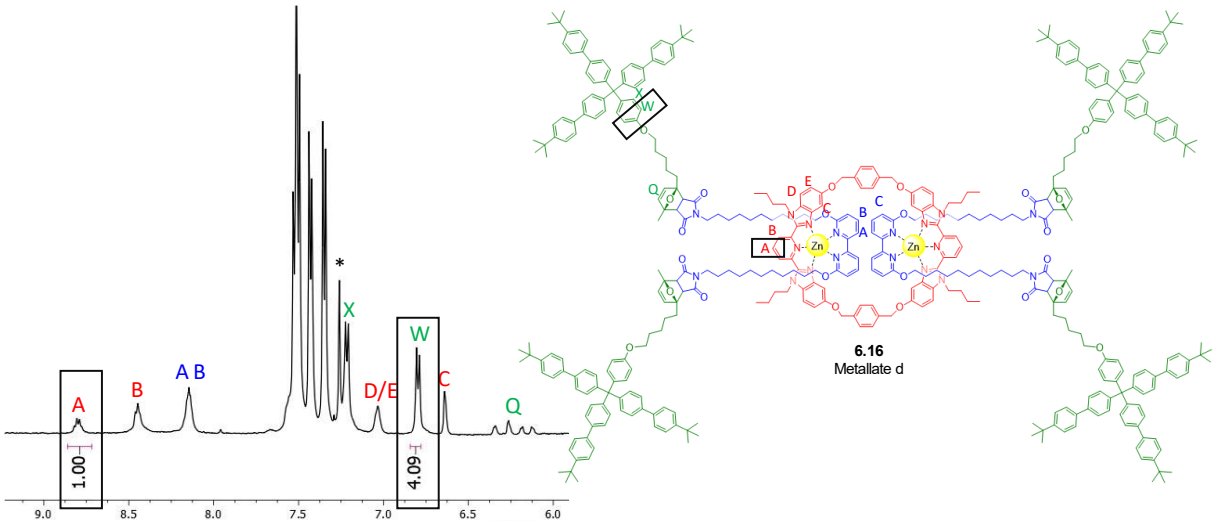

Figure 6.10. Partial ^{1}H-NMR (500 MHz, 25°C, CD_2Cl_2) of metallated **6.16** shows the absence of the maleimide singlet and the formation of *endo* and *exo* adducts (Q) upon stoppering. Integration of the Bip protons and stopper protons (1:4 A:W) suggests full stoppering of **6.16**.

Demetallation of **6.16** resulted in a mixture of macrocycle **5.24** and Diels-Alder dumbbell **6.11** (Figure 6.11, left). The NMR overlay shows no upfield shift in the aromatic protons that would be expected for the interlocked product.[9] The integration of *exo* and *endo* isomers between 6.0 and 6.5 ppm is close to 1:1 for the demetallated **6.16** product mixture. The small signal at 6.7 ppm (corresponding to maleimide) was also seen in the formation of **6.11** and is likely due to the instability/thermoreversibility of this system.

Demetallation of **6.16** resulted in a mixture of macrocycle **5.24** and Diels-Alder dumbbell **6.11** (Figure 6.11, left). The NMR overlay shows no upfield shift in the aromatic protons that would be expected for the interlocked product.[9] The integration of *exo* and *endo* isomers between 6.0 and 6.5 ppm is close to 1:1 for the demetallated **6.16** product mixture. The small signal at 6.7 ppm (corresponding to maleimide) was also seen in the formation of **6.11** and is likely due to the instability/thermoreversibility of this system.

Performing the acid-catalyzed rearrangement reaction on metallated **6.16** (see Experimental) resulted in a decrease in the *endo* and *exo* adduct peaks (Figure 6.12, outlined in

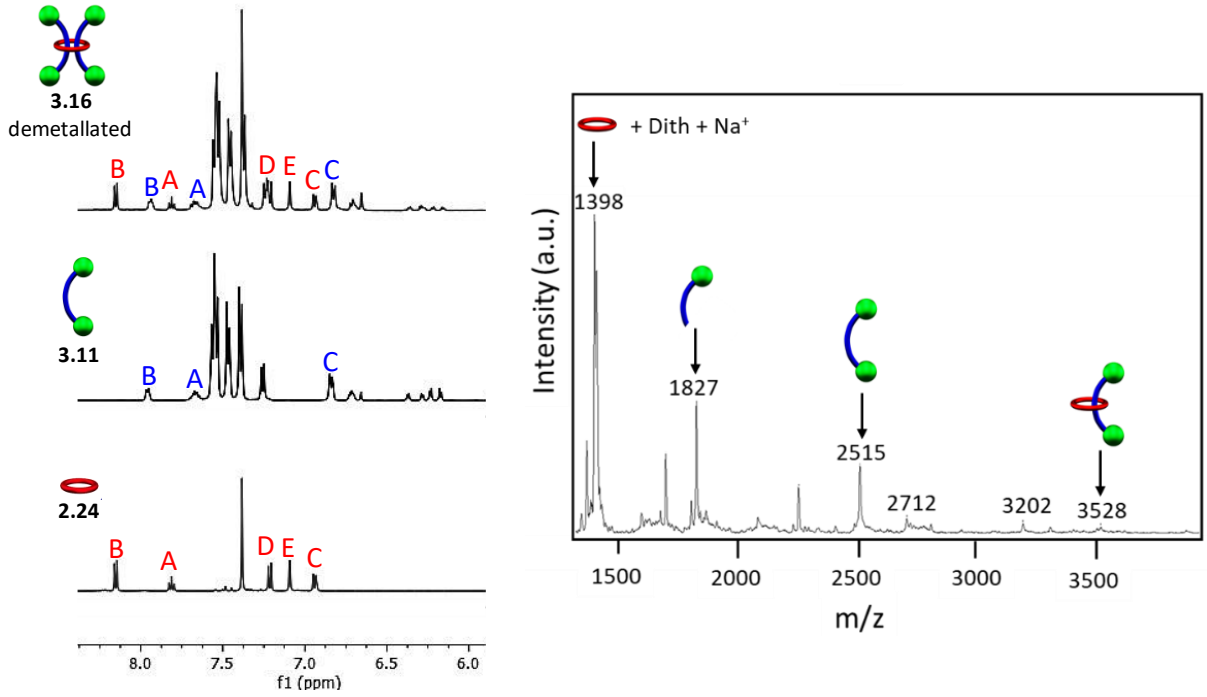

Figure 6.11. Partial ^{1}H-NMR overlay (500 MHz, 25°C, CD_2Cl_2) of demetallated **6.16** with dumbbell **6.11** and 42-atom ring **5.24** for comparison (left). MALDI-TOF MS (Dithranol, sodium trifluoroacetate) of the demetallated Diels-Alder **6.16** product mixture (right).

green) suggests the successful formation of phthalimide **6.17**; however, the metallated protons between 8.1 and 8.9 ppm corresponding to the Bip and Bip are also gone. This is likely due to the acidic conditions that can protonate the nitrogen atoms on Bip and Bipy; therefore, rotaxane **6.17** was demetallated (see Experimental) so that the component mixture could be analyzed via NMR and MALDI-TOF.

The NMR spectrum on demetallated **6.17** is inconclusive; no peaks in the aromatic region correspond to either Bip or Bipy component (Figure 6.13). If the nitrogen atoms were protonated with *p*-TsOH, as hypothesized from dumbbell experiments, the demetallation process would recover the expected aromatic peaks between 7.6 and 8.15 ppm. MALDI-TOF confirmed a mixture of components but no doubly-threaded [3]rotaxane (see Experimental). Another potential reason for the lack of product formation is the cleavage of the Bipy ligand under acid-catalyzed (*p*-TsOH)

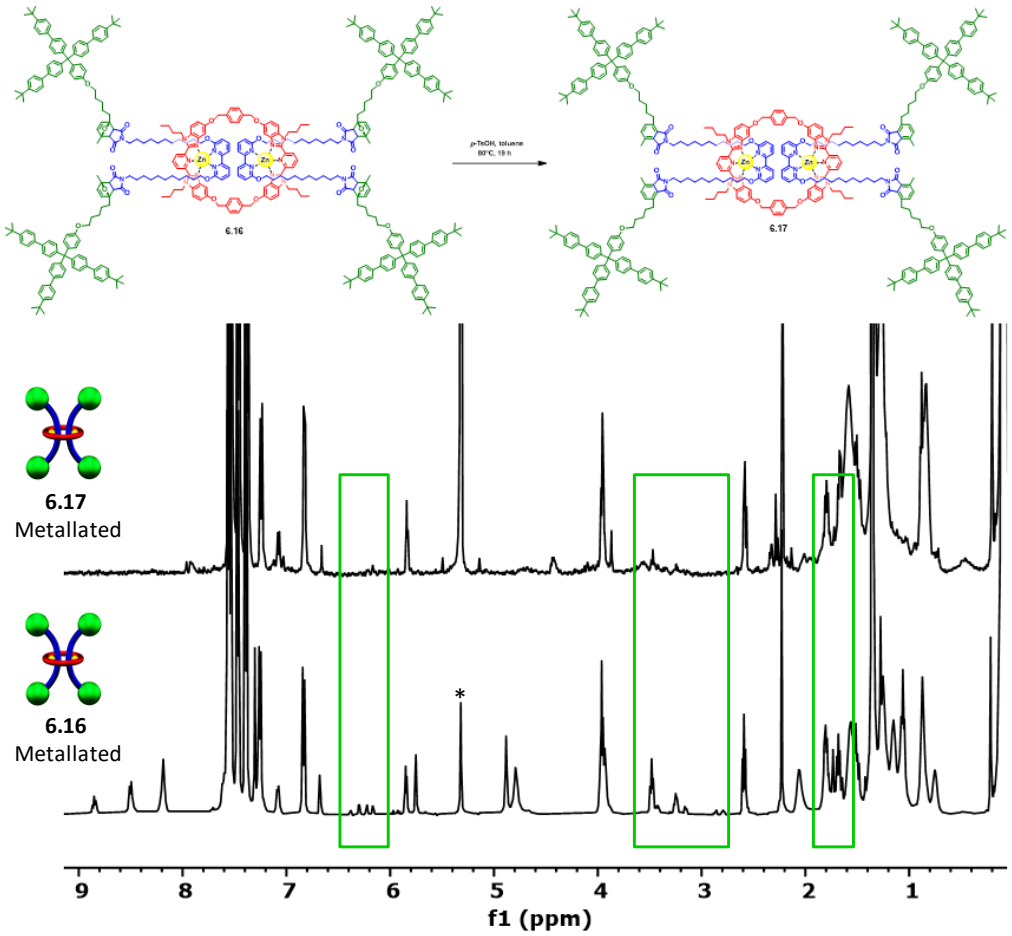

Figure 6.12. Synthesis of phthalimide **6.17** from metallated **6.16** with *p*-TsOH (top). ^{1}H-NMR overlay (500 MHz, 25°C, CD_2Cl_2) of **6.16** and acid rearrangement reaction mixture **6.17** showing a decrease in *endo* and *exo* adduct peaks (outlined in green) (bottom).

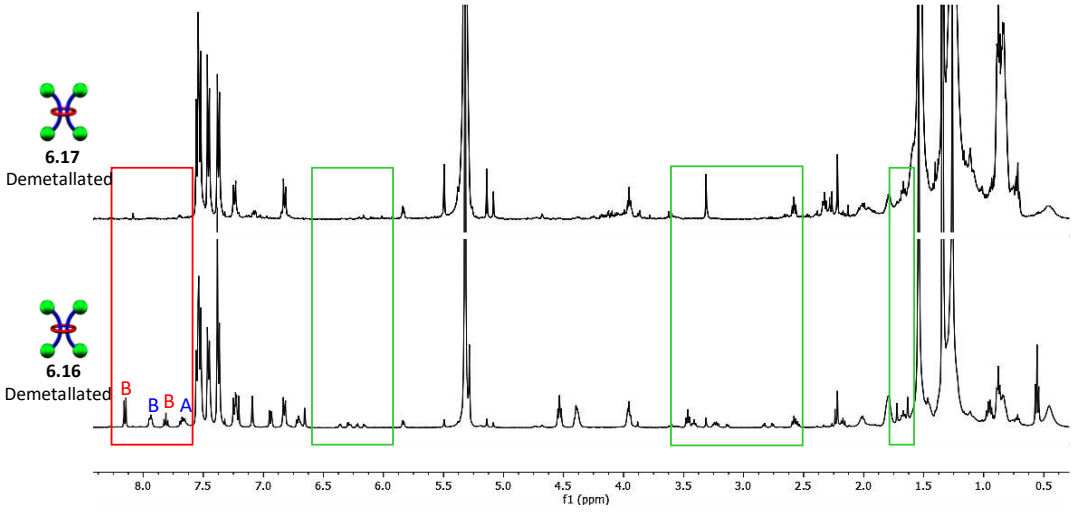

Figure 6.13. ^{1}H-NMR overlay (500 MHz, 25°C, CD_2Cl_2) of demetallated **6.17** and demetallated **6.16** for comparison, showing the disappearance of Diels-Alder adduct peaks (outlined in green) and aromatic protons on Bip and Bipy ligands (outlined in red).

conditions; these results necessitate further investigation into the effect of metal ions on the rearrangement.

6.3 Conclusions

The dynamic maleimide-furan bond would be an exciting addition to the MIP field because of its potential use as a reversible stoppering system for slide-ring materials. Implementing these dynamic bonds into other interlocked components in the group could lead to future reversible network topologies. The benefit of using maleimide-furan cycloadducts is their ability to rearrange into thermally stable phthalimide groups. Optimizing this process is critical for creating slide-ring networks that can function in various environments without falling apart.

Synthesizing a furan-functionalized stopper **6.7** permitted Diels-Alder stoppering with the maleimide thread **5.13** synthesized in Chapter 5. ^{1}H-NMR spectra confirmed the formation of **6.11** as a mixture of *endo* and *exo* dumbbell products. The acid-catalyzed dehydration of Diels-Alder adducts on **6.11** led to stable phthalimides in **6.12** and reduced *endo*/*exo* proton peaks in the NMR spectrum. Stoppering the metallated [3]rotaxane **6.16** resulted in a mixture of (metallated) isomers with similar proton signals in the NMR spectrum as the dumbbell; however, the acid-catalyzed procedure to form the stable rotaxane **6.17** was unsuccessful. Extending these acid-catalyzed conditions to the metallated dumbbell complex **6.11$_2$:Zn(II)** revealed demetallation, suggesting that Zn^{2+} ions could affect the rearrangement (see Experimental).

The challenge of this two-step stoppering method lies in the reaction kinetics for the thermoreversible Diels-Alder and the aromatization that requires an elevated temperature (Figure 6.14). Formation of the phthalimide requires the rate constant for the rearrangement to be greater than that of the retro Diels-Alder (i.e., $k_2 > k_{-1}$). Because both reactions occur at elevated

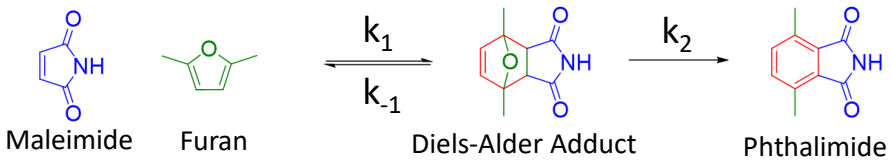

Figure 6.14. Thermoreversibility and stabilization challenge in this [3]rotaxane system.

temperatures, the rotaxane will never form if the retro Diels-Alder occurs faster than aromatization to the phthalimide (i.e., $k_{-1} > k_2$). Thus, rearranging a demetallated Diels-Alder [3]rotaxane could form a mixture of non-interlocked components; the retro Diels-Alder would remove the stoppers, and result in a mixture of thread, ring, and stopper because there are no metal ions.

Integrating the *exo* and *endo* signals of dumbbell **6.11** revealed a 1:2 ratio of *endo*:*exo* isomers (6.0 – 6.5 ppm); targeting *exo* isomers at higher temperatures could aid the dehydration process that leads to rearrangement. Kinetic NMR experiments on a solution of **6.11** at different temperatures would provide more information on the thermoreversibility of this system; repeating the same experiment on **6.11$_2$:Zn(II)** and rotaxane **6.16** would determine how Zn^{2+} affects thermoreversibility.

Future experiments would include screening different aromatization conditions (i.e., Brønsted and Lewis acid catalysts and other metal triflates)[234] and metal-ligand complexes to tune overall kinetics (i.e., $k_2 > k_{-1}$). However, the prospect of catalyst-free click conditions led to a more successful stoppering approach using Nitrile-Oxide/Alkyne Cycloaddition (NOAC, discussed in Chapters 2 and 4) to access thermally stable bonds between components in one step. Catalyst-free conditions are best for preparing polymer materials because removing the catalyst can be difficult.[10] Thus, the final chapter will discuss future directions for developing fully interlocked networks using NOAC polymerization and larger stoppers (based on **6.10**) to keep doubly-threaded rings threaded in the MIP architecture.

6.4 Experimental

6.4.1 Materials and Methods

All chemicals were purchased from Sigma-Aldrich and used without further purification unless otherwise mentioned. Zinc di[bis(trifluoromethyl sulfonyl)imide] was purchased from Strem Chemicals and stored in a nitrogen desiccator. Maleimide and 2,2'-bipyridine-6,6'-diol were purchased from TCI America. Solvents for chromatography were purchased from Fisher-Scientific. 2,6-bisbenzimidazolylpyridine ligands[11] were prepared following literature procedures. Deuterated solvents and diisopropyl azodicarboxylate were purchased from ACROS Organics. Tetrahydrofuran (THF) was dried over sodium and benzophenone. Dichloromethane was distilled over calcium hydride before use. Dimethylformamide (DMF) was dried with activated 4Å molecular sieves before use. All synthesized components were stored in a freezer at -8°C before use.

Matrix Assisted Laser Desorption/Ionization Mass Spectrometry (MALDI-TOF MS) was measured by a Bruker AutoFlex III or Bruker Ultraflextreme MALDI-TOF-TOF spectrometer in linear (or reflectance) mode using dithranol as matrix and silver or sodium trifluoroacetate as ionizer (or no ionizer).

Room Temperature Nuclear Magnetic Resonance Spectroscopy was performed using a Varian Inova 600 MHz spectrometer (at Case Western Reserve University), Bruker Ascend AVANCE III 500 MHz spectrometer, a Bruker AVANCE II+ 500 MHz spectrometer, or a Bruker DRX 400 MHz spectrometer at the University of Chicago NMR facilities. ^{1}H NMR spectra were referenced to the residual protonated solvent signal, and ^{13}C NMR spectra were referenced to the deuterated solvent carbon resonance signal.

6.4.2 Synthetic Procedures

6.4.2.1 Synthesis of protected maleimide **6.1**

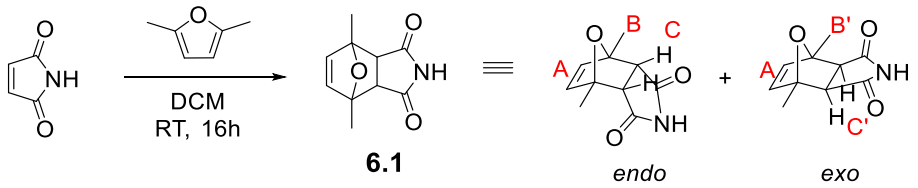

A round-bottom flask was charged with maleimide (2.0 g, 20.60 mmol) and dry DCM (200mM, 100 mL) and then flushed with argon. 2,5-Dimethylfuran (1.1 equiv., 2.18 g, 2.41 mL, 22.66 mmol) was injected into the flask, turning the colorless solution a pale yellow. After 16 hours, the DCM (and any residual, unreacted furan) was removed via rotary evaporation and dried under vacuum to reveal **6.1** as a white powder in quantitative yield. ^{1}H NMR (500 MHz, $CDCl_3$) δ 6.3 (s, 2H, A), 3.3 (s, 2H, C), 2.9 (s, 2H, C'), 1.8 (s, 6H, B), 1.7 (s, 6H, B').

6.4.2.2 Synthesis of protected-maleimide thread **6.3**

Stirring a mixture of maleimide and 2,5-dimethylfuran at room temperature gives a mixture of Diels-Alder adduct isomers that can withstand basic Williamson ether conditions[1,8] Furan-protected maleimides can react under basic conditions to form linkers that can attach to the phenolic ends of different Bip derivatives. Furan and 2,5-dimethylfuran stir at room temperature to form furan-maleimide **6.1**; alkylating (with base) creates the brominated linker **6.2** as a mixture of *endo* and *exo* isomers.

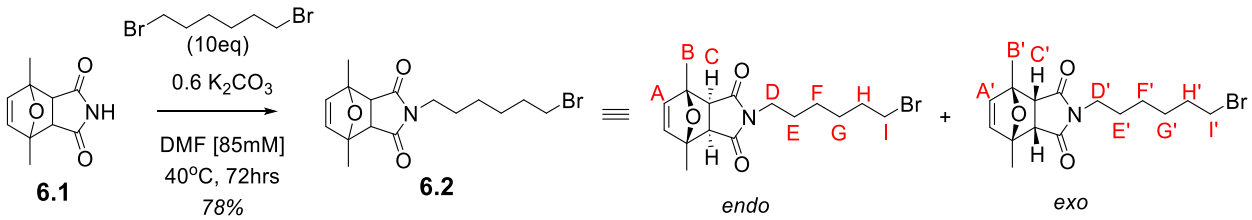

Adding a smaller amount of base (0.6 equivalents with respect to the maleimide proton) limits any chances of base-catalyzed maleimide hydrolysis. Refluxing Williamson ether syntheses

helps push reactions forward but could cause the retro Diels-Alder to occur; maleimide hydrolysis in the presence of base would prevent product formation. Therefore, the reaction was heated slightly to 40°C and left to react for a longer time to prevent the retro Diels-Alder from occurring.

A mixture of **6.1** (2.0 g) and K_2CO_3 (0.6 eq) was added to a round bottom flask with a stir bar and put under argon flow. Excess 1,6-dibromohexane (10 eq) was injected into the flask, followed by dry DMF (85 mM). The solution was placed in a heating block and warmed to 40°C. After 72 hours, the reaction was cooled to room temperature, and the solvent was removed under vacuum. The crude mixture was purified using column chromatography (hexanes:ethyl acetate gradient) to make **6.2** as a mixture of *endo* and *exo* adducts in 78% yield by mass. **6.1** only has one proton signal (7.3 ppm) for the vinyl bond because the maleimide is not functionalized. Based on integrations of the *exo/endo* methyl (B'/B) and bridgehead protons (C'/C) were used to assign the singlets at 6.15 (A) and 6.3 ppm (A'); the smaller signals correspond to the *exo* isomers of **6.2**.

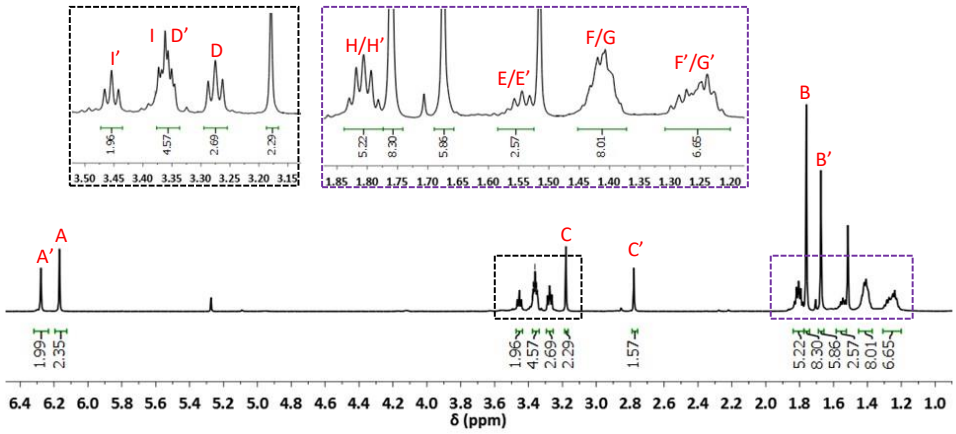

Figure 6.15. ^{1}H-NMR (600 MHz, 25°C, $CDCl_3$) of protected-maleimide linker **6.2** *endo* and *exo* (prime) isomers. Peak labeling was based on the bridgehead protons assignments for **6.1**.

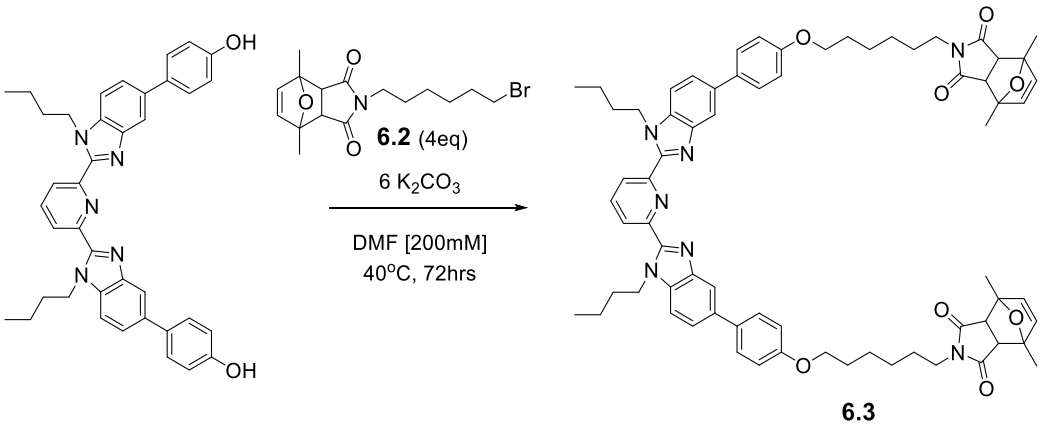

6.3

Functionalizing Bip with **6.2** yields the furan-protected thread **6.3** as a mixture of *exo* and *endo* isomers. Careful attention to reaction temperature is essential when working with furan-maleimide conjugates such as **6.2**. The stability of these adducts under basic conditions permits Williamson ether conditions; however, the elevated temperatures used to push Bip functionalization reactions forward would result in the retro Diels-Alder. Therefore, the temperature was only raised slightly to 40°C, like in the previous step, and left for a longer time (72 hours).

6.4.2.3 Synthesis of phthalimide **6.5**

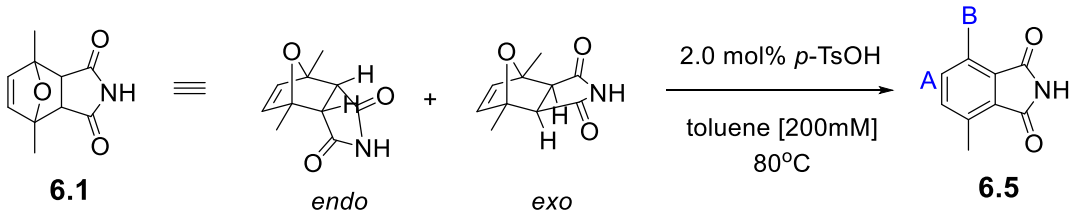

6.1 ≡ *endo* + *exo* → **6.5**

Diels-Alder adduct **6.1** was dissolved in toluene (200 mM), added to a small vial with a stir bar, and put under argon flow. A catalytic amount (2.0 mol%) of *p*-TsOH was added, and the reaction was placed in a sand bath at 80°C. The reaction was left overnight and cooled to room temperature before removing the solvent under vacuum. The crude product **6.5** was dissolved in $CDCl_3$ for NMR analysis. ^{1}H NMR (500 MHz, $CDCl_3$) δ 7.3 (s, 2H, A), 2.7 (s, 6H, B).

6.4.2.4 Synthesis of furan stopper **6.7**

Given the success of 2,5-dimethylfuran as a protecting group for maleimide thread **5.6** discussed above, furans were alkylated to make reactive linkers that could attach to the phenolic triaryl component **2.11**. Efficient alkylation of furan moieties is commonly achieved with *n*-butyllithium. Employing 1-chloro-5-iodopentane results in a chlorinated alkyl furan; the iodine is a better leaving group than chlorine, so it reacts with the *n*-butyllithium first to form a chlorinated product **6.6** that can further react with other components.

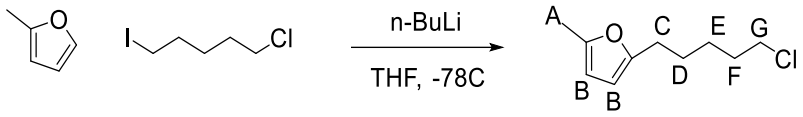

6.6

2-(5-Chloropentyl)-5-methylfuran **6.6** was synthesized via furan alkylation with *n*-butyllithium according to a literature procedure.[12] 2-Methylfuran (0.97 g, 1.07 mL, 11.81 mmol) and 40 mL of dry THF were added to a flame-dried schlenk flask under argon with a stir bar. The solution was cooled to -78°C with a dry ice/acetone bath, and 2.5 M *n*-butyllithium in hexanes (5.59 mL, 14.0 mmol) was added, slowly turning the solution orange and then pale yellow. The reaction was left to warm to -5°C over 2.5 hours, after which 1-chloro-5-iodopentane (2.50 g, 1.50 mL, 10.75 mmol) was injected. After stirring at RT for 21 hours, the orange reaction mixture was quenched with 3 mL of saturated ammonium chloride solution, which turned the solution red. The product was extracted with ethyl acetate and dried over sodium sulfate. The solvent was removed via rotovap, the resulting dry material was dissolved in chloroform, and the solid salt was removed by filtration. The filtrate was dried, and the residue purified by column chromatography (silica gel, hexanes to 10% ethyl acetate in hexanes as eluent), revealing 2-(5-chloropentyl)-5-methylfuran **6.6** as a clear, colorless oil in 86% yield by mass. ^{1}H NMR (500 MHz, $CDCl_3$) δ 5.87 – 5.81 (m, 2H, B), 3.54 (t,

J = 6.7 Hz, 2H, G), 2.58 (t, J = 7.5 Hz, 2H, C), 2.25 (d, J = 0.8 Hz, 3H, A), 1.89 – 1.75 (m, 2H, F), 1.70 – 1.59 (m, 2H, D), 1.54 – 1.40 (m, 2H, E).

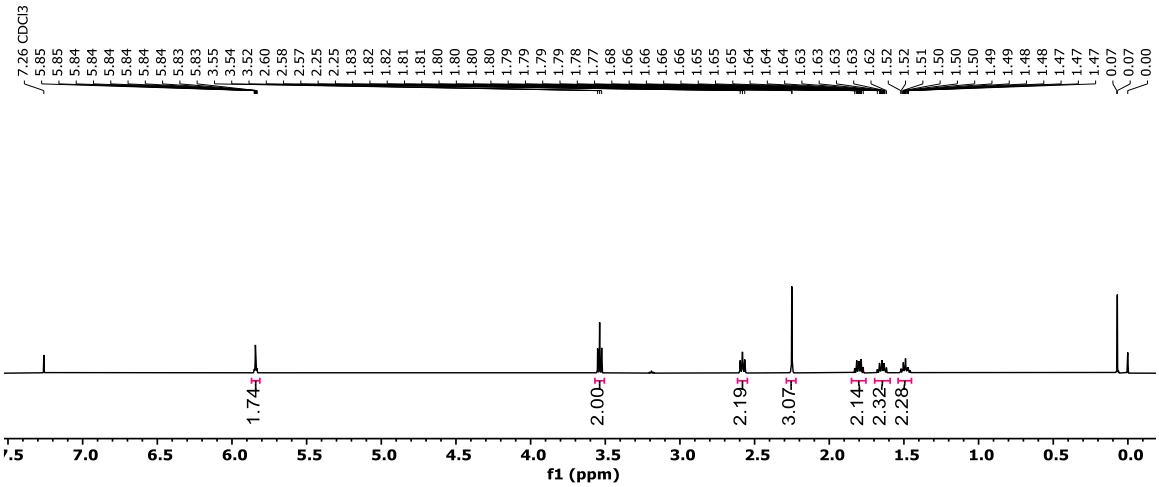

Figure 6.16. ^{1}H-NMR (500 MHz, 25°C, $CDCl_3$) of the purified 2-(5-chloropentyl)-5-methylfuran product **6.6**.

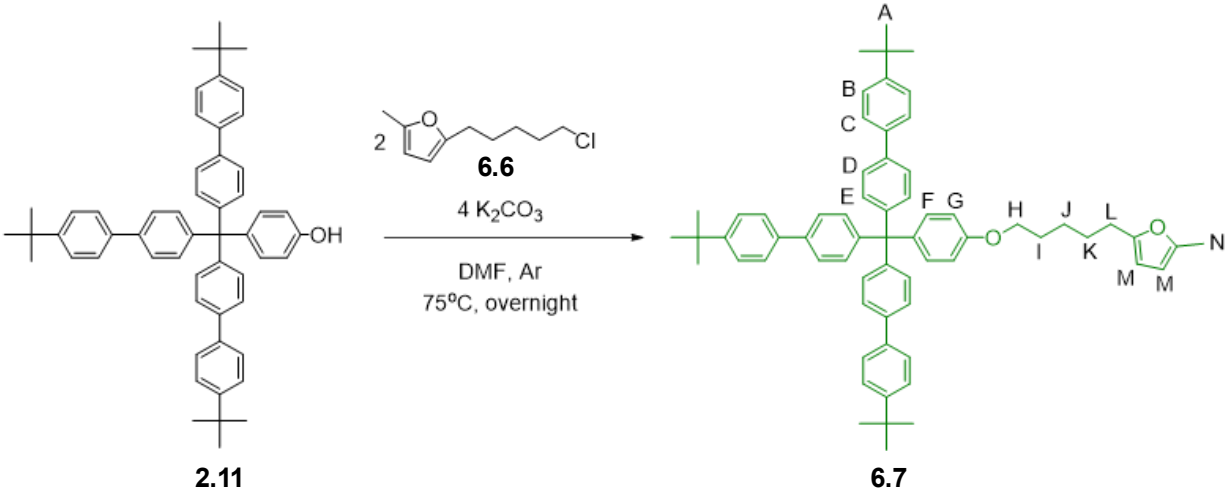

A 25 mL oven-dried round bottom flask was charged with phenol stopper **2.11** (0.50 g, 0.68 mmol), 2-(5-chloropentyl)-5-methylfuran **6.6** (0.255 g, 1.36 mmol), and K_2CO_3 (0.38 g, 2.73 mmol). The flask was put under argon flow, dry DMF (14 mL) was injected, and the reaction was heated to 75°C. The next day, the reaction was cooled to room temperature, and the solvent was removed under reduced pressure. The residue was dissolved in $CHCl_3$, and the insoluble material (salts) was removed by filtration. The filtrate was collected, and the solvent was removed under reduced

pressure. The resulting material was purified using column chromatography (silica gel, hexanes to 40% hexanes in chloroform as eluent) to reveal furan stopper **6.7** as a white powder in 48% yield by mass. ^{1}H NMR (500 MHz, $CDCl_3$) δ 7.58 – 7.53 (m, 6H, B), 7.53 – 7.48 (m, 6H, C), 7.48 – 7.42 (m, 6H, D), 7.35 – 7.30 (m, 6H, E), 7.22 – 7.16 (m, 2H, F), 6.84 – 6.79 (m, 2H, G), 5.86 – 5.81 (m, 2H, M), 3.95 (t, *J* = 6.5 Hz, 2H, H), 2.60 (t, *J* = 7.5 Hz, 2H, L), 2.24 (d, *J* = 0.9 Hz, 3H, N), 1.81 (dt, *J* = 14.2, 6.6 Hz, 2H, I), 1.69 (p, *J* = 7.6 Hz, 2H, K), 1.57 – 1.47 (m, 2H, J), 1.35 (s, 27H, A). MALDI-MS: 991.6 ([M]+Ag^+).

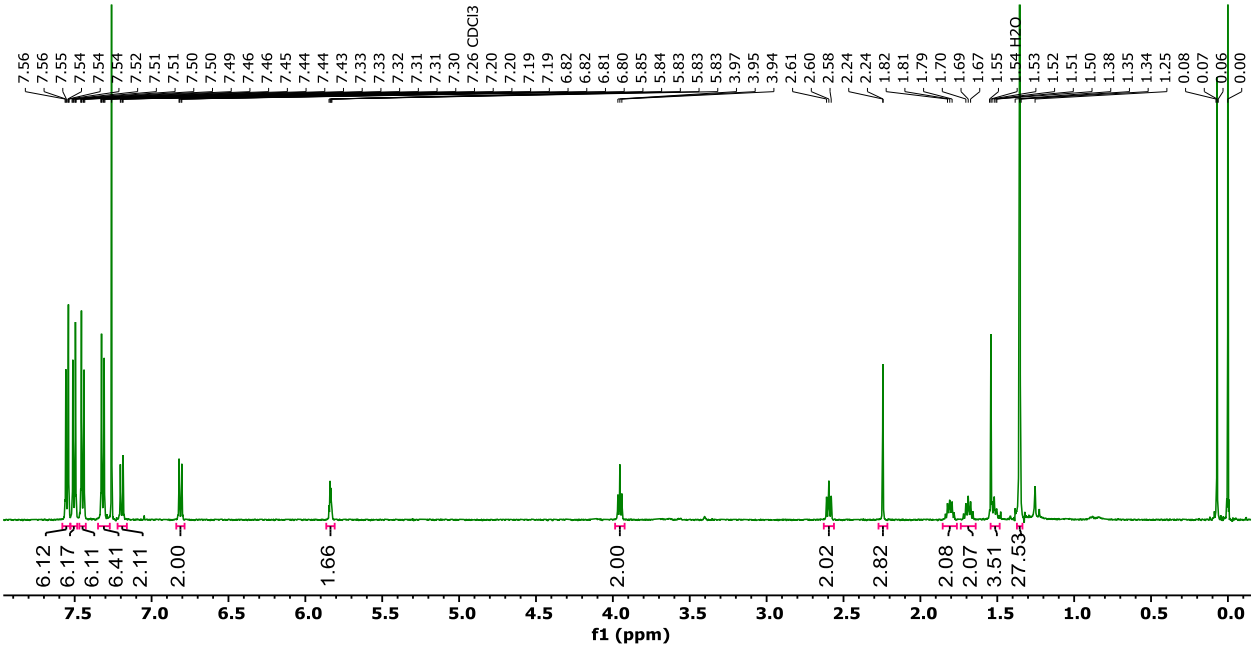

Figure 6.17. ^{1}H-NMR (500 MHz, 25°C, $CDCl_3$) of furan stopper **6.7**.

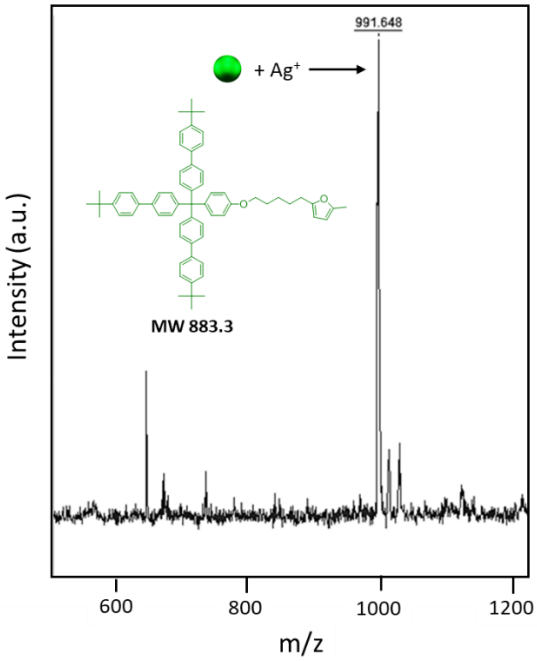

Figure 6.18. MALDI-TOF MS (Dithranol, silver trifluoroacetate) of furan stopper **6.7**.

6.4.2.5 Synthesis of furan double stopper **6.10**

Dialkylation of furan with 1-chloro-5-iodopentane afforded linker **6.8** that was used to react with two triaryl stoppers to make a double-stopper **6.9** component. Tetramethylethylenediamine (TMEDA) helps activate organolithium reagents; *n*-butyllithium forms hexamers in hexane, but the addition of TMEDA results in a solvated tetramer that affects the dilithiation of furan to achieve high yields.[13]

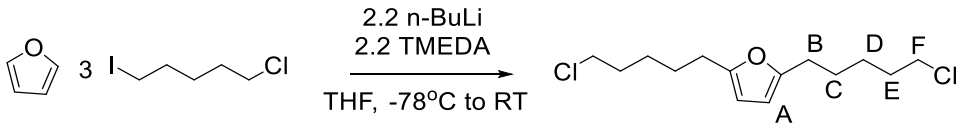

6.8

2,5-Bis(5-chloropentyl)furan was synthesized via dialkylation of furan based on a literature procedure.[14] A mixture of furan (1.0 g, 1.07 mL, 10.2 mmol) and tetramethylethylenediamine (2.61 g, 3.37 mL, 22.4 mmol) in 40 mL dry THF was added to a 100mL flame-dried schlenk flask and cooled to -78°C using a dry ice/acetone bath. 2.5 M n-butyllithium in hexanes (8.97 mL, 22.4 mmol) was added slowly, and the reaction was refluxed at 65°C for 1 hour. The resulting brown

suspension was allowed to cool to RT and was then cooled with an ice bath. 1-Chloro-5-iodopentane (7.11 g, 4.28 mL, 30.6 mmol) in 10 mL THF was added dropwise, and the reaction was left to stir at room temperature overnight, forming a yellow-orange solution. The flask was submerged in an ice bath and quenched with DI water, changing the color to red. The product was extracted with ether, dried over sodium sulfate, and filtered. The orange filtrate was collected and dried under vacuum, and then the residue was purified using column chromatography (silica gel, hexanes to 40% hexanes in chloroform as eluent) as a clear oil in 40% yield by mass. ^{1}H NMR (500 MHz, $CDCl_3$) δ 5.86 (s, 2H, A), 3.54 (t, J = 6.7 Hz, 4H, F), 2.59 (t, J = 7.5 Hz, 4H, B), 1.85 – 1.75 (m, 4H, E), 1.70 – 1.60 (m, 4H, C), 1.57 – 1.44 (m, 4H, D).

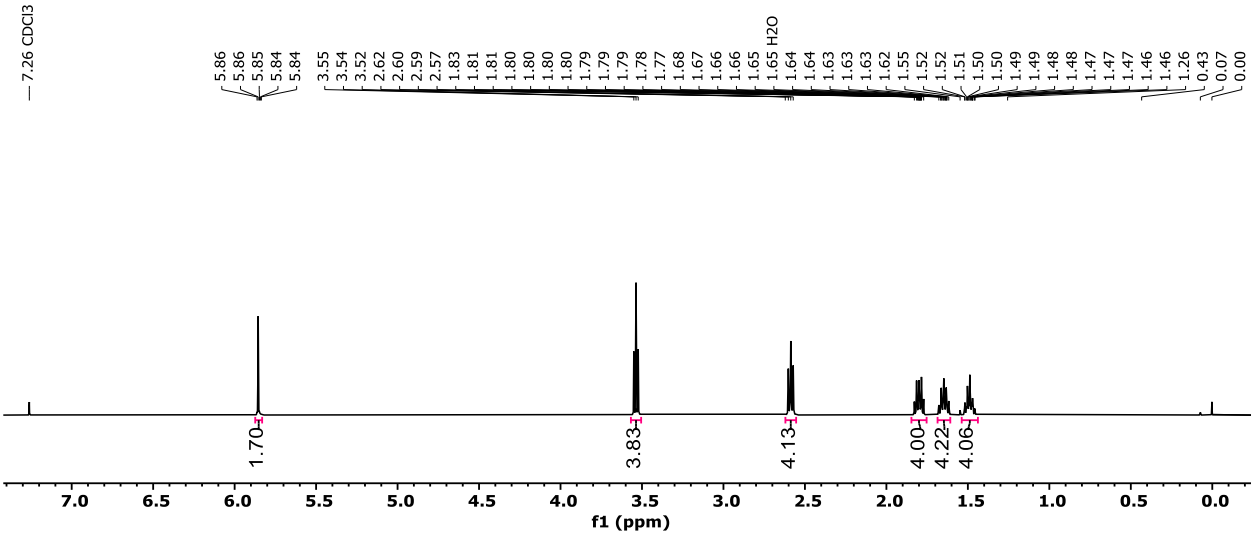

Figure 6.19. ^{1}H-NMR (500 MHz, 25°C, $CDCl_3$) of 2,5-bis(5-chloropentyl)furan **6.8**.

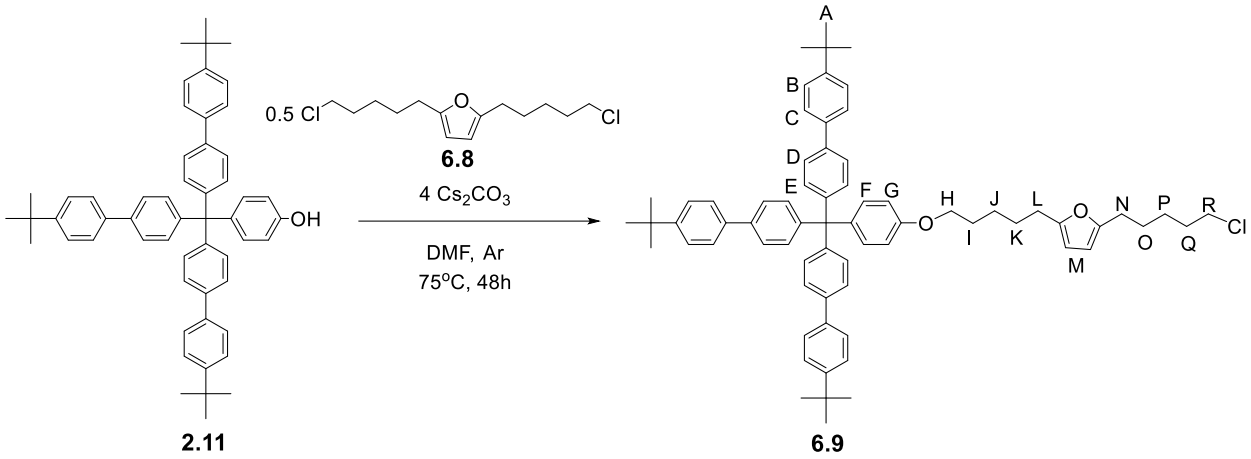

A 5 mL oven-dried conical vial was charged with phenol stopper **2.11** (0.0773 g, 0.105 mmol), 2,5-bis(5-chloropentyl)furan **6.8** (0.015 g, 0.0527 mmol), and Cs_2CO_3 (0.137 g, 0.42 mmol). The flask was put under argon flow, dry DMF (1.05 mL, 100mM) was injected, and the reaction was heated to 75°C resulting in a yellow solution. After 48 hours, the reaction was cooled to room temperature, and the solvent was removed under reduced pressure. The residue was dissolved in $CHCl_3$, and the insoluble material (salts) was removed by filtration. The filtrate was collected, and the solvent was removed under reduced pressure. The resulting material was purified using column chromatography (dry loaded on silica gel, 10% hexanes in chloroform to 100% chloroform as eluent) to reveal chlorinated furan stopper **6.9** as a white solid. ^{1}H NMR (500 MHz, $CDCl_3$) δ 7.53 – 7.48 (m, 6H, B), 7.48 – 7.43 (m, 6H, C), 7.42 – 7.37 (m, 6H, D), 7.27 (d, J = 8.4 Hz, 6H, E), 7.18 – 7.12 (m, 2H, F), 6.80 – 6.73 (m, 2H, G), 5.80 (s, 2H, M), 3.91 (t, J = 6.4 Hz, 2H, H), 3.47 (t, J = 6.7 Hz, 2H, R), 2.54 (dt, J = 9.8, 7.5 Hz, 4H, L+N), 1.80 – 1.69 (m, 4H, I+Q), 1.67 – 1.55 (m, 4H, K+O), 1.52 – 1.41 (m, 4H, J+P), 1.31 (s, 27H, A).

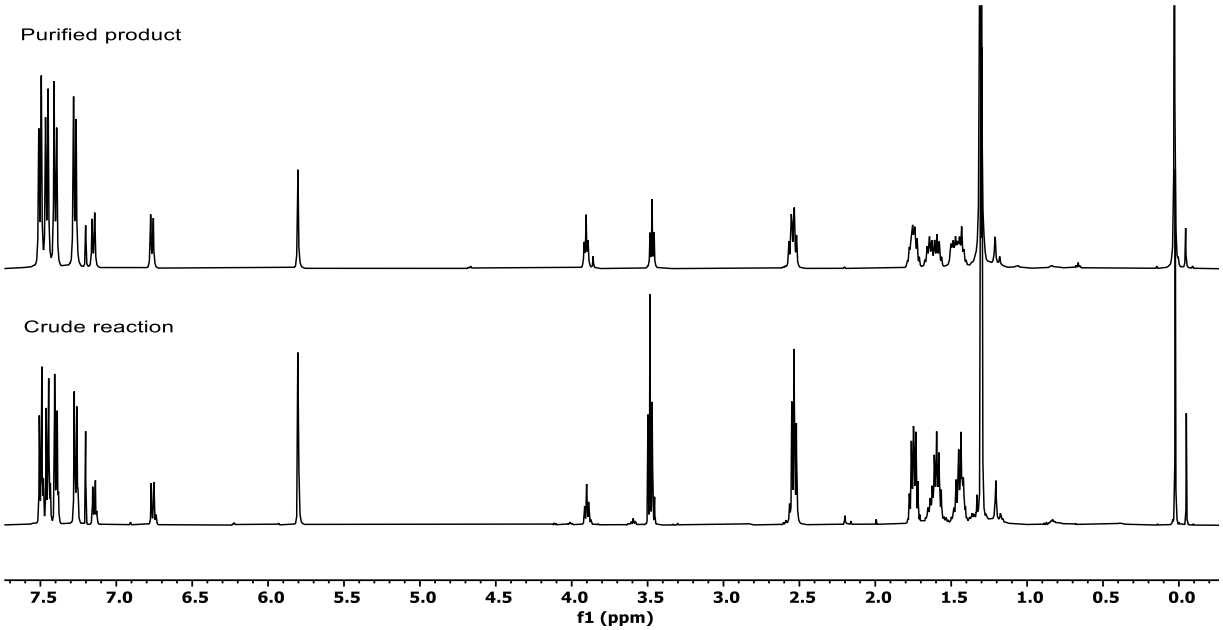

Figure 6.20. ^{1}H-NMR (500 MHz, 25°C, $CDCl_3$) of the crude reaction (bottom spectrum) and the chlorinated furan stopper **6.9** (top spectrum).

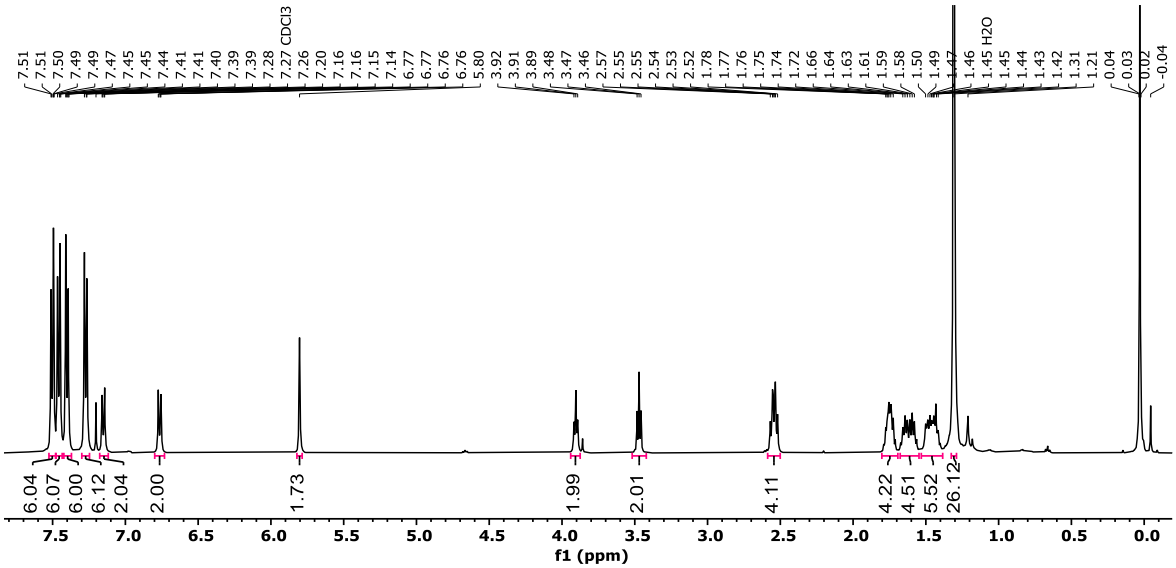

Figure 6.21. ^{1}H-NMR (500 MHz, 25°C, $CDCl_3$) of chlorinated furan stopper **6.9**.

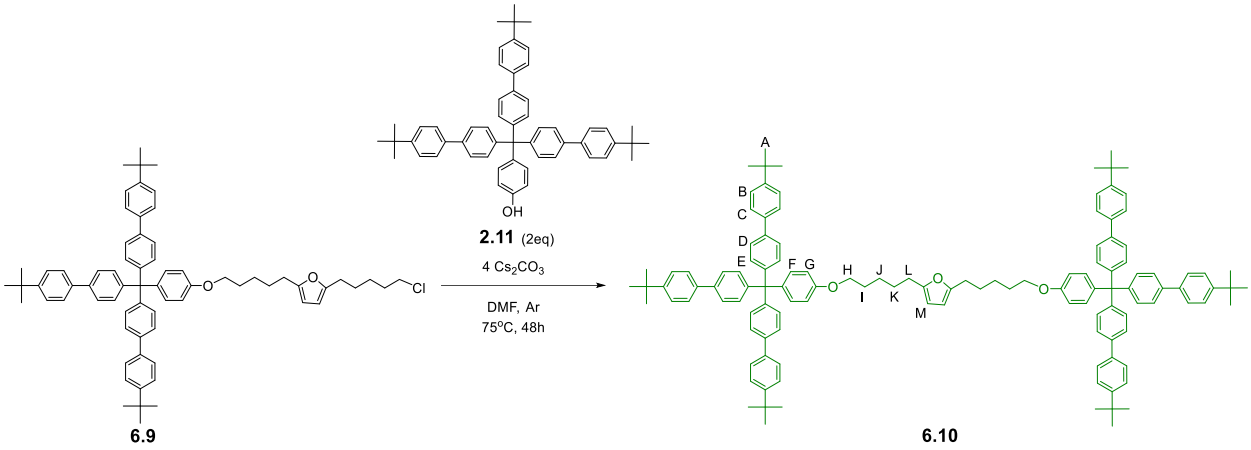

A 5 mL oven-dried conical vial was charged with chlorinated stopper **6.9** (0.080 g, 0.082 mmol), phenol stopper **2.11** (0.121 g, 0.165 mmol), and Cs_2CO_3 (0.107 g, 0.329 mmol). The flask was put under argon flow, dry DMF (0.82 mL, 100mM) was injected, and the reaction was heated to 75°C resulting in a yellow solution. After 48 hours, the reaction was cooled to room temperature, and the solvent was removed under reduced pressure. The residue was dissolved in $CHCl_3$, and the insoluble material (salts) was removed by filtration. The filtrate was collected, and the solvent was removed under reduced pressure. The resulting material was purified using column chromatography (dry loaded on silica gel, 10% hexanes in chloroform to 100% chloroform as eluent) to reveal double stopper **6.10** as a white solid. ^{1}H NMR (500 MHz, $CDCl_3$) δ 7.58 – 7.52 (m, 12H, B), 7.53 – 7.48 (m, 12H, C), 7.44 (m, 12H, D), 7.32 (m, 12H, E), 7.21 – 7.17 (m, 4H, F), 6.83 – 6.77 (m, 4H, G), 5.85 (s, 2H, M), 3.94 (t, J = 6.4 Hz, 4H, H), 2.60 (t, J = 7.6 Hz, 4H, L), 1.80 (m, 4H, I), 1.69 (p, J = 7.8 Hz, 4H, K), 1.54 – 1.49 (m, 4H, J), 1.35 (d, J = 1.8 Hz, 54H, A).

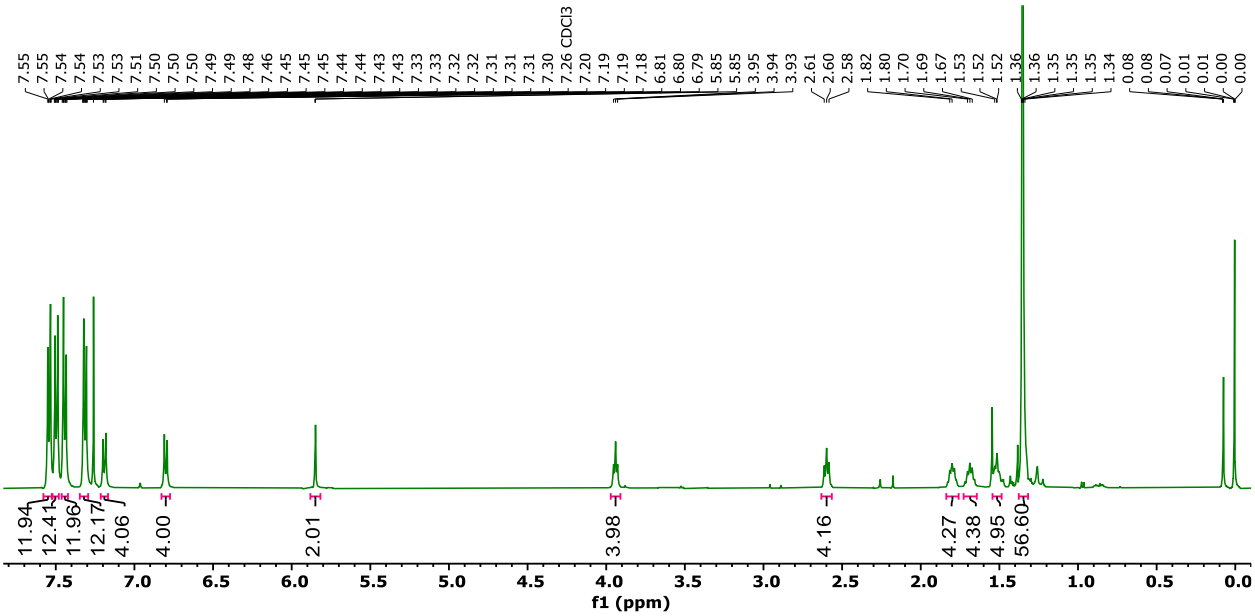

Figure 6.22. ^{1}H-NMR (500 MHz, 25°C, $CDCl_3$) of furan double-stopper **6.10**.

This synthesis serves as a proof-of-concept, showing that a larger stopper group can be made from attaching two smaller components to a reactive group that should be big enough to prevent the larger ditopic rings from dethreading in the [3]rotaxane. The double-stopper synthesis was further optimized in collaboration with Jerry Hertzog to form a series of metastable doubly-threaded [3]rotaxanes.[9]

6.4.2.6 Synthesis of Bipy Diels-Alder dumbbell **6.11**

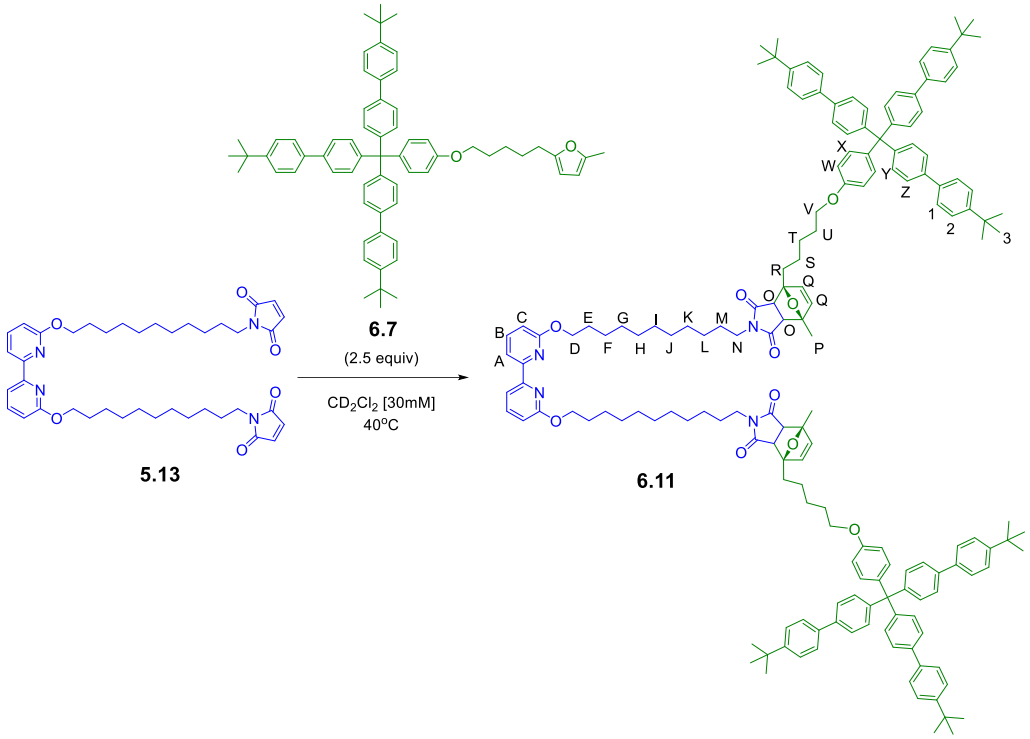

Bipy maleimide thread **5.13** (0.010 g, 0.015 mmol) and furan stopper **6.7** (0.032 g, 0.0364 mmol) were dissolved in 500 µL of CD_2Cl_2 and added to an NMR tube. The NMR tube was heated to 40°C and the spectrum was taken 48 hours later at room temperature to reveal the expected formation of dumbbell **6.11** as a mixture of *endo* (prime) and *exo* (unprime) isomers. ^{1}H NMR (500 MHz, CD_2Cl_2) δ 8.00 – 7.93 (m, 2H, A), 7.70 – 7.64 (m, 2H, B), 7.55 (ddt, *J* = 10.4, 8.5, 2.0 Hz, 24H, 2+1), 7.47 (dt, *J* = 8.5, 1.6 Hz, 12H, Z), 7.43 – 7.36 (m, 12H, Y), 7.30 – 7.24 (m, 4H, X), 6.84 (dq, *J* = 9.1, 2.0 Hz, 4H, W), 6.75 – 6.68 (m, 2H, C), 6.37 (d, *J* = 5.5 Hz, 0.5H, Q), 6.29 (d, *J* = 5.5 Hz, 0.5H, Q), 6.24 (d, *J* = 5.5 Hz, 1H, Q'), 6.18 (d, *J* = 5.6 Hz, 1H, Q'), 4.45 – 4.36 (m, 4H, D), 3.97 (tt, *J* = 6.5, 4.1 Hz, 4H, V), 3.51 – 3.46 (t, 0.5H, N), 3.44 (t, *J* = 7.2 Hz, 1H, N'), 3.30 – 3.21 (m, 3.5H, N+N'+O'+R'), 3.18 – 3.12 (m, 1H, O'), 2.84 (d, *J* = 6.4 Hz, 0.5H, O), 2.77 (d, *J* = 6.4 Hz, 0.5H, O), 2.60 (t, *J* = 7.6 Hz, 0.5H, R), 2.24 (s, 1H, P), 2.10 – 1.85 (m, 2.5H, R+R'), 1.81 (td, *J* = 8.9, 4.4 Hz, 8H, E+U), 1.74 (s, 3H, P'), 1.65 (s, 2H, P), 1.61 – 1.55 (m, 8H, F+S), 1.52 –

1.45 (m, 4H, M), 1.43 – 1.38 (m, 8H, G+T), 1.36 (s, 54H, 3), 1.29 (d, *J* = 8.2 Hz, 20H, H-L).

MALDI-TOF MS: 2561.8 ([M]+Ag^+), 2367.1 ([M]+Ag^+-(4-tert-butylbiphenyl)).

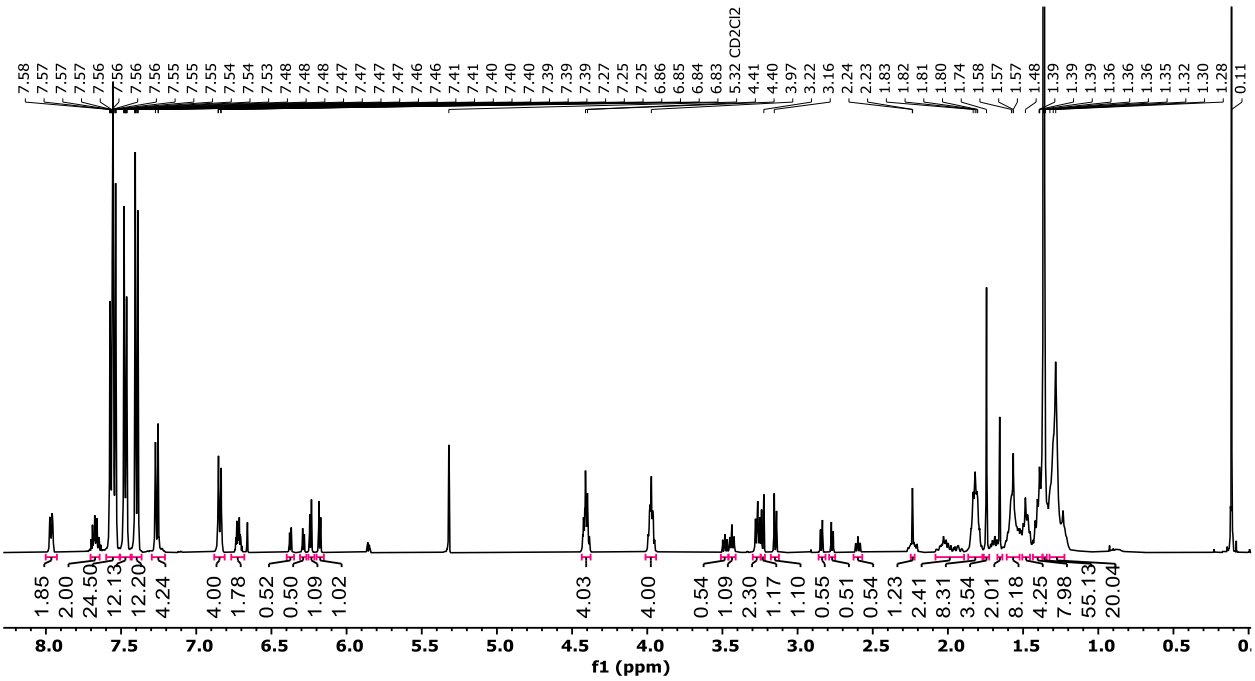

Figure 6.23. ^{1}H-NMR (500 MHz, 25°C, CD_2Cl_2) of Bipy Diels-Alder dumbbell **6.11**.

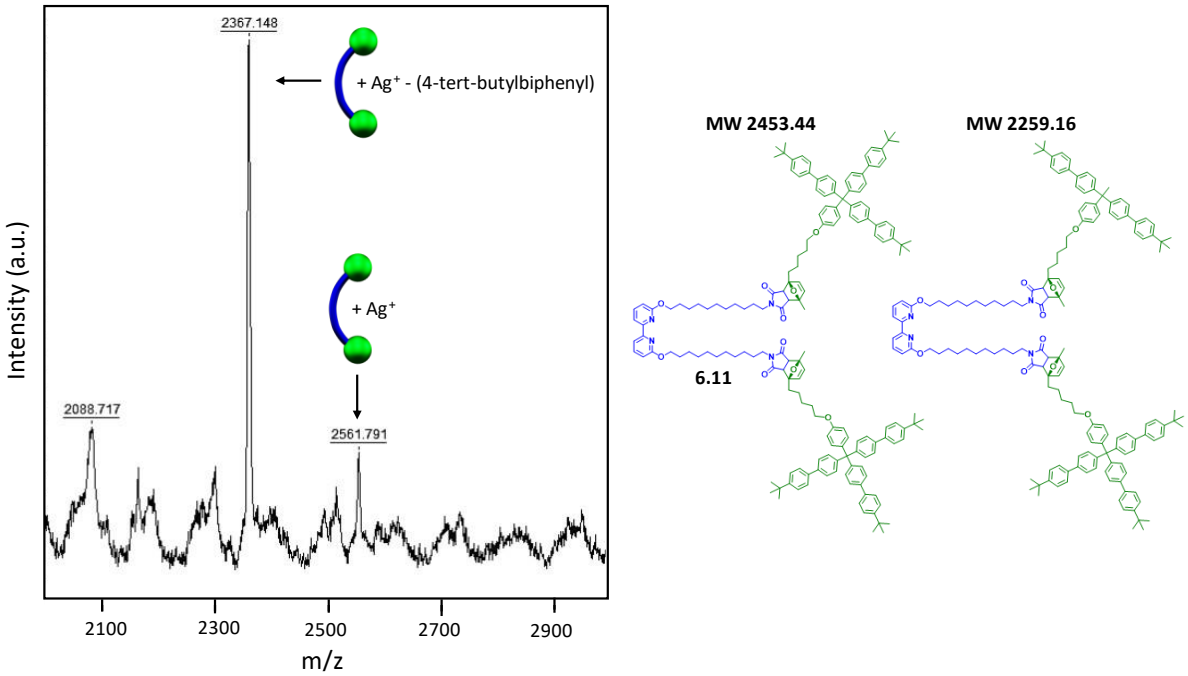

Figure 6.24. MALDI-TOF MS (Dithranol, silver trifluoroacetate) of **6.11** indicating fragmentation of one of the biphenyl groups on the stopper. The chemical structure of this fragmented stopper is on the far right.

6.4.2.7 Synthesis of Bipy phthalimide dumbbell **6.12** with *p*-TsOH

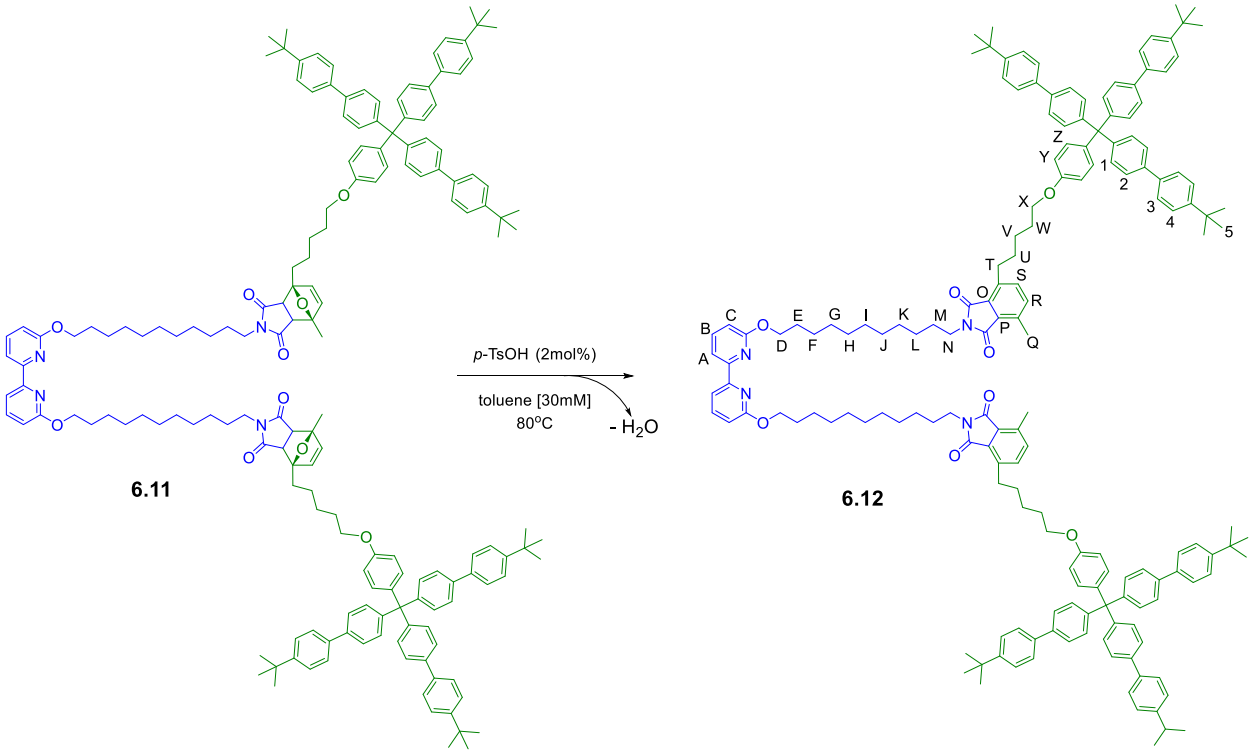

Diels-Alder **6.11** was dissolved in 500 µL of toluene and added to a 4mL vial under argon flow. A catalytic amount (2.0 mol%) of *p*-TsOH was added and the reaction was heated to 80°C. The next day, the solvent was removed under vacuum and the crude product was analyzed via NMR and MALDI-TOF. ^{1}H NMR (500 MHz, $CDCl_3$) δ 7.61 – 7.51 (m, 25H), 7.51 – 7.44 (m, 13H), 7.38 – 7.32 (m, 13H), 7.25 – 7.19 (m, 4H), 6.87 – 6.81 (m, 4H), 5.87 (t, J = 3.1 Hz, 3H), 3.98 (t, J = 6.4 Hz, 4H), 2.68 – 2.59 (m, 4H), 2.27 (s, 5H), 1.84 (dt, J = 15.1, 7.1 Hz, 6H), 1.72 (p, J = 7.7 Hz, 6H), 1.58 – 1.50 (m, 12H), 1.38 (s, 56H), 1.28 (s, 16H), 0.90 (dd, J = 16.4, 9.7 Hz, 6H), 0.10 (s, 37H).

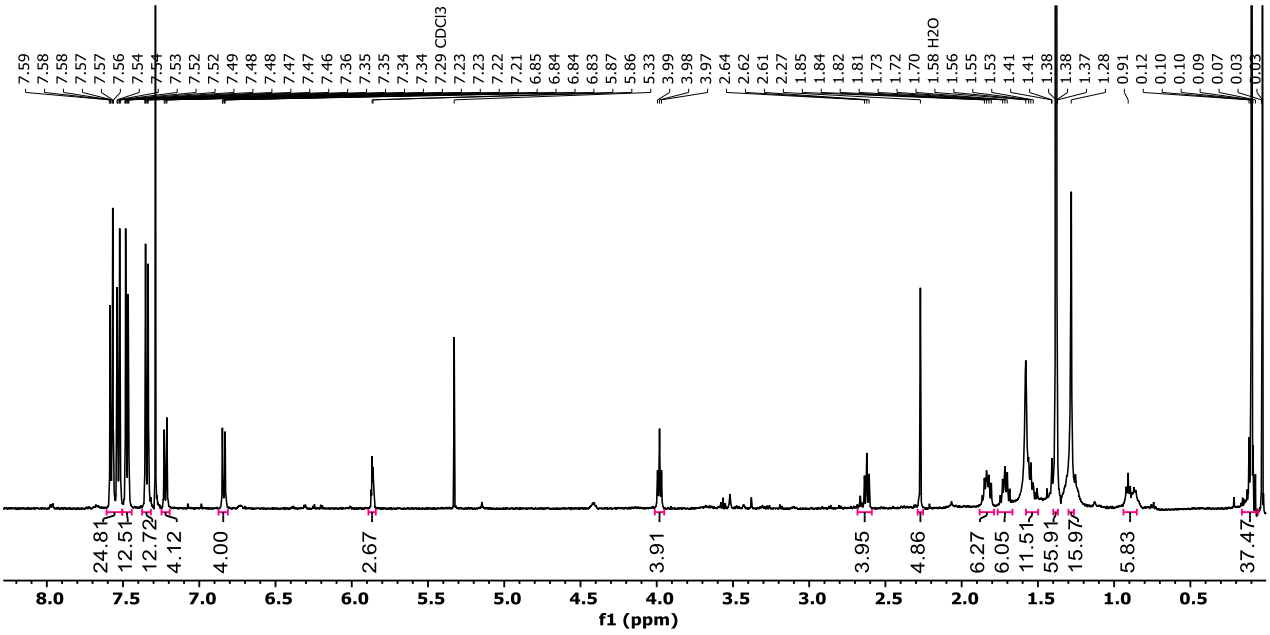

Figure 6.25. ^{1}H-NMR (500 MHz, 25°C, $CDCl_3$) of Bipy phthalimide dumbbell **6.12**.

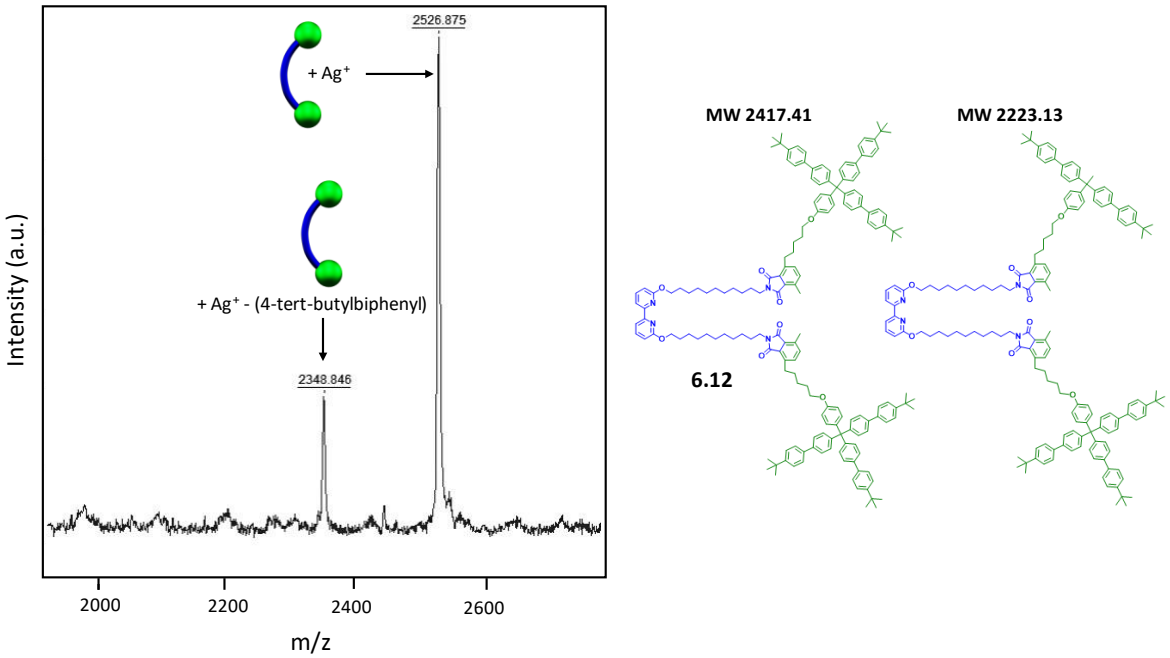

Figure 6.26. MALDI-TOF MS (Dithranol, silver trifluoroacetate) of Bipy phthalimide dumbbell **6.12**.

6.4.2.8 Synthesis of Bipy phthalimide dumbbell **6.12** with $Sc(OTf)_3$

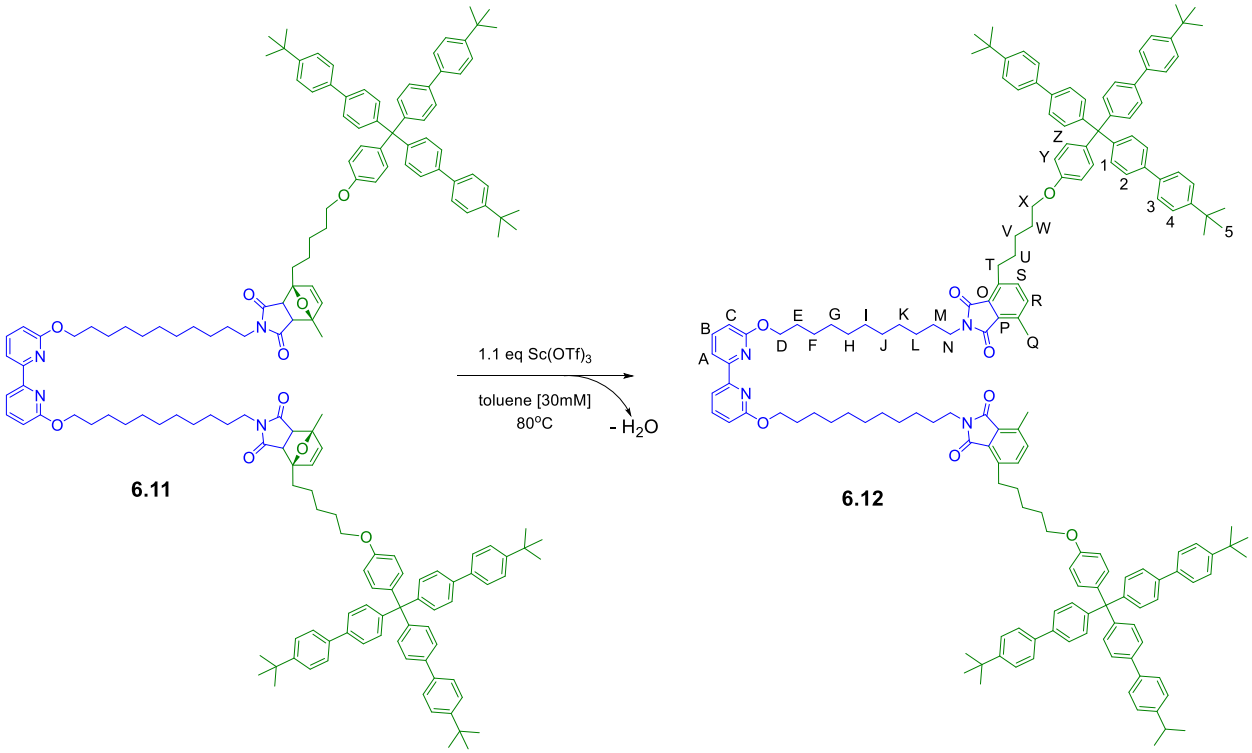

6.11 (0.0067 g, 0.0027 mmol) and $Sc(OTf)_3$ (0.00148 g, 0.0030 mmol) were added to a 4 mL vial equipped with a condenser and put under argon flow. Toluene (90 µL) was injected, and the reaction was heated to 80°C and stirred overnight. The solvent was removed under vacuum and the remaining solid was dissolved in CD_2Cl_2 for NMR analysis.

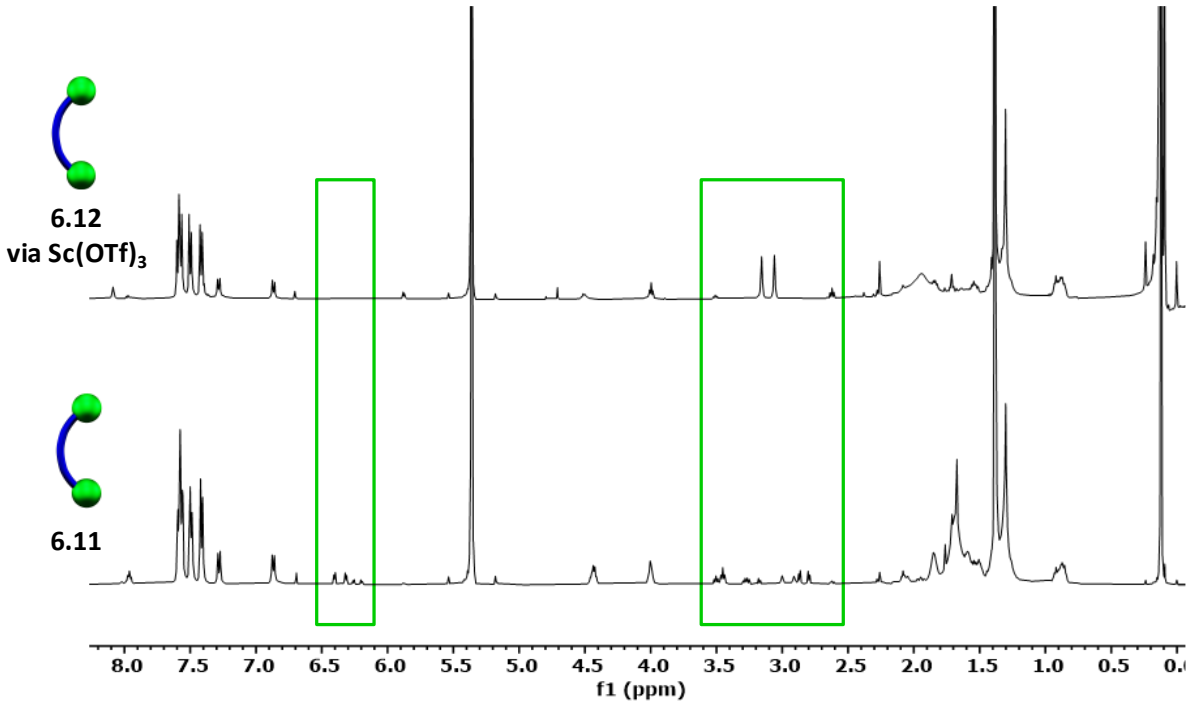

Figure 6.27. ^{1}H-NMR (500 MHz, 25°C, CD_2Cl_2) of **6.11** before (bottom) and **6.12** after treating with scandium triflate (top).

6.4.2.9 Synthesis of **6.11$_2$:Zn(II)**

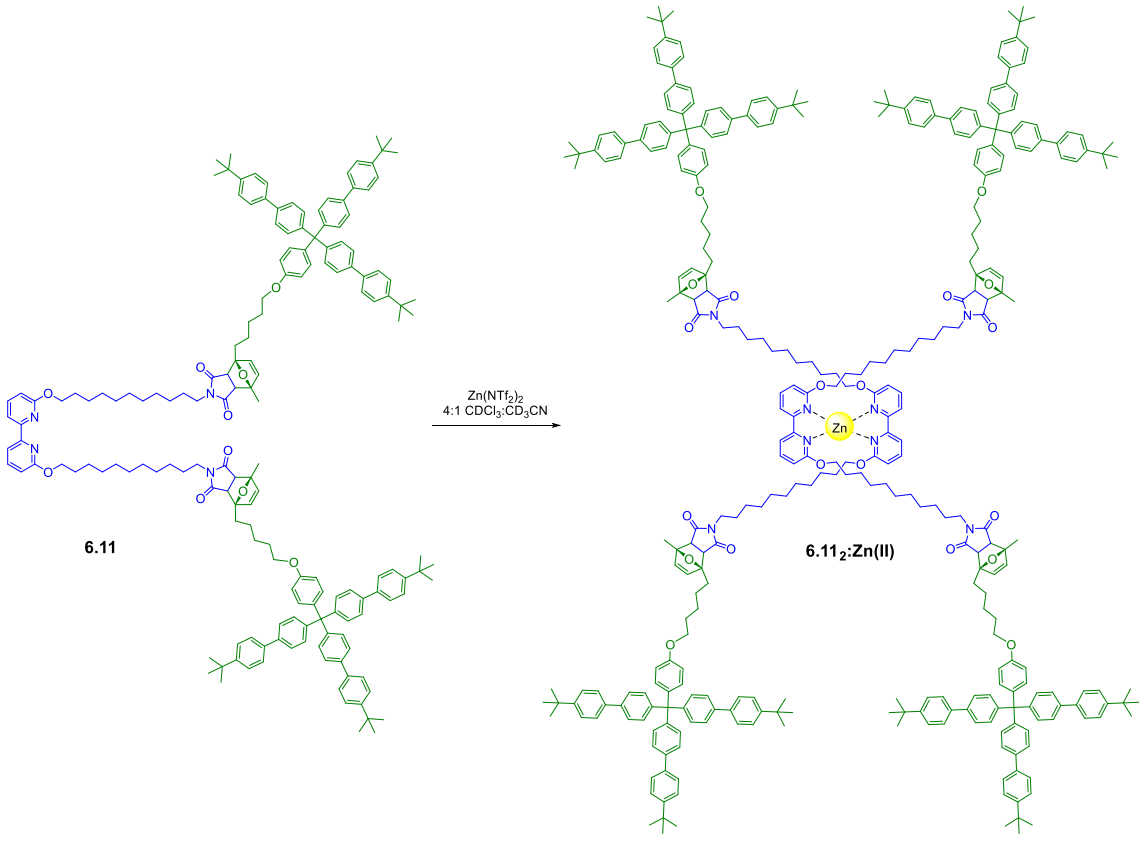

Diels-Alder dumbbell **6.11** (2.0 mg, 0.00082 mmol) was dissolved in 400 µL $CDCl_3$**.** A stock solution of $Zn(NTf_2)_2$ (30mM in 2:1 $CDCl_3$:CD_3CN) was added until no free Bipy peaks appeared at ~0.5 equiv. of the metal ion. The complete disappearance of the free Bipy aromatic protons at 7.97 and 7.66 ppm (and the corresponding growth of the peaks at 8.41 and 8.19 ppm) indicates that all Bipy ligands are bound with zinc in a 2:1 Bipy:metal ratio. The resulting **6.11$_2$:Zn(II)** complex was dried under vacuum to obtain a yellow powder that was used without further purification.

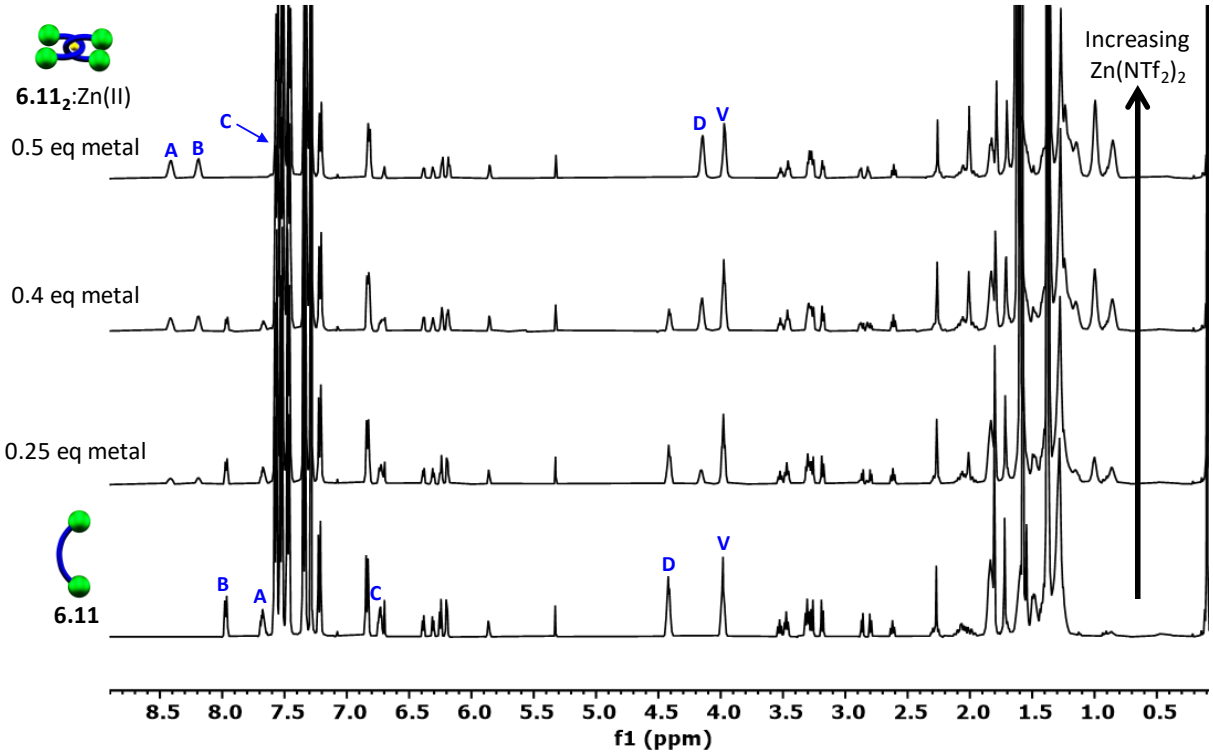

Figure 6.28. ^{1}H-NMR overlay (500 MHz, 25°C, Solvent: 0, 7.5, 12, 15% d_3-MeCN in $CDCl_3$ increasing upwards) of metal addition to form **6.11$_2$:Zn(II)**.

6.4.2.10 Synthesis of **6.12$_2$:Zn(II)**

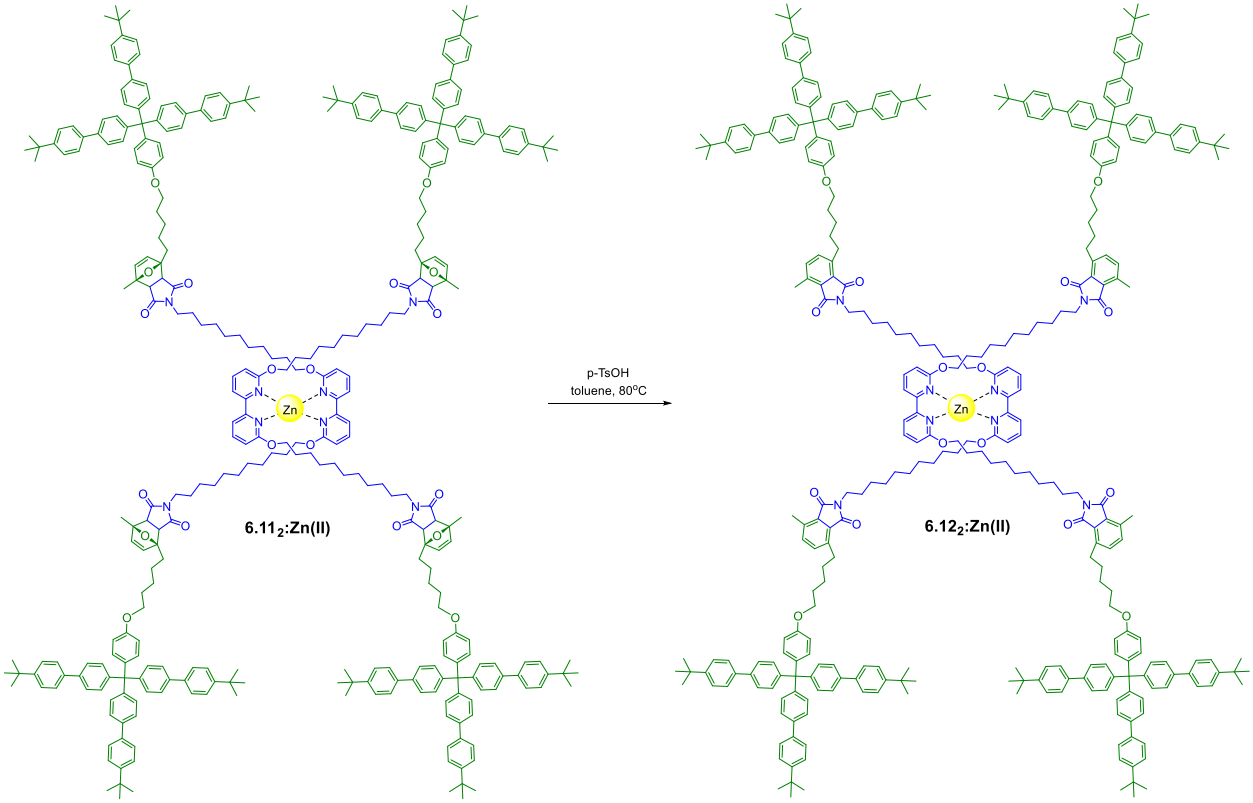

The metallated dumbbell **6.11$_2$:Zn(II)** was used to evaluate the dehydration mechanism in the presence of metal ions. **6.11$_2$:Zn(II)** was added to a conical vial with a stir bar and a catalytic amount of *p*-TsOH. The vial was put under argon flow and toluene (100 µL) was injected. The vial was heated in a silicone oil bath at 80°C overnight, after which the solvent was removed under vacuum and the crude **6.12$_2$:Zn(II)** sample was dissolved in $CDCl_3$ for NMR analysis.

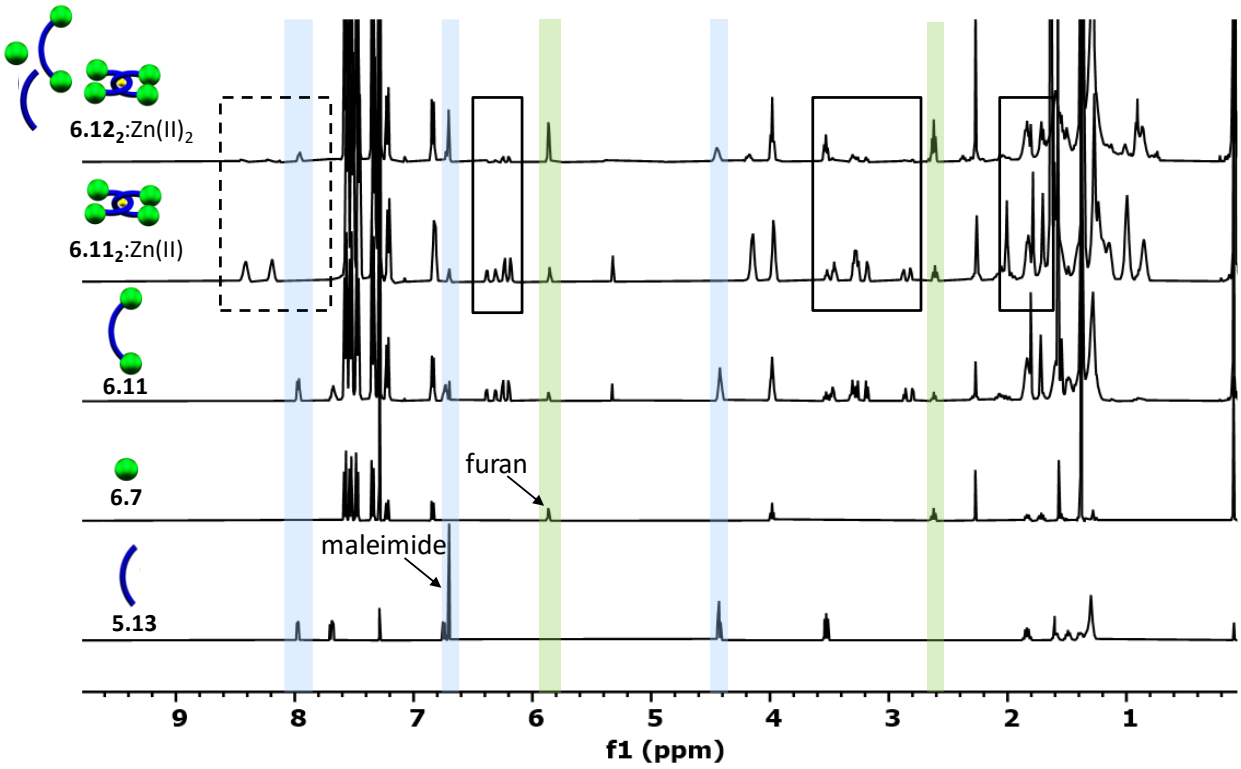

Figure 6.29. ^{1}H-NMR overlay (500 MHz, 25°C, $CDCl_3$) of rearrangement reaction results. The top spectrum corresponds to the crude rearrangement product **6.12$_2$:Zn(II)** from **6.11$_2$:Zn(II)** showing a decrease in dumbbell conjugation peaks (solid black boxes) and an increase in free Bipy thread **5.13** (dashed black box).

The stacked spectra in Figure 6.36 suggest the retro Diels-Alder occurs at the elevated temperature required for the dehydration reaction, allowing the complex to dethread before the adducts in **6.11$_2$:Zn(II)** can rearrange to form the stable product. While there is a reduction in signals corresponding to the Diels-Alder adduct (solid black boxes), the increase in unmetallated aromatic Bipy peaks (dashed black box) suggests dethreading under these conditions. The presence of the maleimide singlet at 6.7 ppm (**5.13** peaks highlighted in blue) and furan at 5.8 ppm (**6.7** peaks highlighted in green) is further evidence of the retro Diels-Alder occurring.

6.4.2.11 Bip and Bipy Titrations with Zn(II)

Zinc bistriflimide ($Zn(NTf_2)_2$) and zinc triflate ($Zn(OTf)_2$) were used to assemble doubly-threaded pseudo[3]rotaxanes in Chapter 5: **5.23:5.2$_2$:Zn(II)$_2$**, **5.24:5.11$_2$:Zn(II)$_2$**, and

5.24:5.13$_2$:Zn(II)$_2$. The bistriflimide counterion is non-coordinating, making it a common choice for chelating two tridentate Bip ligands. Preliminary titration experiments on the 42-atom macrocycle **5.24** suggest the ring cavity is too small to hold two Bip threads, necessitating the synthesis of a smaller Bipy thread **5.13** to form the pseudo[3]rotaxanes developed in Chapter 5. Switching to the smaller, Bipy ligands for threading the tighter, 42-atom ring **5.24** results in a pentacoordinate system; it was hypothesized that a triflate counterion could come in and stabilize the open coordination site on the Bipy:Bip complex.

To better understand these metal-ligand systems, a series of titrations (A-D; Figure 6.30) was performed to monitor complex formation under different conditions and assign all ^{1}H signals for reference. Each ligand was metallated to form 2:1 ligand: metal complexes **6.13** and **6.14** (Figures 6.30a and 6.30b). In another experiment, metal was added to a 1:1 mixture of ligands, forming **6.13** before the mixed complex **6.15** assembles (Figure 6.30c). Bip was then added to a

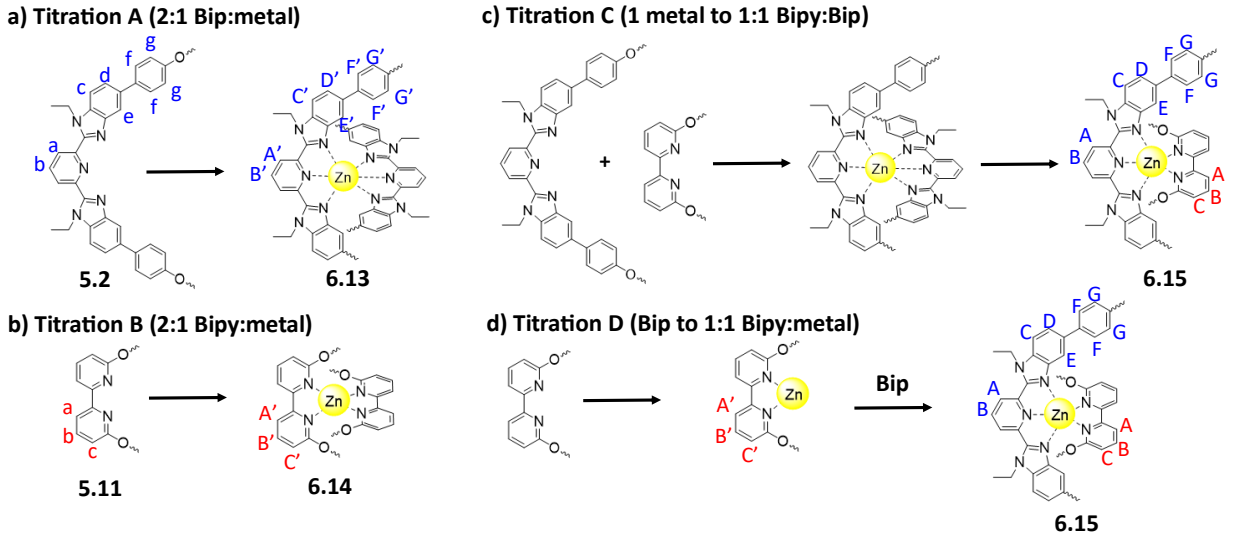

Figure 6.30. Titrating Bip (**5.2**) and Bipy (**5.11**) ligands with Zn(NTf$_2$)$_2$ and Zn(OTf)$_2$. a) Titration A of Bip ligand **5.2** with metal results in 2:1 Bip:metal **6.13**. b) Titration B of Bipy **5.11** with metal results in **6.14**. c) Titration C of a 1:1 mixture of Bip:Bipy with metal results in Bip complexing first, and then **6.15** forms. d) Titration D of a 1:1 mixture of Bipy:metal with Bip **5.2** forms **6.15**.

1:1 mixture of Bipy:metal (Figure 6.30d) to determine how the order of component addition affects the formation of **6.15**.

A general procedure for Titrations A and B is as follows: 0.005 g of Bip **5.2** and 0.005 g of Bipy **5.11** were weighed out into separate vials, and each dissolved in 400 µL $CDCl_3$ before adding to an NMR tube. A half equivalent of $Zn(NTf_2)_2$ (or $Zn(OTf)_2$) was weighed out and dissolved in 200 µL of 15% d_3-MeCN in $CDCl_3$. The zinc solution was added in 50 µL increments until **6.13** or **6.14** formed as a single metallated species in solution.

Titrations C and D both target the mixed ligand complex **6.15** but with different orders of component addition to provide more information on how this mixed complex forms in solution. For Titration C, Bip **5.2** (0.0059 g) was dissolved in 400 µL $CDCl_3$ and added to an NMR tube. One equivalent of Bipy **5.11** (0.0083 g) was added to a vial and dissolved in 100 µL $CDCl_3$. The Bipy solution was slowly added until an exact 1:1 stoichiometric ratio of **5.2:5.11** formed. Then, one equivalent of $Zn(NTf_2)_2$ (or $Zn(OTf)_2$) was weighed out and dissolved in 200 µL of 15% d_3-MeCN in $CDCl_3$. The zinc solution was added in 50 µL increments, monitoring the formation of **6.15**. For Titration D, Bipy **5.11** was dissolved in 400 µL $CDCl_3$ and added to an NMR tube. The $Zn(NTf_2)_2$ (or $Zn(OTf)_2$) solution was added slowly until an exact 1:1 ratio of Bipy:metal formed. Bip **5.2** was dissolved in 200 µL $CDCl_3$ and slowly added to the NMR tube, monitoring the formation of **6.15**.

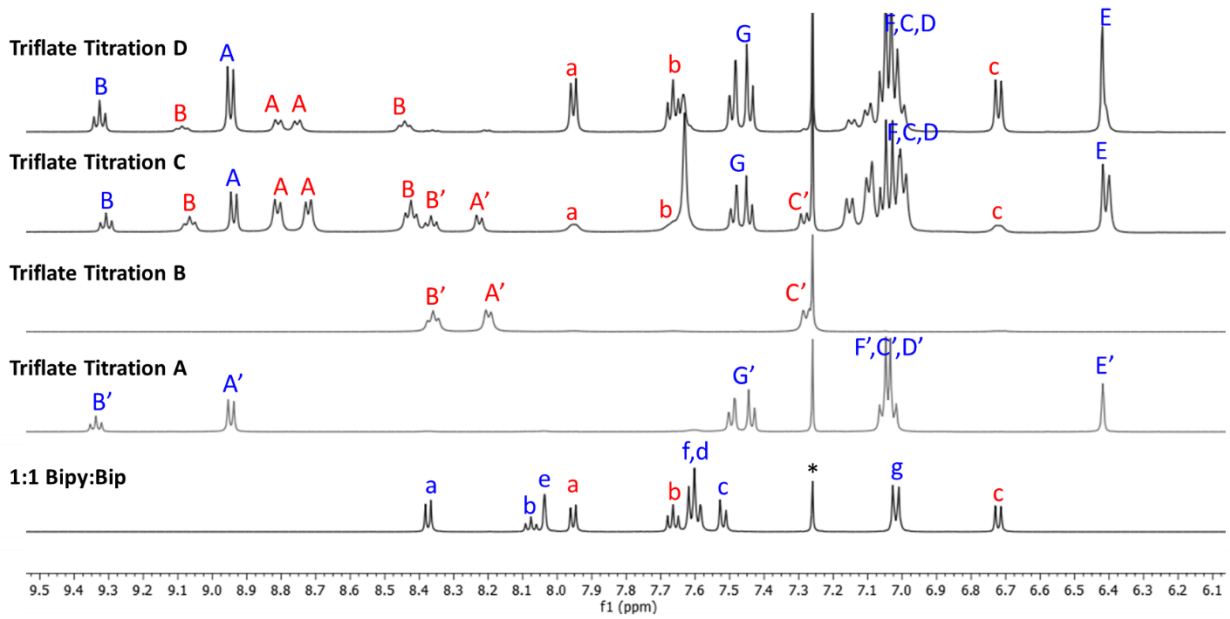

Figure 6.31. ^{1}H-NMR (500 MHz, 25°C, 15% d_3-MeCN in $CDCl_3$) titrations with $Zn(OTf)_2$.

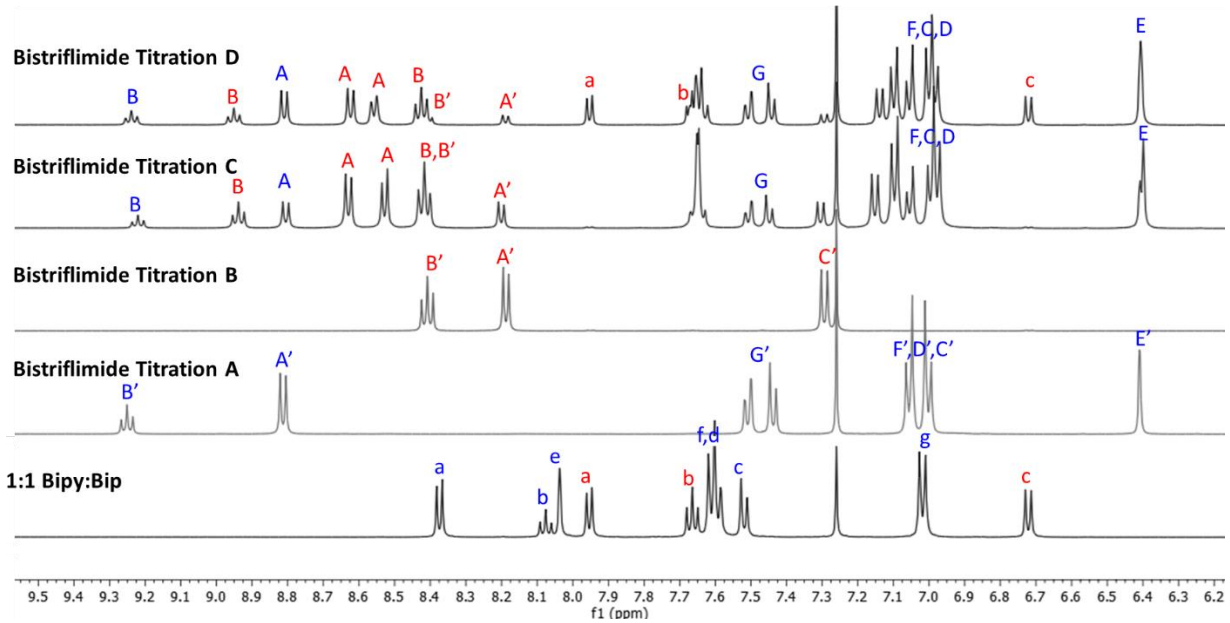

Figure 6.32. ^{1}H-NMR (500 MHz, 25°C, 15% d_3-MeCN in $CDCl_3$) titrations with $Zn(NTf_2)_2$.

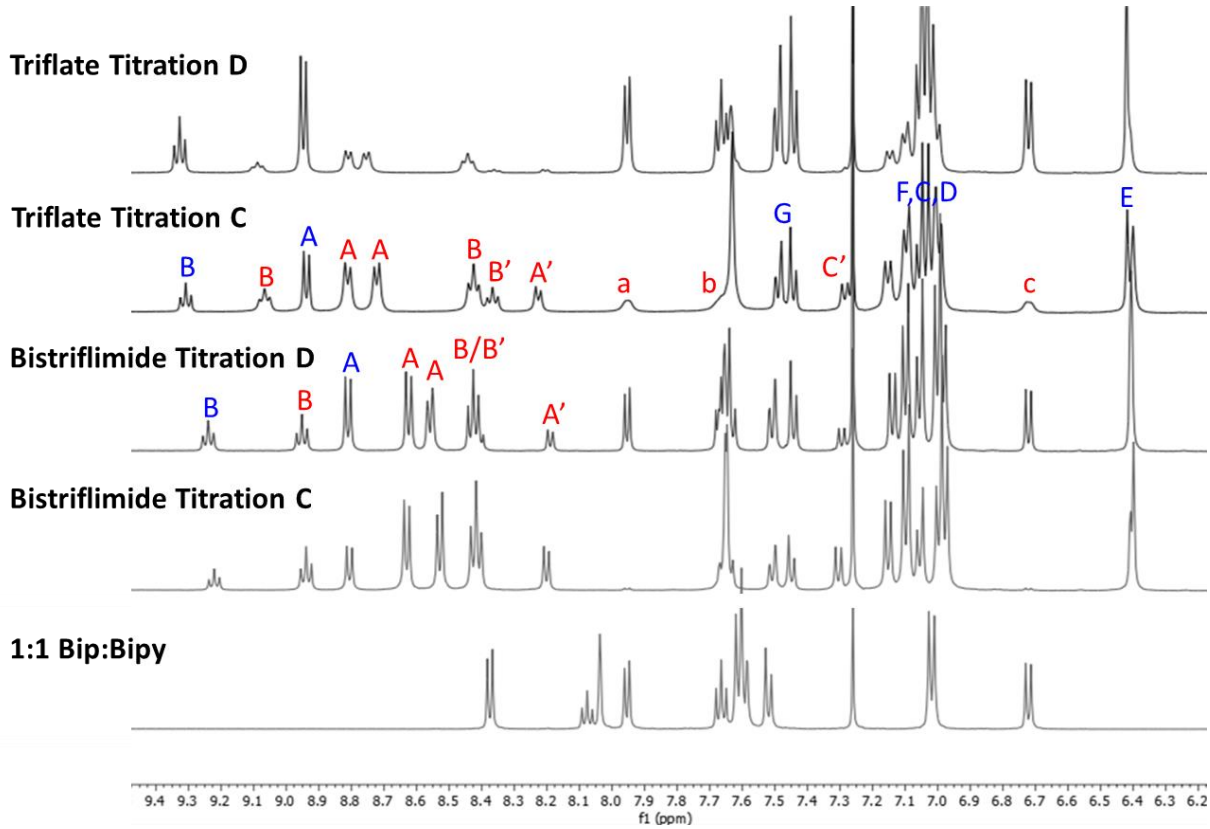

Figure 6.33. ^{1}H-NMR (500 MHz, 25°C, 15% d3-MeCN in $CDCl_3$) titrations with $Zn(OTf)_2$ vs. $Zn(NTf_2)_2$.

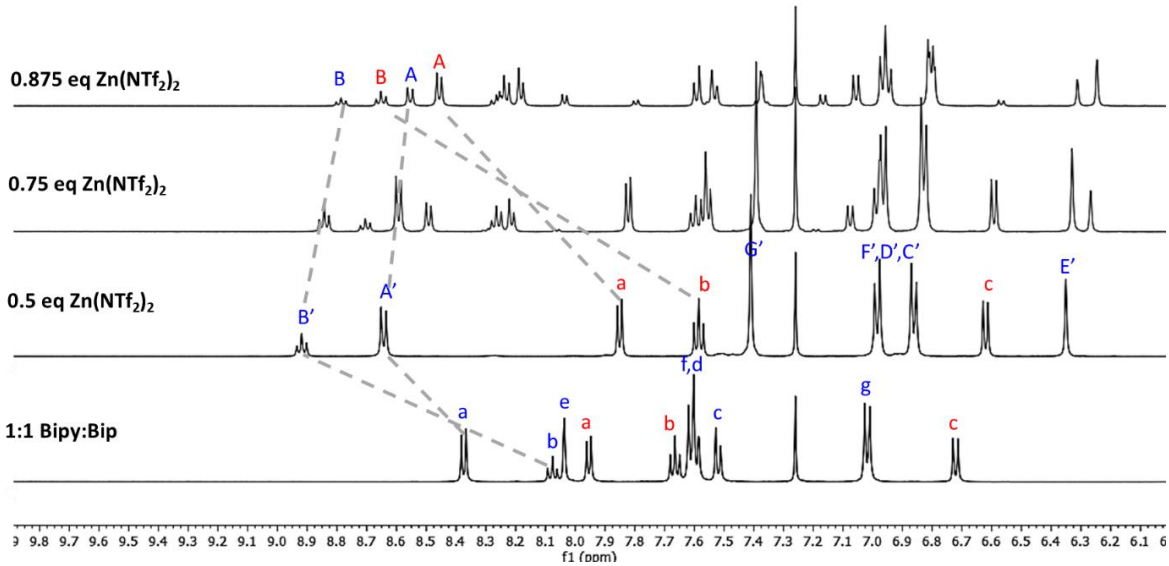

Figure 6.34. ^{1}H-NMR (500 MHz, 25°C, 15% d_3-MeCN in $CDCl_3$) of **5.2:5.11** titration with $Zn(NTf_2)_2$ (Titration C) showing the formation of **6.13** before Bipy starts to metallate above 0.5 eq metal.

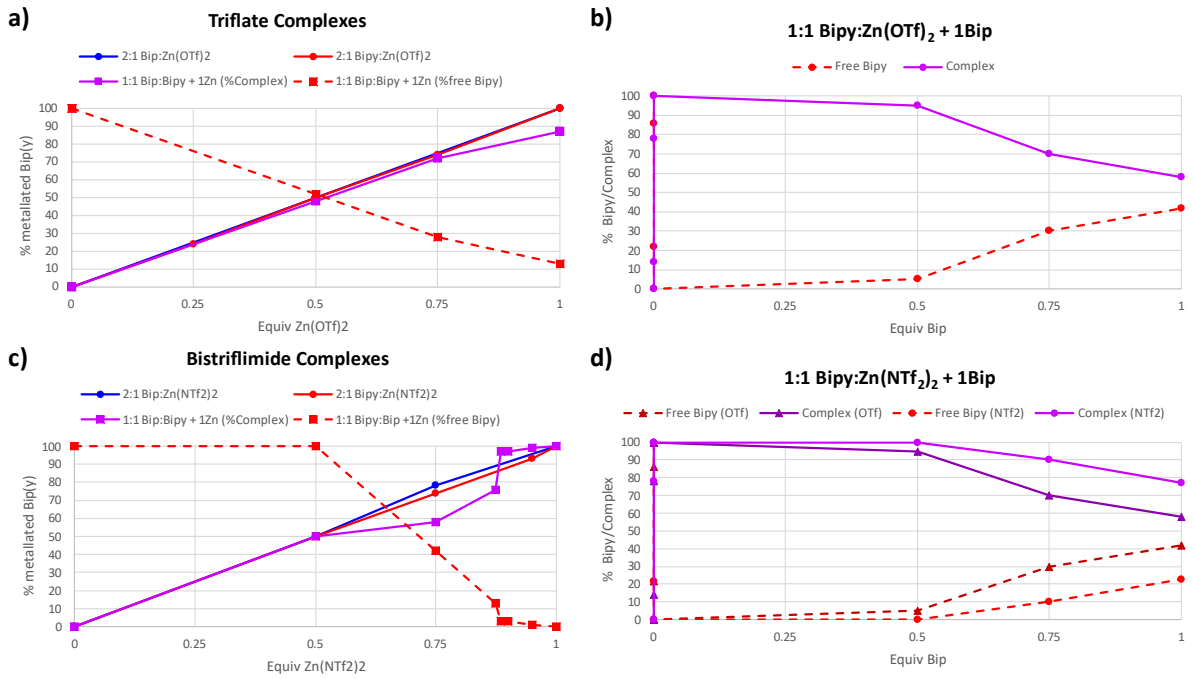

Figure 6.35. Titration plots. a) Triflate Titration C showing free Bipy **5.11**. b) Triflate Titration D: Bip **5.2** limits the formation of **6.15** as free Bipy **5.11** starts to appear. c) Bistriflimide Titration C shows the formation of **6.13** before Bipy **5.11** starts to metallate. d) Bistriflimide Titration D: Bip **5.2** limits the formation of **6.15**, but not as significantly as triflate.

Plotting NMR integrations in Titrations C and D helps show how the order of added components changes the formation of mixed complex **6.15**. Adding $Zn(OTf)_2$ to 1:1 mixture of **5.2:5.11** results in the preferential formation of **6.13** due to the stronger ligand binding with the tridentate vs. bidentate ligand. Then the amount of free Bipy **5.11** decreased as the mixed complex formed; however, not all the Bipy was chelated with 1 equivalent of $Zn(OTf)_2$. The strength of tridentate complex **6.13** appears to be weaker with triflate and stronger with bistriflimide; **5.11** did not start chelating until 0.5 equivalents of $Zn(NTf_2)_2$ were added to the solution (Figure 6.34, Figure 6.35c). Adding Bip **5.2** to a 1:1 complex of **5.11:Zn(II)** (Titration D) results in the formation of free (unbound) Bipy as Bip starts binding to the metal ions. The effect is more significant in the $Zn(OTf)_2$ system, resulting in a greater amount of free **5.11** (and less **6.15**) than in the $Zn(NTf_2)_2$ system.

The best mixed complex results come from Titration C using zinc bistriflimide; there are no peaks corresponding to **6.14** or any of the unmetallated ligands **5.11** and **5.2**. These results also suggest the addition of $Zn(NTf_2)_2$ into the stoichiometric mixture of components is the best route to making mixed ligand complexes such as **6.15**. Based on these titrations, **5.24:5.13$_2$:Zn(II)$_2$** formed from $Zn(NTf_2)_2$ was used for Diels-Alder stoppering.

6.4.2.12 Synthesis of metallated Diels-Alder [3]rotaxane **6.16**

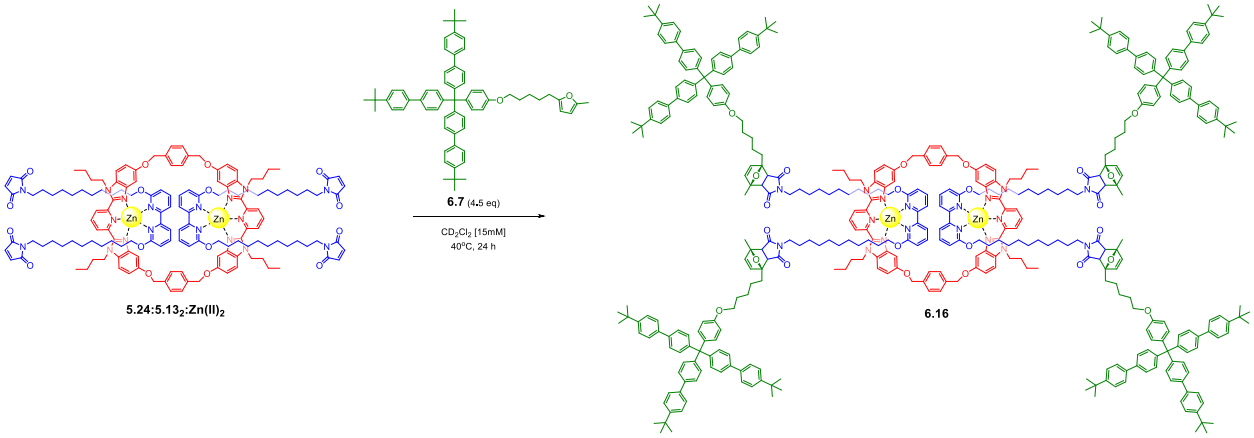

5.24:5.13$_2$:Zn(II)$_2$ (0.003 g, 0.0008 mmol) and furan stopper **6.7** (0.0032 g, 0.0036 mmol) were dissolved in 50 µL of CD_2Cl_2 and added to an NMR tube. The NMR tube was placed in an oil bath preheated to 40°C. After 24 hours, the sample containing **6.16** was diluted with 350 µL of CD_2Cl_2 for crude NMR analysis. The crude sample was washed with 3:1 hexanes:chloroform (5 mL, x3) to remove unreacted components. The solution was passed through a syringe filter and the solid was dried under vacuum. The solution containing the wash was also dried under vacuum. NMR confirmed removal of excess furan stopper; about one equivalent of stopper was recovered by mass.

6.4.2.13 Demetallation of Diels-Alder [3]rotaxane **6.16**

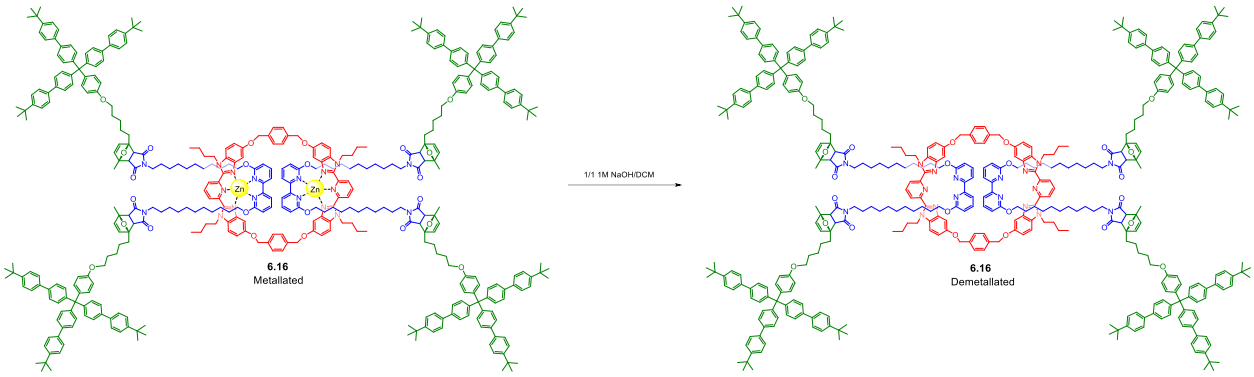

The metallated Diels-Alder [3]rotaxane **6.16** was dissolved in 8 mL of DCM and added to a vial with 8 mL of 1M NaOH to demetallate. The mixture was stirred overnight at room temperature. Afterward, the organic layer was isolated, and the solvent was removed under vacuum, leaving behind the crude, demetallated **6.17** that was dissolved in CD_2Cl_2 for NMR and MALDI-TOF analysis.

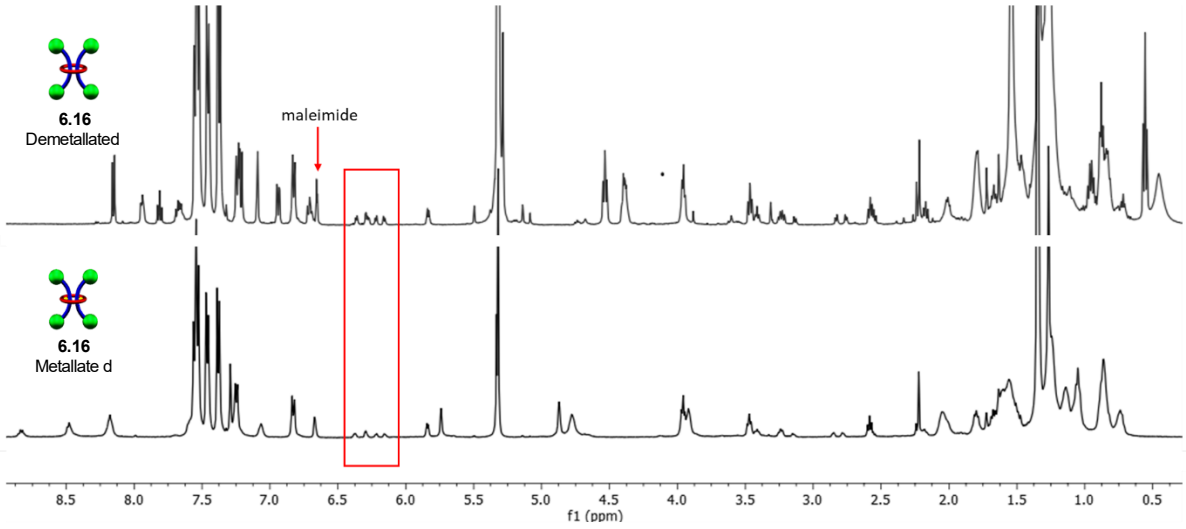

Figure 6.36. ^{1}H-NMR overlay (500 MHz, 25°C, CD_2Cl_2) of metallated (bottom spectrum) and demetallated **6.16** (top spectrum). Demetallation resulted in the formation of free thread and no rearrangement of the Diels-Alder adducts (red box).

6.4.2.14 Synthesis of metallated phthalimide [3]rotaxane **6.17**

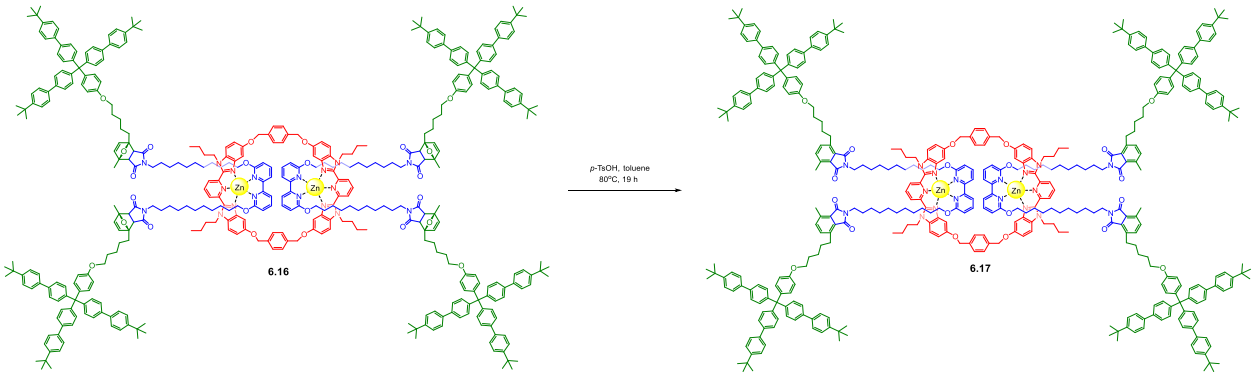

A catalytic amount of *p*-toluenesulfonic acid (*p*-TsOH) was added to a 4 mL conical vial with a stir bar and purged with argon. Metallated **6.16** (0.00067 g) was dissolved in 100 µL of toluene and syringed into the reaction vial. The reaction was heated to 80°C and stirred for 19 hours. The reaction was cooled to room temperature, and the toluene was removed via rotary evaporation. The crude sample **6.17** was dissolved in 400 µL CD_2Cl_2 for NMR analysis.

6.4.2.15 Demetallation of phthalimide [3]rotaxane **6.17**

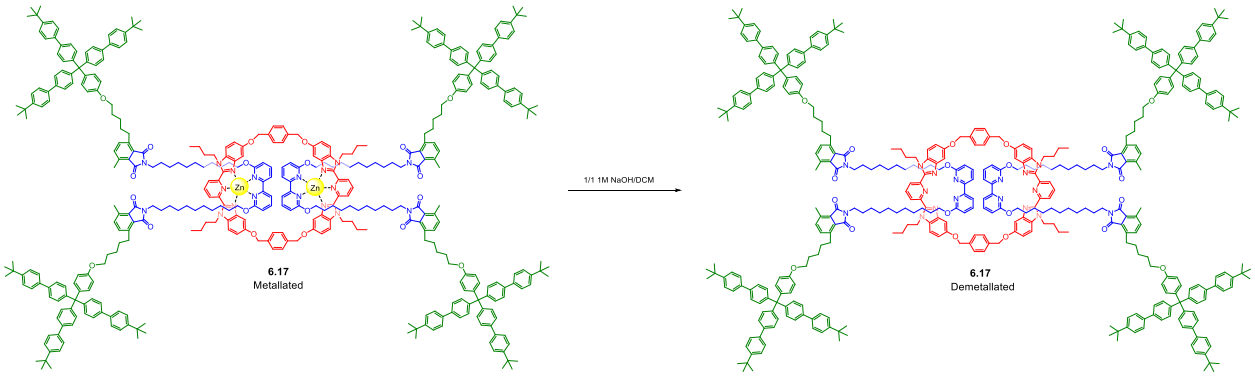

The metallated phthalimide [3]rotaxane **6.17** was dissolved in 8 mL of DCM and added to a vial with 8 mL of 1M NaOH to demetallate. The mixture was stirred overnight at room temperature. Afterward, the organic layer was isolated, and the solvent was removed under vacuum, leaving behind a crude residue that was dissolved in CD_2Cl_2 for NMR analysis.

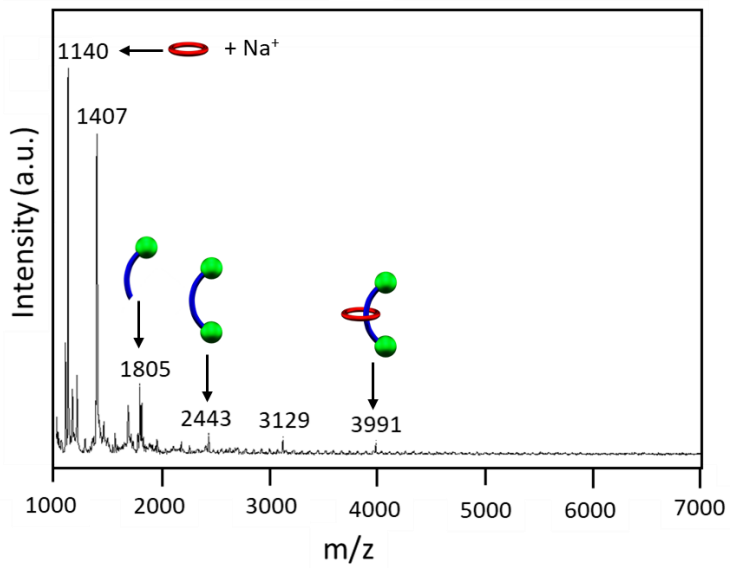

Figure 6.37. MALDI-TOF MS (Dithranol, sodium trifluoroacetate) of demetallated phthalimide **6.17**.

6.5 References

(1) Sánchez, A.; Pedroso, E.; Grandas, A. Maleimide-Dimethylfuran Exo Adducts: Effective Maleimide Protection in the Synthesis of Oligonucleotide Conjugates. *Org. Lett.* **2011**, *13* (16), 4364–4367. https://doi.org/10.1021/ol201690b.

(2) Chen, X.; Dam, M. A.; Ono, K.; Mal, A.; Shen, H.; Nutt, S. R.; Sheran, K.; Wudl, F. A Thermally Re-Mendable Cross-Linked Polymeric Material. *Science (80-.).* **2002**, *295* (5560), 1698–1702. https://doi.org/10.1126/science.1065879.

(3) Chujo, Y.; Sada, K.; Saegusa, T. Reversible Gelation of Polyoxazoline by Means of Diels-Alder Reaction. *Macromolecules* **1990**, *23* (10), 2636–2641. https://doi.org/10.1021/ma00212a007.

(4) Ding, X.; Nguyen, S. T.; Williams, J. D.; Peet, N. P. Diels–Alder Reactions of Five-Membered Heterocycles Containing One Heteroatom. *Tetrahedron Lett.* **2014**, *55* (51), 7002–7006. https://doi.org/10.1016/j.tetlet.2014.10.114.

(5) Song, S.; Wu, G.; Dai, W.; Guan, N.; Li, L. Diels-Alder and Dehydration Reactions of Furan Derivatives with Ethylene Catalyzed by Liquid Brønsted Acids and Lewis Acids. *J. Mol. Catal. A Chem.* **2016**, *420*, 134–141. https://doi.org/10.1016/j.molcata.2016.04.023.

(6) Takata, T. Polyrotaxane and Polyrotaxane Network: Supramolecular Architectures Based on the Concept of Dynamic Covalent Bond Chemistry. *Polym. J.* **2006**, *38* (1), 1–20. https://doi.org/10.1295/polymj.38.1.

(7) Ding, X.; Nguyen, S. T.; Williams, J. D.; Peet, N. P. Diels–Alder Reactions of Five-Membered Heterocycles Containing One Heteroatom. *Tetrahedron Lett.* **2014**, *55* (51), 7002–7006. https://doi.org/10.1016/j.tetlet.2014.10.114.

(8) Gandini, A. The Furan/Maleimide Diels-Alder Reaction: A Versatile Click-Unclick Tool in Macromolecular Synthesis. *Prog. Polym. Sci.* **2013**, *38* (1), 1–29. https://doi.org/10.1016/j.progpolymsci.2012.04.002.

(9) Hertzog, J. E.; Maddi, V. J.; Hart, L. F.; Rawe, B. W.; Rauscher, P. M.; Herbert, K. M.; Bruckner, E. P.; de Pablo, J. J.; Rowan, S. J. Metastable Doubly Threaded [3]Rotaxanes with a Large Macrocycle. *Chem. Sci.* **2022**, *00*, 1–12. https://doi.org/10.1039/d2sc01486f.

(10) Mandoli, A. *Recent Advances in Recoverable Systems for the Copper-Catalyzed Azide-Alkyne Cycloaddition Reaction (CuAAC)*; 2016; Vol. 21. https://doi.org/10.3390/molecules21091174.

(11) McKenzie, B. M.; Miller, A. K.; Wojtecki, R. J.; Johnson, J. C.; Burke, K. A.; Tzeng, K. A.; Mather, P. T.; Rowan, S. J. Improved Synthesis of Functionalized Mesogenic 2,6-Bisbenzimidazolylpyridine Ligands. *Tetrahedron* **2008**, *64* (36), 8488–8495. https://doi.org/10.1016/j.tet.2008.05.075.

(12) Kazancioglu, E. A.; Kazancioglu, M. Z.; Fistikci, M.; Secen, H.; Altundas, R.

Photooxygenation of Azidoalkyl Furans: Catalyst-Free Triazole and New Endoperoxide Rearrangement. *Org. Lett.* **2013**, *15* (18), 4790–4793. https://doi.org/10.1021/ol402163u.

(13) Haynes, R. K.; Vonwiller, S. C.; Luderer, M. R. Tetramethylethylenediamine. In *Encyclopedic Dictionary of Polymers*; Springer New York: New York, NY, 2011; pp 739–739. https://doi.org/10.1007/978-1-4419-6247-8_11714.

(14) Kitamura, C.; Abe, Y.; Ohara, T.; Yoneda, A.; Kawase, T.; Kobayashi, T.; Naito, H.; Komatsu, T. Synthesis and Crystallochromy of 1, 4, 7, 10-Tetraalkyltetracenes: Tuning of Solid-State Optical Properties of Tetracenes by Alkyl Side-Chain Length. *Chem. - A Eur. J.* **2010**, *16* (3), 890–898. https://doi.org/10.1002/chem.200901668.

7 NOAC Polymerization of Fully Interlocked Doubly-Threaded Slide-Ring and Polycatenane Materials

7.1 Introduction

Polycatenanes[1–6] are a less well-developed MIP class that utilizes mechanical bonding between two or more catenated macrocycles within the polymer architecture. Catenanes can be incorporated directly into the polymer backbone or act as crosslinking units to form polycatenanes (PCs), such as poly[2]catenanes (Figure 7.1a, top left), polymeric [2]catenanes (Figure 7.1a, top right), poly[*n*]catenanes (Figure 7.1a, bottom left), and Olympic gels (Figure 7.1a, bottom right) which are a class of polycatenane networks (PCNs).

Olympic gels are networks formed entirely from interlocked rings, making them a significant synthetic challenge.[7–9] However, they are theoretically predicted to have swelling and elastomeric properties dependent on the distribution of overlapping non-catenated rings.[10] Rings

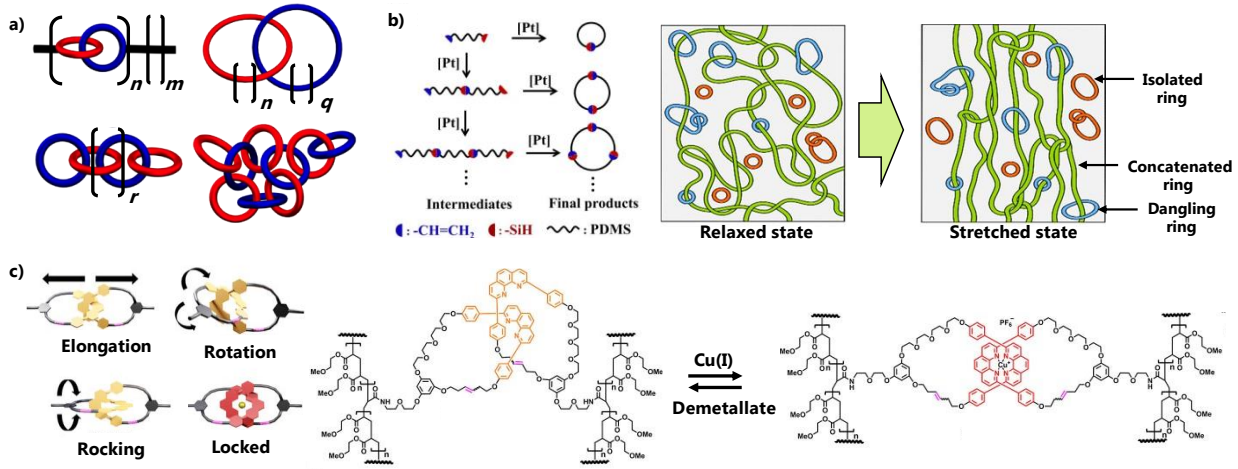

Figure 7.1. Polycatenane materials. a) Various polycatenane architectures: a poly[2]catenane (top left), a polymeric [2]catenane (top right), a poly[*n*]catenane (bottom left), and an Olympic gel, a class of polycatenane networks (PCNs) comprised entirely of catenated rings (bottom right). b) Platinum-catalyzed hydrosilylation reaction of α-monovinyl-ω-monohydride terminated polydimethylsiloxane (PDMS) yields an elastic concatenated ring network with isolated (red), concatenated (green), and dangling (singly-threaded, blue) rings. c) Metallation and demetallation of poly[2]catenane networks provides a way to switch between locked metallated [2]catenane crosslinks (red) and [2]catenanes (yellow) that can elongate, rotate, and rock after demetallation. Adapted from Refs. 5 and 11 with permission from American Chemical Society.

of varying size can be made from the platinum-catalyzed hydrosilylation reaction of α-monovinyl-ω-monohydride terminated polydimethylsiloxane (PDMS) (Figure 7.1b, left).[11] The concatenation of PDMS rings during the reaction results in a concatenated ring network containing dangling ends and a soluble fraction containing isolated rings (Figure 7.1b, right). The presence of elastically active concatenated rings increased polymer elasticity depending on the molecular weight of PDMS in the network, suggesting that incorporating cyclic components can tune material properties.

Replacing fixed (covalent) crosslinks with catenated crosslinks, such as the [2]catenanes in Figure 7.1c,[5] imbues networks with mobility elements present in the catenane moiety, including elongation, rotation, and rocking. Controlling the mobility of the interlocked crosslink through metallation/demetallation[5] or intercomponent hydrogen bonding[4] leads to mechanically adaptive networks that can reversibly switch between rigid and flexible states.

Poly[*n*]catenanes are macroscopic chains that have been synthesized in the Rowan Group using a Bip-based metallosupramolecular polymer (MSP) template and ring-closing metathesis (RCM) to form the interlocked PC **7.1** after demetallation (Figure 7.2).[12] Gel permeation chromatography (GPC) analysis of the interlocked products (obtained in *ca.* 70-80% yield) showed poly[*n*]catenane **7.1** as a mixture of linear and cyclic poly[*n*]catenane with an average DP_n of 12 and 8, respectively (Figure 7.2b and 7.2c). The largest M_n fraction contained a highly branched poly[*n*]catenane network with up to 130 rings, corresponding to an average DP_n of 55. This PC synthesis is highly tunable; the **7.1** architectures can be targeted by varying the concentration of the ring-closing step,[13] or by altering the size (and flexibility) of the ring and thread, which is an ongoing study.

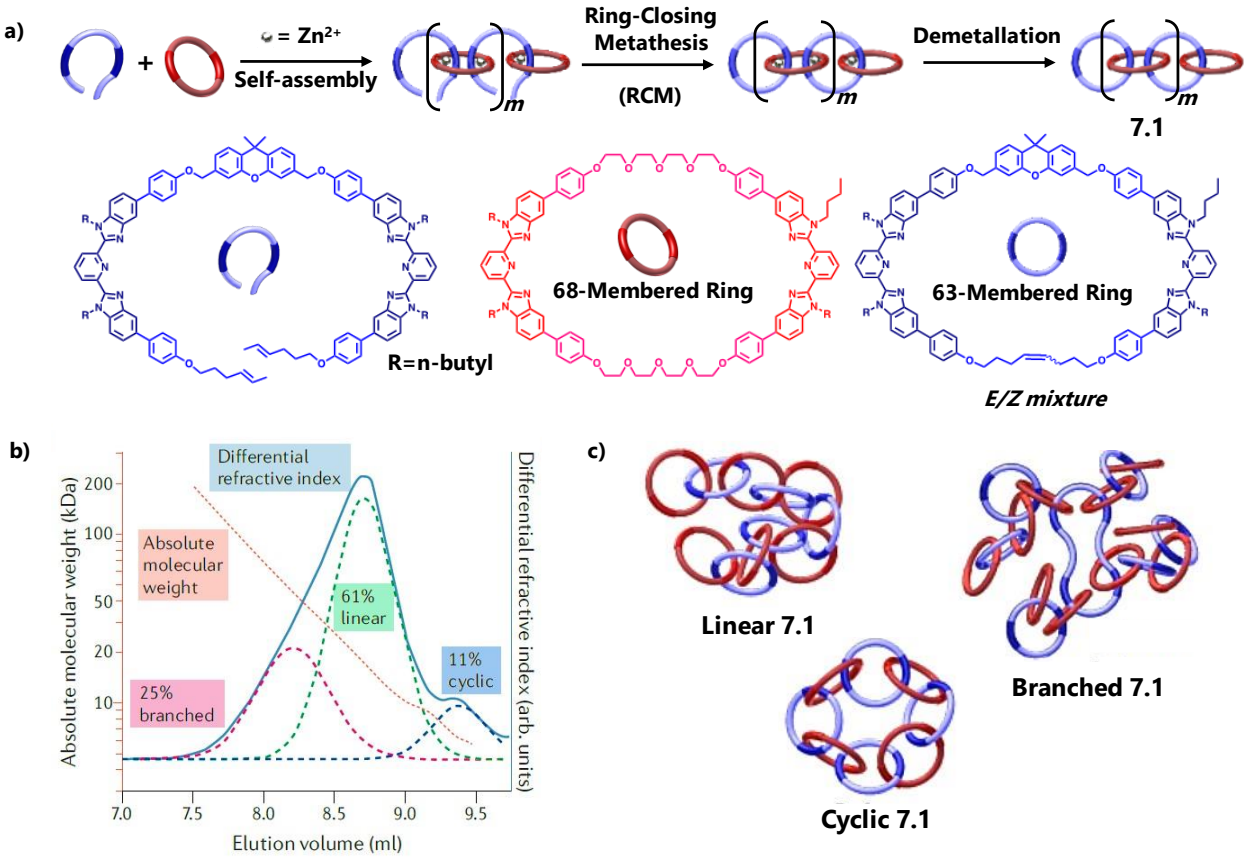

Figure 7.2. Poly[*n*]catenanes and Olympic Gels. a) Synthetic steps used to access the metallosupramolecular polymer (MSP) template and interlocked poly[*n*]catenane **7.1** (top), and the chemical structures of the thread (blue), 68-atom macrocycle (red), and the 63-atom ring closed thread (bottom). b) The gel permeation chromatography (GPC) trace of **7.1** suggests three unique architectures: c) linear, cyclic, and branched poly[*n*]catenane products. Adapted from Ref.12 with permission from The American Association for the Advancement of Science.

This chapter aims to explore possible routes to access doubly-threaded interlocked MIPs using ditopic Bip rings and demonstrate how nitrile-oxide/alkyne cycloaddition (NOAC) click chemistry can assemble PCNs directly from MSP or PC **7.1**. The last half of this chapter focuses on designing a highly versatile NOAC assembly of doubly-threaded SRNs with larger stoppers to incorporate singly-threaded and concatenated rings into the polymer architecture.

7.2 Fully Interlocked Polycatenane Materials

Branched poly[*n*]catenane networks (PCNs) form during the linear poly[*n*]catenane synthesis,[13,14] and NOAC polymerization can be used to specifically target PCNs by crosslinking the internal alkenes on **7.1**. The SR-PCN system developed in Chapter 2 employs [1,3] dipolar cycloaddition between nitrile-oxide monomer and alkyne chain ends on the P3R to form isoxazole linkages between components (Figure 7.3a, top). Cycloaddition can also occur between a nitrile-oxide and an alkene dipolarophile to form an isoxazoline ring (Figure 7.3a, bottom). [2,3] Cycloaddition reactions of nitrile-oxides have also been reported using intramolecular reactions with alkenes and internal alkenes to form 2-isoxazolines, as shown in Figure 7.3b.[15–17] Nitrile-

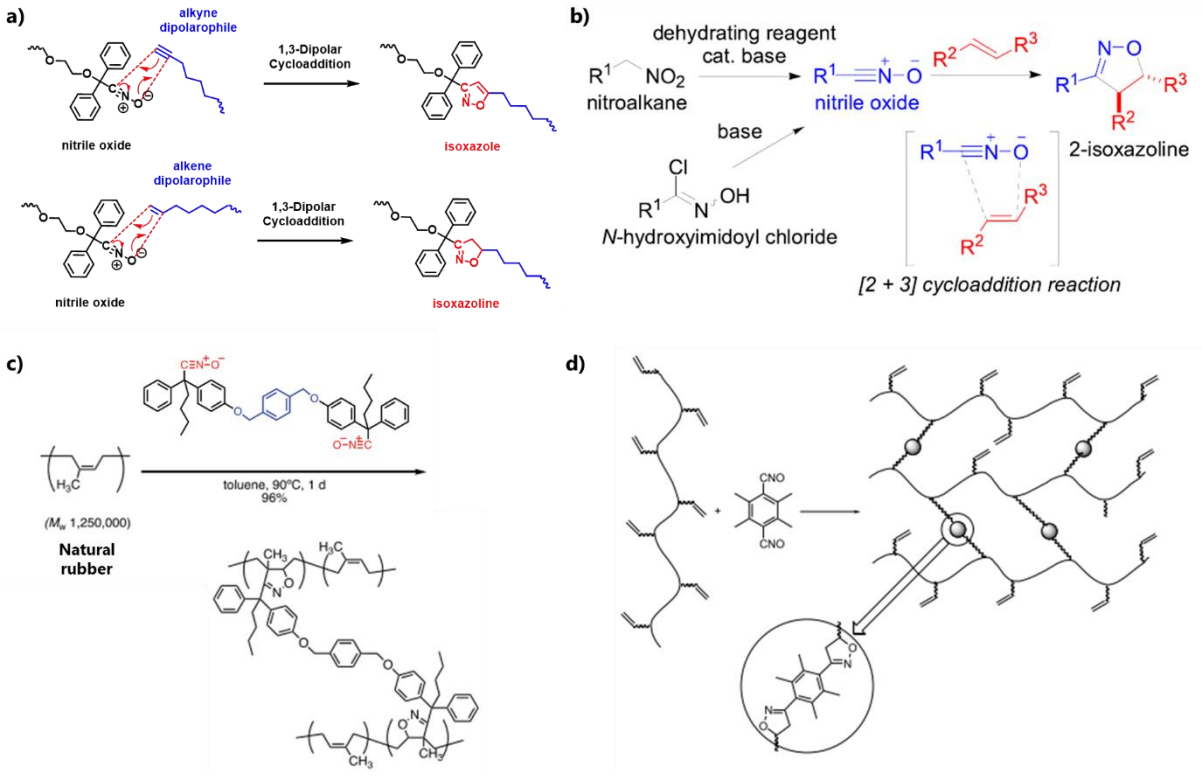

Figure 7.3. a) Nitrile-oxide click with alkyne forms isoxazoles (top), and with alkenes forms isoxazolines (bottom). b) [2+3] Cycloaddition reaction of nitrile-oxide with alkenes to form isoxazoline.[17] c) Crosslinking of natural rubber with ditopic nitrile-oxides.[18] d) Low-temperature curing of liquid polybutadiene with ditopic nitrile-oxides.[19] Adapted from Ref. 17 with permission from Elsevier, Ref. 18 with permission from Royal Society of Chemistry, and Ref. 19 published by MDPI.

oxide/alkene click has also been used to make networks by crosslinking natural rubber with di- and tri-topic nitrile-oxides (Figure 7.3c)[18] and through low-temperature curing of liquid polybutadiene (Figure 7.3d).[19]

As such, branched PCNs can be targeted synthetically by crosslinking the internal alkenes on PC **7.1** with nitrile-oxide monomer **2.5**, forming triethylene glycol linkages between polycatenane chains (Figure 7.4a). The metallated polycatenane could provide better results because the metal ions keeps the internal alkenes exposed rather than sterically hindered within the interlocked rings. The acyclic diene metathesis (ADMET) polymer **7.2** (prepared by Dr. Marissa Tranquilli) was chosen for a proof-of-concept study because it contains the same internal alkenes as poly[*n*]catenane **7.1** (Figure 7.4b).

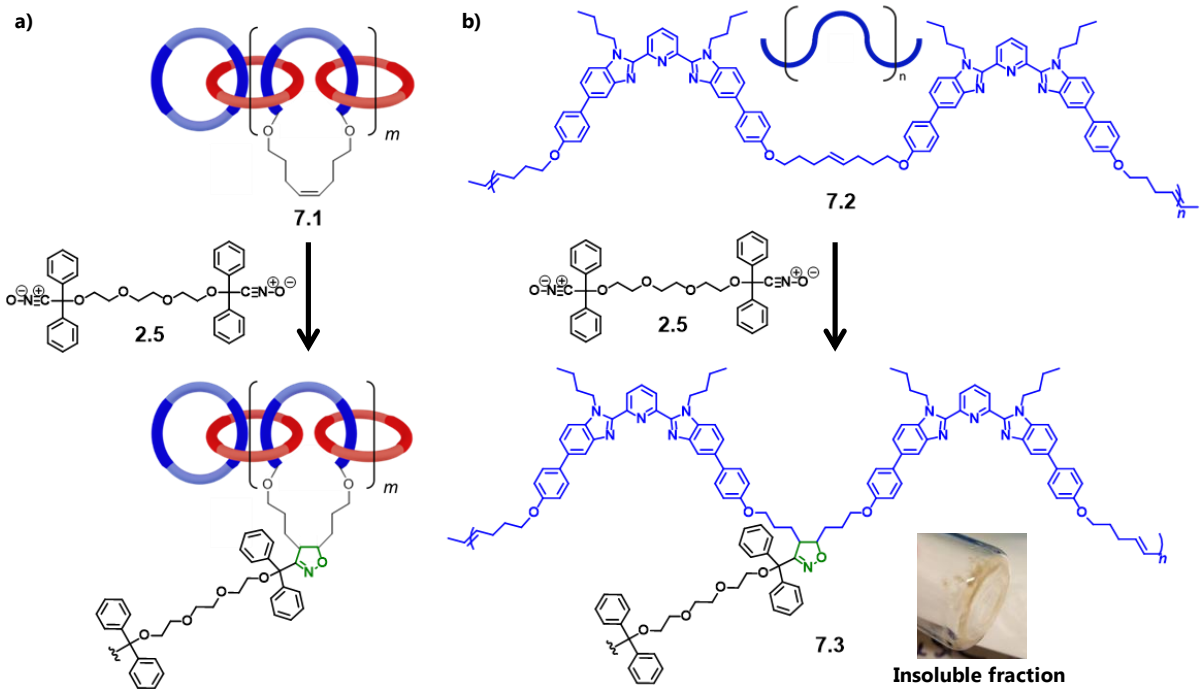

Figure 7.4. a) Proposed route to branched poly[*n*]catenanes via 1,3-dipolar cycloaddition of nitrile-oxide monomer **2.5** with alkenes on **7.1**. b) Proof-of-concept reaction of ADMET **7.2** (1488 g/mol, 3 alkenes per molecule, prepared by Dr. Marissa Tranquilli) with nitrile oxide **2.5** to form the crosslinked ADMET polymer **7.3**.

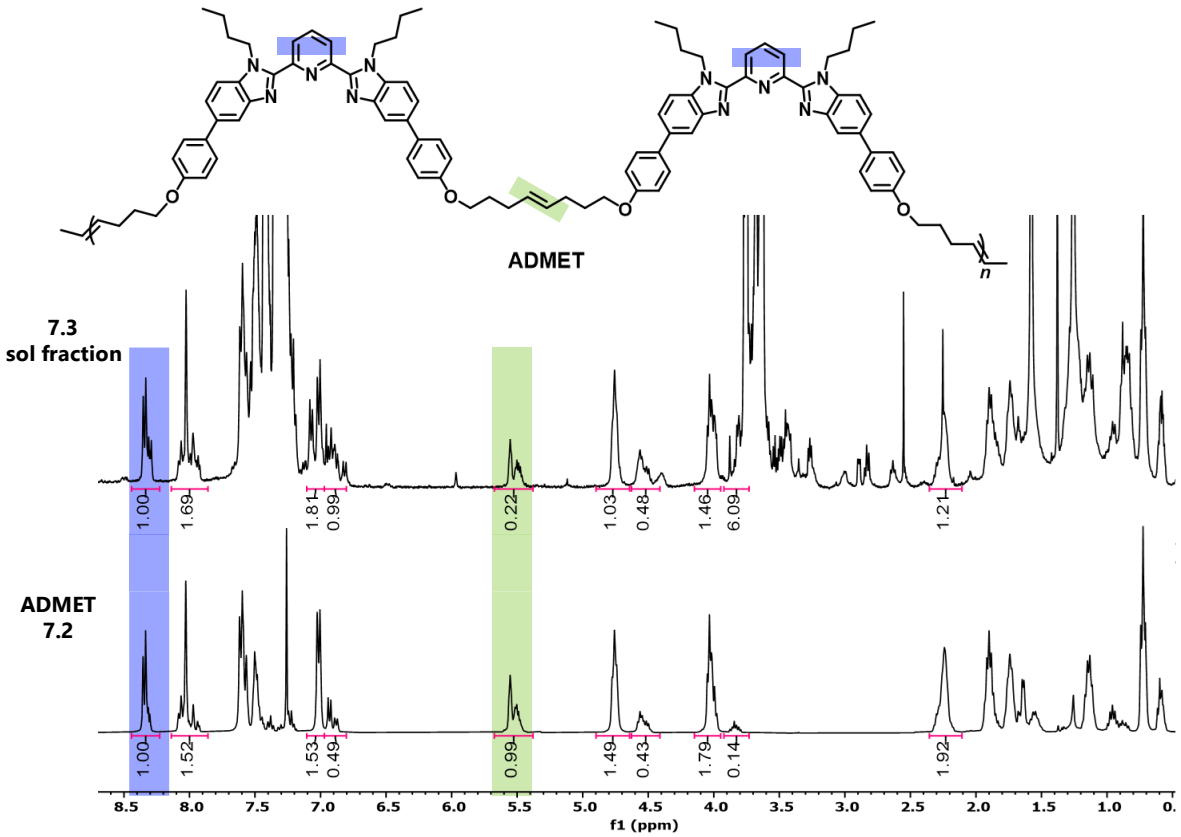

Figure 7.5. ^{1}H-NMR of the acyclic diene metathesis (ADMET) polymer **7.2** (bottom). The soluble fraction **7.3** resulting from the 1,3-dipolar cycloaddition of nitrile-oxide monomer **2.5** with alkenes on ADMET. Conversion is based on integrating meta-Bip protons (8.34 ppm, blue) and the internal alkene region (5.45 – 5.60 ppm, green).

ADMET **7.2** was reacted with **2.5** using similar reaction conditions employed in the SR-PCN synthesis (see Experimental for details). The lower molecular weight components were extracted into chloroform fraction for NMR analysis (Figure 7.5). The reduced integration of the internal alkenes between 5.45 – 5.60 ppm suggests the formation of an ADMET polymer product, such as **7.3**. A small amount of insoluble material was left in the vial, suggesting that this procedure can crosslink poly[*n*]catenanes to form networks (Figure 7.4b, bottom right).

Fully interlocked PCNs, or Olympic gels, can also be accessed using catalyst-free NOAC, as proposed in Figure 7.6. Previous work by Dr. Marissa Tranquilli investigated the concentration of the RCM reaction and found insoluble polycatenane byproducts formed during the synthesis of **7.1** at 10 mM (Figure 7.6a), suggesting network formation during RCM. Reacting the dangling

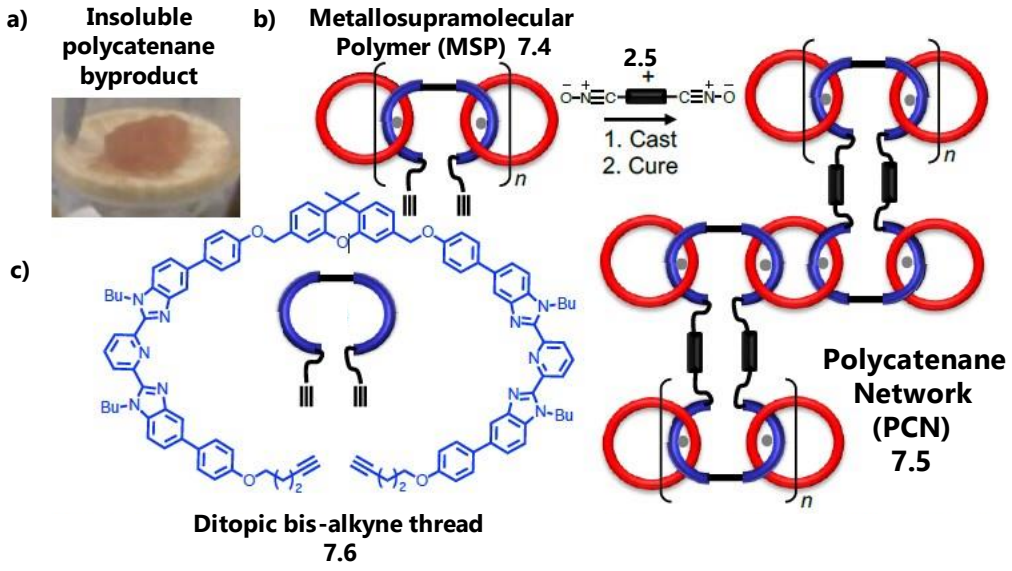

Figure 7.6. Proposed route to fully interlocked PCNs. a) Insoluble byproduct from synthesizing linear poly[*n*]catenane **7.1**. b) Metallosupramolecular polymer (MSP) **7.4** with dangling alkynes that can react monomer **2.5** to form PCN **7.5** akin to Olympic gels. c) Chemical structure of the proposed ditopic bis-alkyne thread **7.6** that can react with **2.5** to form large blue ring crosslinks.

alkynes on MSP **7.4** with nitrile-oxide **2.5** should form fully interlocked PCN **7.5**, akin to Olympic Gels (Figure 7.6b). The proposed ditopic thread with dangling alkynes (**7.6**, Figure 7.6c) should provide access to larger blue rings in the network that essentially act as crosslinking sites in PCN **7.5** after demetallation.

7.3 Fully Interlocked Doubly-Threaded Slide-Ring Materials

Incorporating pseudo[3]rotaxanes into a fully interlocked SRN requires switching out the 4-arm PEG covalent crosslink for a larger stopper group to prevent the doubly-threaded rings from falling out of the network. This dissertation aimed to put the pieces in place for synthesizing and properly characterizing the doubly-threaded slide-ring architectures proposed at the end of Chapter 1: **1.28** and **1.29**. Figure 7.7 shows the proposed synthetic design for preparing doubly-threaded slide-ring gels **7.7** and **7.8** with larger stoppers instead of covalent crosslinks, which should lead to networks with increased ring mobility. As seen in Chapter 2, catalyst-free nitrile-oxide/alkyne

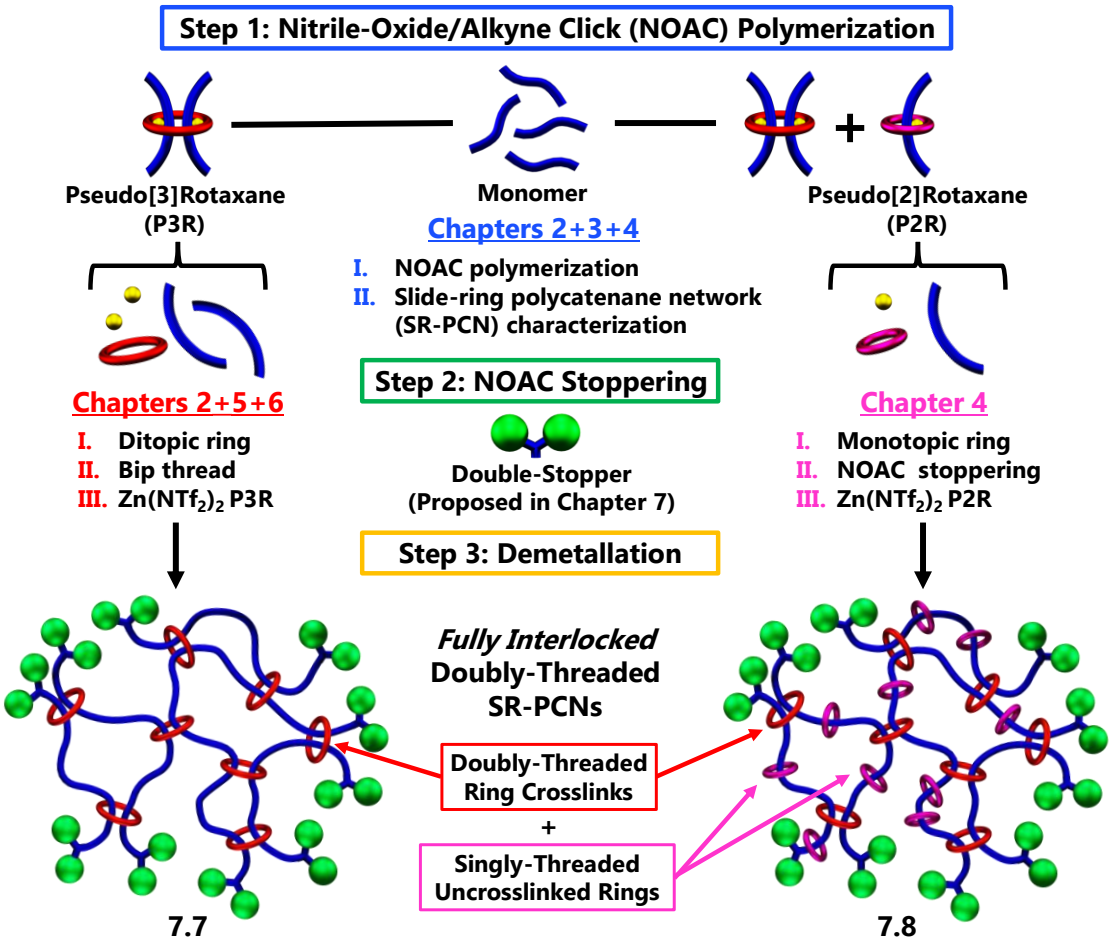

Figure 7.7. Preparation of fully interlocked doubly-threaded SRNs **7.7** and **7.8** using larger stoppers instead of covalent crosslinks.

cycloaddition is an excellent choice for assembling MIPs using metal templating because the reaction will proceed without disrupting the ligand complex. Furthermore, there is no catalyst or reagent to remove after polymerization, simplifying sample preparation. NOAC works in various solvents, providing room for optimizing sample preparation for further mechanical and rheological testing. Based on the success in forming SR-PCNs from P3R **2.1:2.2$_2$:Zn(II)$_2$**, adding a final stoppering step after the click polymerization should result in the fully-interlocked topology after demetallation.

The key to forming stable doubly-threaded SRNs without fixed crosslinks lies in matching the sizes of the stopper and macrocycle. The stoppering experiments explored in Chapters 4-6

suggested targeting a bulkier stopper to make [2]rotaxanes from the monotopic 36-atom ring **4.8** and [3]rotaxanes from ditopic 42- and 46-atom rings **5.24** and **2.1**. Collaborating with Dr. Jerry Hertzog resulted in synthesizing a series of metastable doubly-threaded [3]rotaxanes[20] using the same ditopic ring **2.1** and a "double stopper" architecture comprising two triaryl stopper groups, based on the furan double-stopper **6.10** developed in Chapter 6. With all the other SR-PCN components in hand, an alkyne-functionalized double-stopper should provide access to the fully interlocked doubly-threaded systems. An alkyne-terminated benzyl core **7.9** (see Experimental) permits the click addition of two azide-functionalized stoppers (**7.10**) to build the larger stoppering architecture **7.13** shown in Figure 7.8.

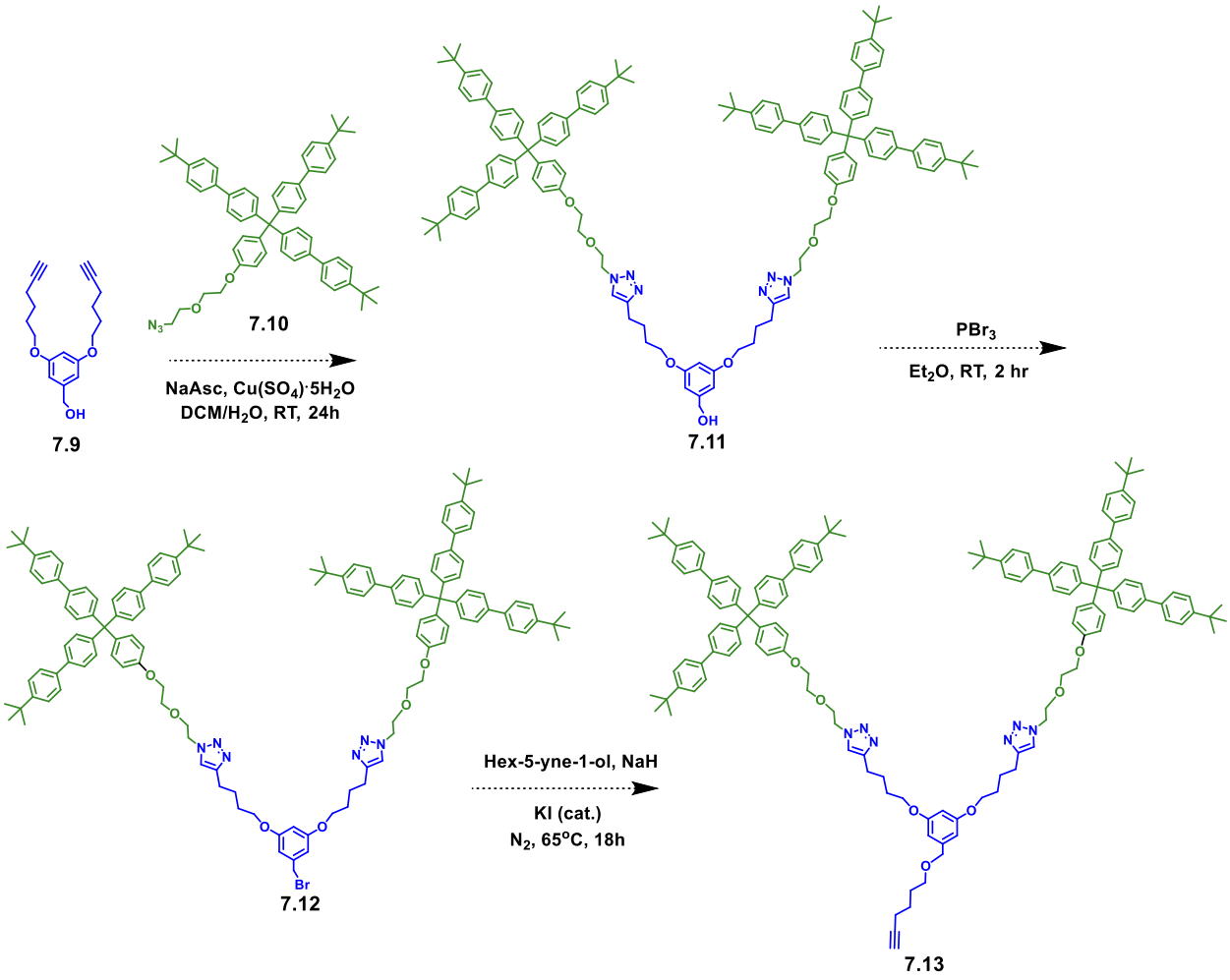

Figure 7.8. Proposed synthesis of double-stopper **7.13**.

In addition to characterizing the SR-PCN comprised only of ditopic rings, the monotopic rings can be added to probe the entropic elasticity exhibited in Ito's CD/PEG SRNs. Translating the pseudo[2]rotaxane (P2R) components and NOAC polymerization conditions from Chapter 4 will provide a way to tune properties based on the number of singly-threaded rings between doubly-threaded crosslinks (Figure 7.9). Varying the ring density on main-chain polyrotaxanes can be done by varying the polymerization ratio of monomer (or thread) and P2R components before the final stoppering step. Adding P3R to the click polymerization would result in a doubly-threaded

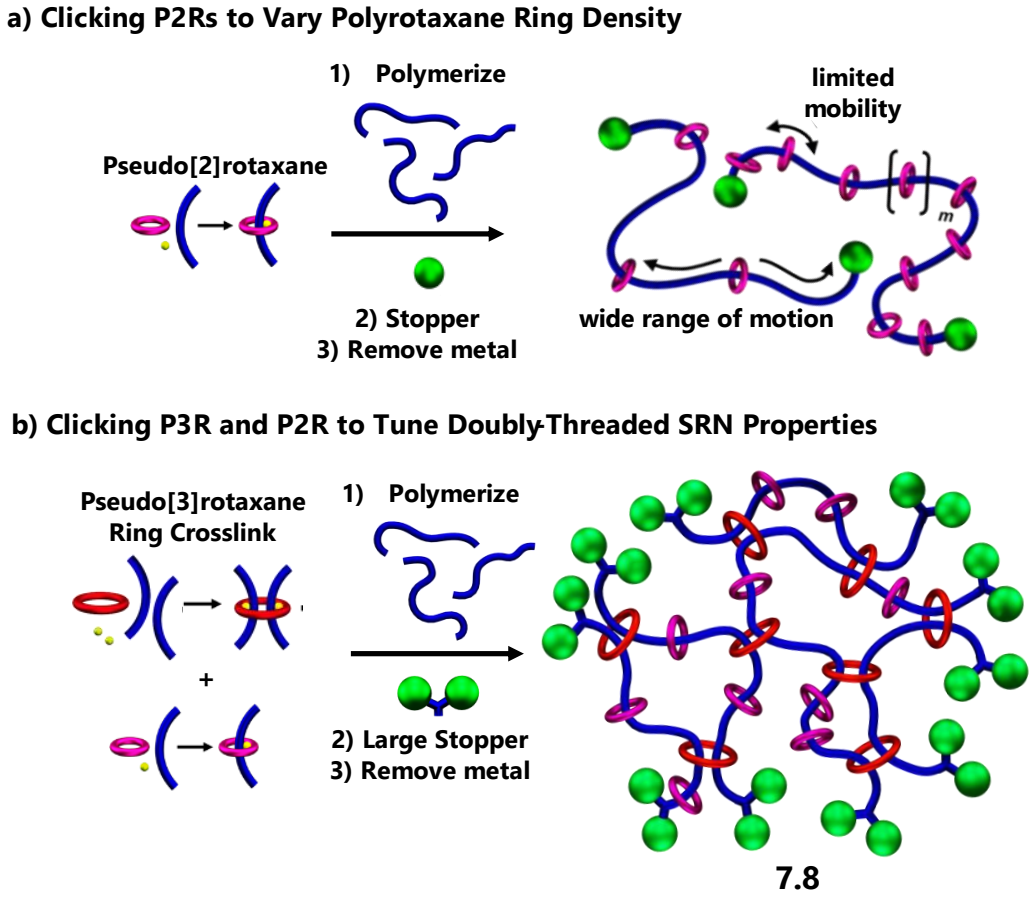

Figure 7.9. Probing entropic elasticity in SRN **7.8** with pseudo[2]rotaxanes. a) Varying free ring density via clicking pseudo[2]rotaxanes together yields metastable polyrotaxanes with varying ring coverage in Chapter 4. b) Preventing dethreading in doubly-threaded SRNs with larger stoppers and dialing in uncrosslinked (pink) rings to probe entropic elasticity in **7.8**.

slide-ring gel with singly-threaded rings embedded in the network (i.e., **7.8**). Thus, optimizing the ratio of different pseudo[*n*]rotaxanes into the polymerization affords a system with precise control over the number and valency of threaded rings in the MIP network.

In addition to singly-threaded rings, catenated rings can be incorporated into the doubly-threaded SRNs. The first step of the NOAC polymerization forms partially functionalized P3R

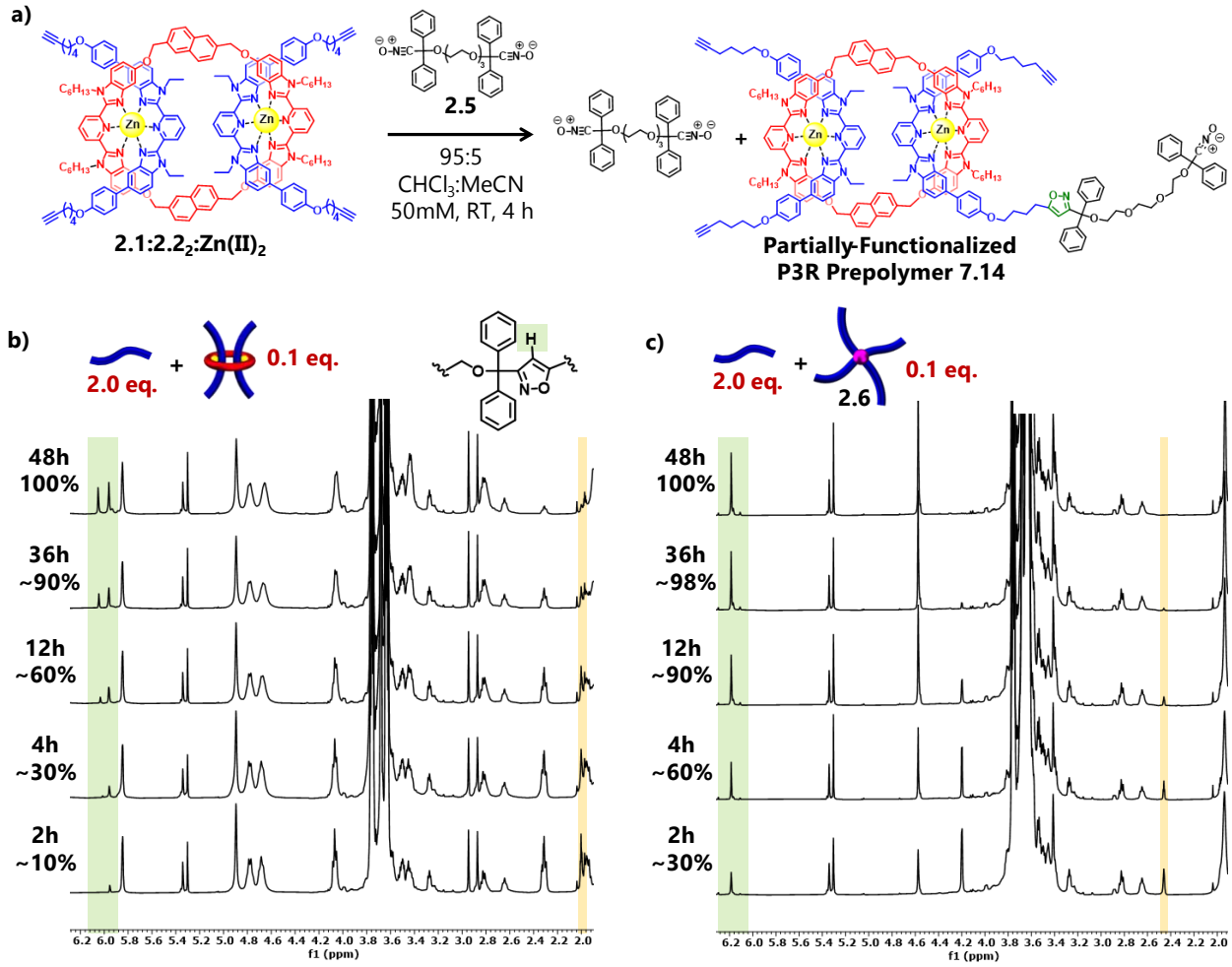

Figure 7.10. a) Synthesis of partially-functionalized P3R prepolymer **7.14**. b) Partial ^{1}H-NMR overlay (500 MHz, 25°C) of 2.0 eq. of monomer **2.5** and 0.1 eq. P3R **2.1:2.2$_2$:Zn(II)$_2$** dissolved in 5/95 v/v MeCN/CHCl$_3$ at 50mM. Conversion is based on integrations of the isoxazole proton peaks (5.96 and 6.03 ppm, green) and the metallated Bip protons on **2.1** in P3R (8.51 ppm, not shown) because the alkyne peak (1.99 ppm, yellow) is buried, preventing accurate integration. c) 2.0 eq. of **2.5** and 0.1 eq. of 4-arm PEG **2.6** dissolved in 5/95 v/v MeCN/CHCl$_3$ at 50mM. Conversion is based on the integrations of the isoxazole proton (6.19 ppm, yellow) and the alkyne peak (2.46 ppm, green).

prepolymers **7.14** in the solution that can form catenanes at longer reaction times (Figure 7.10a). Monitoring the reaction of **2.1:2.2$_2$:Zn(II)$_2$** and **2.5** via NMR revealed multiple peaks in the isoxazole region (Figure 7.10b). However, as expected, the control reaction between **2.5** and the covalent PEG **2.6** only showed one isoxazole peak (Figure 7.10c).

After 4 hours, only 30% of the P3R was reacted, but there was a 60% conversion for the tetra-PEG crosslinker sample. Therefore, nitrile-oxide monomer and P3R were left to react for 24 hours to improve conversion before adding the tetra-PEG crosslinker. The resulting SR-PCN **7.15** exhibited poor gel fraction (GF < 10%, see Experimental), so the soluble fractions were characterized further. MALDI-TOF analysis of the demetallated soluble fraction revealed signals corresponding to a [2]catenane **7.16** and [3]catenanes **7.17** and **7.18** (Figure 7.11a). The flexibility of the triethylene glycol units on prepolymer **7.14** permits the formation of ring-closed thread, resulting in [2]catenane **7.16** or [3]catenane **7.17** if both threads ring close (Figure 7.11b, top). The larger [3]catenane can form when two **7.14** prepolymers come in close contact, resulting in a larger blue ring comprised of two threads and two monomers (Figure 7.11b, bottom).

^{1}H-NMR revealed a collection of new aromatic peaks in the demetallated soluble fraction of **7.15** between 8.15 – 7.65 ppm (Figure 7.12, purple box). Similar shifts are observed in this region for [3]catenanes[21] and poly[*n*]catenanes[13,14] assembled from similar Bip components. These upfield shifted peaks likely correspond to the aromatic Bip protons on catenanes **7.16** – **7.18** detected by MALDI-TOF. The isoxazole linkages in the catenated rings show a different singlet in the NMR spectrum compared to the linear (not ring-closed) thread components (Figure 7.12, green box), as seen in Figure 7.10b.

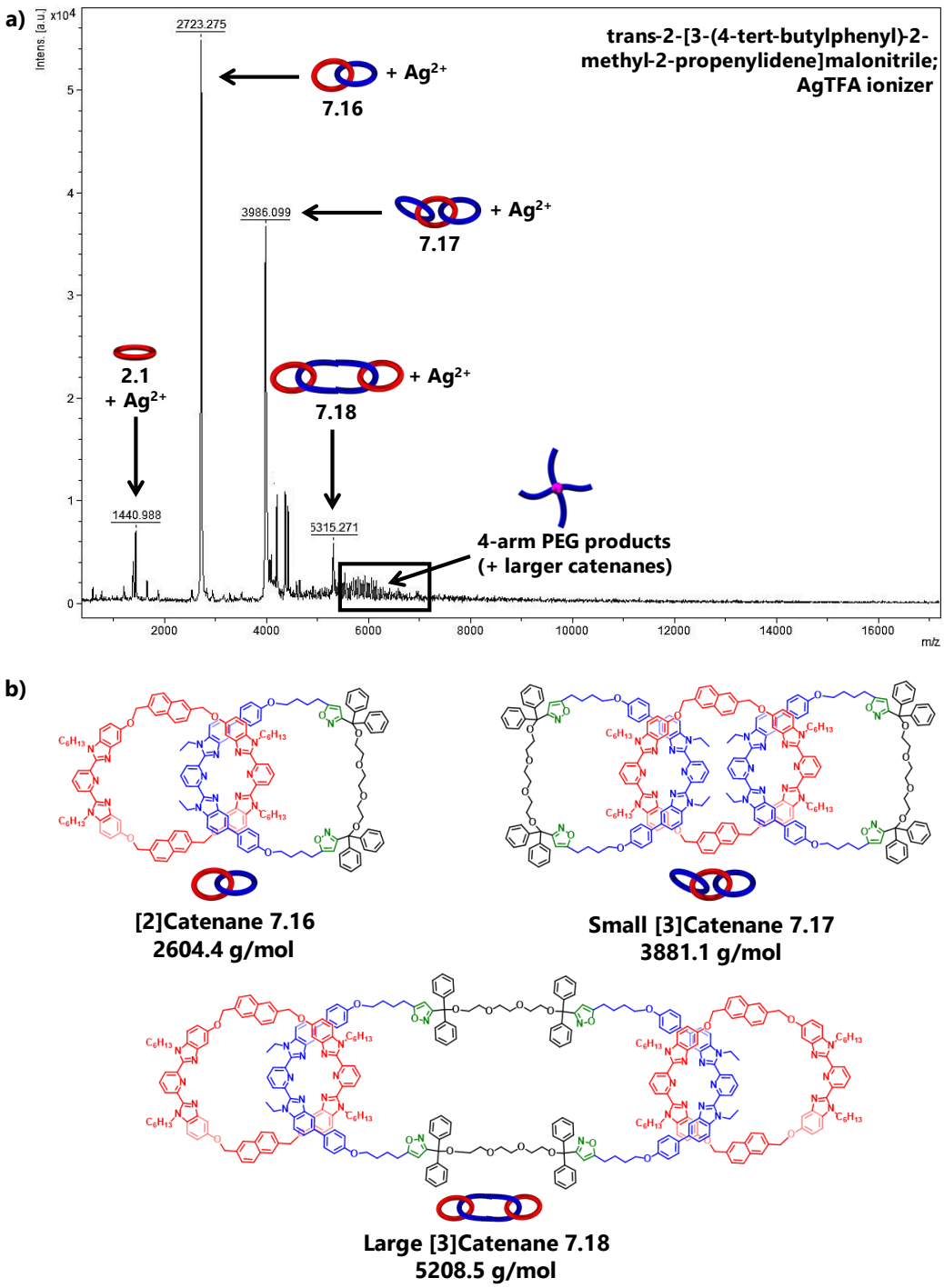

Figure 7.11. a) MALDI-TOF MS (trans-2-[3-(4-tert-butylphenyl)-2-methyl-2-propenylidene] malonitrile matrix, silver trifluoroacetate ionizer) of the demetallated SR-PCN **7.15** soluble fraction, revealing a mixture of catenated products: b) [2]catenane **7.16** (2604.4 g/mol) and small [3]catenane **7.17** (3881.1 g/mol), and the larger [3]catenane **7.18** (5208.5 g/mol) in the soluble fraction after demetallation.

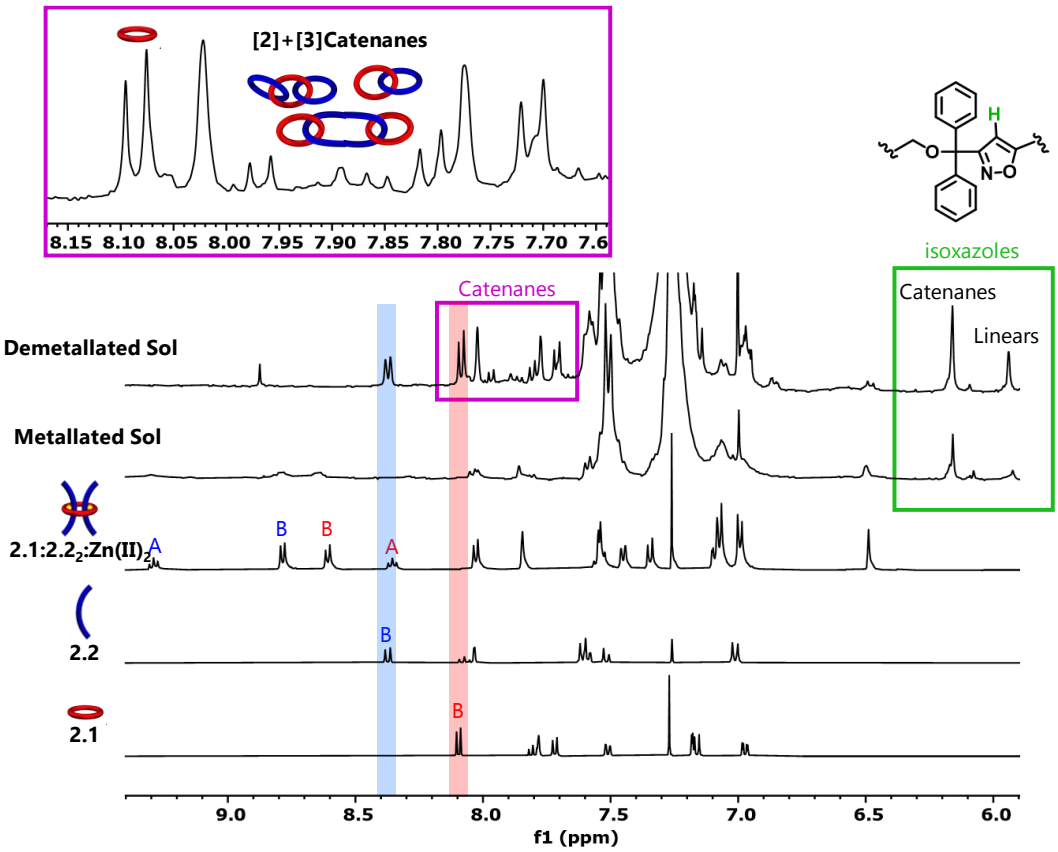

Figure 7.12. Partial ^{1}H-NMR overlay (400 MHz, 25°C, $CDCl_3$) of the demetallated soluble fraction of **7.15** (top spectrum) with the metallated soluble fraction, P3R, thread **2.2,** and macrocycle **2.1** for comparison. P3R **2.1:2.2$_2$:Zn(II)$_2$** (0.3 eq) and **2.5** (2.0 eq) reacted for 24 hours before adding 4-arm PEG **2.6** (0.7 eq), resulting in a metallated 70/30 gel with poor GF (<20%) and a mixture of catenated products in the soluble fraction. The more upfield isoxazole peak (5.94 ppm) likely corresponds to linear, and the downfield (6.16 ppm) peak likely corresponds to the catenanes (green box). The interlocked region (8.15 – 7.65 ppm)[21] shows the formation of a mixture of [2-3]catenanes **7.16-7.18** (purple box) upon the addition of TBAOH to demetallate the rings.

The formation of large [3]catenane **7.18** suggests there could be [3]catenane crosslinks in the SR-PCNs. Catenation of prepolymer **7.14** during the polymerization could lead to concatenated rings in the SR-PCNs that would not appear in the soluble fraction. Tuning the P3R topology to limit catenation could help improve the gel fraction of the current SR-PCN system. This P3R could also target smaller catenanes for incorporation into other polymers. Changing the flexibility of the polymer and dangling chain ends on the thread would be one route to explore different catenane product distributions.

The current network synthesis is not designed to access SR-PCNs with higher ring content (Y > 30 mol%) because increasing the P3R crosslinker reduces the covalent PEG crosslinker in the network, preventing rings from dethreading. The mechanical properties of SR-PCN gels **2.8**$_{X/Y}$ with higher ring content (Y > 30 mol%) were not studied in Chapter 2 because of the difficulty in obtaining consistent, reproducible data with these very soft samples. However, the SR-PCNs **7.19**$_{60/40}$ and **7.19**$_{50/50}$, were synthesized using the same procedure outlined in Chapter 2 (see

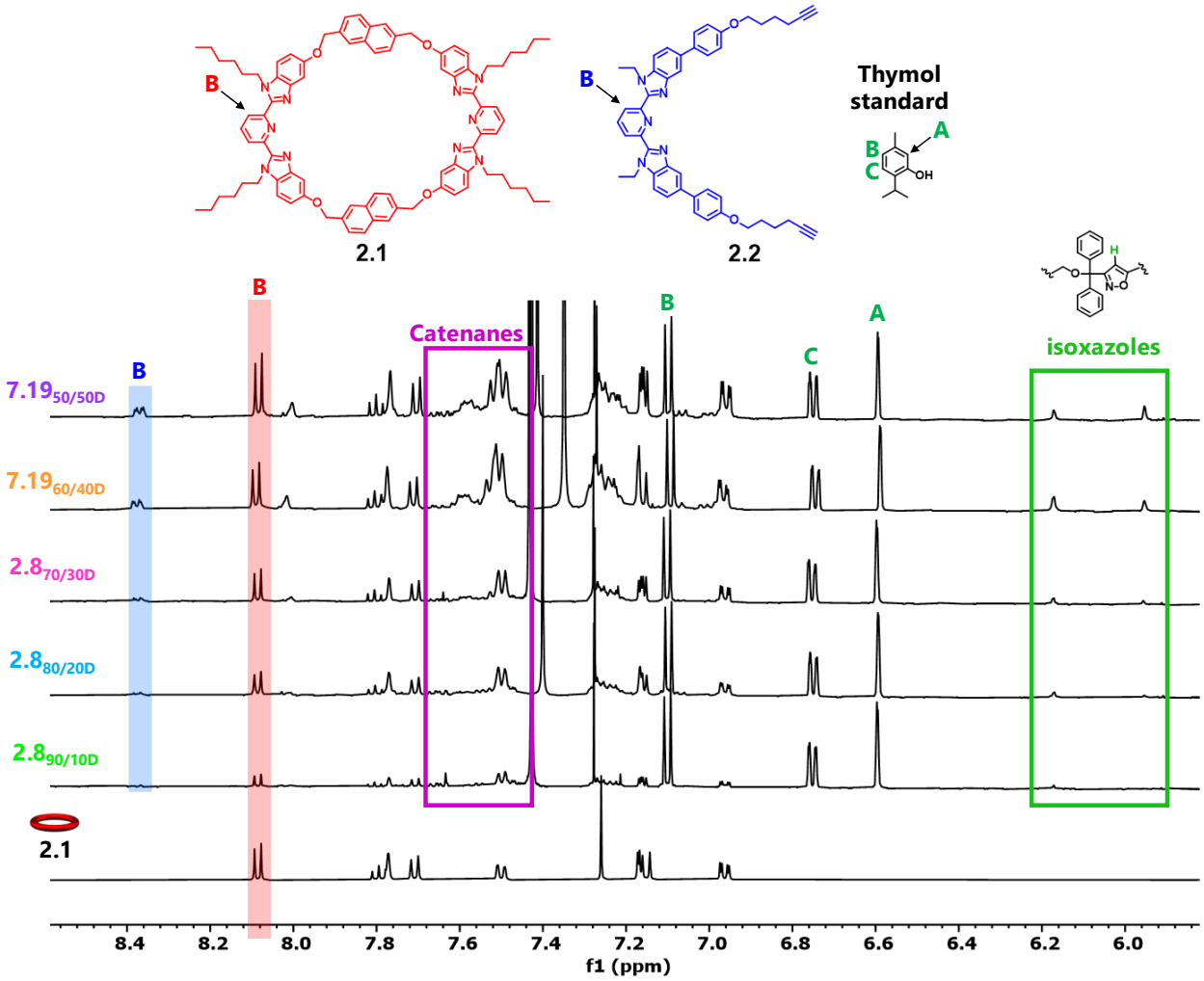

Figure 7.13. Demetallated soluble fractions of **2.8**$_{90/10D}$, **2.8**$_{80/20D}$, **2.8**$_{70/30D}$, **7.19**$_{60/40D}$, and **7.19**$_{50/50/D}$ from qNMR experiments (with a thymol standard), showing an increase in thread **2.2** (blue), macrocycle **2.1** (red), and the appearance of new peaks in the interlocked region (purple box) with the addition of rings. Two isoxazole peaks also appear (green box), which suggests the formation of linear and catenated (i.e., [2] and [3]catenanes) isoxazole products in the soluble fraction.

Experimental, Table 7.1) to determine their gel fraction, ring content, and thermal properties. The decrease in gel fraction (GF, see Experimental) likely accounts for the weaker, softer **7.19$_{60/40}$** and **7.19$_{50/50}$** gels. Perhaps not surprisingly, the number of rings (macrocycle **2.1**, $X_{MC,total}$) in the soluble fraction increases for **7.19$_{60/40}$** and **7.19$_{50/50}$** (see Experimental, Table 7.2) due to increasing the percentage of P3R crosslinker in the first polymerization step, which also results in the formation of catenanes not connected to the network that ultimately end up in the soluble fraction. ^{1}H-NMR of the demetallated soluble fractions for **7.19$_{60/40}$** and **7.19$_{50/50}$** (Figure 7.13) revealed similar peaks in the interlocked region and a second isoxazole singlet corresponding to the catenated products, similar to Figure 7.12.

SR-PCNs **7.19$_{60/40D}$**, and **7.19$_{50/50/D}$** with more rings follow similar trends in thermal properties as **2.8$_{90/10D}$**, **2.8$_{80/20D}$**, **2.8$_{70/30D}$** (see Experimental, Table 7.3). At higher ring content, a cold crystallization event appears in the demetallated SR-PCN, possibly due to the larger mobility elements present in this network (Figure 7.14d).

The addition of the catenated rings leads to several possible convoluted structural changes giving rise to the complex relaxation phenomenon discussed in Chapter 2. First, the demetallation removes the metal-ligand coordination, allowing the catenated rings to move freely along the network between covalent crosslinks. Second, adding the ring crosslinker reduces the overall covalent crosslinking density, permitting the catenated rings to move farther along the network. Third, the highly-aromatic thread likely results in a higher persistence length of the network between covalent crosslinks, allowing the rings to slide with less hindrance by the reptating network backbone. Rationalized as an increase in network mobility, the faster P3R relaxation occurs as more ring crosslinks replace the covalent crosslinks and likely provide an additional chain-sliding mechanism for energy damping. Because of the asymmetry between the contour

length of a PEG arm and a thread (calculated to be 9.8 nm and 3.2 nm, respectively), the ring density increases with the increasing number of ring crosslinks between covalent crosslinks (Figure 7.15).

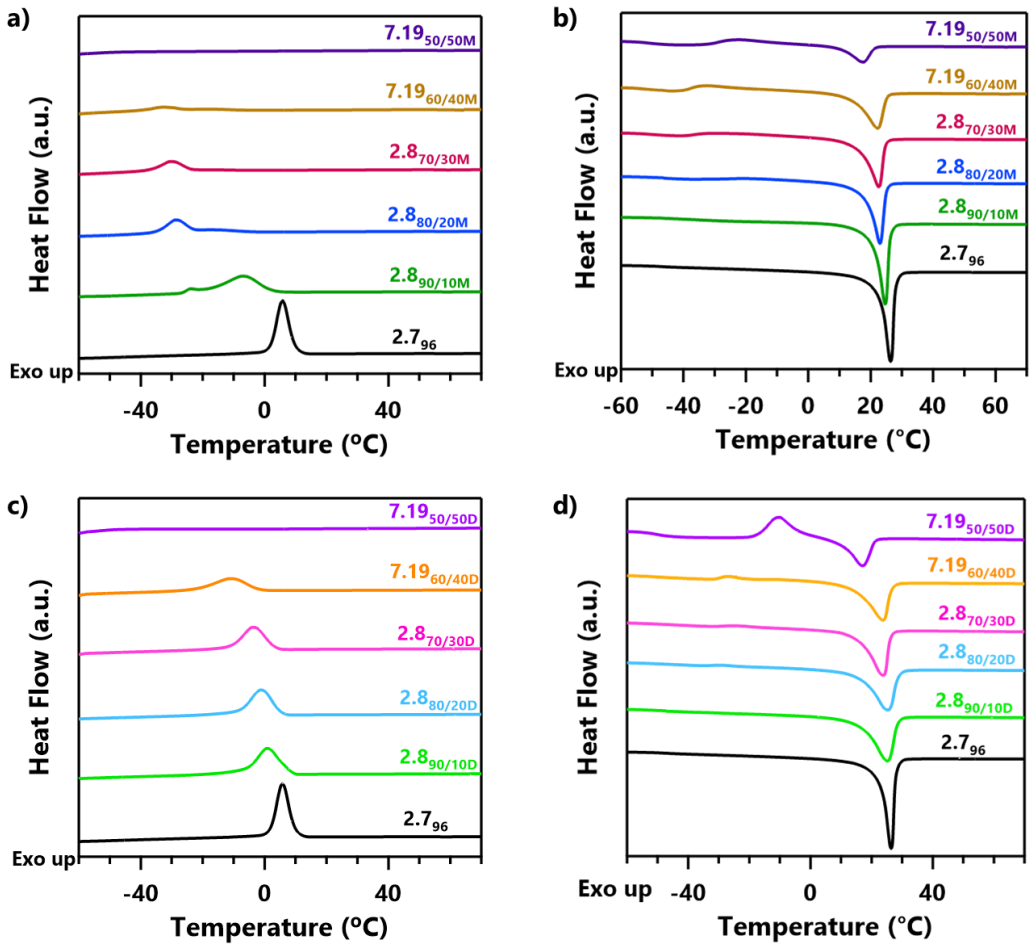

Figure 7.14. Differential scanning calorimetry (DSC) curves during a) cooling and b) second heating for the dried covalent **2.7$_{96}$** (black) and metallated SR-PCNs: **2.8$_{90/10M}$** (green), **2.8$_{80/20M}$** (blue), **2.8$_{70/30M}$** (red), **7.19$_{60/40M}$** (dark orange), and **7.19$_{50/50M}$** (dark purple). DSC curves during c) cooling and d) second heating for the dried covalent **2.7$_{96}$** (black) and demetallated SR-PCNs: **2.8$_{90/10D}$** (light green), **2.8$_{80/20D}$** (light blue), **2.8$_{70/30D}$** (pink), **7.19$_{60/40D}$** (orange), and **7.19$_{50/50D}$** (purple) (exotherm up, ramp rate = 10°C/min, curves offset for ease of viewing).

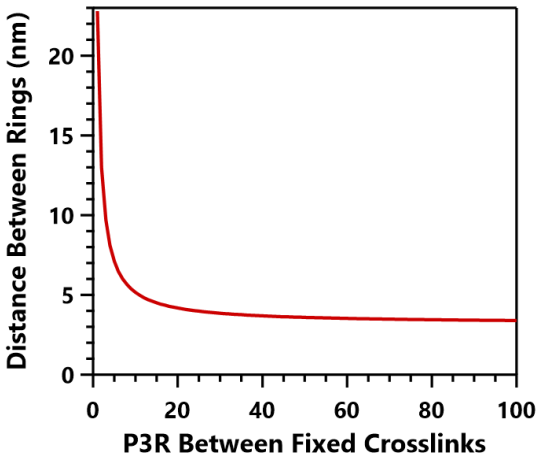

Figure 7.15. The average available distance between evenly distributed rings as a function of the number of MC crosslinks between covalent crosslinks. Calculated as $Distance = \left(2L_{c,PEG} + nL_{c,thread}\right)/n$, where L_c is the calculated contour length ($L_{c,\,PEG}$ = 9.8 nm and $L_{c,\,thread}$ = 3.2 nm) and n is the number of MC crosslinks between fixed crosslinks.

7.3.1 Proposed Scattering Studies

Two-dimensional SANS experiments have provided more evidence for the pulley-effect in topological gels.[22,23] Polymer gels experience an anisotropic scattering pattern, referred to as an abnormal butterfly, with prolate (elongated spheroid) patterns parallel to the stretching direction. Since polymer gels are essentially large inhomogeneous structures, these inhomogeneities are amplified upon stretching, which causes the abnormal butterfly pattern to start appearing. With increasing crosslinking density, the scattering intensity of the polymer gel will also increase at the small angle region. The scattering pattern will reduce to a normal butterfly pattern (prolate patterns perpendicular to the stretching direction) without spatial inhomogeneities. Homogeneous polymeric materials exhibit the normal butterfly due to polymer chains orienting along the direction of elongation or flow. Slide-ring gels have also experienced a normal butterfly pattern resulting from the pulley effect: the sliding of freely movable crosslinks limits spatial inhomogeneities in the network (Figure 7.16a). SRNs with high crosslinking densities (crosslinker concentrations at 2 wt% with respect to the polyrotaxane solution) start to experience abnormal

butterfly patterns, deviating from the previously observed normal butterfly pattern (Figure 7.16b). This normal-to-abnormal butterfly pattern transition suggests increasing the crosslink density reduces ring sliding, and spatial inhomogeneities cannot be reduced if the ring crosslinks do not move effectively enough.[24]

SANS studies are widely used for determining gel structure because the deuteration of the sample can control the scattering length.[25] In CD/PEG-based SRNs, polymers can be isolated from the rings by changing the solvent to add contrast to one component and cancel out the other, resulting in three partial scattering functions (Figure 7.16c).[26] Decomposition of the scattering

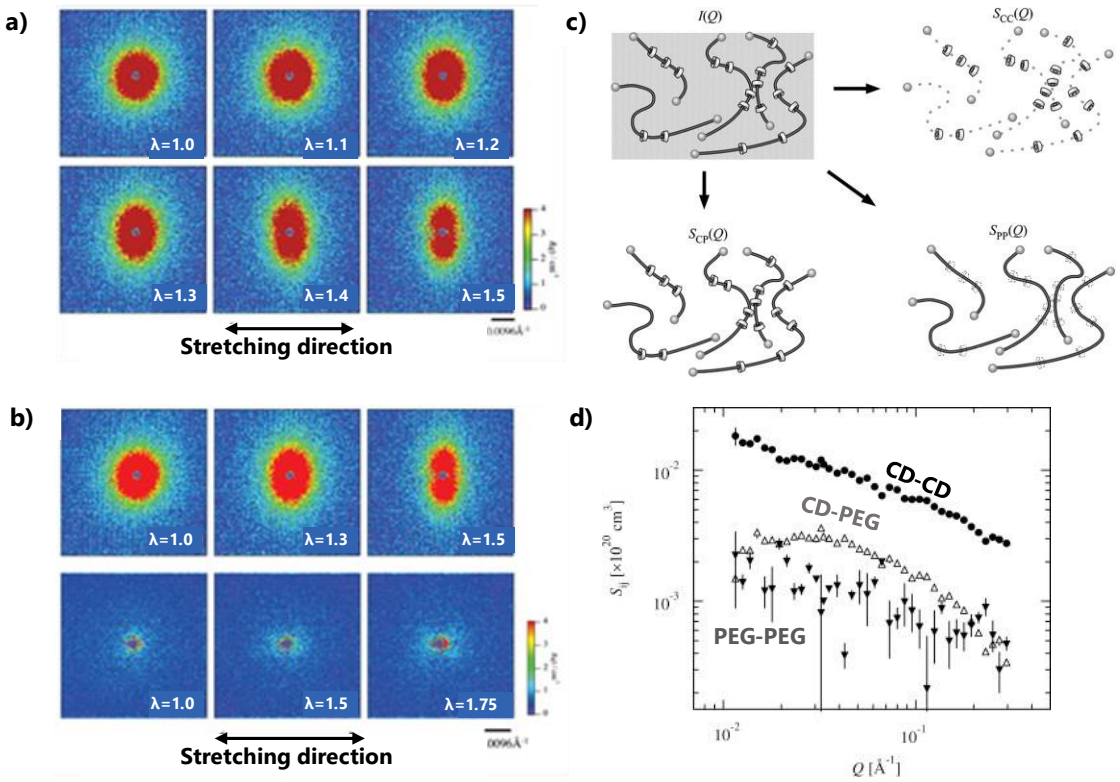

Figure 7.16. SANS isointensity patterns of CD/PEG SRNs with a) varying stretching ratios (λ), and b) normal butterfly patterns found at low crosslinking density (top), but abnormal and lower scattering intensity at higher crosslinking density (bottom). c) Polyrotaxane in solution showing the decomposition of scattering intensity I(Q) into three partial scattering functions plotted in d) with CD-CD interactions at the top, CD-PEG in the middle, and PEG-PEG at the bottom.[25] Adapted from Ref. 23 with permission from American Chemical Society, and Ref. 26 with permission from Elsevier.

intensity I(Q) is decomposed into three partial scattering functions S(Q) relating to CD-CD (Figure 7.16c, top), CD-PEG (Figure 7.16c, middle), and PEG-PEG interactions (Figure 7.16c, bottom).[26] These scattering results suggest SRNs experience an overall entropy resulting from the oriental entropy of the polymer backbone and the alignment entropy associated with the rings.

SAXS experiments have also been used to clarify the structure of ring crosslinks in CD/PEG SRNs by changing the swelling solvent.[27] Synchrotron radiation X-rays provide SAXS with shorter exposure times than SANS experiments, allowing SR-PCNs to be tested in a broader range of swelling solvents. SAXS measurements on stretched SR-PCNs in different solvents should provide more insight into our gels' alignment tendencies at different ring densities, as seen in the CD/PEG-based systems shown in Figure 7.17a. Vertically elliptic patterns appear in 2D SAXS experiments for polymer gels; however, slide-ring gels maintain an isotropic pattern. Aggregations of cyclodextrins create crosslinking junctions that cannot move, suppressing the pulley effect and resulting in similar SAXS patterns to those of chemical gels with fixed crosslinks. When the gel is stretched in a good solvent, polymer chains can pass freely through ring crosslinks

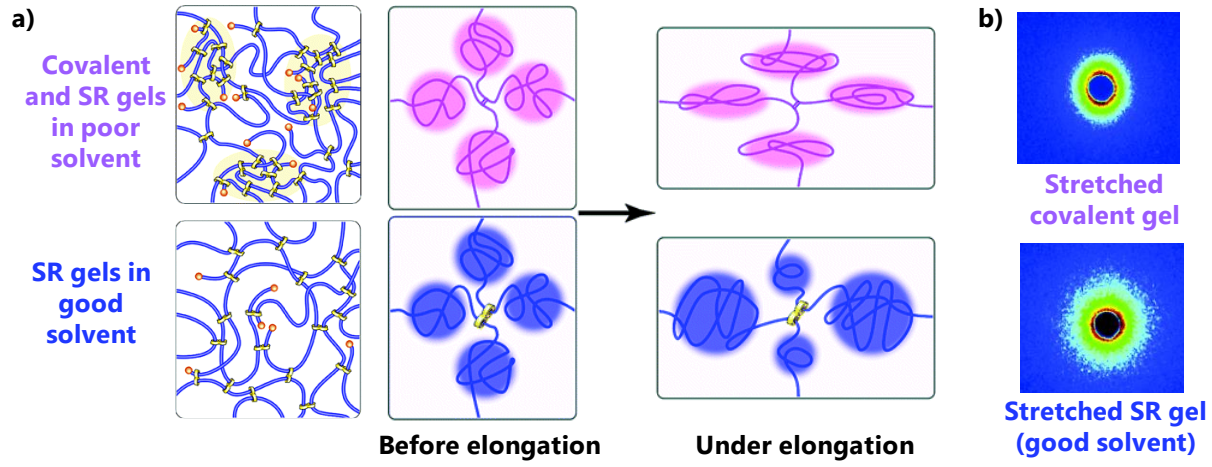

Figure 7.17. CD/PEG SRN SAXS experiments.[25] a) Schematics of SRNs in poor (water) (top, purple) solvent with CD aggregates and good (DMSO) (bottom, blue) solvent before and under elongation (right). b) SAXS patterns of the stretched covalent gel (top) with elliptic pattern and the stretched SRN (bottom) in good solvent, showing no anisotropy. Adapted from Ref. 25 with permission from American Chemical Society.

because fixed chemical crosslinks do not suppress them. The tension between the extended horizontal regions and the vertically compressed areas can then equilibrate to maximize entropy, resulting in the isotropic profile. CD/PEG SRNs exhibit isotropic patterns before and after stretching in good solvents but exhibit elliptic patterns in poor solvents like covalent gels (7.17b).

The segmental and monomer dynamics of polymer gels with controlled inhomogeneity have been studied under uniaxial deformation using quasi-elastic neutron scattering (QENS). To clarify the effect of the homogeneity of a network structure on the polymer dynamics in gels, homogeneous (homo-gel) and heterogeneous (hetero-gel) networks were prepared (Figure 7.18).[28] The homogenous gels (Figure 7.18a) were made from crosslinking N-hydroxy-succinimide

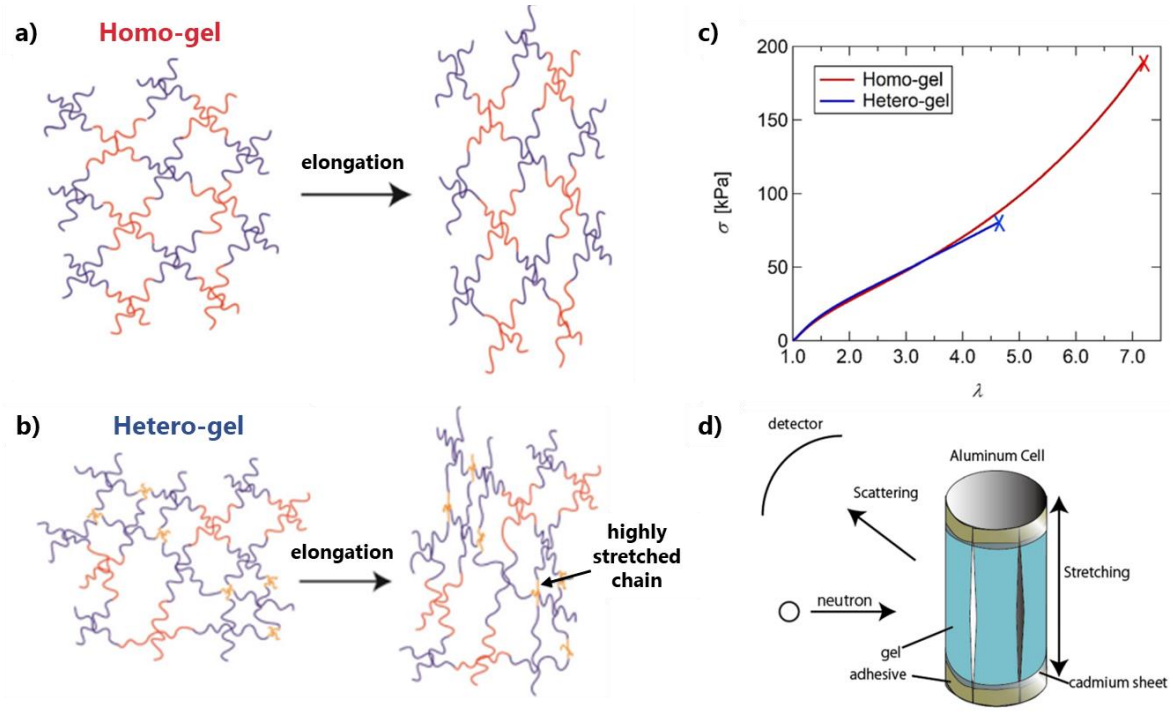

Figure 7.18. Homogeneous vs. heterogeneous polymer gels under elongation.[28] a) Homo-gels made from crosslinking N-hydroxy-succinimide (NHS)-terminated tetra-PEG (blue) and amino-terminated tetra-PEG (red) with the same total molecular weight. b) Hetero-gels made from the same NHS- and amino-terminated tetra-PEGs, and amino-terminated tetra-PEG with a smaller molecular weight (yellow). c) Stress-strain response of homo- (red) and hetero-gels (blue, showing a better response for the homo-gel. d) Schematic of the experimental setup for quasi-elastic neutron scattering (QENS) measurements of gels during stretching. Adapted from Ref. 28 with permission from Royal Society of Chemistry.

(NHS)-terminated tetra-PEG (blue) and amino-terminated tetra-PEG (red) with the same total molecular weight (20 kDa). The heterogeneous gels (Figure 7.18b) were made from the same NHS- and amino-terminated tetra-PEGs, and amino-terminated tetra-PEG with a smaller molecular weight (yellow). The strand length in the hetero-gel is not uniform like in the homo-gel, but bimodal, resulting in stresses concentrating on shorter strands under stretching with a lower strain at break (Figure 7.18c). Figure 7.18d shows a schematic of the experimental setup for QENS measurements performed with the incident neutron beam and scattering vector perpendicular to the stretching direction of the gels. The homo-gels only showed a broad quasi-elastic component, but the highly stretched strands in the hetero-gel resulted in a small elastic peak. This study suggests QENS could help detect stress concentrations in the SR-PCNs, which will be valuable for comparing failure mechanisms in the covalent vs. interlocked gels. Contrast matching would provide separation between the QENS of the network and the macrocycles in SR-PCNs **2.8**$_{\mathbf{X/YM}}$ vs. **2.8**$_{\mathbf{X/YD}}$. Inelastic methods such as spin echo would be required to capture the slower relaxations in the SR-PCN system.

Two-dimensional small-angle X-ray scattering (SAXS) studies performed on SRNs in water elude to the relaxation of conformational anisotropy upon uniaxial deformation.[27] Increasing the PEG concentration in SRNs enhances the interactions between PEG chains in the network, imparting tough hydrogels with rapid self-reinforcement.[29] SRN hydrogels (2% CD coverage; CD/PEG molar ratio = 8) were prepared with different PEG volume fractions: SR-0.18 with a lower PEG content and SR-0.38 with a higher PEG content. The WAXS and SAXS patterns for the SR-0.18 during a load-unloading cycle are provided in Figure 7.19a and SR-0.38 in Figure 7.19b. The WAXS profiles (Figure 7.19c) show the planar zigzag PEG (Figure 7.19d) that appears in both PEG networks. However, a new peak for the SR-0.38 suggests the formation of 7/2 helix

PEG (Figure 7.19e) at higher PEG content. Similar studies would elucidate information on the conformation of PEG chains during the deformation of SR-PCNs **2.8**$_{X/YM}$ vs. **2.8**$_{X/YD}$.

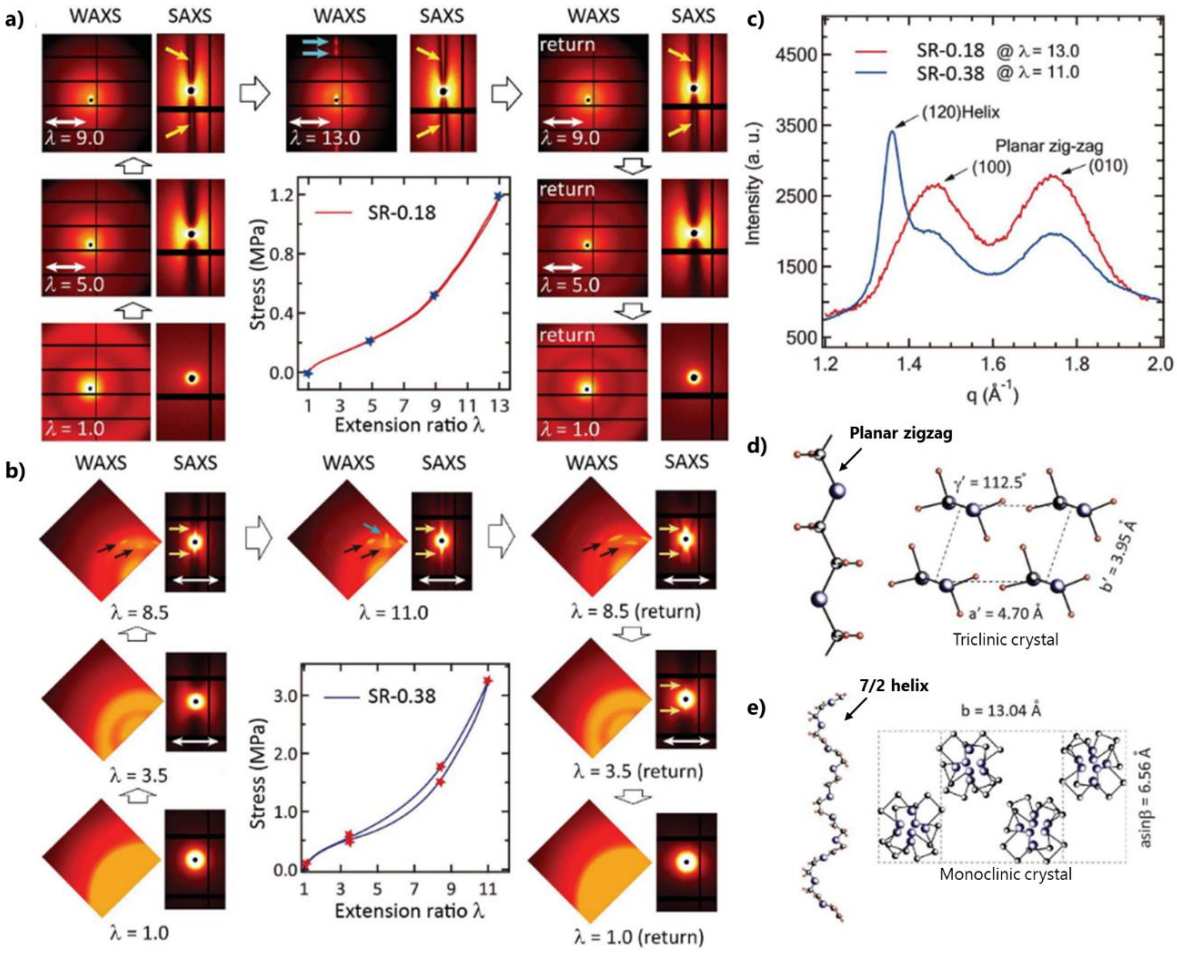

Figure 7.19. Structural transition of SRN hydrogels under cyclic loading.[29] WAXS and SAX patterns of a) SR-0.18 and b) SR-0.38 during a loading-unloading cycle (white arrows denote stretching direction). c) WAXS profiles of SRNs in the direction perpendicular to stretching. d) Structure of the planar zigzag PEG and its triclinic crystal. e) Structure of 7/2 helix PEG and its monoclinic crystal. Adapted from Ref. 29 with permission from The American Association for the Advancement of Science.

7.4 Conclusions

Copolymerization of pseudo[3]rotaxanes and other functional components offers a simple way to include doubly-threaded moieties into a network structure to dive deeper into the complex structure-property relationships identified in this new class of materials. Future studies should compare stress concentrations of covalent and SR-PCNs with controlled homogeneity, akin to the homo-gels in Figure 7.18a. Inhomogeneity in the current SR-PCNs increases stress concentrations in the network; however, the great advantage of the SR-PCN synthesis is the ability to tune the molecular weight of components to target networks with more homogeneity. Previous work on CD-SRNs has shown that the local segmental relaxations of the chain between the rings drive the frequency response and are related to the apparent molecular weight between mobile ring crosslinks.[30–34] Varying the mesh size distribution, defined as the linear distance between two adjacent crosslinks,[35,36] should affect solvent transport through the SR-PCN and the poroelastic rate of draining, respectively, as discussed in Chapters 2 and 3. The mesh size decreases as P3R **2.1:2.2$_2$:Zn(II)$_2$** increases because less tetra-PEG (**2.6**, 5.3 kg mol^{-1}) is added to the crosslinking reaction. The molecular weight difference between P3R and tetra-PEG **2.6** can account for the contour length between crosslinks. Adding linear PEG macromonomers to the current mixture would increase homogeneity and form regions with highly stretched chains like those seen in the hetero-gels (Figure 7.18b). A more straightforward approach would involve clicking two tetra-functional crosslinkers (i.e., P3R **2.1:2.2$_2$:Zn(II)$_2$** and tetra-PEG **2.6**) with similar molecular weights but different functionalities.

The ability to control every handle in the system, including deuteration, makes this system an infinitely better platform for the general study of SRNs. The SR-PCN system allows chemists to design fully interlocked doubly-threaded MIP networks with new components, including singly-

threaded rings (as discussed in Chapter 4), to tune elastomeric properties. Furthermore, the macrocycle synthesis allows control over the ring's size, conformation, and valency (Chapters 4 and 5) that should influence SR-PCN properties; for example, shrinking the ring size is expected to shift the high-frequency transition to a lower frequency, as the rings will take longer to move in the network. Maleimide click chemistry (explored in Chapters 5 and 6) offers a simple way to functionalize SR-PCNs to make dynamic MIP networks or click (singly- or doubly-threaded) rings together to form figure-of-eight crosslinks in the doubly-threaded network.

The SR-PCN system opens the door to future research into the mechanics and applications of networks comprised of doubly-threaded rings and has sparked the interest of several postdocs in the Rowan Group. Perhaps the most exciting future direction for fully interlocked doubly-threaded MIPs is formulating coatings for scratch-resistant and self-healing applications. SRNs are unique for the ability of movable ring crosslinks to slide along the polymer backbone, maintaining flexibility and elasticity upon damage and deformation, resulting in scratch-healing properties. However, because SRNs are highly flexible and elastic, coatings are typically modified with polycaprolactone, polyols, and isocyanates to lower the glass-transition temperature.[37] The NOAC polymerization of SR-PCNs was designed to be highly versatile so that different monomers can be added and the number of doubly-threaded (and singly-threaded) rings can be optimized to target the elasticity and toughness required for applications such as scratch-healing. Therefore, this straightforward synthetic approach will be a promising platform for understanding the structure-property relationships in SR-PCNs to design specific formulations for different applications.

7.5 Experimental

7.5.1 Materials and Methods

All chemicals were purchased from Sigma-Aldrich and used without further purification unless otherwise mentioned. Benzophenone imine was purchased from Oakwood Chemical. Zinc di[bis(trifluoromethylsulfonyl)imide] was purchased from Strem Chemicals and stored in a nitrogen desiccator. Sodium hydride, dry powder, was purchased from Sigma-Aldrich and stored in a nitrogen desiccator. 4-arm PEG-Alkyne (5.0 kg/mol) was purchased from Creative PEGWorks and characterized via ^{1}H-NMR and MALDI-TOF to verify the molecular weight. Solvents for chromatography were purchased from Fisher-Scientific. Deuterated solvents and nitromethane were purchased from ACROS Organics. Nitrile-oxide monomer **2.5**[38] and 2,6-bisbenzimidazolylpyridine ligands[39] were prepared following literature procedures. Tetrahydrofuran (THF) was dried over sodium and benzophenone. Dichloromethane was distilled over calcium hydride before use. Dimethylformamide (DMF) was dried with activated 4Å molecular sieves before use. All synthesized components were stored in a freezer at -8°C before use.

Matrix-Assisted Laser Desorption/Ionization Mass Spectrometry (MALDI-TOF MS) was measured by a Bruker Ultraflextreme MALDI-TOF-TOF spectrometer in linear (or reflectance) mode using dithranol or trans-2-[3-(4-tert-butylphenyl)-2-methyl-2-propenylidene]malononitrile (DCTB) as matrix and sodium trifluoroacetate or silver trifluoroacetate as ionizer (or no ionizer).

Room Temperature Nuclear Magnetic Resonance Spectroscopy was performed using a Bruker Ascend AVANCE III 500 MHz spectrometer, a Bruker AVANCE II+ 500 MHz spectrometer, or a Bruker DRX 400 MHz spectrometer at the University of Chicago NMR facilities. ^{1}H NMR spectra were referenced to the residual protonated solvent signal.

Thermogravimetric Analysis (TGA) was performed using a TA Instruments Discovery Thermogravimetric Analyzer in the Soft Matter Characterization Facility at the University of Chicago. Samples were tested under a nitrogen atmosphere using platinum pans. Tests were conducted using a 10°C/min ramp from 30°C to 700°C.

Differential Scanning Calorimetry (DSC) was performed using a TA Instruments Discovery 2500 Differential Scanning Calorimeter in the Soft Matter Characterization Facility at the University of Chicago. Dried gel samples were prepared in aluminum Tzero pans from TA Instruments and were sealed. Typical test conditions involved a heat-cool-heat procedure (200°C/-90°C/200°C) run at 10°C/min with a 5 min isotherm between each ramp.

7.5.2 Synthetic Procedures

7.5.2.1 Synthesis of ADMET polymer **7.3**

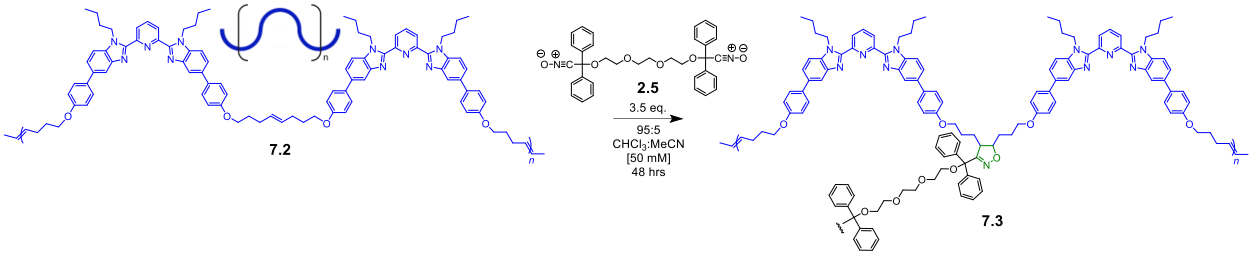

ADMET **7.2** (0.005 g, 1488 g/mol) and nitrile-oxide monomer **2.5** (0.00664 g, 3.5 equiv.) were added to a small vial with a stir bar. A solution of 5:95 (v/v) acetonitrile:chloroform (235 µL, 50mM w.r.t. monomer) was added, and the solution was left to stir at room temperature for ~48 hours. Crude **7.3** was dried under vacuum, and $CDCl_3$ was added to extract low molecular weight components into the soluble fraction for NMR analysis.

7.5.2.2 Synthesis of double-stopper core **7.9**

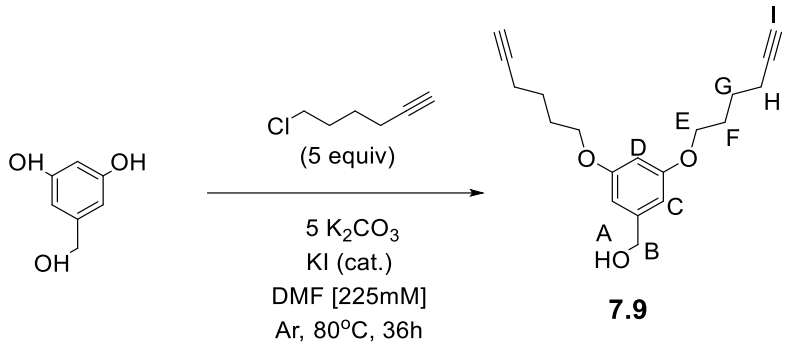

3,5-Dihydroxybenzyl alcohol (2.0 g, 14.3 mmol), K_2CO_3 (9.86 g, 71.4 mmol), and KI (catalytic amount) were added to an oven-dried 250 mL round bottom flask under argon. Dry DMF (60 mL) was injected, and the flask was placed into a heating block and heated to 80°C. Once the solution reached temperature, 6-chloro-1-hexyne (8.32 g, 8.65 mL, 71.4 mmol) was injected dropwise. After 36 hours, the reaction was cooled to room temperature, after which the solvent was removed, and the remaining residue was triturated with chloroform. After vacuum filtration, the filtrate was collected, and the solvent was removed under vacuum. The resulting material was purified using column chromatography (silica gel, hexanes to chloroform gradient) to yield **7.9** in 40% yield. ^{1}H NMR (400 MHz, $CDCl_3$) δ 6.50 (d, J = 2.2 Hz, 2H, C), 6.37 (t, J = 2.3 Hz, 1H, D), 4.62 (s, 2H, B), 3.97 (t, J = 6.2 Hz, 4H, E), 2.27 (td, J = 7.0, 2.7 Hz, 4H, H), 1.97 (t, J = 2.7 Hz, 2H, I), 1.94 – 1.85 (m, 4H, F), 1.76 – 1.67 (m, 4H, G), 1.64 (s, 1H, A).

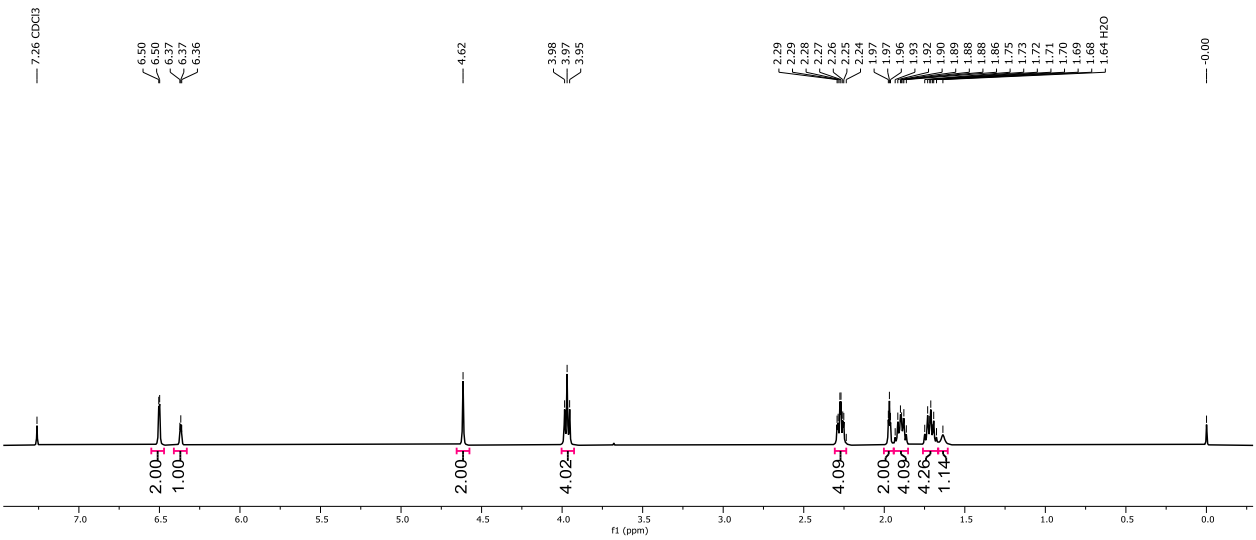

Figure 7.20. ^{1}H-NMR (400 MHz, 25°C, $CDCl_3$) of bis-alkyne double-stopper core **7.9**.

7.5.2.3 Synthesis of P3R prepolymer **7.14**

Nitrile-oxide monomer **2.5** (0.010 g, 0.0177 mmol) and 0.05 equivalent P3R **2.1:2.2$_2$:Zn(II)$_2$** (0.00355 g, 0.00089 mmol) were dissolved in 95/5 $CDCl_3$/CD_3CN at 50 mM (~350 µL) and added to an NMR tube. The sample was submitted to the NMR queue and set to acquire a full ^{1}H spectrum after 0.5, 1, 2, 3, 4, 8, 12, 22, 24, 30, 36, and 48 hours. For the control experiment, nitrile-oxide **2.5** (0.010 g, 0.0177 mmol) and 0.05 equivalent 4-arm PEG **2.6** (0.00443 g, 0.00089 mmol, 5.0 kg/mol) were dissolved in 95/5 $CDCl_3$/CD_3CN at 50 mM (~350 µL) and added to an NMR tube. The sample was submitted to the NMR queue and set to acquire a full ^{1}H spectrum after 0.5, 1, 2, 3, 4, 8, 12, 22, 24, 30, 36, and 48 hours.

7.5.2.4 Synthesis of SR-PCN **7.15**

Nitrile-oxide monomer **2.5** (0.010 g, 0.0177 mmol) and 0.15 equivalent P3R **2.1:2.2$_2$:Zn(II)$_2$** (0.0106 g, 0.00266 mmol) were dissolved in 250 µL 95/5 chloroform/acetonitrile and added to a vial with a stir bar. The mixture was capped, covered in parafilm, and left to stir for 24 hours at room temperature. The covalent PEG crosslinker **2.6** (0.0310 g, 0.0062 mmol, 5.0 kg/mol) was dissolved in ~100 µL 95/5 chloroform/acetonitrile and added to the vial with the

viscous prepolymer solution. The stir bar was removed, and the vial was recapped and covered in parafilm. The solution was left to gel for 48 hours at room temperature. Chloroform (1000 µL) was added to the vial containing **7.15** to dissolve low molecular weight products into the metallated soluble fraction. The solution was split into two separate vials, each containing 500 µL. A solution of TBAOH (2 µL, 1M in MeOH) was added to one of the vials to demetallate the sample, turning the yellow solution colorless.

7.5.2.5 Synthesis of Higher Ring Content SR-PCNs **7.19$_{X/Y}$**

The polymerization procedure from Chapter 2 was used to synthesize the SR-PCNs used in this Chapter: P3R **2.1:2.2$_2$:Zn(II)$_2$** (n_{P3R}, Table 7.1) and nitrile-oxide **2.5** (0.010 g, 0.0177 mmol) were dissolved in 95:5 $CHCl_3$:MeCN (~250 µL) and added to a glass shell vial with a stir bar and capped. The solution was left to stir at room temperature for 4 hours. During the first step, the ditopic nitrile-oxide monomer **2.5** (2.0 eq) reacts with terminal alkynes on **2.1:2.2$_2$:Zn(II)$_2$**, (Y

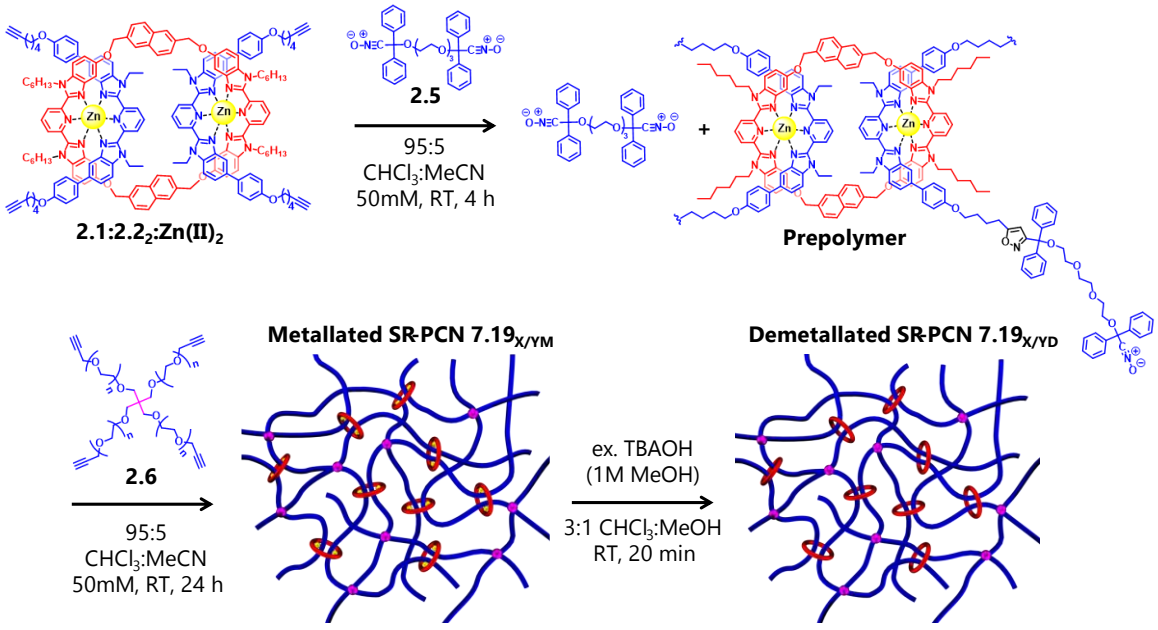

Figure 7.21. Nitrile-oxide/alkyne cycloaddition (NOAC) polymerization of **7.19$_{60/40M}$** and **7.19$_{50/50M}$** (Y = 0.4 and 0.5 mol%), and demetallation with a dilute solution of tetrabutylammonium hydroxide (TBAOH) to the demetallated doubly-threaded SR-PCNs **7.19$_{60/40D}$** and **7.19$_{50/50D}$**.

mol%) to form isoxazole prepolymers/oligomers in the presence of the excess monomer (Figure 7.21, top).

The 4-arm PEG-Alkyne **2.6** (M_n = 5 kgmol^{-1}, n_{PEG} mol) was dissolved in 95:5 $CHCl_3$:MeCN (~100 µL) and added to the vial. A viscous solution formed within minutes; the stir bar was removed, and then the vial was capped and left to gel at room temperature for ~48 hours. The gels dried in a fume hood overnight. The metallated SR-PCNs **7.19$_{60/40M}$** and **7.19$_{50/50M}$** were washed by submerged in a large beaker full of 200 mL of chloroform at 48°C on a hot plate. A watch glass was placed on top of the beaker, and the gels were left heating for 4 hours to ensure the complete extraction of low molecular weight components into the soluble fraction.

Table 7.1. Composition of covalent **2.7$_{GF}$** and metallated SR-PCN series **2.8$_{X/YM}$** and **7.19$_{X/YM}$**

Covalent/ SR-PCN	Nitrile-oxide monomer **2.5**	P3R **2.1:2.2$_2$:Zn(II)$_2$** n_{P3R} mol	4-arm PEG **2.6** n_{PEG} mol
2.7$_{96}$	0.010 g, 1.8E-05 mol	0	0.047 g, 8.9E-06 mol
2.8$_{90/10M}$	0.010 g, 1.8E-05 mol	0.0035 g, 8.9E-07 mol	0.042 g, 8.0E-06 mol
2.8$_{80/20M}$	0.010 g, 1.8E-05 mol	0.0071 g, 1.8E-06 mol	0.038 g, 7.1E-06 mol
2.8$_{70/30M}$	0.010 g, 1.8E-05 mol	0.011 g, 2.7E-06 mol	0.033 g, 6.2E-06 mol
7.19$_{60/40M}$	0.010 g, 1.8E-05 mol	0.014 g, 3.5E-06 mol	0.028 g, 5.3E-06 mol
7.19$_{50/50M}$	0.010 g, 1.8E-05 mol	0.018 g, 4.4E-06 mol	0.023 g, 4.4E-06 mol

7.5.2.5.1 Demetallation Procedure

To demetallate, the washed, metallated SR-PCNs **7.19$_{X/YM}$** were submerged in 35 mL of chloroform and 5 mL of methanol in a Teflon dish. 10 µL of tetrabutylammonium hydroxide solution (1M in MeOH) was added dropwise to demetallate the rings. After 20 minutes, the SR-PCNs were transferred to a second Teflon dish containing 40 mL of 50/50 chloroform/methanol for 2-3 hours, changing the solvent every 30 minutes (for a total of 6 washes). Then the gels were

submerged in a large beaker full of ~200 mL of chloroform at 48°C on a hot plate. A watch glass was placed on top of the beaker, and the gels were left heating for 4 hours to ensure the complete extraction of metal, salts, and any soluble fractions of the network.

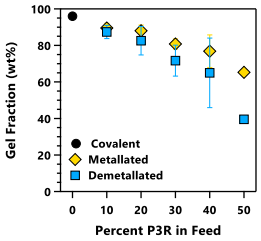

Figure 7.22. Gel fractions for the covalent gel **2.7**$_{96}$ (black circle), metallated SR-PCNs (**2.8**$_{90/10M}$, **2.8**$_{80/20M}$, **2.8**$_{70/30M}$, **7.19**$_{60/40M}$, and **7.19**$_{50/50M}$, yellow diamonds), and demetallated SR-PCNs (**2.8**$_{90/10D}$, **2.8**$_{80/20D}$, **2.8**$_{70/30D}$, **7.19**$_{60/40D}$, and **7.19**$_{50/50D}$, light blue squares) calculated from Equation 2.1.

7.5.3 Quantifying Ring Content

The final number of rings incorporated within the network after demetallation was determined from the molar ratio of a reference molecule (thymol), with a known structure and mass, to the macrocycle (MC) in the metallated and demetallated soluble fractions. The relationship between the number (moles) of MC in the soluble fraction and thymol is related to the integral of the diagnostic proton peak and the number of protons contributing to the peak, Equation 2.2:

$$X_{MC} \times \frac{N_{MC}}{I_{MC}} = X_{thymol} \times \frac{N_{thymol}}{I_{thymol}} \tag{2.2}$$

where X_{MC} is the number of moles of MC in the soluble fraction, X_{thymol} is the number of moles of thymol (known), I is the integrated area of the diagnostic proton peak, and N is the number of

protons contributing to the peak. X_{thymol} is known, the integrals are measured via quantitative ^{1}H-NMR (qNMR), and N corresponding to those integrals are known. The doublet on the macrocycle pyridine ring (N=4) at 8.08 ppm was used as the diagnostic signal for the soluble fractions. Thymol was chosen for its diagnostic singlet (N=1) at 6.58 ppm that does not overlap with any other signals in the soluble fractions (Figure 7.13).

Rearranging Equation 2.2 and incorporating the relationship between moles and mass ($X_{thymol} = W_{thymol}/MW_{thymol}$) provides a simple relationship between the mass of the standard and the moles of MC in the soluble fraction, Equation 2.3:

$$X_{MC} = \frac{1}{4}\left(\frac{I_{MC}}{I_{thymol}}\right) \times \frac{W_{thymol}}{MW_{thymol}} \tag{2.3}$$

The average number (moles) of macrocycle (X_{MC}) present in each metallated and demetallated soluble fraction is listed in Table 7.2 and plotted in Figure 7.23a. The metallated soluble fraction from washing the crude metallated gels, and the demetallated soluble fraction from washing the demetallated gels were used to calculate X_{MC} in each sol, i.e., $X_{MC,met}$ and $X_{MC,demet}$. Demetallating the metallated soluble fractions provided cleaner NMR spectra with more reliable MC integrations. To do this the metallated soluble fractions were dissolved in 3 mL of DCM, and 3 µL of TBAOH solution (1M in MeOH) was added to each sample. Each soluble fraction was washed with 15 mL of DI water and then the organic layer was dried under high vacuum. Each (metallated and demetallated) soluble fraction was dissolved in 600 µL of $CDCl_3$ and added to an NMR tube. An external standard was used to prevent molecular interactions with the soluble fractions. A thymol standard for quantitative NMR *Trace*CERT® (0.00050 g, 150.22 g/mol) was dissolved in 200 µL of $CDCl_3$ to make the reference solution that was added to a Wilmad® coaxial insert. The same coaxial insert was added to each NMR tube containing the (metallated or

demetallated) soluble fraction and the outside of the insert was wiped with isopropyl alcohol between samples to prevent contamination. The soluble fractions from three SR-PCN series were used to calculate the average I_{MC} for each X/Y. The integral of the thymol singlet (N=1) at 6.58 ppm was set to I_{thymol}=1, and the average integrals of the MC doublet (N=4) at 8.08 ppm (I_{MC}) for each soluble fraction are listed in Table 7.2.

The total number (moles) of rings that were washed out of the network ($X_{MC,total}$) is determined by adding $X_{MC,sol}$ in the metallated (i.e., $X_{MC,met}$) and demetallated (i.e., $X_{MC,met}$) soluble fractions, Equation 2.4:

$$X_{MC,total} = X_{MC,met} + X_{MC,demet} \tag{2.4}$$

The total percentage of MC lost from the network was calculated using $X_{MC,\text{total}}$ and the total number of rings added to the polymerization as P3R crosslinker (n_{P3R}), Equation 2.5:

$$\text{Total percent MC lost} = \frac{X_{MC,total}}{n_{P3R}} \times 100 \tag{2.5}$$

The percent of MC lost during demetallation was determined from $X_{MC,met}$ and $X_{MC,demet}$ using Equation 2.6:

$$\text{Percent MC lost during demetallation} = \frac{X_{MC,demet}}{n_{P3R} - X_{MC,met}} \times 100 \tag{2.6}$$

To better understand the sample, a number percent of possible MC crosslinks is calculated using Equation 2.7, plotted in Figure 7.23b, to provide a sense of how the sample compares to an ideal MC content, which assumes 100% incorporation based on the crosslinker feed ratio (plotted as a solid red line in Figure 7.23b for comparison).

$$\text{Percent MC Crosslinks} = \frac{n_{P3R} - X_{MC,total}}{n_{P3R} - X_{MC,total} + n_{PEG}} \times 100 \tag{2.7}$$

where n_{PEG} is the total number (moles) of 4-arm PEG-Alkyne crosslinker (**2.6**) added to the polymerization.

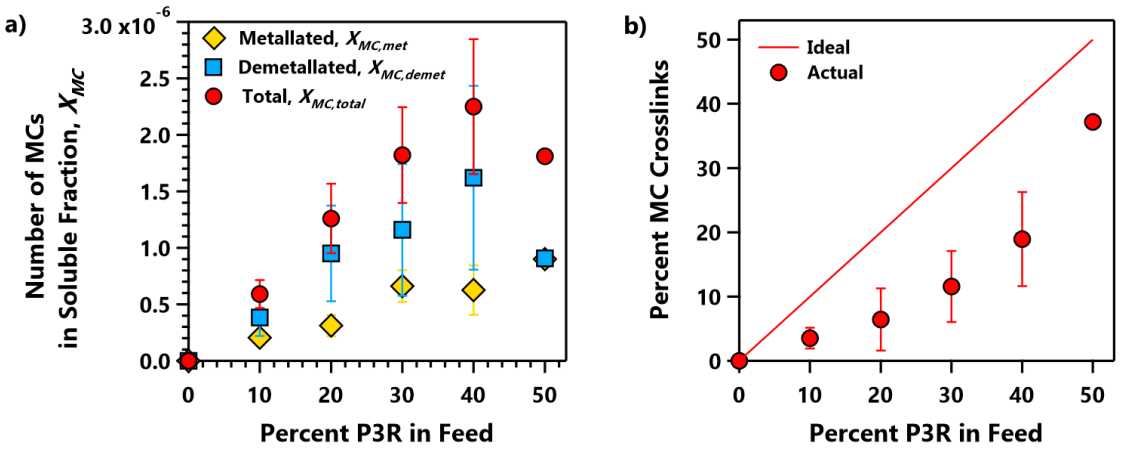

Figure 7.23. a) The average number (moles) of macrocycle (MC) in the metallated ($X_{MC,met}$, yellow diamonds) and demetallated ($X_{MC,demet}$, light blue squares) soluble fractions determined from qNMR experiments and Equation 2.3. The total number of MC in the soluble fraction ($X_{MC,total}$) is plotted in red (circles). The limited GF and the more considerable amount of P3R crosslinker required to synthesize **7.19**$_{50/50}$ limited the number of samples; however, the error increases with Y, and thus a large error is expected when Y reaches 50 mol%. b) The percent of MC crosslinks in the network, calculated from Equation 2.7, plotted against the percent of total crosslinker in the feed that is P3R (100 x [**2.1:2.2**$_2$**:Zn(II)**$_2$]/([**2.1:2.2**$_2$**:Zn(II)**$_2$] + [**2.6**])) content. The ideal percent of MC crosslinks (solid red line), assuming 100% incorporation based on the crosslinker feed ratio, is plotted for comparison.

Table 7.2. Quantitative NMR experiment parameters

SR-PCN	n_{P3R} (mol)	n_{PEG} (mol)	$I_{MC,met}$	$I_{MC,demet}$	$X_{MC,met}$ (mol)	$X_{MC,demet}$ (mol)	$X_{MC,total}$ (mol)
2.8$_{90/10}$	8.9E-07	8.0E-06	0.26	0.45	2.1E-07	3.9E-07	5.9E-07
2.8$_{80/20}$	1.8E-06	7.1E-06	0.40	1.13	3.1E-07	9.5E-07	1.3E-06
2.8$_{70/30}$	2.7E-06	6.2E-06	0.85	1.37	6.6E-07	1.2E-06	1.8E-06
7.19$_{60/40}$	3.5E-06	5.3E-06	0.80	1.89	6.3E-07	1.6E-06	2.3E-06
7.19$_{50/50}$	4.4E-06	4.4E-06	1.15	0.94	3.0E-07	9.1E-07	1.8E-06

7.5.4 Thermal Characterization

Thermal properties (Table 7.3) of the dry, SR-PCNs were extracted from the TGA curves in Figure 7.24 and the DSC thermograms in Figure 7.14. Glass transition temperature T_g was determined from the half-height midpoint of the thermal transition during the second heating cycle. The melting and crystallization temperatures T_m and T_c (°C) were determined from the peak maxima obtained during the second heating/cooling cycle, and the enthalpies of fusion ΔH_f (J/g) (defined as the melting enthalpy per gram) and crystallization ΔH_c were calculated from the peak areas. The final plateau of the TGA curve determined the residual mass percentage for each sample.

The degree of crystallinity (DC) for the dry, demetallated SR-PCNs was calculated from ΔH_f using Equation 2.8:

$$\text{DC}\ (\%) = \frac{\Delta H_f}{\Delta H_f^0} \times 100 \tag{2.8}$$

where ΔH_f is the enthalpy of fusion per gram of PEG in the network and ΔH_f^0 is the enthalpy of fusion of perfectly crystalline poly(ethylene oxide) that is calculated from T_m using Equation 2.9:[40]

$$\Delta H_f^0 = 178.6 + 0.629\, T_m - 2.93 \times 10^{-3}\, T_m^2 \tag{2.9}$$

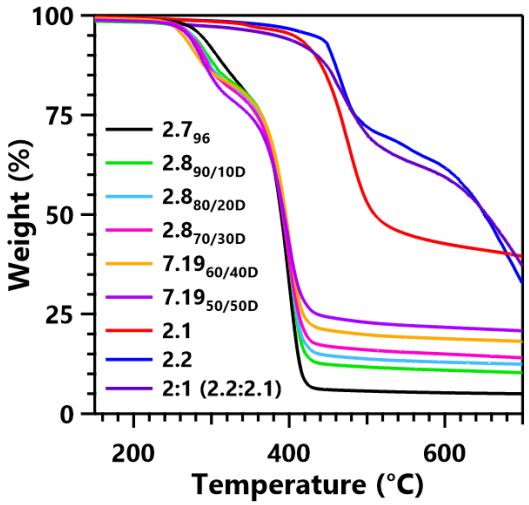

Figure 7.24. Thermogravimetric analysis (TGA) curves for dried covalent **2.7$_{96}$** and demetallated SR-PCNs **2.8$_{90/10D}$** (light green), **2.8$_{80/20D}$** (light blue), **2.8$_{70/30D}$** (pink), **7.19$_{60/40D}$** (orange), **7.19$_{50/50D}$** (purple), macrocycle **2.1** (red), thread **2.2** (blue), and 2:1 stoichiometric mixture of **2.2:2.1** (dark purple) (ramp rate = 10°C/min).

Table 7.3. Thermal properties of dried covalent **2.7$_{GF}$** and SR-PCN series **2.8$_{X/Y}$** and **7.19$_{X/Y}$**

Covalent/ SR-PCN	T_g (°C)	T_m (°C)	ΔH_f (J/g)	DC (%)	T_c (°C)	ΔH_c (J/g)	Residual Mass (%) (from TGA)
2.7$_{96}$	-48	26	61	32	6	54	5
2.8$_{90/10M}$	-41	25	54	28	-7	51	-
2.8$_{90/10D}$	-52	25	53	28	0	47	9
2.8$_{80/20M}$	-46	23	53	27	-29	35	-
2.8$_{80/20D}$	-46	24	51	26	-3	44	12
2.8$_{70/30M}$	-53	23	51	27	-30	18	-
2.8$_{70/30D}$	-50	24	50	26	-4	43	18
7.19$_{60/40M}$	-52	22	42	22	-33	15	-
7.19$_{60/40D}$	-52	21	41	22	-15	27	21
7.19$_{50/50M}$	-51	17	18	10	-22	11	-
7.19$_{50/50D}$	-50	17	31	16	-10*	22*	21

*cold crystallization temperature/enthalpy

7.6 References

(1) Hart, L. F.; Hertzog, J. E.; Rauscher, P. M.; Rawe, B. W.; Tranquilli, M. M.; Rowan, S. J. Material Properties and Applications of Mechanically Interlocked Polymers. *Nat. Rev. Mater.* **2021**, *6* (6), 508–530. https://doi.org/10.1038/s41578-021-00278-z.

(2) Zhang, K.; Lackey, M. A.; Cui, J.; Tew, G. N. Gels Based on Cyclic Polymers. *J. Am. Chem. Soc.* **2011**, *133* (11), 4140–4148. https://doi.org/10.1021/ja111391z.

(3) Oike, H.; Mouri, T.; Tezuka, Y. A Cyclic Macromonomer Designed for a Novel Polymer Network Architecture Having Both Covalent and Physical Linkages. *Macromolecules* **2001**, *34* (18), 6229–6234. https://doi.org/10.1021/ma010291b.

(4) Xing, H.; Li, Z.; Wu, Z. L.; Huang, F. Catenane Crosslinked Mechanically Adaptive Polymer Gel. *Macromol. Rapid Commun.* **2018**, *39* (1), 1–6. https://doi.org/10.1002/marc.201700361.

(5) Nosiglia, M. A.; Colley, N. D.; Danielson, M. K.; Palmquist, M. S.; Delawder, A. O.; Tran, S. L.; Harlan, G. H.; Barnes, J. C. Metalation/Demetalation as a Postgelation Strategy To Tune the Mechanical Properties of Catenane-Crosslinked Gels. *J. Am. Chem. Soc.* **2022**, *144* (22), 9990–9996. https://doi.org/10.1021/jacs.2c03166.

(6) Liu, G.; Rauscher, P. M.; Rawe, B. W.; Tranquilli, M. M.; Rowan, S. J. Polycatenanes: Synthesis, Characterization, and Physical Understanding. *Chem. Soc. Rev.* **2022**, *51* (12), 4928–4948. https://doi.org/10.1039/D2CS00256F.

(7) Raphaël, E.; Gay, C.; de Gennes, P.-G. Progressive Construction of an "Olympic" Gel. *J. Stat. Phys.* **1997**, *89* (1–2), 111–118. https://doi.org/10.1007/BF02770756.

(8) Vilgis, T. A.; Otto, M. Elasticity of Entangled Polymer Loops: Olympic Gels. *Phys. Rev. E* **1997**, *56* (2), R1314–R1317. https://doi.org/10.1103/PhysRevE.56.R1314.

(9) Fischer, J.; Lang, M.; Sommer, J.-U. The Formation and Structure of Olympic Gels. *J. Chem. Phys.* **2015**, *143* (24), 243114. https://doi.org/10.1063/1.4933228.

(10) Lang, M.; Fischer, J.; Werner, M.; Sommer, J.-U. Olympic Gels: Concatenation and Swelling. *Macromol. Symp.* **2015**, *358* (1), 140–147. https://doi.org/10.1002/masy.201500013.

(11) Hu, P.; Madsen, J.; Huang, Q.; Skov, A. L. Elastomers without Covalent Cross-Linking: Concatenated Rings Giving Rise to Elasticity. *ACS Macro Lett.* **2020**, *9* (10), 1458–1463. https://doi.org/10.1021/acsmacrolett.0c00635.

(12) Wu, Q.; Rauscher, P. M.; Lang, X. L.; Wojtecki, R. J.; de Pablo, J. J.; Hore, M. J. A.; Rowan, S. J. Poly[n]Catenanes: Synthesis of Molecular Interlocked Chains. *Science (80-.).* **2017**, *358* (6369), 1434–1439. https://doi.org/10.1126/science.aap7675.

(13) Tranquilli, M. M.; Wu, Q.; Rowan, S. J. Effect of Metallosupramolecular Polymer

Concentration on the Synthesis of Poly[n]Catenanes. *Chem. Sci.* **2021**, *12* (25), 8722–8730. https://doi.org/10.1039/d1sc02450g.

(14) Wu, Q.; Rauscher, P. M.; Lang, X.; Wojtecki, R. J.; De Pablo, J. J.; Hore, M. J. A. A.; Rowan, S. J.; Wu, Q.; De Pablo, J. J.; Wojtecki, R. J.; Rowan, S. J.; Rauscher, P. M. Poly[n]Catenanes: Synthesis of Molecular Interlocked Chains. *Science (80-.).* **2017**, *358* (6369), 1434–1439. https://doi.org/10.1126/science.aap7675.

(15) Hashimoto, T.; Maruoka, K. Recent Advances of Catalytic Asymmetric 1,3-Dipolar Cycloadditions. *Chem. Rev.* **2015**, *115* (11), 5366–5412. https://doi.org/10.1021/cr5007182.

(16) Kanemasa, S. Cornerstone Works for Catalytic 1,3-Dipolar Cycloaddition Reactions. *Heterocycles* **2010**, *82* (1), 87. https://doi.org/10.3987/REV-10-666.

(17) Umemoto, N.; Imayoshi, A.; Tsubaki, K. Development of Regioselective [2 + 3] Cycloaddition Reactions of Nitrile Oxides with Alkenes Using Intramolecular Reactions through Oxime Groups [1]. *Tetrahedron* **2022**, *120*, 132833. https://doi.org/10.1016/j.tet.2022.132833.

(18) Sogawa, H.; Monjiyama, S.; Wang, C.-G.; Tsutsuba, T.; Takata, T. New Synthetic Route to OH-Functionalized Nitrile N -Oxide and Polyfunctional Nitrile N -Oxides for Click Crosslinking and Decrosslinking of Natural Rubber. *Polym. Chem.* **2018**, *9* (34), 4382–4385. https://doi.org/10.1039/c8py00904j.

(19) Li, P.; Wang, X. Study on Nitrile Oxide for Low-Temperature Curing of Liquid Polybutadiene. *Materials (Basel).* **2022**, *15* (9), 3396. https://doi.org/10.3390/ma15093396.

(20) Hertzog, J. E.; Maddi, V. J.; Hart, L. F.; Rawe, B. W.; Rauscher, P. M.; Herbert, K. M.; Bruckner, E. P.; de Pablo, J. J.; Rowan, S. J. Metastable Doubly Threaded [3]Rotaxanes with a Large Macrocycle. *Chem. Sci.* **2022**, *00*, 1–12. https://doi.org/10.1039/d2sc01486f.

(21) Wojtecki, R. J.; Wu, Q.; Johnson, J. C.; Ray, D. G.; Korley, L. T. J.; Rowan, S. J. Optimizing the Formation of 2,6-Bis(N-Alkyl-Benzimidazolyl)Pyridine-Containing [3]Catenates through Component Design. *Chem. Sci.* **2013**, *4* (12), 4440. https://doi.org/10.1039/c3sc52082j.

(22) Karino, T.; Shibayama, M.; Okumura, Y.; Ito, K. SANS Study on Pulley Effect of Slide-Ring Gel. *Phys. B Condens. Matter* **2006**, *385–386*, 807–809. https://doi.org/10.1016/j.physb.2006.06.095.

(23) Karino, T.; Okumura, Y.; Zhao, C.; Kataoka, T.; Ito, K.; Shibayama, M. SANS Studies on Deformation Mechanism of Slide-Ring Gel. *Macromolecules* **2005**, *38* (14), 6161–6167. https://doi.org/10.1021/ma050624v.

(24) Karino, T.; Okumura, Y.; Ito, K.; Shibayama, M. SANS Studies on Spatial Inhomogeneities of Slide-Ring Gels. *Macromolecules* **2004**, *37* (16), 6177–6182. https://doi.org/10.1021/ma049598b.

(25) Shinohara, Y.; Kayashima, K.; Okumura, Y.; Zhao, C.; Ito, K.; Amemiya, Y. Small-Angle X-Ray Scattering Study of the Pulley Effect of Slide-Ring Gels. *Macromolecules* **2006**, *39* (21), 7386–7391. https://doi.org/10.1021/ma061037s.

(26) Mayumi, K.; Ito, K. Structure and Dynamics of Polyrotaxane and Slide-Ring Materials. *Polymer (Guildf).* **2010**, *51* (4), 959–967. https://doi.org/10.1016/j.polymer.2009.12.019.

(27) Ito, K. Novel Entropic Elasticity of Polymeric Materials: Why Is Slide-Ring Gel so Soft. *Polym. J.* **2012**, *44* (1), 38–41. https://doi.org/10.1038/pj.2011.85.

(28) Aomura, K.; Yasuda, Y.; Yamada, T.; Sakai, T.; Mayumi, K. Quasi-Elastic Neutron Scattering Study on Dynamics of Polymer Gels with Controlled Inhomogeneity under Uniaxial Deformation. *Soft Matter* **2023**, *19* (1), 147–152. https://doi.org/10.1039/D2SM00784C.

(29) Liu, C.; Morimoto, N.; Jiang, L.; Kawahara, S.; Noritomi, T.; Yokoyama, H.; Mayumi, K.; Ito, K. Tough Hydrogels with Rapid Self-Reinforcement. *Science (80-.).* **2021**, *372* (6546), 1078–1081. https://doi.org/10.1126/science.aaz6694.

(30) Fleury, G.; Schlatter, G.; Brochon, C.; Travelet, C.; Lapp, A.; Lindner, P.; Hadziioannou, G. Topological Polymer Networks with Sliding Cross-Link Points: The "Sliding Gels". Relationship between Their Molecular Structure and the Viscoelastic as Well as the Swelling Properties. *Macromolecules* **2007**, *40* (3), 535–543. https://doi.org/10.1021/ma0605043.

(31) Kato, K.; Ito, K. Dynamic Transition between Rubber and Sliding States Attributed to Slidable Cross-Links. *Soft Matter* **2011**, *7* (19), 8737. https://doi.org/10.1039/c1sm06212c.

(32) Kato, K.; Yasuda, T.; Ito, K. Viscoelastic Properties of Slide-Ring Gels Reflecting Sliding Dynamics of Partial Chains and Entropy of Ring Components. *Macromolecules* **2013**, *46* (1), 310–316. https://doi.org/10.1021/ma3021135.

(33) Fleury, G.; Schlatter, G.; Brochon, C.; Hadziioannou, G. Unveiling the Sliding Motion in Topological Networks: Influence of the Swelling Solvent on the Relaxation Dynamics. *Adv. Mater.* **2006**, *18* (21), 2847–2851. https://doi.org/10.1002/adma.200600107.

(34) Kato, K.; Karube, K.; Nakamura, N.; Ito, K. The Effect of Ring Size on the Mechanical Relaxation Dynamics of Polyrotaxane Gels. *Polym. Chem.* **2015**, *6* (12), 2241–2248. https://doi.org/10.1039/C4PY01644K.

(35) Cuccia, N. L.; Pothineni, S.; Wu, B.; Méndez Harper, J.; Burton, J. C. Pore-Size Dependence and Slow Relaxation of Hydrogel Friction on Smooth Surfaces. *Proc. Natl. Acad. Sci.* **2020**, *117* (21), 11247–11256. https://doi.org/10.1073/pnas.1922364117.

(36) Peppas, N. A.; Bures, P.; Leobandung, W.; Ichikawa, H. Hydrogels in Pharmaceutical Formulations. *Eur. J. Pharm. Biopharm.* **2000**, *50* (1), 27–46. https://doi.org/10.1016/S0939-6411(00)00090-4.

(37) Noda, Y.; Hayashi, Y.; Ito, K. From Topological Gels to Slide-ring Materials. *J. Appl. Polym. Sci.* **2014**, *131* (15), app.40509. https://doi.org/10.1002/app.40509.

(38) Tsutsuba, T.; Sogawa, H.; Kuwata, S.; Takata, T. Kinetically Stabilized Aliphatic Nitrile *N* -Oxides as Click Agents: Synthesis, Structure, and Reactivity. *Chem. Lett.* **2017**, *46* (3), 315–318. https://doi.org/10.1246/cl.161098.

(39) McKenzie, B. M.; Miller, A. K.; Wojtecki, R. J.; Johnson, J. C.; Burke, K. A.; Tzeng, K. A.; Mather, P. T.; Rowan, S. J. Improved Synthesis of Functionalized Mesogenic 2,6-Bisbenzimidazolylpyridine Ligands. *Tetrahedron* **2008**, *64* (36), 8488–8495. https://doi.org/10.1016/j.tet.2008.05.075.

(40) Domszy, R. C.; Mobbs, R. H.; Leung, Y. K.; Heatley, F.; Booth, C. Crystallinity and Fusion of Low Molecular Weight α,ω-Alkoxy-Poly (Ethylene Oxide): Octadecoxy to Triacontanoxy End-Groups. *Polymer (Guildf).* **1979**, *20* (10), 1204–1214. https://doi.org/10.1016/0032-3861(79)90144-7.